Dynamics and Energetics of Electron Transfer Across Microelectrode/Monolayer Interfaces

Joseph P. O'Kelly B.Sc.(Hons.)

A Thesis presented at Dublin City University
for the degree of Doctor in Philosophy

under the supervision of
Dr Robert J. Forster

School of Chemical Sciences
Dublin City University

December 1998

This thesis is dedicated to my parents

I hereby certify that this material, which I now submit for the assessment on the programme of study leading to the award of Doctor in Philosophy is entirely my own work and has not been taken from the work of others save to the extent that such work has been cited and acknowledged within the text of my work.

Signed: Joseph O'Kelly ID No.: 94970343

Date: 26-1-99

Acknowledgements

First and foremost, I wish to extent my deep and sincere gratitude to my supervisor Dr Robert Forster for his help, guidance, advice, intuitive discussions, and attention to detail throughout the course of this work. Thanks for everything. I also wish to thank the academic staff in DCU and the technical staff particularly Veronica, Mick, Maurice, Damien, Ann, and everyone else thanks for your assistance throughout.

Thanks to the old timers who were around when I started in DCU and made me feel welcome and at home; Tom, Teresa, Noel, Frances, Mikey, Rachel, Suzanne, Siobhan, Mary, Dave and all the rest. And to the newer recruits; Luke, Bronagh, Christine, Stefano, Mike, Ben and all the rest.

To the RFG; Dominic, Conor, Tim, Richard, Nick, Aoife and the others in WG30, Paddy and Darren.

Thanks also to the lads in 106 Iveragh Road, especially Luke and Conor, who looked after me so well, dragging me down to the pub when all I wanted to do was work!!

Also, to my colleagues in the NMRC during the writing of this thesis, especially Karen for her support and good humour.

To the lads on the hurling teams in Commercials and DCU; I wouldn't have kept sane without you.

To my family especially mum and dad, thanks for everything, for supporting me and putting up with me.

Finally, thanks to Maura for your love, patience, and understanding.

Abstract

Dynamics and Energetics of Electron Transfer Across Microelectrode/Monolayer Interfaces

An overview of the literature in relation to the thermodynamics and kinetics of electron transfer across electrode/monolayer interfaces, microelectrodes, modified electrodes - in particular self-assembled monolayers of transition metal complexes and anthraquinones on various electrodes, and the background theory into the various electrochemical techniques used, is presented in Chapter 1.

Various metal complexes have been designed to form monolayers suitable for investigations into heterogeneous electron transfer across electrode/monolayer interfaces. These complexes include $[Os(bpy)_2Cl_2]$, $[Os(bpy)_2(p3p)_2]^{2+}$, and $QCat^{2-}$Ru-1,2 where bpy is dipyridyl, p3p is trimethylenedipyridine, and QCat is alizarin (1,2-dihydroxy-9,10-anthraquinone). Characterization of these complexes using HPLC, CV, UV-vis, NMR and CHN is described in Chapter 2.

Fabrication of platinum, gold, and carbon fibre microelectrodes and their characterization is illustrated in Chapter 3.

The adsorption characteristics and general electrochemistry of Anthraquinone-2,7-disulphonate adsorbed onto mercury electrodes is described in Chapter 4. The electrochemical response of these monolayers is examined as a function of solution pH. The dependence of the surface coverage of 2,7-AQDS on its bulk concentration is studied and an adsorption isotherm fitted. By measuring the potential dependence of C_{dl} as the bulk concentration of 2,7-AQDS is systematically varied, an insight into the potential dependence of the free energy of adsorption, ΔG_{ads}^{*}, has been obtained.

Chapter 5 describes monolayers containing the Os^{2+}/Os^{3+} redox couple adsorbed onto Pt and Au microelectrodes. Adsorption and desorption was examined as were the heterogeneous electron transfer rate constants. Reaction entropies and enthalpies were also determined. Results indicate that adsorption/desorption characteristics differ with substrate, that heterogeneous electron transfer can be described using Marcus theory, and that the rate of electron transfer is pH dependent.

The final experimental chapter describes the electrochemistry of solution phase and surface confined $QCat^{2-}$Ru-1,2. Diffusion coefficients, transfer coefficients and rate constants were determined for the solution phase species at Pt and Hg electrodes. Monolayers of the complex were adsorbed onto carbon fibre microelectrodes and the reaction entropy, enthalpy, and rate constants probed.

Contents

Chapter 1

Review of Microelectrodes and Electrode/Monolayer Interfaces

1.1 Introduction

Many important and interesting processes occur at the electrode-solution interface. Some of these processes include corrosion of metals, charging of batteries, electroplating of metals, and the operation of electroanalytical sensors. Scientists have long been interested in electrochemical interfaces because of their importance in generating and storing electrical energy and for synthesis. Therefore, a major research focus in modern electrochemistry involves deliberately modifying the electrode-solution interface. The objective is to immobilise, in a rational fashion, a chemical with known and desired properties, on the electrode surface so that the electrode will then possess the chemical, electrochemical, optical, and other properties of the immobilised species.[1] In order to achieve this objective, the electrode is coated with a thin film of material. This material can vary dramatically from metal oxides and metal deposits to polymers, enzymes, and inorganic or organic materials.

Two methods of deposition are commonly used. First, Langmuir-Blodgett in which the molecules are spread on an air-water interface, compressed and transferred to a solid substrate. Second, spontaneous adsorption or self-assembly onto the surface of an electrode of molecules in solution. Structurally well defined films on solid surfaces allow experimentalists to simplify and model a large variety of interfacial phenomena that are often difficult to study at bare electrodes. Well ordered films offer the possibility of precise control of spacing and orientation on a molecular level, a feature of current interest in electron transfer reactions.[2,3] If it is assumed that the local microenvironment at the electrode surface can be controlled, then the sensitivity and/or specificity of electrode reactions can be influenced. This control may provide fundamental information on the mechanisms of interfacial electron transfer and of electron and ion transport in thin films,[2,3] as well as provide advantageous information for electroanalytical chemistry.[4,5]

Experimental progress has been accelerated by recent advances in the technology of surface characterisation, including the emergence of various surface

sensitive techniques based upon spectroscopy, diffraction of electrons and protons, and electrochemistry. Virtually any combination of substrate and adsorbate can now be studied. These advances in experimental capabilities, instrumentation, and electrode dimensions have allowed electrochemical experiments to be carried out on the nanosecond timescale.[2,3] Therefore, studies of electrode-solution interfaces in which the role of structure in electrochemical behaviour can now be evaluated. Recent work has focussed on surface and adsorbed layer structure,[6] elemental composition, purity, stoichiometry,[7] packing density,[7] molecular characteristics,[8] surface chemical bonding,[9,10] surface layer chemical stability,[11] electrochemical reactivity and mechanistic aspects of heterogeneous electron transfer.[12,13] Surface electrochemical research is contributing to progress in the interfacial sciences. Studies of the electrical double layer are guiding the development of interfacial theory and have stimulated interest in the role of the electrical double layer in electrode kinetics. Intriguing facts concerning the electrochemistry of solvents, ions, solutes, and the chemisorption of organic molecules have been revealed.[7,14]

Many research groups have concentrated on the fundamental aspect of heterogeneous electron transfer in order to try and elucidate those factors that control electron transfer. In order to do this, redox active probes are employed. One of the first publications to demonstrate the modification of an electrode surface with a redox active moiety was by Lane and Hubbard.[15] The now popular technique of self-assembly is employed by numerous groups in order to provide redox active films. These films provide a high degree of structural order that can be manipulated to provide films of various thickness, densities and compositions.

Thin films of a species which are only one layer thick, or *monolayers*, were the first form of modified electrode to be studied.[16] However, due to problems of instability these systems proved unpopular and polymer modified electrodes soon gained acceptance as the interface of choice to study issues such as heterogeneous electron transfer. In recent times, the use of monolayers in the modification of electrodes for the study of interfacial processes has again become popular due to new immobilisation strategies. Alkanethiol monolayers are probably the most widely

studied electrode/monolayer interface due to their stability on gold, their high degree of organisation, and their potential application as the building blocks for novel microstructures. Examples of molecular absorption that have received attention are;[16] electroactive organic compounds, adsorbed putative electrochemical intermediates, anionic and cationic surfactants, non-aqueous solvents, surface chemical modification agents, typically alkenes, alkynes and aromatics, and various hydrocarbons having chemisorbable substituents.[14,17]

This chapter has three major objectives. Firstly, to review the work that has been carried out on the modification of electrodes with redox active monolayers namely, inorganic transition metal complexes; and organic molecules, for the purpose of investigating interfacial processes. Secondly, to illustrate why the development of microelectrodes has aided the explosion of research into interfacial processes. Thirdly, it is hoped that an insight into the electrochemical techniques that have been employed to study the electrode/monolayer interface in the course of this work is presented.

1.2 The Electrical Double Layer

1.2.1 Structure and Thermodynamics of the Electrode-Solution Interface.

The electrode-solution interface has been shown experimentally to behave like a capacitor with charges of equal magnitude and opposite sign on the electrode and solution side of the interface. Whether the charge on the electrode is positive or negative with respect to the solution depends on the potential across the interface and the composition of the solution. The whole array of charged species and oriented dipoles that exist at the electrode-solution interface is called the *electrical double layer*.[18,19,20] Here, the modern day interpretation of the structure and thermodynamics of the double layer is presented.

When a potential is applied across the electrode-solution interface a current, known as the charging or *capacitive* current, flows until the required charge has built up at the interface to satisfy Equation 1:

$$\frac{q}{E} = C \qquad (1)$$

where q is the charge on the capacitor, E is the potential across the capacitor, and C is the capacitance. It is only when this charge has been realised that the desired electrode reaction can take place. A *Faradaic* current then flows which is due to the reaction. The double layer is typically less than 1000 Å and its capacitance depends on the structure of this very thin region. The double layer capacitance also depends on the potential, the composition of the solution, the solvent, and the electrode material.[18] Therefore, probing the double layer capacitance gives an insight into the change in interfacial charge distribution that accompanies monolayer formation and the relative perfection of monolayers attached to the electrode surface.

The currently accepted model of the double layer region owes its existence to the models presented in a number of earlier works.[21,22,23,24,25,26] The modern day model describes an interfacial region whose structure depends on the applied potential, the electrolytic solution, and the electrode. As shown in Figure 1, three regions exist; the electrode layer, the compact layer, and the diffuse layer. The electrode layer is homogeneous, and its excess charge resides in a thin two-dimensional layer at the electrode surface neighbouring the solution. The compact layer consists of a thin region next to the electrode surface. This layer is only one or two molecular diameters in thickness and contains solvent molecules and sometimes a fractional monolayer of neutral molecules or specifically adsorbed ions. These specifically adsorbed ions are usually anions, but some evidence suggests that some cations (e.g., caesium) may also be specifically adsorbed.[20] Specifically adsorbed ions are generally considered to be unsolvated, especially in the direction of the electrode and the locus of the electrical centres of the adsorbed ions is called the Inner Helmholtz Plane (IHP) which is at a distance x_1. The adsorption forces are short range, although the detailed nature of these forces has not yet been completely resolved. The total charge density ($\mu C\ cm^{-2}$) from specifically adsorbed ions in this inner layer is σ^i.

The diffuse layer consists of the region between the bulk solution and the plane of nearest approach for solvated ions. Solvated ions can only approach the electrode to a distance x_2; the locus of centres of these nearest solvated ions is called the outer Helmholtz plane (OHP). The interaction of these non-specifically adsorbed ions with the electrode involves long range electrostatic forces. Because of thermal motion, the ions in diffuse layer are distributed in a three dimensional region which can be regarded as the ionic atmosphere of the electrode. The charge density in the diffuse layer is σ^d, and while the diffuse layer is independent of the chemical nature of the ion, its thickness depends on the concentration of the ion as the charge on the solution and electrode sides of the double layer must be balanced;

$$\sigma^S = \sigma^i + \sigma^d = -\sigma^M \qquad (2)$$

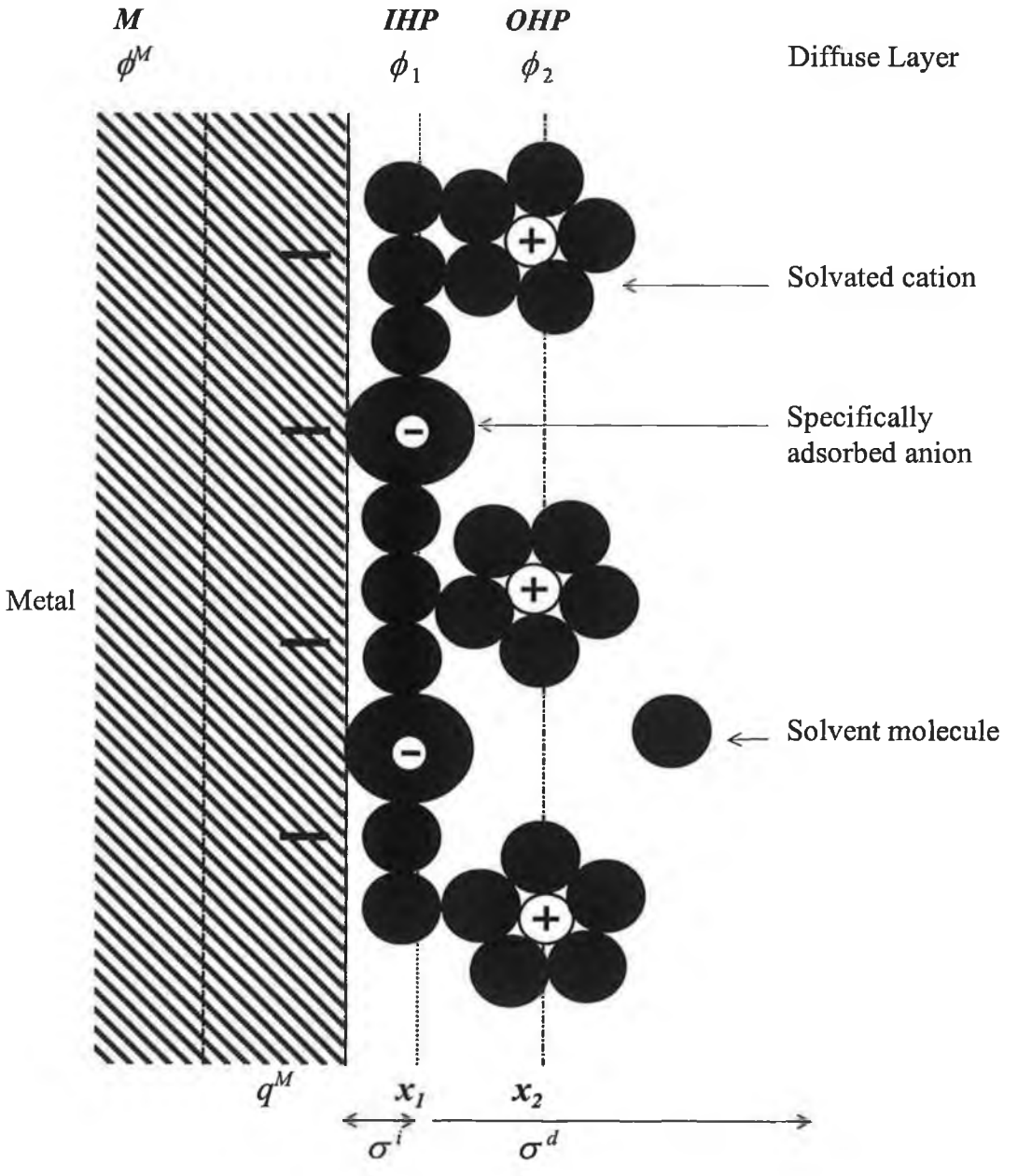

Figure 1 The electrode-solution, double layer region.

where σ^S is the total excess charge density on the solution side of the double layer and σ^M is the total excess charge density on the electrode side of the double layer.

In mathematical terms the double layer can be represented as two capacitors in series, representing the compact and diffuse layer capacitance, C_H and C_D, respectively:

$$\frac{1}{C_{dl}} = \frac{1}{C_H} + \frac{1}{C_D} \tag{3}$$

where C_{dl} is the total differential capacitance which is the derivative of the curve of σ^M vs. potential (E) and whose minimum value occurs at the potential of zero charge (PZC).† C_{dl} can be measured by making a small change in potential, thus causing a small change in charge density. The differential capacitance is a more useful quantity than the integral capacitance, C_i, which is the average of C_{dl} over the potential range PZC to E. The value of C_H is typically independent of applied potential, but C_D varies in a V-shaped fashion as shown in Figure 2. C_{dl} shows complicated behaviour and is dominated by the smaller of the two components because of the reciprocal nature of Equation 3. In low electrolyte concentration solutions (< 0.1 M), a V-shaped dependence of C_{dl} is observed near PZC. This V-shaped minimum in capacitance decreases with decreasing electrolyte concentration. Consequently, the diffuse layer contribution to C_{dl} only becomes apparent in dilute solutions. In higher electrolyte concentrations (> 0.1 M), the diffuse layer becomes so large that the contribution from C_D to C_{dl} becomes negligible and only the potential independent contribution from C_H is seen.

† The PZC is the potential at which no excess charge exists on the electrode surface i.e. E = PZC = 0.

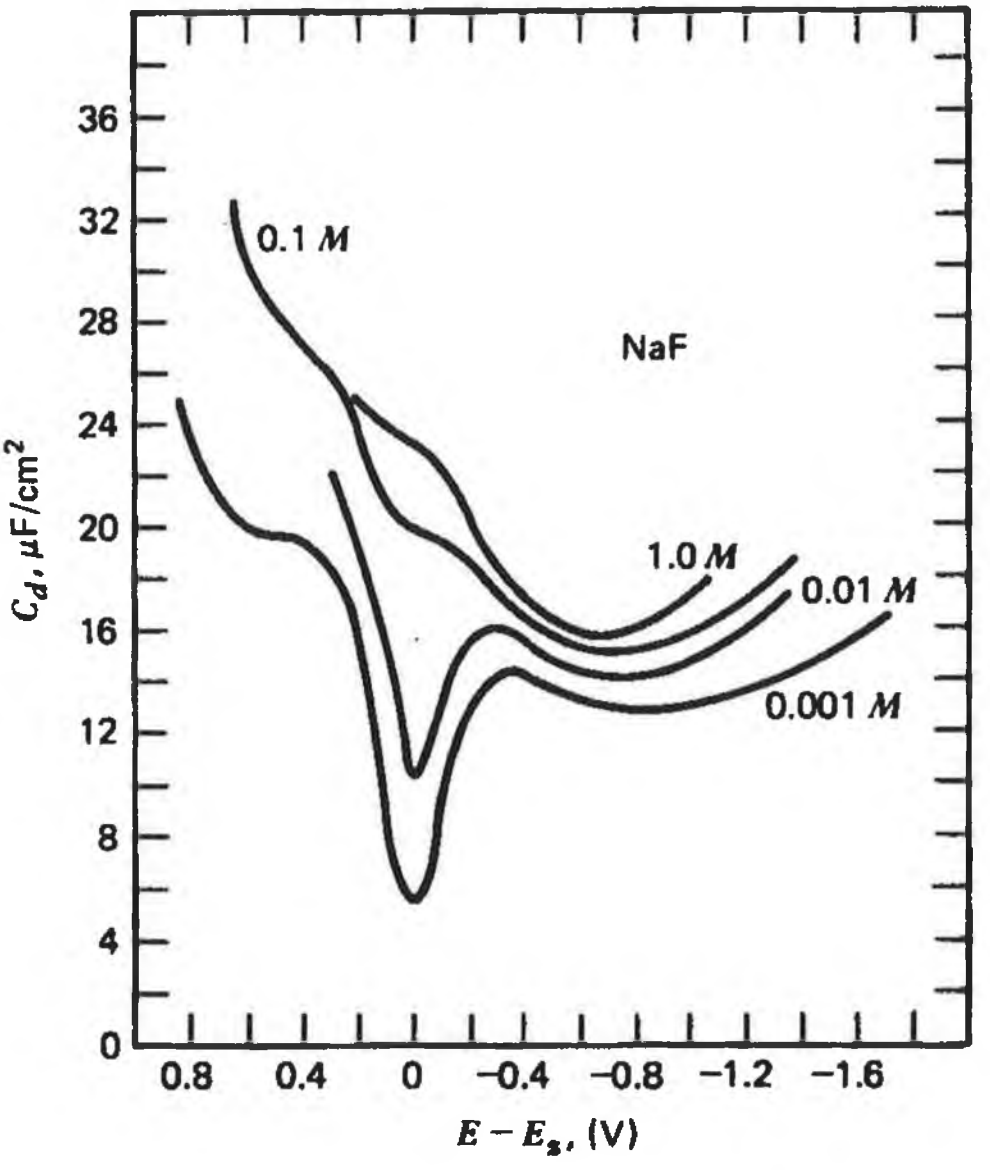

Figure 2 Differential capacitance versus potential for sodium fluoride solutions in contact with mercury.

1.2.2 Specific Adsorption

Adsorption is the formation of some type of bond between the adsorbate and the electrode surface. The interaction may be merely electrostatic (e.g., the adsorption of cations or anions on a surface of opposite charge) or charge-dipole in nature (e.g., the adsorption of amines, thiourea, or benzene) or due to the formation of a covalent bond. Moreover, one sees great variations in the strength of the bonding and the reversibility of the adsorption process. Specific interactions are very short range in nature and specifically adsorbed species are tightly bound to the electrode surface, normally unsolvated, and their locus in at the inner Helmholtz plane. Electrode reactions are most strongly affected when the adsorbate is the electroactive species, a reaction intermediate, or the product, but the adsorption of species apparently not directly involved in the electrode process can also change the rate of electron transfer.

Figure 3 Specific adsorption of molecules onto an electrode surface.

The extent of adsorption is usually expressed as the surface coverage, Γ, i.e., the fraction of the surface covered by adsorbate. The surface coverage by an adsorbate is related to its concentration in solution by an isotherm. There are several isotherms that differ in the extent and method of taking into account lateral interactions between adjacent adsorbed species. The Langmuir isotherm assumes

that the free energy of adsorption is independent of coverage, while the Frumkin isotherm assumes that the free energy of adsorption increases linearly with coverage. Isotherms are discussed at length in many articles[18,20,27] and shall be discussed in greater detail in Chapter 3.

Adsorption must be considered as a competition between all species, including solvent, in the system for sites on the electrode surface. Hence, Γ may depend on the solvent, electrolyte, adsorbate structure and concentration and the concentration of any other species in the system as well as the nature of the electrode. Moreover, the surface coverage will change, sometimes sharply, with electrode potential. This change arises because at each potential the electrode will have a characteristic surface charge and this charge will lead to the organisation of ions within the molecular dimensions of the surface, i.e., the formation a double layer. If the electrode is positively charged it will promote adsorption of anions, while a negatively charged surface will enhance cation adsorption. In addition, the charge on the electrode can interact with dipoles in solution leading to their adsorption and orientation at the surface. Neutral molecule adsorption occurs strongly where competition from charged species is at a minimum, when the electrode is uncharged, i.e., at the PZC.

The structure of the monolayers can be controlled with a high degree of precision, particularly in the plane perpendicular to the electrode surface. The thickness of the self assembled monolayer, and the position of functional groups can be controlled to approximately 1 Å in favourable cases (the incremental distance of adding one methylene group). By working with phase separated mixed self-assembled monolayers, one can generate disordered regions of controllable size, and the average composition of the monolayer can be controlled.

Because the thickness of self-assembled monolayers can be controlled with high precision, and electrochemically active functional groups can be introduced, they have been shown to be useful substrates for studies of mechanisms of electron transport and tunnelling.[28,29,30] Also, the amount of the electrode covered by a self-

assembled monolayer can be controlled, by varying the composition of the deposition solution and the deposition times, thus enabling studies of molecular orientation dependence on adsorption to be carried out.[14]

1.2.3 Recent literature on Interfacial Processes

Over the past number of decades, a number of theories have been developed describing electron transfer between an electrode and a freely diffusing species in a solution into which the electrode has been immersed. Recently, several articles describing the processes occurring at the double layer when an electrode is modified with a thin film have been presented.[31,32,33,34,35,36,37,38,39,40] De Levie has discussed the double layer structure of condensed two dimensional films. He presents a dynamic double layer unlike the static double layer of early models.[31] Capacitance measurements have been used to examine the growth of monolayers from a nucleus to a full monolayer. The film capacitance is typically independent of the nature and concentration of the electrolyte used suggesting that the film may not contain electrolyte ions.

A model describing the potential distribution across the metal/monolayer interface has been presented.[32] The traditional Frumkin correction for the effect of potential difference driving an electrode reaction, is given by Equation 4:[19]

$$k^{o} = k^{o}_{true} exp\left[\frac{(\alpha n - z)F\phi_2}{RT}\right] \qquad (4)$$

where k^{o} is the experimental rate constant, k^{o}_{true} is the true rate constant, α is the transfer coefficient, z is the ionic charge, ϕ_2 is the potential at the OHP, F is Faraday's constant, R is the gas constant and T is the absolute temperature. This model does not consider molecularly structured interfaces where ionic sites are often incorporated into the interface and where redox sites can change the charge distribution to a significant extent as they undergo electron transfer.

Figure 4 shows an irreversibly adsorbed electroactive film in contact with an electrolytic solution. White and co-workers have developed an analytical expression which describes the interfacial potential distribution, a consideration which has been absent from previous models of the interface which attempted to explain the non-ideal voltammetry often observed for surface confined species. This model describes the case of an electrode modified with an impermeable monolayer of low dielectric constant across which the potential may decrease linearly before decaying exponentially in the solution phase. Expressions are presented for both capacitive and Faradaic currents and cyclic voltammograms are thereby produced that take into consideration change in potential across the electrode/monolayer interface. An inclusive equation, describing both the Faradaic and capacitive current is given by

$$i_t = \nu A\left(1+\frac{\partial\sigma_{PET}}{\partial\sigma_M}\right)C_T \qquad (5)$$

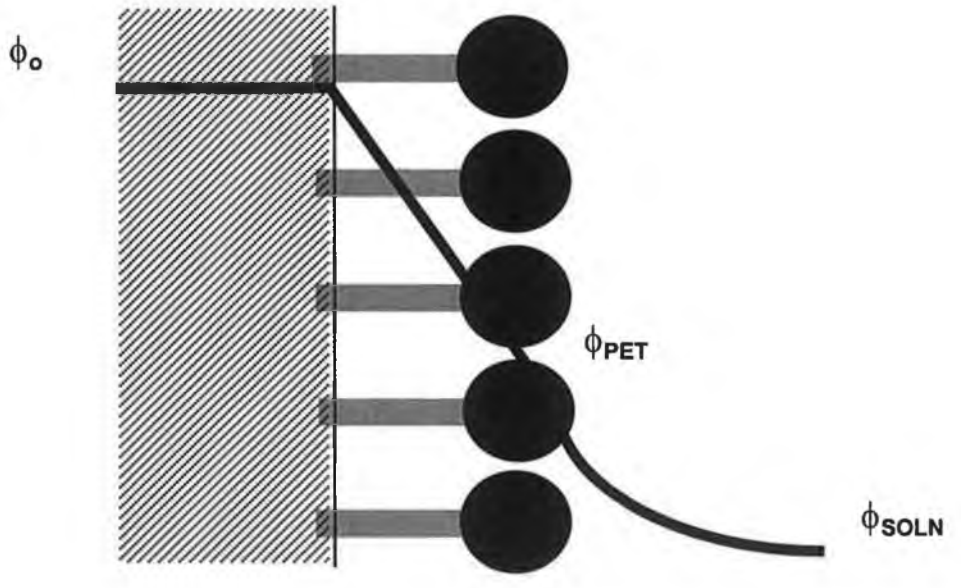

Figure 4 Smith and White model of electrode/monolayer interface.

where i_t is the voltammetric current, ν is the scan rate, A is the electrode area, σ_{PET} is the charge density at the plane of electron transfer (PET), σ_M is the charge density on the electrode surface, and C_T is the potential dependent interfacial capacitance. The

use of this model in determining the composition of an electrode-monolayer interface using capacitance measurements is discussed later.

The influence of interfacial potential distribution on electron transfer kinetics has also been investigated.[34] As with the previous study, this paper examines the non-ideality of the voltammetric response for a monolayer adsorbed onto an electrode surface. The non-zero electrostatic potential difference between the electrode and electroactive moiety causes the current-time transients from chronoamperometric experiments to decay in a more complex way than the single exponential manner expected. Moreover, Tafel plots with lower than expected slopes are anticipated, a phenomenon which shall be discussed in Chapter 6.

Using a quite simple two-capacitor model of the double layer, representing an ideal capacitor - the capacitance of the monolayer - and that of the diffuse layer (described by Gouy-Chapman theory), Becka and Miller have extracted reliable data about diffuse layer potentials.[35] Using capacitance data taken from cyclic voltammetric experiments diffuse layer potentials were determined which showed excellent agreement with calculations based on the two-capacitor model. While each of the above contributions do make a certain number of underlying assumptions they have proved useful for analysing and predicting models of interfacial composition, potential distribution, and voltammetric behaviour.

The study of the double layer is more complicated than that of homogeneous chemistry because it is necessary to include processes involving the interface, e.g., heterogeneous electron transfer, adsorption, atom deposition or reconstruction. Moreover, experimental approaches to the study of the double layer are complicated by the quite small portion of an experimental system contained in the interfacial zone and the small numbers of species that are active there.[36]

1.3 Review Of Monolayer Modified Electrodes

While the following review is by no means exhaustive, the intention is to give an insight into some of the important work that has been carried out in the area of monolayer modified electrodes over the past 15 to 20 years.

1.3.1 *Alkanethiol Modified Electrodes*

Alkanethiol modified electrodes constitute the most important member of a new class of chemically stable monolayers that have followed Murray's pioneering work.[16] These were the first systems used to investigate the thermodynamics and kinetics of electron transfer across metal/monolayer interfaces in any great detail and as such have been very important in elucidating many interesting phenomena occurring at the interface.

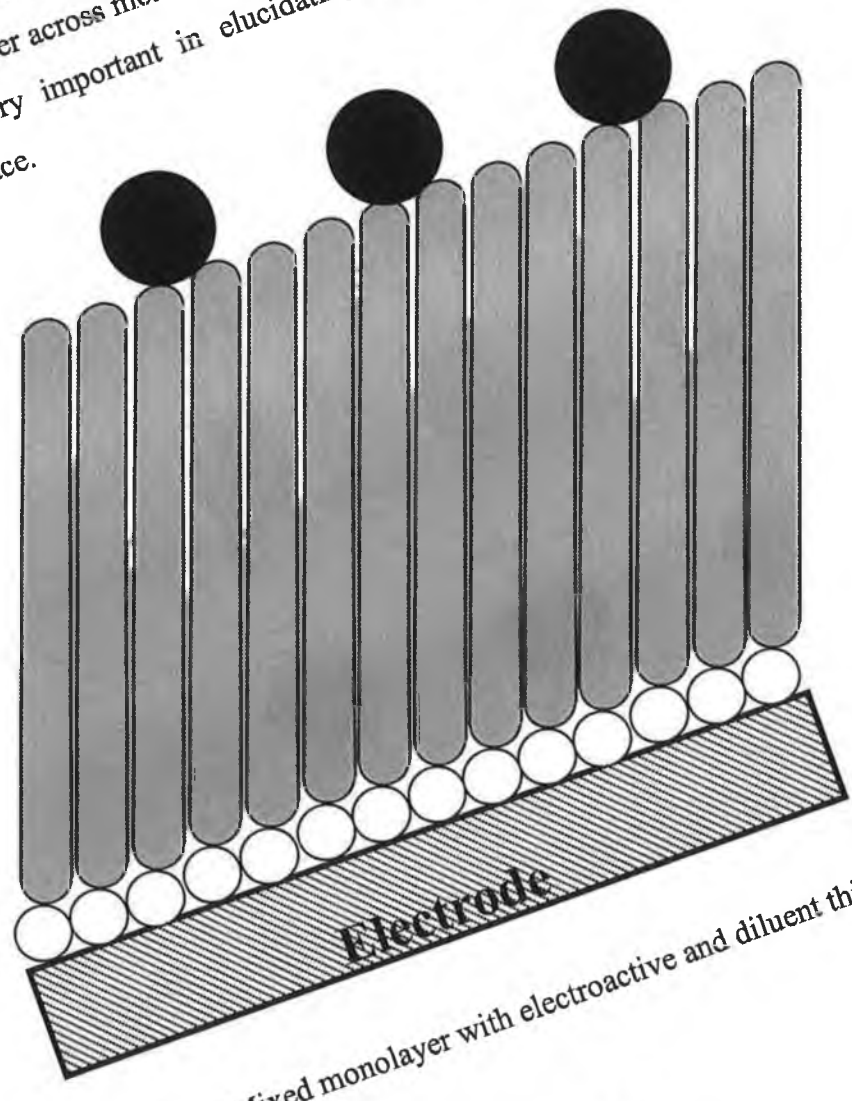

Figure 5 Mixed monolayer with electroactive and diluent thiols.

Alkanethiols on gold are the most extensively studied type of system and were first described as ordered organic monolayer systems and proposed for the study of organic surfaces by Nuzzo, Allara, and co-workers.[41,42,43] Although they have also been studied on silver,[44,45,46,47,48,49] copper[44,49] and mercury[50] the majority of work has been carried out using gold substrates because of their structural definition and fairly simple synthetic manipulation which allows research to be carried out in which variation in organic functionality is important. The use of copper and silver is complicated as reproducible films are difficult to produce due to the sensitivity of these systems to exposure to air of the solution containing the adsorbate.[49] Differences also occur in the metal-sulphur bond which causes different tilt angles and orientations[47] and therefore may cause differences in kinetic parameters, although this may yield interesting and valuable information on the effect of metal substrate (see Chapter 5). Mercury electrodes have been shown to provide extremely good surfaces for the rapid, reproducible adsorption of hexadecanethiol monolayers which are almost entirely defect free.[50] Also, adsorption of the monolayer extends the potential of mercury oxidation anodically to approximately 0.4 V making these systems attractive for the investigation of such issues as distance dependent heterogeneous electron transfer.[51]

Monolayers of alkanethiols are typically formed by adsorption of an alkanethiol or dialkyl disulphide onto gold from solution.[52,53] The fate of the alkanethiol hydrogen in monolayer formation is relatively undefined, although it is thought to be lost. Formation of the monolayer on a gold surface is a reasonably fast process, monolayers being formed from 1 mM solutions of the adsorbate in solvents such as ethanol and hexadecane in one hour at room temperature.[54,55,56] Much of the early work on alkanethiols by Nuzzo, Allara, and others was carried out in order to examine the adsorption processes, the relative perfection of the monolayers and the use of these monolayers for the study of interfacial processes.

Sabatani et al[57] examined the use of thiols and silanes for forming stable monolayers on gold as barriers to gold oxidation. The pinholes left in the monolayer assembly were found to act as microelectrode arrays and were used for the

determination of heterogeneous electron transfer rate constants. Pinhole radii and separations have been determined although deviations from the predictions for microelectrode arrays, attributable to grouping of pinholes in patches, are evident.[58] Permanently pacifying the pinholes of thiol monolayers on gold was carried out in order to establish these monolayers as effective barriers to direct electron transfer between the electrode and a redox active species.[59] Residual currents observed after passivation were assigned to electron tunnelling through the monolayer to a redox active species. The defect density and permeability of alkanethiol monolayers were further studied by looking at electron transfer to solution phase redox active species using various long chain thiols.[12] The use of long chain thiols incorporating different functional groups was used to determine the importance of steric and electrostatic interactions in determining the packing of chains.

Adsorption/desorption processes involving thiols on gold also generated much early interest.[46,60,61] Wrighton, Whitesides and co-workers examined the preferential adsorption of alkane thiols onto gold over silicon nitride and the adsorption/desorption processes occurring when a monolayer of one ferrocene alkanethiol is desorbed into hexane while another ferrocene alkanethiol is then adsorbed.[62] Potential control of adsorption of thiol monolayers was also reported.[63] Controlling the potential, and hence the thermodynamics, of monolayer formation provided monolayers with surface coverages reproducible to within 2% compared to 10% using the self-assembly technique. Also, the extent of coverage has been observed to depend on the applied potential.

Collard and Fox have studied competitive adsorption using mixed monolayers immersed in solutions of electroactive and electroinactive alkanethiols which exchange with the surface confined species.[64] Creager and Rowe have investigated the competition between the adsorption of electroactive and electroinactive alkanethiols, and between long and short chain thiols.[65,66] The electroinactive species is adsorbed preferentially as is the longer chain thiol. Changes in redox potential accompany a change from shorter to longer alkanethiols due to the increasingly non-polar nature of the monolayer. Whitesides also has

examined the competitive adsorption of alkanethiols and has concluded that this competition results in monolayers predominantly composed of one type of alkanethiol.[67] A more complicated experiment in which different metal electrodes have been placed into the same mixture of adsorbates has yielded some interesting orthogonal self-assembly results.[68] Platinum and gold electrodes have been placed in a solution containing both 12-ferrocenyldodecyl isocyanide, I, and bis[10-(ferrocenylcarbonyl)-decyl] disulfide, II, with I being more selective for Pt and II being more selective for Au. In a more recent contribution, Wrighton has followed on this earlier work by producing a more selective surface attachment regime using Au and ITO electrodes.[69] Thiols show excellent selectivity for Au while carboxylic and phosphonic acids show selectivity for ITO.

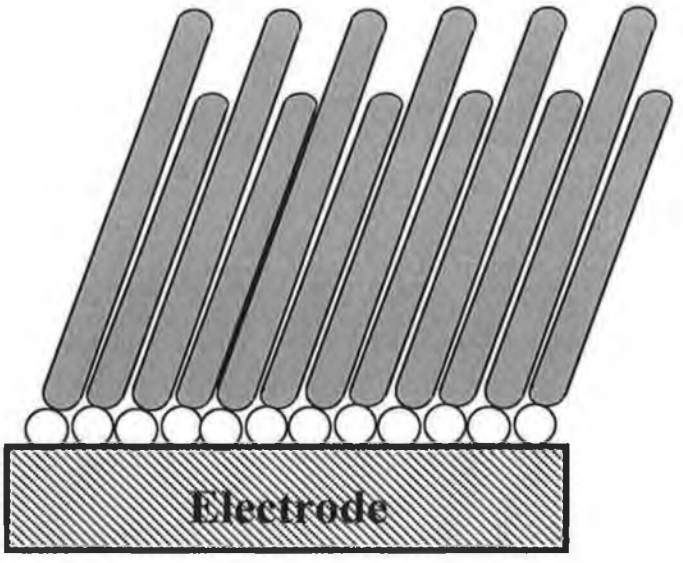

Figure 6 Mixed monolayer with long and short chain thiols.

An important area of research concerning monolayers of alkanethiols on gold has been the investigation of thermodynamic and kinetic parameters. Because alkanethiols spontaneously adsorb onto gold producing well-defined monolayers often with near-ideal electrochemistry, they are extremely useful for the examination of the thermodynamics and kinetics of electron transfer.

The effect of electrolyte has been examined using an electroactive ruthenium moiety attached to an alkanethiol.[70] It has been observed that the surface confined and solution phase species were solvated to the same extent. Finklea has recorded single exponential current-time decays indicating first order kinetics. The rate of electron transfer did not appear to be affected by anion identity. Creager has also looked at the thermodynamics of self-assembled monolayers, examining the effect of electrolyte and chain length on the redox behaviour of ferrocene alkanethiol monolayers.[71] Shifts in redox potentials were attributed to ion pairing effects and the increasingly non-polar nature of the monolayers when long chain alkanethiols were incorporated.

Chidsey has played an important role in developing our understanding of electron transfer across monolayer modified electrodes.[28,29,72] He provided one of the first comprehensive investigations into the kinetics of electron transfer between an electrode and a surface confined species using a ferrocene alkanethiol monolayer on gold to provide measurements of the heterogeneous electron transfer rate constant, its dependence on temperature and potential, reorganisation energies, etc.[28] Some of the first single exponential current-time decays indicating first order kinetics for a surface confined species were presented. Distance dependent electron transfer has also been reported by using thiols of different length[72] and by incorporating electroactive species into chains at different positions.[73] In a noteworthy series of publications Miller and co-workers have examined the adsorption of densely packed electroinactive monolayers of alkanethiols with terminal hydroxy groups. These monolayers appear to have little or no defect sites or pinholes and as such act as effective tunnelling barriers to electron transfer to redox active species in solution.[30,74,75] They found that the mechanism of this electron transfer was dominated by electron transfer through the hydroxy thiol monolayer and that it was possible to measure electron transfer rate constants of the solution phase species across the thickness of the layer. Because of the distance dependence of electron transfer rate constants kinetic measurements were also possible at large overpotentials and it has been postulated that these blocked electrodes may be useful for measurements in highly resistive solutions due to the low current densities

observed.[74] As mentioned above, Finklea has examined electron transfer kinetics as a function of electrolyte identity using an electroactive ruthenium moiety attached to an alkanethiol.[70] In a later paper, a comprehensive examination of the electron transfer kinetics of mixed monolayers consisting of electroactive and electroinactive components has been undertaken.[76,77] The electrochemistry of these ruthenium terminated thiols suggests the presence of "fast" redox centres. Tafel plots like those in Chidsey's work[28] indicate a through-bond tunnelling mechanism. More recently Finklea has produced a paper describing multiple electron tunnelling paths across self-assembled monolayers of alkanethiols with attached ruthenium redox centres.[78] By varying the chain length of the electroactive moiety as well as that of the diluent chains various interesting heterogeneous electron transfer results were obtained. For monolayers consisting of diluent chains longer than electroactive chains a through-bond tunnelling mechanism is believed to dominate. However, when the electroactive chain is longer a multiple tunnelling pathway is believed to occur, consisting of coupling with the diluent chain and one through-space step dominating.

Murray and Creager have examined the electrochemistry of electroactive alkanethiol monolayers in non-aqueous environments.[48,79,80] At reduced temperatures ferrocene alkanethiol monolayers are stable and the rate of heterogeneous electron transfer qualitatively tracks that of aqueous electrolyte systems, the rate constants decreasing with decreasing temperature and increasing chain length. While kinetic dispersion was absent in Chidsey's initial report in aqueous electrolyte[28] it was reported by Finklea in non-aqueous electrolyte.[76] Both Murray and Creager have also produced articles on the use of voltammetry in obtaining quantitative heterogeneous electron transfer results based on Marcus theory for ferrocene alkanethiol monolayers.[81,82] The shape of the peak currents and peak potentials of voltammograms and their dependence on sweep rate can be explained by Butler-Volmer theory only when the reorganisation energy is very high, or when the applied overpotential is less than approximately 30% of the reorganisation energy. Simulated voltammograms show that the Marcus theory of electron transfer accounts for the changing shape; broadened peaks and shifting peak potentials, not accounted for in Butler-Volmer theory at large overpotentials.

1.3.2 Electrodes Modified with Osmium and Ruthenium Polypyridyl Complexes

Although there has been a substantial amount of work carried using osmium and ruthenium redox centres incorporated into polyvinyl pyridine polymers, little research has been carried out into the use of these transition metals in forming polypyridyl monolayers in comparison to the work that has been carried out using ferrocene alkanethiol monolayers. However, in recent times a few research groups, namely those of Abruña and co-workers and Forster and co-workers have carried out some notable work in this area. Monolayers consisting of polypyridyl osmium complexes have been most widely employed due to their accessible redox potentials compared with their ruthenium counterparts, which are often complicated by problems of electrode oxidation. The most common type of monolayers employed utilise osmium complexes of the type shown in Figure 7(a) and 7(b).

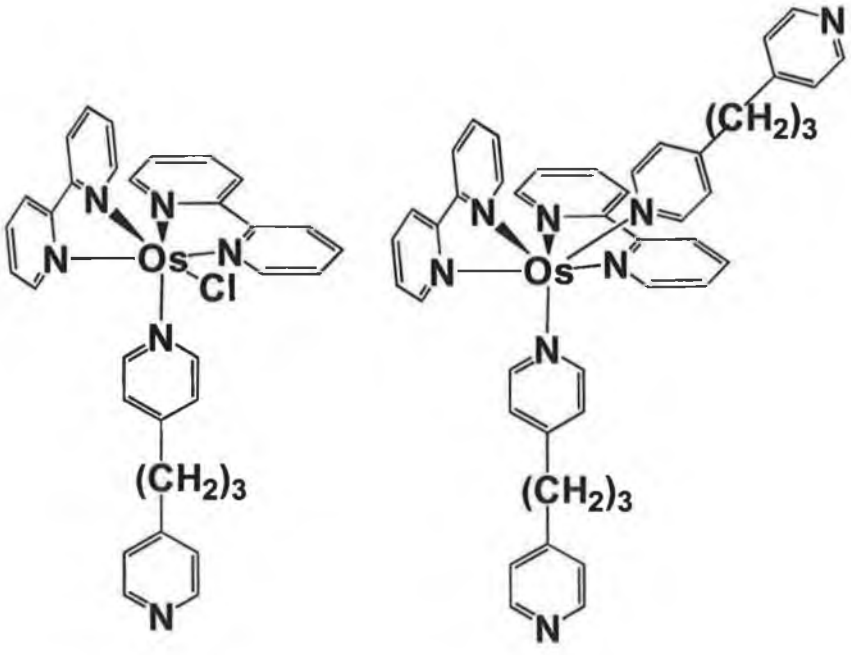

Figure 7 Osmium complexes: (A) $[Os(bpy)_2(Cl)L]^+$ and (B) $[Os(bpy)_2L_2]^{2+}$.

Abruña has studied the thermodynamics of electron transfer involving osmium complexes of Type (A) extensively. Some of this work is reviewed here. In conjunction with Acevedo, Abruña has carried out a study of solvent effects on the formal potential of $[Os(bpy)_2(dipy)Cl]^+$ where dipy is 4,4-trimethylenedipyridine.[83] Formal potentials were recorded using cyclic voltammetry in six organic and aqueous solvents. Charge injection was also used to examine the effect of oxidation state on double layer capacitance. These results suggest the formation of evenly spread submonolayers as opposed to island formation. Also, there appeared to be no dependence of surface coverage on the ionic strength of the deposition solution but there was on pH. The lower the pH, the lower the surface coverage. Capacitance results suggest higher ionic permeability for the higher charged oxidation state.

Abruña has also studied the formation and structure of these self-assembling complexes using scanning tunnelling microscopy (STM) and electrochemical scanning tunnelling microscopy (ECSTM).[84] Again the formal potential was observed to shift positively suggesting uniformity of layer growth. Also, a Frumkin isotherm was found to be fit the experimental data - suggesting small repulsive interactions between neighbouring sites. Microscopy confirms the CV results indicating that incomplete monolayers form as uniformly spread layers and not as islands of more concentrated aggregates. The fully formed monolayer consists of solvated complex molecules which are constantly and rapidly reordering.

The adsorption of other similar type osmium complexes where the ligand is either 4,4-dipyridine (pypy), 1,2-bis(4-pyridyl)ethane (dipyH2), *trans*-1,2-bis(4-pyridyl)ethylene (py=py), or 1,3-bis(4-pyridyl)-propane (dipy) have also studied by Abruña and co-workers.[85] The dependence of the adsorption process on deposition potential, pH, and ionic strength was investigated. As in the previous contributions, electrostatic repulsive forces are believed to exist. They are believed to account for (i) variations in the adsorption isotherms, (ii) shifts in the formal potential as a function of surface coverage, and (iii) differences in surface coverage between the reduced and oxidised forms of the complexes. Free energies of adsorption were independent of potential but the surface coverage was affected by

electrode rinsing. Surface coverage decreased with decreasing pH due to protonation of the free nitrogen on the pyridine group, and ionic strength did not affect the adsorption isotherms.

The introduction of a new series of osmium polypyridyl complexes has been described by Abruña.[86] The complexes are of the type $[Os(bpy)_2Cl(Py\text{-}(CH_2)_n\text{-}SH](PF_6)$ and are capable of forming self assembled monolayers on silver, gold and platinum. Again the effect of electrode potential on the amount of material deposited onto the electrode surface during deposition was investigated. The amount of material deposited onto the electrode at potentials negative of the potential of zero charge (PZC) was found to depend on the applied potential during deposition while the amount of material adsorbed at potentials positive of PZC was found to be independent of applied potential. It would appear that that the most dominant interactions taking place in the adsorption process are electrostatic attraction and repulsion. From the plots of surface coverage of these osmium containing polypyridyl thiol complexes versus deposition potential it is also possible to determine PZC of the electrode.

The adsorption and desorption of these complexes was further studied with regard to solution pH and ionic strength of the deposition solution and a model for the adsorption based on the Freundlich isotherm was postulated.[87] In the pH range 1-5 the surface coverage was independent of pH. It was also found to be independent of ionic strength of the deposition solution. The adsorption of the complex provided some interesting results when an adsorption isotherm was fitted to the surface coverage versus concentration results. It was found that a Freundlich isotherm which does not require a saturation or maximum coverage best described the results observed. Desorption of the complexes resulted in an exponential decrease in coverage with time. The temperature dependence of the desorption process was used in order to calculate activation energies for desorption which were found to obey Traubes rule which states that the longer the carbon chain of the adsorbed complex the less likely it is to dissolve into aqueous solution.

In a recent publication, Abruña has examined the exchange dynamics of osmium and ruthenium complexes adsorbed onto platinum electrodes.[88] The free energies of the osmium and ruthenium complexes, which differ in metal only, were found to be identical and therefore have the same affinity for the electrode surface. The desorption process was found to be rate determining whereby an adsorbed molecule must desorb in order for another to take up the vacant site, i.e., a dissociative mechanism. The presence of both complexes on the electrode surface was examined as a function of voltammetric wave shape. Increased broadening in the ruthenium wave when coadsorbed with the osmium, compared with only ruthenium complex adsorbed on the electrode, indicates increased repulsive interactions due to the presence and uniformity of spread of osmium molecules throughout the monolayer.

In recent years, Forster has produced a number of important papers on the thermodynamics and kinetics of heterogeneous electron transfer using similar types of monolayer assemblies as model systems. In an extensive pair of papers together with Faulkner, he has examined the equilibrium properties, fundamental electron transfer characteristics, and the effects of solvent, potential and temperature on the electron transfer dynamics of a group of spontaneously adsorbed osmium based monolayers.[2,3] In the first of these papers, the local microenvironment of the redox centres was probed by examining the electrochemical response as a function of supporting electrolyte, solvent, and temperature. Forster found that the extent of ion pairing between the oxidised form of the redox couple and an anion depends not only on the identity of the particular anion and its concentration, but also on the solvent used. Greater solvent ordering was observed for the oxidised form of the monolayers particularly in low dielectric solvents. The kinetics of heterogeneous electron transfer was also explored and it was found that the rate of heterogeneous electron transfer was independent of electrolyte concentration suggesting that ion pairing is an equilibrium process which precedes or follows electron transfer. The kinetics of electron transfer was found to be extremely well behaved across the group of complexes investigated over a wide range of timescales, temperatures, and solvents. The potential dependence of the rate constants was also studied over a wide range of

potentials, transfer coefficients of 0.5 were found at low overpotentials in agreement with the Butler-Volmer formulation. At high overpotentials curvature in the Tafel plots, predicted by Marcus, was observed. From the non-symmetric nature of the Tafel plots at high overpotentials it was concluded that a through space tunnelling mechanism best explained the observed results.

In the second of the two papers, the ability of the Butler-Volmer theory of electrode kinetics to accurately describe electron transfer at high over potentials and as a function of temperature was investigated. Temperature, solvent, and potential effects on the electron transfer dynamics were investigated. In particular, the potential dependence of the electrochemical enthalpy predicted by theory and that experimentally observed was examined. The experimentally determined electrochemical enthalpy was found to be less sensitive to applied potential than predicted by Butler-Volmer theory. This theory ignores the potential dependence of the activation entropy which the authors suggest leads to the difference in the observed and predicted results, thus highlighting a deficiency in the theory. Another worthwhile investigation undertaken in this contribution was the examination of the effect of solvation relaxation on the rate of electron transfer. Results suggest that the electron transfer process is sensitive to the solvents ability to relax dynamically to accommodate the new charge placed on the redox centre. By calculating the transmission coefficient the electron transfer reaction was found to be non adiabatic which was in conflict with the dependence of the rate constant on solvent dynamics and very unexpected. One would expect with a low transmission coefficient that the dynamics of solvent motion would be much too fast to influence the electron transfer rate.

In a more recent paper, Forster and Faulkner have examined the use of chronoamperometry as a tool with which one can separate Faradaic current on a microsecond timescale even though the two species possess identical formal potentials.[4] Binary monolayers based on osmium and ruthenium complexes having near ideal electrochemical responses were formed on platinum microelectrodes. The rate of heterogeneous electron transfer was insensitive to the ratio of the

osmium : ruthenium concentration on the electrode surface. Also, the adsorption of osmium complexes followed the Langmuir adsorption isotherm. Therefore, binary monolayers having the same formal potential could be studied in the knowledge that the surface concentration of the components would not effect the electron transfer rate constants, and that any deviation from Langmuir type behaviour would be due to lateral interactions between adsorbates. These binary monolayers consisted of two osmium complexes differing only in the length of the bridging ligand between the redox centre and the underlying electrode. Thus the formal potentials of both complexes were identical. These monolayers were formed by adsorption of a partial monolayer of one species and thereafter backfilling the assembly by adsorbing the second species. No alteration in the Langmuir behaviour was noted, suggesting that electrode-adsorbate and headgroup-solution interactions, rather than lateral forces, dominate. Potential step chronoamperometric results show three separate current decays corresponding to double layer charging, and the two Faradaic decays due to the two monolayer components. This separation in kinetic response, due to the different bridge lengths, was used to determine the bulk concentrations of the species which could not be accomplished using cyclic voltammetry.

In his most recent paper on osmium containing monolayers, Forster has tackled an interesting topic concerning the heterogeneous kinetics of metal and ligand based redox reactions within osmium-polypyridyl adsorbed monolayers.[89] Cyclic voltammetry yields three distinctive oxidation/reduction couples corresponding to the redox activity of the metal (3+/2+), and the two bipyridyl reactions (2+/1+ and 1+/0). Tafel plots high at overpotential are curved indicating that Marcus theory is an appropriate description of the electron transfer dynamics. The metal based Tafel plot shows asymmetry in the cathodic and anodic branches of the Tafel plot at these large overpotentials, a phenomenon consistent with through space tunnelling. However, the branches of the bipyridyl based Tafel plots were symmetrical suggesting a through bond tunnelling pathway. Although less than unity for all three processes the transmission coefficient was larger for the bipyridyl based reactions which the author suggests may be a consequence of the redox potentials of the bipyridyl groups being comparable to that of the metal-to-electrode

bridging ligand. The proximity of these redox potentials to each other may facilitate virtual coupling (superexchange) between the bridging ligand and the bipyridyl groups.

1.3.3 Adsorption of Quinones onto Electrode Surfaces

There is a long history of electrochemical measurements of solution phase molecules including quinones, diphenols, and polycyclic phenols, etc. However, relatively little research had been carried out on the electrochemistry of surface confined aromatic molecules until the initial ground breaking work of Soriaga and Hubbard.[14,90,91] Since then a number of important contributions have been made to the field of adsorbed aromatics. Here, we are most interested in the electrochemistry of adsorbed anthraquinones and hydroquinones, classified just as quinones for the purpose of this report.

In those initial investigations, Hubbard examined the electrochemistry of a profusion of redox active aromatic molecules. In the first of these papers, the limiting surface coverages, of forty molecules which adsorbed strongly onto platinum electrodes, were presented.[90] These coverages were used to determine the area occupied per molecule on the electrode surface. The results were compared to theoretically calculated areas for different orientations of the molecule on the surface of the electrode. These comparisons lead to the identification of the orientation of a particular molecule when it was adsorbed onto the platinum electrode. The results were of particular interest to other authors whose work on the electrochemistry, particularly the heterogeneous electron transfer kinetics, of adsorbed aromatics often required knowledge of the orientation of the adsorbed species for interpretation of their results. Of particular interest with regard to our current research is that a flat orientation for anthraquinone-1,5-disulphnic acid and anthraquinone-2,6-disulphonic acid was determined for both the oxidised and reduced forms of the species.

The second in this series of papers investigated the coadsorption of an anion, iodide, with aromatic molecules.[14] Orientations before and after exposure to iodide were determined. The results indicated that in general when a flat orientated adsorbed layer of aromatic molecules was exposed to a solution of a strongly surface active anion, such as iodide, changes in coverage, orientation, and/or mode of attachment occur. Changes in coverage, i.e., desorption of the 1,5- and 2,6- anthraquinones occurred. However, these molecules did not undergo any reorientation upon adsorption of iodide possibly due to voids in the adsorbed layers.

The third and final paper in the series dealt with adsorption of aromatic molecules as a function of solute concentration.[91] Most of the molecules investigated underwent transition in orientation upon increasing the adsorbate concentration with each individual orientation being stable over a range of concentrations. In general, at low concentrations the molecules adopted a flat orientation on platinum. On increasing the adsorbate concentration, packing densities, orientations and modes of attachment were observed to change. Again the adsorbed anthraquinones of interest were found to be insensitive to the nature of the environmental changes taking place around them. Their resistance to reorientation is explained by the authors as an entropy effect: in the flat orientation the three fused rings can each interact with the platinum surface, whereas the edgewise orientations would only allow limited association. Steric hindrance due to the sulphonate substituents is not considered as an explanation for the lack of reorientation as 1,5-anthraquinone disulphonic acid could undergo this process quite easily.

Since those initial contributions, Hubbard has continued his work on adsorbed aromatic molecules. Indeed, a number of distinguished articles have been published in which the general theme of adsorbed aromatic molecules has been continued. The temperature dependence of molecular orientation has been discussed and, while other flat orientated molecules showed a strong temperature dependence, the orientation of anthraquinone-1,5-disulphnic acid was observed to be insensitive to temperature.[92] Other papers have dealt with topics ranging from the effect of surface pretreatment with flat orientated intermediates,[93] the potential dependent

surface chemistry of pyridine carboxylic acids,[94] and hydroxypyridines,[95] etc.[6,96] For reviews of Hubbards work the interested reader is invited to examine *Electrochemistry at Well-Defined Surfaces*,[8] and *Electrochemistry at Well-Characterised Surfaces*.[97]

Laviron has carried out some notable theoretical work on the sequence of proton and electron transfer in species that undergo coupled proton/electron transfer reactions.[98,99,100] One experimentally based contribution reported the coupled proton/electron transfer involved in the oxidation/reduction reaction of surface confined benzoquinone/hydroquinone.[101] The kinetics of proton/electron transfer for the benzoquinone/hydroquinone couple surface confined on a platinum electrode was presented. The influence of pH was used to give information about the reaction sequence, i.e., order of addition or removal of electrons and protons. The results were along the lines of earlier predicted theoretical results and indicated that the sequence of proton / electron transfer involved successive two one-proton (H^+) one-electron (e^-) steps. In particular, it was found that at low pH the reaction proceeded by a $H^+e^-H^+e^-$ sequence, at intermediate pH $e^-H^+H^+e^-$, and at high pH $e^-H^+e^-H^+$ for the reduction reaction and the reverse order for the oxidation reaction. The work of Laviron and others has proved instrumental in providing us with insights to the sequence of proton / electron transfer in the system investigated in Chapter 3.

In recent years, Forster has carried out some elegant work on surface confined quinones adsorbed onto mercury microelectrodes. In two papers published on the topic, the electron transfer dynamics and surface coverages of binary anthraquinone monolayers were discussed.[5,102] In the first of these reports, pure and binary monolayers of anthraquinone-2,6-disulphonic acid and anthraquinone-1,5-disulphonic acid (previously studied by Hubbard on platinum) were studied using cyclic voltammetry and chronoamperometry.[102] Because both quinones exhibited identical formal potentials it was not possible to examine surface coverages of binary monolayers using conventional cyclic voltammetric means.

Therefore, chronoamperometry was employed in which the charge passed, Q, during a Faradaic reaction was obtained using Equation 6.

$$i_F(t) = kQ\ exp(-kt) \tag{6}$$

Heterogeneous electron transfer rate constants for the two Faradaic processes revealed a much higher rate constant for 2,6-anthraquinone disulphonic acid. This separation of the Faradaic components on the experimental timescale enabled analysis of the charge passed. The surface coverage was then determined in the usual way, cyclic voltammetry and chronoamperometry revealing indistinguishable coverages and adsorption free energies. The use of surface coverages in conjunction with high speed chronoamperometry in determining solution concentrations of analytes is also demonstrated.

In another paper demonstrating the use of high speed chronoamperometry and surface coverages for determining solution concentrations of analytes, adriamycin and quinizarin monolayers adsorbed onto mercury microelectrodes were examined.[5] The formal potentials of the components of co-adsorbed binary monolayers are too similar to distinguish them voltammetrically and chronoamperometry was required for the analysis of electron transfer dynamics and surface coverages. Again the thermodynamic and kinetic properties of the system under investigation are used in order to extract information concerning their concentrations in solution.

The effect of potential on the adsorption thermodynamics of reversibly adsorbed quinone monolayers has been studied by Forster in two recent papers.[103,104] Adsorption of 2-hydroxyanthraquinone onto mercury microelectrodes was studied using cyclic voltammetry and chronoamperometry.[103] Surface coverages and free energies of adsorption can only be probed at the formal potential, when cyclic voltammetry is employed. Also, cyclic voltammetry can only be used to measure the double layer capacitance when there is no Faradaic current present. Therefore, use of potential step chronoamperometry was exploited in order to examine the potential

dependence of the free energy of adsorption by analysing capacitance data. Results indicate that changing the redox state of the monolayer brings about a change in the free energy of adsorption. Differences in the strength of hydrogen bonding between the reduced and oxidised states are suggested for the observation that the free energy of adsorption is larger in the reduced state of the monolayer.

In the second of these papers, coupled proton and electron transfer of adsorbed anthraquinone-2-carboxylic acid monolayers was examined.[104] The potential dependence of the heterogeneous electron transfer rate constant was examined as a function of electrolyte pH and the resulting Tafel plots indicated that the standard rate constant was influenced by pH verifying that a coupled proton/electron process is taking place. The potential dependence of the double layer capacitance as a function of adsorbate concentration was again used to determine the free energy of adsorption as a function of potential. The free energy was larger for the reduced form of the monolayer, suggesting the influence of hydrogen bonding in dictating relative strengths of adsorption in these systems.

A paper describing the application of quinones as corrosion inhibitors has been presented.[105] In this contribution the authors have investigated the usefulness of adsorbing various quinones onto steel as a method of preventing corrosion in neutral media. The various quinones have made it possible to investigate the effects of molecular size and structure on the effectiveness and mechanism of protective action of the quinones. The quinones of most interest in the context of this thesis, the *para*-quinones adsorbed on the metal surface and were shown to decelerate corrosion. Quinones larger in size and mass had greater inhibitory qualities, however all quinones had a decreased effect on increasing temperature, particularly the *ortho*-quinones.

The general cyclic voltammetric and quartz crystal microgravimetric behaviour of a number of interesting adsorbates containing thiol and hydroquinone moieties has been studied by Soriaga, Scherson and co-workers.[106] Results indicate that water is lost from the electrode surface as the oxidation state of the monolayer is

altered. This would suggest that quinonoid monolayers contain water and this water has a greater affinity for the reduced, hydroquinone, form of the monolayers.

In a stimulating article on the electrochemical properties of 2-mercaptohydroquinone monolayers on gold electrodes, Uosaki and colleagues have investigated the electrochemical response of these adsorbed species as a function of pH in buffered and unbuffered electrolyte solutions, and as a function of adsorption time and concentration of the deposition solution.[107] In summary, the number of adsorbed molecules increases as a function of deposition time and deposition solution concentration. What is of most interest in this paper is the examination of the electrochemical behaviour of the monolayers as a function of pH. In buffered electrolyte a change in redox potential with a slope of -60 mV pH^{-1} is observed. The same result is offered for the unbuffered results although it is difficult to see how these results are derived as there are two sets of redox couples present at intermediate pH. Identifying these couples and determining which are to be used for the plot of redox potential versus pH appears difficult. However, Uosaki overcomes this problem by neglecting these couple altogether and uses only low and high pH data instead. He does go on to give a tentative explanation for the presence of the electrochemical response at intermediate pH, suggesting it as the presence of two different reaction schemes caused by a lack of protons in solution.

For an excellent and oft cited review, the interested reader is pointed in the direction of Chambers' thorough inspection of the literature on the electrochemistry of quinones.[108]

1.4 Microelectrodes

1.4.1 Introduction

The importance of microelectrodes is widely recognised and interest in their application in diverse areas of research has been increasing over the past 15 years.[109] There has been an explosion of interest in the properties of microelectrodes because of their potential use in areas where conventional electrodes cannot be used or expensive alternative instrumentation is needed. Microelectrodes have made both a fundamental and applied impact on electrochemistry unequalled by almost any other electrochemical approach in recent times.[110] The literature now contains many hundreds of papers a year which increase our understanding of the properties of microelectrodes or demonstrate new types of applications. The special features of mass transport to microelectrodes including the distinctive behaviour at short times, and the ability of microelectrodes to minimise distortion of experimental data due to iR drop and charging effects are important advantages of microelectrodes which shall be discussed.

1.4.2 Microelectrode Types

Microelectrodes employed in voltammetry take a variety of different shapes and forms. There are five major microelectrode geometries with the microdisk being the most common, being used in approximately 50% of all applications.[110] The other geometries include, cylinders and arrays, which comprise 20% of investigations each, and bands and rings which comprise the other 10%. The main microelectrode types are shown in Figure 8. The ease of construction and use of microdisks have made them the most frequently used electrodes. Most often these are small flat disks of a metal that are press fitted into a rod of an inert, non conducting material such as glass, teflon or Kel-F that has embedded in it a wire contact. The conductor may be an inert metal, such as platinum or gold; pyrolytic graphite or glassy carbon; a

semi-conductor, such as tin or indium oxide; or a metal coated with a mercury film. Nickel, silver and to a lesser extent silica and ceramics have also been used. Figure 9 shows the construction of a typical construction microelectrode used throughout this work.

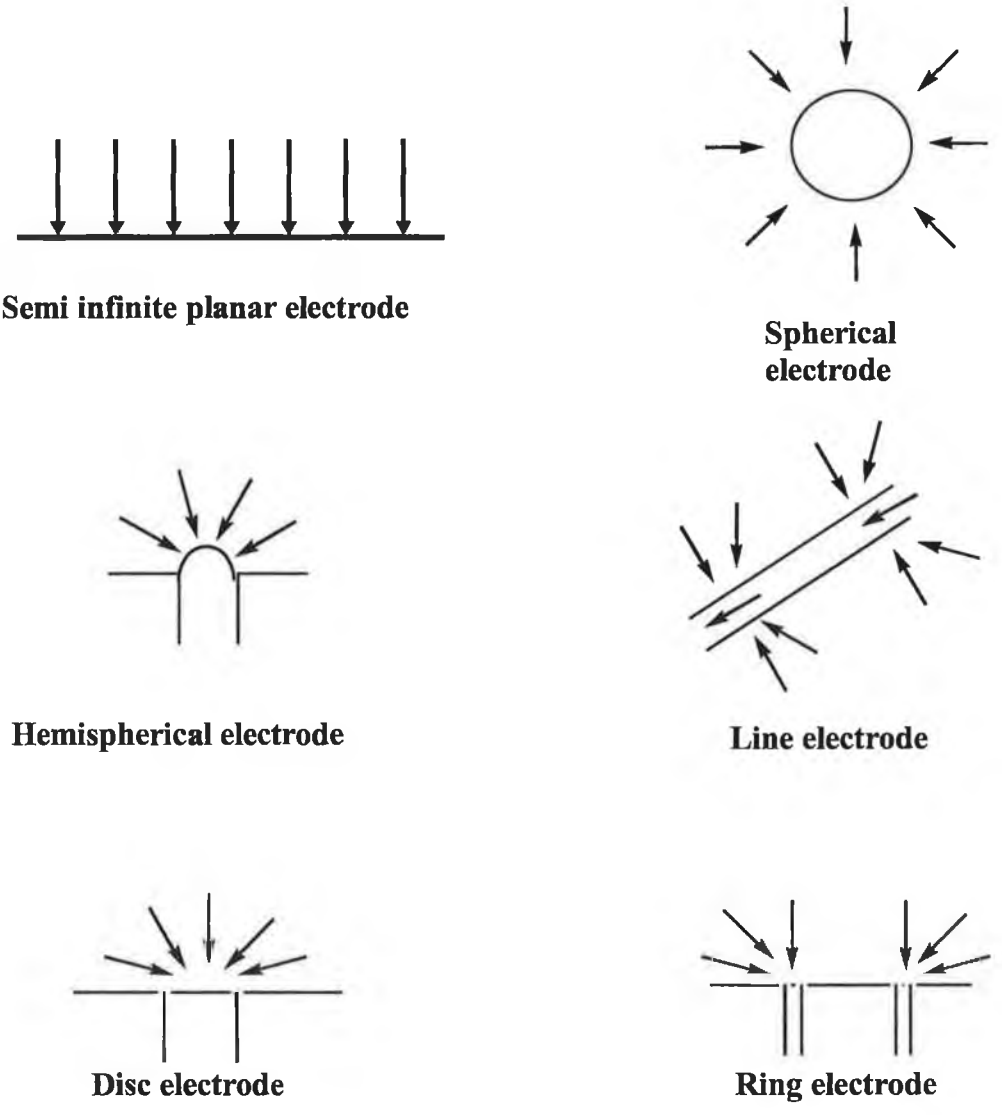

Figure 8 Common microelectrode geometries and their diffusion fields.

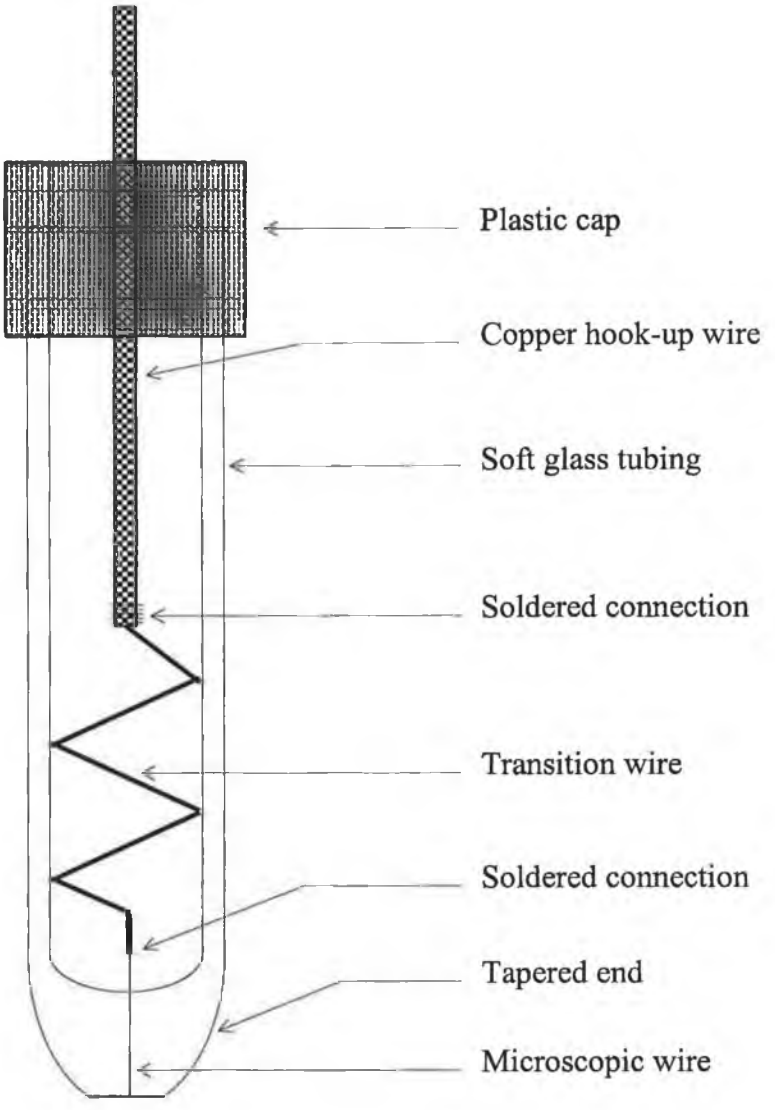

Figure 9 Typical construction of a microelectrode.

As is shown in Figure 10 the range of potentials that can be used with these electrodes in aqueous solutions varies and depends not only upon the electrode material but also upon the composition of the solution in which it is immersed.[27] Generally, the positive potential limitations are caused by the large currents that develop due to oxidation of the water to give molecular oxygen. The negative limits arise from the reduction of water giving hydrogen. Note that relatively large negative potentials can be tolerated with mercury electrodes owing to the high overpotential of hydrogen on this metal.

The criteria for describing an electrode as a microelectrode is that it must have at least one dimension, such as the radius, small enough that its properties, for example, mass transport regime, are a function of size. The critical dimension is generally in the range 0.1-50 μm. The actual physical size of microelectrodes allow

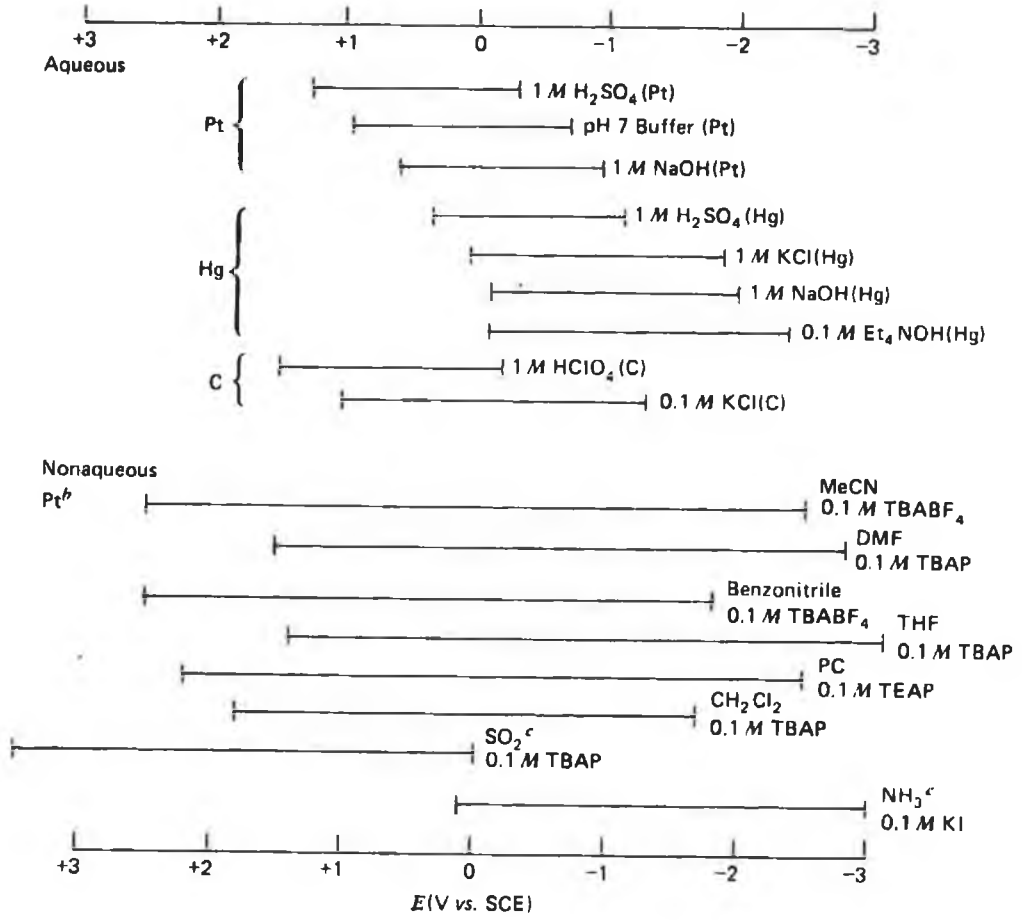

Figure 10 Some supporting electrolytes and their potential ranges in various solvents for various electrodes.

their use in the analysis of very small volumes while they have also been used as components in microelectronic devices.[111] They can also be used as an important interface between electrochemistry and in vivo investigations and clinical treatment.[112] Micro-ion selective electrodes have been used for in vivo monitoring and other microelectrodes have been used to directly stimulate nerves.[113]

1.4.3 Mass Transport Considerations

Although the majority of work throughout this project has involved surface confined species in which mass transport does not play a part, the role of the electrode dimensions in determining diffusion processes is an important consideration. Due to different mass transport regimes being predominant when microelectrodes or macroelectrodes are employed differing electrochemical responses are observed for the two types of electrode. Steady state responses may be observed when a smaller size electrode is used. Shrinking the radius of the electrode affects the diffusion process which may be manifested in the experimental response. Two limiting cases may be distinguished depending on whether the experimental timescale is long or short.

Using Laplace transformations to solve Ficks second law of diffusion, Equation 7 describing current, i, as a function of time, t, is obtained;

$$i(t) = \frac{nFADC}{r} + \frac{nFAD^{1/2}C}{\pi^{1/2}t^{1/2}} \qquad (7)$$

where F is Faradays constant, A is the area of the electrode, D is the diffusion coefficient, and C is the concentration of electroactive species as a function of distance r, and time.[114]

At short times the diffusion layer thickness that is depleted of reactant is smaller than the radius of the electrode. Therefore, the electrode appears to be planar to a molecule at the edge of the diffusion layer and linear diffusion predominates. Thus, the first part of Equation 7 becomes insignificant. The resulting voltammogram is as that of a macroelectrode with the decaying current governed by the Cottrell equation;

$$i = \frac{nFAD^{1/2}C}{\pi^{1/2}t^{1/2}} \qquad (8)$$

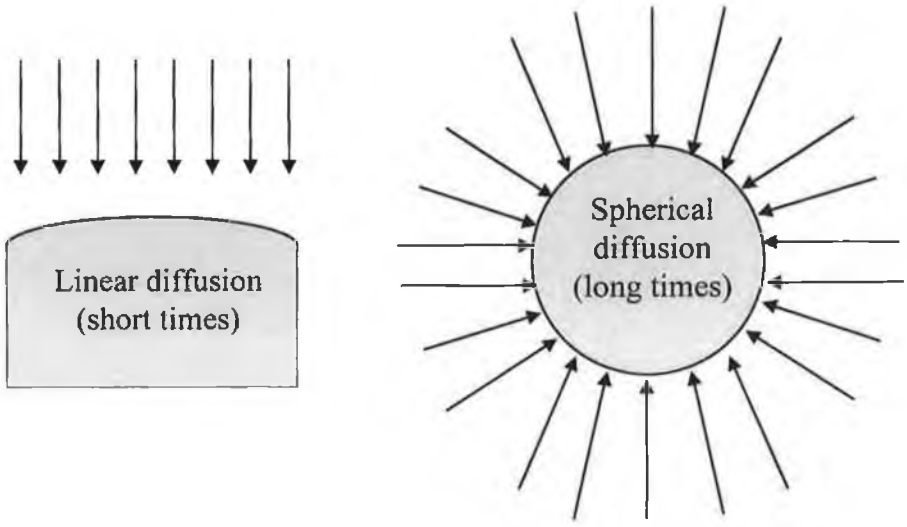

Figure 11 Time dependence of the diffusion field at microelectrodes (A) Linear diffusion at short times and (B) radial diffusion at long times.

At longer times t increases ($t^{-1/2}$ decreases) and the contribution of the Cottrell current to the overall current density will decrease to a negligible value. Under these conditions the current reaches a steady state value, as given by Equation 9:

$$i = \frac{nFADC}{r} \tag{9}$$

At these long times, the spherical character of the electrode becomes important and mass transport is dominated by spherical diffusion as illustrated in Figure 11. The steady state (sigmoidal) response arises because the electrolysis rate is equal to the rate at which molecules diffuse to the electrode surface.

The above treatment considered spherical microelectrodes. Mass transport to microdisk electrodes is more difficult to describe as the centre of the disk is not as accessible to a diffusing molecule as the circumference. Therefore, the flux of material is unequal across the electrode surface. However, the steady state response for the microdisk has been established and is given by:

$$i = 4nFDrC \qquad 10$$

where r is the radius of the disk.

Microelectrode dimensions are such that diffusion converges to achieve steady states, in other words, steady state voltammograms can be recorded under purely diffusive conditions, that is without any involvement of convection. The time required[110] to approach a steady-state is approximately 6A/D for a microdisk of area A and diffusion coefficient D.

For surface confined species the situation is different. Surface confined species, such as monolayers spontaneously adsorbed onto an electrode surface, are a fixed distance from the electrode surface and as such there is no diffusion process taking place. Therefore, the dimensions of the electrode will not impact the observed response in the same manner as for freely diffusing species. However, the size of the electrode will have a bearing on the RC cell time constant and therefore the capacitive current and also on the ohmic drop.

1.4.4 Characteristics of Microelectrodes

Apart from the normal characteristics associated with macroelectrodes, microelectrodes possess several distinct properties which give them a unique position in modern day electrochemistry.[70,114] Several advantages arise from the use of microelectrodes such as reduced capacitance, faster response time of an electrochemical cell (RC time constant), reduced ohmic drop (iR drop) and reduced currents which enable the study of short timescale processes.

RC Time Constant.

As explained in section 1.2.1, when a potential is applied across the electrode-solution interface a current, known as the capacitive current, flows to charge the double layer. This capacitive current must flow through a resistance R. The time taken for this process to occur is known as the cell, or RC, time constant, R representing the total cell resistance and C being the double layer capacitance. When an electrochemical experiment is carried out in which a Faradaic reaction is being monitored, it is desirable to separate on the basis of timescale, the capacitive and Faradaic currents. The capacitive current decays after a potential step according to Equation 11.

$$i_c = \frac{\Delta E}{R} exp\left(\frac{-t}{RC}\right) \tag{11}$$

If the Faradaic reaction is slow compared with RC, then a kinetic separation of the capacitive and Faradaic currents will occur. However, if the RC and the Faradaic processes are of the same timescale the two processes will be convolved making it difficult to accurately probe the dynamics of either process. Therefore, if we wish to monitor fast electrochemical processes how do we reduce RC? Decreasing the size of the electrode will not decrease the cell resistance. In fact, according to equation 12 the resistance will increase on decreasing the electrode radius;[114]

$$R = \frac{1}{4\pi\kappa r} \tag{12}$$

where κ is the specific conductance of the medium. However, because the electrode capacitance is an extensive property and is proportional to the electrode area, or r^2, Equation 13 demonstrates that the product RC decreases with electrode radius.

$$RC \propto \frac{1}{r} r^2 (= r) \tag{13}$$

Hence, microelectrodes can be used to minimise the RC component, by decreasing C relative to R, and therefore fast Faradaic reactions can be monitored.

According to Equation 12 use of higher conductance media will decrease the cell resistance. Therefore, electrolytic solutions of higher molarity will help minimise the overall RC. For example, Forster has reported the use of 2.5 μm platinum microelectrodes to achieve RC time constants of 12 ns in 5 M $HClO_4$.[114]

Ohmic Drop

Ohmic or iR drop quantifies the extent to which the applied potential is weakened when Faradaic and capacitive currents pass through a solution. Because the dimensions of the electrode are so much smaller than at conventional macroelectrodes, and the current decreases with r^2, microelectrodes are less prone to ohmic drop phenomena than macroelectrodes. This allows useful electrochemical measurements to be performed under conditions where no significant Faradaic information could be obtained at classical electrodes. These situations include, solvents of low dielectric constant, absence of supporting electrolyte, large concentrations of electroactive material and submicrosecond voltammetry. The physical size of microelectrodes means that the Faradaic current, is typically in the pA to nA range, which is approximately six orders of magnitude less than that observed at conventional macroelectrodes. These reduced currents are of vital importance in the successful application of microelectrodes. However, it is not only reduced currents that contribute to a reduction in iR drop. The nature of diffusion in short timescale experiments (Equation 9) means that the resistance increases with decreasing electrode radius rather than decreasing electrode area observed at longer times (Equation 8).

1.4.5 Applications of Microelectrodes

Microelectrodes are now used for a wide variety of applications. Due to the short RC cell time constants and reduced iR drop, microelectrodes are finding more and more application in the analysis of real samples today. The applications of microelectrodes due to their reduced size are almost limitless.[110] Under any circumstances where detection or measurement of concentration of an electroactive species is required with a spatial resolution of a few micrometers, microelectrodes constitutes the best tool available.[115] In collector-generator systems or in electrochemiluminescence experiments one electrode is used to probe and examine the chemical content of the diffusion layer of another.[115] Several applications of similar principle have been developed in which a mobile microelectrode is used to detect chemical emission or consumption by another object such as another electrode,[116,117] a living tissue or single cell[70,118,119] or an event such as corrosion.[110] Microelectrodes can be used to monitor local hydrodynamics of a solution near a surface or in a small channel with micrometer resolution.[120] Similarly, their small size, large signal to noise ratio, and insensitivity to convection make them ideally suited for use as electrochemical detectors in liquid chromatography.[121,122,123]

Apart from these and many other applications based on the unique size of microelectrodes, the two characteristics of reduced RC time constants and reduced ohmic drop are responsible for some of the more specific applications of microelectrodes. They include the application of microelectrodes to electrochemistry in highly resistive/low conductivity media and electrochemistry in the low to sub microsecond time scale, i.e., fast kinetics.

Highly Resistive/Low Conductivity Media.

The application of microelectrodes to electrochemistry in highly resistive and low conductivity media takes advantage of the fact that the small currents observed at microelectrodes results in reduced iR drop. Even in organic solutions where there is no supporting electrolyte added, iR drop is still comparable to the response observed for macroelectrodes in aqueous solutions containing electrolyte.[114,115] For example, a

macroelectrode with a 3 mm radius immersed in an organic solution with a resistance of 100 Ω will experience the same iR drop as a 30 μm radius microelectrode immersed in a solution of $1x10^6$ Ω provided that all other conditions are equal. Samples of high resistivity which have been explored include those of large viscosity including; gels, polymers, epoxy resins, frozen materials, living tissues, and food/nutrients, while those of low dielectric constant include; hexane, toluene, and other solvents as well as oils and lubricants.[115]

Electrochemistry in the Low to Sub Microsecond Time Scale - Fast Kinetics.

Many significant events, such as electron and proton transfers, ligand exchanges, isomerisations, and ejection of leaving groups, occur on the low to sub microsecond time domains. In order to be able to probe these processes techniques capacle of operating in at least these timescales must be employed. Modern electrochemical methods using microelectrodes provide conceptually the most convenient way to resolve kinetics of chemical reactions in which electron transfer is involved.[124] The literature now contains many examples in which the of the use of microelectrodes in elucidating the kinetics of electron transfer of solution phase and surface confined species using non steady state techniques has been investigated. Microelectrodes are employed for this purpose due to their insensitivity to iR drop and because RC cell time constants are considerably reduced. These two important advantages have opened up sub microsecond frontiers to transient electrochemistry. Although the double layer capacitance increases proportionally with increasing scan rate in a voltammetric experiment, distortion of the observed response does not occur until scan rates at least three orders of magnitude larger than those normally used at macroelectrodes are used.[114] These non steady state techniques provide more information about chemical and electrochemical reactions than do their steady state counterparts. For example, cyclic voltammetry allows the creation of the diffusion layer created on a forward scan to be examined for intermediates on the reverse scan. Heterogeneous electron transfer rate constants can also be accurately probed by examining the separation in peak potentials at high scan rates. Although the effects of resistance and capacitance can never be entirely eliminated several strategies have been used to decrease their influence.[125] Potential step techniques have also proved

popular in the examination of electrode kinetics as they provide a straight forward approach for extracting useful data.

1.4.6 Conclusion

Microelectrodes offer considerable advantages over electrodes of classical dimensions. Experiments involving microelectrodes are cheap to perform and simple to carry out, and are based on sound fundamental principles. They greatly improve the quality of electrochemical data, have applications in many fields of science and allow experiments that were almost inconceivable several years ago to be performed on a routine basis. These improved characteristics have opened up new horizons to electrochemistry. They have been used to increase the sensitivity of anodic stripping voltammetry in environmental analysis, to investigate rapid electron transfer and coupled chemical reactions, to study electrode reactions in low conductivity solvents and media without added electrolyte, to probe the mechanism of electrode reactions under conditions close to those prevailing in industrial electrochemical processes and to map the local potential/current distribution in electrolysis cells and in medicine as in vivo sensors. Microelectrodes can be used successfully to solve problems of chemical reactivity which could not be solved with conventional electrodes or would have required sophisticated techniques. By miniaturising an electrode one may investigate in true time and in their true environment processes that occur on a sub microsecond timescale.

1.5 Electrochemical Techniques

1.5.1 Cyclic Voltammetry (CV)

Cyclic voltammetry is perhaps the most powerful and widely used electrochemical technique in use today. For generations it has been used successfully by physical and analytical electrochemists in the course of their work. Traditionally a qualitative technique, it has found ever more application in quantitative work as instrumental, experimental, and electrode advances have been achieved. In particular, it has found widespread application in the investigation and characterisation of modified electrode processes, especially in the study of mechanisms and rates of electron transfer.[126]

In cyclic voltammetry, the current response of an electrode is excited by a triangular waveform such as that shown in Figure 12.[27] The potential is varied linearly versus a reference electrode until it reaches a specified potential, whereupon the scan direction is inverted and the potential is reversed to its original value. This potential *cycling* is often repeated several times. Depending on the composition of the sample and whether oxidation or reduction of this sample is initially required, the initial direction of the scan may be positive or negative. Typical experimental time scales in cyclic voltammetry vary from hundreds of seconds down to microseconds. In CV experiments the cell current is recorded as a function of the applied potential (and therefore time).

The type of CV recorded will depend very much on the conditions under which the experiment was carried out. Depending on what type of mass transport is taking place due to the size of electrode used, the scan rate employed, and whether the solution is hydrodynamic or acquiescent the voltammogram will acquire a different shape. Because a range of electrode sizes and experimental time scales have been used throughout the course of this work it is beneficial to look at what happens under the different circumstances.

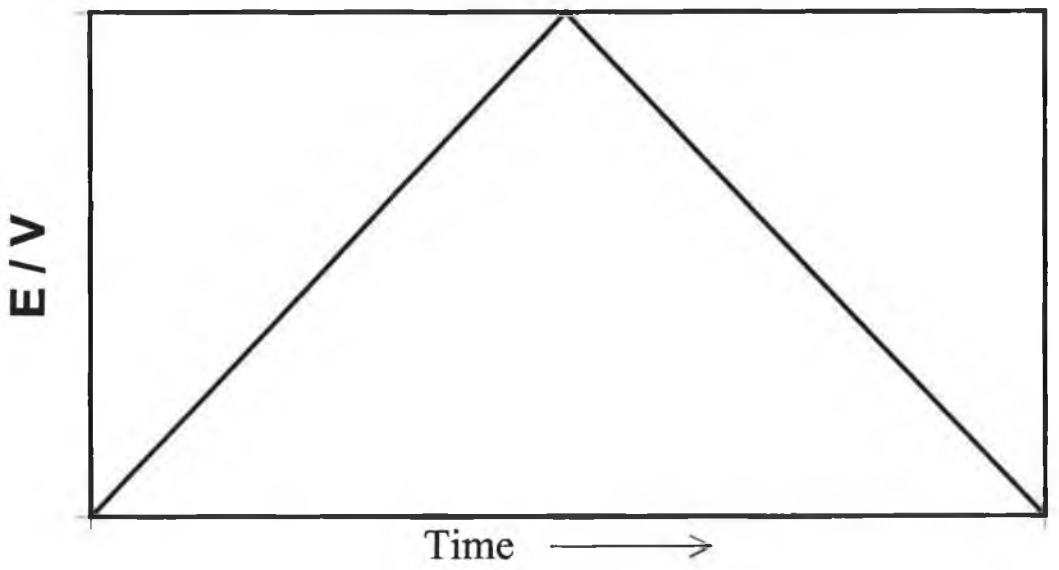

Figure 12 Triangular waveform

Solution Phase CV.

An electrochemical cell in which only reactant, R, is initially present is considered. A redox reaction occurs because a potential is applied causing R to be oxidised or reduced to the product, O. When the potential is scanned towards the formal potential, $E^{o\prime}$, the concentration of R at the electrode surface decreases while that of O increases and a concentration gradient is set up. However, at all times there is still a very large excess of R out in the bulk solution. At $E^{o\prime}$, there exists 50% R and 50% O at the electrode surface, the gradients are steeper and therefore an increase in current is observed. Past $E^{o\prime}$, the concentration of R is essentially negligible at the electrode surface while that of O has increased substantially. A cyclic voltammogram for a reversible, freely diffusing solution phase species, recorded at high sweep rate is shown in Figure 13. Because of the short experimental time scale linear diffusion predominates. When the surface concentration of R approaches zero the current cannot rise any further. R is continually being transported to the electrode surface by linear diffusion but has to travel further and further as time passes, the concentration gradients begin to fall causing the current to decay and a peak shaped response dictated by semi-infinite diffusion, is observed. On the reverse

sweep there is a high concentration of O at the electrode surface. This continues to be formed until the applied potential nears $E^{o\prime}$ at which point O is converted back to R. The same regime is then followed as with the forward scan.

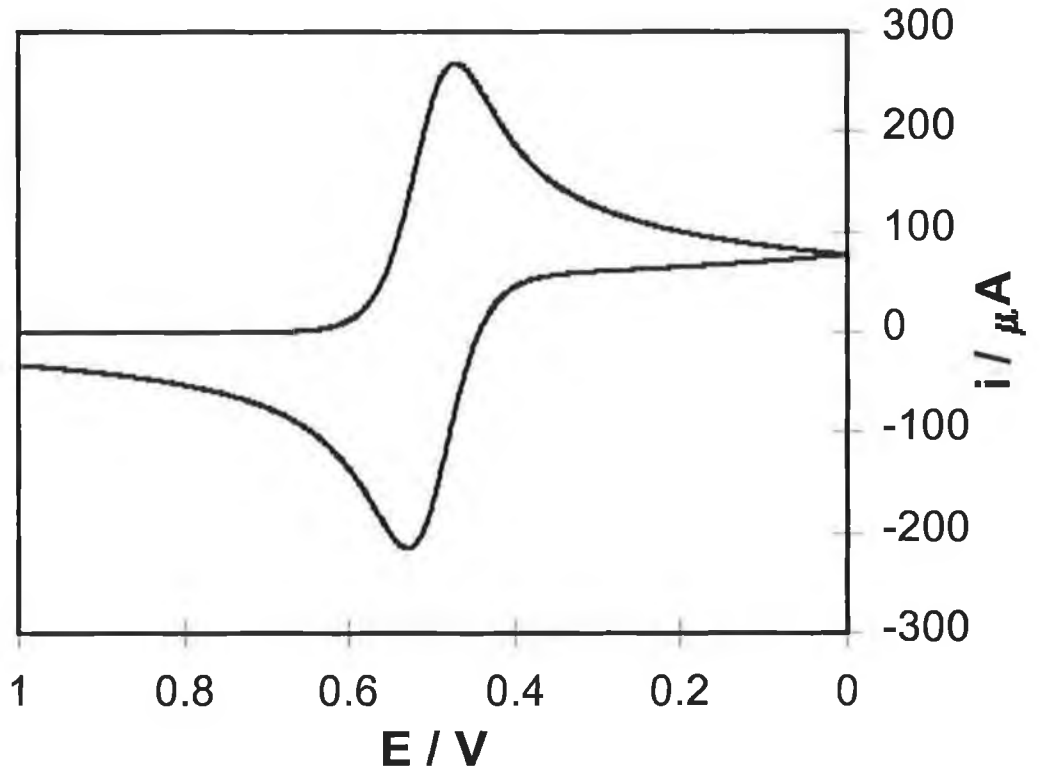

Figure 13 Cyclic voltammogram of a freely diffusing species at high scan rate.

A typical cyclic voltammogram for a reversible, freely diffusing solution phase species, recorded at low scan rate is shown in Figure 14. In this experiment, the sweep rate is sufficiently low for a *steady state* response to be observed. A steady state response is observed when either the solution is being stirred, hydrodynamic voltammetry, or the electrode area is sufficiently small for spherical or radial diffusion to occur. As hydrodynamic voltammetry has not been employed in the course of this work we will confine our discussion to steady state responses due to small electrode areas. As stated above, concentration gradients are set up when the applied potential is varied. In this case the reactant has sufficient time to reach the electrode, become oxidised or reduced, and diffuse away from the

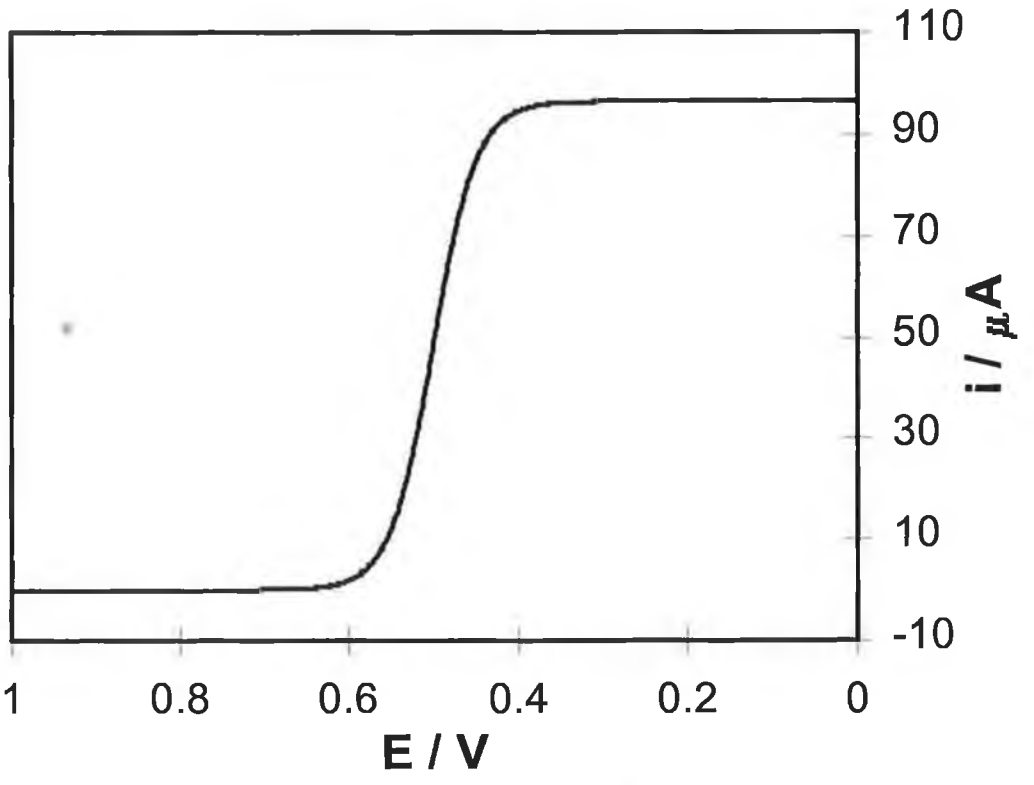

Figure 14 Cyclic voltammogram of a freely diffusing species at low scan rate.

electrode, while there is always sufficient reactant available for the reaction to proceed due to the large the spherical diffusion volume which exists. As the concentration of the reactant nears zero (past $E^{o\prime}$) the current cannot increase further and reaches a plateau whereby the observed current becomes independent of applied potential indicating a steady state response. The reverse scan tracks back along the forward scan.

A number of important parameters, which are important in quantifying reversible solution phase CVs recorded at high and low scan rate, can now be identified. The peak current, i_p, in a high sweep rate, semi-infinite diffusion, CV is given by the Randles-Sevcik equation;[18]

$$i_p = 0.443nFAC\left(\frac{nF}{RT}\right)^{1/2} v^{1/2} D_o^{1/2} \qquad (14)$$

or at 25 °C, for n the number of electrons, R the gas constant in J mol^{-1} K^{-1}, F the Faraday constant in coulombs, A the electrode area in cm^2, D_o the diffusion coefficient of the electroactive species in cm^2/sec, C the concentration of electroactive species in mol/cm^3, and v the scan rate in V/sec, i_p in amperes is

$$i_p = (2.69 \times 10^5) n^{3/2} A D_o^{1/2} v^{1/2} C \qquad (15)$$

It can be seen from the above equations that the peak current, i_p, depends on the square root of scan rate, v, i.e., $i_p \propto v^{1/2}$ for diffusion controlled CVs. Also, the ratio of anodic and cathodic currents, i_{pa} and i_{pc}, respectively is unity;

$$\frac{i_{pa}}{i_{pc}} = 1 \qquad (16)$$

while another noteworthy condition is that the peak-to-peak separation, ΔE_p, for a reversible reaction is $59/n$ mV.

For steady state processes the current observed, the limiting current, i_L, is given by

$$i_L = 4nFD_o rC \qquad (17)$$

where r is the radius of the electrode.

Surface confined CV.

A cyclic voltammogram of a surface confined species, Figure 15, looks radically different from the diffusion controlled CV shown in Figure 13. The major differences between this CV and that of a solution phase one are that the peaks are sharp and symmetrical, the current rising from essentially zero to a peak value and then falling again to zero, and there is no peak-to-peak separation. The symmetrical peaks arise because there is a fixed amount of reactant at the electrode surface

available to undergo a reaction that is not hindered by mass transfer limitations. The peak current for a surface confined CV is given by;

$$i_p = \frac{n^2 F^2}{4RT} \Gamma v A \tag{18}$$

where Γ is the surface coverage. The charges under the anodic and cathodic peaks are equal and can be used to calculate Γ, which is a measure of the area of the electrode surface covered with the electroactive species,

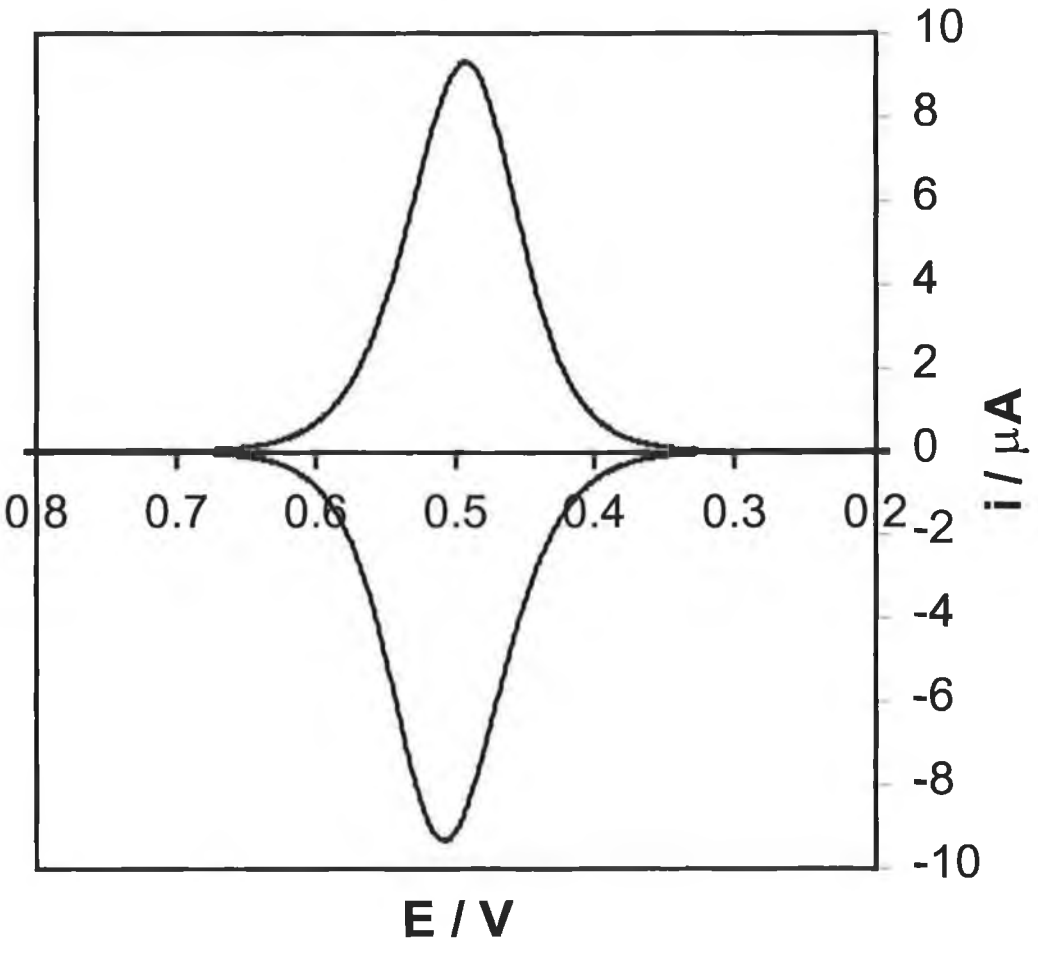

Figure 15 Cyclic voltammogram of a redox active surface confined species.

$$\Gamma = \frac{Q}{nFA} \tag{19}$$

where Q is the charge under either the oxidation or reduction peak in coulombs. Peak width at height (maximum), fwhm, for a surface confined species is 90.6/n mV and is a useful parameter for determining the ideality of the electrochemical response, influence of interactions, and the number of electrons involved in the oxidation/reduction reaction. The peak current for a reversible surface confined reaction varies linearly with scan rate, $i_p \propto \nu$.

Applications of cyclic voltammetry are wide and varied. They include applications in the study of electrode kinetics,[81,82] determination of diffusion coefficients,[127] examination of microelectrode performance[128,129] and determination of electrode areas.[130]

1.5.2 Potential Step Chronoamperometry (CA)

As the name suggests, chronoamperometry involves the application of a potential step and analysis of the resulting current-time decay, or transient. The major differences between CV and CA are that instead of varying the potential linearly as in CV, the potential is changed instantaneously in CA and the resulting current is recorded as a function of time. CA experiments usually involve stepping the potential to a region where all of the reactant, R, at the electrode surface is oxidised or reduced to the product, O, and this generates a large initial current. The concentration gradients decrease with time because of an ever increasing depletion layer, causing the current to decrease. The current decay for a reaction involving a solution phase species follows the Cottrell equation;[18]

$$i(t) = \frac{nFAD_o^{1/2}C}{\pi^{1/2}t^{1/2}} \tag{20}$$

It is clear from this equation that the current, i, decays with square root time, t. Therefore a plot of i, versus $t^{1/2}$ is linear, should pass through the origin, and the slope provides the diffusion coefficient of the electroactive species.

For a reaction involving a surface confined species, the capacitive current, i_C, is given by;

$$i_C = \frac{\Delta E}{R}\exp\left(\frac{-t}{RC}\right) \tag{21}$$

where ΔE is the magnitude of the potential amplitude, R is the total cell resistance and C is the double layer capacitance. Therefore, from a plot of the logarithm of the current versus time both the resistance and capacitance can be determined. The Faradaic current, i_F, is given by;

$$i_F(t) = kQ\,exp(-kt) \tag{22}$$

where k is the rate constant and Q is the total charge passed during the Faradaic reaction. From a semi-log of current versus time, k and Q can be determined from the slope and intercept respectively. Chronoamperometry has been used by several research groups in preference over cyclic voltammetry due to its ease of application and sensitivity in providing information about the relative perfection of adsorbed monolayers.

1.5.3 Normal Pulse Voltammetry (NPV)

The basis of pulse voltammetry is the potential step.[27,131] Pulse voltammetric techniques were initially developed to provide enhanced sensitivity in analytical applications as compared to classical polarography.[20] The objective in pulse polarographic techniques was to synchronize the pulses with the drop growth and reduce capacitive current contribution by sampling at the end of drop life. After

applying a potential pulse the capacitive current decays faster than the Faradaic current thus the current is measured at the end of the pulse. Therefore, the sensitivity is increased and better characteristics for analytical applications are achieved.

The techniques of differential pulse and normal pulse are the most popular due to their sensitivity and ease of application, and it normal pulse voltammetry which has been used in this research. In normal pulse voltammetry a fixed potential, E_1, at which no Faradaic reaction takes place is applied to the electrode, and then a short duration pulse is applied and the current recorded shortly before the potential is returned to E_1. Since the current is measured towards the end of the pulse lifetime, the capacitive current has died away and only Faradaic current is recorded. After another period of time at E_1 the process is repeated with a slightly larger pulse and this process is continued using equal increment pulse increases until the potential range of interest has been examined. The current-potential response takes the shape of a steady state voltammogram, Figure 14, except that the currents are significantly larger due to the greater mass transport afforded by this technique.[18]

For the evaluation of kinetic parameters associated with heterogeneous electron transfer between an electrode and a solution phase species, normal pulse voltammetry can be used. The current-potential relationship for the NPV of freely diffusing species for the oxidation process is given by;[132,133]

$$E = E^* \pm \frac{RT}{\alpha \pm nF} ln \left\{ X \left[\frac{1.75 + X^2 \left[1 + exp(\pm\xi) \right]^2}{1 - X\left[1 - exp(\pm\xi) \right]} \right]^{1/2} \right\} \qquad (23)$$

With

$$E^* = E^o \pm \frac{RT}{\alpha \pm nF} ln \left\{ \frac{4}{3^{1/2}} \frac{k^o \tau^{1/2}}{D} \right\} \qquad (24)$$

where E is the electrode potential, E^o is the reversible half wave potential, α is the anodic transfer coefficient, k^o is the standard heterogeneous electron transfer rate constant, ξ a dimensionless parameter expressed as

$$\xi = \left\{\left(\frac{nF}{RT}\right)\left(E - E^o\right)\right\} \tag{25}$$

τ the sampling time, D is the diffusion coefficient as determined by cyclic voltammetry, and X is the ratio of the current at the potential E to the anodic limiting diffusion controlled current.

A plot of the right hand side of Equation 23 versus E is linear with a slope of

$$\left(\left(\frac{RT}{\alpha nF}\right)^{-1}\right) \tag{26}$$

and an intercept of E*. Assuming D is the same for the anodic and cathodic processes, and using the value of the formal potential from CV, k^o and α can be evaluated. This method of estimating the kinetic parameters of a system have been used successfully by several authors.[134,135,136]

1.5.4 Spectroelectrochemistry

The principle disadvantage in using electrochemical techniques alone for the elucidation of reaction mechanisms and the determination of kinetic parameters is that that such purely electrical measurements lack molecular specificity, i.e., the resultant current observed after an electrochemical experiment is carried out does not supply information about the identity of reaction products or intermediates. Therefore, it is obvious that techniques that can provide information of this type are necessary. Spectroscopic techniques such as IR and NMR have long been employed

to provide information on the identity time dependence of reaction intermediates in conventional solution chemistry.

In recent times, a considerable effort has been expended in adapting some of these spectroscopic techniques so that they can be applied *in situ* in an electrochemical cell. In addition, new techniques for the study of the electrode/solution interface have been developed. This field, known as spectroelectrochemistry, is currently a very active area of electrochemical research, and many of the techniques developed are now being routinely applied.[20]

In its simplest and most widely used form, spectroelectrochemistry involves obtaining the UV-visible-Near InfraRed spectra of electrogenerated species in solution by passing a probe light beam directly through an optiaclly transparent working electrode. In this way, the change in the absorbed light density as a result of the production or consumption of a species in the electrode process can be measured directly. Such an approach relies on the existence of optically transparent electrodes (OTEs) which fall essentially into three categories:[137,138,139,140]

1. Metal minigrids
2. Thin coatings of semiconductors or metals on glass
3. Reticulated vitreous carbon

Minigrids of Platinum, gold, silver, etc. can comprise several hundred wires/cm and allow up to 80% transmittance of the incident light. They can be used in both UV-visible-NIR and IR cells and behave as a planar electrode providing that the time of the spectral data collection is sufficient to allow the diffusion layers around each wire to overlap.

Thin layers of metals such as Pt, Au, Ag or even carbon, do give planar surfaces but they do have the disadvantage of balancing good conductivity with a sufficiently high transmittance. Thin layers of certain oxides such as SnO_2 (ITO) on glass substrates exhibit good conductivity, yet are almost completely transparent in

the visible. At first sight this may seem a contradiction in terms: a transparent metal. However, ITO is metallic by virtue of its extensive doping but transparent because the bandgap of the material is in the UV, and the free carrier adsorption is primarily in the IR. Coated-glass OTEs allow simple cell designs, with the OTE forming one of the cell windows.

Spectroelectrochemical cells for use in the UV-visible region are not, of course, constrained by solvent absorption and can thus be of a reasonable size to give acceptable electrochemical behaviour. However, a thin-layer approach is employed. Both the identification of a species and the determination of the kinetics of its formation or decay can be achieved with longer pathlength cells. However, in kinetic experiments, there is the proviso that the experiment can be performed before natural convection currents interfere with the measurements; i.e., the operator must be certain that the removal of a chromophore from the optical path is due to reaction and not due to convection currents. It should be noted that the strength of UV-visible spectroscopy does not lie primarily in the identification of unknown species as the information it provides is not of a molecularly specific nature.

In order to observe a short-lived species it may be necessary to employ a rapid-scanning spectrometer, such as a diode-array instrument (which can routinely acquire a 240-280 nm spectrum within 5ms). In addition, the absorbances of electrogenerated species can be very small and signal-averaging or phase-sensitive detection may be necessary to achieve the required signal-to-noise ratio.

One important advantage that UV-visible spectrometers possess over FTIR instruments is the ability to monitor the absorbance at a particular wavelength or over a wavelength range as a function of time. This allows kinetic measurements to be made on a relatively fast timescale with signal averaging being used to increase the signal-to-noise if necessary. A typical experiment in an OTE cell would generally involve stepping the potential from a potential where the reactant is stable to a potential where reaction occurs at a diffusion controlled rate. The absorbance at a wavelength where either the reactant or product absorbs is then followed as a

function of time. This is essentially analogous to the chronocoulometric experiments where linear diffusion of the electroactive species to the electrode is assumed.

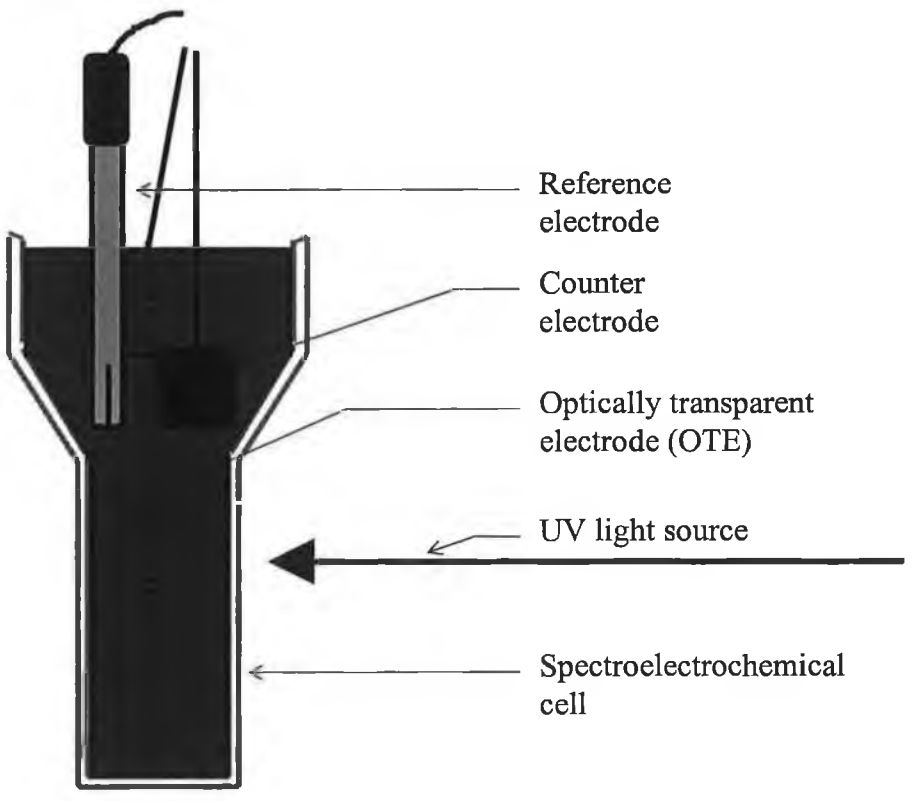

Figure 16 Spectroelectrochemical cell containing reference, counter, and working electrodes.

1.6 References

1 *Electroanalytical Chemistry - A Series Of Advances*, Bard, A. J. Ed. Vol. 13 Wiley, New York.

2 Forster, R. J.; Faulkner, L. R. *J. Am. Chem. Soc.* 1994, 116, 5444.

3 Forster, R. J.; Faulkner, L. R. *J. Am. Chem. Soc.* 1994, 116, 5453.

4 Forster, R. J.; Faulkner, L. R. *Anal. Chem.* 1995, 67, 1232.

5 Forster, R. J. *Analyst*, 1996, 121, 733.

6 Zapien, D. C.; Gui, J. Y.; Stern, D. A.; Hubbard, A. T. *J. Electroanal. Chem.* 1992, 330, 469.

7 Cao, E. Y.; Gao, P.; Gui, J. Y.; Lu, F.; Stern, D. A.; Hubbard, A. T. *J. Electroanal. Chem.* 1992, 339, 311

8 Hubbard, A. T. *Acc. Chem. Res.*, 1980, 13, 177.

9 Soriaga, M. P.; Wilson, P. H.; Hubbard, A. T.; Benton, C. S. *J. Electroanal. Chem.* 1982, 142, 317.

10 Soriaga, M. P. *Chem. Rev.* 1990, 90, 771.

11 Whitesides, G. M.; Ferguson, G. S.; Allara, D.; Scherson, D.; Speaker, L.; Ulman, A. *Crit. Rev. Surf. Chem.* 1993, 3, 49.

12 Chidsey, C. E. D.; Loiacono, D. N. *Langmuir* 1990, 6, 682.

13 Polymeropoulos, E. E.; Sagiv, J. *J. Chem. Phys.*, 1978, 69, 1836

14 Soriaga, M. P.; Hubbard, A. T. *J. Am. Chem. Soc.* 1982, 104, 2742.

15 Lane, R. F.; Hubbard, A. T. *J. Phys. Chem.* 1973, 77, 1401.

16 Murray, R. W. In *Electroanalytical Chemistry* Vol. 13 Bard, A. J. Ed. Marcel Dekker, New York, 1984.

17 Hubbard, A. T. *Crit. Rev Anal. Chem.* 1973, 3, 201.

18 Bard, A. J.; Faulkner, L. R. *Electrochemical Methods: Fundamentals and Applications;* Wiley: New York 1980.

19 Forster, R. J. In *Electrochemistry: Principles and Practice* Smyth, M. R., Cunnane, V. Eds.; Wiley: New York, 1997.

20 Southampton Electrochemistry Group *Instrumental Methods in Electrochemistry;* Ellis Harwood, England, 1985.

21 Von Helmholtz, H. L. F. *Ann. Physik*, 1853, 89, 211.

22 Von Helmholtz, H. L. F. *Ann. Physik*, 1879, 7, 337.

23 Guoy, G. *J. Phys. Radium*, 1910, 9, 457.

24 Guoy, G. *Compt. Rend.*, 1910, 149, 654.

25 Chapman, D. L. *Phil. Mag.*, 1913, 25, 475.

26 Stern, O. *Z. Elektrochem.*, 1924, 30, 508.

27 Brett, C. M. A.; Brett, A. M. O. *Electrochemistry: Principles, Methods, and Applications*; Oxford University Press: New York 1993.

28 Chidsey, C. E. D. *Science* 1991, 251, 919.

29 Porter, M. D.; Bright, T. B.; Allara, D. L.; Chidsey, C. E. D. *J. Am. Chem. Soc.* 1987, 109, 3559.

30 Miller, C.; Cuendet, P.; Gratzel, M. *J. Phys. Chem.* 1991, 95, 877.

31 De Levie, R. *Chem. Rev.* 1988, 88, 599.

32 Smith, C. P. White, H. S. *Anal. Chem.* 1992, 64, 2398.

33 Becka, A. M.; Miller, C. J. *J. Phys. Chem.* 1992, 96, 2657.

34 Creager, S. E.; Weber, K. *Langmuir*, 1993, 9, 844.

35 Becka, A. M.; Miller, C. J. *J. Phys. Chem.* 1993, 97, 6233.

36 Bard, A. J.; Abruña, H. D.; Chidsey, C. E. D.; Faulkner, L. R.; Feldberg, S. W.; Itaya, K.; Majda, M.; Melroy, O.; Murray, R. W.; Porter, M. D.; Soriaga, M. P.; White, H. S. *J. Phys. Chem.*1993, 97, 7147.

37 Xu, J.; Li, H.-L.; Zhang, Y. *J. Phys. Chem.* 1993, 97, 11497.

38 Lui, Y.-P.; Marshall, D. N. *J. Phys. Chem.* 1994, 98, 7162.

39 Andreu, R.; Fawcett, W. R. *J. Phys. Chem.* 1994, 98, 12753.

40 Rowe, G. K.; Creager, S. E. *J. Phys. Chem.*1994, 98, 5500.

41 Nuzzo, R. G.; Allara, D. L. *J. Am. Chem. Soc.* 1983, 105,4481.

42 Chidsey, C. E. D.; Porter, M. D.; Allara, D. L. *J. Electrochem. Soc.* 1986, 113, 130.

43 Nuzzo, R. G.; Fusco, F. A.; Allara, D. L. *J. Am. Chem. Soc.* 1987, 109,2358.

44 Laibinis, P. E.; Whitesides, G. M. *J. Am. Chem. Soc.* 1992, 114, 1990.

45 Walczak, M. M.; Chung, C.; Stole, S. M.; Widrig, C. A.; Porter, M. D. *J. Am. Chem. Soc.* 1991, 113, 2370.

46 Widrig, C. A.; Chung, C.; Porter, M. D. *J. Electroanal. Chem.* 1991, 310, 335.

47 Bryant, M. A.; Pemberton, J. E. *J. Am. Chem. Soc.* 1991, 113, 8284.

48 Curtin, L. S.; Peck, S. R.; Tender, L. M.; Murray, R. W.; Rowe, G. K.; Creager, S. E. *Anal. Chem.* 1993, 65, 386.

49 Laibinis, P. E.; Whitesides, G. M.; Allara, D. A.; Tao, Y.-T.; Parikh, A. N.; Nuzzo, R, G. *J. Am. Chem. Soc.* 1991, 113, 7152.

50 Demoz, A.; Harrison, D. J. *Langmuir* 1993, 9, 1046.

51 See Chapter 4

52 Bain, C. D.; Biebuyck, H. A.; Whitesides, G. M. *Langmuir* 1989, 5, 723.

53 Biebuyck, H. A.; Whitesides, G. M. *Langmuir* 1993, 9, 1766.

54 Bain, C. D.; Evall, J.; Whitesides, G. M. *J. Am. Chem. Soc.* 1989, 111, 7155.

55 Bain, C. D.; Troughton, E. B.; Tao, Y.-T.; Evall, J.; Whitesides, G. M.; Nuzzo, R. G. *J. Am. Chem. Soc.* 1989, 111, 321.

56 Bain, C. D. Whitesides, G. M. *J. Am. Chem. Soc.* 1989, 111, 7164.

57 Sabatani, E.; Rubinstein, I.; Maoz, R.; Sagiv, *J. Electroanal. Chem.* 1987, 219, 365

58 Finklea, H. O.; Snider, D. A.; Fedyk, J.; Sabatani, E.; Gafni, Y.; Rubenstein, I. *Langmuir* 1993, 9, 3660.

59 Finklea, H. O.; Snider, D. A.; Fedyk, J. *Langmuir* 1990, 6, 371.

60 Dubois, L.H.; Zegarski, B.R.; Nuzzo, R.G. *J. Am. Chem. Soc.* 1990, 112, 570.

61 De Long, H. C.; Buttry, D. A. *Langmuir* 1992, 8, 2491.

62 Hickman, J. J.; Ofer, D.; Zou, C.; Wrighton, M. S.; Laibinis, P. E.; Whitesides, G. M. *J. Am. Chem. Soc.* 1991, 113, 1128.

63 Weisshaar, D. E.; Lamp, B. D.; Porter, M. D. *J. Am. Chem. Soc.* 1992, 114, 5860.

64 Collard, D. M.; Fox, M. A. *Langmuir* 1991, 7, 1192.

65 Creager, S. E.; Rowe, G. K. *Anal. Chim. Acta* 1991, 246, 233.

66 Rowe, G. K.; Creager, S. E. *Langmuir* 1994, 10, 1186.

67 Folkers, J. P.; Laibinis, P. E.; Whitesides, G. M.; Deutch, J. *J. Phys. Chem.* 1994, 98, 563.

68 Hickman, J. J.; Laibinis, P. E.; Auerbach, D. I.; Zou, C.; Gardner, T. J.; Whitesides, G. M.; Wrighton, M. S. *Langmuir* 1992, 8, 357.

69 Gardner, T. J.; Frisbie, C. D.; Wrighton, M. S. *J. Am. Chem. Soc.* 1995, 117, 6927.

70 Finklea, H. O.; Ravencroft, M. S.; Snider, D. A. *Langmuir* 1993, 9, 223.

71 Rowe, G. K.; Creager, S. E. *Langmuir* 1991, 7, 2307.

72 Chidsey, C. E. D.; Bertozzi, C. R.; Putvinski, T. M.; Mujsce, A. M. *J. Am. Chem. Soc.* 1990, 112, 4301.

73 Bunding Lee, K. A. *Langmuir* 1990, 6, 709.

74 Miller, C.; Gratzel, M. *J. Phys. Chem.* 1991, 95, 5225.

75 Becka, A.M.; Miller, C.J. *J. Phys. Chem.* 1992, 96, 2657.

76 Finklea, H. O.; Hanshew, D. D. *J. Am. Chem. Soc.* 1992, 114, 3173.

77 Finklea, H. O.; Hanshew, D. D. *J. Electroanal. Chem.* 1993, 347, 327.

78 Finklea, H. O.; Liu, L.; Ravencroft, M. S.; Punturi, S. *J. Phys. Chem.* 1996, 100, 11852.

79 Groat, K. A.; Creager, S. E. *Langmuir* 1993, 9, 3668.

80 Carter, M. T.; Rowe, G. K.; Richardson, J. N.; Tender, L. M.; Terrill, R. H.; Murray, R. W. *J. Am. Chem. Soc.* 1993, 115, 10364.

81 Weber, K.; Creager, S. E. *Anal. Chem.* 1994, 66, 3164.

82 Tender, L. M.; Carter, M. T.; Murray, R. W. *Anal. Chem.* 1994, 66, 3173.

83 Acevedo, D.; Abruña, H. D. *J. Phys. Chem.* 1991, 95, 9590.

84 Hudson, J. E.; Abruña, H. D. *J. Phys. Chem.* 1996, 100, 1036.

85 Acevedo, D.; Bretz, R. L.; Tirado, J. D.; Abruña, H. D. *Langmuir* 1994, 10, 1300.

86 Bretz, R. L.; Abruña, H. D. *J. Electroanal. Chem.* 1995, 388, 123.

87 Bretz, R. L.; Abruña, H. D. *J. Electroanal. Chem.* 1996, 408, 199.

88 Tirado, J. D.; Abruña, H. D. *J. Phys. Chem.* 1996, 100, 4556.

89 Forster, R. J. *Inorg. Chem.* 1996, 35, 3394

90 Soriaga, M. P.; Hubbard, A. T. *J. Am. Chem. Soc.* 1982, 104, 2735.

91 Soriaga, M. P.; Hubbard, A. T. *J. Am. Chem. Soc.* 1982, 104, 3937.

92 Hubbard, A. T.; Stickney, J. L.; Soriaga, M. P.; Chia, V. K. F.; Rosasco, S. D.; Schardt, B. C.; Solomun, T.; Song, D.; White, J. H.; Wieckowski, A. *J. Electroanal. Chem.* 1984, 168, 43.

93 Soriaga, M. P.; Hubbard, A. T. *J. Phys. Chem.* 1984, 88, 1089.

94 Stern, D. A.; Laguren-Davidson, L.; Frank, D. G.; Gui, J. Y.; Lin, C.-H.; Lu, F.; Salaita, G. N.; Walton, N.; Zapien, D. C.; Hubbard, A. T. *J. Am. Chem. Soc.* 1989, 111, 877.

95 Gui, J. Y.; Stern, D. A.; Lin, C.-H.; Goa, P.; Hubbard, A. T. *Langmuir* 1991, 7, 3183.

96 Salaita, G. N.; Hubbard, A. T. *Catalysis Today* 1992, 12, 465.

97 Hubbard, A. T. *Chem. Rev.* 1988, 88, 633.

98 Laviron, E. *J. Electroanal. Chem.* 1981, 124, 9.

99 Laviron, E.; Roullier, L. *Electroanal. Chem.* 1983, 157, 7.

100 Laviron, E. *J. Electroanal. Chem.* 1983, 146, 15.

101 Laviron, E. *J. Electroanal. Chem.* 1984, 164,213.

102 Forster, R. J. *Langmuir*, 1995, 11, 2247.

103 Forster, R. J. *Anal. Chem.* 1996, 68, 3143.

104 Forster, R. J. *J. Electrochem. Soc.* 1997, 144, 1165.

105 Slavcheva, E.; Sokolova, E.; Raicheva, S. *J. Electroanal. Chem.* 1993, 360, 271.

106 Mo, Y.; Sandifer, M.; Sukenik, C.; Barriga, R. J.; Soriaga, M. P.; Scherson, D. *Langmuir* 1995, 11, 4626.

107 Sato, Y.; Fujita, M.; Mizutani, F.; Uosaki, K. *J. Electroanal. Chem.* 1996, 409, 145.

108 Chambers, J. Q. In *The Chemistry of Quinonoid Compounds*, *Vol II*; Patai, S., Rappoport, Z. Eds.; Wiley: New York, 1988; Ch 12.

109 Fleishmann, M.; Pons, S.; Rolison, D. R.; Schmidt, P. P. Eds. *Ultramicroelectrodes,* Datatech Systems, USA, 1987.

110 Montenegro, M. I.; Queiros, M. A.; Daschbach, J. L. Eds. *Microelectrodes: Theory and Applications*, Kluwer Academic, Netherlands 1991.

111 Carter Ed. Molecular Electronic Devices II; Marcel Dekker: New York, 1987.

112 Wightman, R. M.; Amatore, C.; Engstrom, R. C.; Hale, P. D.; Kristensen, E.W.; Kuhr, W. G.; May, L. J. *Neuroscience* 1988, 25, 513.

113 Ferris, C. D. " Introduction to Bioelectrodes" Plenum Press, 1974.

114 Forster, R. J. *Chem. Soc. Rev.* 1994, 289.

115 *Physical Electrochemistry, Principles, Methods and Applications*, Ed. I . Rubinstein, Marcel Dekker Inc. 1995, 27.

116 Engstrom, R. C.; Weber, M.; Wunder, D. J.; Burgess, R.; Winquist, S. *Anal. Chem.* 1986, 158, 844.

117 Liu, H.-Y.; Fan, F.-R. F.; Lin, C. W.; Bard, A. J. *J. Am. Chem. Soc.* 1986, 108, 3838.

118 Amatore, C.; Kelly, R. S.; Kristensen, E. W.; Kuhr, W. G.; Wightman, R. M. *J. Electroanal. Chem.* 1986, 213, 31.

119 Schroeder, T. J.; Jankowski, J. A.; Kawagoe, K. T.; Wightman, R. M.; Lefrou, C.; Amatore, C. *Anal. Chem.* 1993, 65, 2711.

120 Kristensen, E. E.; Wilson, R. L.; Wightman, R. M. *Anal. Chem.* 1986, 58, 986.

121 Knecht, L. A.; Guthrie, E. J.; Jorgenson, J. W. *Anal. Chem.* 1984, 56, 479.

122 White, J. G.; St. Claire, R. L.; Jorgenson, J. W. *Anal. Chem.* 1986, 58, 293.

123 White, J. G.; Jorgenson, J. W. *Anal. Chem.* 1986, 58, 293.

124 Xu, C. Ph.D. Thesis, *University of Illinois Urbana Champaign*, 1992.

125 Andrieux, C. P.; Hapiot, P.; Saveant, J-M. *Chem. Rev.* 1990, 90, 723.

126 Brown, A. P.; Anson, F. C. *Anal. Chem.* 1977, 49, 1585.

127 Moressi, M. B. Fernández, H. *J. Electroanal. Chem.* 1994, 369, 152.

128 Chen, X.; Zhuang, J.; He, P. *J. Electroanal. Chem.* 1989, 271, 257.

129 Wipf, D. O.; Michael, A. C.; Wightman, R. M. *J. Electroanal. Chem.* 1989, 269, 15.

130 Trasatti, S.; Petrii, O. A. *J. Electroanal. Chem.* 1992, 327, 354.

131 He, P.; Avery, J. P.; Faulkner, L. R. *Anal. Chem.* 1982, 54, 1313.

132 Vetter, K. J. *Electrochemical Kinetics*, Academic Press, New York and London, 1987.

133 Matsuda, H. *Bull. Chem. Soc. Jpn.*, 1980, 53, 3439.

134 Forster, R. J. Ph.D. Thesis, Dublin City University, 1990.

135 Clarke, A. P. Ph.D. Thesis, Dublin City University, 1992.

136 Forster, R. J.; Vos, J. G. *J. Electroanal. Chem.* 1991, 314, 135.

137 Heineman, W. R. *Anal. Chem.* 1978, 50, 390.

138 De Angelis, T. P.; Hurst, R. W.; Yacynych, A. M.; Mark, Jr., H. B.; Heinman, W. R.; Mattson, J. S. *Anal. Chem.* 1977, 49, 1395.

139 Cieslinski, R.; Armstrong, N. R. *Anal. Chem.* 1979, 51, 565.

140 Murray, R. W.; Heinman, W. R.; O'Dom, G. W. *Anal. Chem.* 1967, 39, 1666.

Chapter 2

Synthesis and Characterisation of Redox Active Self-Assembling Complexes

2.1 Introduction

2.1.1 Metal complexes

Metal complexes are of great practical importance. They are used in metal-ion sequestration or removal, solvent extraction, dyeing, leather tanning, electroplating, catalysis, water softening, and other industrial processes. New processes are found regularly in which metal complexes are used. Biochemistry contains many examples of metal complexes at work. For example, a cobalt complex is responsible for vitamin B_{12}, an iron complex makes up the haemoglobin in blood, and a magnesium complex is responsible for chlorophyll.[1] For these and other reasons, metal complexes have been studied extensively by scientists for generations. Many research groups are involved the synthesis of model systems which mimic the activity of naturally occurring assemblies. If we can understand how electron transfer in these systems works, we may be able to synthetically produce more sophisticated systems for the production of, for example, light harvesting systems, optoelectronic devices, molecular electronic components, etc. In this chapter, we report the synthesis and characterisation of two metal complexes. We have studied the thermodynamics and kinetics of electron transfer in these model systems to understand those issues, such as distance, bridging ligand structure, etc. that dictate the rate of electron transfer across interfaces. This information is of fundamental interest and is directly important for the development of molecular electronics.

2.1.2 Anthraquinones

Many pigments and dyes of historical interest exhibit the capability of forming co-ordination complexes. The production and use of pigments and dyes has developed from an ancient craft into a modern day science. From a co-ordination chemistry point of view, the most important class of dyes, has historically been the red colours.[2] All the red colorants, whether they be of animal or vegetable origin, are derivatives of anthraquinone (Scheme 1). The dye *Madder* which is principally red in colour originates from the roots of the *Rubia tinctorum* plant.[3] The roots of this plant were known as *alizari*, hence the name *alizarin* which is the principle red colouring matter in madder.[3] In most sources that describe dyeing with anthraquinone or its many derivatives, the use of a metallic salt is mentioned. This information serves to illustrate just how long the use of anthraquinones and their metal complexes have been known and used for practical purposes. We have characterised a surface active anthraquinone with the ultimate objective of investigating the intricate proton/electron transfer reactions which take place in monolayers of these materials. Also, we have synthesised and characterised a metal complex of an anthraquinone and examined the electrochemistry of this novel material.

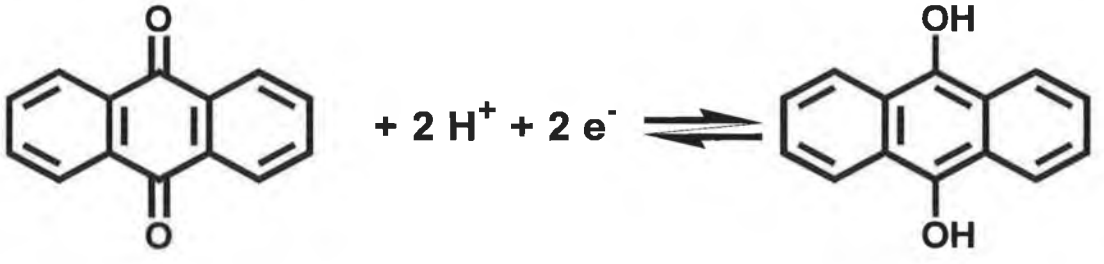

Scheme 1 Anthraquinone (left) and its reduced form hydroquinone (right).

2.2 Synthesis and Characterisation

2.2.1 Materials and Instrumentation

Cyclic Voltammetry (CV)

Cyclic voltammetry was performed using either a CH Instruments Model 660 or an EG&G M270 potentiostat/galvanostat. Voltammograms were obtained on reaction solutions using platinum microelectrodes without adding of supporting electrolyte. Solution phase cyclic voltammetry of osmium complexes was performed in methanol with 0.1 M $LiClO_4$ as supporting electrolyte. The voltammetry of alizarin and $QCat^{2-}$Ru-1,2 was performed in DMF with 0.1 M $TEABF_4$, while the analysis of 2,7-AQDS was performed in 1.0 M $HClO_4$. In all cases a Ag/AgCl reference electrode and a platinum counter electrode were employed.

High Performance Liquid Chromatography (HPLC)

HPLC was carried out using a Waters 510 HPLC pump equipped with a 20 μl injector loop and a partisil SCX radial PAK cartridge. A Waters 990 photodiode array detector interfaced with a NEC PAC III computer was used for detection and readout. The detection wavelength was 280 nm and a flow rate of 1.8 ml per minute was used. A mobile phase consisting of 80:20 acetonitrile:water (v/v) containing 0.1 M $LiClO_4$ was employed. This mobile phase has been optimised in DCU over several years and is the standard mobile phase used.

Absorption Spectroscopy (UV)

UV-vis spectra were obtained using a Shimadzu UV-3100 spectrophotometer interfaced with an IBM compatible 486 computer running UVPC personal spectroscopy software. Quartz cells of 1 cm path length were used. Baseline spectra were run using the blank solvent. The same solvent was also used as the reference. In all cases spectroscopic grade solvents or Milli-Q water was used.

Nuclear Magnetic Resonance Spectroscopy (NMR)

Proton NMR were carried out using a Bruker AC 400 MHz spectrometer. Samples weighing 25-30 mg were dissolved in approx. 2 ml d-D_2O or d-DMSO as indicated.

2.2.2 Synthesis and Characterisation of Transition Metal Complexes

Use of transition metal complexes is proving popular for the formation of molecular thin films on electrode surfaces.[4,5,6,7] Many articles exist in which the formation of transition metal containing, polymeric films on electrode surfaces has been described.[8,9,10,11] However, in recent times the modification of electrode surfaces with monolayers of transition metal complexes has become prominent leading to the development of organised structures. One only has to look at the abundance of work that has been carried out using ferrocene alkanethiols as reviewed in Chapter 1.[12] However, the use of osmium and ruthenium polypyridyl complexes for the formation of redox active monolayers has not received the same attention as the ferrocene alkanethiol counterparts. Only a few research groups has explored the use of these complexes for the formation of monolayer films.[13,14,15,16,17,18,19,20,21,22] Moreover, until very recently little research has been carried out on the use of these monolayers for modelling interfacial processes. Here, we continue this research by examining the electrochemistry of osmium and ruthenium containing monolayers on a variety of surfaces. In order to do this, the complexes $[Os(bpy)_2(p3p)_2]^{2+}$ and $QCat^{2-}$Ru-1,2, where Os is osmium, Ru is ruthenium, bpy is 2,2-bipyridyl, p3p is 4,4-trimethylenedipyridine, and Cat is 1,2-dihydroxy-9,10-anthraquinone have been synthesised and characterised.

2.2.3 Synthesis and Characterisation of $[Os(bpy)_2(p3p)_2]^{2+}$

The complex $[Os(bpy)_2Cl_2]$. was synthesised according to a method reported previously.[23] This parent complex is a useful starting material for the synthesis of complexes of the type $[Os(bpy)_2LCl_2]^{n+}$, $[Os(bpy)_2L_2]^{n+}$, $[Os(bpy)_2LL']^{n+}$ since the chloride can be selectively removed in two successive steps, where L and L' are ligands.

Synthesis of $[Os(bpy)_2Cl_2]Cl$

$$K_2[OsCl_6] + 2\ bpy + 2H_2O \xrightarrow{DMF} [Os(bpy)_2Cl_2]Cl.2H_2O + 2\ KCl + products$$

$$[Os(bpy)_2Cl_2]Cl.2H_2O \xrightarrow{heat} [Os(bpy)_2Cl_2]Cl + 2H_2O$$

1.9g $K_2[OsCl_6]$ (3.95 mmol) and 1.3g bpy (8.3 mmol) were suspended in DMF (40 cm^3) contained in a 100 cm^3 round bottomed flask. The suspension was refluxed for 1 hr while being stirred magnetically. After approx. 20 min crystals of KCl began to appear and the solution darkened. After 1 hr of refluxing the solution was allowed to cool for 1 hr. KCl was removed by filtration and 20 cm^3 ethanol was added to the filtrate in a 1 l beaker. The complex was precipitated out by slow addition of 500 cm^3 diethylether while stirring rapidly. The precipitate was filtered and air-dried.

Synthesis of $[Os(bpy)_2Cl_2]$

$$2\ [Os(bpy)_2Cl_2]Cl.2H_2O + Na_2S_2O_4 \longrightarrow 2\ [Os(bpy)_2Cl_2] + 2H_2SO_4 + 2H_2O$$

1 g $[Os(bpy)_2Cl_2]Cl.2H_2O$ (1.55 mmol) was dissolved in a mixture of 20 cm^3 DMF and 10 cm^3 methanol in a 500 cm^3 beaker. A dilute aqueous solution of $Na_2S_2O_4$ (2 g, 1.1 mmol in 200 cm^3) was added slowly with stirring over half an hour. The

solution was then cooled in an ice bath while the side of the beaker was scratched with a glass rod until crystals of the complex appeared. The crystals were filtered and washed with 2x10 cm^3 H_2O, 2x10 cm^3 methanol and 2x10 cm^3 diethylether.

Characterisation of $[Os(bpy)_2Cl_2]$

HPLC analysis yielded a single chromatographic peak (100%) at 1.94 min. That a single peak is observed indicates the formation of a single product. The retention time is consistent with that expected for a neutral species under these conditions.

A UV absorbance spectrum of the complex is shown in Figure 1 and is typical of an N_6 complex containing a group 6 transition metal. The sharp band at 300 nm is indicative of a π to π^* (bpy to bpy*) transition. The broad bands between 350 and 650 nm are indicative of metal-to-ligand-charge-transfer (MLCT) bands. The multiple peaks and the broadness shown suggests the influence of spin orbit coupling.

Figure 2 shows an NMR of $[Os(bpy)_2Cl_2]$. It reveals, as expected, eight proton peaks, each integrating for two protons, corresponding to the 8x2 polypyridyl protons on the complex split into four doublets and four triplets. Each pyridyl moiety shows two doublets representing the protons nearest the nitrogen, and two triplets representing the protons furthest from the nitrogen atom. That all the peaks are sharp and show no broadening indicates that the complex is pure and contains no Os^{3+}.
(Enlarged data is presented in Appendix 1)

Cyclic voltammetry of $[Os(bpy)_2Cl_2]$ is shown in Figure 3. A single redox couple is observed at approx. 0.0 V. This is characteristic of a one electron transfer involving an osmium complex containing two neutral ligands and two electronegative atoms.[24]

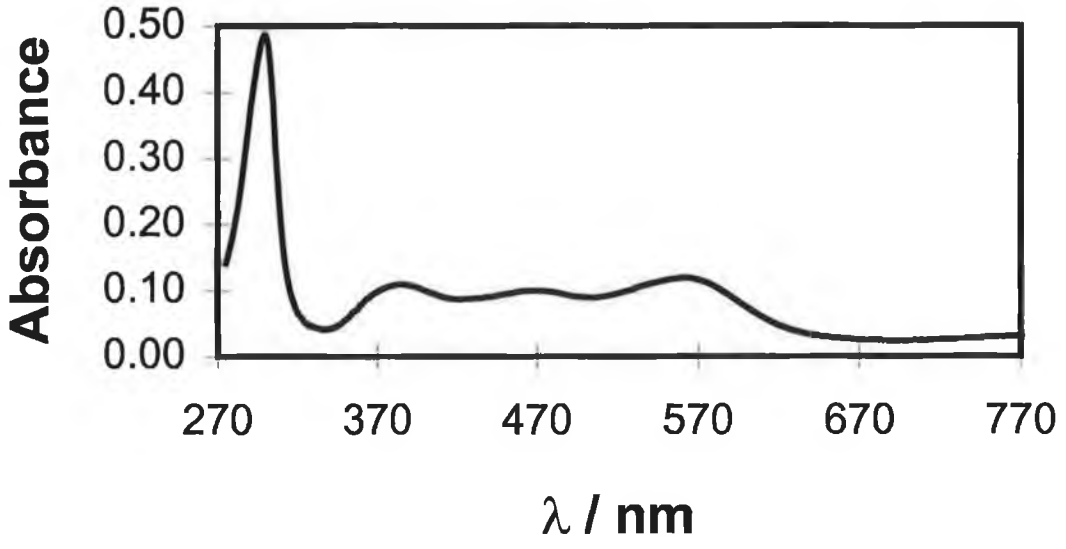

Figure 1 UV- visible spectrum of $[Os(bpy)_2Cl_2]$ in DMF.

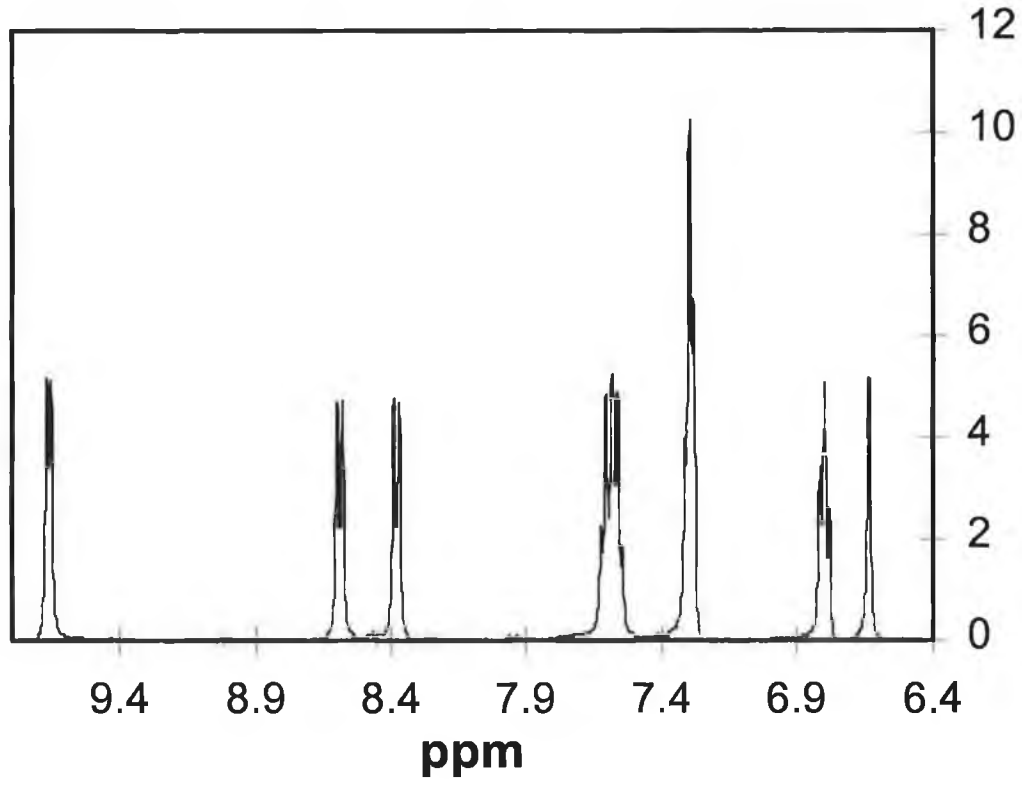

Figure 2 NMR of $[Os(bpy)_2Cl_2]$ in d-DMSO.

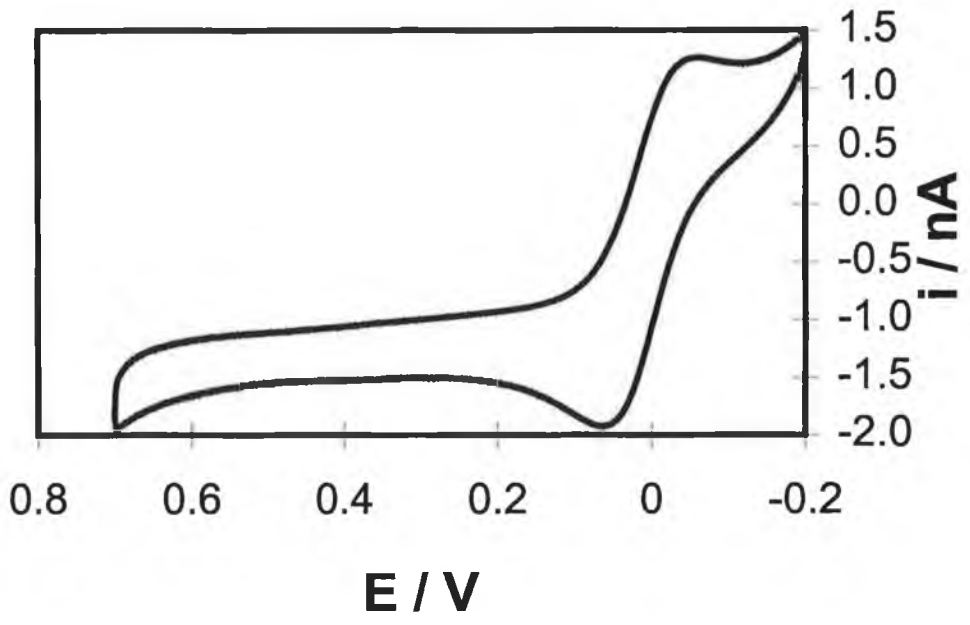

Figure 3 Cyclic voltammogram of $[Os(bpy)_2Cl_2]$ in methanol using a 25 μm radius platinum electrode. The supporting electrolyte is 0.1 M $LiClO_4$. The initial potential is -0.20 V and the scan rate is 0.100 V/s.

Synthesis of $[Os(bpy)_2(p3p)_2]^{2+}$

50 mg of $[Os(bpy)_2Cl_2]$ in 40 cm^3 methanol (0.09 mmol) was placed in a 250 cm^3 round bottomed flask and refluxed for 10 min to insure complete dissolution. 70 mg of 4,4-trimethylenedipyridine (98%, Aldrich) was dissolved in methanol (0.036 mmol), and 150 cm^3 milli-Q water added before refluxing the mixture for 15 hr. After approx. 10-12 hr the solution turned from red-brown to dark green. The reaction was monitored by HPLC and cyclic voltammetry until completion. Upon completion of the reaction, the volume was reduced by rotary evaporation to approx. 5 cm^3. Ammonium hexafluorophosphate (95+%, Aldrich) was added and the dark green product was collected by filtration. This was then washed with diethylether to remove of any remaining p3p. The product was recrystallised from aqueous methanol to give green-black crystals with a yield of 66 mg (82%).

Characterisation of $[Os(bpy)_2(p3p)_2]^{2+}$

Analysis of the complex yielded a single chromatographic peak (97%) at 3.27 min. This retention time is consistent with the charge on the complex being 2+.

A UV absorbance spectrum of the complex is shown in Figure 4 and is indicative of an N_6 complex containing neutral ligands.[24]

Figure 5 shows an NMR of $[Os(bpy)_2(p3p)_2]^{2+}$. The integration reveals 44 protons corresponding to the 8 protons on each dipyridyl and the 14 protons on each 4,4-trimethylenedipyridine. The trimethylene protons can be observed at the more negative ppm while the dipyridine and bipyridyl protons are observed at the more positive end of the scale. (An enlarged NMR is presented in Appendix 1)

Figure 6 shows a cyclic voltammetry of pure $[Os(bpy)_2(p3p)_2]^{2+}$. A single redox couple is observed at approx. 0.640 V which is characteristic of a one electron transfer involving an N_6 osmium complex.[24] The positive shift compared to the redox potential of $[Os(bpy)_2Cl_2]$ is expected due to the replacement of the electronegative chloride ions.

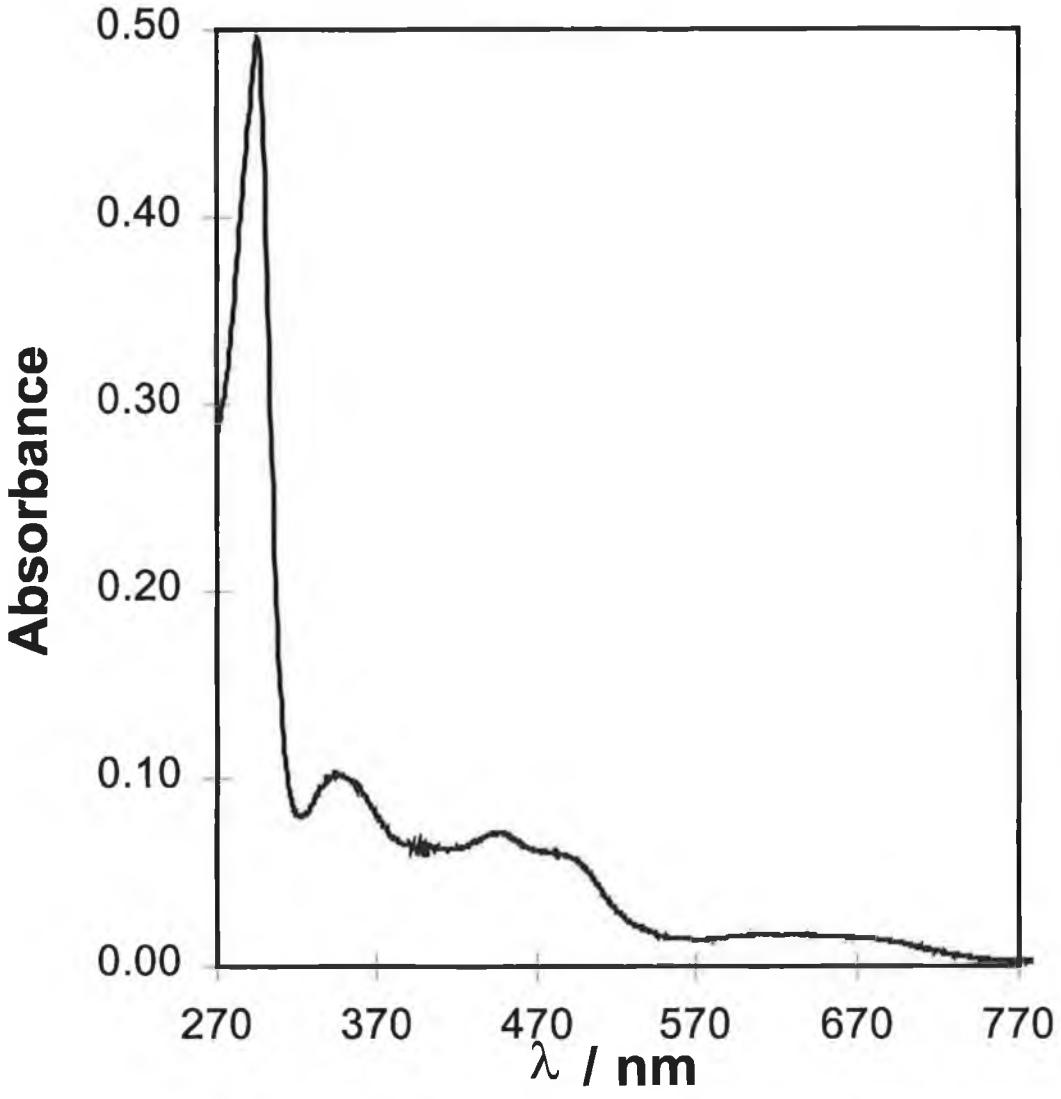

Figure 4 UV- visible spectrum of $[Os(bpy)_2(p3p)_2]^{2+}$ in DMF.

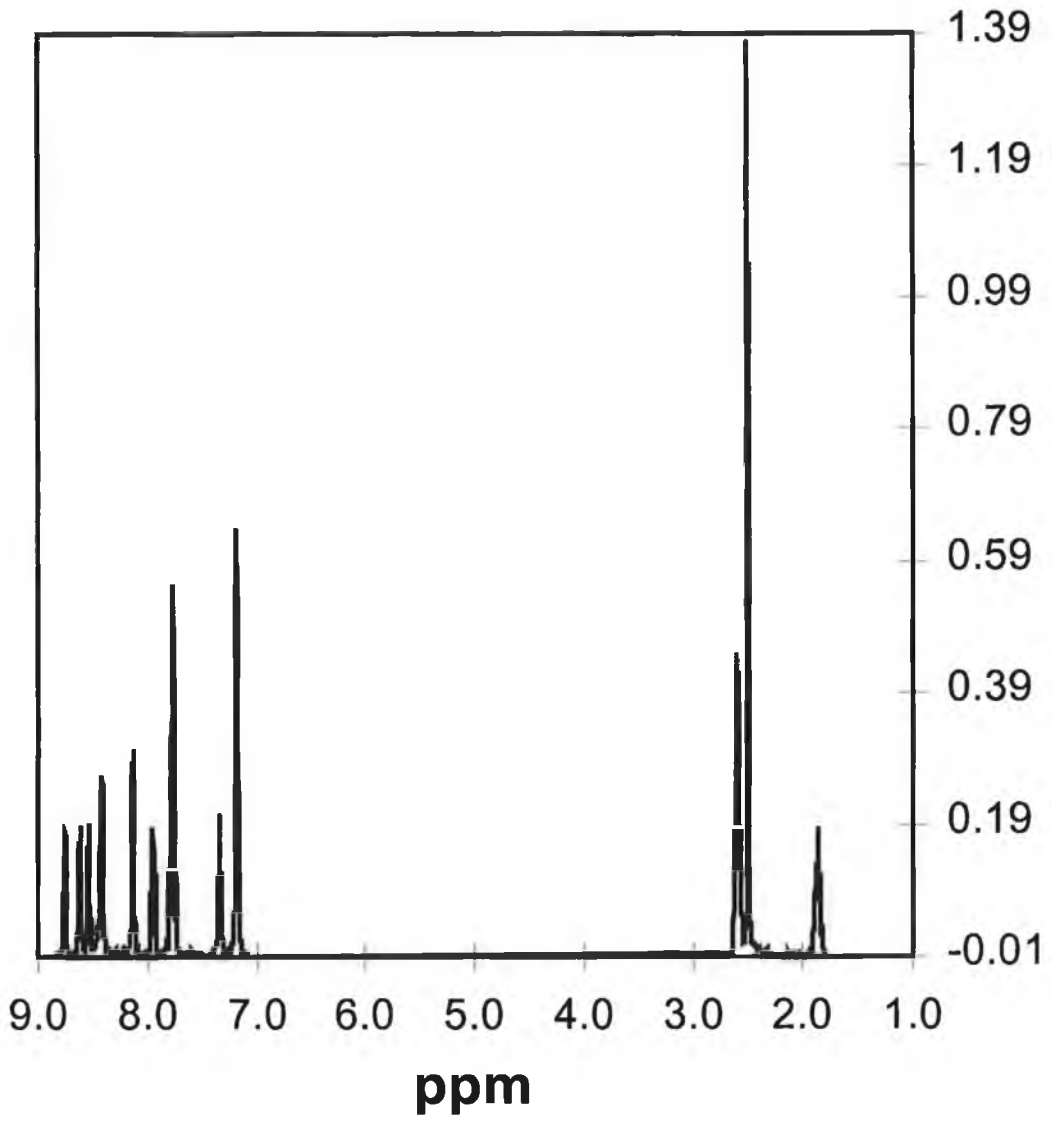

Figure 5 NMR of $[Os(bpy)_2(p3p)_2]^{2+}$ in d-DMSO.

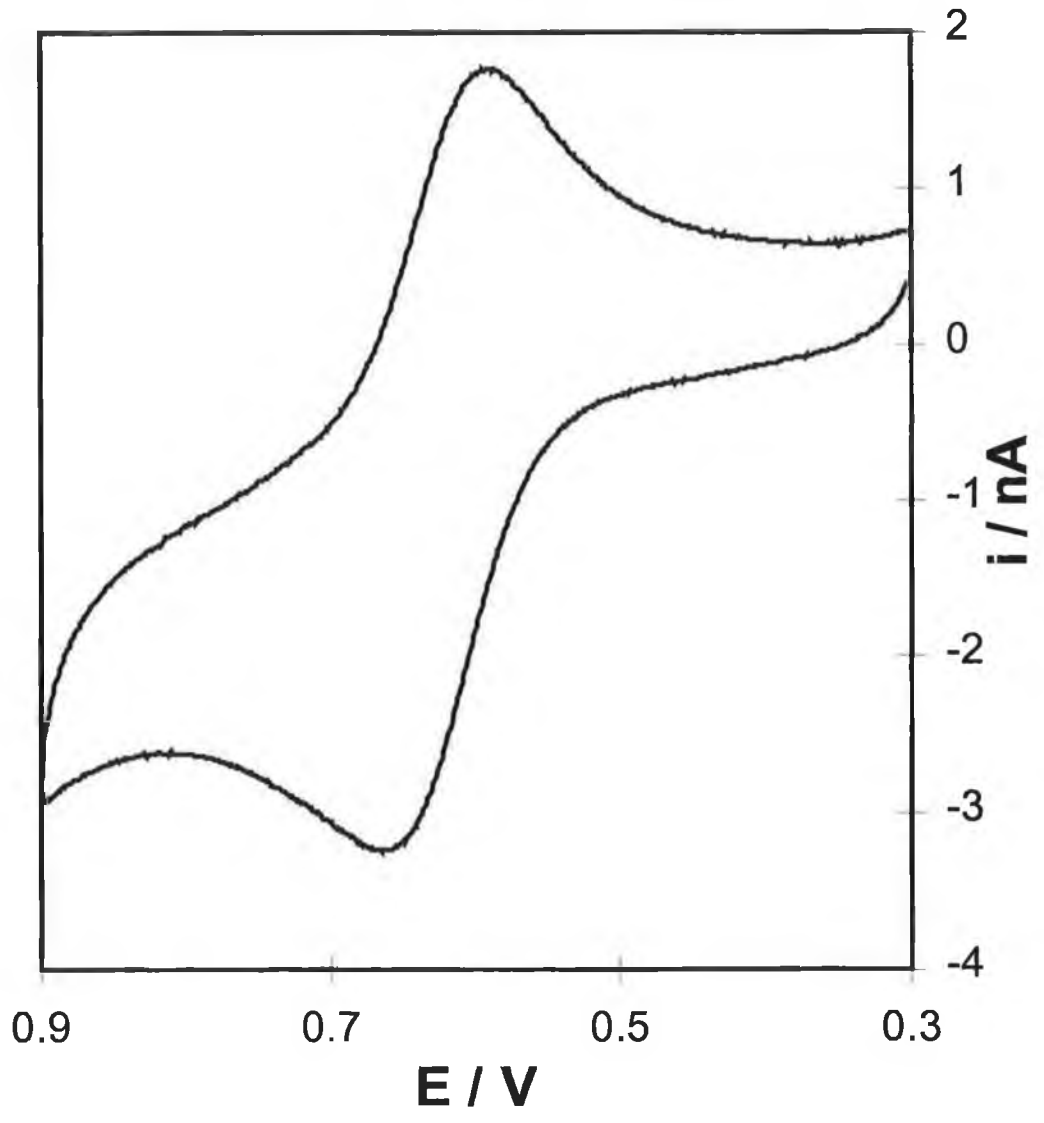

Figure 6 Cyclic voltammogram of pure $[Os(bpy)_2(p3p)_2]^{2+}$ at a 25 μm radius platinum electrode in methanol. The supporting electrolyte is 0.1 M $LiClO_4$ and the scan rate is 0.100 V/s.

2.2.4 Synthesis and Characterisation of $QCat^{2-}$-Ru-1,2

In order to accomplish the synthesis of $QCat^{2-}$Ru-1,2, $[Ru(bpy)_2Cl_2]$ and alizarin (1,2-dihydroxy-9,10-anthraquinnone) were required. $[Ru(bpy)_2Cl_2]$ was kindly provided by Christine O'Connor from DCU, while alizarin was purchased from Aldrich.

Characterisation of Alizarin

Alizarin was purchased from Aldrich (98%). HPLC analysis gave a single chromatographic peak at 1.68 min corresponding to a neutral compound. UV and NMR of the compound are shown in Figures 7 and 8 while CV is shown in Figure 9. The UV also corresponds to that expected for a neutral ligand. This suggests that the protons on the hydroxy groups remain attached even in organic solvents. The NMR reveals two singlets positive of 10 ppm which represent the hydroxy protons. Two triplets between 7.7 and 8.5 ppm and two doublets between 7.0 and 7.7 ppm represent the other protons on the molecule. Cyclic voltammetry provides two redox couples that appear to represent oxidation/reduction for each of the two ketonic moieties which are typically separated in non aqueous media. The redox reactions of the hydroxy groups are not observed within the potential range available.

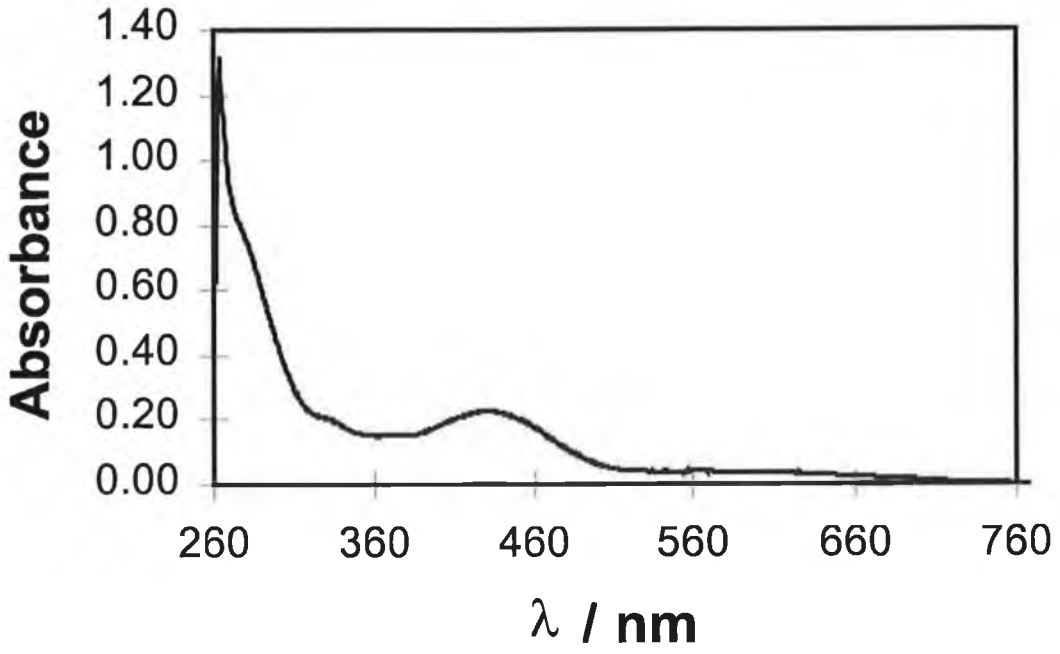

Figure 7 UV- visible spectrum of alizarin in DMF.

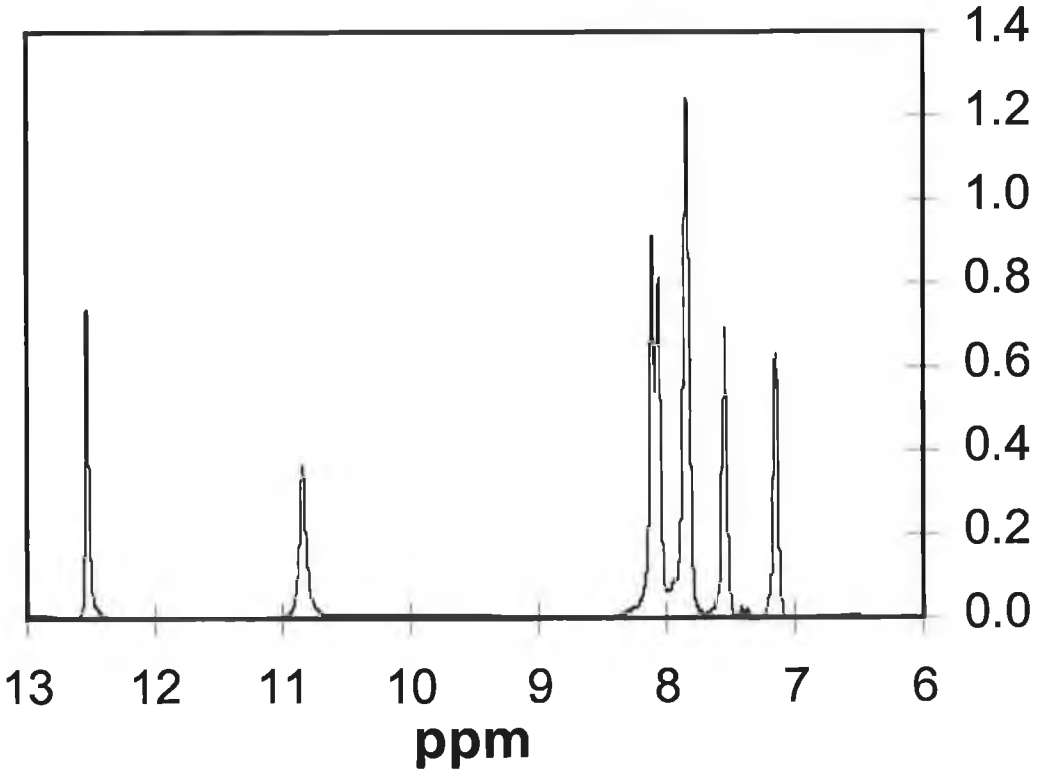

Figure 8 NMR of alizarin in d-DMSO.

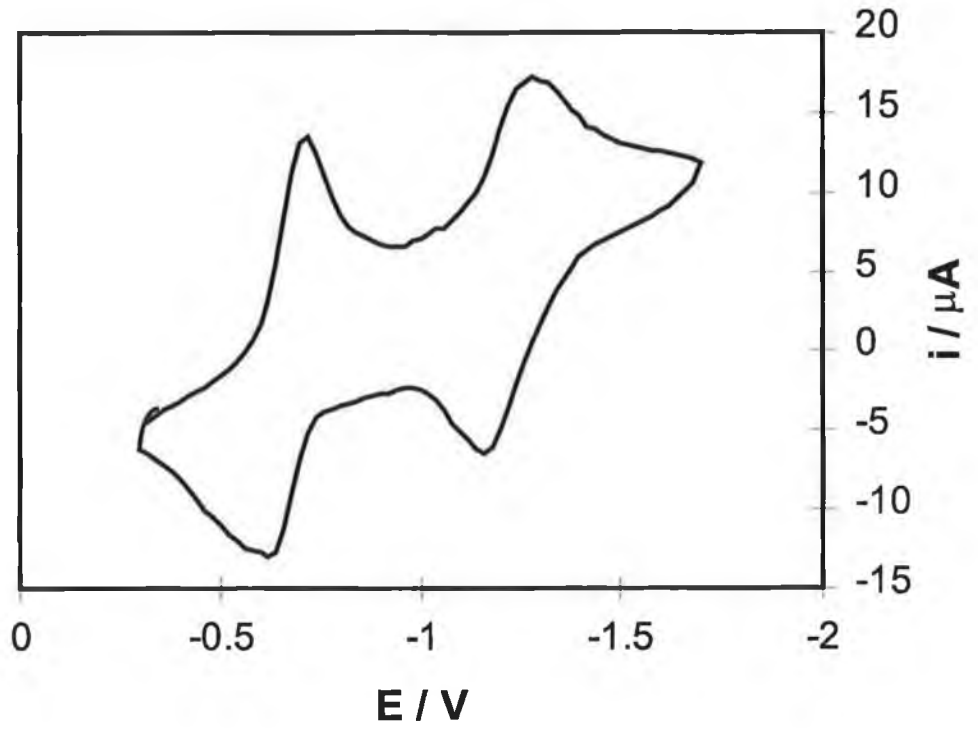

Figure 9 Cyclic voltammogram of alizarin at a 0.017 cm^2 mercury electrode in DMF. The supporting electrolyte is 0.1 M $TEABF_4$. The initial potential is -0.250 V.

Characterisation of [Ru(bpy)$_2$Cl$_2$]

$[Ru(bpy)_2Cl_2]$ was obtained from Christine O'Connor at DCU. HPLC, UV, NMR, and cyclic voltammetry were carried out to confirm the purity of the complex. HPLC of $[Ru(bpy)_2Cl_2]$ provided a single peak at 2.04 min. Figures 10 and 11 show the UV and NMR of $[Ru(bpy)_2Cl_2]$ which are similar to those reported above for the osmium, while Figure 12 shows the CV of the complex in methanol. That the redox potential is 0.38 V, is consistent with the expected difference between an osmium based complex ($[Os(bpy)_2Cl_2]$) and its ruthenium counterpart.

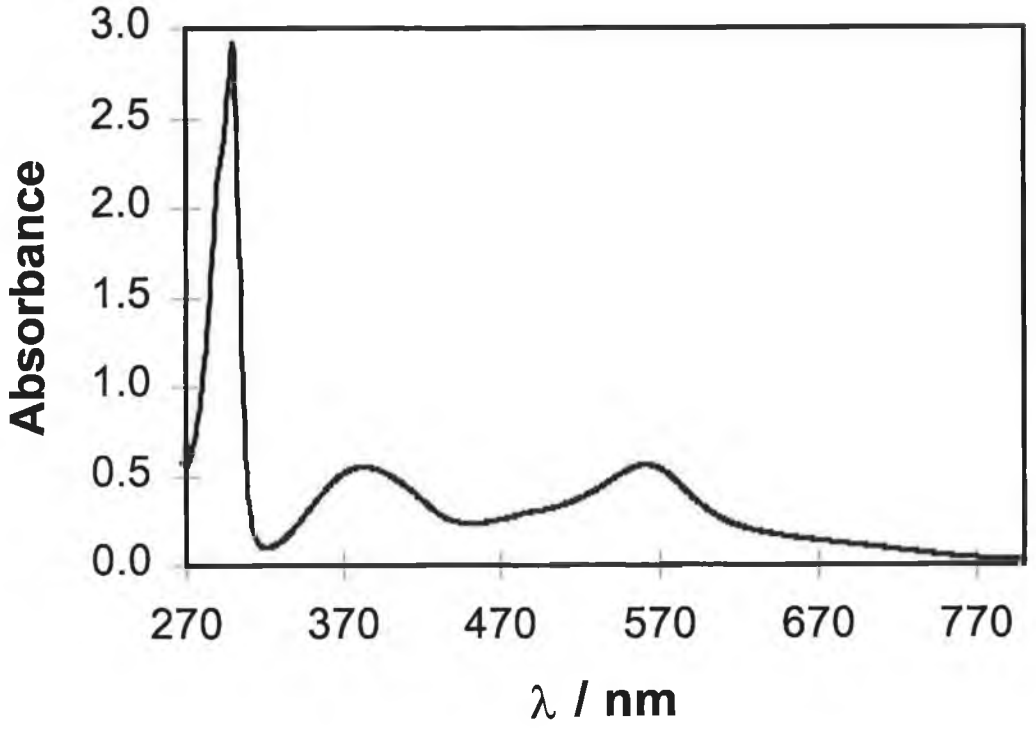

Figure 10 UV of $[Ru(bpy)_2Cl_2]$ in DMF.

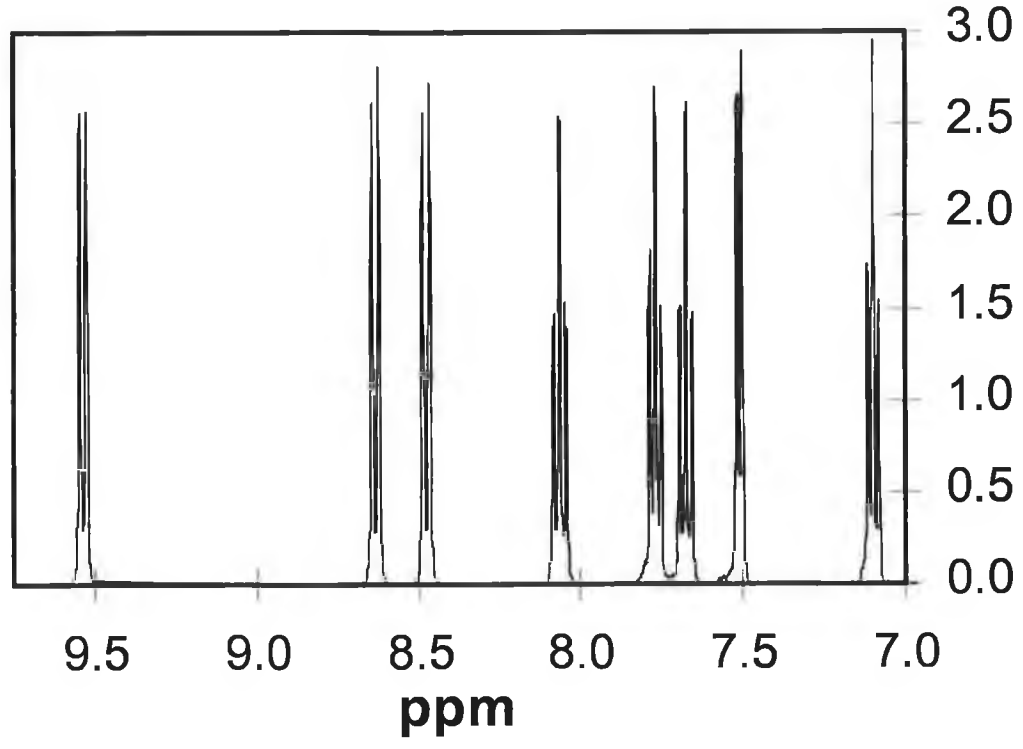

Figure 11 NMR of $[Ru(bpy)_2Cl_2]$ in DMSO.

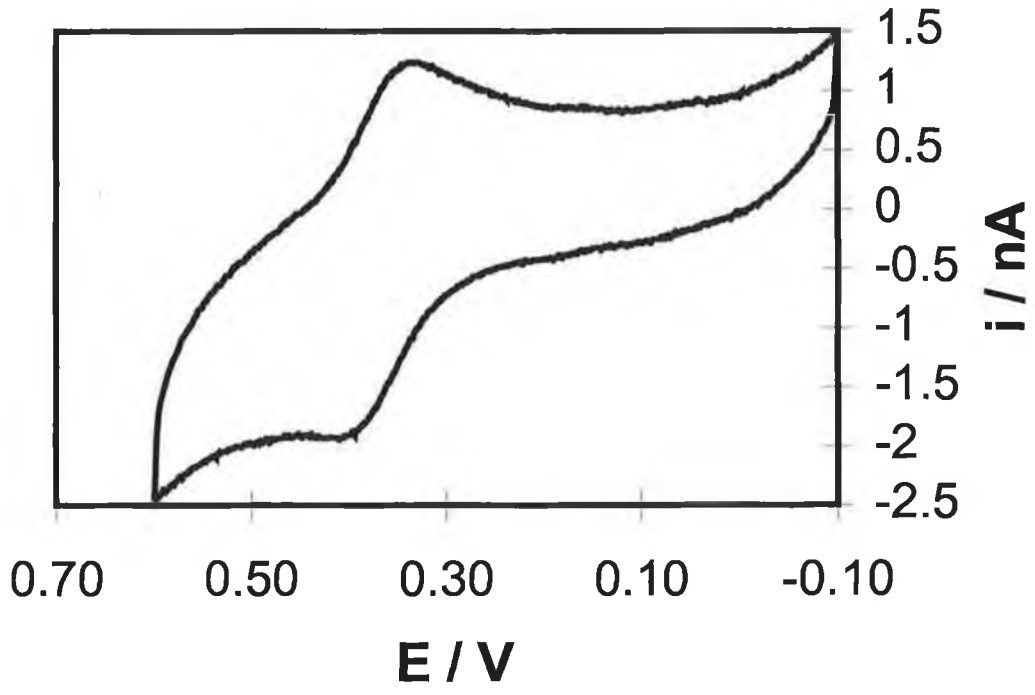

Figure 12 Cyclic voltammogram of $[Ru(bpy)_2Cl_2]$ at a 25 μm radius platinum electrode in methanol. The scan rate is 0.5 V/s and the initial potential is -0.1 V.

Synthesis of $QCat^{2-}$-Ru-1,2

To 280 mg (0.58 mmol) of $[Ru(bpy)_2Cl_2]$ in 20 methanol, 150 mg (0.62 mmol) of alizarin was added followed by a potassium hydroxide pellet in 20 ml milli-Q water. The mixture was refluxed for 72 hours under nitrogen after which time 2 ml acetic acid and 0.5 ml trichloroacetic acid was added. The solvent was evaporated down to approx. 5 ml the dark blue precipitate was filtered and washed with diethylether and milli-Q water. The yield was 92 %.

Characterisation of $QCat^{2-}$-Ru-1,2

As revealed by Lever and co-workers,[25] it is possible to form two isomers of this complex. However, the synthetic method employed here gives the isomer in which ruthenium is bound to the 1,2 position. The 1,2 isomer is of more interest to us in our research as we had previously examined the electrochemistry of anthraquinone-2,7-disulphonic acid. This compound has the two ketonic oxygens available for oxidation/reduction reactions and we therefore wished to look at the effect of combining a similar type anthraquinone to a transition metal centre, keeping the two ketonic oxygens available. Moreover, the selected route represents a more convenient synthetic method of obtaining the desired complex than that used by Lever.[25]

HPLC of the product revealed a single peak at 2.07 min. which is consistent with a neutral complex species. CHN analysis as shown in Table 1 shows the expected and observed elemental composition of the 1,2 isomer. The close agreement between the expected and observed compositions is consistent with the formation of the 1,2 isomer. CHN analysis indicates that charge compensating counterions are absent indicating that the ligand carries a 2- charge that compensates for the 2+ charge on the metal centre. This data suggests the alizarin moiety contains two semi-quinone groups. Cyclic voltammetry of the complex is shown in Figure 13 and 14. In total, six redox couples are observed. The redox couples at the most negative potentials are assumed to represent the reduction and oxidation of the bipyridyl fragments. All of the couples appear to be at least quasi-reversible. The reversibility of each of the couples is examined in more detail in Chapter 6.

Table 1 CHN analysis of $QCat^{2-}$Ru-1,2

$QCat^{2-}$Ru-1,2	Expected %	Found %
Carbon	62.7	63.4
Hydrogen	3.4	3.9
Nitrogen	8.6	8.2

Where the electrochemical activity of the ligand is preserved upon co-ordination, assigning the other redox couples can be difficult. Therefore, we have used spectroelectrochemistry to help elucidate the origin of the other voltammetric processes. The spectroelectrochemical cell employed throughout this work was a 1 mm glass cell with a reservoir. The working electrode (platinum grid) was placed in the cell and the counter and reference electrodes in the reservoir. Scheme 3 shows the design of the cell. Figure 15 shows UV spectra of the species at the open circuit potential (OCP) of –0.3 V. At the OCP no redox activity occurs and no change in the UV is expected. That the UV's overlaid in Figure 15 are indistinguishable confirms that no redox activity occurs at this potential. The shape and wavelength of the bands in Figure 15 are very similar to that reported by Lever and co-workers for $QCat^{2-}$Ru-1,2 but are markedly different from that of $QCat^{2-}$Ru-1,9.[25] The band at 280 nm represents ligand to ligand charge transfer while the other bands at 360 nm and the intense broad doubly peaked band at 620 nm represent metal to ligand charge transfer.

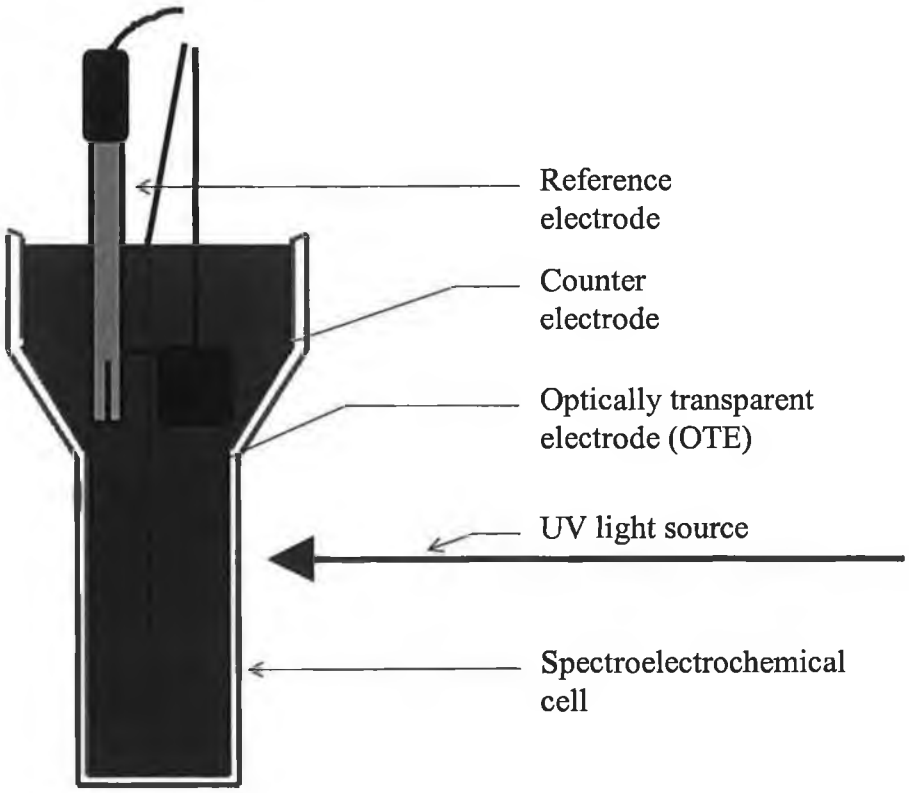

Scheme 2 Typical set-up of a spectroelectrochemical cell.

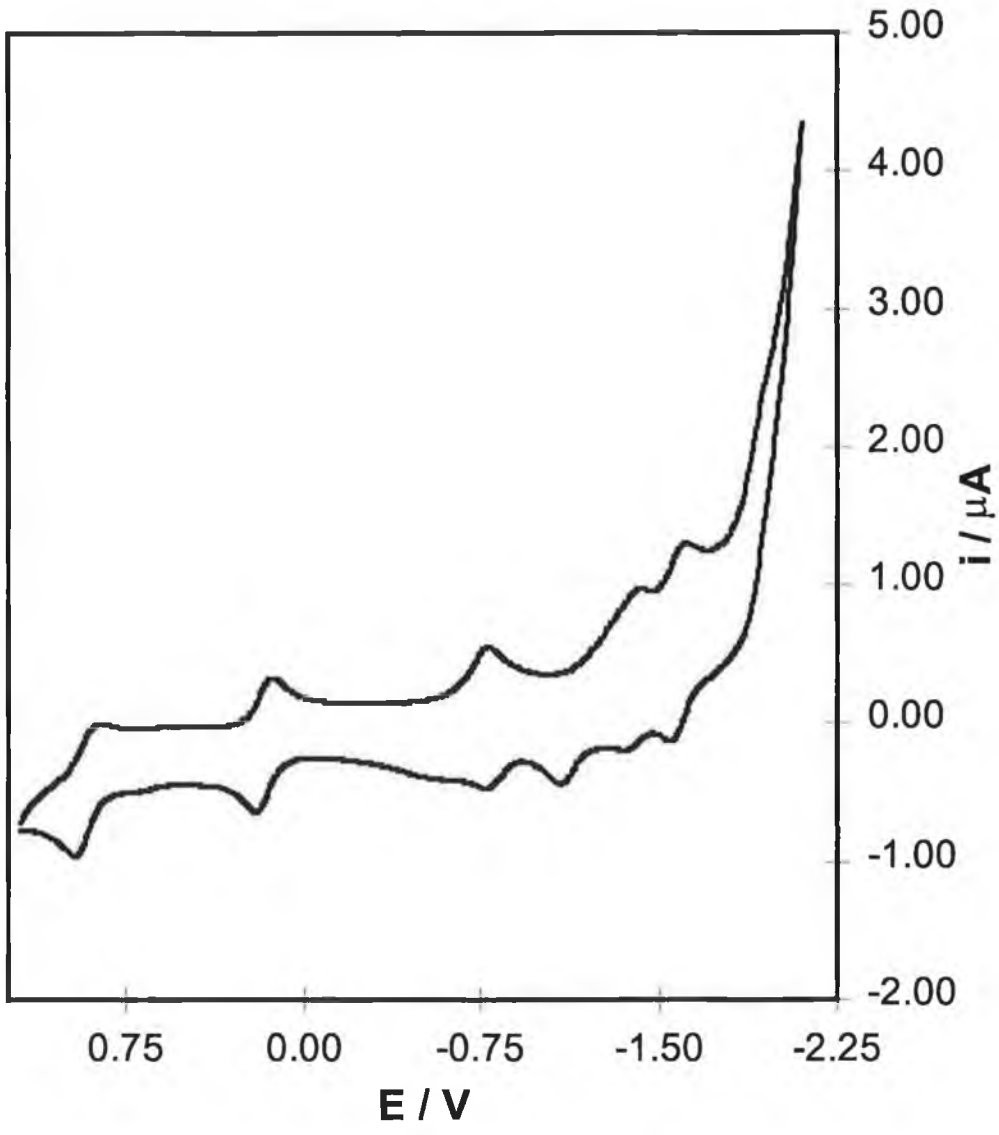

Figure 13 Cyclic voltammogram of a 25 μm platinum microelectrode immersed in a 1 mM solution of $QCat^{2-}$(Ru-1,2) in DMF. Anodic currents are up and cathodic currents are down. The supporting electrolyte is 0.1 M $TEABF_4$ and the scan rate is 0.5 V/s. The initial potential is –0.30 V.

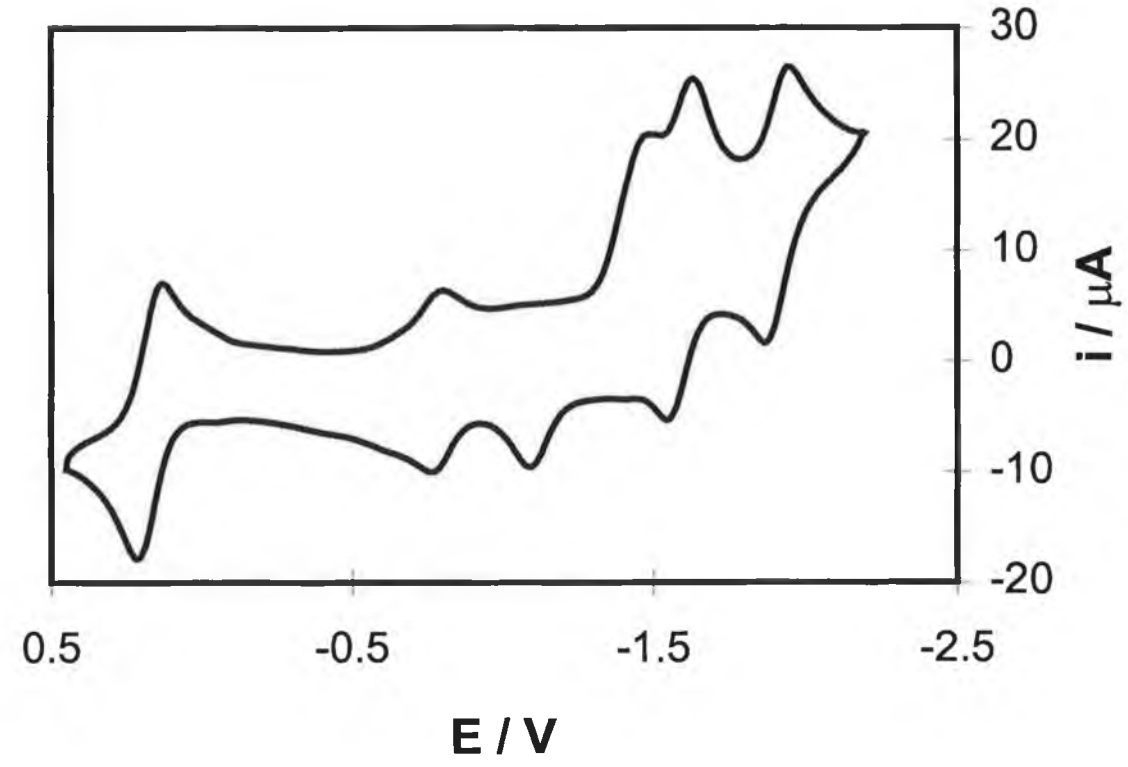

Figure 14 Cyclic voltammogram of $QCat^{2-}$(Ru-1,2) in DMF at a mercury electrode.

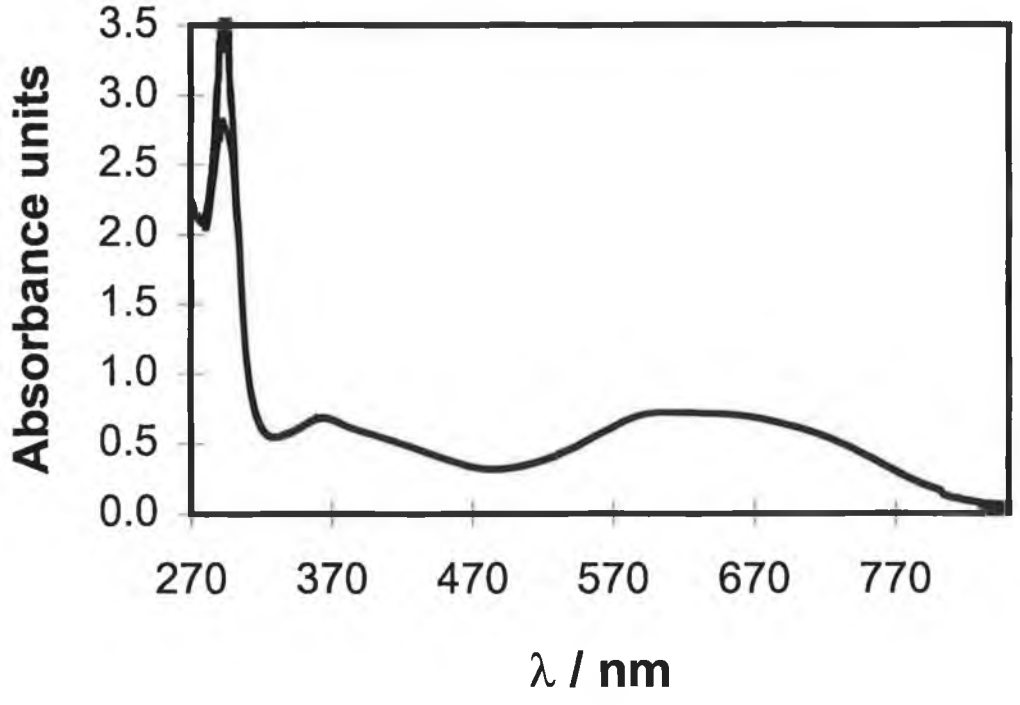

Figure 15 UV spectrum of $QCat^{2-}$(Ru-1,2) in DMF at the open circuit potential (OCP) -0.30 V. Spectra shown are up to 3 hours after application of the applied potential though no distinction can be made.

Figure 16 shows spectra of the complex at a potential of +0.50 V as a function of time. The potential of 0.5 V was chosen because it represents oxidation of the first redox couple positive of the OCP. Therefore, information about the origin of the redox couple at approx. 0.2 V can be obtained. Figure 16 shows that upon application of the 0.5 V potential, the metal to ligand charge transfer bands at 360 and 620 nm decrease with time while a band at 930 nm appears. The decrease in intensity of the broad band at 620 nm and the emergence of the band at 930 nm implies that the oxidation step that occurs at 0.2 V involves the formation of a new metal to ligand charge transfer band at the expense of the original higher energy transition. At this potential, the metal is in the 2+ state (in the 3+ state, no bands would be visible in the visible region). Therefore, at 0.5 V these UV spectra may represent the collapse of a Ru^{2+} to semiquinone band and the formation of the resulting Ru^{2+} to quinone band.

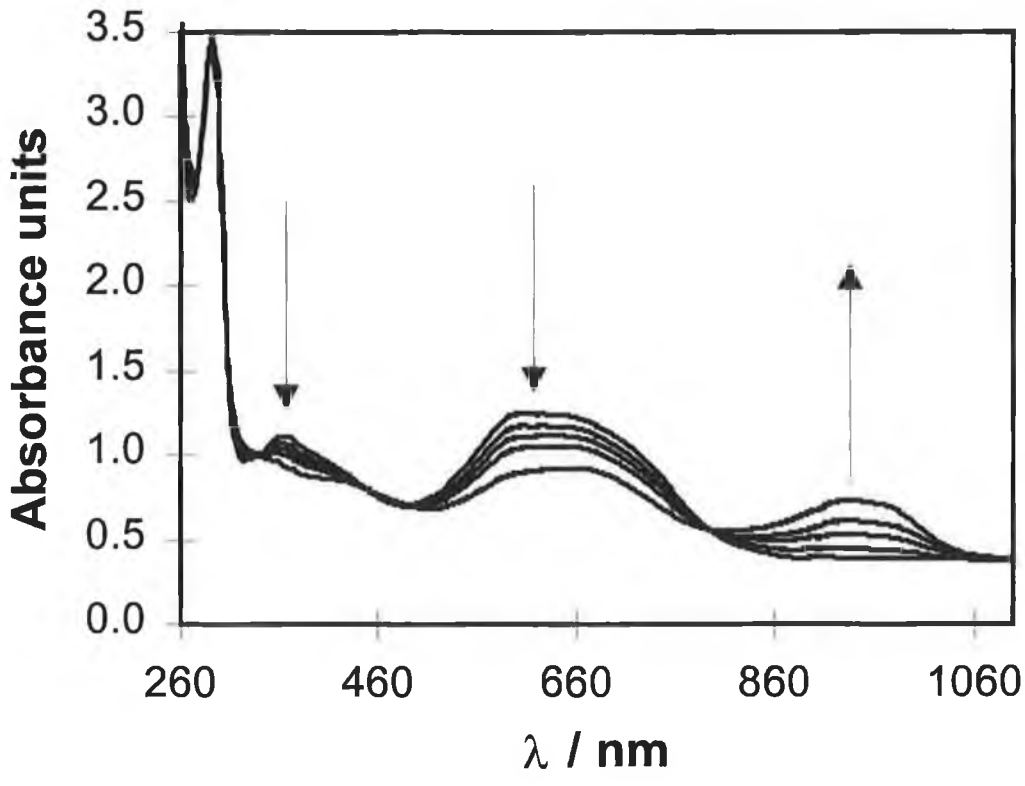

Figure 16 UV spectrum of $QCat^{2-}$(Ru-1,2) in DMF at a potential of +0.50 V as a function of time. The spectra at 660 nm, from top to bottom, represent times of 0, 0.5, 6, 10, and 195 minutes after the cell was turned on at 0.5 V.

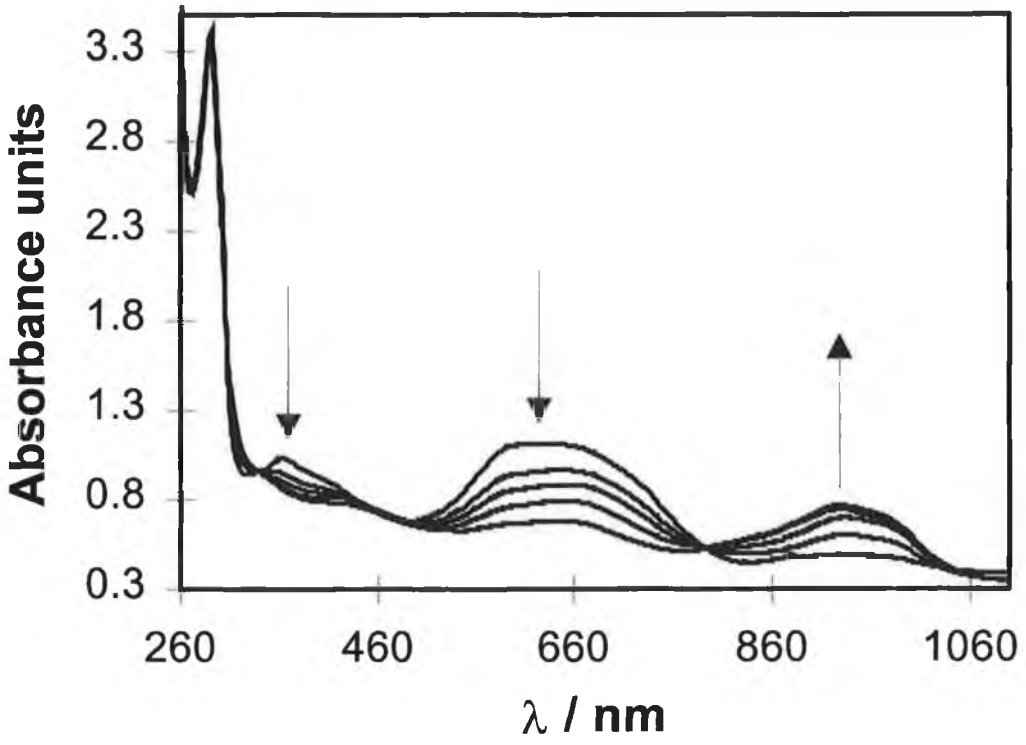

Figure 17 UV spectrum of $QCat^{2-}$(Ru-1,2) in DMF at a potential of +1.20 V. The spectra represent, from top to bottom at 660 nm, times of 0, 0.5, 3, 15, and 39 minutes respectively.

Figure 17 shows UV spectra as a function of time at +1.2 V, i.e., positive of the redox couple at 0.9 V. These spectra have been recorded directly after those at 0.2 V. In this case, the MLCT bands disappear completely while the band at 930 nm grows in intensity similarly to that seen in Figure 16. In fact, the change in absorbance, ΔA, in the bands at 660 nm and 930 nm at 0.2 V and 0.5 V is indistinguishable. That is, a change in absorbance of 0.4 A.U. is observed for decreases in the 660 nm band at 0.2 V and at 0.5 V. These observations indicate that that two similar MLCT transitions take place at 0.2 V and at 0.5 V. These transitions are summarised in Scheme 2.

At the open circuit potential of –0.3 V the complex exists as $QCat^{2-}$Ru-1,2, is neutral, the ruthenium centre is in the 2+ state and two semi-quinones exist in the 1

and 2 positions. At 0.2 V a one electron transfer reaction takes place involving metal to ligand charge transfer. This corresponds to oxidation of the semi-quinone on the anthraquinone (band at 660 nm decreases) to a quinone (band at 930 nm appears). At 0.9 V, the corresponding reaction occurs with the semi-quinone in the 1 position.

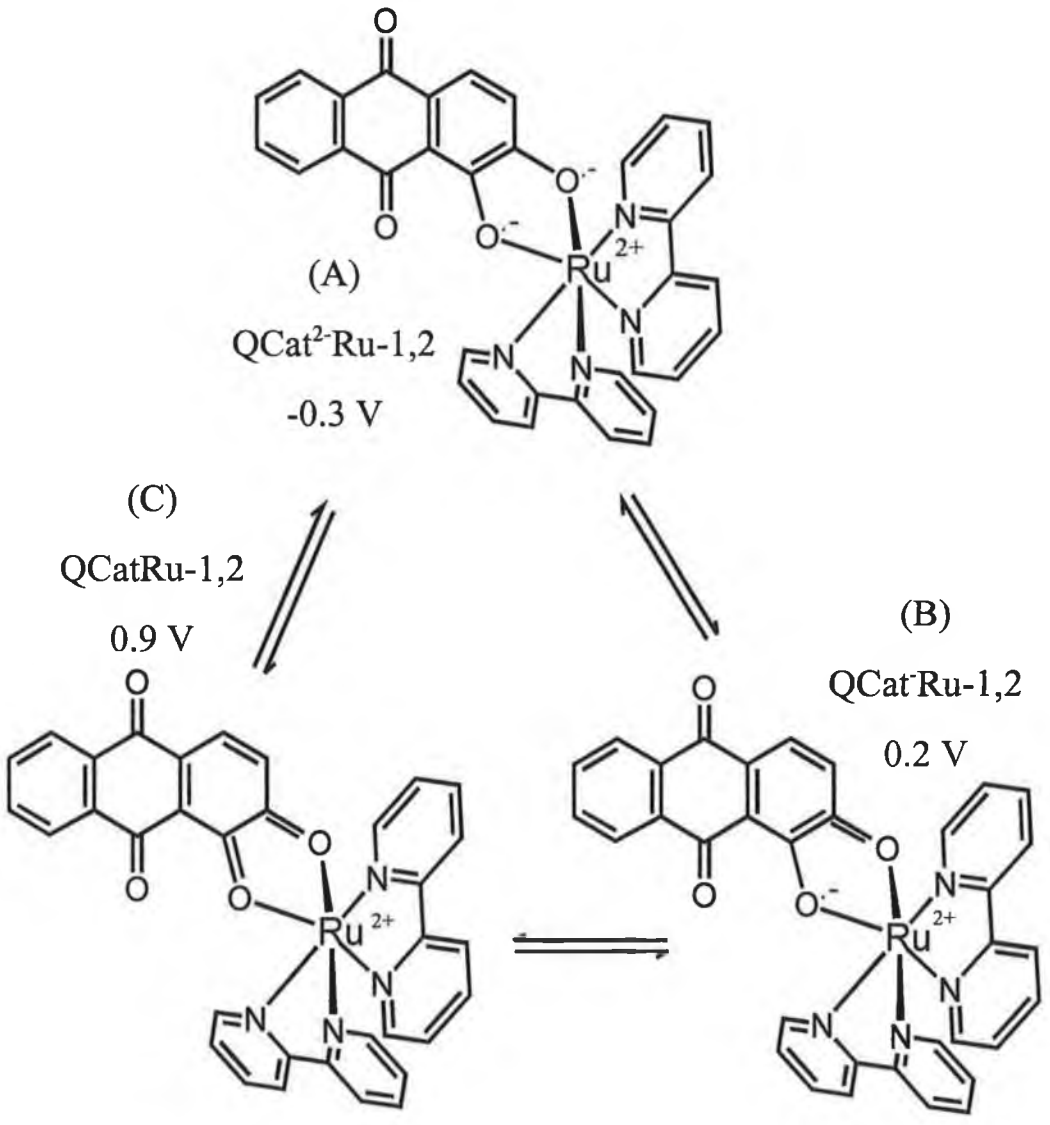

Scheme 3 $QCat^{2-}$Ru-1,2 as synthesised (A), at a potential of 0.2 V, and at a potential of 0.9 V.

It appears that the $Ru^{2+/3+}$ redox couple exists at more potentials positive of the range probed in this work. This is further supported by a previous report on this complex.[25] Therefore, we suggest that the two redox couples observed at positive potentials represent oxidation/reduction reactions of two ligand based oxygen atoms.

At a potential of –1.2 V a similar type behaviour to that observed at the positive potentials can be observed. Figure 18 shows UV spectra of $QCat^{2-}$(Ru-1,2) as a function of time at –1.2 V. This potential probably represents reduction of the semi-quinone in the 1 position to the catechol moiety. The UV spectra in Figure 17 would then represent the loss of the ruthenium to semi-quinone transition at 660 nm, and the appearance of a catechol to bipyridyl transition at 930 nm. The corresponding reaction at –2 V is shown in Figure 19 for the reduction of the second semiquinone reaction.

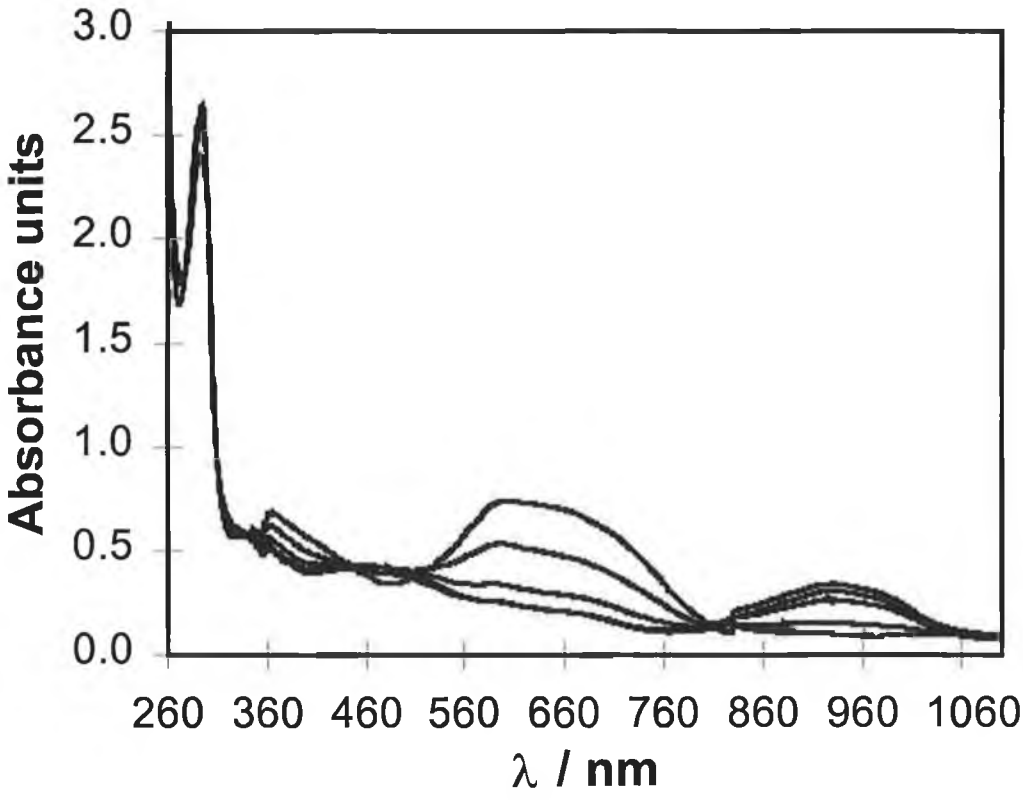

Figure 18 UV spectra of $QCat^{2-}$(Ru-1,2) in DMF at a potential of -1.20 V. The spectra represent, from top to bottom at 660 nm, times of 0, 20, 40, and 80 min.

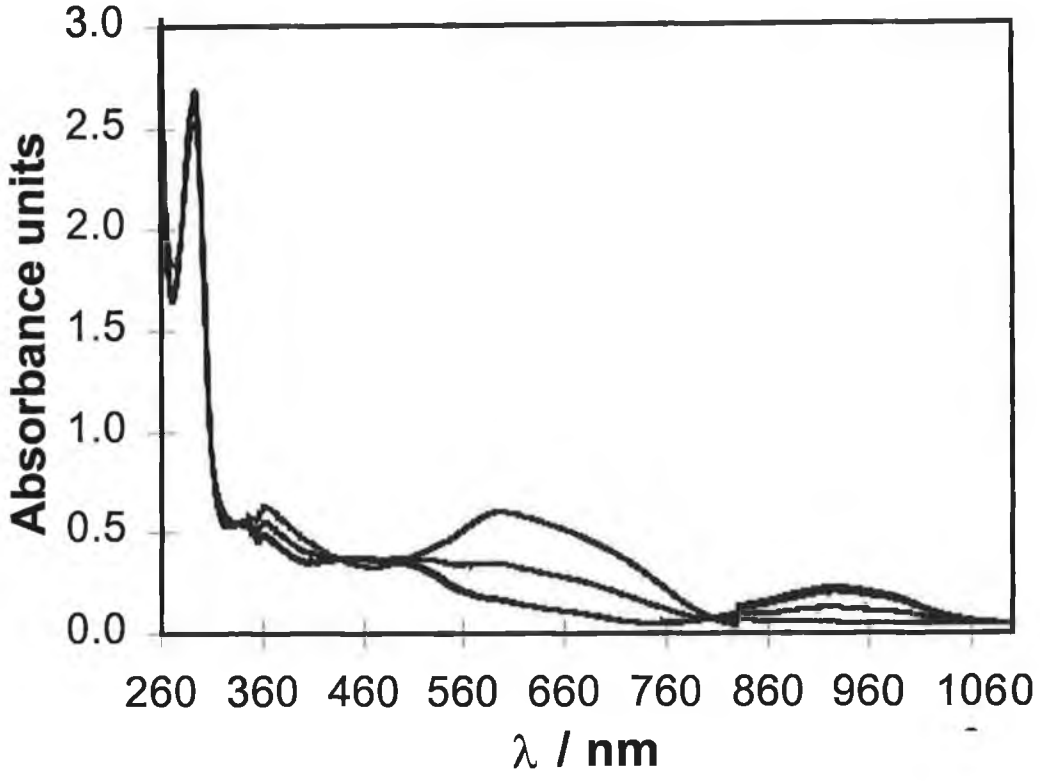

Figure 19 UV spectrum of $QCat^{2-}$(Ru-1,2) in DMF at a potential of –2.0 V.

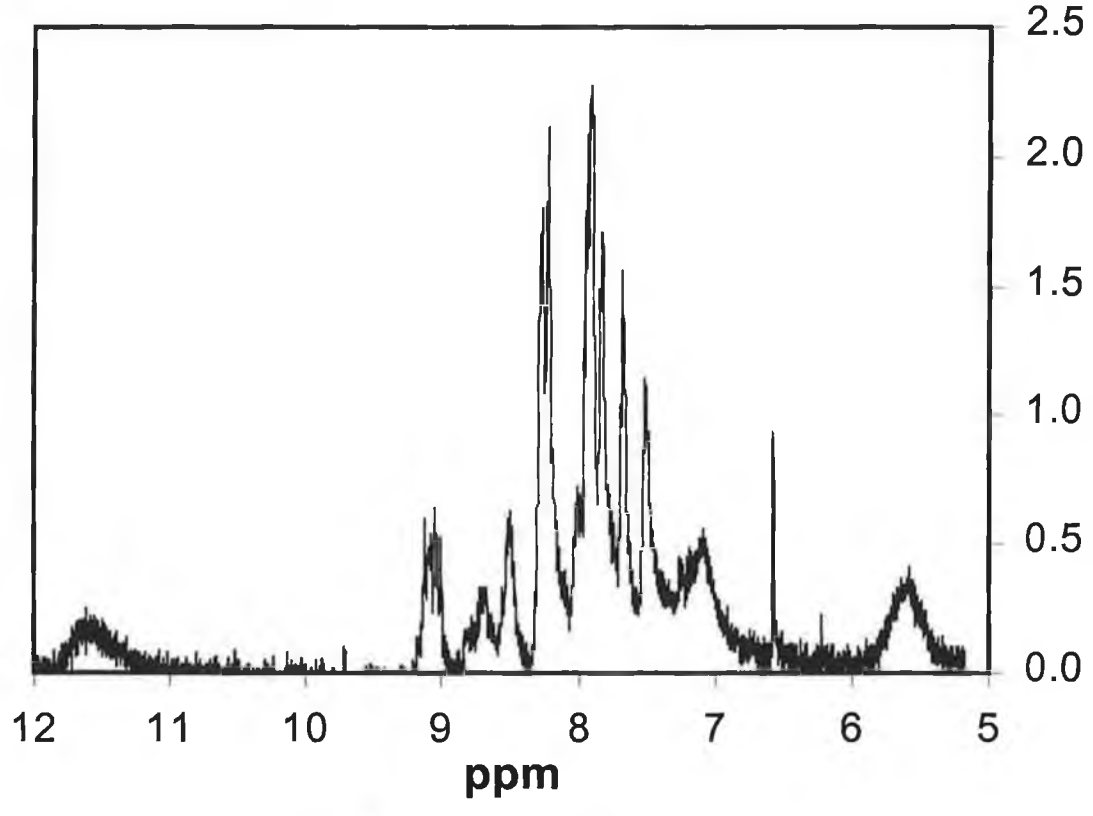

Figure 20 NMR of $QCat^{2-}$(Ru-1,2) in d-DMSO.

An NMR of $QCat^{2-}$-Ru-1,2 is shown in Figure 20. The spectrum is distorted due to the presence of the semi-quinone moieties in the complex. However, integration of the peaks gives the correct integration expected for the complex. Sixteen protons for the bipyridyl fragments and six protons on the anthraquinone moiety are accounted for in this spectrum. On the basis of the above characterisation, we have assigned our complex as $QCat^{2-}$Ru-1,2.

2.2.5 Characterisation of Anthraquinone-2,7-disulphonic acid

Anthraquinone-2,7-disulphonic acid was purchased from BASF (Ludwigshafen, Germany). In order to satisfy ourselves of the integrity of the product HPLC, UV, NMR and CV were performed on the compound. HPLC revealed a single peak at 1.9 min., typical for a neutral species of this molecular weight. UV shown in Figure 21 is indicative of an anthraquinone as seen by Figure 7 of alizarin. The NMR reveals a singlet at 8.05 representing the two protons in the 1 and 8 positions. The doublets at 7.85 and 7.70 represent the protons in the 3 and 4, and the 2 and 5 positions, respectively. The CV in Figure 22 shows a single redox couple with a peak-to-peak separation of 40 mV. This is typical for a reaction involving two electrons, which is expected for the 2-proton, 2-electron transfer exhibited by many anthraquinones in acidic solutions.

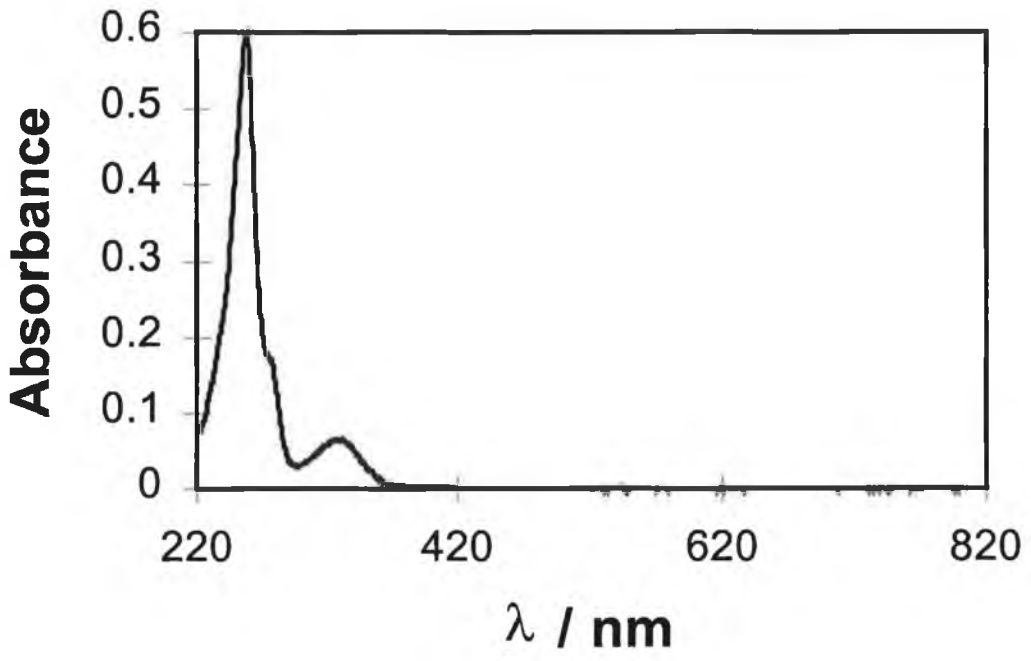

Figure 21 UV of Anthraquinone-2,7-disulphonic acid in DMF.

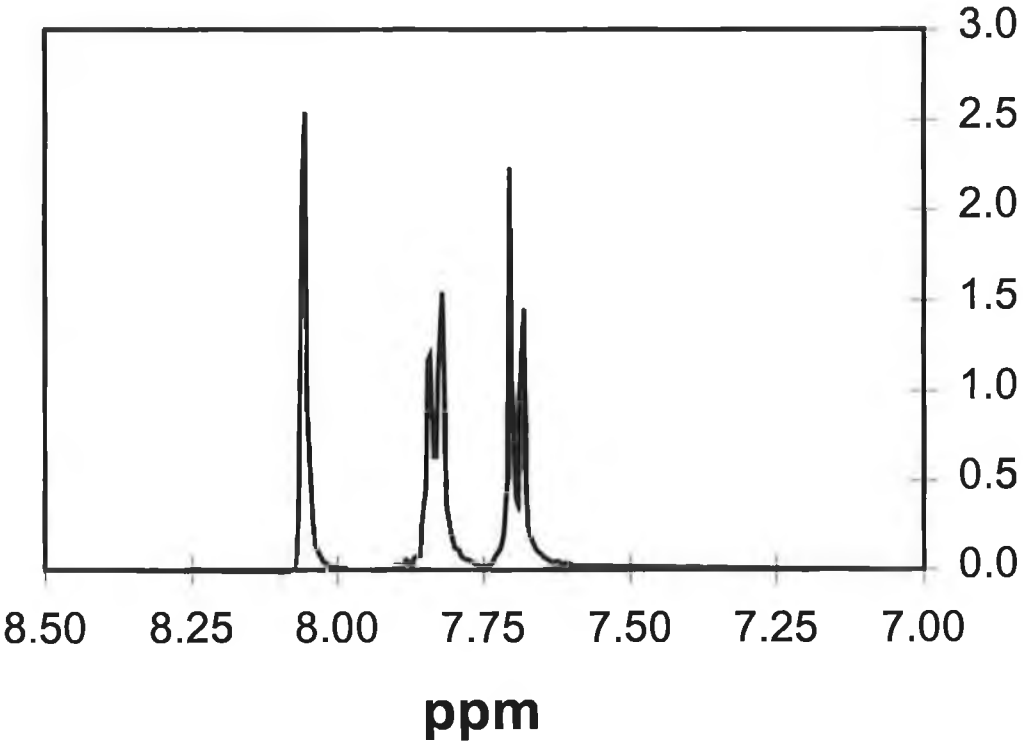

Figure 22 NMR of 2,7-AQDS in D_2O.

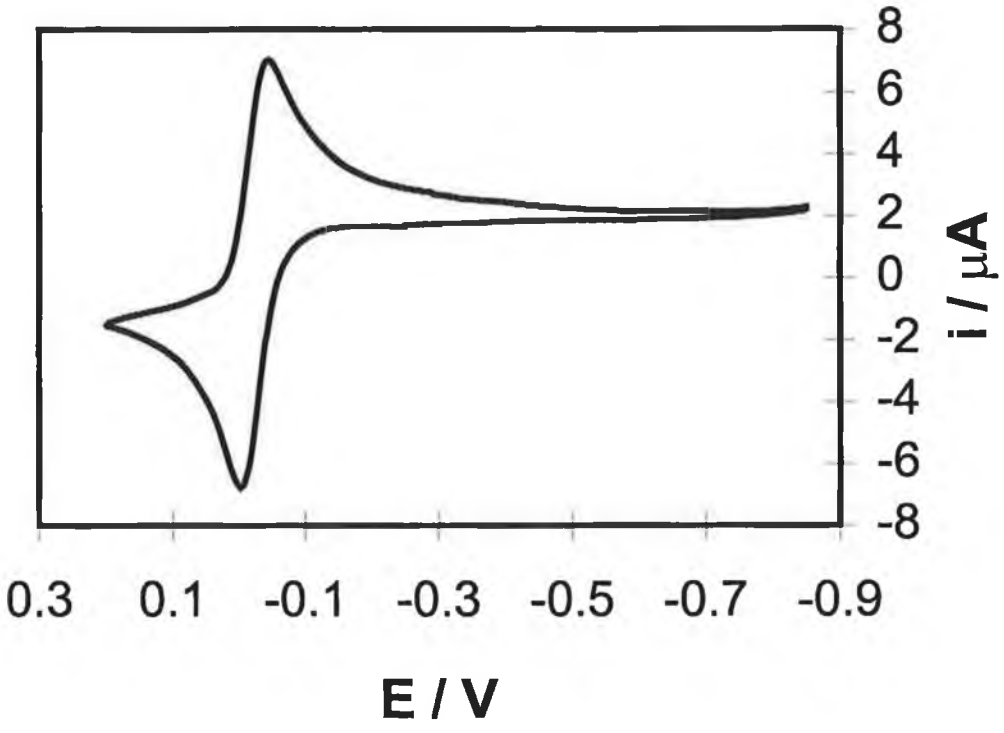

Figure 23 Cyclic voltammogram of a 0.017 cm^2 mercury electrode in a solution of 2,7-AQDS in 1 M $HClO_4$. Anodic currents are down and cathodic currents are up. The initial potential is –0.3 V and the scan rate is 0.5 V/s.

2.3 References

1 Kauffman, G. B. *Theories of co-ordination compounds,* Wiley, New York 1994.

2 Price, R. in *Comprehensive Coordination Chemistry: The Synthesis, Reactions, Properties & Applications of Coordination Compounds*; Wilkinson, G., Ed.; Pergamon Press, New York, 1987.

3 Orna, M. V.; Kozlowski, A. W.; Baskinger, A.; Adams, T. *Co-ordination Chemistry of Pigments and Dyes of Historical Interest,* Elsevier, 1987.

4 Finklea, H. O.; Hanshew, D. D. *J. Am. Chem. Soc.* 1992, 114, 3173.

5 Miller, C.; Gratzel, M. *J. Phys. Chem.* 1991, 95, 5225.

6 Bunding Lee, K. A. *Langmuir* 1990, 6, 709.

7 Chidsey, C. E. D.; Bertozzi, C. R.; Putvinski, T. M.; Mujsce, A. M. *J. Am. Chem. Soc.* 1990, 112, 4301.

8 Forster, R. J.; Vos, J. G. *J. Electroanal. Chem.* 1991, 314, 135.

9 Leech, D.; Forster, R. J.; Smyth, M. R.; Vos, J. G. *J. Mater. Chem.* 1991, 1, 629.

10 Forster, R. J.; Vos, J. G. *Macromolecules* 1990, 23, 4372.

11 Forster, R. J.; Kelly, A. J.; Vos, J. G.; Lyons, M. E. G. *J. Electroanal. Chem.* 1989, 270, 365.

12 See Chapter 1 references 26-72.

13 Acevedo, D.; Bretz, R. L.; Tirado, J. D.; Abruña, H. D. *Langmuir* 1994, 10, 1300.

14 Hudson, J. E.; Abruña, H. D. *J. Phys. Chem.* 1996, 100, 1036.

15 Bretz, R. L.; Abruña, H. D. *J. Electroanal. Chem.* 1995, 388, 123.

16 Bretz, R. L.; Abruña, H. D. *J. Electroanal. Chem.* 1996, 408, 199.

17 Forster, R. J. *Inorg. Chem.* 1996, 35, 3394.

18 Forster, R. J.; Faulkner, L. R. *Anal. Chem.* 1995, 67, 1232.

19 Forster, R. J.; Faulkner, L. R. *J. Am. Chem. Soc.* 1994, 116, 5453.

20 Forster, R. J.; Faulkner, L. R. *J. Am. Chem. Soc.* 1994, 116, 5444.

21 Tirado, J. D.; Abruña, H. D. *J. Phys. Chem.* 1996, 100, 4556.

22 Acevedo, D.; Abruña, H. D. *J. Phys. Chem.* 1991, 95, 9590.

23 Ferguson, G. F. *Inorg. Synth.* 1986, 24, 291.

24 Weldon, F. Ph.D. Thesis *Dublin City University*, 1998.

25 Del Medico, A.; Auburn, P. R.; Dodsworth, E. S.; Lever, A. B. P.; Peitro, W. J. *Inorg. Chem.* 1994, 33, 1583.

Chapter 3

Fabrication and Characterisation of Microelectrodes

3.1 Fabrication of Microelectrodes

3.1.1 Introduction

The construction of microelectrodes has received widespread attention over the last 15 years.[1,2,3,4,5,6,7,8,9,10,11,12,13,14,15] Many papers now appear each year dealing with the construction of microelectrodes, their properties and their applications. Chapter 1 provides a description of microelectrodes, their common geometries, applications and their advantages over conventionally sized electrodes. In this chapter, the fabrication and characterisation of microelectrodes using mercury, platinum, gold and carbon fibre is presented.

Several methods have been presented for the fabrication of microelectrodes depending on the type and size of the electrode required. For example, in the construction of platinum microelectrodes, Wightman[16,17] and co-workers have sealed the microscopic electrode wire in soft glass using a coil of resistively heated nichrome wire or Bunsen burner flames and made the electrical connection between the electrode wire and the hook-up wire by injecting silver epoxy into the glass tubing. The construction of microelectrodes of diameter less than 10 μm using electrode wire of 75 μm has been described by Pendley and Abruña.[18] In this work, 3-4 cm of 75 μm Pt wire was placed in a 6-7 cm length of borosilicate pipette. The assembly was then placed in four loops of nichrome wire on a pipette puller and stretched. The resulting microelectrodes were of less than 10 μm diameter. Robinson and McCreery have reported the construction of carbon fibre microelectrodes for use in spectroelectrochemical experiments.[19] They used the barrels of disposable pipettes in which to house the electrodes. The carbon fibre was sealed in the bottom of the electrode casing using wax and the electrical connection to the hook-up wire was made by placing mercury in the glass pipette. Wightman[20] and Martin[21] have studied the sealing procedures used in the fabrication of microelectrodes. They found that sealing the electrode with silanes at the electrode wire/glass interface was necessary due to seepage of electrolyte solution up between

the electrode wire and the glass housing which caused excessive capacitive currents. Excess silane was polished off the active electrode area and a high quality seal appeared to be achieved. Tschuncky and Heinze have provided a comprehensive procedure for the construction of microelectrodes in which stray capacitance is minimised.[22] Instead of using conductive paint or epoxy which can cause stray capacitance they have soldered the microscopic wire to the hook-up wire. A description of a more elaborate shielded microelectrode construction is also given.

The construction of mercury microelectrodes has also received much attention over the past number of years. Although very narrow capillaries have been employed to produce hanging mercury drops of small dimensions, these electrodes have not decreased in area sufficiently to be considered microelectrodes. The most popular approach to the fabrication of mercury microelectrodes is the deposition of mercury onto a solid microelectrode. Mercury has been deposited onto carbon fibres,[23] platinum,[24,25] iridium[26] and gold.[27,28] Wightman[29] and Baldo[30] have used platinum electrodes held at a potential of 0.00 V in a solution containing Hg(I) ions to produce mercury microelectrodes. Stojek and co-workers have used a $HClO_4$ solution containing Hg(II) ions for the successful deposition of mercury onto silver and for the preparation of silver-mercury amalgams.[31] Birke and Huang also used Hg(II) ions for deposition onto gold.[32]

Due to their increasingly common usage, and developments in their construction, microelectrodes with increasingly small dimensions and greater quality of construction are being produced on an ongoing basis. Improved fabrication methods and lower RC cell time constants means that an increasing number of experiments can be carried out on a greater variety of samples.

3.1.2 Fabrication of Platinum and Gold Microelectrodes

Platinum and gold microelectrodes were constructed using a procedure similar to that reported by Xu and Faulkner.[33] Platinum and gold wire of 25 μm radius was purchased from Goodfellows. A diagram of the cross section of a microelectrode is shown in Figure 1.

The general procedure for the fabrication of 25 μm radius platinum and gold microelectrodes is as follows;

- A length of soft glass is cut into several pieces 14 - 16 cm in length. These pieces are soaked in dilute nitric acid in order to clean them. After cleaning in nitric acid (usually for several hours) they are rinsed in Milli-Q water and soaked in acetone for several hours, and finally rinsed with Milli-Q water.

- After cleaning, the dry glass is heated over a Bunsen until soft. A taper is drawn in the centre of the glass tube and allowed cool. The glass is broken at the centre of the taper and reheated to seal the tapered end.

- The transition wire of approx. 4 cm in length is soldered to the 3-4 cm hook-up wire. The transition wire is stripped of its outer plastic coating and bent into a zig-zag shape (Figure 1) using a pair of tweezers. This zigzag shape is designed to prevent breaking of the microscopic wire or the electrical connections due to vibrations while the electrode is being polished. Every effort is made to minimise handling of the wires during construction. The microscopic wire of 1-2 cm is then carefully soldered to the transition wire. The wiring of the electrode is then cleaned by soaking in acetone and allowed to dry. It is then placed into the soft glass body with the microscopic wire reaching the tip of the sealed taper.

- A vacuum tube is placed over the open end of the assembly and a vacuum applied while the tapered end is sealed in a flame. The glass is allowed to collapse around the microwire to a length of approx. 5 mm. A plastic cap is glued on to the top of

the electrode to help stabilise the hook-up wire and the prevent contamination of the interior of the assembly.

- With the embedded microwire in the glass casing, the electrode is ground down with fine emery paper until the wire is exposed the tip of the glass appears flat. Electrical connection is tested by running a cyclic voltammogram in blank electrolyte solution. Once connection has been established, electrodes are left to stand in Milli-Q water overnight to ensure no seepage of liquid into the electrode casing occurs.

In the fabrication of 25 μm radius electrodes high success rates should be obtained. We have consistently achieved success rates of over 90% using the method described above.

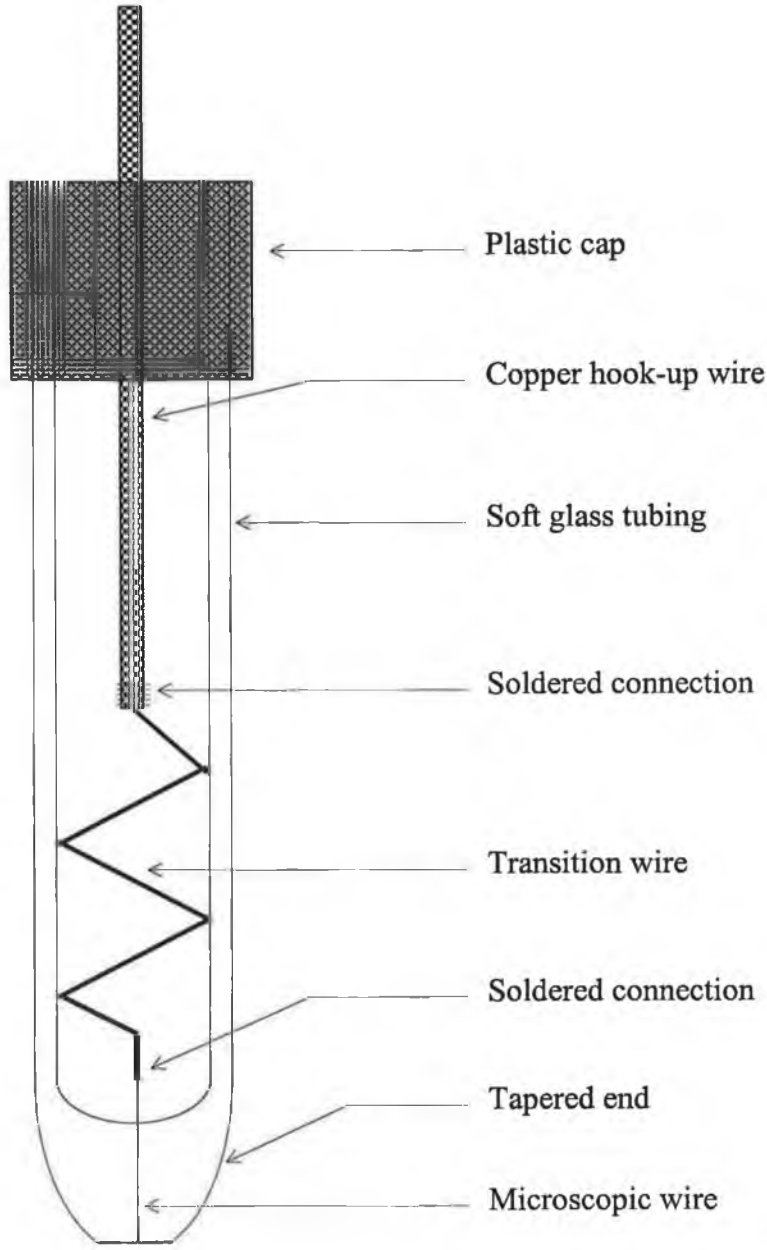

Figure 1 Cross section of a microelectrode.

Dimensions: length of electrode including protruding hook-up wire; 7-9 cm
width of glass casing; i.d. 4 mm, o.d. 5 mm.

3.1.3 Fabrication of Carbon Fibre Microelectrodes

Carbon fibre microelectrodes were fabricated in a similar way to the platinum and gold microelectrodes. Several carbon fibres of similar length are taken from a fibre bundle and attached to a hook-up wire using solder or using conductive silver paint, and placed in an electrode casing as described above. The glass is sealed in the same way as for the metallic electrodes. However, while sealing the soft glass around the micro fibres gas bubbles as shown in Figure 2 often tended to form in the glass. This caused difficulties when the electrodes were polished as a bubble at the fibres could be exposed thus increasing the accessible area of the electrode (Figure 3). Another problem which arose in the construction of the carbon fibre microelectrodes was that it was not possible to fabricate a single fibre electrode. Problems arose in the handling of such thin, brittle single fibres. Even when they were successfully soldered onto a hook-up wire, sealing the glass caused the fibre to burn. Therefore, the success rate for the construction of carbon fibre microelectrodes was lower than that for the Au and Pt electrodes at approx. 70%.

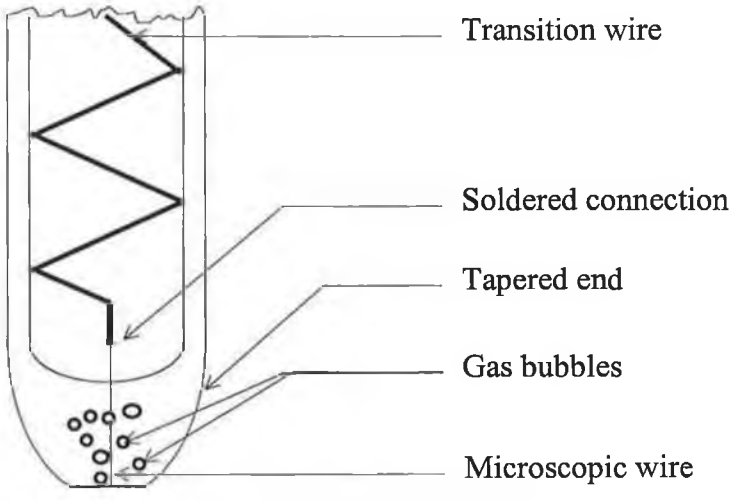

Figure 2 Construction of carbon fibre microelectrodes indicating the presence of gas bubbles which complicated the construction.

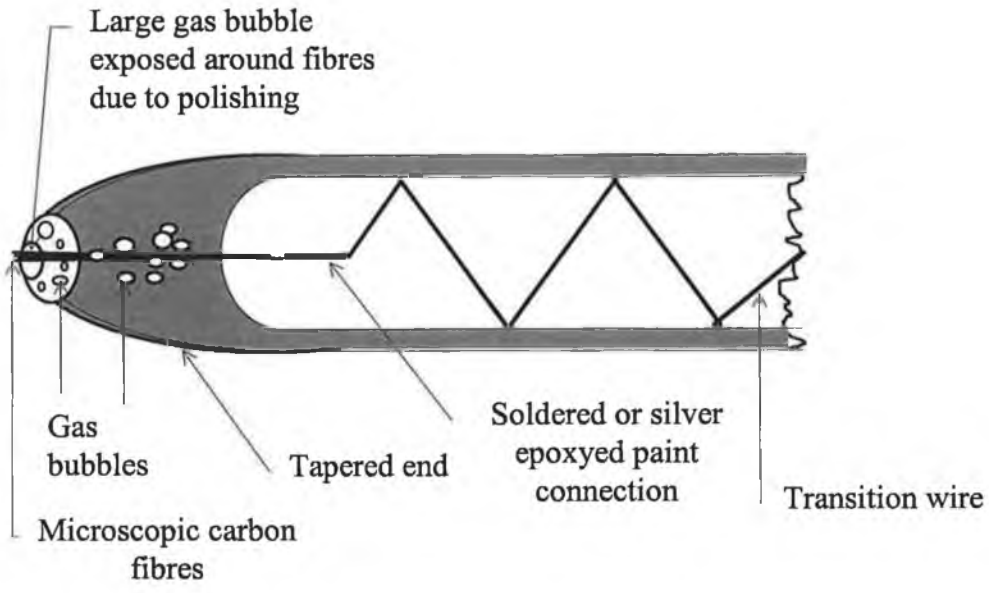

Figure 3 Construction of carbon fibre microelectrodes. Polishing of electrodes could lead to the opening of a gas bubble exposing a greater electrode area.

3.1.4 Fabrication of Mercury Microelectrodes

Mercury microelectrodes have been widely employed in electrochemistry for several reasons. One is the relatively large negative potential range unique to mercury. Mercury microelectrodes take several forms. The simplest of these is a mercury film electrode formed by electrodeposition of the mercury onto a disk electrode.

Several attempts were made at constructing mercury microelectrodes, none of them being entirely successful. The construction of mercury microelectrodes in acidic media using both Hg(I) and Hg(II) has been described in detail previously.[27,29,30,31] Our attempts included;

- Electrodeposition of Hg onto platinum electrodes using a solution containing Hg II ions.
- Electroless deposition of Hg onto platinum; leaving a platinum electrode to stand in the above solution or in a mercury pool.
- Electro and electroless deposition onto gold.

Electrodeposition onto platinum was carried out using microelectrodes between 5 and 25 μm radius. Firstly, deposition onto a microelectrode which had been polished and electrochemically cleaned was attempted. A background CV is shown in Figure 4. It can be seen that mercury has indeed been deposited on the platinum surface. However, these electrodes performed badly and were very unstable, the mercury drop falling off repeatedly. A CV of an attempt to deposit anthraquinone-2,7-disulphonic acid is shown in Figure 5. The electrochemical response is poor compared with that observed using a conventional mercury electrode. Electroless deposition of mercury by placing the electrode into a pool of mercury proved ineffectual.

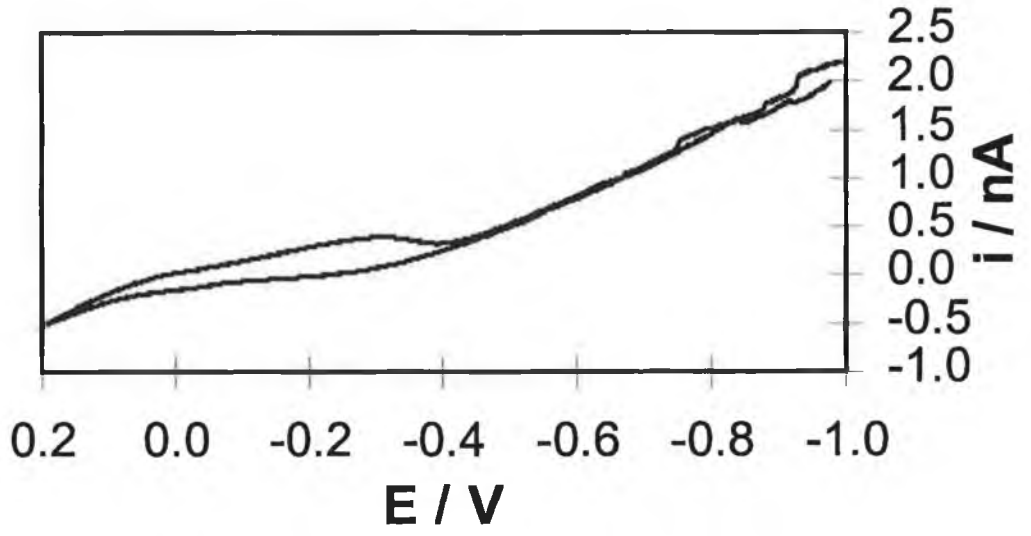

Figure 4 Background CV of a mercury electrode formed by placing a platinum electrode in a solution of Hg(II) ions and holding the potential at –0.1 V.

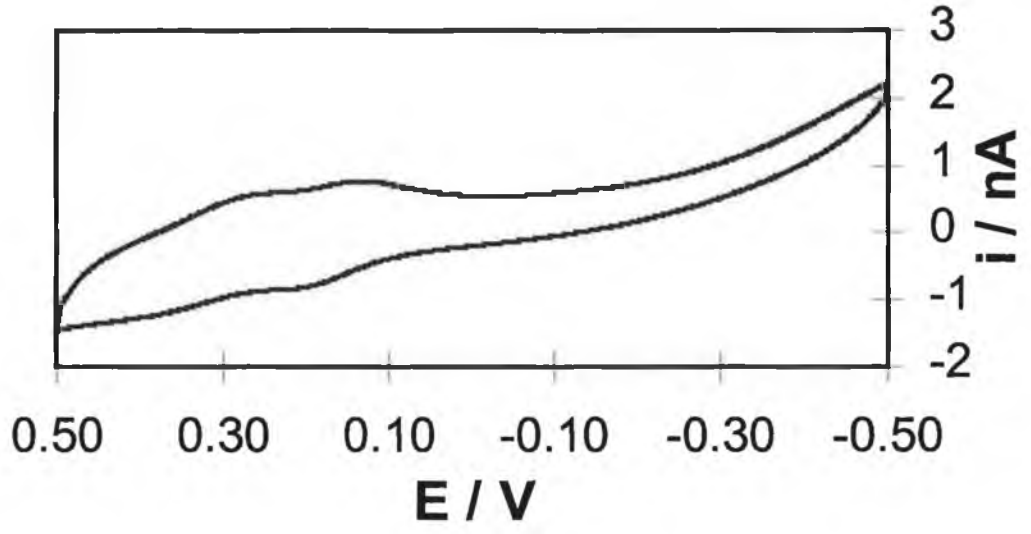

Figure 5 CV of a mercury electrode placed in a μM solution of anthraquinone-2,7-disulphonic acid. The scan rate is 0.5 V/s and the initial potential is –0.5 V.

The final method of fabricating platinum based mercury microelectrodes involved etching the platinum back from the tip of the electrode using aqua-regia solution and then depositing the mercury. The presence of the glass body around the mercury might make it less likely to become dislodged. Although little success was achieved, it was found that silanising the inner glass body improved the stability of the assembly. Figure 6 shows a cyclic voltammogram of a mercury microelectrode fabricated in this way.

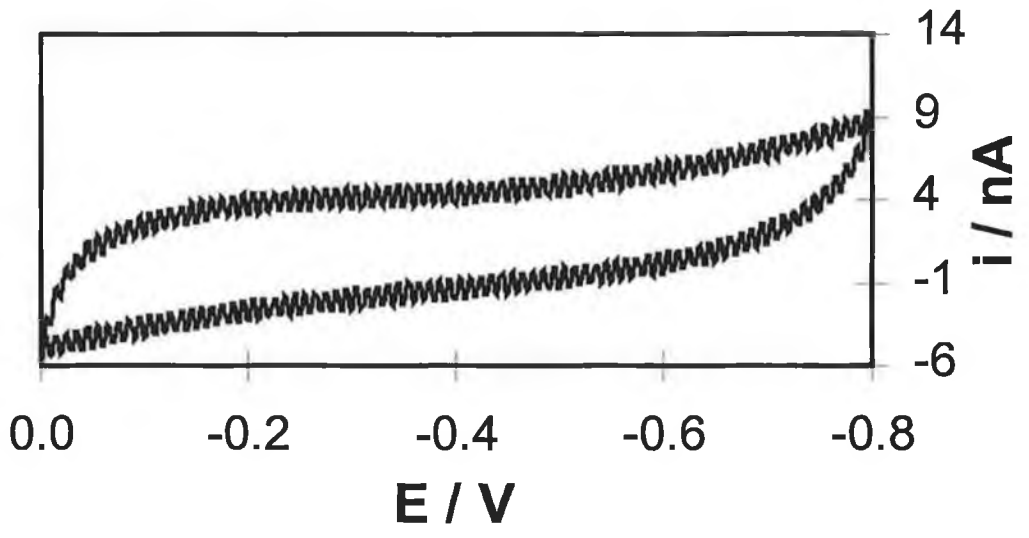

Figure 6 CV of a mercury microelectrode in 0.1 M $LiClO_4$. The scan rate is 0.5 V/s and the initial potential is –0.8 V.

The small currents observed are probably due to partial silanisation of the platinum. Figure 7 shows the same electrode placed in a solution containing 2,7-AQDS. There appears to be some surface confined behaviour analogous to that expected for the compound attached to a clean mercury electrode. However, this type of electrode proved unstable and irreproducible.

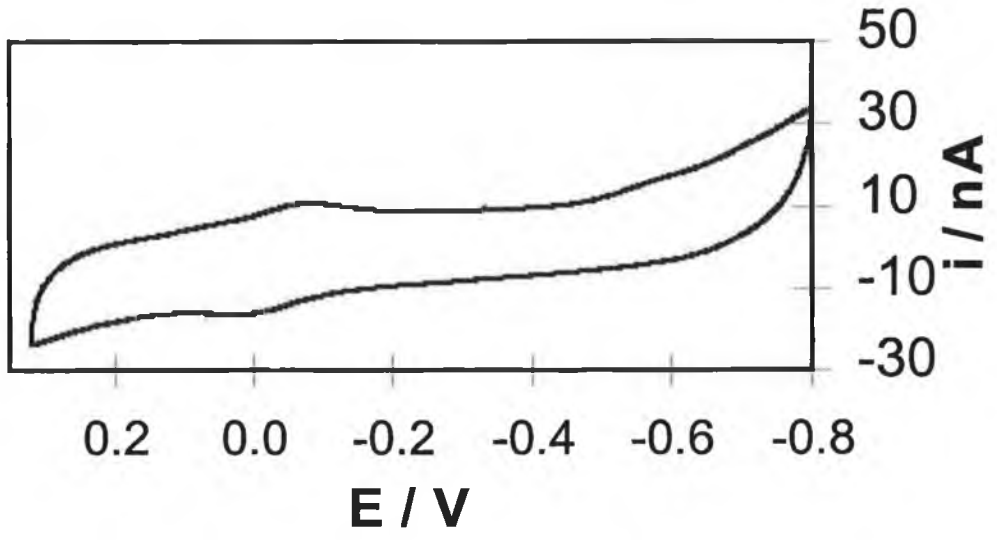

Figure 7 CV of a mercury microelectrode immersed in a solution of 2,7-AQDS. The scan rate is 1 V/s and the initial potential is -0.8 V.

Since platinum based mercury microelectrodes proved difficult to fabricate, gold based electrodes were attempted. Figure 8 shows a background CV of a gold based mercury electrode. Despite these initially positive results, over a period of time the background CV changed until it appeared as Figure 9. Upon examination, it appeared that mercury had formed an amalgam with the gold. Hence, it was no longer a gold based mercury electrode but a mercury-gold amalgam which was changing composition over time until the gold had dissolved in the mercury. Therefore, gold is generally unsuitable for fabricating stable mercury microelectrodes.

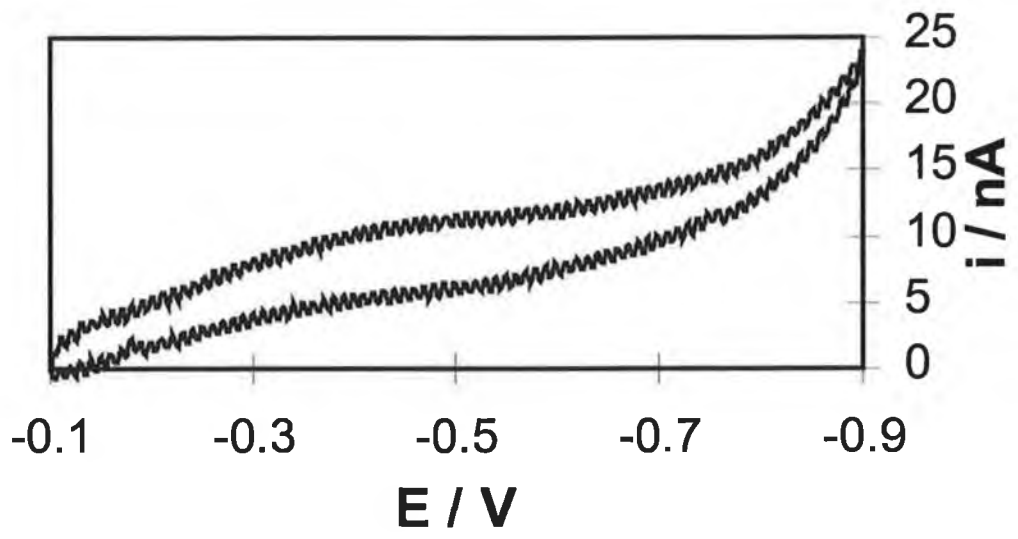

Figure 8 Background CV of a gold based mercury microelectrode immersed in 0.1 M $LiClO_4$. The scan rate is 0.5 V/s and the initial potential is –0.9 V

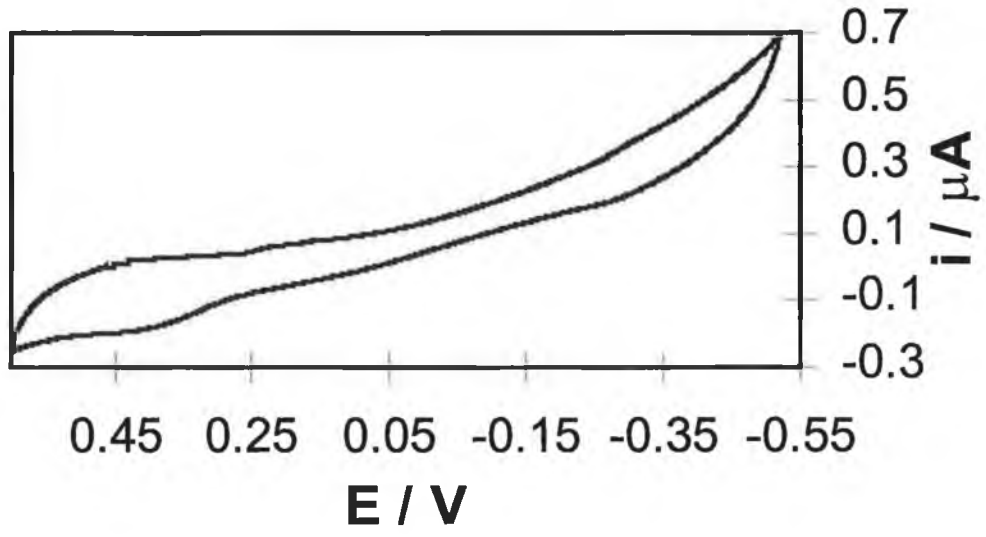

Figure 9 Background CV of a mercury-gold amalgam electrode immersed in 0.1 M $LiClO_4$. The scan rate is 0.1 V/s and the initial potential is –0.5 V.

In summary, small amounts of mercury were observed on 25 μm radius Pt electrodes. Larger deposits were also witnessed, though these suffered from stability problems. Deposition onto 25 μm gold electrodes was unsuccessful due to an amalgam being formed between the mercury and the gold thus changing the electrode composition over time. Construction of mercury microelectrodes was unsuccessful using Hg(II), although recent results from our laboratory suggest that Hg(I) is much more successful in the production of mercury microelectrodes. Finally, after attempting to fabricate mercury microelectrodes we focussed on interfacing a model 660 potentiostat to the dropping mercury electrode (DME). This permitted computer control of the set-up allowing a wide range of experiments to be carried out.

3.2 Characterisation of Microelectrodes

3.2.1 Polishing and Electrochemical Cleaning of Solid Electrodes

After platinum, gold and carbon fibre microelectrodes have been fabricated and left overnight in Milli-Q water, they are polished mechanically using wet alumina (Buehler, Chicago Illinois) on felt pads (Buehler). Polishing is carried out in order to obtain a smooth electrode surface.

Starting with alumina of 12.5 μm particle size, electrodes are successively polished using alumina of size, 5.0, 1.0, 0.3, 0.05 μm. During each polishing step the electrodes are sonicated in Milli-Q water and cyclic voltammograms recorded in 0.1 M $HClO_4$ or H_2SO_4. The purpose of these voltammograms is to observe whether the area of the electrode is decreasing, and to see if the background remains flat, a flat background in the CV is indicative of low resistance. If the background current in the CV becomes sloped, continued polishing on the current, or a higher particle size, alumina is necessary. In some cases when a sloped CV background is observed the only solution is to grind the electrode tip down further with fine sandpaper.

Figure 10 shows representative cyclic voltammograms of a gold electrode immersed in a solution of 0.1 M H_2SO_4. These voltammograms represent, from top to bottom on the right hand side, the electrode after exposure of the microwire, after polishing with 300 grid sandpaper, and after polishing with alumina, respectively. Initially, the peak at approx. 0.9 V is small indicative of a small electrode area or an unreactive surface, and the background current is sloped due to high resistance. After initial polishing with emery paper, the resistance decreases and the active area increases. Finally, after polishing with alumina the electrode area decreases, as does the resistance, yielding an electrode of acceptable quality. Figure 11 indicates how the electrochemical response of a platinum electrode immersed in a 0.1 M $HClO_4$ solution varies with polishing. The electrode resistance appears to be low and the area decreases with increased polishing as indicated by the decreasing currents.

When the electrode area only decreases minimally with continued polishing, a switch is made to a lower particle size alumina. During switches between different particle size alumina the electrode is sonicated in Milli-Q water. To ensure that a microdisk electrode is formed, polishing is carried out with the electrode held at an angle of 90° to the polishing pad and sweeping Figure of 8 movements are employed. The electrode is also turned periodically and moved to a different starting location on the pad to ensure uniform polishing.

After the electrode has been polished and sonicated, a final CV in 0.1 M H_2SO_4 or $HClO_4$ is recorded to obtain the microscopic/electrochemical area of the electrode. Finally, electrodes were cycled between the region 0.0 and 0.9 V in 0.1 M $LiClO_4$ to desorb any adsorbed hydrogen. These background CVs should appear flat and featureless such as that in Figure 12 of a platinum and gold electrode cycled in 0.1 M $LiClO_4$.

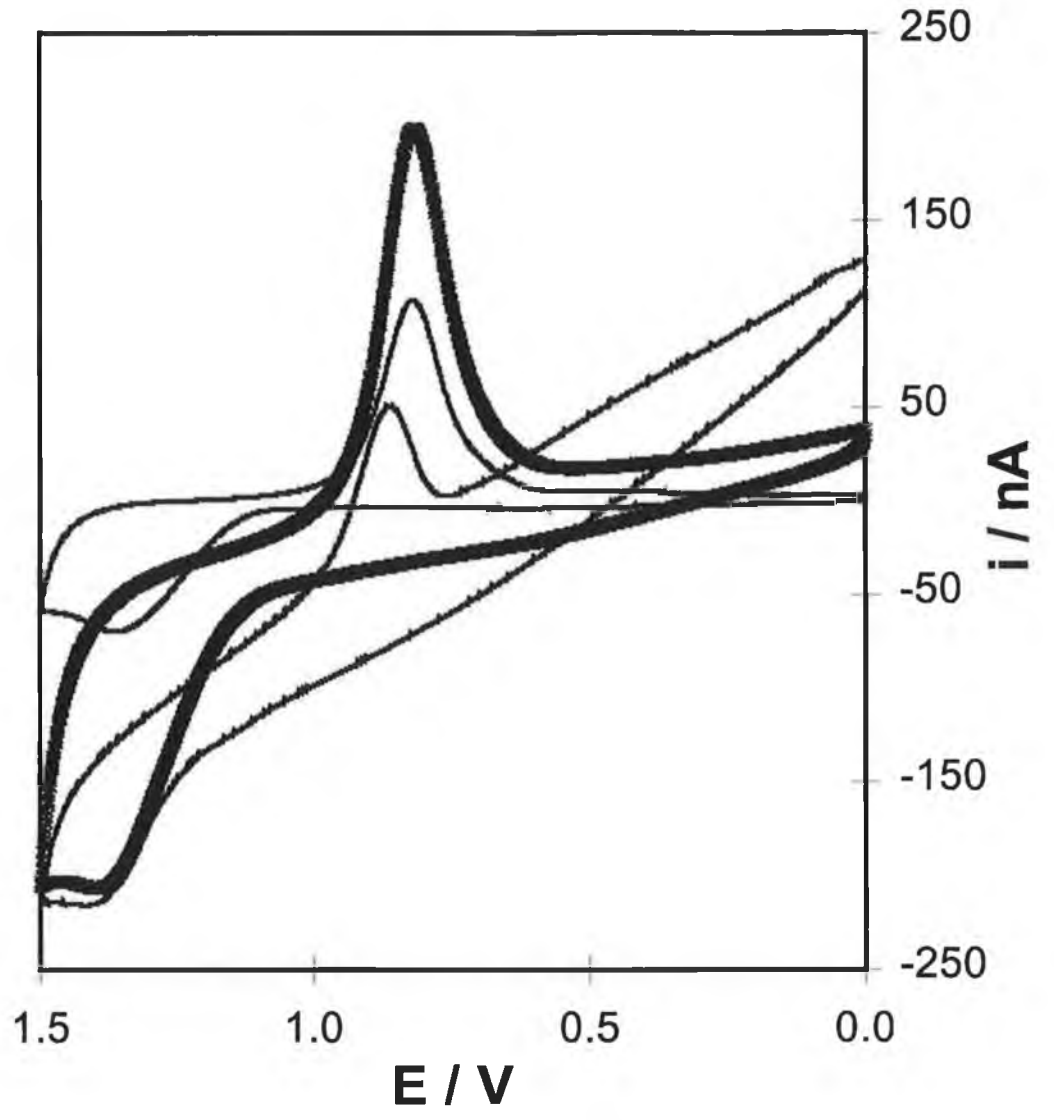

Figure 10 Cyclic voltammograms of a gold microelectrode immersed in 0.1 M H_2SO_4. The voltammograms from top to bottom at 0.0 V represent the electrode after initial exposure of the gold microwire, after polishing with sandpaper, and after polishing with alumina, respectively. The scan rate is 0.5 V/s and the initial potential is 0.0 V.

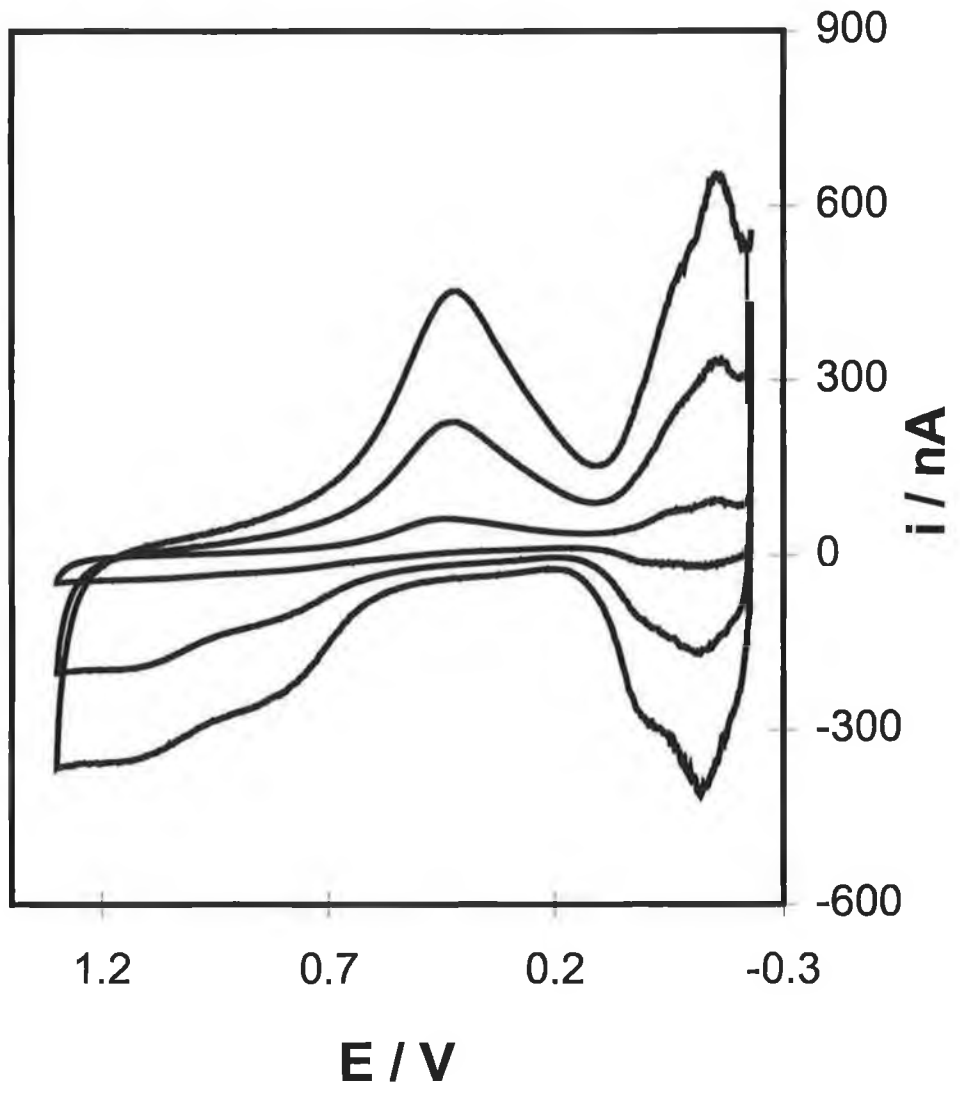

Figure 11 Cyclic voltammograms of a platinum microelectrode immersed in 0.1 M $HClO_4$. The voltammograms, from the largest to the smallest currents, represent the electrode at different stages of polishing. The currents, and therefore the electrode area, decrease with continued polishing. The scan is 1 V/s and the initial potential is -0.230 V.

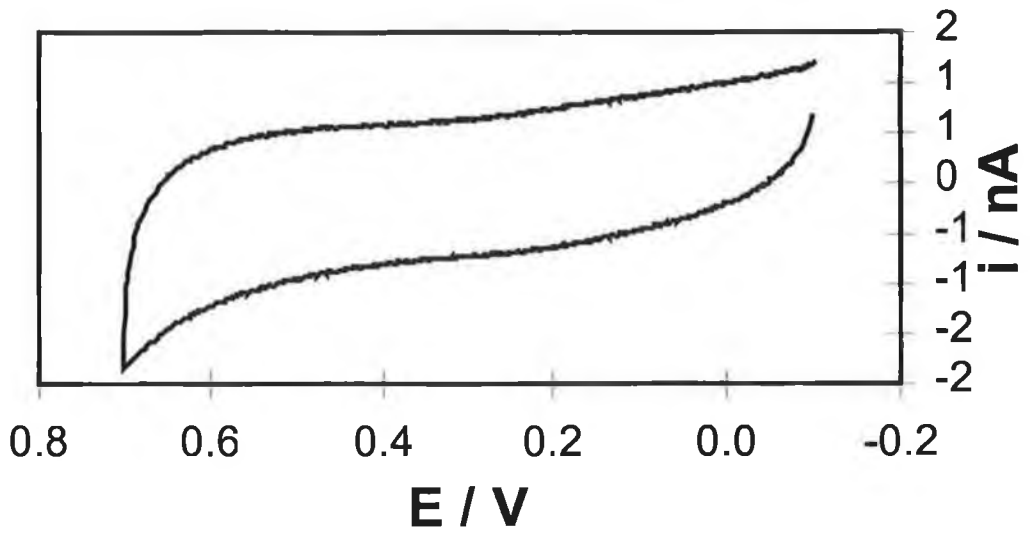

Figure 12(a) Cyclic voltammogram of a bare 25 μm radius platinum electrode in 0.10 M $LiClO_4$. The initial potential is -0.10 V and the scan rate is 0.5 V/s.

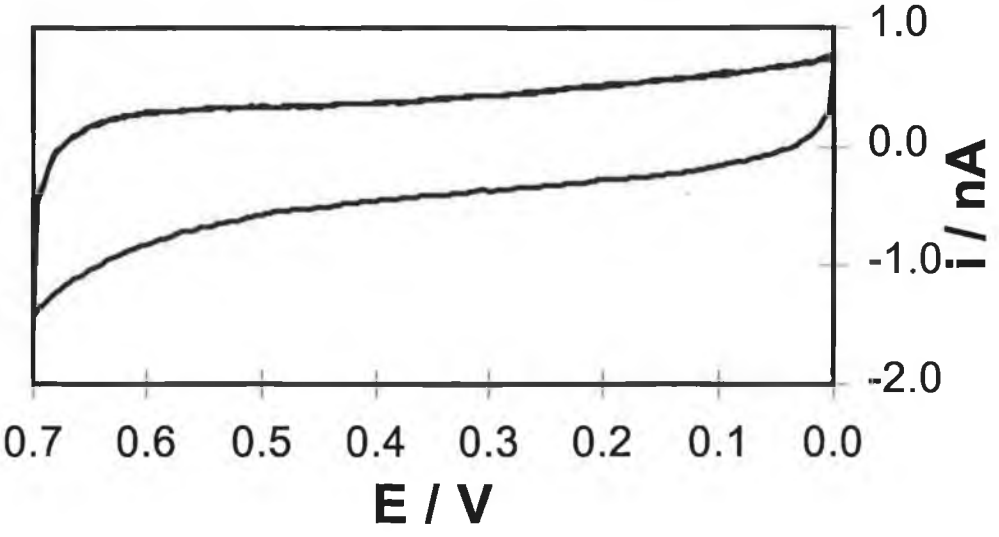

Figure 12(b) Cyclic voltammogram of a bare 25 μm radius gold electrode in 0.10 M $LiClO_4$. The initial potential is 0.0 V and the scan rate is 0.5 V/s.

3.2.2 Measurement of Real Surface Area

Most double layer parameters are extensive quantities and have to be referred to the unit area of the interface. Therefore, knowledge of the *real* or *microscopic* surface area of the electrodes is necessary. Different methods have been proposed to normalise experimental data specifically when dealing with solid electrodes.[34]

The *geometric surface area,* A_g, of an electrode is the surface area which can be determined with ordinary tools designed to measure a length. It is defined as the projection of the real surface on a plane parallel to the macroscopic visible phase boundary.[34] Therefore, A_g is calculated on the basis of known geometric dimensions of the object constituting the electrode whose resolution is normally that of macroscopic measurements. However, it is only in the case of liquids that the real surface area coincides with the geometric area. Where solids are concerned, the electrode surface is rarely atomically smooth requiring that the microscopic area be determined.

Depending on how the real surface area of an electrode is measured and the theory behind the measurement technique, various definitions of *real surface area* can be attached to the expression. Thus, for a given system, various "real surface areas" can in principle be defined, depending on the characteristic dimension of the probe used. These differences exist even if phenomena of surface reconstruction, relaxation and faceting, which often occur during adsorption or electrochemical measurements, are not considered.[34] The most appropriate approach relies on a method which best approaches the experimental situation to which the area determined is to be used, i.e., capacitance measurements in studies of double layer structure.

Electrochemical Techniques used for Determining Real Surface Area

Platinum electrodes: Hydrogen adsorption from solution

The hydrogen adsorption method is used for a few transition metals showing hydrogen adsorption in potential regions prior to massive H_2 evolution. The experimental technique employed is cyclic voltammetry or current step (chronopotentiometry).[35] The method was first established for platinum electrodes,[36] but it has been extended to Rh and Ir ,[37] and to Ni.[38]

The charge under the voltammetric peaks for hydrogen adsorption or desorption (Q_f), corrected for double layer charging, is assumed to correspond to adsorption of one hydrogen atom on each metal atom of the surface. The charge associated with a one-to-one hydrogen-metal correspondence per unit surface area (Q_f^s) is calculated on the basis of the distribution of metal atoms on the surface. This is well defined for a perfect single crystal face[39] whereas it is taken as an average value between the main low-index faces for polycrystalline surfaces (Polycrystalline solid materials consist of an ensemble of randomly oriented crystallites which are the smallest units of single crystals). The resulting value is typically very close to that of the (100) face.[40] The true surface area, A, is derived from Equation 1.

$$A = \frac{Q_f}{Q_f^s} \qquad (1)$$

In the case of polycrystalline Pt the accepted value of Q_f^s is 210 $\mu C\ cm^{-2}$, based on the assumption that the density of atoms on such a surface is $1.31 \times 10^{15}\ cm^{-2}$.[41]

The method assumes that the point where hydrogen adsorption is complete can be exactly identified. Moreover, the technique assumes that there is a definite quantitative relationship between the charge measured and the amount of substance deposited i.e. that total charge transfer takes place between the adsorbate and the

metal. This assumption may not be entirely correct. However, this is the only method which enables an *in situ* estimate of the real surface area of *d*-metal electrodes to be obtained. The total inaccuracy and lack of reproducibility of these measurements can be expected to be ±10%.[40,42] The reliability of the method depends very much on the cleanliness of the electrode surface and hence of the solution used.

Figure 13 shows a typical cyclic voltammogram recorded in 0.1 M $HClO_4$ in which the formation of adsorbed hydrogen, oxidation of this adsorbed hydrogen and formation of adsorbed oxygen/platinum oxide is clearly visible. The area under the two hydrogen adsorption peaks is integrated after correcting for the background charging current. This value, expressed in microcoulombs, is then divided by 210 μC cm^{-2} to provide the real electrode area in cm^2. The surface roughness can be calculated by dividing this *real* area by 1.9634 x 10^{-5} cm^2, the geometric area of a 25 μm radius electrode.

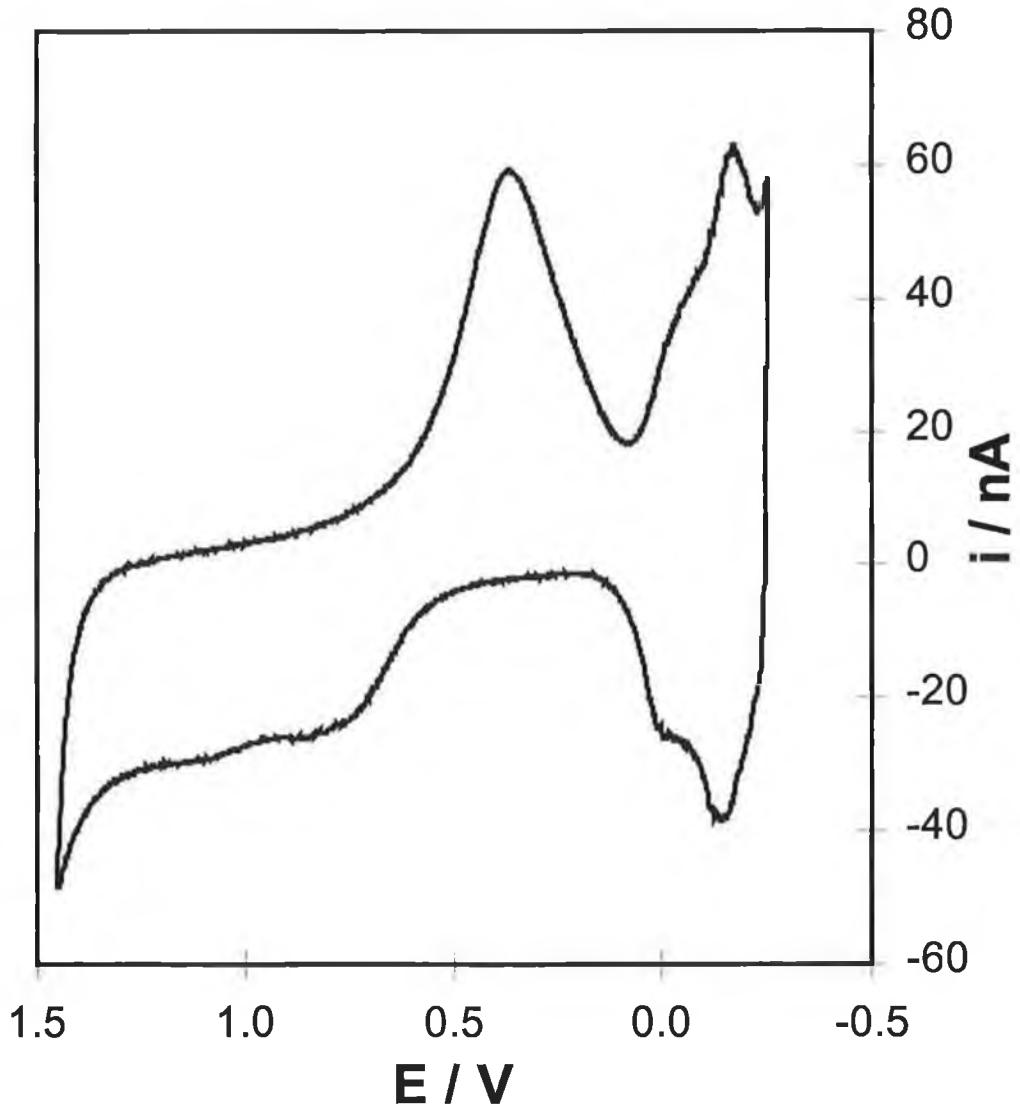

Figure 13 Cyclic voltammogram of a platinum microelectrode immersed in 0.1 M solution of $HClO_4$. The initial potential is -0.250 V and the scan rate is 1 V/s. The electrode area has been calculated as being 33 x 10^{-6} cm^2 giving a surface roughness of 1.7.

Gold electrodes: Oxygen adsorption from solution

This method is applicable for metals showing well developed regions for oxide monolayer formation and reduction. In addition to some *d*-metals, it has been used for gold for which the previous technique cannot be applied since no hydrogen adsorption region is recognisable.

The oxygen adsorption method is based on the same principles as the hydrogen adsorption method. Oxygen is assumed to be chemisorbed in a monoatomic layer before O_2 evolution in a one-to-one ratio with surface metal atoms. This implies that the charge associated with the formation or reduction of the layer is:

$$Q_O = 2eN_A\Gamma_O A \tag{2}$$

where N_A is the Avogadro constant, and Γ_O, the surface concentration of atomic oxygen, is assumed to be equal to N_M, the surface density of metal atoms. From the value of N_M per unit surface area, the value of Q_O^S, the reference charge, is calculated so that;

$$A = \frac{Q_O}{Q_O^S} \tag{3}$$

The accepted value for polycrystalline platinum is 420 μC cm^{-2} and that for polycrystalline gold is 390 ± 10 μC cm^{-2}.[43]

The oxygen adsorption method is less reliable than that based on hydrogen adsorption, but in some cases it is the only applicable method (e.g. Au, Pd). The reliability decreases as the affinity for the metal increases and therefore should be best for gold.

Gold microelectrodes were characterised using the oxygen adsorption from solution method described above. Cyclic voltammograms of a gold electrode of

geometric area 1.963 x 10^{-5} cm^2 immersed in 0.1 M H_2SO_4 are shown in Figure 14. The area under the oxygen adsorption wave is determined after background correction and is divided by 390 μC cm^{-2} to provide the microscopic electrode area.

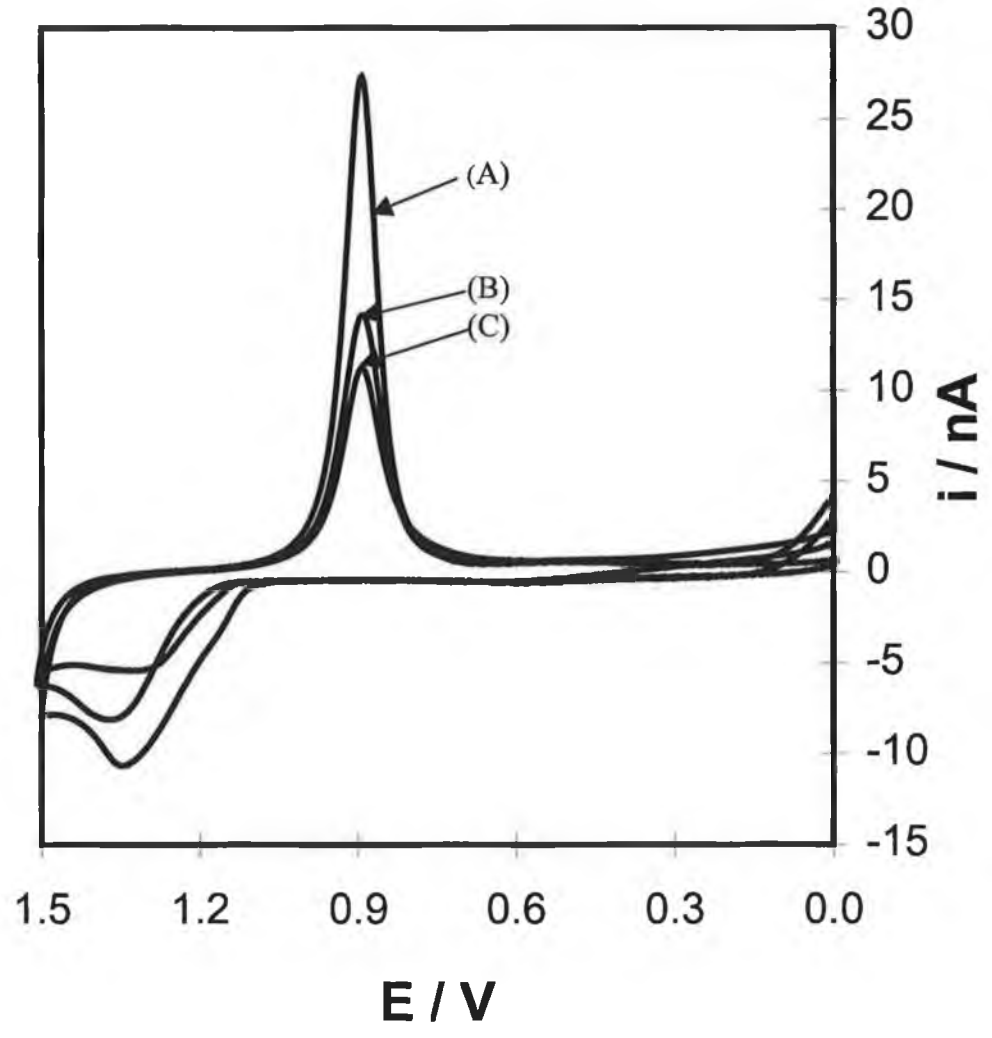

Figure 14 Cyclic voltammograms of a gold microelectrode immersed in 0.1 M H_2SO_4. The initial potential is 0.00 V and the scan rate is 0.10 V/s. Using peak (C) the electrode area has been calculated as 32 x 10^{-6} cm^2 giving a surface roughness of 1.6.

Mercury electrodes: Redox-Active Probe Method

Mercury surfaces are atomically smooth. Therefore, the real and geometric areas are identical and methods relating the Faradaic current to electrode area can be used. In this method, a non-adsorbing, redox active probe is employed to determine the area of the electrode electrochemically. The probe in question must be completely soluble in the solvent used and must be of known concentration. Cyclic voltammograms are run at various sweep rates and the currents obtained are used to obtain the electrode radius. Slow sweep rate (long timescale) voltammograms give rise to steady state currents (sigmoidal-shaped responses) which are governed by Equation 5 which is used to obtain the limiting/steady state current.

$$i_L = 4nFDrC \tag{5}$$

where n is the number of electrons involved in the reaction, F is Faradays constant, D is the diffusion coefficient in $cm^2\ sec^{-1}$, r is the radius of the electrode in cm, and C is the concentration of the redox probe present in solution in mol cm^{-3}.

At higher sweep rates (short timescales) the peak shaped response gives the peak current:

$$i_p = (2.69 \times 10^5)\, n^{3/2} D^{1/2} v^{1/2} C A \tag{6}$$

where A is the area of the electrode in cm^2. By combining both equations to form Equation 7 we are able to determine the radius of the electrode without prior knowledge of the diffusion coefficient of the redox-active species.

$$r = \left(\frac{4 i_p^{\,2}}{2.69 \times 10^5 i_L n^2 v C \pi^2} \right)^{1/3} \tag{7}$$

In the determination of the surface area of the mercury electrodes used in this work a 10 mM solution of 1,4-Benzoquinone in which 0.1 M $TEABF_4$ was used as

supporting electrolyte, was employed to obtain the voltammograms necessary for the calculation of the electrode area. Figure 15 portrays typical cyclic voltammograms of 1,4-benzoquinone recorded at slow and fast sweep rates. Using these currents and equation 7 an electrode radius of 0.035 cm was obtained.

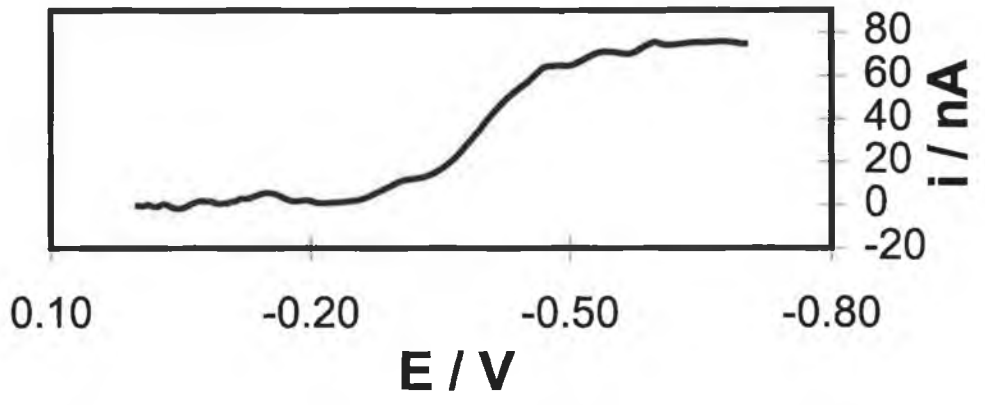

Figure 15(a) Cyclic voltammogram of a 10 mM solution of 1,4-benzoquinone in DMF. The supporting electrolyte is 0.10 M $TEABF_4$. The initial potential is -0.70 V and the scan rate is 0.005 V/s.

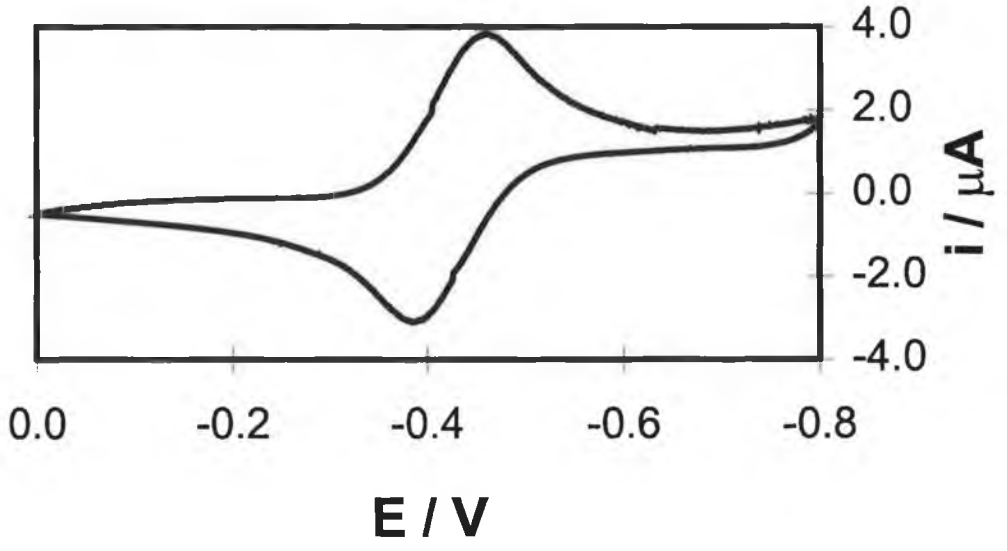

Figure 15(b) Cyclic voltammogram of a 10 mM solution of 1,4-benzoquinone in DMF. The supporting electrolyte is 0.10 M $TEABF_4$. The initial potential is -0.80 V and the scan rate is 0.100 V/s.

Non-Electrochemical Techniques used for Determining Real Surface Area

Mercury electrodes: Drop Weight Method

The drop weight method is that classically used with liquid metal electrodes such as mercury, gallium, and gallium liquid alloys (In-Ga, Ti-Ga, etc.).[44,45] Electrodes may be static (hanging or sessile drop) or dynamic (falling drop). A large number of drops are collected and weighed. This is carried out with the capillary immersed in a cell containing water as drops fall erratically when the capillary is left in air. The weight of the liquid metal is then calculated and related back to the number of drops collected. The weight of one drop is found and this related to the volume and hence radius and area of a sphere.

In the determination of the surface area of the mercury electrodes used in this work, one hundred drops of mercury were dispensed into an electrochemical cell containing a known weight of water. This measurement was repeated five times and the collected drops were dried and weighed. The results were as follows;

Average weight of 100 drops: 0.2825 g
density of Hg: 13.546 g/cm^3
Volume of 1 drop of Hg: 0.02076 cm^3

$4/3\pi r^3 = 0.02076$ cm^3
$r = 0.0367$ cm
$A = 4\pi r^2 = 0.017$ cm^2

The results yielded a mercury drop of radius and surface area of 0.0367 cm and 0.017 cm^2 respectively. These results were experimentally indifferent from those obtained using the redox-active probe method described above.

Carbon Fibre Microelectrodes

It is difficult to obtain the real surface area of carbon fibre microelectrodes. The methods used above for determining the area of gold and platinum electrodes are not applicable as carbon undergoes neither hydrogen or oxygen adsorption from solution. The redox active probe method is since the surface is rarely atomically smooth. For these reasons, the microscopic area of our carbon fibre microelectrodes has not been accurately determined. However, the capacitance of the microelectrodes has been investigated to obtain some insight into the surface roughness. In characterising these electrodes background charging currents were monitored throughout the polishing routine to determine whether the electrode areas and resistances were decreasing. Figure 16 shows typical cyclic voltammograms of a carbon fibre microelectrode immersed in 0.10 M $LiClO_4$ as the electrode is being continually polished. The current decreases systematically until it reaches a point where continued polishing decreases the current minimally. The current in Figure 17 is similar to that observed for a 25 μm radius platinum or gold electrode although the sloped background suggests high resistance. In order to further characterise carbon fibre microelectrodes the RC cell time constants were determined.

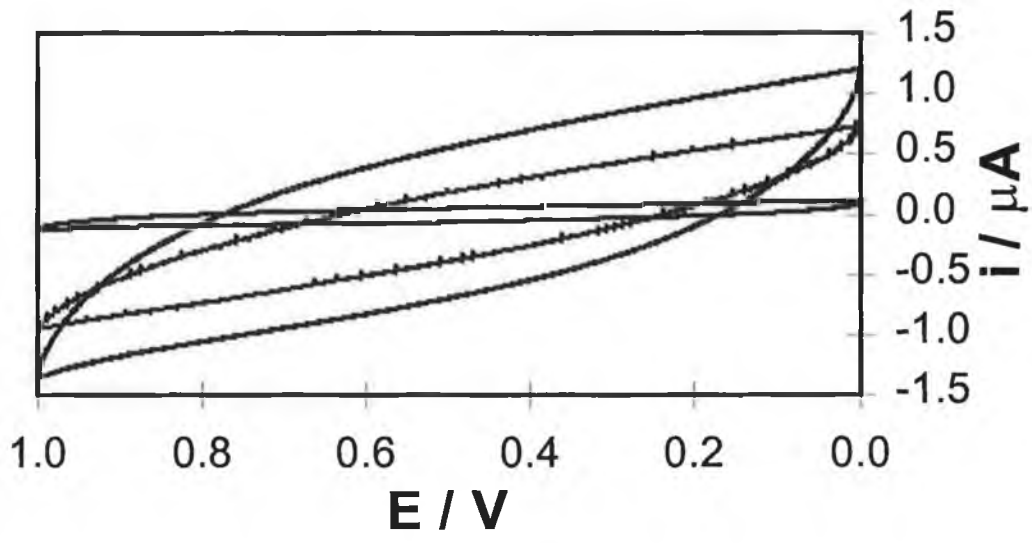

Figure 16 Cyclic voltammogram of a carbon fibre microelectrode immersed in 0.1 M $LiClO_4$. The initial potential is 0.0 V and the scan rate is 0.5 V/s

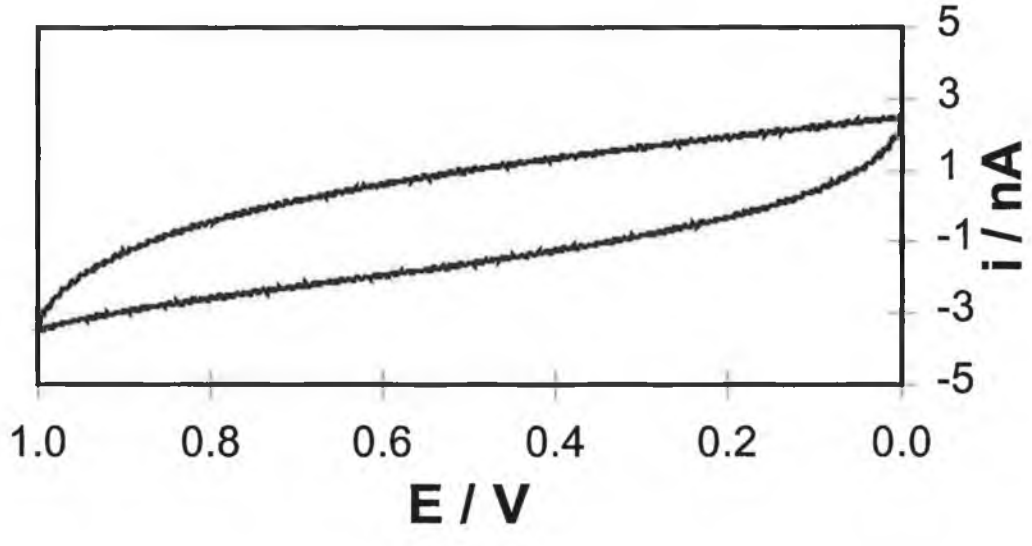

Figure 17 Cyclic voltammogram of a fully polished carbon fibre microelectrode immersed in 0.1 M $LiClO_4$. The initial potential is 0.0 V and the scan rate is 0.5 V/s.

3.2.3 RC Cell Time Constants

As explained in Chapter 1 section 1.4.4, determining RC cell time constants is important if high speed electrochemical measurements are to be made. Every electrochemical measurement has a lower time limit that is imposed by the RC cell time constant. The RC cell time constant which is the product of the solution resistance, R, and the double layer capacitance, C, of the working electrode must be short enough so that it does not interfere with the Faradaic reaction. Also, the resistance of these microelectrodes must be low enough so that the observed response is not influenced by iR drop. In the fabrication of microelectrodes soldering is preferred to other methods of electrical connection such as conducting paint, injecting mercury etc. as it produces less stray capacitance, thus keeping the RC cell time constant of the electrode at a minimum.

According to Equation 8, the solution resistance for a microdisk electrode, R, is inversely proportional to the radius of the electrode, r.

$$R = \frac{1}{4\kappa r} \tag{8}$$

where κ is the conductivity of the solution. Therefore, decreasing the size of the electrode will not decrease the resistance, in fact the resistance is increased. However, solution resistance is also inversely proportional to the conductivity of the solution. Therefore, by investigating the electrochemical response as a function of electrolyte concentration we can study the effect of conductivity on the resistance and RC of microelectrodes.

To characterise the electrolyte and potential dependence of the cell resistance using platinum and gold microelectrodes, a large number of cyclic voltammetric and chronoamperometric measurements were made over a wide range of conditions. The supporting electrolyte employed was $LiClO_4$ at concentrations between 0.05 and

1.0 M. Potentials chosen were the potential of zero charge, PZC, of the electrode, and potentials 0.150 V negative and positive of the PZC.

The cyclic voltammograms in Figure 18 show the effect of electrolyte concentration on the background charging current of platinum and gold microelectrodes immersed in varying concentrations of $LiClO_4$. Cyclic voltammetry is a useful technique for examining the effect of electrolyte concentration on capacitance.

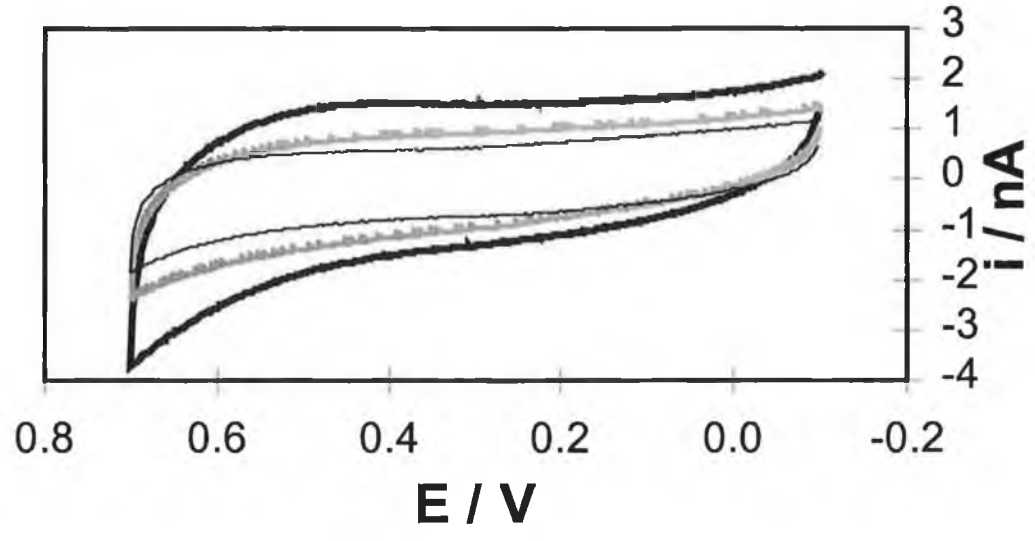

Figure 18(a) Cyclic voltammograms of a 25 μm radius platinum electrode immersed in $LiClO_4$. The concentrations, for the highest to lowest currents, are 1.0, 0.5, and 0.1 M $LiClO_4$.

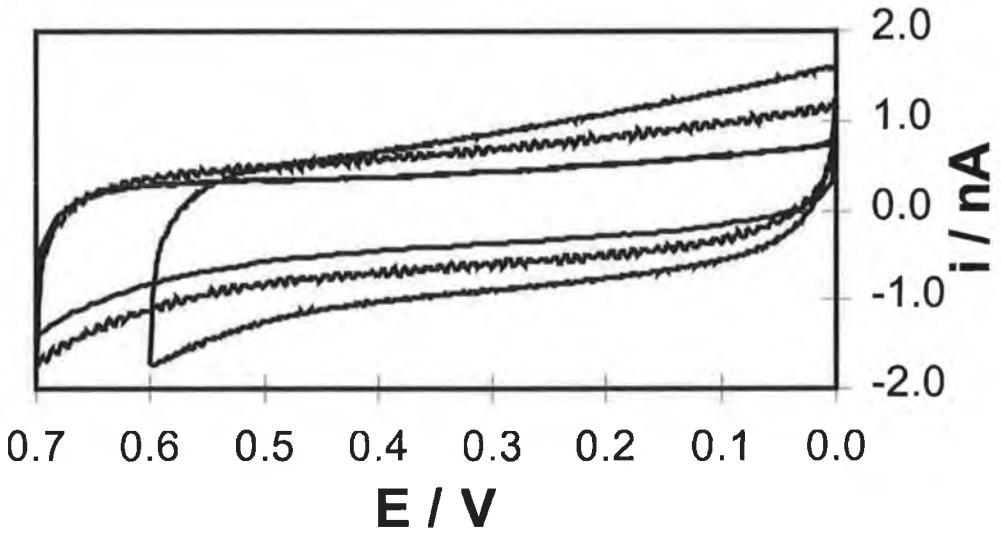

Figure 18(b) Cyclic voltammograms of a 25 μm radius gold electrode immersed in $LiClO_4$. The concentrations, for the highest to lowest currents, are 1.0, 0.5, and 0.1 M $LiClO_4$.

However, a more sensitive technique, which provides information on both the capacitance and resistance as a function of both electrolyte concentration and applied potential, is potential step chronoamperometry. Figure 19 shows the dependence of the chronoamperometric response for a gold electrode as a function of electrolyte concentration. There is an obvious change in the response as a function of concentration that correlates with the changes observed in the cyclic voltammetric response. The charging current, i_c, decays exponentially in time according to Equation 9.

$$i_c = \frac{\Delta E}{R} exp\left(\frac{-t}{RC}\right) \tag{9}$$

where ΔE is the magnitude of the potential step, R is the resistance, C is the capacitance. According to Equation 9 a semi-log plot of these transients should be linear and the slope of this plot provides the RC cell time constant associated with the experiment. The intercept of the semi-log plot provides the resistance of the cell. The insert of Figure 19 provides semi-log plots of the current-time transients. These

are linear over at least two lifetimes thus allowing meaningful quantitative analysis of the dependence of both the resistance and RC on electrolyte concentration. The increasing slope with electrolyte concentration indicates that RC is decreasing while the larger the intercept, the larger the resistance.

Figure 20 shows the potential dependent response for a platinum electrode immersed in 0.1 M $LiClO_4$ as a function of applied potential. There appears to be little difference in the responses positive, negative or at the PZC, a fact confirmed by the semi-log plots in Figure 21.

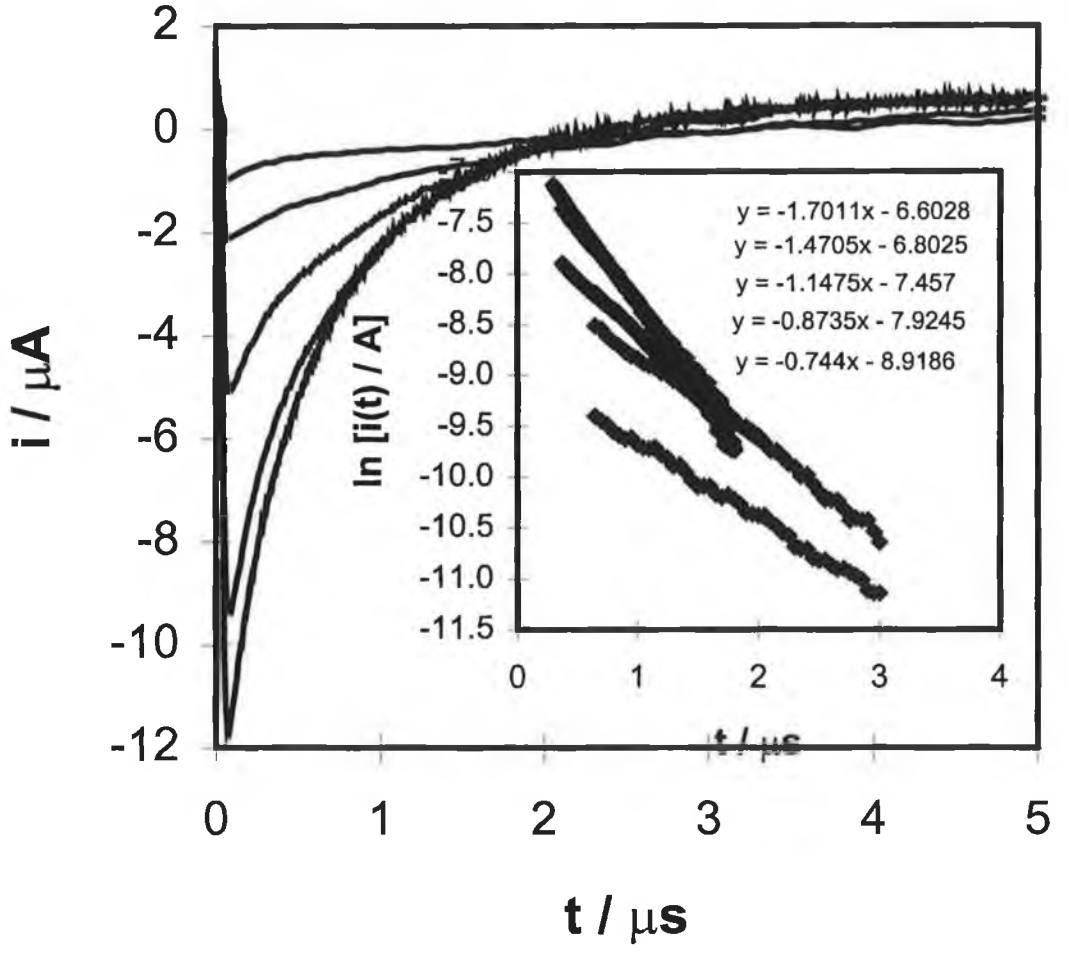

Figure 19 Dependence of the chronoamperometric response for a 25 μm radius gold electrode on electrolyte concentration. The current-time transients from top to bottom on the left hand side, represent the electrode in 0.05, 0.1, 0.25, 0.5, and 0.75 M $LiClO_4$. The insert which shows the semi-log plots of the transients are, from top to bottom, 0.75, 0.5, 0.25, 0.1, and 0.05 M $LiClO_4$.

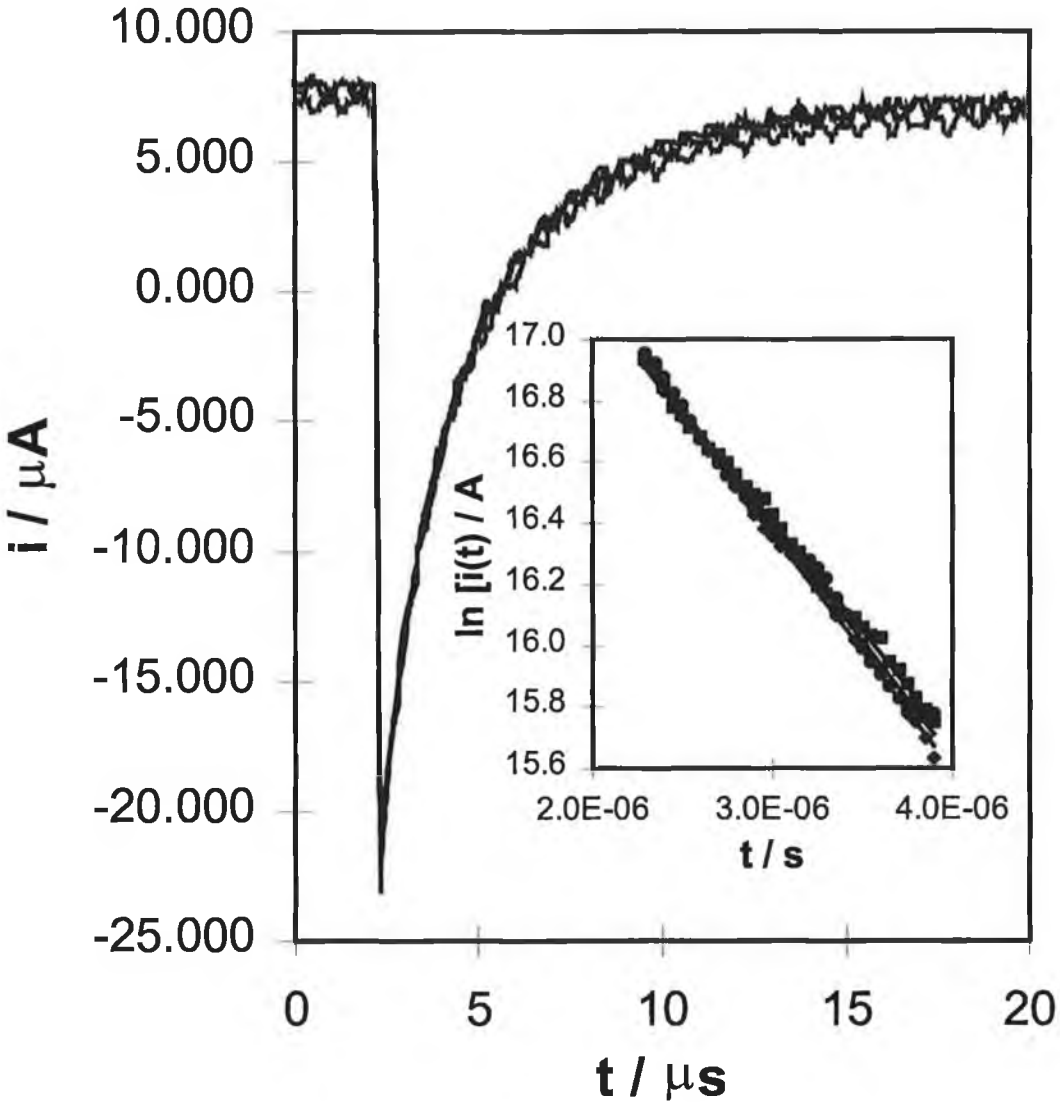

Figure 20 Dependence of the chronoamperometric response for a 25 μm radius platinum electrode applied potential. The electrolyte is 0.1 M $LiClO_4$ and the current-time transients were recorded using a pulse amplitude of 30 mV at the PZC and potentials 150 mV positive and negative of the PZC. The semi-log plots provide resistance and capacitance data.

Figures 21 and 22 show the decrease in RC cell time constants with increasing electrolyte concentration for clean gold and platinum microelectrodes immersed in aqueous lithium perchlorate. As expected the RC time constant decreases significantly over the range 0.05 to 1.00 M $LiClO_4$. The largest decrease in RC occurs on increasing the electrolyte concentration from 0.05 to 0.25 M. In this range the RC decreases from 8 to 2 μs. For electrolyte concentrations above 0.25 M the decrease in RC is much smaller; decreasing by approximately 1 μs between 0.25 and 1.00 M.

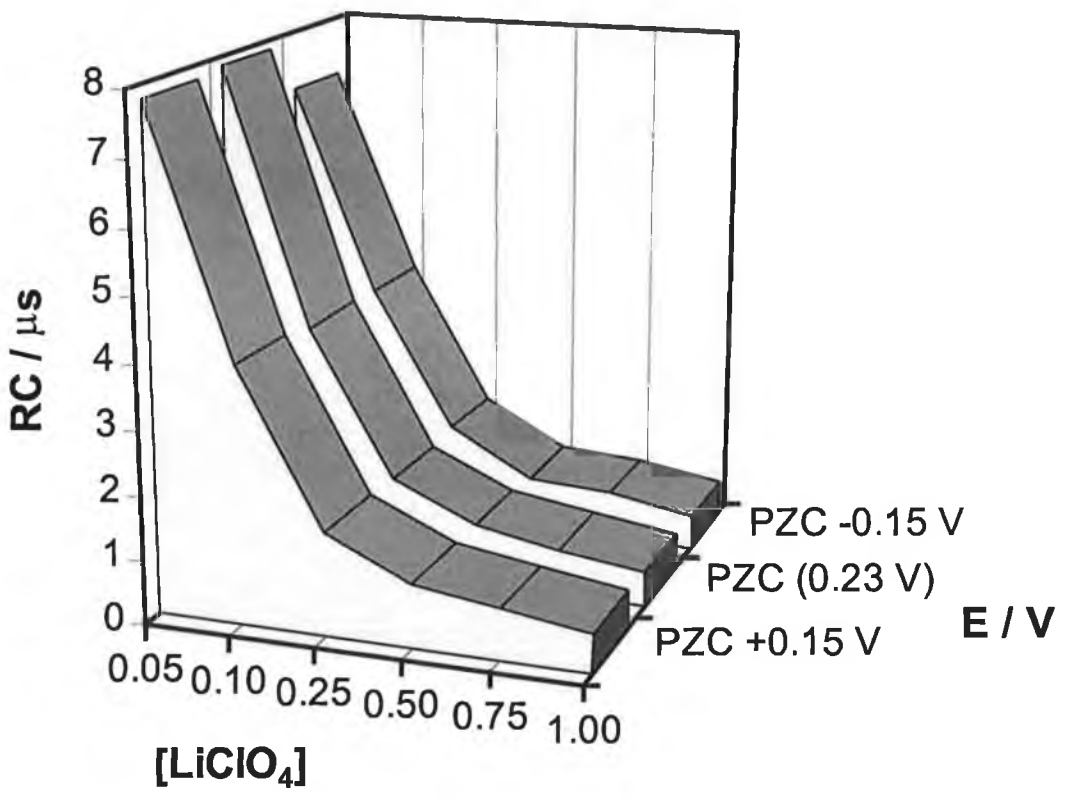

Figure 21 RC cell time constant of a 25 μm radius gold electrode as a function of electrolyte concentration and applied potential. Measurements were made by stepping the potential 30 mV in a positive potential direction.

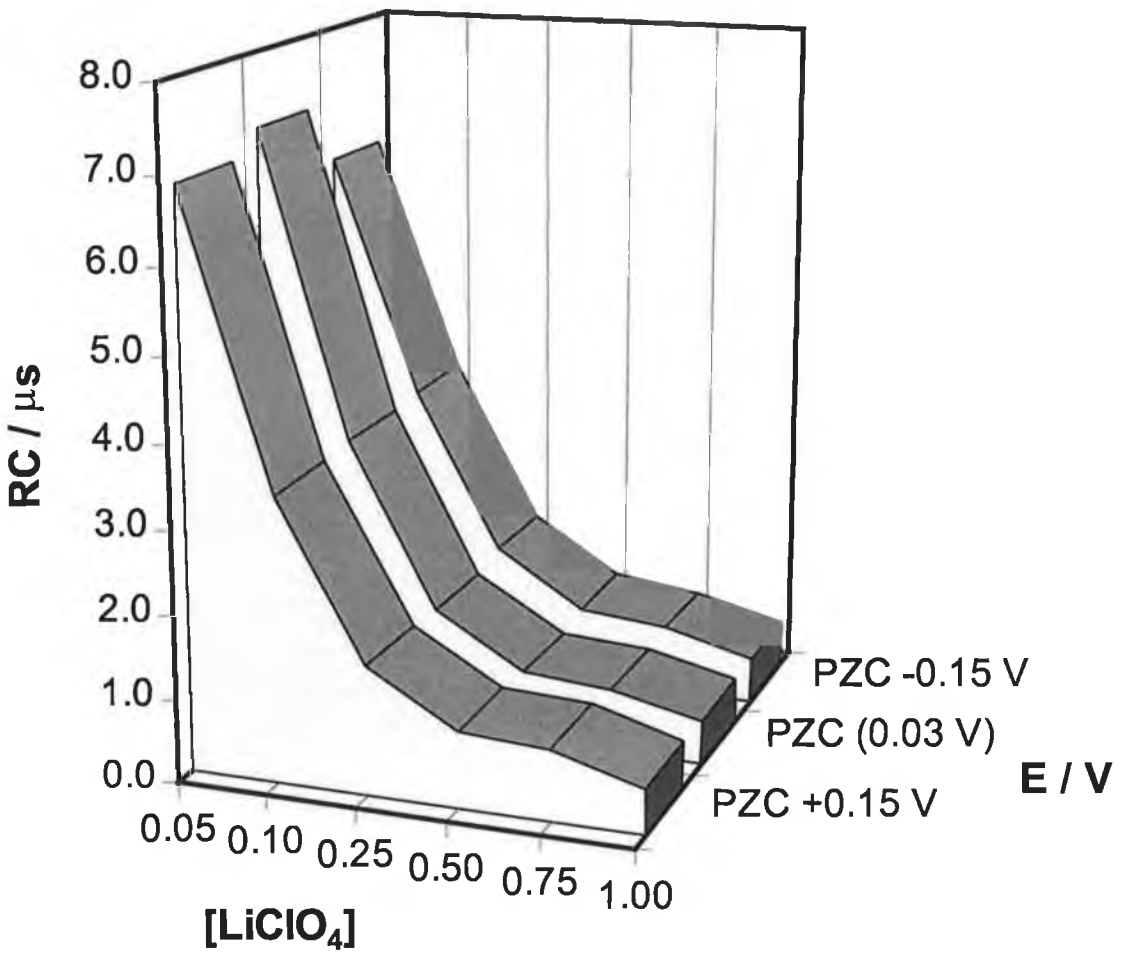

Figure 22 RC of a 25 µm radius Pt electrode as a function of electrolyte concentration and applied potential. Conditions are as in Figure 15(a)

Significantly, Figures 21 and 22 indicate that increasing the electrolyte concentration, and therefore the conductivity of the solution, lowers the RC of the electrode by as much as sixteen fold over the concentration range 0.05 to 1.00 M. RC values as low as 500 ns are possible for 25 µm radius gold or platinum electrodes in 1.00 M $LiClO_4$. This effect is common to both types of electrode to an almost identical degree.

The resistance of these electrodes has also been studied and compared with theoretical values for the electrolyte employed. Figure 23 shows the influence of electrolyte concentration on the resistance of platinum and gold microelectrodes. As expected the resistance decreases with increasing concentration. The theoretical resistance, calculated using Equation 8 is also shown. It can be seen that the theoretical and measured resistances agree closely with one another.

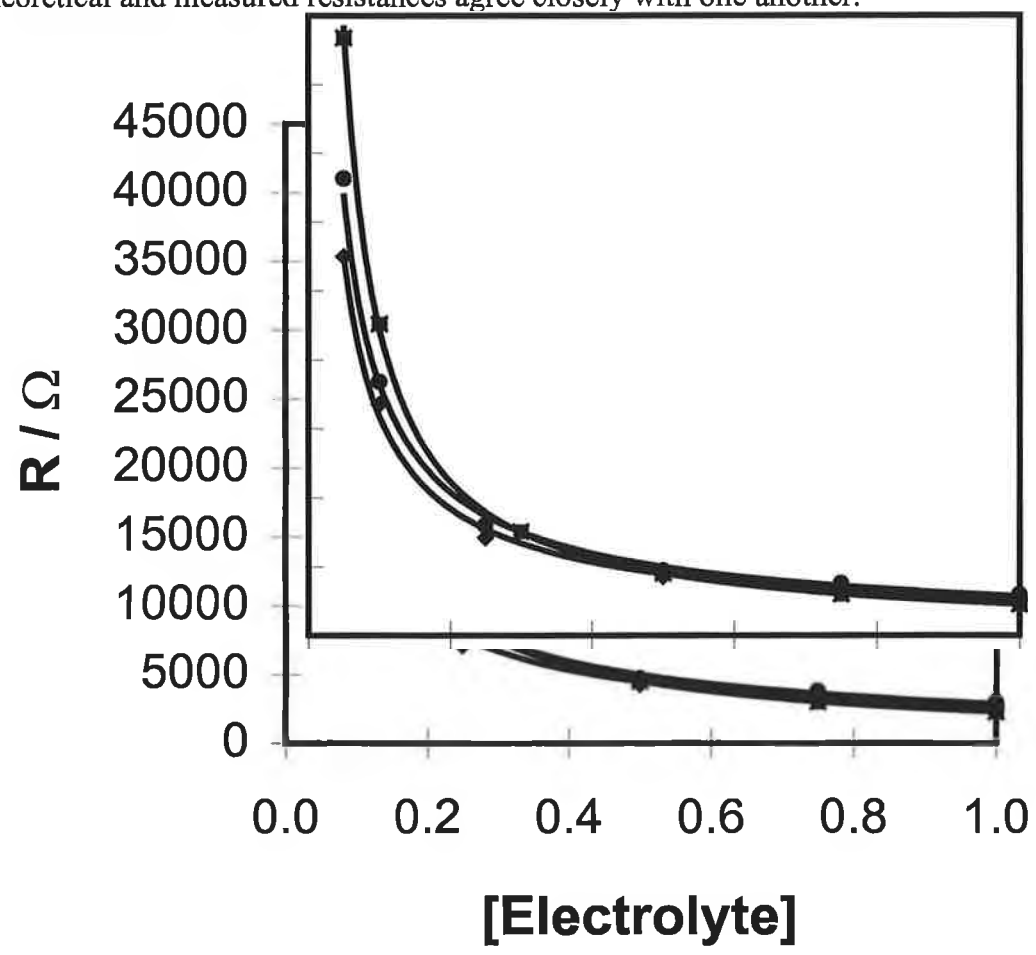

Figure 23 Dependence of resistance on the concentration of supporting electrolyte. The lines from top to bottom on the right hand side represent theoretical resistance for a 25 μm radius electrode with a roughness of 4, a 25 μm radius gold electrode, and a 25 μm radius platinum electrode respectively.

Carbon fibre and mercury electrodes have also been characterised with regard to RC cell time constant. Figure 24 shows a typical current-time transient and semi-log plot used to determine the RC cell time constant of a carbon fibre

microelectrode. That the current decays exponentially and the semi-log plot is linear over at least two lifetimes suggests that this data together with Equation 9 may be used to determine the RC cell time constant accurately. For a typical carbon fibre microelectrode the resistance and RC were in the range of 14000 Ω and 20 μs respectively. These data are consistent with a microelectrode with a radius of less than 100 μm. Figure 25 shows the corresponding plots for a mercury electrode. Due to the increased size of the mercury electrode, the experimental timescale is longer and the RC larger at approximately 150 μs.

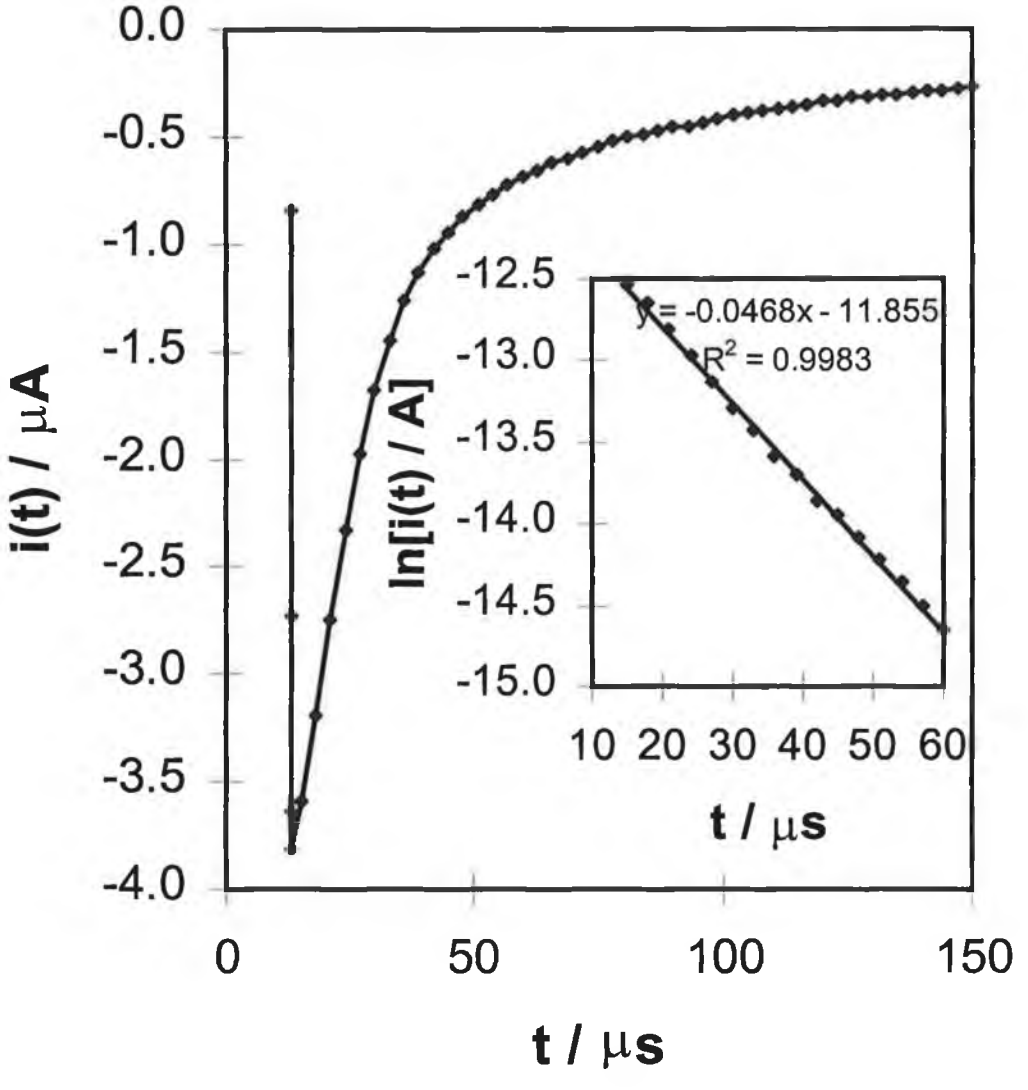

Figure 24 Current time transient and semi-log of bare carbon fibre electrode in 0.1 M $LiClO_4$. The RC time constant is 21 μs. The pulse amplitude is 100 mV and is being stepped in a positive potential direction. The initial potential is 0.30 V.

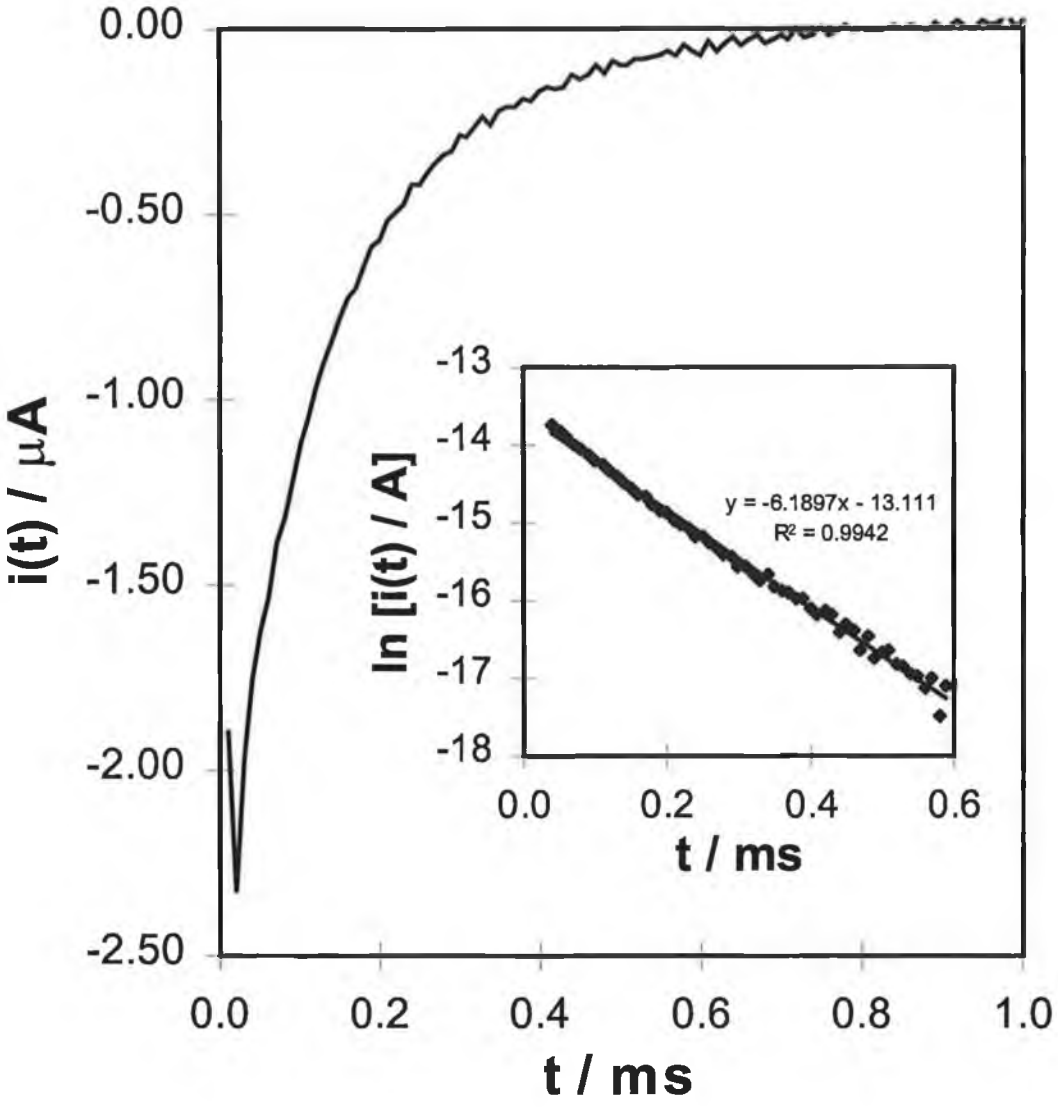

Figure 25 Current-time transient and semi log plot for a mercury electrode in contact with 0.05 M NaF. The pulse amplitude is 30 mV and is being stepped in a negative potential direction. The initial potential is -0.20 V.

3.2.4 Determination of Potential of Zero charge

In order to fully characterise electrodes it is important that the potential of zero charge of the constructed electrodes corresponds with literature values. The potential of zero charge is the potential at which there is no excess charge on the electrode surface and is distinctive for electrodes of different material. A well known method for determining the PZC is that first proposed by Frumkin.[46] It involves the measurement of the differential capacity minimum. As we know from Chapter 1, the double layer capacitance, C_{dl}, exhibits complex behaviour and is governed by the smaller of the two components on the right hand side of Equation 10;

$$\frac{1}{C_{dl}} = \frac{1}{C_H} + \frac{1}{C_D} \qquad (10)$$

where C_H is the capacitance associated with the compact layer while C_D is the capacitance of the diffuse layer. In dilute electrolyte solutions (< 0.1 M) C_D is sufficiently small to significantly influence the double layer capacitance. Since only C_D is normally influenced by potential, the potential dependence of C_{dl} can be used to identify the PZC as a sharp decrease in the C_{dl} vs. E curve.

Figures 26, 27, and 28 show the C_{dl} vs. E curves associated with Hg, Pt and Au electrodes. The experimentally determined PZC associated with these plots are recorded in Table 1 together with values taken from the literature. There is excellent agreement between experiment and theory in all cases. The PZC for carbon fibre microelectrodes was not obtained as problems exist due to redox active surface quinones which makes measurement of the PZC for carbon electrodes meaningless.

Table 1 Potentials of zero charge for platinum, gold, and mercury electrodes.

Electrode	Literature Value	Experimental value
Platinum	0.03 V[47]	0.03 V
Gold	0.20 V[48]	0.021 V
Mercury	-0.47 V[49]	-0.45 V

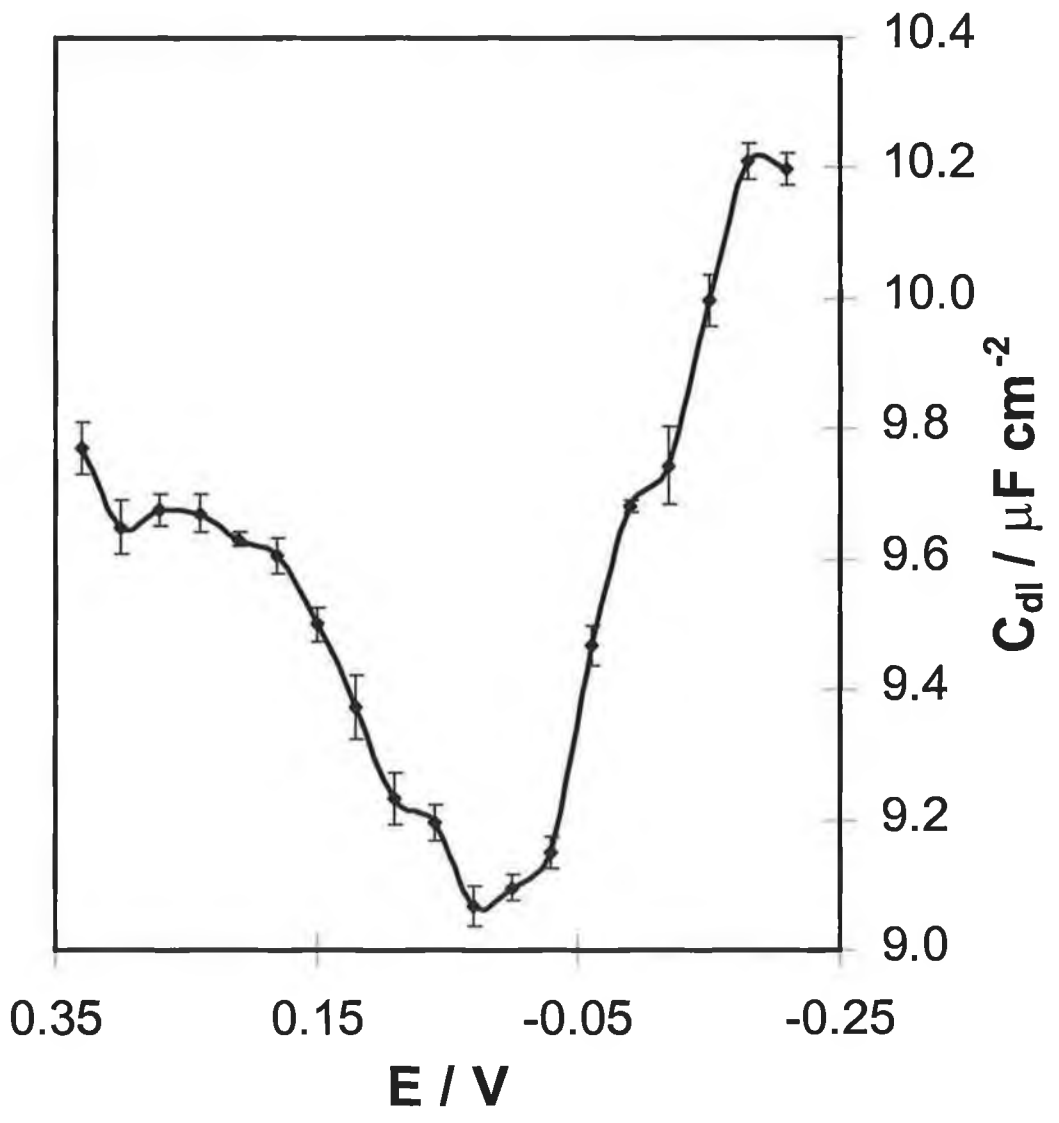

Figure 26 PZC of 25 μm platinum electrode. Chronoamperometry using a pulse amplitude of 60 mV was used to obtain individual points. The supporting electrolyte is 0.05 M NaF. Error bars represent data from at least three separate experiments.

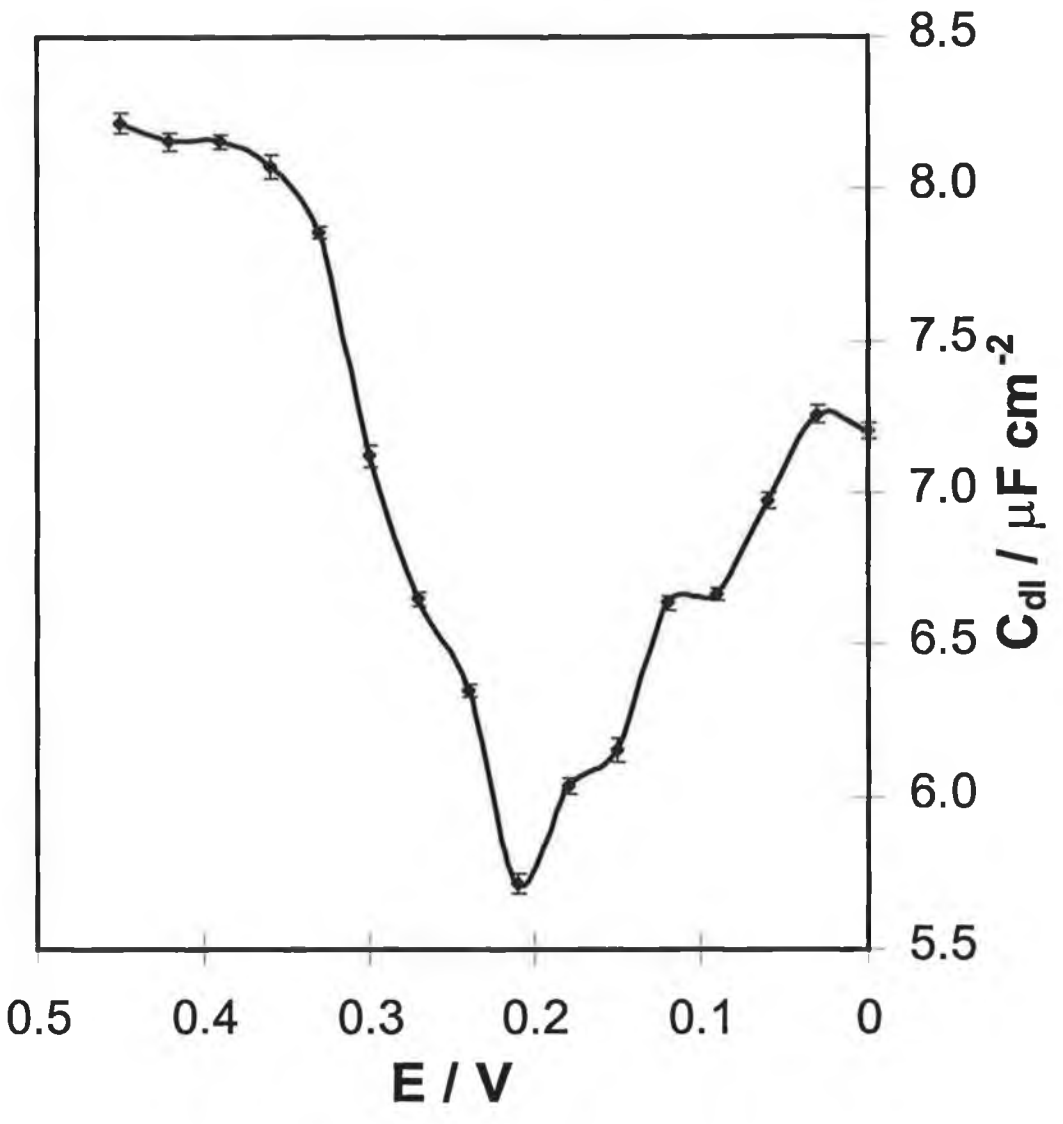

Figure 27 PZC of 25 μm gold electrode. Chronoamperometry using a pulse amplitude of 60 mV was used to obtain individual points. The supporting electrolyte is 0.05 M NaF. Error bars represent data from at least three separate experiments.

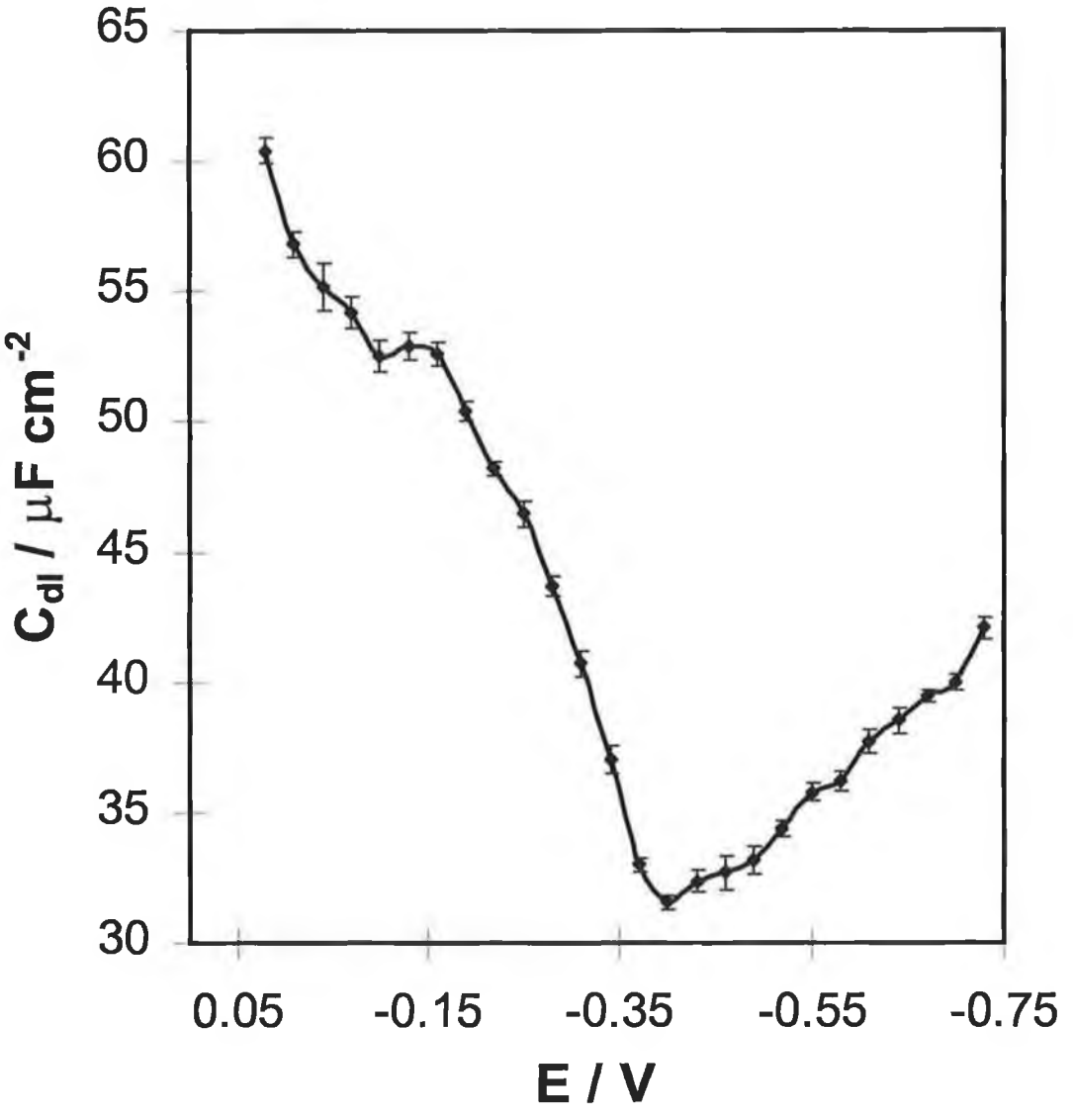

Figure 28 PZC of 25 μm mercury electrode. Chronoamperometry using a pulse amplitude of 60 mV was used to obtain individual points. The supporting electrolyte is 0.05 M NaF. Error bars represent data from at least three separate experiments.

3.3 Conclusion

This chapter has shown that microelectrodes with a 25 μm radius can be fabricated routinely with a high success rate. From the point of view of monitoring fast electrochemical experiments the overall RC time constant of the electrochemical cell is of utmost importance. In particular, the ability to resolve the Faradaic and non-Faradaic components of current-time responses and the reduction of iR drop are of uppermost consideration. We have shown that our 25 μm radius Pt and Au electrodes have RC time constants as low as 500 ns. This indicates that these microelectrodes are suitable for examining fast electron transfers involving immobilised redox active species.

3.4 References

1 Montenegro, M. I.; Queiros, M. A.; Daschbach, J. L. Eds. *Microelectrodes: Theory and Applications*, Kluwer Academic, Netherlands 1991.

2 Brett, C. M. A.; Brett, A. M. O. *Electrochemistry: Principles, Methods, and Applications*; Oxford University Press: New York 1993.

3 Carter Ed. Molecular Electronic Devices II; Marcel Dekker: New York, 1987.

4 Wightman, R. M.; Amatore, C.; Engstrom, R. C.; Hale, P. D.; Kristensen, E.W.; Kuhr, W. G.; May, L. J. *Neuroscience* 1988, 25, 513.

5 Ferris, C. D. " Introduction to Bioelectrodes" Plenum Press, 1974.

6 Forster, R. J. *Chem. Soc. Rev.* 1994, 289.

7 Amatote, C. In *Physical Electrochemistry, Principles, Methods and Applications*, Ed; Rubinstein, I. Marcel Dekker INC., 1995

8 Engstrom, R. C.; Weber, M.; Wunder, D. J.; Burgess, R.; Winquist, S. *Anal. Chem.* 1986, 158, 844.

9 Amatore, C.; Kelly, R. S.; Kristensen, E. W.; Kuhr, W. G.; Wightman, R. M. *J. Electroanal. Chem.* 1986, 213, 31.

10 Liu, H.-Y.; Fan, F.-R. F.; Lin, C. W.; Bard, A. J. *J. Am. Chem. Soc.* 1986, 108, 3838.

11 Schroeder, T. J.; Jankowski, J. A.; Kawagoe, K. T.; Wightman, R. M.; Lefrou, C.; Amatore, C. *Anal. Chem.* 1993, 65, 2711.

12 Kristensen, E. E.; Wilson, R. L.; Wightman, R. M. *Anal. Chem.* 1986, 58, 986.

13 White, J. G.; Jorgenson, J. W. *Anal. Chem.* 1986, 58, 293.

14 White, J. G.; St. Claire, R. L.; Jorgenson, J. W. *Anal. Chem.* 1986, 58, 293.

15 Knecht, L. A.; Guthrie, E. J.; Jorgenson, J. W. *Anal. Chem.* 1984, 56, 479.

16 Howell, J. O.; Wightman, R. M. *Anal. Chem.* 1984, 56, 524.

17 Wipf, D. O.; Michael, A. C.; Wightman, R. M. *J. Electroanal. Chem.* 1989, 269, 15.

18 Pendley, B. D.; Abruña, H. D. *Anal. Chem.* 1990, 62, 782.

19 Robinson, R. S.; McCreery, R. L. *Anal. Chem.* 1981, 53, 997.

20 Wehmeyer, K. R.; Wightman, R. M. *J. Electroanal. Chem.* 1985, 196, 417.

21 Cheng, I. F.; Schimpf, J. M.; Martin, C. R. *J. Electroanal. Chem.* 1990, 284, 499.

22 Tschuncky, P.; Heinze, J. *Anal. Chem.* 1995, 67, 4020.

23 Cushman, M. R.; Bennett, B. G.; Anderson, C. W. *Anal. ChIm. Acta* 1981, 130, 323.

24 Baranski, A. S.; Quon, H. *Anal. Chem.* 1986, 58, 407.

25 Wehmeyer, K. R.; Wightman, R. M. *Anal. Chem.* 1985, 57, 1989.

26 Golas, J.; Galus, Z.; Osteryoung, J. *Anal. Chem.* 1987, 59, 389.

27 O'Shea, T.; Lunte, S. M. *Anal. Chem.* 1993, 65, 247.

28 Lu, W.; Baranski, A. S. *J. Electroanal. Chem.* 1992, 335, 105.

29 Wightman and Wipf In *Voltammetry at ultramicroelectrodes*

30 Baldo, M. A.; Daniele, S.; Corbetta, M.; Mazzocchin, G. A. *Electroanalysis* 1995, 7, 980.

31 Ciszkowska, M.; Donten, M.; Stojek, Z. *Anal. Chem.* 1994, 66, 4112.

32 Birke, R. L.; Huang, Z. *Anal. Chem.* 1992, 64, 1513.

33 Xu, C. Ph.D. Thesis, *University of Illinois Urbana Champaign*, 1992.

34 Trasatti, S.; Petrii, O. A. *J. Electroanal. Chem.* 1992, 327, 354.

35 Frumkin, A. N. in Advances in Electrochemistry and Electrochemical Engineering, Vol 3, Wiley-Interscience, New York 1963.

36 Gilman, S. *J. Phys. Chem.* 1963, 67, 78.

37 Gilman, S. *J. Phys. Chem.* 1967, 71, 4339.

38 Pshchenichnikov, A. G. *Mat. Chem. Phys*. 1989, 22, 121.

39 Motoo, S.; Furuya, N. *J. Electroanal. Chem.* 1984, 167, 309.

40 Hayes, M.; Kuhn, A. T. *Appl. Surf. Ssi.* 1980, 6, 1.

41 Biegler, T.; Rand, D. A. J.; Woods, R. *J. Electroanal. Chem.* 1971, 29, 269.

42 Barna, G. G.; Frank, S. N.; Teherani, T. H. *J. Electrochem. Soc.* 1982, 129, 746.

43 Michri, A. A.; Pshchenichnikov, A. G.; Burshtein, R. Kh. Elektrokhimiya 1972, 8, 364.

44 Broadhead, J.; Hills, G. J.; Kinniburgh, D. R. *J. Appl. Electrochem.* 1971, 1, 147.

45 Grahame, D. C. *J. Am. Chem. Soc.* 1957, 79, 701.

46 Vorsina, M.; Frumkin, A. N. C. R. (Dokl.) Acad. Sci. (USSR) 1939, 24, 924.

47 Bretz, R. L.; Abruña, H. D. *J. Electroanal Chem.* 1995, 123, 388

48 Hamelin, A. *J. Electroanal Chem.* 1987, 234, 93.

49 Bard, A. J.; Faulkner, L. R. *Electrochemical Methods : Fundamentals and Applications*, Wiley, New York, 1980.

Chapter 4

Potential and pH dependent Electrochemistry of Anthraquinone-2,7-disulphonic acid

4.1 Introduction

The role of electron transfer in molecular electronics,[1,2,3] biological processes,[4,5,6,7,8] photophysics[9] and sensor technology[10] has received much attention over the past two decades. Depositing monomolecular films using self-assembly or spontaneous adsorption approaches represents an important approach to controlling the properties of the electrode/solution interface.[2,11,12,13,14] Immobilised, redox-active monolayers to form highly ordered materials offer the possibility of being able to control electron transfer distance, mass transfer effects, and the local microenvironment, thus enabling the processes that influence heterogeneous electron transfer to be fully understood. Two of the processes that may influence electron transfer in quinonoid systems are the strength with which the adsorbed species is bound to the electrode surface and the pH of the contacting electrolyte solution.[15,16,17,18,19,20] While numerous investigations have focused on the physical and chemical properties of these films,[15,21,22] much less is known about the kinetics and thermodynamics of adsorption in systems of this type. Molecular adsorption onto metal electrodes is known to be profoundly influenced by the specific properties of the substrate and by the state of charge of the surface.[23,24,25] In particular, the applied potential plays an important role in determining the stability and configuration of adsorbates.[26,27,28,29,30] For redox active monolayers, the applied potential may influence the adsorption process, not only by changing metal-adsorbate interactions, but also by changing adsorbate-adsorbate interactions through changes in the redox composition of the film.[31] The role of applied potential in interfacial electrochemistry has received much attention over the past number of years.[32,33,34,35] Some recent research has been carried out on the importance of potential on the formation of adsorbed monolayers.[31] However, little is known about how the applied potential influences the structure of spontaneously adsorbed monolayers, particularly the strength of adsorption.

The most popular approach to addressing these difficult issues relies on measurements taken over a potential window where the adsorbate is electroinactive. A significant drawback of this approach is that information about how the redox composition affects the metal-adsorbate or metal-solvent interactions cannot be

easily obtained. In recent years, there has been a stronger focus on using Faradaic rather than capacitance measurements to probe these issues. This situation is somewhat surprising given the sensitivity of the interfacial capacitance to the presence of adsorbates. One of the difficulties associated with obtaining accurate capacitance data on redox active films is the difficulty in separating Faradaic and capacitive currents when making measurements close to the formal potential. Recently, we have demonstrated that that by using high speed chronoamperometry it is possible to efficiently time resolve, and therefore separate, these current contributions under a wide range of experimental conditions.[36,37] Therefore, probing the potential dependence of the interfacial capacitance as the bulk concentration, and hence surface coverage, of a surface active molecule is systematically varied, can provide a useful insight into potential dependent adsorption of electroactive species. In this contribution, we apply this approach to studying the effect of potential on the formation of anthraquinone-2,7-disulphonic acid (2,7-AQDS, Scheme 1) monolayers.

The potential dependence of the differential capacitance of metal electrodes can exhibit well defined maxima at certain voltages in the presence of physically adsorbed neutral molecules.[38] These peaks are interpreted as evidence of adsorption/desorption at the electrode surface. However, the capacitance behaviour of organic monolayers that are chemisorbed to the electrode surface is quite different and adsorption/desorption peaks are absent because a more or less permanent film is formed.[39] We are interested in measuring the interfacial capacitance to diagnose the strength of 2,7-AQDS adsorption over a wide range of potentials encompassing regions where the film is electroactive and regions far from the formal potential of the quinone/hydroquinone redox reaction.

The ability to time-resolve capacitive and Faradaic currents makes it possible to probe the potential dependence of the interfacial capacitance as the bulk concentration, and hence surface coverage, of a surface active molecule is systematically varied. In this way, we have obtained a useful insight into the

potential dependent adsorption of electroactive species that are reversibly adsorbed onto electrode surfaces.

Scheme 1

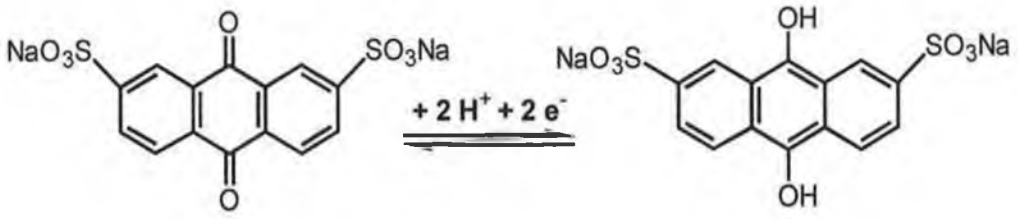

4.2 Experimental

4.2.1 Materials and procedures

The disodium salt of anthraquinone-2,7-disulphonic acid (2,7-AQDS) was obtained from BASF. All electrolytes were prepared using Milli-Q purified water. Unless otherwise stated, Milli-Q purified water was used as the solvent and the electrolyte was 0.1 M $LiClO_4$. In experiments where the pH dependence of the voltammetric response was probed, the pH of the contacting electrolyte solution was systematically varied by addition of either conc. $HClO_4$ or NaOH. Spontaneously adsorbed monolayers were formed by immersing the electrodes in the supporting electrolyte solution containing the anthraquinone at the desired concentration, typically in the low μM range. Since adsorption is reversible in this system, subsequent experiments were carried out with this concentration of 2,7-AQDS present in solution. Where surface confined studies of 2,7-AQDS have been carried out, the highest concentration of anthraquinone in solution was 10 μM. To ensure that the current observed is dominated by the redox reactions of the monolayer rather than the solution phase anthraquinone, experiments designed to probe the concentration dependence of the surface coverage were performed at relatively short timescales. For example, for the dropping mercury electrode used in this study, the maximum contribution from diffusion to the voltammetric peak current is less than 2% even in 10 μM 2,7-AQDS solutions for scan rates greater than 10 V/s. All measurements were undertaken when the surface coverage had reached equilibrium with the bulk concentration of 2,7-AQDS, i.e., when repeated voltammetric cycling revealed an unchanging peak current.

4.2.2 Apparatus

All measurements were performed using conventional three-electrode electrochemical cells thermostated to 25 ± 0.2 °C using a Julabo F10-HC refrigerated circulating bath. The electrolytic solutions were degassed using nitrogen and a blanket of nitrogen was maintained over the solution during all experiments. All potentials are quoted with respect to a BAS Ag/AgCl gel-filled reference electrode. Cyclic voltammetry was performed using a PAR EG&G model 273 potentiostat/galvanostat interfaced to a PAR EG&G model 270 mercury electrode. Chronoamperometry was carried out using a CH Instruments Model 660 Electrochemical Workstation. The area of the mercury electrode was determined by recording cyclic voltammograms of 1,4-benzoquinone under radial and semi-infinite linear diffusion conditions as explained in Chapter 3. Using the values obtained for the limiting and peak currents, an electrode area of 0.017 ± 0.002 cm^2 was obtained. This value agrees with that obtained by dispensing, and then subsequently drying and weighing, one hundred mercury drops.

4.3 Results and discussion

4.3.1 General electrochemical properties

Figure 1 shows representative cyclic voltammograms for a mercury electrode immersed in a 5 μM solution of 2,7-AQDS in 1.0 M HClO4. The peak shapes are independent of scan rate up to at least 20 V/s and the peak height varies linearly with sweep rate, ν, rather than the $\nu^{1/2}$ dependence expected for a freely diffusing species.[23] These voltammograms are consistent with those expected for an electrochemically reversible reaction involving a surface confined redox-active species.[40,41] Therefore, consistent with previous reports on structurally related anthraquinones[42, 43] it appears that 2,7-AQDS adsorbs onto the surface of the mercury electrode to give an electroactive film.

For a surface confined species in which there are no interactions between adsorbates, and an equilibrium is rapidly established between the applied potential and the redox composition of the film, a zero peak-to-peak splitting and a full width at half maximum (FWHM) of 90.6/n, where n is the number of electrons transferred, are expected.[23] That we typically observe a peak-to-peak splitting (ΔE_{peak}) and an FWHM of 8 ± 2 and 57 ± 1 mV, respectively, at scan rates slower than 3 V/s in 1 M $HClO_4$ suggests that the electrochemical response is near ideal in this system. Peak shapes do not change significantly when cycled repeatedly at temperatures up to 40 °C, over at least 30 minutes, indicating that adsorbed films of 2,7-AQDS are both electrochemically and thermally stable.

The magnitude of the FWHM suggests that this redox reaction involves the transfer of two electrons, at least in low pH electrolytes and that lateral interactions are not significant. This result is consistent with previous work[36,37] which revealed

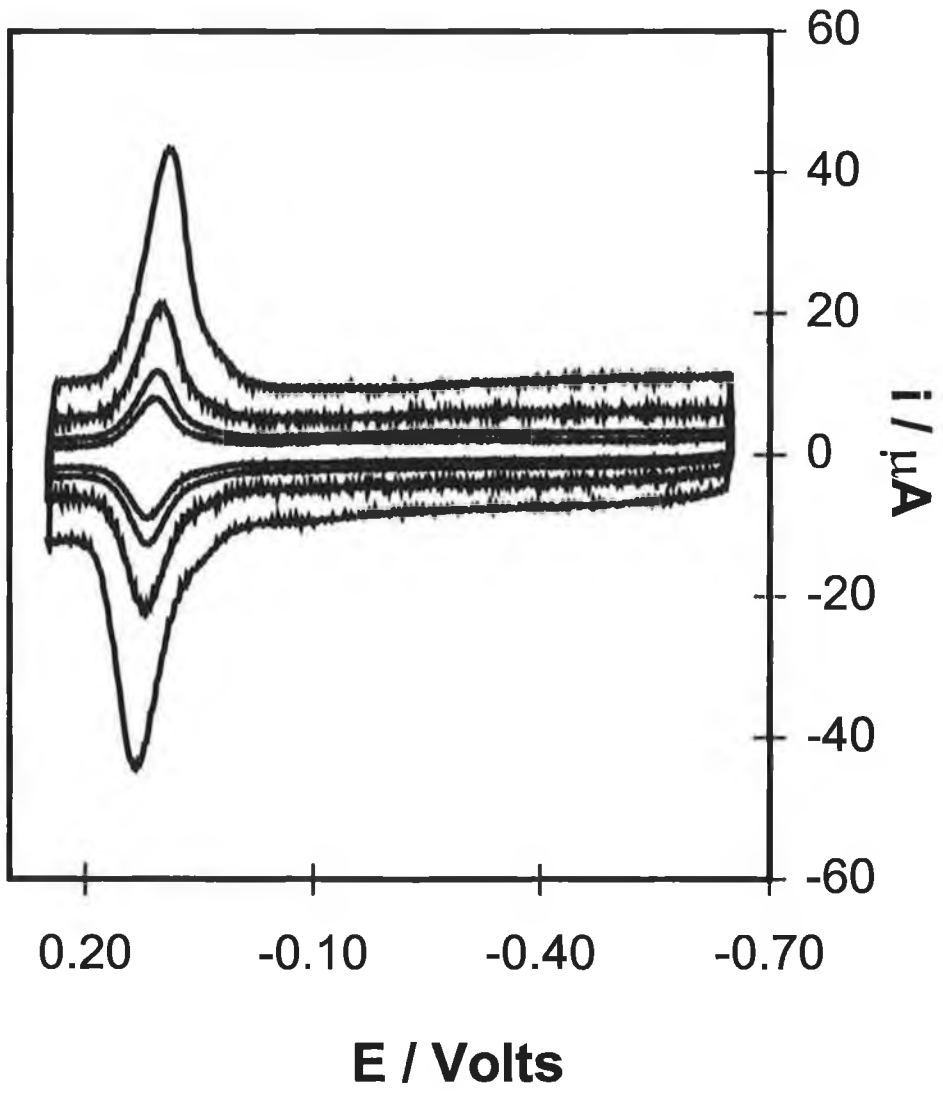

Figure 1. Cyclic voltammograms for a mercury electrode immersed in a 5 μM solution of 2,7-AQDS in 1.0 M $HClO_4$. Scan rates from top to bottom are 20, 10, 5, and 3 V/s. Cathodic currents are up and anodic currents are down. The initial potential is –0.650 V and the electrode area is 0.017 cm^2.

that in acidic solutions reduction of anthraquinone monolayers proceeds by a two-proton, two-electron transfer mechanism (Scheme 1) a behaviour that is consistent with that observed by Laviron for solution phase benzoquinone.[44] This monolayer behaviour is also consistent with the two-electron two-proton redox reactions in the scheme of squares (Scheme 2) used by Laviron to describe the redox reactions of solution phase quinones.[17] Therefore, at low pH the electrochemical response of 2,7-AQDS is considered to be almost ideal. In order to accurately diagnose the electron transfer mechanism of surface confined monolayers, it is important that pure single component films are obtained. Therefore, it is significant that there are no other electroactive species present in the potential region examined in Figure 1.

When the time constants of the voltammetric experiment and electron transfer are comparable, one expects the rate of electron transfer across the metal/film interface to influence the voltammetric response.[23] A shift in both the anodic and cathodic peak potentials, that cannot be attributed to iR drop or diffusion, and a non unity slope magnitude in a plot of the peak current, i_p, versus the scan rate is evidence that the electrode kinetics influence the overall response. Figure 2 shows that the experimental i_p increases linearly with increasing v up to 20 V/s with an absolute slope of near unity ($|\text{slope}| = 0.98 \pm 0.06$) thereby indicating that over this range the experimental timescale is longer than that for electron transfer. For scan rates above 20 V/s, the slope observed in a plot of i_p versus v decreases significantly as the influence of heterogeneous electron transfer kinetics becomes apparent, and the current tends to become independent of the scan rate for values greater than approximately 200 V/s. The scan rate at which the peak current begins to vary significantly from unity can be used to estimate the rate of heterogeneous electron transfer, k^o, using Equation 1;

$$k^o \approx \frac{Fv}{RT} \qquad (1)$$

where F is Faraday's constant, v is the voltammetric scan rate, R is the gas constant

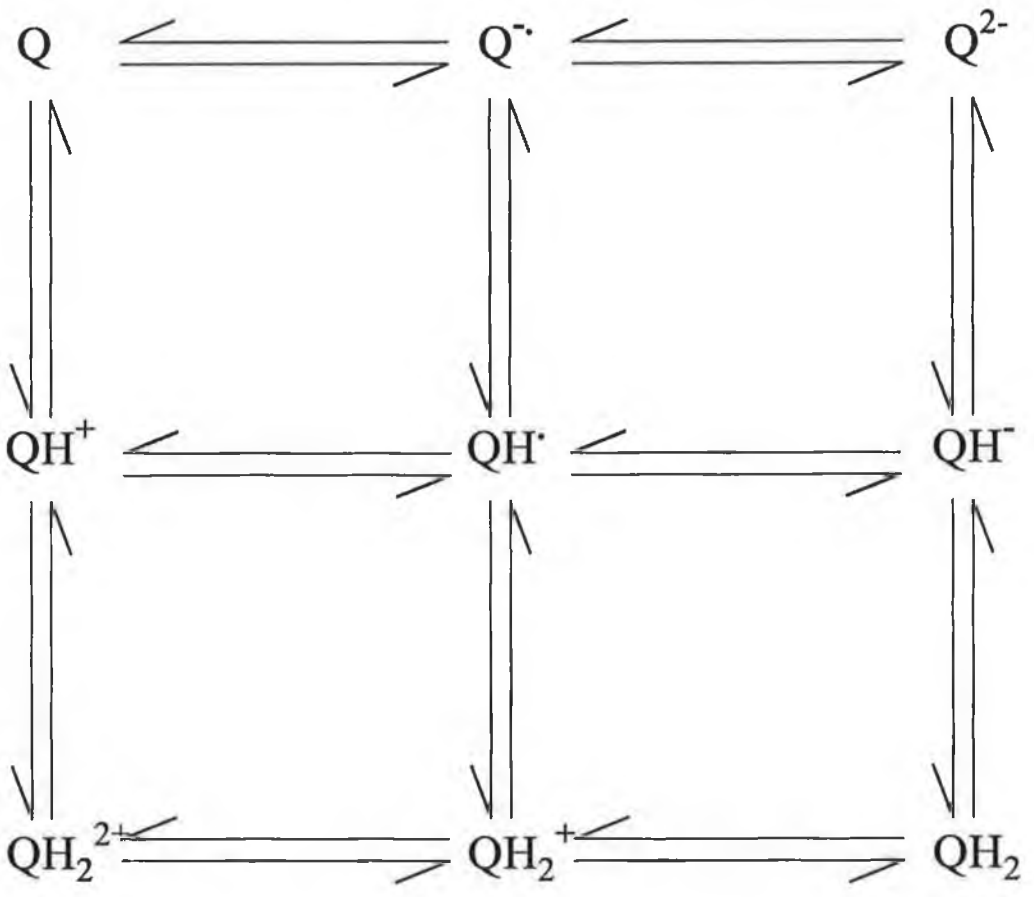

Scheme 2 3x3 scheme of squares illustrating the coupled proton/electron transfer processes involved in the possible oxidation/reduction reactions of quinones.

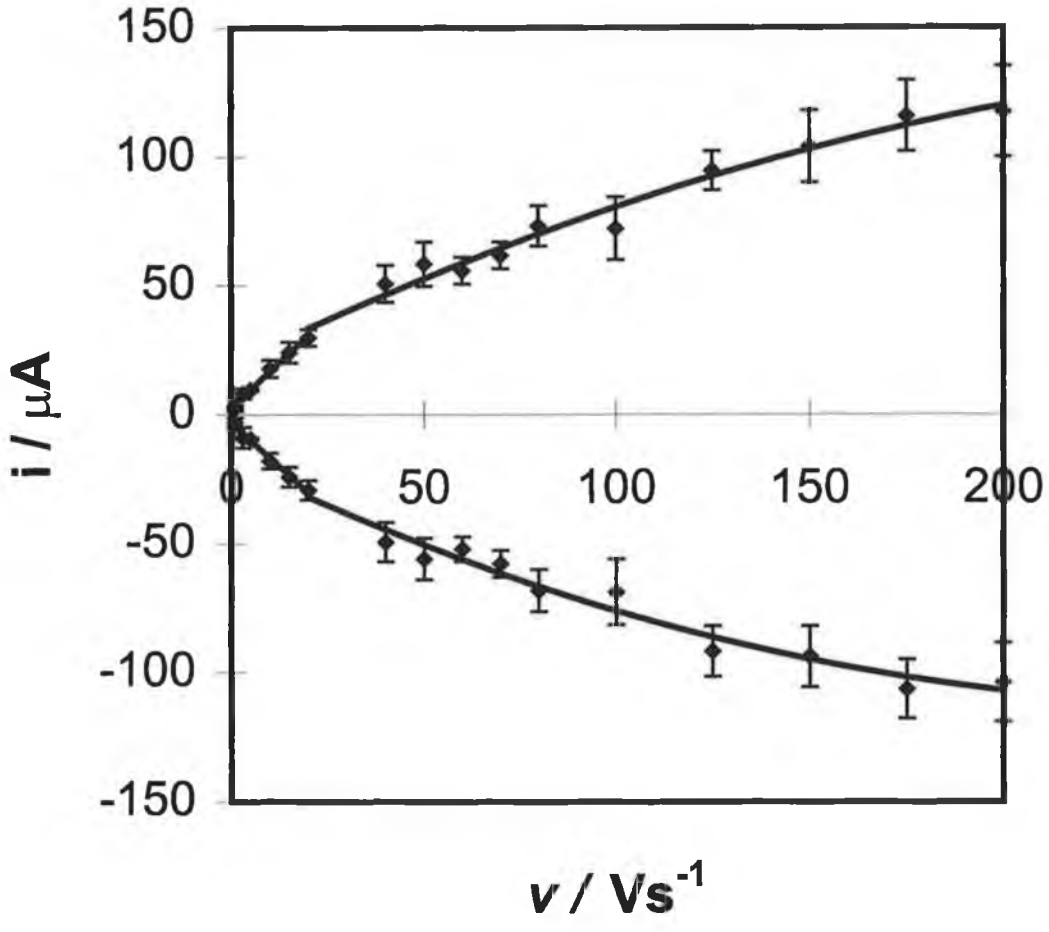

Figure 2 Peak currents as a function of voltammetric sweep rate. Cathodic currents are up and anodic currents are down.

and T is the absolute temperature. Given that the time constant for a cyclic voltammetry experiment in which the scan rate is 20 V/s is approximately 1 ms, these observations suggest that the standard electron transfer rate constant, k^o, is at least 800 s^{-1}. That electron and proton transfer are coupled in these systems, and that the heterogeneous kinetics are not adequately described by simple Butler-Volmer kinetics, complicates fitting of the data to, for example Laviron's model,[40] to extract accurate heterogeneous rate constants.

For potentials far from E°′, the voltammetric response is dominated by the double layer charging current, i_c. The charging current observed in the absence of dissolved 2,7-AQDS is at least twice as large as that observed when its bulk concentration is 10 μM. Therefore, that i_c is independent of the applied potential between approximately 0.25 and -0.65 V suggests that the anthraquinone moieties remain adsorbed over the entire potential range investigated and desorb only at potentials negative of -0.65 V.[39] Figure 3 illustrates that at low surface coverages the current increases at positive potentials due to the onset of mercury oxidation. However, increasing the surface coverage of the anthraquinone shifts the potential at which mercury oxidation occurs to more positive potentials suggesting that film formation may inhibit mercury oxidation.

Figure 1 is consistent with the redox chemistry of 2,7-AQDS involving the transfer of two electrons and two protons at low pH. However, when the concentration of protons available in solution decreases the redox chemistry may not be proton dependent. Having characterised monolayers of 2,7-AQDS in low pH media we now concentrate on cyclic voltammetric characterisation in higher pH electrolyte.

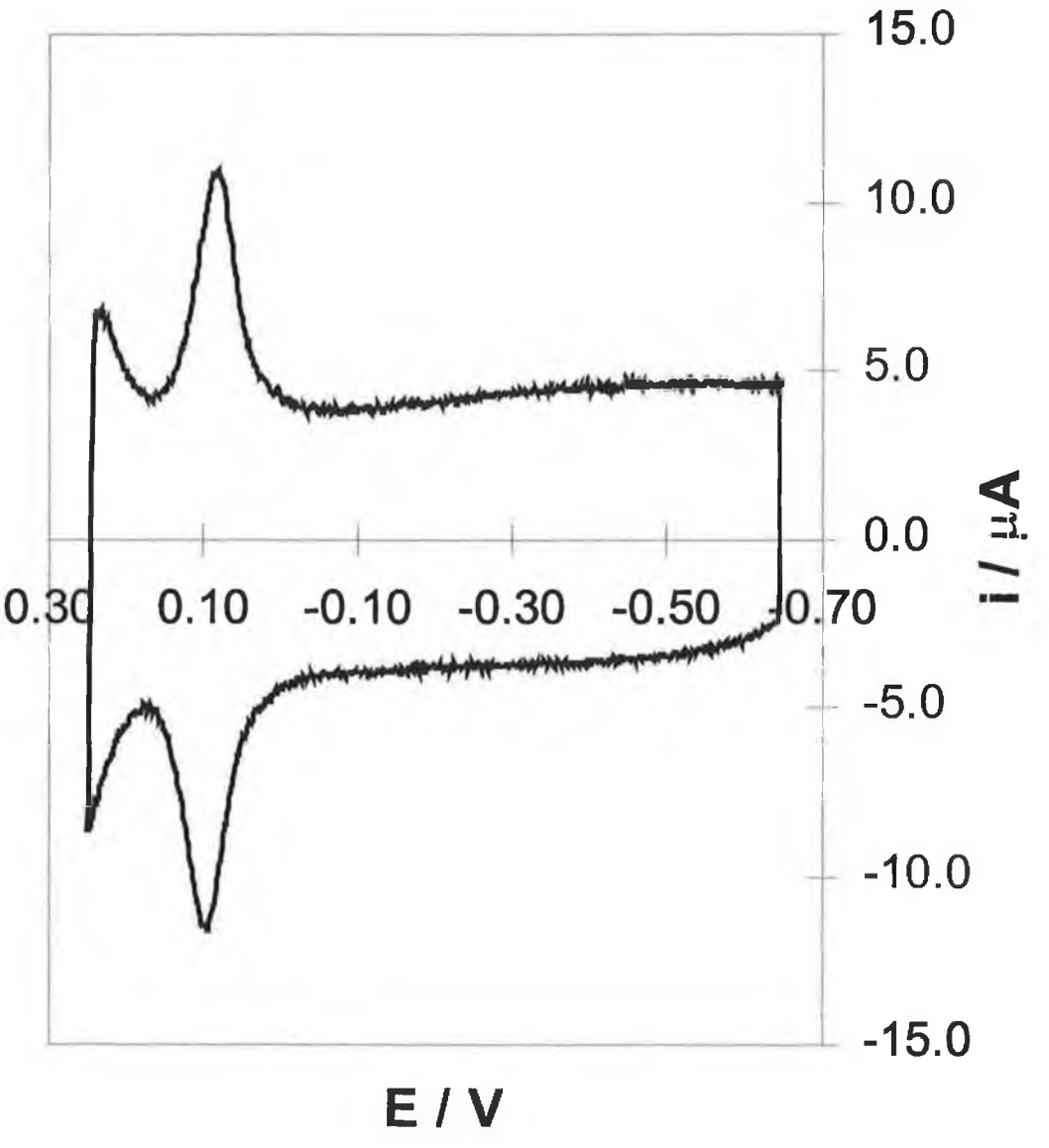

Figure 3 Cyclic voltammogram of 2,7-AQDS showing the onset of mercury oxidation at potentials positive of $E^{o\prime}$. The surface coverage is 1.4×10^{-11} mol cm^{-2} and the scan rate is 10 V/s.

4.3.2 pH Dependence of Voltammetric Response

Laviron and others have developed theory describing *coupled* proton and electron transfers, whereby transfer of an electron precedes or is followed by transfer of a proton. Moreover, it has been found that reaction schemes can be worked out to provide information about the sequence of steps involved in the two-electron, two-proton process which many anthraquinones undergo. In particular, Laviron has developed models of electrochemical systems where fast protonation steps are coupled to one- and two-electron transfer. Scheme 2 illustrates the 3x3 nine-membered scheme of squares which has been developed with the view to explaining the intricate proton and electron transfer reactions which can take place in the redox reactions of quinones.[17,45] So that we might be able to understand the complicated steps involved in the reduction and oxidation of 2,7-AQDS we have studied the pH dependence of the voltammetric response in both buffered and unbuffered electrolyte. By making voltammetric measurements over a wide range of solution pH's, we have attempted to probe whether this 3x3 square scheme provides an appropriate description of coupled electron and proton transfer in these monolayers.

The pH dependence of cyclic voltammograms for surface confined 2,7-AQDS in unbuffered electrolyte is shown in Figure 4. At a pH of 1.1 the voltammetric response of monolayers of 2,7-AQDS is centred at 0.00 V and is unusually ideal. As the pH of the contacting electrolyte is increased, the voltammetric wave initially shifts in a negative potential direction suggesting that, as with previously studied systems of this type, the electrochemical response is proton dependent.[20,24,42,43,46] In the very narrow pH range 3.9 to 4.1 two two-electron waves are observed. The sum of the charges under these two peaks, 390 ± 5 nC, is identical to that found under each of the single two-electron peak observed at high or low pH. This observation suggests that over the entire pH range investigated, the

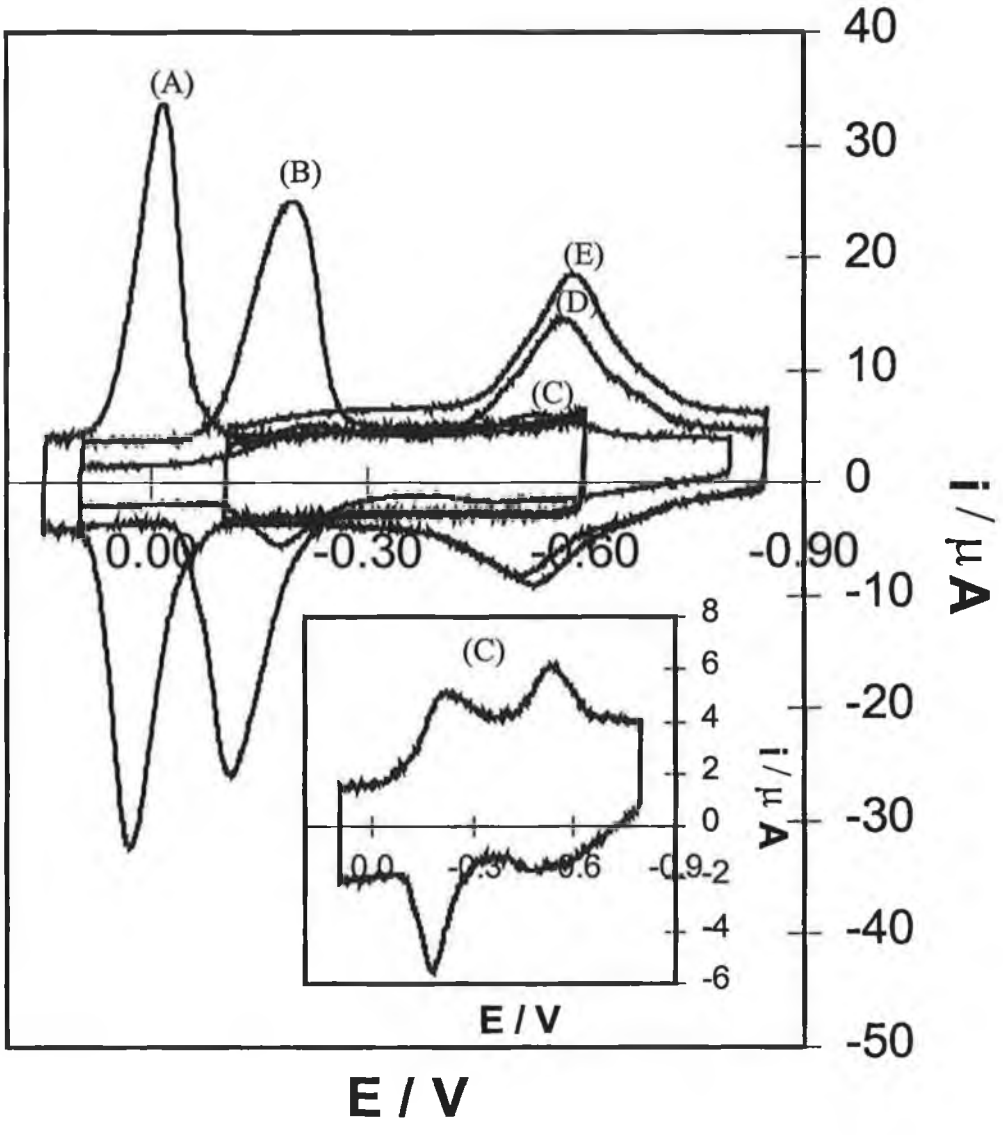

Figure 4. Cyclic voltammograms for a 0.017 cm^{-2} mercury electrode immersed in a 5μM of 2,7-AQDS as the pH of the unbuffered contacting electrolyte solution is varied. The pH are (A) 1.1, (B) 2.8, (C) 4.1, (D) 6.2, and (E) 9.1. The insert shows more clearly the CV at a pH of 4.1 (C). The pH was varied by the addition of small aliquots of either $HClO_4$ or NaOH. The scan rate is 10 V/s and the supporting electrolyte is 0.1 M $LiClO_4$. Cathodic currents are up and anodic currents are down. The initial potential is –0.650 V.

redox reactions involve the transfer of two electrons but that for $3.9 \leq pH \leq 4.1$, two chemically distinct species, the redox chemistry of both involving two electrons, co-exist on the electrode surface.

If each electron transferred in our 2,7-AQDS system is coupled to proton transfer a shift in $E^{o'}$ of 59 mV pH^{-1} is expected. A plot of formal potential of surface confined 2,7-AQDS as determined using slow scan rate cyclic voltammetry as a function of unbuffered electrolyte pH is shown in Figure 5. At a pH of 0.9 a formal potential of 31 ± 1 mV is observed. Over the pH range 0.9 to 3.9 $E^{o'}$ depends linearly on pH, the slope is 76 ± 2 mV pH^{-1}. Although this value is larger than the 59 mV shift expected for a Nernstian response for a reaction involving the transfer of equal numbers of protons and electrons, coupled proton/electron transfer this observation does confirm that the reaction involves a coupled proton/electron reaction mechanism. Intramolecular proton transfer from the sulphonate groups to the quinones would result in pH independent formal potentials. Therefore, because a large negative slope is observed intramolecular proton transfer from the sulphonate groups is ruled out.

Between pH 3.9 and 4.0 there is a dramatic shift in the formal potential from -183 ± 15 to -509 ± 4 mV. This shift is consistent with that observed by Bailey and Richie for solution phase quinones[20] and appears to represent the pK_a of 4.0 for $QH^{\bullet}$. This value for the pK_a is supported by Laviron's and Vetter's measurements.[18,44,47] Over the pH range 4.0 to 13.7 the formal potential is independent of pH within experimental error. This indicates that electron transfer is independent of proton transfer over this pH range and that above a pH of 4.0 the reduction pathway predominantly involves electron transfer followed by proton transfer (eHeH). This switching of the mechanism is further supported by our observation of two redox couples in the pH range 3.9 to 4.0 and our calculations that protons are less readily available for protonation of the monolayer at elevated pH.

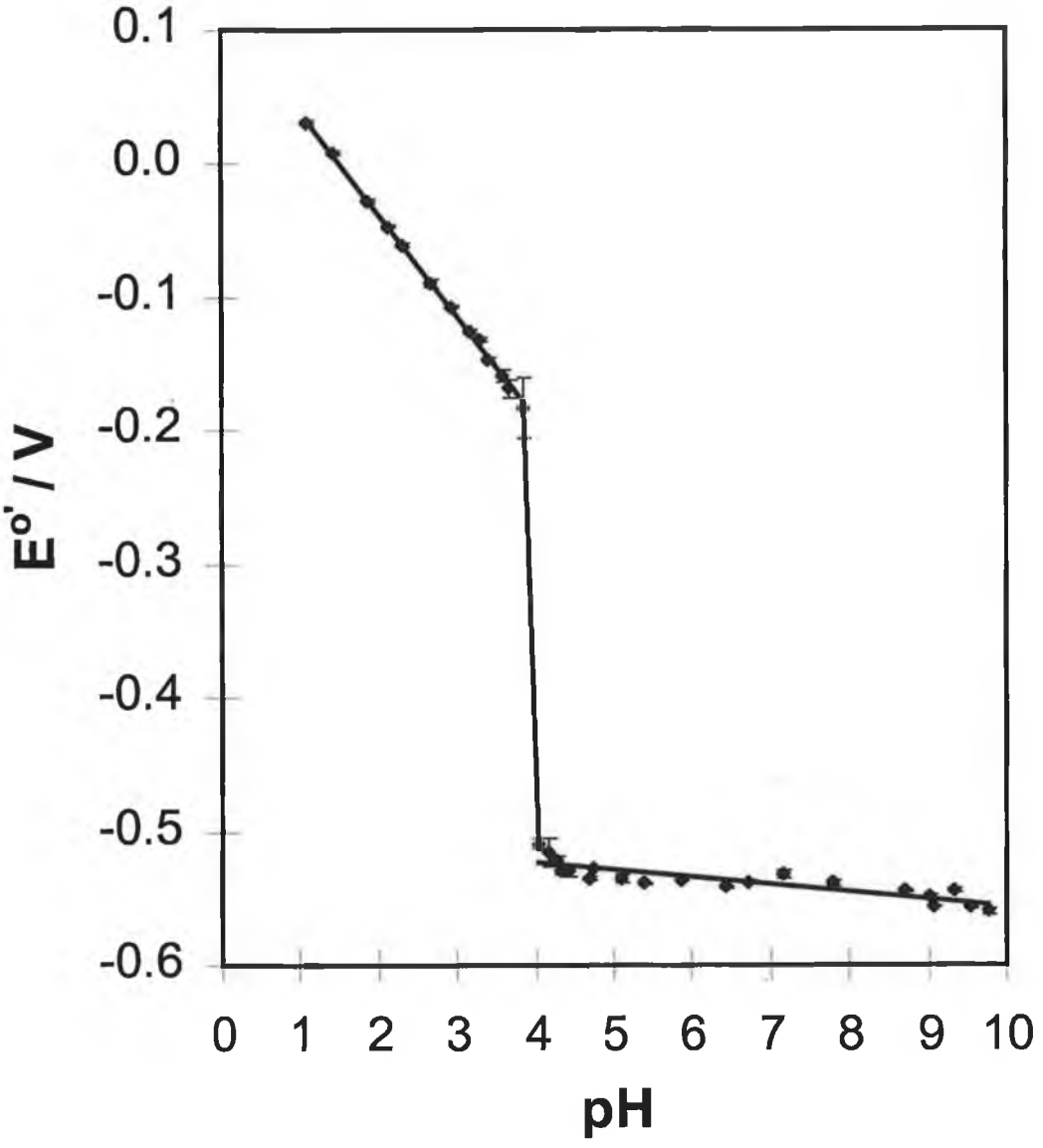

Figure 5 Formal potential of 2,7-AQDS as a function of pH in unbuffered 0.1 M $LiClO_4$.

Solution phase cyclic voltammetry in unbuffered electrolyte was carried out to determine whether the same response would be observed in solution as for the surface confined experiment and to investigate whether the apparent pK_a for dissolved and surface confined 2,7-AQDS was the same. Figure 6 indicates a similar trend in the cyclic voltammetric response for solution phase and adsorbed species. The $E^{o'}$ vs. pH shown in Figure 7 plot shows a slope of 78 ± 5 mV pH^{-1} up to pH of 4.7. Two redox couples were observed in the pH range 4.7 to 5.9 indicating the change in reduction pathway and the formal potential is almost independent of pH above 5.9. The pK_a for dissolved 2,7-AQDS appears to occur approximately 0.5 pH unit higher than for the surface confined 2,7-AQDS. Up to a pH of 3.9 the formal potentials for solution phase and surface confined 2,7-AQDS are indistinguishable. However, above pH 3.9 formal potentials for solution phase 2,7-AQDS were shifted in a positive potential direction compared to the surface confined formal potentials indicating that at higher pH monolayers of 2,7-AQDS are more stable in the reduced form.[42]

Figure 8 shows the cyclic voltammetric response of 2,7-AQDS in buffered electrolyte. Up to a pH of approximately 10.5 the response is well behaved and the FWHM values suggests that the redox reaction involves the transfer two electrons. At pH values above 10.5 the voltammetric response becomes less well behaved with the oxidation peak of the CV becoming considerably broadened. Figure 9 shows the variation in formal potential with pH for surface confined 2,7-AQDS in buffered electrolyte. From a pH of 1.0 to 10.6 $E^{o'}$ depends linearly on pH with a slope of 63 ± 3 mV which is indistinguishable from a slope of 59 mV expected for a coupled proton/electron transfer. Between pH 10.6 and 12.0 a slope of 25 + 4 mV was obtained, the expected slope for a two-electron, one-proton transfer being 29.5 mV. The change in slope at pH 10.6 appears to represent the pK_a of QH^-. Above a pH of 12.0 $E^{o'}$ is independent of pH which would suggest that the pK_a of the Q^{2-} is at pH 12.0. These results are consistent with those of Bailey and Ritchie who found pK_a values of 9.9 and 11.9 for QH^- and Q^{2-} in 1,4-benzoquinone.[20] and those of Laviron who also predicted that the pK_a of the QH^- and Q^{2-} occur at a pH 9.85 and 11.4, respectively.

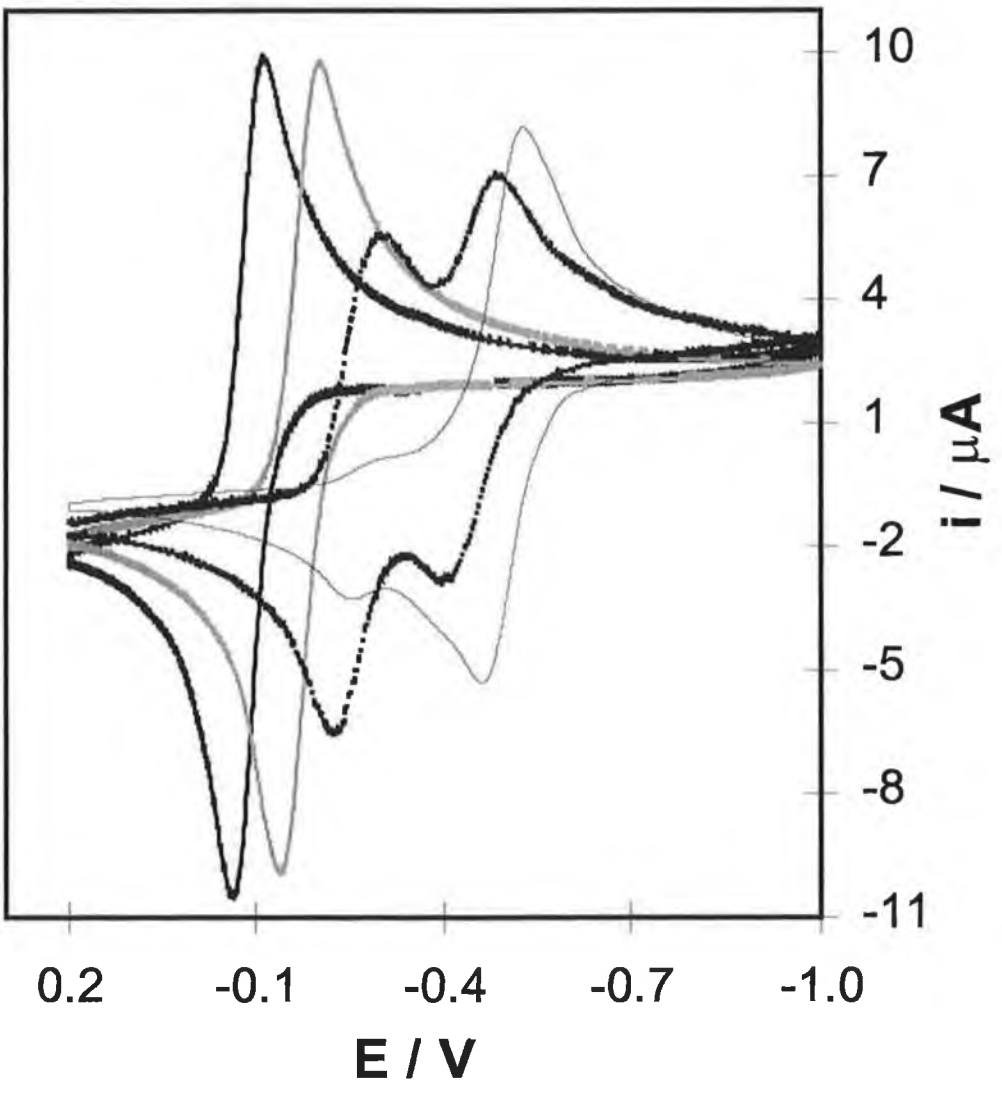

Figure 6 Cyclic voltammograms for a mercury electrode immersed in a 5 mM solution of 2,7-AQDS as the pH of the unbuffered contacting electrolyte solution is varied using either $HClO_4$ or NaOH. The pH from left to right are 2.8, 3.5, 4.8, and 6.06. The scan rate is 0.1 V/s and the supporting electrolyte is 0.1 M $LiClO_4$. Cathodic currents are up and anodic currents are down. The initial potential is –0.650 V.

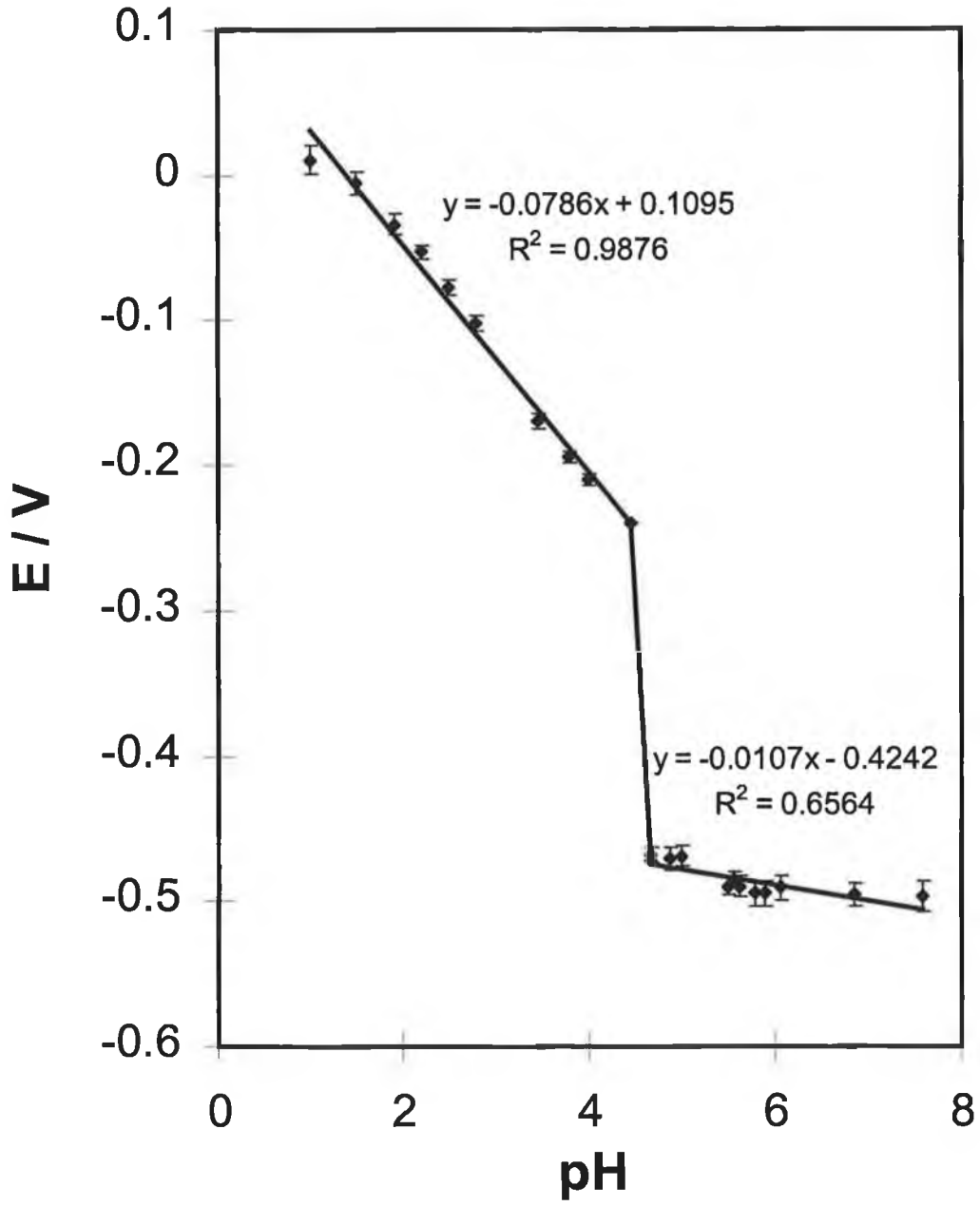

Figure 7 Dependence of the formal potential of 2,7-AQDS on the pH of unbuffered 0.1 M $LiClO_4$.

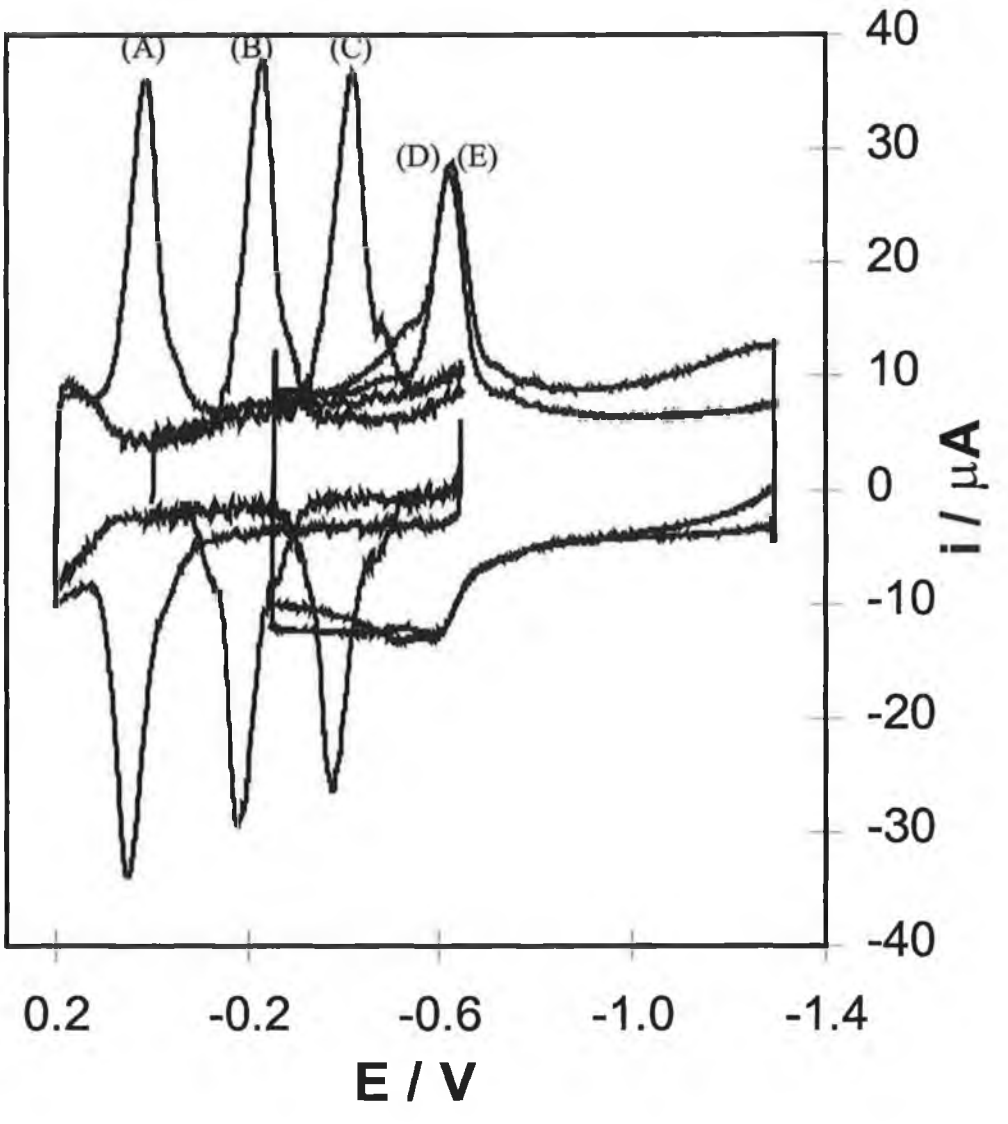

Figure 8 Cyclic voltammograms for a 0.017 cm^{-2} mercury electrode immersed in 2,7-AQDS as the pH of the buffered contacting electrolyte solution is varied. The pH from left to right are (A) 1.4, (B) 4.9, (C) 7.8, (D) 11.2, and (E) 13.0. Buffers were made up according to Fluka and the supporting electrolyte was 0.1 M $LiClO_4$. The pH was varied by the addition of small aliquots of either $HClO_4$ or NaOH. The scan rate is 10 V/s. Cathodic currents are up and anodic currents are down. The initial potential is –0.650 V.

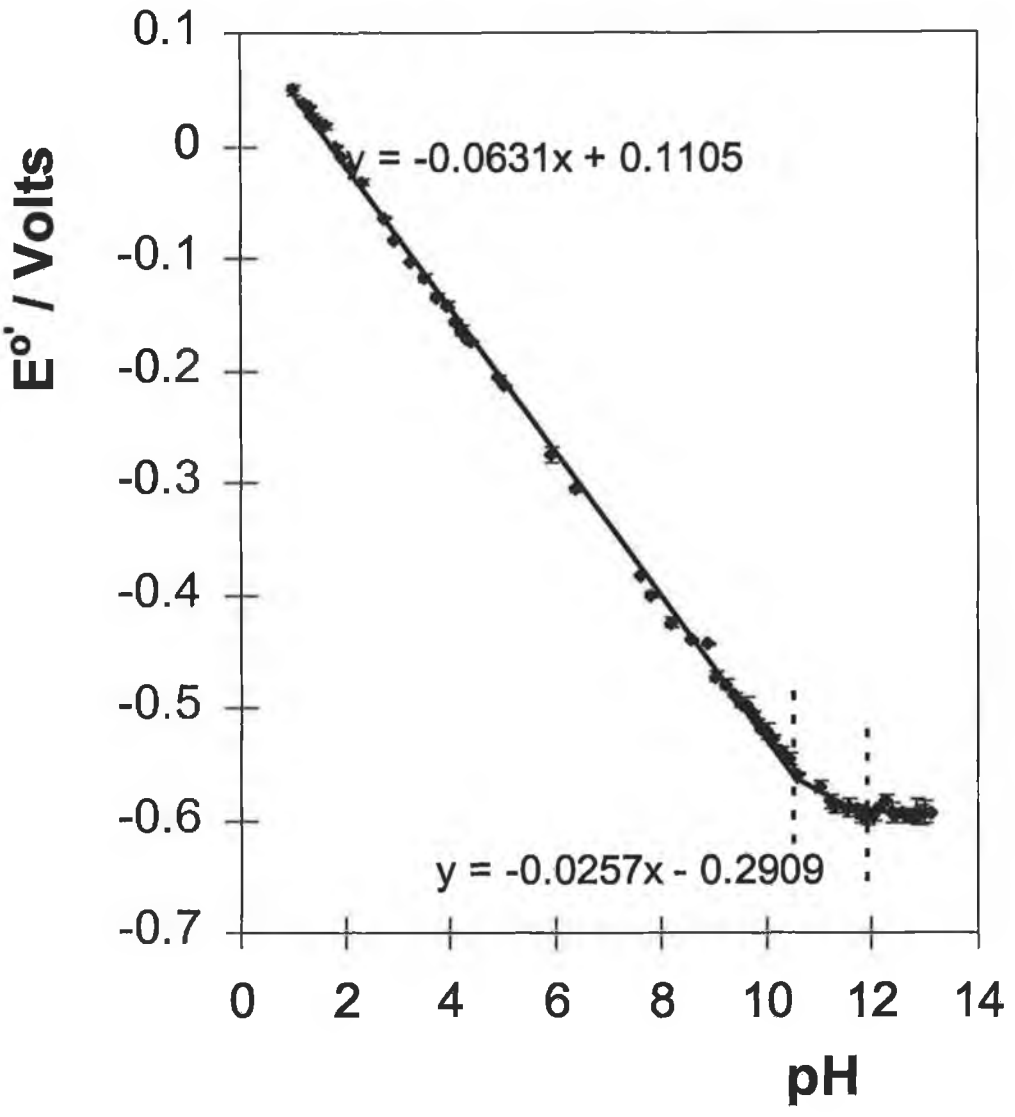

Figure 9 Dependence of the formal potential of surface confined 2,7-AQDS on pH in buffered electrolyte.

Although the pH dependent redox switching mechanism of 2,7AQDS both as a solution phase and adsorbed species has not yet been fully elucidated, it would appear that the reduction reaction involves a $H^+e^-H^+e^-$ mechanism at low pH and an $e^-H^+e^-H^+$ mechanism at higher pH. Some of the pK_a's on Laviron's scheme have been identified although further work is required to confirm the assignments. Further investigations will focus on determining whether the pH range 3.9 to 4.1 represents the pK_a of the semi-quinone moiety and whether the independence of the formal potential above pH 4.1 is indicative of a change in the sequence of electron/proton transfer, which at low pH is thought to be $H^+e^-H^+e^-$.[18,44,47]

The following section investigates the concentration dependent electrochemistry of 2,7-AQDS monolayer films using adsorption isotherms.

4.3.3 Adsorption Isotherms

The total charge, Q, introduced or withdrawn to reduce or oxidise the immobilised species, is found from the area under the voltammetric peak after correcting for the background charging current.[23] This charge, together with the surface area of the electrode, is used to calculate the surface coverage, Γ;

$$\Gamma = \frac{Q}{nFA} \qquad (2)$$

where n is the number of electrons transferred and A is the electrode area.

The surface coverage provides information about the packing density of the monolayer and can be used to determine the area occupied by individual adsorbates. The area occupied may provide an insight into the orientation of the compound on the electrode surface, which is of interest since 2,7-AQDS may bind to the surface in either a flat or edge-on orientation.[24] Molecular orientation has important implications in the chemistry of adsorbed compounds, e.g., the oxidation pathway for adsorbed aromatics on Pt is known to depend on their orientation.[48]

The limiting surface coverage, Γ_s, for 2,7-AQDS, obtained at equilibrium from cyclic voltammetry in an electrolytic solution with a relatively high concentration of 2,7-AQDS in solution (10 μM) was $7.2 \pm 0.6 \times 10^{-11}$ mol cm^{-2}. This surface coverage gives an area of occupation per molecule of 230 ± 12 Å^2 and an average radius per molecule of 8.6 ± 0.2 Å. This area is consistent with an area of 180 ± 9 Å^2 found by Forster[49] for molecules of 1,5-AQDS and 2,6-AQDS and the range found by Faulkner and coworkers[42] (210 ± 10 Å^2) for 2,6-AQDS. This consistency suggests that the substitution pattern of the anthraquinone does not significantly affect the packing density. It is perhaps important to note that Soriaga and Hubbard[50] observed a limiting coverage of 131 ± 7 Å^2 for 2,6-AQDS adsorbed in a flat orientation on platinum which may be due to a difference in surface bonding at Pt and Hg indicating that the nature of the electrode material influences the

monolayer structure significantly. The area occupied corresponds to an effective radius of the 2,7-AQDS molecule that is larger than that given by an energy minimised model of the compound which predicts a radius of 5.5 Å and hence an area per molecule of 95 $Å^2$. While solvation may account for some of the difference in areas it does not provide a complete explanation and the maximum coverage attained may not correspond to dense packing of the adsorbate. The kinetics of adsorption of 2,7-AQDS onto mercury have not been studied extensively but adsorption is rapid (less than 1 second) and reversible from aqueous solution.

In order to define the adsorption isotherm, the surface coverage of 2,7-AQDS at equilibrium was determined using the area under the voltammetric peak, after correcting for the contribution from double layer charging, as the solution concentration of the anthraquinone was systematically varied. Figure 10 shows the corresponding cyclic voltammograms. The change in surface coverage associated with these variations in solution concentration is reflected in Figure 11 which demonstrates how the surface coverage increases as the solution concentration of 2,7-AQDS is varied from $5.5x10^{-8}$ to $9.0x10^{-6}$ M. These data show that the surface coverage does not increase beyond the plateau value even if the bulk concentration of 2,7-AQDS is increased significantly. This result indicates that this system tends to form monolayers rather than multilayers. Moreover, that Γ is essentially independent of the bulk 2,7-AQDS concentration, C_b, for 10 $\mu M < C_b < 10$ mM suggests that concentration induced molecular reorientation does not occur in this system unlike the situation frequently found for quinones on platinum.[51]

The Langmuir isotherm[23,52] describes equilibrium adsorption for the situation where lateral interactions between the adsorbed molecules are absent or are independent of the surface coverage, the electrode surface is homogeneous, and the limiting surface coverage is dictated simply by the size of the adsorbate. That the voltammetric response illustrated in Figure 1 is nearly ideal, and that both adsorption and desorption of the anthraquinone occurs rapidly and reversibly, suggests that the Langmuir isotherm may be an appropriate description of adsorption in this case.

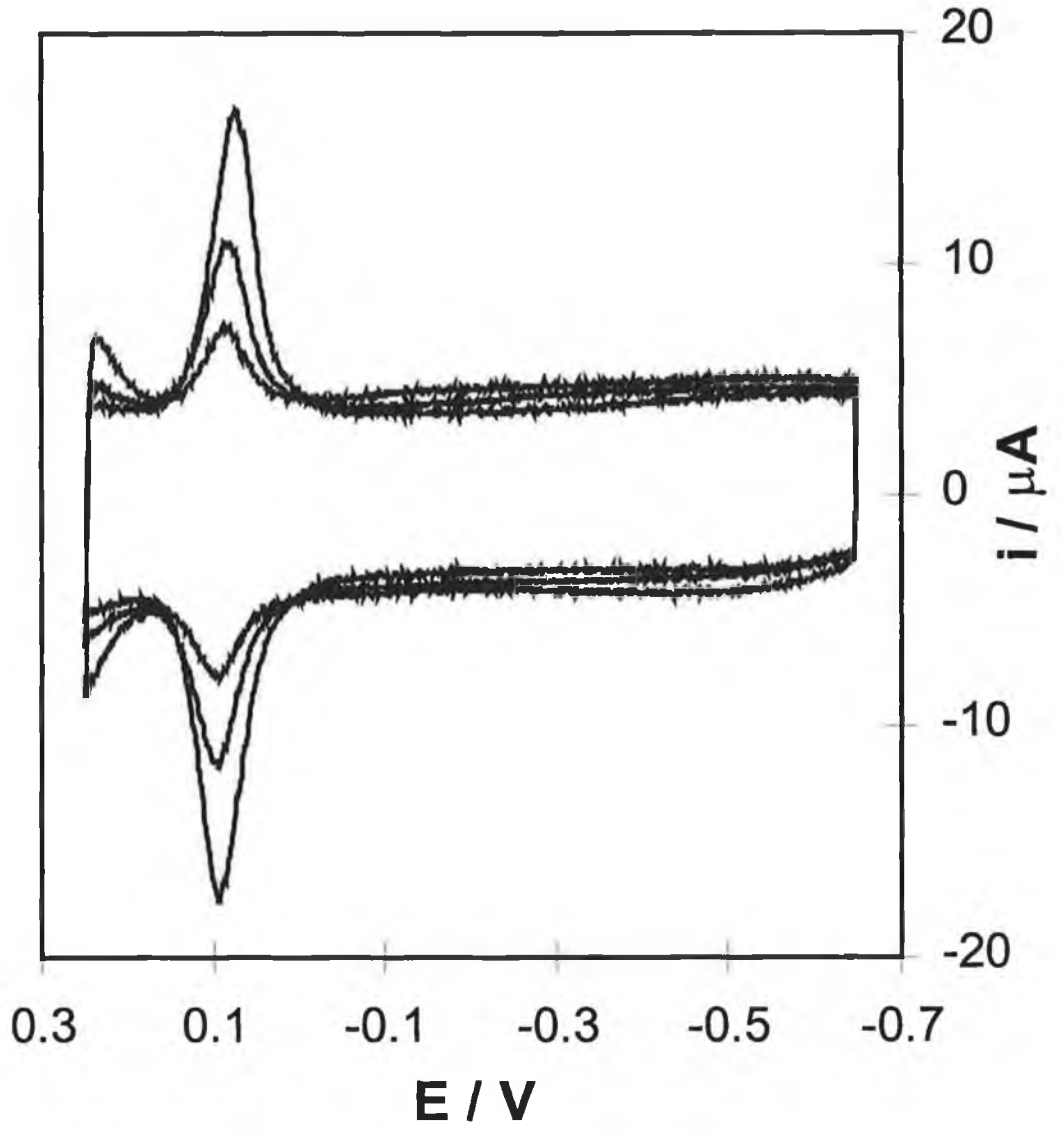

Figure 10 Cyclic voltammograms of a mercury electrode immersed in 1.0 M $HClO_4$ solutions containing 2, 5, and 7 μM 2,7-AQDS.

This isotherm is described by the following expression:

$$\frac{\Gamma_i}{\Gamma_s - \Gamma_i} = \beta_i C_i \qquad (3)$$

where Γi and C_i are the adsorption coefficient and the solution phase concentration of species i, respectively. In the following discussions, activity coefficients are incorporated into the adsorption coefficient. The line in Figure 11 is the best fit Langmuir isotherm. That satisfactory agreement between experiment and theory is obtained suggests that this model may provide an appropriate description of the experimental data.

The Langmuir isotherm predicts that a plot of C_i / Γ_i vs. C_i should be linear, and that the saturation surface coverage, Γ_s, and the adsorption coefficient, β_i, can be obtained from the slope and intercept, respectively:

$$\frac{C_i}{\Gamma_i} = \frac{1}{\Gamma_s} C_i + \frac{1}{\Gamma_s \beta_i} \qquad (4)$$

The inset of Figure 11 shows that a plot of this type is satisfactorily linear ($R^2 = 0.98$) and the slope yields an estimate of $8.7 \pm 0.5 \times 10^{-11}$ mol cm^{-2} for the saturation surface coverage, Γ_s. This value agrees with the cyclic voltammetric surface coverage of $7.2 \pm 0.6 \times 10^{-11}$ mol cm^{-2}, measured in a 10 μM 2,7-AQDS solution, to within 20%. The adsorption coefficient, β_i, which describes the strength of adsorption, is $5.2 \pm 0.5 \times 10^5$ M^{-1}. Significantly, the adsorption coefficient for the system investigated here is an order of magnitude smaller than that found for 2,6-AQDS ($5.2 \pm 0.7 \times 10^6$ M^{-1}).[42] This observation suggests that while the location of the sulphonate groups does not significantly affect the monolayer coverage (vide supra) it may be an important factor in determining the strength of adsorption, perhaps by disrupting adsorbate-electrode interactions.

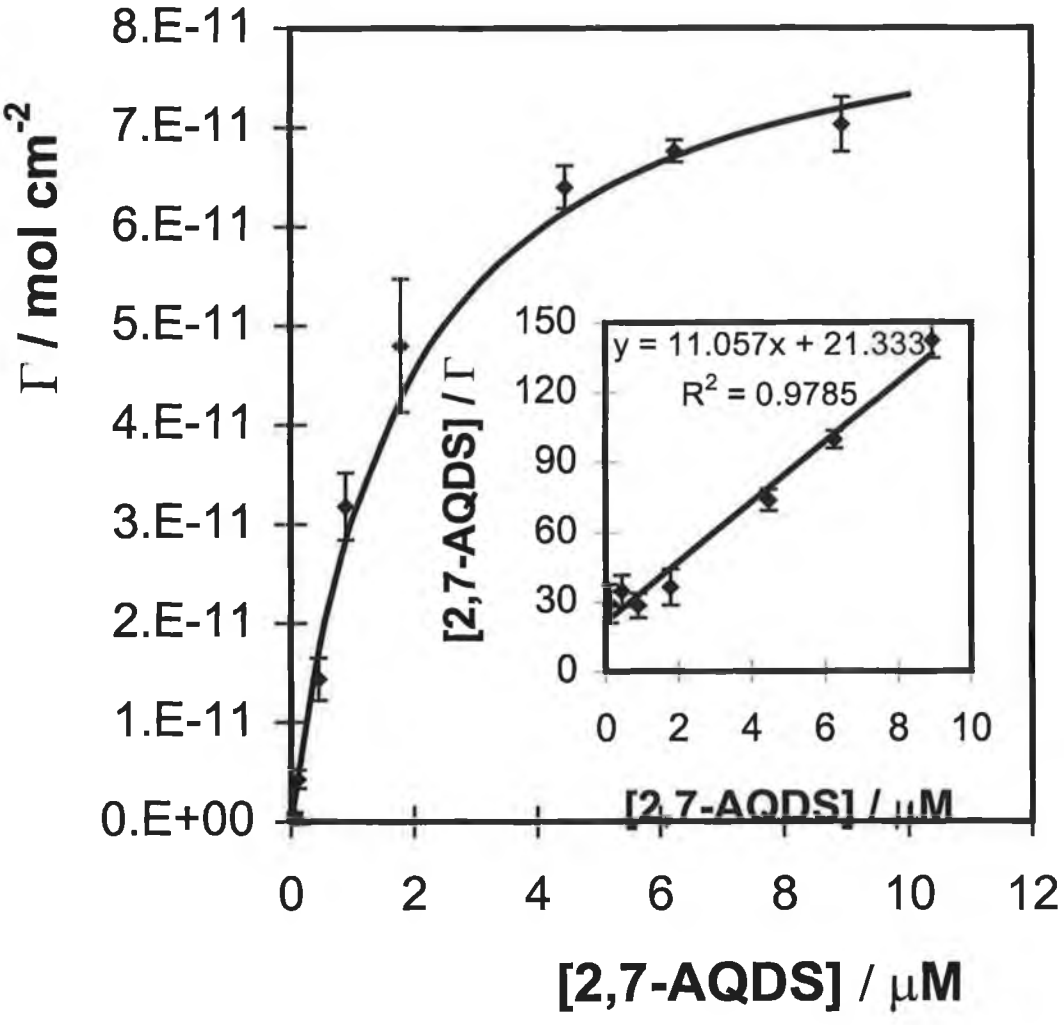

Figure 11 Relationship between surface coverage and bulk concentration of 2,7-AQDS. The solid is the best-fit line to the Langmuir isotherm. The inset illustrates data plotted according to the linearised Langmuir isotherm. The supporting electrolyte is 1.0 M $HClO_4$.

The adsorption coefficient can be used to calculate the free energy of adsorption, ΔG_{ads};

$$-\Delta G_{ads}^{\neq} = RT \ln \beta_i \qquad (5)$$

which includes contributions from concentration independent adsorbate-adsorbate and potential dependent adsorbate-electrode interactions. The free energy of adsorption at $E^{o\prime}$ is 32.8 ± 0.3 kJ mol^{-1}.

4.3.4 Potential Dependence of Adsorption Strength

Voltammetry can provide a powerful insight into the effect of the applied potential on the surface coverage and strength of adsorption when a molecule adsorbs irreversibly onto an electrode surface.[31,53] This understanding can be achieved because the applied potential can be controlled during monolayer deposition and the surface coverage can be measured in a blank electrolyte solution that does not contain any of the adsorbate of interest. This approach is not useful when adsorption is reversible since transferring the coated electrode into blank electrolyte would change the equilibrium surface coverage. However, the double layer capacitance, C_{dl}, is sensitive to the nature and extent of surface modification and its potential dependence can be measured in the presence of the dissolved anthraquinone.[36,54] Therefore, we have used potential step chronoamperometry to investigate how the double layer capacitance, C_{dl}, depends on the applied potential as the concentration of 2,7-AQDS in solution is systematically varied. While recognising that chronoamperometry is not an especially sensitive technique for measuring the interfacial capacitance, it has the advantage that double layer charging and Faradaic currents can be time-resolved[36] and the technique is easily implemented.

Chronoamperometry

In these experiments, the potential was stepped from an initial value E_i using a pulse amplitude of 30 mV and the resulting current response was recorded. Between successive measurements, E_i was increased by 30 mV from -0.700 to +0.100 V. The charging current, i_c, decays exponentially in time according to Equation 6:[55]

$$i_c(t) = \left(\frac{\Delta E}{R}\right) exp\left(\frac{-t}{RC_{dl}}\right) \qquad (6)$$

where ΔE is the pulse amplitude and R is the total cell resistance.

Equation 6 predicts that when the potential is stepped in a region where the redox composition of the monolayer does not change, i.e., far from E°′, a plot of the logarithm of the current observed versus time should be linear with the slope and intercept providing the RC cell time constant and resistance of the cell, respectively. When the potential is stepped in a region close to E°′, the current response at short times is dominated by double layer charging with Faradaic current due to oxidation of the adsorbed 2,7-AQDS moieties occurring at longer times.[37] Therefore, a plot of the logarithm of the short timescale current vs. time should be linear. Figure 12 shows a typical current-time transient for a potential step of 30 mV at a potential of 0.4 V. A semi-log plot of this transient is shown as the inset in Figure 12 and it linear with a R^2 of 0.9982. Figure 13 shows how semi-log plots depend on the applied potential for monolayer modified mercury electrodes. The resistance and double layer capacitance were determined from the intercepts and slopes of these lines, respectively, and the data are presented in Table 1.

Table 1 Effect of potential on the total cell resistance and interfacial capacitance observed for a mercury electrode modified with a close packed monolayer of 2,7-AQDS.

Potential (V)	Resistance (Ω)	Capacitance ($\mu F\ cm^{-2}$)
-.220	760(35)	11.6(0.9)
-.340	750(20)	13.1(1.0)
-.430	700(25)	15.8(1.1)
-.520	770(20)	14.7(0.8)
-.670	770(28)	12.6(0.9)

Resistance and capacitance values quoted are the average of at least three independent chronoamperometric experiments on separate monolayers. The errors are quoted in parentheses.

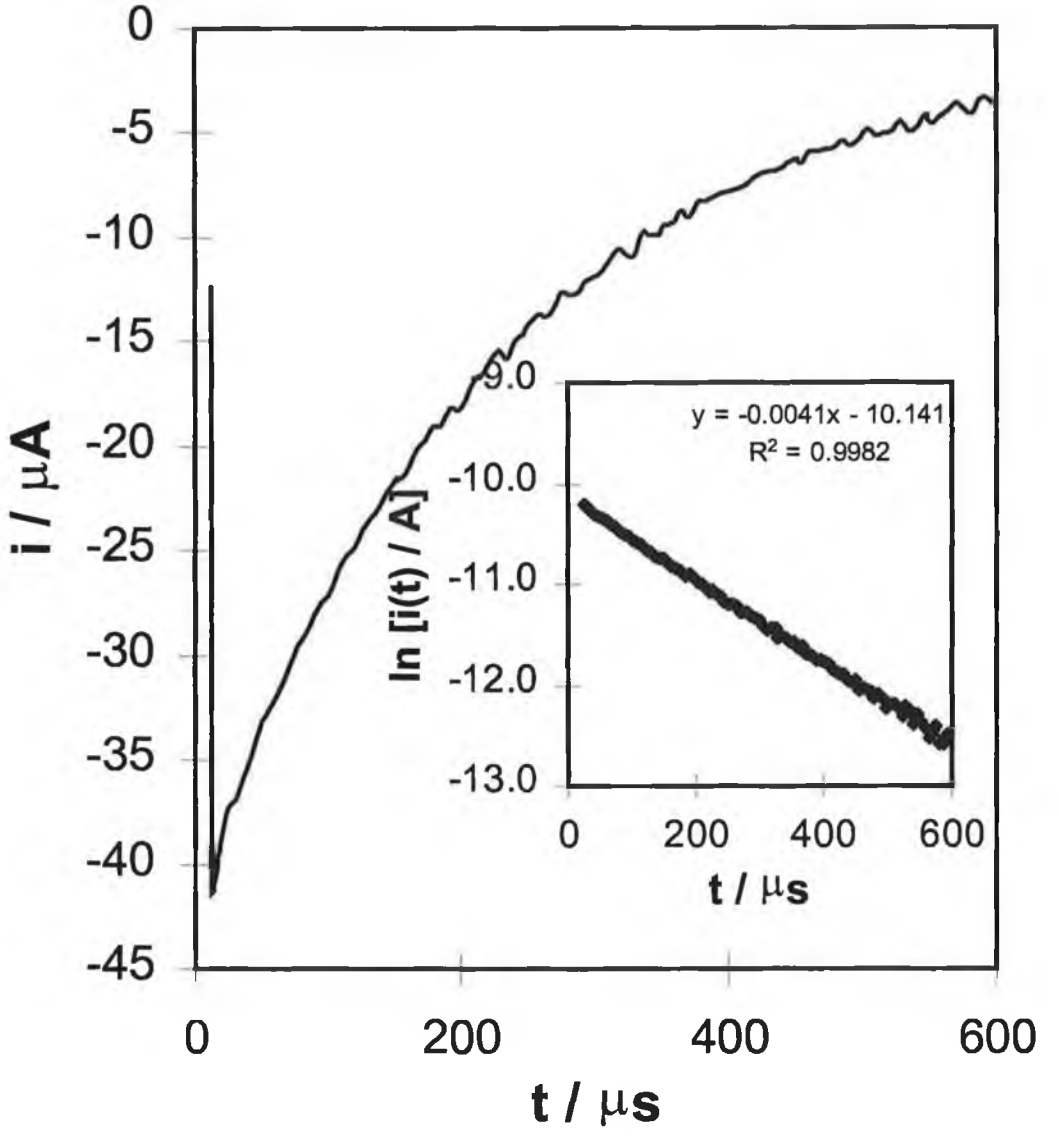

Figure 12 Chronoamperometric current-time response for a mercury electrode modified with monolayer of 2,7-AQDS. The potential is 0.400 V and a pulse amplitude of 30 mV was employed. The inset shows the semi-log plot of the transient.

Figure 13 reveals that the intercepts of semi-log plots are independent of the applied potential. Moreover, Table 2 shows that the resistance changes by less than 25 % as the composition of the electrolyte solution is systematically varied from one that does not contain any dissolved 2,7-AQDS to one where the anthraquinone concentration is 10 μM. That the resistance, R, is relatively independent of both the applied potential and the anthraquinone concentration suggests that the solution resistance dominates the total cell resistance and that the film resistance makes only a minor contribution.

Table 2. Effect of 2,7-AQDS concentration on the total cell resistance and interfacial capacitance as measured at –0.43 V.

[2,7-AQDS] (μM)	Resistance (Ω)	Capacitance (μF cm^{-2})
0	684(38)	33.1(1.8)
1	756(43)	27.8(1.8)
2	766(51)	25.8(2.1)
7	803(39)	17.2(1.3)
10	890(55)	15.8(0.8)

Resistance and capacitance values quoted are the average of at least three independent chronoamperometric experiments on separate monolayers. The errors are quoted in parentheses.

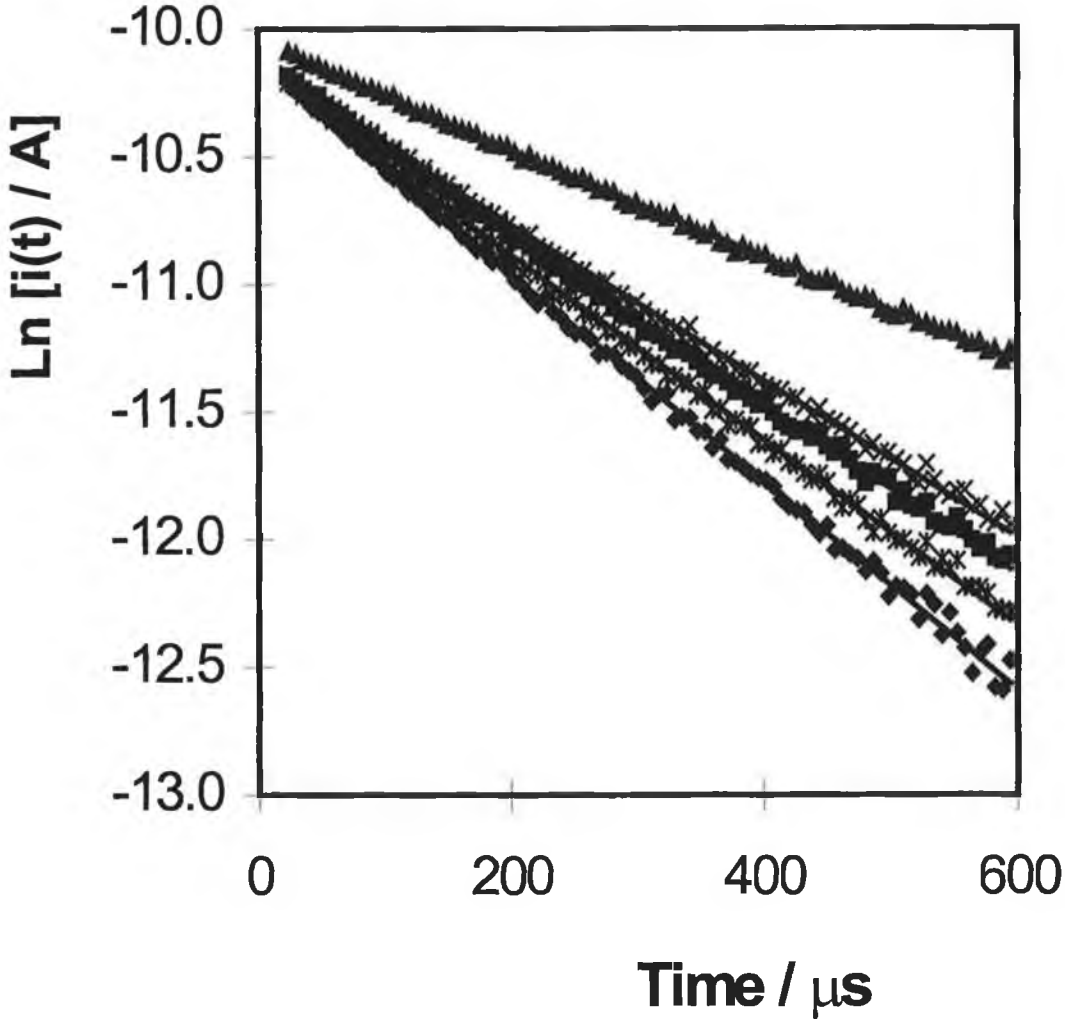

Figure 13 Effect of applied potential on plots of the logarithm of the capacitive current vs. time for mercury electrodes modified with dense monolayers of 2,7-AQDS.

Interfacial Capacitance

For an electrode coated with a modifying film, both the diffuse layer capacitance from solution, C_{dif}, and the film capacitance, C_{film}, may contribute to the overall double layer capacitance:[39,56]

$$\frac{1}{C_{dl}} = \frac{1}{C_{film}} + \frac{1}{C_{dif}} \tag{7}$$

Only the diffuse layer capacitance depends on the applied potential and the concentration of supporting electrolyte[23] and the effect of monolayer assembly on the interfacial potential distribution can be diagnosed by measuring C_{dl} as both the applied potential and the bulk concentration of 2,7-AQDS are systematically varied.

The slopes of the best fit lines to the semi-log plots of Figure 13 depend on the applied potential indicating that the double layer capacitance is potential dependent. Figure 14 illustrates the potential dependence of the interfacial capacitance as the bulk concentration of 2,7-AQDS is systematically varied. This figure shows that strikingly different voltage dependences are observed for the monolayer modified electrodes compared to the pristine metal surfaces. In particular, the double layer capacitance is measurably smaller for the coated electrode than for an unmodified interface over the entire potential range investigated, e.g., at the formal potential, the capacitance decreases from 31 $\mu F\ cm^{-2}$ for the bare electrode to 17 $\mu F\ cm^{-2}$ for a 10 μM solution, and only the clean mercury surfaces show a pronounced minimum. The reduced capacitance in the presence of 2,7-AQDS is consistent with the cyclic voltammetry data presented earlier which indicated that the surface coverage increases from approximately half of a monolayer to approximately limiting monolayer coverage as the bulk concentration of the anthraquinone is increased from 2 to 10 μM. The data illustrated in this figure are highly reproducible and no detectable hysteresis was observed between successive potential scans, or if the direction of scanning was reversed. These observations

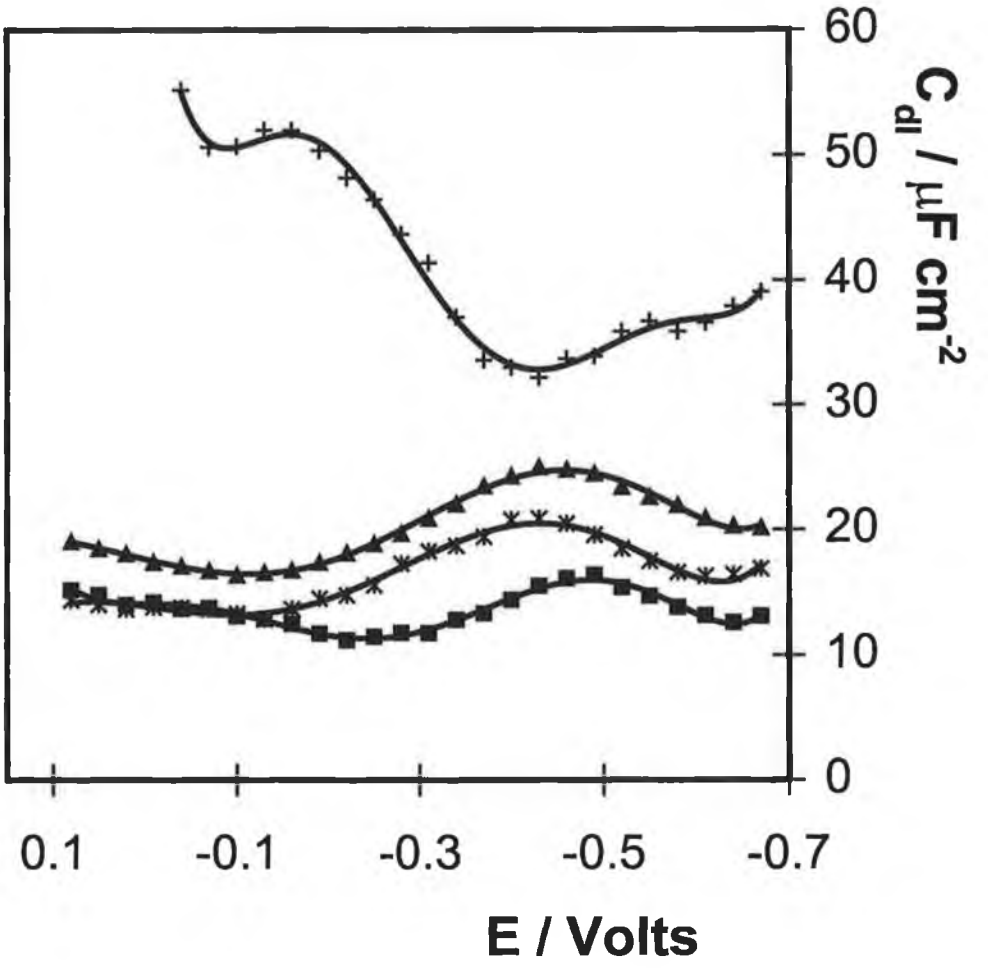

Figure 14 Double layer capacitance as a function of applied potential as the concentration of 2,7-AQDS in solution is systematically varied. The curves, from top to bottom, represent the capacitance of electrodes immersed in a 0.05 M NaF containing 0, 2, 5, and 10 μM 2,7-AQDS. Typical error bars are less than 2 μF cm^{-2}.

suggest that either the structure of the film is static or that it rapidly equilibrates with the applied potential.

A minimum in C_{dl} is expected at the potential of zero charge (PZC) which represents the potential at which there is no excess charge on either the electrode or solution sides of the interface.[23] Figure 14 reveals that for the clean mercury interface a minimum in the capacitance occurs at –415 ± 15 mV. This value of the PZC is consistent with that expected for a mercury electrode in contact with a dilute, non-surface active electrolyte.[23]

The pK_a's of the hydroquinone groups within the reduced form of the adsorbate are 7.7 and 10.5.[57,58] However, the pK_a's for the oxidised or quinone form of the monolayer are approximately 6 pH units lower. Therefore, given that the sulphonic acid groups are deprotonated at the pH of this study (5.5), the reduced monolayer is electrostatically neutral while the oxidised form has a charge of 2-. Under these circumstances, one would expect the potential of zero charge for the monolayer to depend on its redox composition. However, it is not possible to identify the PZC for the anthraquinone derivatised electrodes since, even in the presence of 2,7-AQDS concentrations as low as 2 μM, no well-defined minimum in the interfacial capacitance is observed over the potential range investigated. We note that the formal potential in 0.05 M NaF is -415 mV, i.e., the PZC observed for the bare electrode, and $E^{\circ\prime}$ for the monolayer, are coincident, making it difficult to determine the effect of monolayer formation on the PZC.

Figure 14 shows that a distinct maximum in C_{dl} is observed at approximately -415 mV. That a distinctive peak is observed suggests that this behaviour is not due to imperfections within the anthraquinone monolayer or voltage dependent penetration of water or ionic species into the film. An alternative explanation is that the surface coverage is lower at this potential. To investigate this possibility, we have probed how the interfacial capacitance depends on the bulk concentration, and hence surface coverage, of 2,7-AQDS. The dependence of the interfacial capacitance on the surface coverage can be described using the parallel capacitor model

originally proposed by Delahay.[59] In this model, the double layer capacitance for incomplete monolayers is represented by an equivalent circuit composed of two capacitors in parallel representing the contributions from the bare and modified fractions of the electrode surface:

$$C_{dl} = C_{mono} + (C_{bare} - C_{mono})(1 - \theta) \quad (8)$$

where C_{bare} and C_{mono} are the capacitances of the bare and densely coated electrodes respectively, and θ is the fractional surface coverage. Figure 15 illustrates how the interfacial capacitance, as measured at the formal potential, changes as the bulk concentration is systematically varied from 1 to 10 μM. The capacitance decreases from 31 μF cm^{-2} for the bare electrode to 17 μF cm^{-2} when the concentration in solution is 10 μM. Figure 11 demonstrated that the Langmuir isotherm provides an adequate description of the dependence of the surface coverage of 2,7-AQDS on its bulk concentration. We have combined Delahay's parallel capacitor model with the Langmuir isotherm to allow the potential dependence of Γ to be probed through measurements of C_{dl}. Equation 9 summarises this model:[37]

$$\frac{[2,7-AQDS]}{(C_{bare}-C_{dl})} = \frac{1}{C_{mono}}[2,7-AQDS] + \frac{1}{C_{mono}\beta_i} \quad (9)$$

where [2,7-AQDS] represents the solution concentration of 2,7-AQDS. According to Equation 9, the slope and intercept obtained from a plot of [2,7-AQDS] / (C_{bare} - C_{dl}) vs [2,7-AQDS] can be used to determine the capacitance corresponding to a close packed monolayer and the adsorption coefficient, respectively. The inset of Figure 15 illustrates a plot of this type using values of C_{dl} measured at E°′. This plot is linear (R^2 = 0.9936) suggesting that the parallel capacitor model provides an accurate description of adsorption for 2,7-AQDS films. The slope of the inset in Figure 6 reveals a capacitance for a dense monolayer, C_{mono}, of 22 μF cm^{-2} which compares favourably with the value of 17 μF cm^{-2} obtained directly from chronoamperometry where the bulk concentration of 2,7-AQDS is 10 μM.

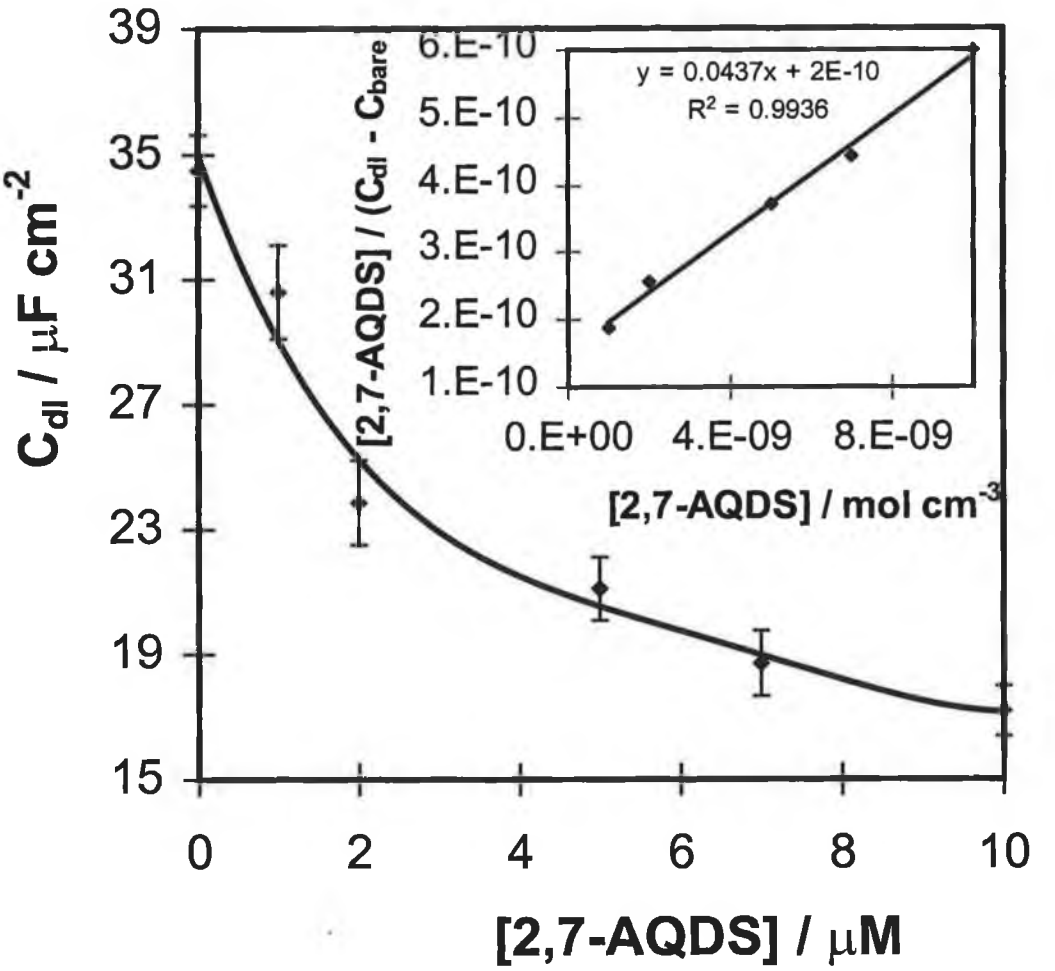

Figure 15 Dependence of the double layer capacitance as measured at the formal potential on the bulk concentration of 2,7-AQDS. The inset illustrates data linearised according to a parallel capacitor model. The supporting electrolyte is 0.05 M NaF.

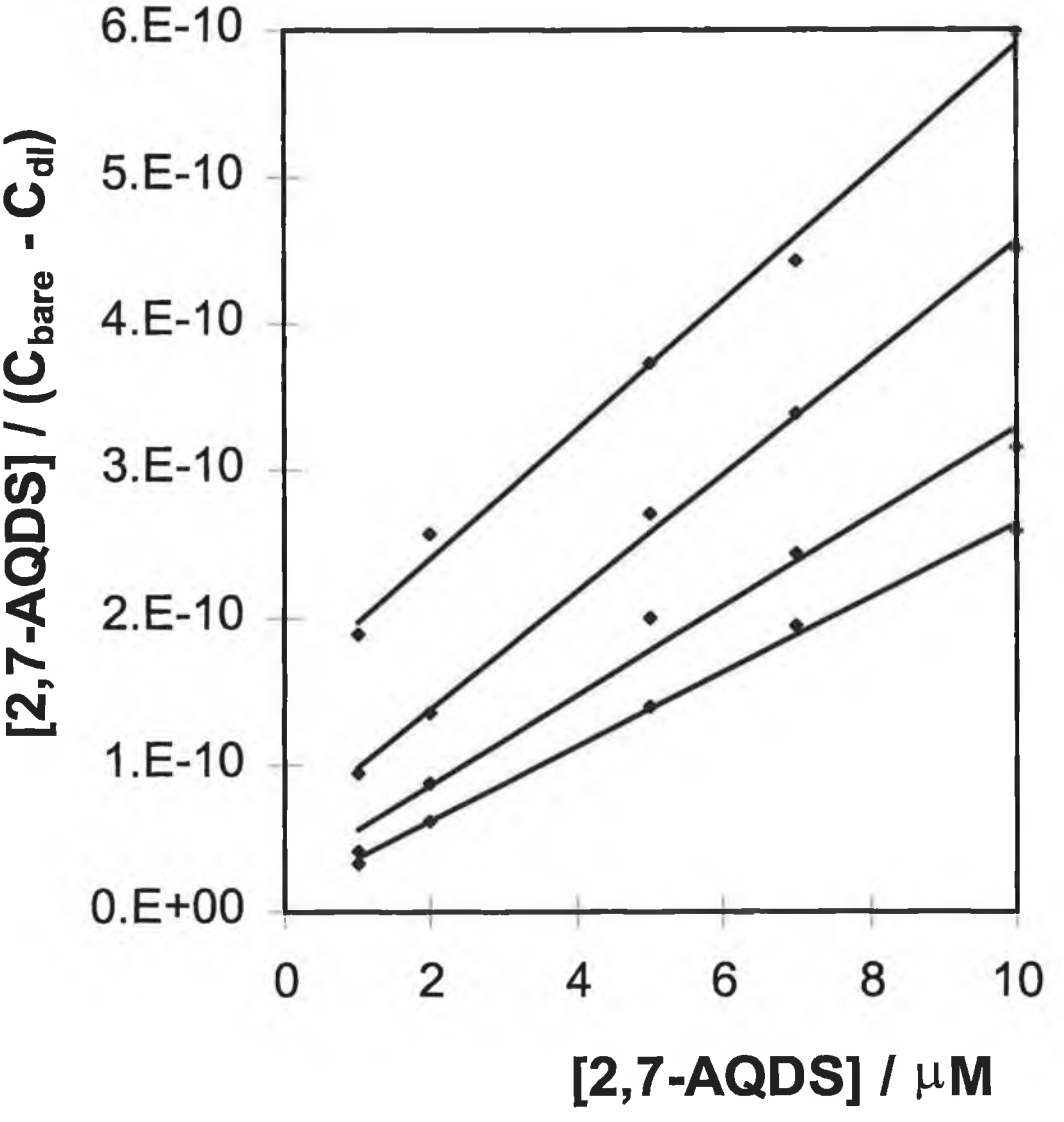

Figure 16 Potential dependence of capacitance data linearised according to the parallel capacitor model. From top to bottom, the potentials are, -0.460, -0.520, -0.310, and –0.190 V respectively. The supporting electrolyte is 0.05 M NaF.

The adsorption coefficient of 2.2 ± 0.5 x 10^5 M^{-1} obtained from the intercept of this plot is in reasonable agreement with the value of 5.6 ± 0.5 x 10^5 M^{-1} obtained from the linearised Langmuir isotherm (Figure 11). That the capacitance and voltammetric results agree, indicates that measurements of C_{dl} can be used to probe the strength of adsorption in this system, at least at E°′.

Figure 16 shows data obtained at potentials away from E°′ and reveals that plots of [2,7-AQDS] / (C_{bare} - C_{dl}) vs [2,7-AQDS] are linear at all potentials investigated. This linearity suggests that the parallel capacitor model provides a meaningful insight into the potential dependence of both C_{mono} and β.

4.3.5 Free energy of adsorption

That adsorption in this system is described by the Langmuir adsorption isotherm suggests that adsorbate-adsorbate interactions are either absent or do not depend strongly on the redox composition of the monolayer or the surface coverage. However, it is possible that adsorbate-electrode interactions depend on the applied potential, thus making the free energy of adsorption, $\Delta G_{ads}^{\neq}$ potential dependent. The intercepts of the plots shown in Figure 16 have been used in conjunction with Equations 5 and 9 to determine the potential dependence of the free energy of adsorption and the data are illustrated in Figure 17. At potentials far from E°′, where only the oxidised or reduced form of the monolayer exist, the free energy of adsorption is large, but is insensitive to the applied potential. For example, $\Delta G_{ads}^{\neq}$ differs by only 1.5 kJ mol^{-1} when measured at -0.21 or -0.67 V, where the monolayer is fully oxidised and reduced, respectively. This observation suggests that $\Delta G_{ads}^{\neq}$ is relatively insensitive to the applied potential provided that only a single redox form exists on the electrode surface.

The most striking feature of Figure 17 is that the absolute value of $\Delta G_{ads}^{\neq}$ reaches a minimum at approximately -415 mV, i.e., the adsorbates are least strongly bound at this potential. This potential corresponds to both the PZC of the bare mercury surface and the formal potential of the quinone/hydroquinone redox reaction. Unlike potentials that are significantly positive or negative of the formal potential, at E°′, the monolayer may contain three distinct forms of the adsorbate, namely the quinone, hydroquinone and semiquinone forms. Capacitance data do not allow us to discriminate between these different redox states preventing a complete interpretation of the available data. However, a minimum in $\Delta G_{ads}^{\neq}$ at the PZC is not expected since the oxidised form of the adsorbate has a 2- charge due to dissociation of the two sulphonic acid groups. Under these circumstances, one would expect $\Delta G_{ads}^{\neq}$ to be larger at potentials positive of the PZC. While future studies will report results at other pHs where the PZC and E°′ are not co-incident, it is likely that the interactions between the electrode and the co-adsorbed quinones, hydroquinones and

perhaps semiquinones that exist at E°′, as well as, acid/base reactions influence the observed response.

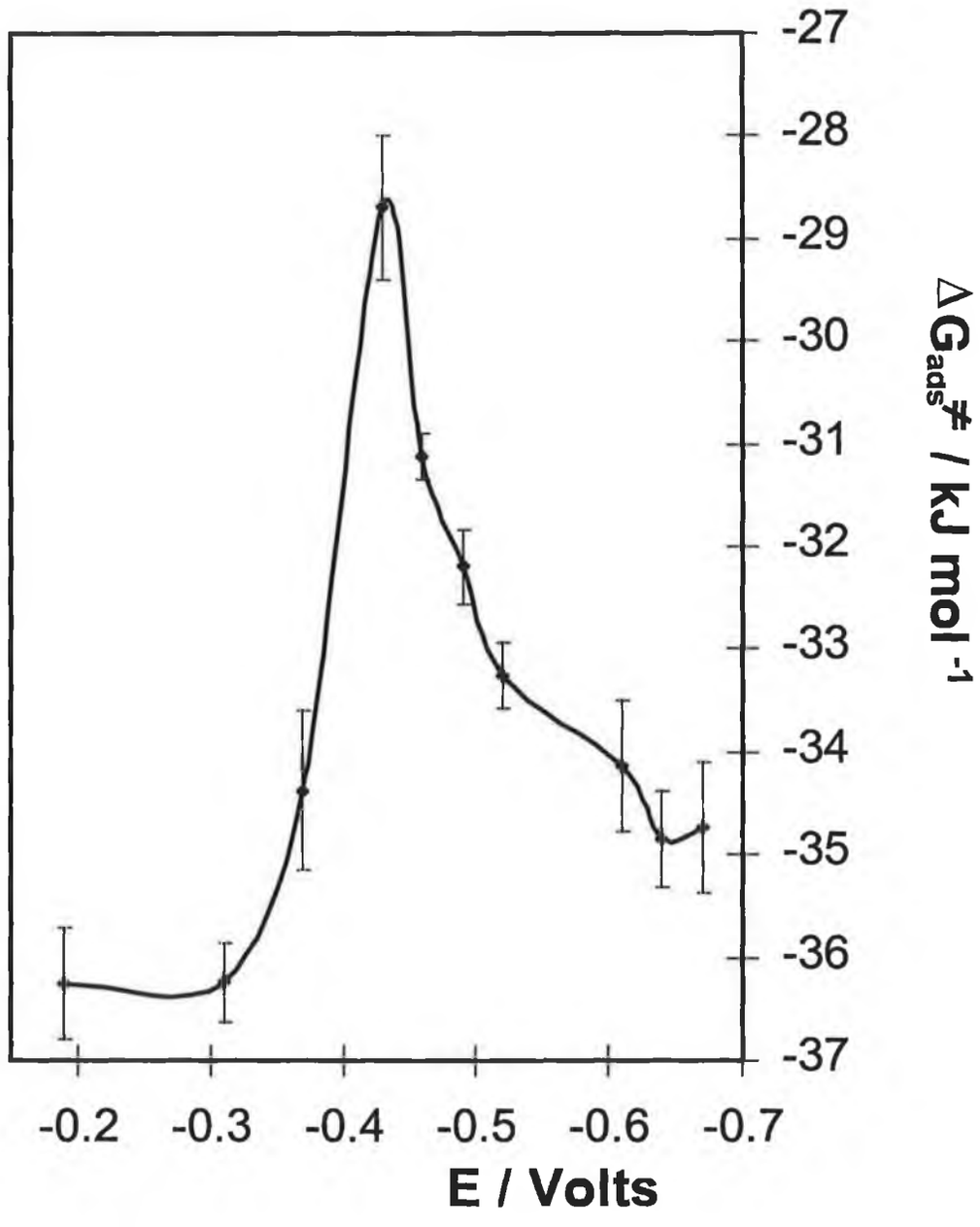

Figure 17 Dependence of the free energy of adsorption on the applied potential. The supporting electrolyte is 0.05 M NaF.

4.4 Conclusions

The electrochemistry of anthraquinone-2,7-disulphonate monolayers has been investigated and found to be unusually ideal under conditions of low electrolyte pH. In particular, the effects of adsorbate concentration and the applied potential on the adsorption strength have been probed. The dependence of the surface coverage on the bulk concentration of 2,7-AQDS is adequately described by the Langmuir adsorption isotherm. The area occupied per molecule suggests that molecules of 2,7-AQDS bind to the surface of the electrode in a flat orientation and that reorientation does not occur, at least not for bulk concentrations up to 10 μM. This resistance to orientation most likely arises because of entropy considerations. In the flat orientation, each of the fused rings can interact with the mercury surface, whereas a perpendicular adsorbate would permit only limited anthraquinone-electrode interaction but more extensive lateral interactions through π-stacking.

The pH dependence of the formal potential indicates that for the reduction of the anthraquinone, the coupled proton/electron reaction proceeds via a $H^+e^-H^+e^-$ pathway up to a pH of 3.9 and that at higher pHs the reduction pathway involves $e^-H^+e^-H^+$ mechanism. The pK_a of the semi-quinone moiety, $QH^\cdot$, appears to lie between pH 3.9 and 4.0 while that of the singly and doubly deprotonated dihydroxyanthracene moieties are 10.6 and 12.0, respectively.

The double layer capacitance has been probed as a function of applied potential and solution concentration of 2,7-AQDS. While C_{dl} depends on the concentration of 2,7-AQDS it appears to be only weakly dependent on potential. The concentration dependence of C_{dl} is described by a parallel capacitor model, which has been used to probe the potential dependence of the free energy of adsorption. The potential dependence of the free energy of adsorption indicates that molecules of the compound are least strongly bound at -415 ± 15 mV which coincides with the formal potential of 2,7-AQDS in 0.05 M NaF and the PZC of the unmodified mercury interface. However, the applied potential and the charge on the

electrode appear to have little effect on $\Delta G^{\neq}$. In contrast, our data suggest that changing the redox composition of the monolayer has a significant influence over the magnitude of $\Delta G^{\neq}$ with destabilising lateral interactions between the reduced and oxidised forms of the compound causing a decrease in the free energy of adsorption.

Monolayers of this type represent useful model systems to address outstanding questions regarding how electrons and protons transfer through membranes. Control of how solution phase chemicals interact with these thin films, and what dictates their redox activity, are expected to impact our understanding of mechanisms of biological reactions.

4.4 References

1 Shimidzu, T.; Iyoda, T.; Segawa, H.; Honda, K. in *Photochemical Processes in Organised Molecular Systems* Honda, K. Ed., Elsevier: Amsterdam, 1991, 411.

2 Murray, R. W. In *Molecular design of Electrode Surfaces*; Murray, R. W., Ed.; Wiley: New York, 1992.

3 Gardner, T. J.; Frisbie, C. D.; Wrightom, M. S. *J. Am. Chem. Soc.* 1995, 117, 6927.

4 Erdelen, C. *et al, Langmuir*, 1994, 10, 1246.

5 Lang, H.; Duschl, C.; Vogel, H. *Langmuir*, 1994, 10, 197.

6 Marques, E. P.; Zhang, J.; Tse, Y.-H.; Methcalfe, R. A.; Pietro, W. J.; Lever, A. B. P. *J. Electroanal. Chem.* 1995, 395, 133.

7 Dong, X.-D.; Lu, J.; Cha, C. *J. Electroanal. Chem.* 1995, 381, 195.

8 Schlereth, D. D.; Katz, E.; Schmidt, H.-L. *Electroanalysis*, 1995, 7, 46.

9 Schott, J. H.; Arana, C. R.; Abrûna, H. D.; Petach, H. H.; Elliott, C. M.; White, H. S. *J. Phys. Chem.* 1992, 96, 5222.

10 Song, Z.; Clark, R. A.; Bowden, E. F.; Tarlov, M. J. *J. Phys. Chem.* 1993, 97, 6564.

11 Ulman, A. *An Introduction to Ultrathin Organic Films From Langmuir -Blodgett to Self-Assembly*, Academic Press: United Kingdom, 1991.

12 Porter, M. D.; Bright, T. B.; Allara, D. L.; Chidsey, C. E. D. *J. Am. Chem. Soc.* 1987, 109, 3559.

13 Chidsey, C. E. D.; Loiacono, D. N. Langmuir 1990, 6, 682.

14 Duevel, R. V.; Corn, R. M. *Anal. Chem.* 1992, 64, 337.

15 Forster, R. J.; O'Kelly, J. P. *J. Phys. Chem.* 1996, 100, 3695.

16 Laviron, E. *J. Electroanal. Chem.*, 1981, 124, 9.

17 Laviron, E. *J. Electroanal. Chem.*, 1983, 146, 15.

18 Vetter, K. J. *Z. Elektrochem.*, 1952, 56, 797.

19 Jacq, J. *J. Electroanal. Chem.*, 1971, 29, 149.

20 Bailey, S. I.; Ritchie, I .M. *Electrochim. Acta.*, 1985, 30, 3.

21 Nuzzo, R. G.; Dubois, L. H.; Allara, D. L. *J. Am. Chem. Soc.* 1990, 112, 558.

22 Tour, J. M.; Jones, L.; Pearson, D. L.; Lamba, J. J.; Burgin, T. P.; Whitesides, G. M.; Allara, D. L.; Parikh, A. N.; Atre, S. V. *J. Am. Chem. Soc.* 1995, 117, 9529.

23 Bard, A. J.; Faulkner, L. R. *Electrochemical methods: Fundamentals and Applications*, Wiley, New York, 1980.

24 Zhang, J.; Anson, F. C. *J. Electroanal. Chem.* 1992, 331, 945.

25 Keita, B.; Nadjo, L. *J. Electroanal. Chem.* 1984, 163, 171.

26 Conway, B. E. *Chem. Soc. Rev.*, 1992, 253.

27 Parsons, R. *Chem. Rev.* 1990, 90, 813.

28 Gui, J. Y.; Stern, D. A.; Lin, C.; Gao, P.; Hubbard, A. T. *Langmuir*, 1991, 7, 3183.

29 Salaita, G. N.; Hubbard, A. T. *Catalysis Today*, 1992, 12, 465.

30 Cao, E. Y.; Gao, P.; Gui, J.Y.; Lu, F.; Stern, D. A.; Hubbard, A.T. *J. Electroanal. Chem.* 1992, 339, 311.

31 Bretz, R. L.; Abruña, H. D. *J. Electroanal. Chem.* 1995, 388, 123.

32 Creager, S. E.; Weber, K. *Langmuir*, 1993, 9, 844.

33 Stolberg, L.; Morin, S.; Lipowski, J.; Irish, D. E. *J. Electroanal. Chem.* 1991, 307, 241.

34 Hamelin, A.; Weaver, M. J. *J. Electroanal. Chem.* 1987, 223, 171.

35 Xiaoping, G.; White, H. S.; Shaowei, C.; Abrûna, H. D. *Langmuir*, 1995, 11, 4554.

36 Forster, R. J. *Analyst* 1996, 121, 733.

37 Forster, R. J. *Anal. Chem.* 1996, 68, 3143.

38 De Levie, R. Advances in *Electrochemistry and Electrochemical Engineering*, Vol. 13, Wiley, New York, 1986, p. 1.

39 Widrig, C. A.; Chung, C.; Porter, M. D. *J. Electroanal. Chem.* 1991, 310, 335.

40 Laviron, E. *J. Electroanal. Chem.*, 1974, 52, 395.

41 Brown, P.; Anson, F. C. *Anal. Chem.*, 1977, 49, 158.

42 He, P.; Crooks, R. M.; Faulkner, L. R. *J. Phys. Chem.* 1990, 94, 1135.

43 Forster, R. J. *J. Electrochem. Soc.*, 1997, 144, 1165.

44 Laviron, E. *J. Electroanal. Chem.*, 1984, 164, 213.

45 Jacq, J. *J. Electrochim. Acta.*, 1967, 12, 1345.

46 Xu, C. Ph.D. Thesis, *University of Illinois Urbana Champaign*, 1992.

47 Roullier, L; Laviron, E. *J. Electroanal. Chem.*, 1983, 157, 7.

48 Soriaga, M. P.; Stickney, J. L.; Hubbard, A. T. *J. Electroanal. Chem.*, 1983, 144, 207.

49 Forster, R. J. *Langmuir* 1995, 11, 2247.

50 Soriaga, M. P.; Hubbard, A. T. *J. Am. Chem. Soc.* 1982, 104, 3937.

51 Soriaga, M. P.; White, J. H.; Hubbard, A. T. *J. Phys. Chem.* 1983, 87, 3048.

52 Trassatti, S. *J. Electroanal. Chem.*, 1974, 53, 335.

53 Avecedo, D.; Bretz, R. L.; Tirado, J. D.; Abruña, H. D. *Langmuir*, 1994, 10, 1300.

54 Forster, R. J. *Electrochemical Society Proceedings*, 1996, 96, 65.

55 Wightman, R. M.; Wipf, D. O. *Electrochemical Chemistry*, Bard, A. J. Ed.: Marcel Dekker: New York, 1989, Vol. 15

56 Smith, C. P.; White, H. S. *Anal. Chem.*, 1992, 64, 2398.

57 Gamage, R. S. K. A.; McQuillan, A. J.; Peake, B. M. *J. Chem. Soc. Faraday Trans.* 1991, 87, 3653.

58 Dean, J. A. Handbook of Organic Chemistry, McGraw Hill, New York, 1987.

59 Delahay, P.; Ttrachtenberg, I. *J. Am. Chem. Soc.* 1957, 79, 2355.

Chapter 5

pH Modulated Heterogeneous Electron Transfer Across Metal/Monolayer Interfaces

5.1 Introduction

The field of molecular electronics ranges from well-defined and well-understood phenomena such as nonlinear optical responses, to the tantalising, and conceptually more difficult, areas of computing and information storage at the molecular level.[1-3] Supramolecular assemblies, constructed using single electroactive molecules as building blocks, offer a striking way to create electrically conducting materials whose organised architecture makes them suitable for developing molecular electronic devices.

Progress toward this strategic goal demands not only the development of new synthetic approaches that yield highly ordered materials[4-10] but also careful attention to those elementary processes that dictate the rate of heterogeneous electron transfer across metal/monolayer interfaces.[11-20] However, it is only recently that it has been possible to *directly* probe those factors that govern the rate of electron transfer processes that are complete within a few billionths of a second. In fact, coupling recent advances in the design and fabrication of microelectrodes and electrochemical instrumentation that operate on a nanosecond timescale, with chemical systems that are organised on a molecular level, promise to revolutionise investigations into electron transfer processes.[21-26]

Toward the objective of understanding those factors that influence heterogeneous electron transfer, we have formed osmium containing monolayers by spontaneously adsorbing $[Os(bpy)_2\ (p3p)_2]^{2+}$ complexes (Chart 1), where bpy is 2,2′-bipyridyl and p3p is 4,4′-trimethylenedipyridine, onto clean platinum and gold microelectrodes. For simplicity, we denote these monolayers as $(p3p)_2$. These adsorbed monolayers are stable for long periods at elevated temperatures in aqueous perchlorate solutions allowing those factors that control the rate and pathway for electron transfer across metal/monolayer interfaces to be probed in considerable detail. Moreover, it appears that only one of the pyridine groups binds to the electrode surface, while the other is available for protonation, thus allowing chemical effects on heterogeneous electron transfer to be explored.

We have used chronoamperometry, performed on a microsecond timescale, to probe the structure of the modified interface, focusing particularly on the extent to which solvent and ions permeate the interior of the monolayer. These investigations are doubly important, since they provide an insight into the relative perfection of the monolayer and allow one probe the interfacial potential distribution.[27-29] High speed chronoamperometry has also been used to investigate the dynamics of heterogeneous electron transfer across the electrode/monolayer interface. When the supporting electrolyte concentration is greater than about 0.1 M, these chronoamperometric responses are remarkably well-behaved with heterogeneous electron transfer being characterised by a single rate constant over more than two lifetimes.

Significantly, the solution pH modulates the rate of heterogeneous electron transfer, apparently by protonating the pyridine moiety of the unbound p3p ligand. We have investigated the origin of this pH sensitivity by systematically probing the pH dependence of the free energy of activation $\Delta G^{\neq}$ and the degree of electronic coupling between the remote redox centres and the electrode. Surprisingly, our investigation suggests that changes in the pre-exponential factor with pH rather than the activation barrier cause the heterogeneous electron transfer rate constant to depend on the extent of monolayer protonation.

Investigations of this type are especially important for improving our understanding of those processes that limit the rate of electron transfer within biological systems where subtle changes in the chemical microenvironment surrounding the redox site can dramatically alter the electron transfer rates.[30-31]

5.2 Experimental Section

5.2.1 Apparatus

Electrochemical cells were of conventional design and were thermostated within ± 0.2 °C using a Julabo F10-HC refrigerated circulating bath. All potentials are quoted with respect to a BAS Ag/AgCl gel-filled reference electrode, the potential of which was 35 mV more positive than that of the saturated calomel electrode (SCE). Cyclic voltammetry was performed using a CH Instruments Model 660 or an EG&G Model 273 potentiostat/galvanostat and a conventional three-electrode cell. All solutions were degassed using nitrogen, and a blanket of nitrogen was maintained over the solution during all experiments. The degree of monolayer protonation was altered by systematically varying the pH of the contacting electrolyte solution over the range 5.1 to 1.1 by addition of conc. $HClO_4$ to $LiClO_4$ solutions. These solutions were not pH buffered to avoid difficulties with competitive adsorption effects from buffer ions.

As described previously,[32] a custom built function generator-potentiostat, with a rise time of less than 10 ns, was used to apply potential steps of variable pulse width and amplitude directly to a two-electrode cell. A Pt foil and an Ag/AgCl reference electrode were combined to form a counter electrode. The foil lowered the resistance and provided a high frequency path.

For the temperature resolved experiments, a nonisothermal cell was used in which the reference electrode was isolated from the main compartment by a salt bridge and held at constant temperature. The nonisothermal salt bridge contained saturated KCl since it has a low resistance, and the salt remains soluble at the lowest temperature employed (-5 °C). The high electrolyte concentration and the design of the bridge minimise any systematic error in the reported temperature effects on $E^{\circ\prime}$ due to changes in the liquid junction potential with temperature.[33]

Microelectrodes were fabricated as described in Chapter 3. Typically, the surface roughness factor was between 1.3 and 1.6. Obtaining the real, as opposed to the projected or geometric, surface area of the electrodes is important if the area occupied per molecule is to be accurately measured. RC cell time constants, measured in blank electrolyte solution, were between 0.03 and 3 μs depending on the electrode radius and the supporting electrolyte concentration. The interfacial kinetics were measured only at times greater than about 5 to 10 RC. In chronoamperometry experiments, the initial potential was either 0.000 V or +1.000 V depending on whether oxidation or reduction kinetics were being probed.

Spontaneously adsorbed monolayers were typically formed by immersing the electrodes in a methanol/water solution of the metal complex for 8-12 hr. No precautions were taken to exclude oxygen during monolayer formation. Before electrochemical measurements were made, the modified electrodes were rinsed with the electrochemical solvent to remove unbound material. Subsequent measurements were performed in blank electrolyte solutions.

Chart 1

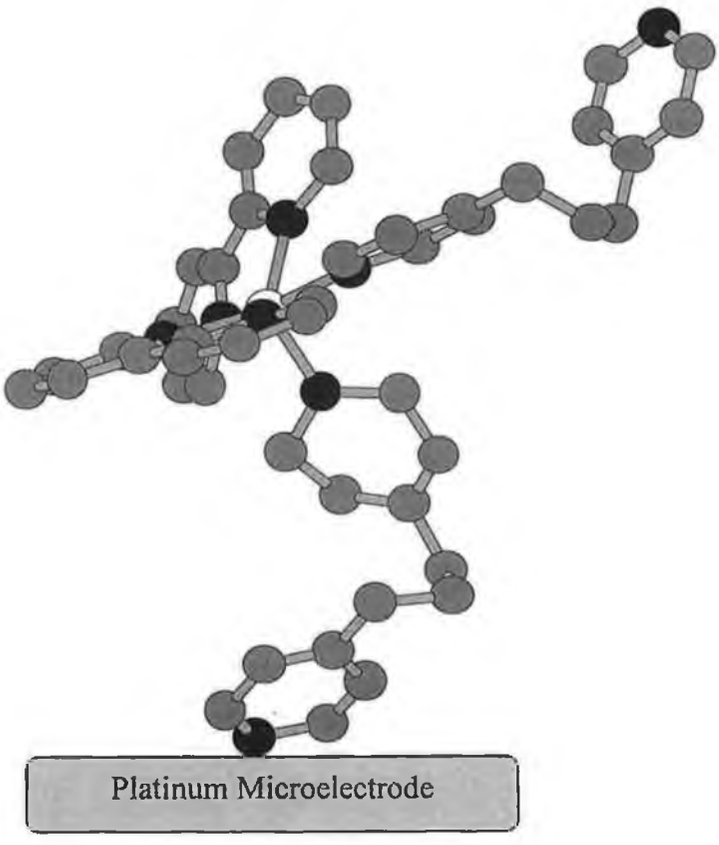

5.3 Results and Discussion

5.3.1 General Electrochemical Properties

Figure 1 shows representative cyclic voltammograms for a spontaneously adsorbed $(p3p)_2$ monolayer, where the supporting electrolyte is 0.1 M $LiClO_4$ (pH = 4.8) that does not contain any dissolved $[Os(bpy)_2(p3p)_2]^{2+}$. This voltammetric response is consistent in all respects with that expected for an electrochemically reversible reaction involving a surface-confined species.[34-35] For example, the peak shapes are independent of scan rate, at least over the range 1 to 50 V/s, and the peak height scales linearly with the scan rate υ, unlike the $\upsilon^{1/2}$ dependence expected for a freely diffusing species. Therefore, it appears that the osmium complex adsorbs onto the surface of the platinum microelectrode to give an electroactive film. Where there are no lateral interactions between surface confined redox centres and a rapid equilibrium is established with the electrode, a zero peak-to-peak splitting (ΔE_{peak}) and a FWHM of 90.6 mV are expected for a reaction involving the transfer of a single electron. As discussed previously for $[Os(bpy)_2\ Cl\ pNp]^+$ monolayers,[32] where pNp is 4,4′-dipyridyl or 1,2-bispyridylethane, we consistently observe a nonzero ΔE_{peak} even at low scan rates, e.g., ΔE_{peak} is 12±3 mV at a scan rate of 500 mV/s. Feldberg has interpreted nonzero peak-to-peak splitting in terms of Unusual Quasi-Reversibility (UQR).[36] In this model, hysteresis is observed in cyclic voltammetry because some rate processes, e.g., heterogeneous electron transfer, ion movement, changes in monolayer structure that accompany redox switching etc., are slow compared to the timescale of the experiment. We do not consider this issue in detail here except to note that neither heterogeneous electron transfer, or double layer assembly (vide infra), limit the voltammetric response at these scan rates. In general, the voltammetric response is consistent with that expected for a rapid, reversible electron transfer to an immobilised redox active species. The peak height and peak area of the voltammograms do not change by more than 15 % when cycled repeatedly over a 10 hr period at temperatures up to 40 °C, indicating that the monolayers are both electrochemically and thermally stable. We observe only a 20-30 mV difference

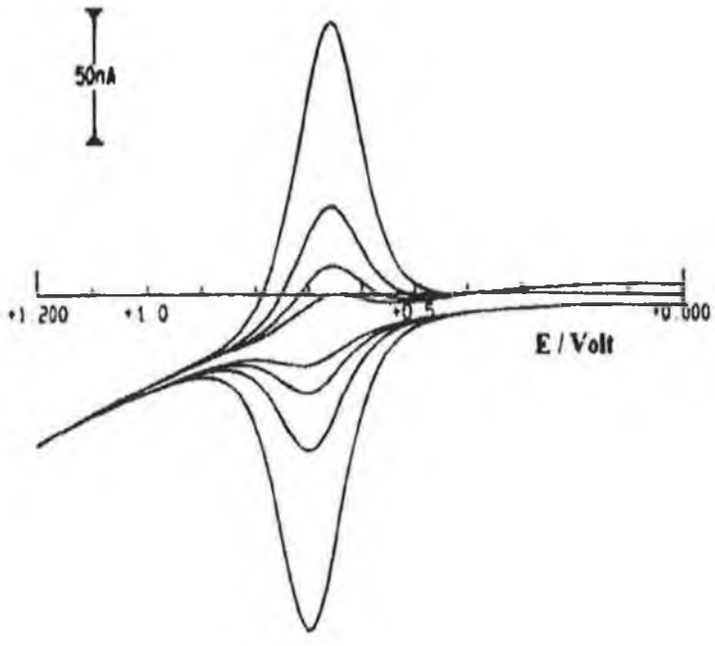

Figure 1 Scan rate dependence of cyclic voltammetry for a spontaneously adsorbed $(p3p)_2$ monolayer. The scan rates are (top to bottom) 50, 20, 10 and 5 V/s. The surface coverage is 9.8×10^{-11} mol cm^{-2}. The supporting electrolyte is 0.1 M $LiClO_4$ at a pH of 4.8. The radius of the platinum microelectrode is 25 μm. The cathodic currents are up, and the anodic currents are down. Each cycle begins at the negative limit.

between the formal potentials of the solution-phase model compound, $[Os(bpy)_3]^{2+}$, and the monolayer, suggesting that the redox centres within the monolayer are solvated.

The total charge introduced or withdrawn to reduce or oxidise the monolayer can be found from the area under the voltammetric peak after correcting for the background charging current. This charge, together with the real surface area, can then be used to calculate the surface coverage, or the number of moles of $[Os(bpy)_2(p3p)_2]^{2+}$ per cm^2. The surface coverage provides important information about the packing density of the monolayer and may provide a limited insight into the way that the complex adsorbs onto the electrode surface. This is important since the cis configuration of the p3p ligands makes it possible for adsorption to occur through one or both of the p3p ligands.

The surface coverage, Γ, as experimentally determined from the area under the cyclic voltammetric wave, was found to be $1.05\pm0.08 \times 10^{-10}$ mol cm^{-2}, corresponding to an area occupied per molecule of 166 ± 12 $Å^2$. When the additional contributions to the molecular volume are considered, e.g., a solvent shell or a counterion, this area of occupation is consistent with that expected for a close packed monolayer in which the radius of the metal complex (crystallographic data[37-39] indicate that the radii of osmium and ruthenium polypyridyl complexes are of the order of 6.7 Å), rather than the length of the bridging ligands, dictates the surface coverage. This area of occupation is smaller than that found for adsorbed $[Os(bpy)_2\ Cl\ (p3p)]^+$ complexes[32] (240 $Å^2$) and is indistinguishable from that found for adsorbed $[Os(bpy)_2$ pyridine $(p3p)]^{2+}$ complexes,[40] both of which contain only one p3p bridging ligand. Molecular modelling of the $[Os(bpy)_2\ (p3p)_2]^{2+}$ complex suggests that if both p3p ligands adsorbed onto the electrode surface, then its area of occupation would be at least 214 $Å^2$, a value that is approximately 30 % larger than that experimentally observed. These observations suggest that only one of the p3p ligands is bound to the electrode surface. This conclusion is supported by our observation (vide infra) that the heterogeneous electron transfer rate, k, depends on the pH of the contacting

electrolytic solution. This pH sensitivity of k contrasts with structurally related $[Os(bpy)_2$ pyridine p3p$]^{2+}$ monolayers where the heterogeneous electron transfer dynamics are independent of the solution pH.

As described previously,[32,41,42] the ideality of the electrochemical response can be further probed by using chronocoulometry to determine the redox composition as a function of the applied potential.[43] The slopes of plots of ln ([Ox] / [Red]) vs potential are independent of the pH, maintaining a value of 57±3 mV/decade, as the pH of the contacting electrolyte solution is changed from 5.05 to 1.07. This slope is indistinguishable from those predicted for a one electron transfer reaction by the Nernst equation,[43] confirming that the thermodynamic aspects of electron transfer at these metal/monolayer interfaces are nearly ideal under the experimental conditions employed.

The formal potential for the $Os^{2+/3+}$ redox reaction shifts from 0.638 to 0.654 V as the pH is systematically varied from 5.05 to 1.07. That $E^{\circ\prime}$ shifts in a positive potential direction indicates that protonation stabilises the reduced state of the complex. This small shift in $E^{\circ\prime}$ is consistent with the methylene spacer groups effectively blocking electronic communication between the two pyridine rings (vide infra). Moreover, the small shift in $E^{\circ\prime}$ suggests that the electrostatic effects of protonating the unbound pyridine ring are relatively unimportant. This behaviour probably arises because the high dielectric constant of water, and the high supporting electrolyte concentration, efficiently screen the charge on the pyridinium ion that is located 9 - 10 Å away from the osmium redox centre.

5.3.2 Adsorption-desorption processes of $[Os(bpy)_2(p3p)_2]^{2+}$

The adsorption, and to a lesser extent desorption, of a number of osmium containing monolayers has been the focus of several studies in the recent past. In particular Abruña and coworkers have carried out extensive studies of complexes similar to $[Os(bpy)_2(p3p)_2]^{2+}$. In the majority of cases, the complex employed has been of the form $[Os(bpy)_2(Cl)L]^+$ where L is a ligand with a pyridine group attached to the central metal atom. One of the first papers to consider adsorption in this type of monolayer was presented by Avecedo and Abruña.[14] In this contribution, they investigated the effects of solvent and surface coverage on the adsorption of $[Os(bpy)_2(p3p)Cl]^+$. Further work by Abruñas group[14,15,44-46] and that of Anson[47] have helped to elucidate the factors that affect the thermodynamics and kinetics of adsorption and desorption in these systems.

In this work, we have investigated the thermodynamics and kinetics of adsorption and desorption of the complex $[Os(bpy)_2(p3p)_2]^{2+}$ which is capable of forming self assembled monolayers on platinum and gold electrodes. The main difference between this complex and that of earlier works is that the chlorine atom of the earlier complexes has been replaced by a 4,4-trimethylenedipyridine ligand making it possible for each osmium site to adsorb through two bridging ligands. The overall charge on the complex is 2+ and the redox potential shifts by approximately 0.35 V positive to 0.70 V. This shift presents significant problems due to oxidation of both platinum and gold at potentials more positive than 0.800 V. However, having a well prepared electrode and a thoroughly degassed electrolyte solution, together with maintaining a blanket of nitrogen over the electrochemical cell during all experiments, minimises problems associated with oxidation of the electrode surface.

Cyclic voltammetry has been the most popular technique for examining adsorption-desorption phenomena due to its non-invasive nature and real-time monitoring of these processes. Typically, we have used cyclic voltammetry employing gold and platinum microelectrodes of 25 μm radius for our experiments.

The potential has been held at a potential of 0.00 V during all experiments. This potential was chosen as it is close to the PZC of both types of electrode and therefore exerts little influence on the adsorption or desorption process. The supporting electrolyte in all cases was 0.1 M $LiClO_4$. Typical deposition solution concentrations were in the low micromolar range. Therefore, it can be assumed that the solution phase contribution to the measured electrochemical response is negligible and the integrated charge under the redox wave, after correcting for double layer charging, is representative of the surface coverage of the electrode. Desorption processes into blank electrolyte solutions can also be monitored.

Adsorption onto platinum

Figure 2 shows voltammograms of a platinum microelectrode immersed in a 10 μM solution of $[Os(bpy)_2(p3p)_2]^{2+}$. That the surface coverage increases over time and the double layer capacitance decreases substantially indicates the formation of an organic monolayer with displacement of solvent and ions from the interface. It can also be seen from Figure 2 that the formal potential of the $Os^{2+/3+}$ redox couple shifts to increasingly more positive potentials with increasing coverage. Anson[35] has interpreted this shift in $E^{o\prime}$ with coverage, as the effect of surface concentration on interactions between the oxidised and reduced forms of the redox couple. This theory of surface activity for immobilised species relates anodic and cathodic peak potentials to surface coverage:

$$E_{peak} = E^{o} + \left(\frac{RT}{nF}\right)\left(r_R - r_O\right)\Gamma_T \qquad (2)$$

where r_R and r_O are interaction parameters representing intermolecular interactions among reduced and oxidised forms, respectively (provided that the interactions between O and R and R and O are equal). In reality, the two peak potentials are not equal and if we take the formal potential, $E^{o\prime}$, to represent E_{peak}, Equation 2 predicts

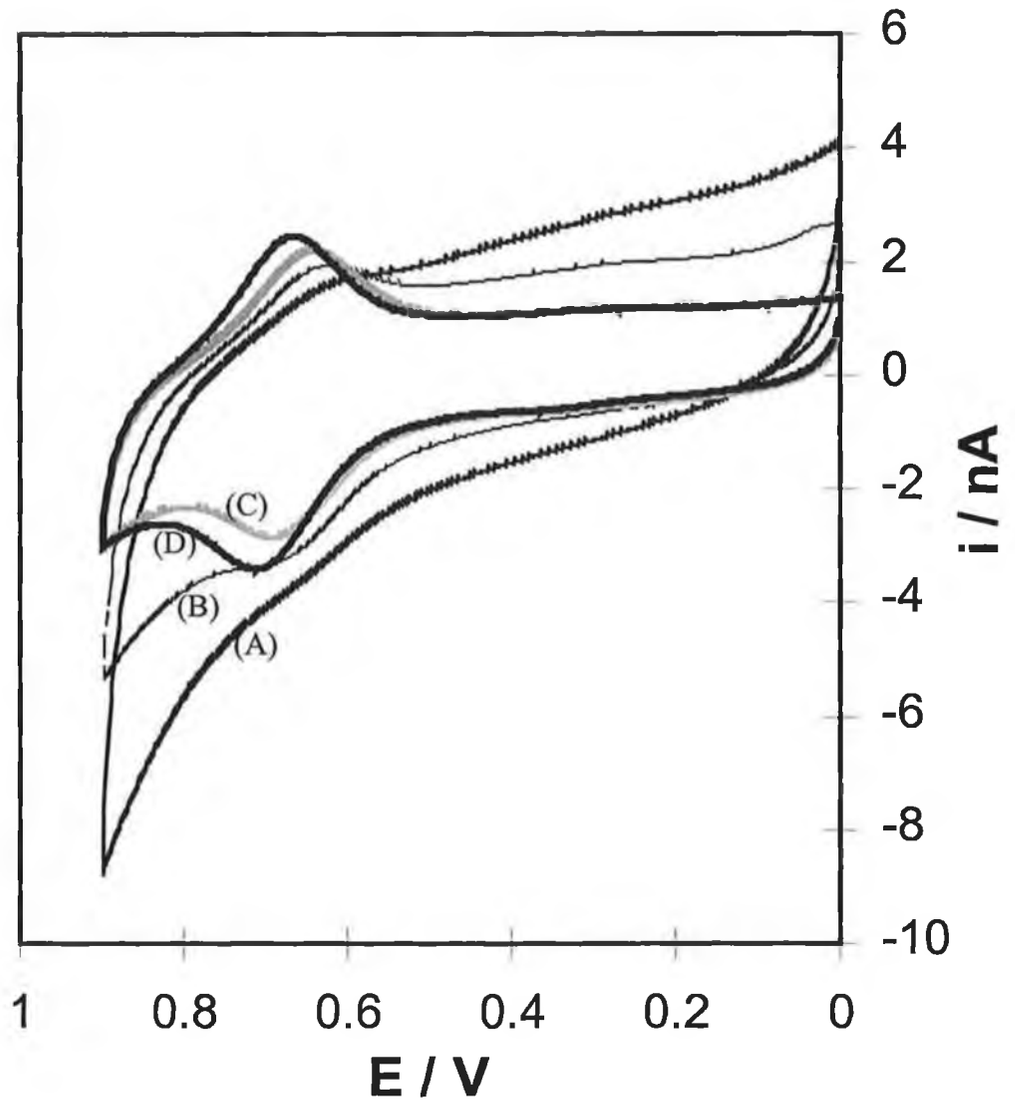

Figure 2 Cyclic voltammograms showing the adsorption of $[Os(bpy)_2(p3p)_2]^{2+}$ from a 10 μM solution of the complex in 2:1 H_2O/DMF onto a 25 μm radius platinum electrode. The voltammograms showing increasing Faradaic current represent deposition times of (A) 5, (B) 20, (C) 200 and (D) 300 minutes respectively. Scans were initiated at 0.00 V and a scan rate of 500 mV/s was employed. The supporting electrolyte is 0.1 M $LiClO_4$.

that $E^{o\prime}$ will shift depending on the relative magnitude of r_R and r_O as the surface coverage, Γ, changes. A positive shift in $E^{o\prime}$ with increasing coverage indicates that the absolute value of r_O is larger than r_R.

Interactions between adsorbed species can be examined by probing the full-width-at-half-maximum (FWHM) values. For positive/attractive interactions between adsorbates FWHM values less than the ideal value of 90.6/n mV are expected, while for negative/repulsive interactions broadened voltammetric peaks with FWHM values greater than 90.6 mV are expected. That the voltammograms in Figure 2 have FWHM values of greater than the ideal value of 90.6/n mV and because $E^{o\prime}$ shifts positive with increasing coverage, it appears that there are repulsive interactions between the oxidised species.[14] This behaviour is consistent with what one would expect on the basis of the charge on the reduced, 2+, and oxidised, 3+, forms of the species. That interactions are present means that a Langmuir isotherm does not provide an appropriate description of adsorption in this system. Also worth mentioning is that the change in $E^{o\prime}$, and therefore intermolecular interactions, with surface concentration suggests that the monolayer is formed by the even spread of adsorbate molecules on the electrode surface as opposed to dense islands which eventually congregate.

As with the adsorption of anthraquinone-2,7-disulphonic acid onto mercury electrodes discussed in the previous chapter, the adsorption of $[Os(bpy)_2(p3p)_2]^{2+}$ appears to insulate the electrode against oxidation and shifts the potential for platinum oxidation to more positive potentials. Figure 2 demonstrates that upon adsorption of the complex, the capacitive current at 900 mV decreases from 9 nA for a bare electrode to approximately 2 nA at full monolayer coverage. This observation further suggests that the monolayers are dense and relatively defect free.

The kinetics of adsorption of $[Os(bpy)_2(p3p)_2]^{2+}$ have also been studied. Figure 3 shows the change in the surface coverage with time. The complex appears to adsorb more rapidly over a short initial period of time, while saturation coverage occurs over a much longer timescale. A full monolayer is formed in 270 minutes

from a 2:1 H_2O/DMF solution. This is substantially longer than the approximate 30 minutes taken for adsorption of a similar mono substituted complex onto gold from what is essentially a 100% aqueous solution. This increase in the time taken for monolayer formation is thought to arise because of the solubility of the complex in DMF. In fact no adsorption occurs from pure DMF. The use of DMF in the adsorption of $[Os(bpy)_2(p3p)_2]^{2+}$ was decided upon because a non-evaporating solvent of known concentration was desired. Also, as we shall see, desorption of the complex into a 100% aqueous environment did not desorb monolayers fully.

Figure 4 shows the adsorption of the complex from a 20 μM solution of the complex. It appears that full monolayer coverage, $\Gamma = 1.1 \times 10^{-10}$ mol cm^{-2} is achieved after approximately 100 minutes. However, upon leaving the electrode immersed in the deposition solution, the coverage increases up approximately 1.5×10^{-10} mol cm^{-2} where a large increase in coverage occurs. Although this experiment did not prove very reproducible, it seems that the sudden increase in coverage may be due to the formation of a second layer, i.e., the beginning of multilayer formation. This hypothesis is consistent with a previous report by Bretz and Abruña who observed multilayer formation of $[Os(bpy)_2Cl(Py\text{-}(CH_2)_n\text{-}SH)]^+$ on platinum.[44]

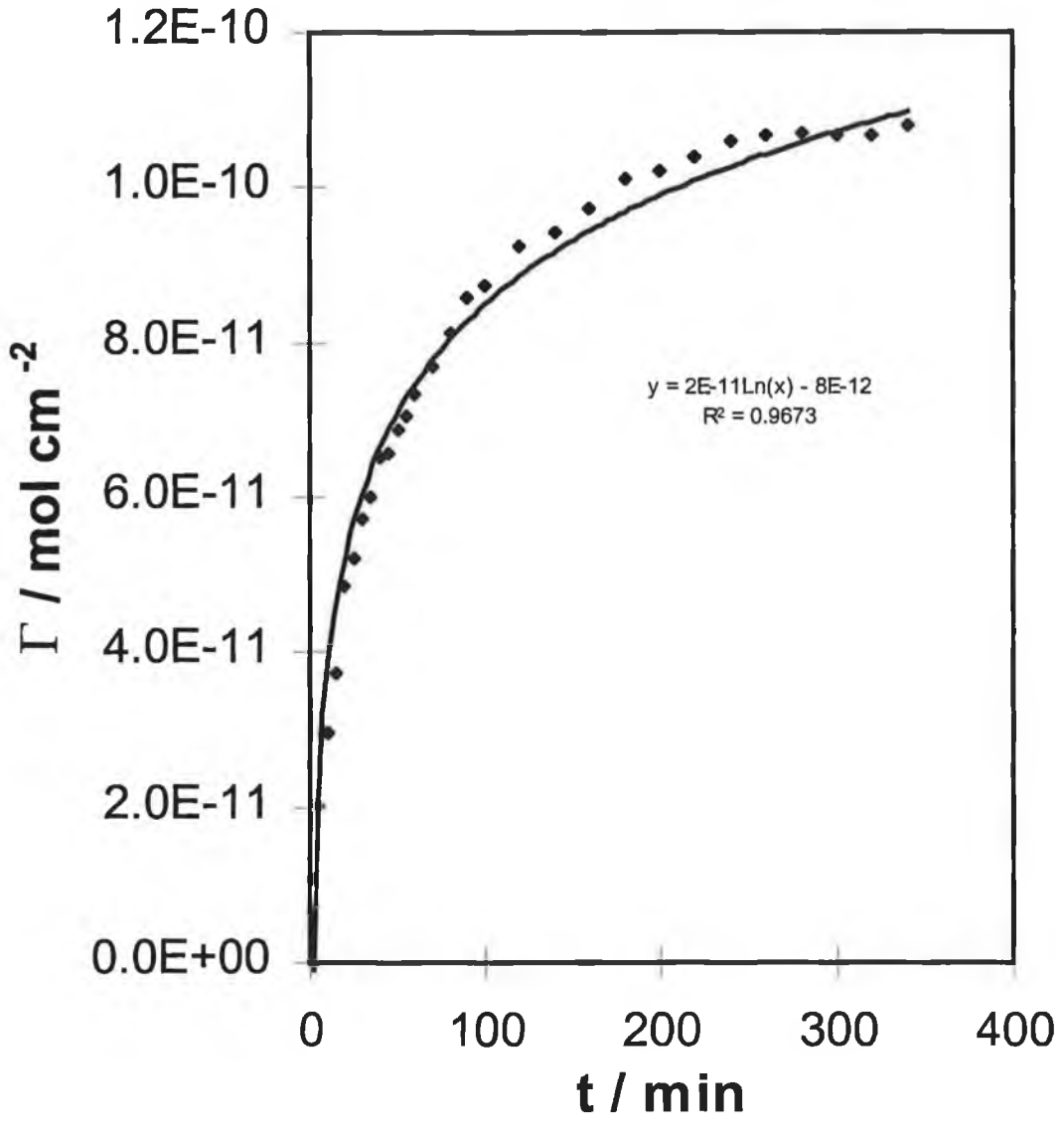

Figure 3 Surface coverage of $[Os(bpy)_2(p3p)_2]^{2+}$ adsorbed onto a 25 μm Pt microelectrode from a 10 μM solution of the complex in 2:1 H_2O/DMF as a function of time. Voltammograms were initiated at 0.00 V and a scan rate of 500 mV/s was employed. The supporting electrolyte is 0.1 M $LiClO_4$. Surface coverages were determined from the voltammograms in Figure 2 by integrating the charge under the redox waves after correcting for double layer charging.

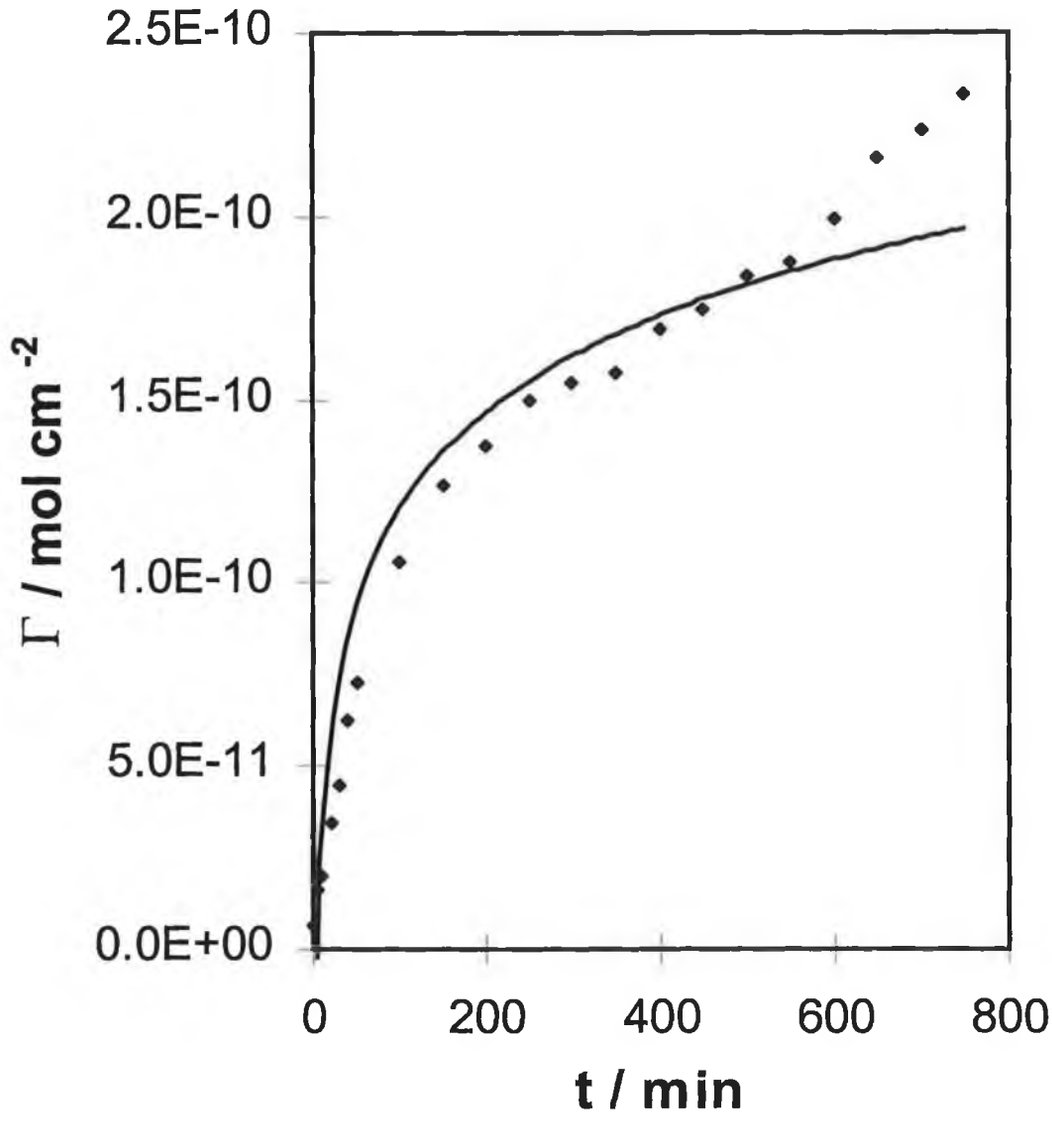

Figure 4 Surface coverage of $[Os(bpy)_2(p3p)_2]^{2+}$ adsorbed onto a 25 μm Pt microelectrode from a 20 μM solution of the complex in 2:1 H_2O/DMF as a function of time. The coverage was determined using slow scan rate cyclic voltammetry. Other conditions are as in Figure 3.

Adsorption onto gold.

Figure 5 shows representative cyclic voltammograms for the adsorption of $[Os(bpy)_2(p3p)_2]^{2+}$ onto gold microelectrodes. A coverage of 0.95 x 10^{-10} mol cm^{-2} was achieved in 130 min. This coverage is experimentally indistinguishable from full coverage on platinum. Similar to adsorption of the complex onto platinum, the capacitance decreases significantly upon monolayer formation. However, the shift in $E^{o\prime}$ with surface coverage is not as pronounced as in the case of the platinum electrode. This may be due to the reduction of repulsive interactions between adsorbates caused by solvation of the monolayer and/or the presence of counter ions, both of which would cause a screening affect, thus reducing the repulsive forces felt by neighbouring molecules. Quantifying the interactions between adsorbates by means of the FWHM values is not feasible here, due to the inaccuracies involved in measuring the FWHM at low surface coverage.

Adsorption of $(p3p)_2$ onto platinum and gold microelectrodes follows a logarithmic path. This makes interpretation of the kinetic order difficult. If adsorption followed first order kinetics, the coverage would increase exponentially with time, while for a second order response the reciprocal of the coverage would be linear with time. However, our results show neither of these dependencies. It is possible that more than one type of kinetics plays a role in the adsorption process. It is also possible that time dependent rates play a part. These and other issues will be dealt with in more detail in future work.

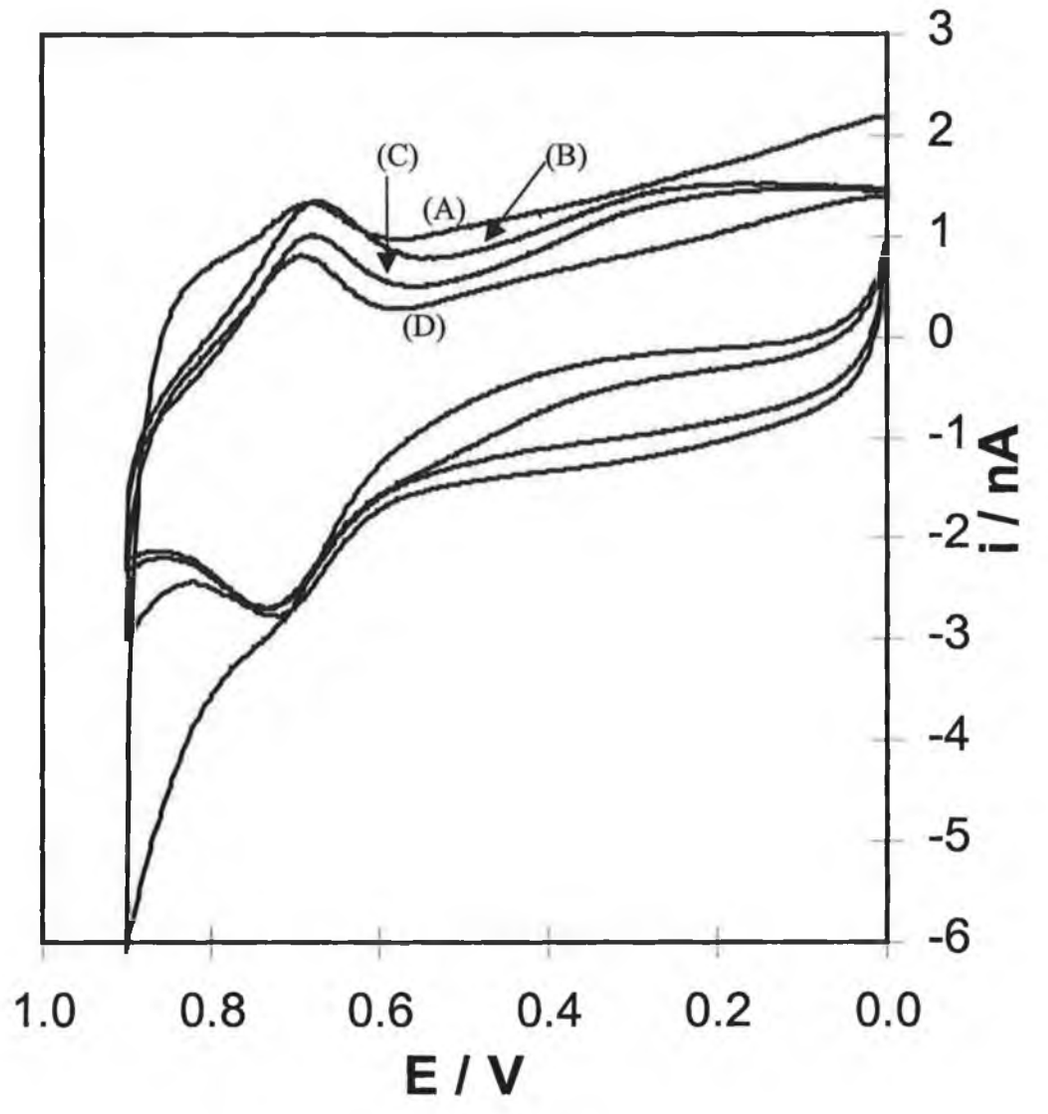

Figure 5 Cyclic voltammograms showing the adsorption of $[Os(bpy)_2(p3p)_2]^{2+}$ from a 10 μM solution of the complex in 2:1 H_2O/DMF onto a 25 μm radius gold electrode. The voltammograms showing increasing Faradaic current represent deposition times of (A) 10, (B) 15, (C) 35 and (D) 60 minutes respectively. Scans were initiated at 0.00 V and a scan rate of 500 mV/s was employed. The supporting electrolyte is 0.1 M $LiClO_4$.

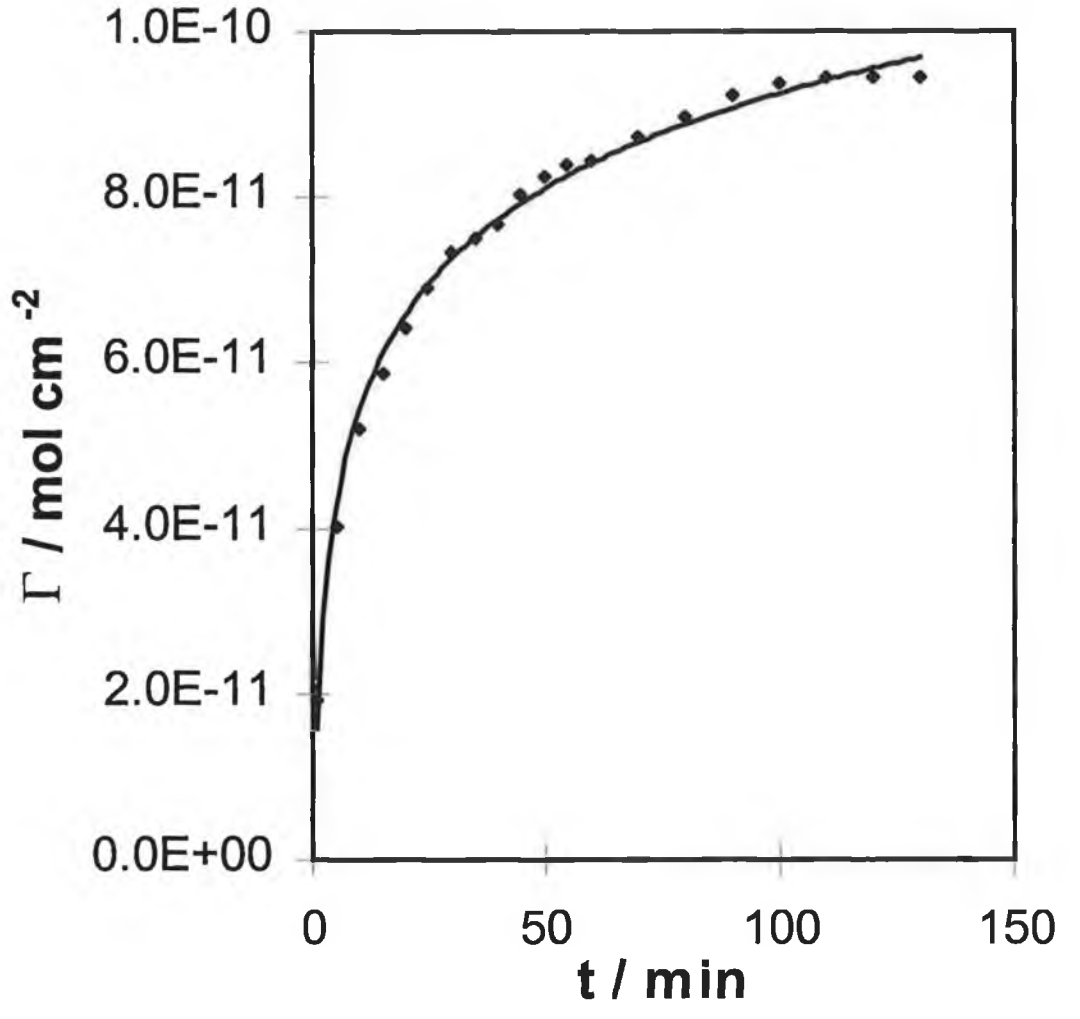

Figure 6 Surface coverage of $[Os(bpy)_2(p3p)_2]^{2+}$ adsorbed onto a 25 μm Pt microelectrode from a 10 μM solution of the complex in 2:1 H_2O/DMF. The supporting electrolyte is 0.1 M $LiClO_4$. Surface coverages were determined from the voltammograms in Figure 5 by integrating the charge under the redox waves after correcting for double layer charging.

Desorption from platinum and gold.

DMF was chosen as the co-solvent because the complex dissolves easily and DMF is non volatile. Thus, the concentration of the deposition solution would be known at all times. Another reason for using DMF was that significantly desorption into 100% aqueous solution occurred only on a timescale of days and in most cases complete desorption did not occur. Therefore, the same solvent mixture was used for the desorption experiments as for the adsorption. This also allows direct comparison of the times required for the two processes to occur.

Figure 7 shows cyclic voltammograms of the desorption of $[Os(bpy)_2(p3p)_2]^{2+}$ from a Pt electrode. The CV showing the highest coverage is that of full monolayer coverage while the CV's showing decreased coverage represent less than complete monolayers after short periods of desorption. As in the case of $[Os(bpy)_2(p3p)_2]^{2+}$ adsorption, the desorption reveals that, while lateral interactions do not completely disappear, decreasing the coverage makes oxidation more facile.

Figure 8 shows desorption of the complex from a gold electrode. In this case, the CV's presented are after some desorption has already taken place. That the capacitance increases substantially for a small decrease in surface coverage suggests that the double layer capacitance is highly sensitive to the double layer structure. However, due to the sloping and changing background, the shift in $E^{o\prime}$ with surface coverage is difficult to determine. Oxidation of the gold electrode surface (as evidenced by the large capacitive currents at 900 mV in Figure 8) occurs as the surface coverage decreases. Therefore, monolayer formation prevents the occurrence of metal oxidation.

The kinetics of desorption of the complex from both Au and Pt microelectrodes has been probed. Figure 9 shows the desorption coverage for $[Os(bpy)_2(p3p)_2]^{2+}$ into a 2:1 H_2O/DMF solution as a function of time at platinum and gold electrodes. The upper curve on the right hand side, showing the least loss of surface coverage, is that for desorption from a Pt electrode while the lower curve on

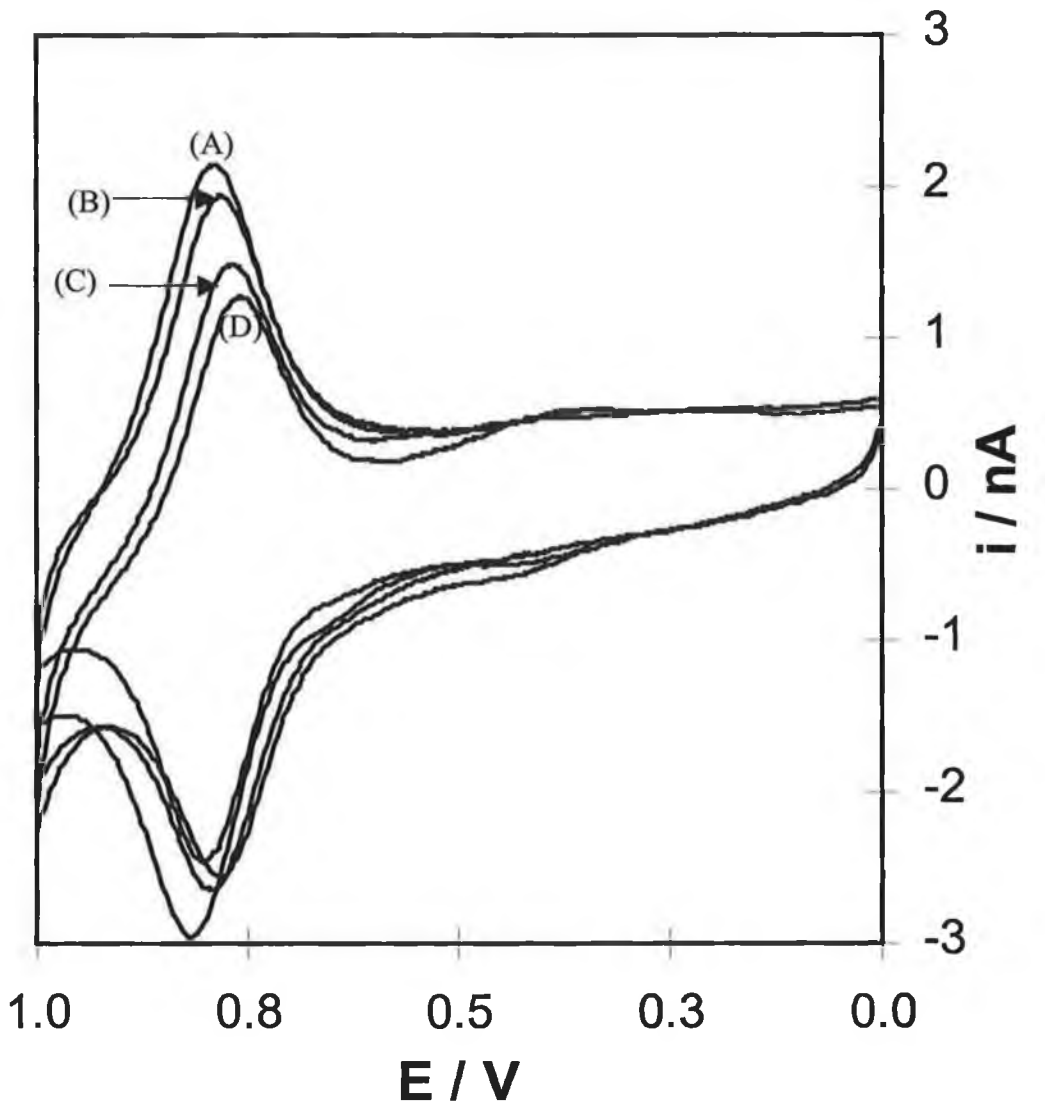

Figure 7 Cyclic voltammograms showing the desorption of $[Os(bpy)_2(p3p)_2]^{2+}$ from a 25 μm radius Pt electrode into a 2:1 H_2O/DMF solution. Cathodic currents are up, anodic currents are down. The voltammograms showing decreasing Faradaic current are, from top to bottom on the cathodic side, represent desorption times of (A) 1, (B) 40, (C) 200 and (D) 390 minutes respectively. Scans were initiated at 0.00 V and a scan rate of 500 mV/s was employed. The supporting electrolyte is 0.1 M $LiClO_4$.

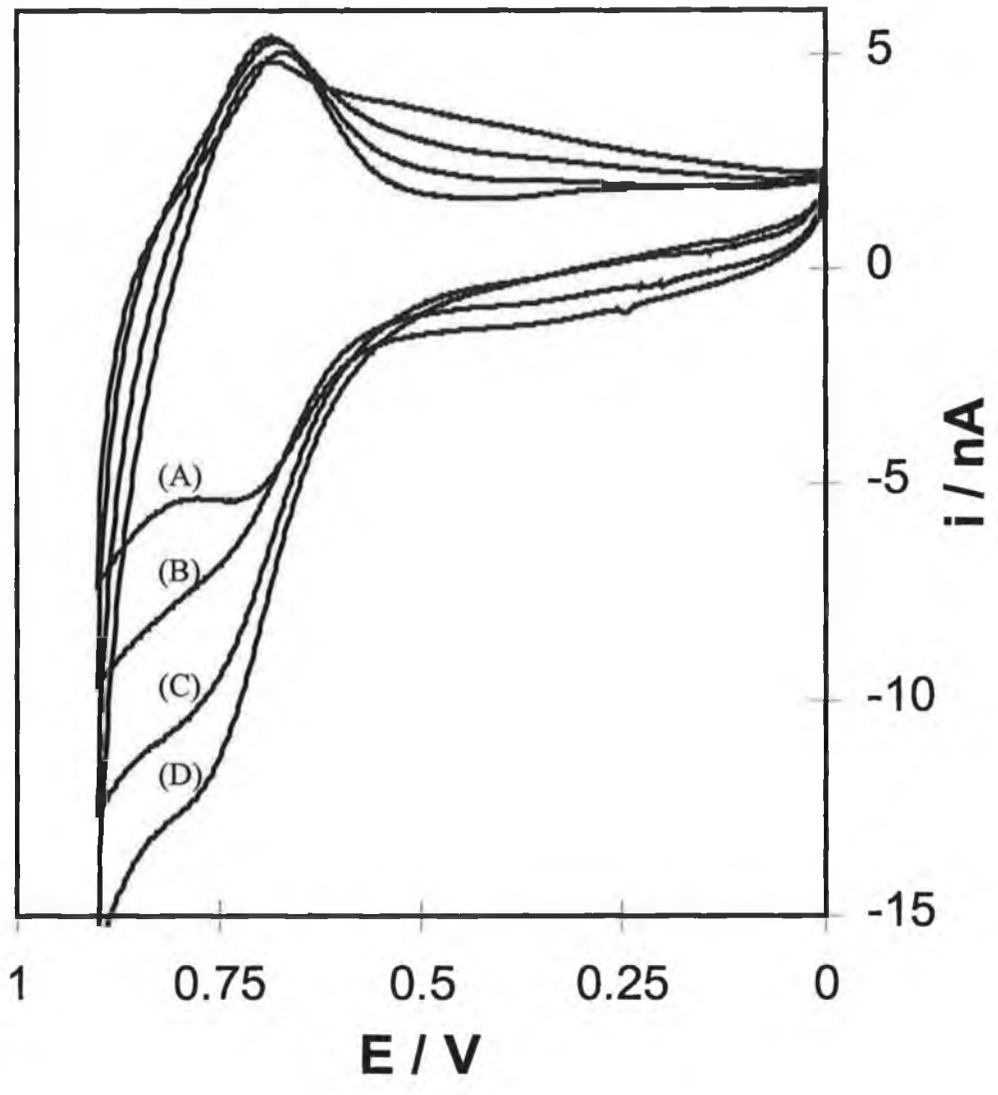

Figure 8 Cyclic voltammograms showing the desorption of $[Os(bpy)_2(p3p)_2]^{2+}$ from a 25 μm radius Au electrode into a 2:1 H_2O/DMF solution. The voltammograms represent desorption times of (A) 20, (B) 185, (C) 390 and (D) 475 minutes respectively. Other conditions are as in Figure 7.

the right hand side is that for desorption from Au. The desorption process in both cases shows an exponential response suggesting that it is a first order kinetic process, i.e., dissolution of the complex into the solvent is the primary reason for desorption and not replacement of the adsorbate with electrolyte ions which would result in a second order mechanism. That the desorption process differs from the adsorption process again suggests that the Langmuir model does not describe the adsorption/desorption processes. The insert of Figure 9 provides the semi-log plots from which the rate of desorption of $[Os(bpy)_2(p3p)_2]^{2+}$ from the electrodes has been determined. For desorption from the gold electrode the desorption rate has been determined at $2.4x10^{-4}$ min^{-1} ($4.1x10^{-5}$ s^{-1}) while desorption from platinum is approximately half at $1.1x10^{-4}$ min^{-1} ($1.79x10^{-5}$ s^{-1}). These values are somewhat slower than the 1.4×10^{-4} s^{-1} reported by Campbell and Anson for desorption of a mono-substituted complex from gold[47] and by Tirado and Abruña for displacement processes at platinum electrodes,[46] and suggests that $[Os(bpy)_2(p3p)_2]^{2+}$ forms very stable monolayers on platinum and gold microelectrodes. Monolayers adsorbed on Pt electrodes desorb more slowly that those on Au. Further work may focus on the potential dependent adsorption of these monolayers onto various electrode materials.

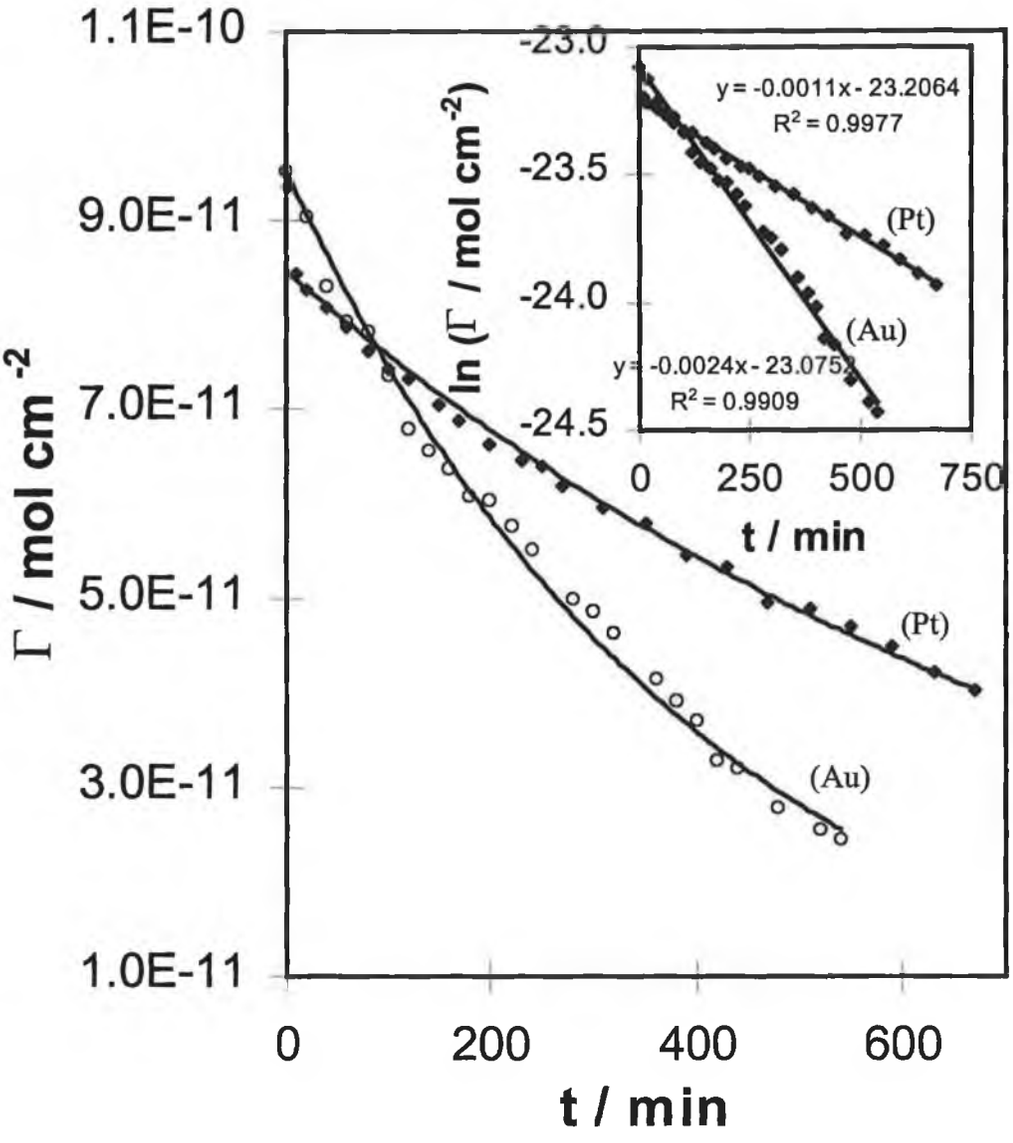

Figure 9 Surface coverage of $[Os(bpy)_2(p3p)_2]^{2+}$ desorbing from 25 μm Pt and Au microelectrodes into a 2:1 H_2O/DMF solution as a function of time. The supporting electrolyte is 0.1 M $LiClO_4$. Surface coverages were determined from the voltammograms in Figure 7 and 8. The insert in Figure shows the semi-log plots for the desorption processes.

5.3.3 Interfacial Capacitance

Probing the double layer capacitance, C_{dl}, gives an insight into the change in interfacial charge distribution that accompanies monolayer formation, the relative perfection of the monolayer, and perhaps its thickness.[27-29,32,48-51] Here, we have used small amplitude potential step chronoamperometry to measure the interfacial capacitance as the electrolyte concentration was systematically varied. The potential step was centred at 0.100 V where the monolayer is redox inactive, and a pulse amplitude, ΔE, of 25 mV was employed. The pulse amplitude is sufficiently small to allow the measured capacitance to be regarded as an approximate differential capacitance. This potential step does not change the redox composition of the monolayer, and only single exponential decays due to double layer charging were observed. This capacitive current was analysed using a plot of ln $i_c(t)$ vs t to obtain the resistance R_u and double layer capacitance C_{dl} according to Equation 2.[52]

$$i_c(t) = \left(\frac{\Delta E}{R_u}\right) exp\left(\frac{-t}{R_u C_{dl}}\right) \qquad (2)$$

For an electrochemical double layer, the differential capacitance increases with a decreasing separation between the electrode surface and the plane of closest approach for ionic charge and increases with increasing dielectric constant.[43] There are two limiting cases for the potential profile across an adsorbed monolayer.[27-29] First, the modified interface could be similar to a bare electrode so that all of the applied potential would be dropped close to the electrode/monolayer interface. In this case, the immobilised redox centre would not experience a large electric field (Chart 2A). Second, as discussed recently by Smith and White,[27] the existence of an impermeable monolayer that has a low dielectric constant may cause the potential to decay linearly across the thickness of the monolayer and then exponentially in the solution phase (Chart 2B). In this case, the surface-confined redox centres would experience a large electric field. An insight into the applicability of either model to our interfaces can be obtained by measuring the interfacial capacitance. This objective is doubly important because we are interested in the electric field effects on

heterogeneous electron transfer, and the interaction of the highly charged protonated complexes with the interfacial electric field.

Chart 2

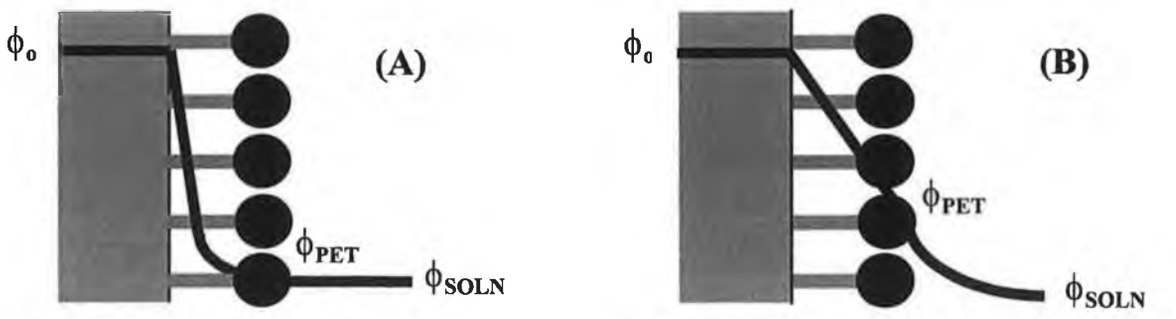

For the model illustrated in Chart 2B,[53-54] the reciprocal total interfacial capacitance, C_T, is given by the sum of the reciprocal capacitances of the film, C_{film}, and the diffuse layer, C_{dif},

$$\frac{1}{C_T} = \frac{1}{C_{film}} + \frac{1}{C_{dif}} \tag{3}$$

$$C_{film} = \frac{\varepsilon_o \varepsilon_{film}}{d} \tag{4}$$

$$C_{dif} = \varepsilon_o \varepsilon_{SOLN} \kappa cosh\left[\frac{ze(\phi_{PET} - \phi_{SOLN})}{2k_B T}\right] \tag{5}$$

where ε_o is the permittivity of free space, ε_{film} and ε_{SOLN} are the film and solution dielectric constants, respectively, d is the monolayer thickness, z is the charge number of the electrolyte ion, e is the absolute electronic charge, k_B is Boltzmann's constant, T is the absolute temperature, and ϕ_{PET} and ϕ_{SOLN} are the potentials at the

plane of electron transfer and in the bulk solution, respectively (Chart 2). The quantity κ is given by $(2n°z^2e^2 / \varepsilon_{SOLN}\varepsilon_0 k_B T)^{1/2}$, where n° is the number concentration of the ions in solution.[16]

Only the diffuse layer capacitance depends on the potential or the concentration of supporting electrolyte. Therefore, the relative importance of that component may be probed by systematically varying the supporting electrolyte concentration and measuring the total capacitance. Table 1 contains the cell time constants, uncompensated cell resistances and double layer capacitances as the concentration of $LiClO_4$ as supporting electrolyte is systematically varied from 0.02 to 1.2 M. Figure 10 shows the dependence of the voltammetric response on the supporting electrolyte concentration and Figure 11 shows the approximate differential capacitance, determined at 0.100 V, as a function of the logarithm of the supporting electrolyte concentration. The double layer capacitance increases approximately linearly with increasing logarithm of the electrolyte concentration for $LiClO_4$ concentrations less than about 0.2 M. This sensitivity clearly indicates that the diffuse layer capacitance contributes significantly to the total interfacial capacitance over this concentration range. The limiting value of C_T at high electrolyte concentration is at least 28 $\mu F\ cm^{-2}$, which may represent the film capacitance (Chart 2B), or if solvent and electrolyte ions freely diffuse into the interior of the monolayer and the double layer sets up as it would at a bare electrode (Chart 2A), it may correspond to the capacitance of the charges held at the outer Helmholtz plane. If this limiting capacitance is dominated by the film capacitance (Chart 2B), then assuming a monolayer thickness of approximately 20 Å, the relative dielectric constant within the film is estimated from Equation 4 as 63. That the relative dielectric constant within the monolayer is comparable to that of water (ε_{SOLN} = 78.5) would suggest that the monolayer is rather permeable to solvent and counterions.

Alternatively, the double layer may set up within the monolayer (Chart 2A), in which case the limiting interfacial capacitance corresponds to the capacitance of the charges held at the Outer Helmholtz Plane. Given that the distance of closest

approach is likely to be of the order of 3 Å, the relative dielectric constant within the double layer would have to decrease from the value of 78.5 for bulk water to approximately 9 before a limiting interfacial capacitance of 28 μFcm^{-2} could be observed. It is important to note that, as discussed above for Chart 2B, this model is consistent with a solvated monolayer interior. Therefore, based on these capacitance data, we conclude that the interior of the monolayer is at least partially solvated. However, the monolayer is not solvated to the extent which precludes interaction between neighbouring adsorbates suggesting that solvent and ions permeate the monolayer but do not electrostatically insulate adjacent charges.

Table 1. Electrolyte Concentration Dependence of the Cell Time Constant R_uC_{dl}, Uncompensated Cell Resistance R_u, and Double Layer Capacitance C_{dl} as Measured at 0.100 V.[a]

[$LiClO_4$], M	**R_uC_{dl}, ns**	**10^{-3} R_u, Ω**	**C_{dl}, pF**
0.02	266(18)	25.1(2.0)	10.6(1.0)
0.05	289(22)	18.3(1.8)	15.8(1.2)
0.10	195(8)	9.6(1.1)	20.4(1.8)
0.15	177(11)	7.1(0.6)	24.9(2.2)
0.21	150(10)	5.2(0.4)	28.7(2.4)
0.26	134(12)	4.1(0.4)	32.6(2.9)
0.29	114(9)	3.7(0.2)	30.8(3.0)
0.35	92(6)	3.1(0.3)	29.9(2.5)
0.40	95(7)	2.8(0.2)	34.5(3.2)
0.61	58(4)	1.8(0.1)	32.8(2.9)
0.80	41(3)	1.3(0.2)	31.7(3.1)
1.0	34(2)	1.1(0.1)	30.5(2.8)
1.2	29(2)	0.9(0.1)	32.8(2.5)

[a] Numbers in parentheses represent the standard deviations for at least three individual monolayers. Supporting electrolyte is lithium perchlorate. The radius of the platinum microelectrode is 5 μm.

As described recently by Creager and coworkers,[28] an insight into the interfacial potential distribution, and hence monolayer permeability, can be obtained by probing the kinetics of heterogeneous electron transfer as the supporting electrolyte concentration is systematically varied. This is possible since a significant potential difference between the plane of the immobilised molecules and the bulk of solution means that only a fraction of the total interfacial drop drives the heterogeneous electron transfer process. In fact, the driving force would be governed by an equilibrium electrode potential that is a function of the electrostatic potential at the site for electron transfer. This means that the driving force for electron transfer changes as the redox reaction proceeds, causing the overall dynamics to deviate from first order kinetics.[28] We note that there are many processes other than interfacial fields that can cause nonexponential current decays, including multiple site geometries, surface activity effects,[34,35] the presence of defect sites,[55] oxidation state dependent dipole moments,[56] or ion-pairing.[57-60] However, an increased supporting electrolyte decreases the double layer thickness κ, and if ions permeate into the monolayer, the situation is approached where all of the applied potential is dropped close to the electrode/monolayer interface. Therefore, one can probe the ideality of the chronoamperometric response without the complication of interfacial electric fields by employing high supporting electrolyte concentrations.

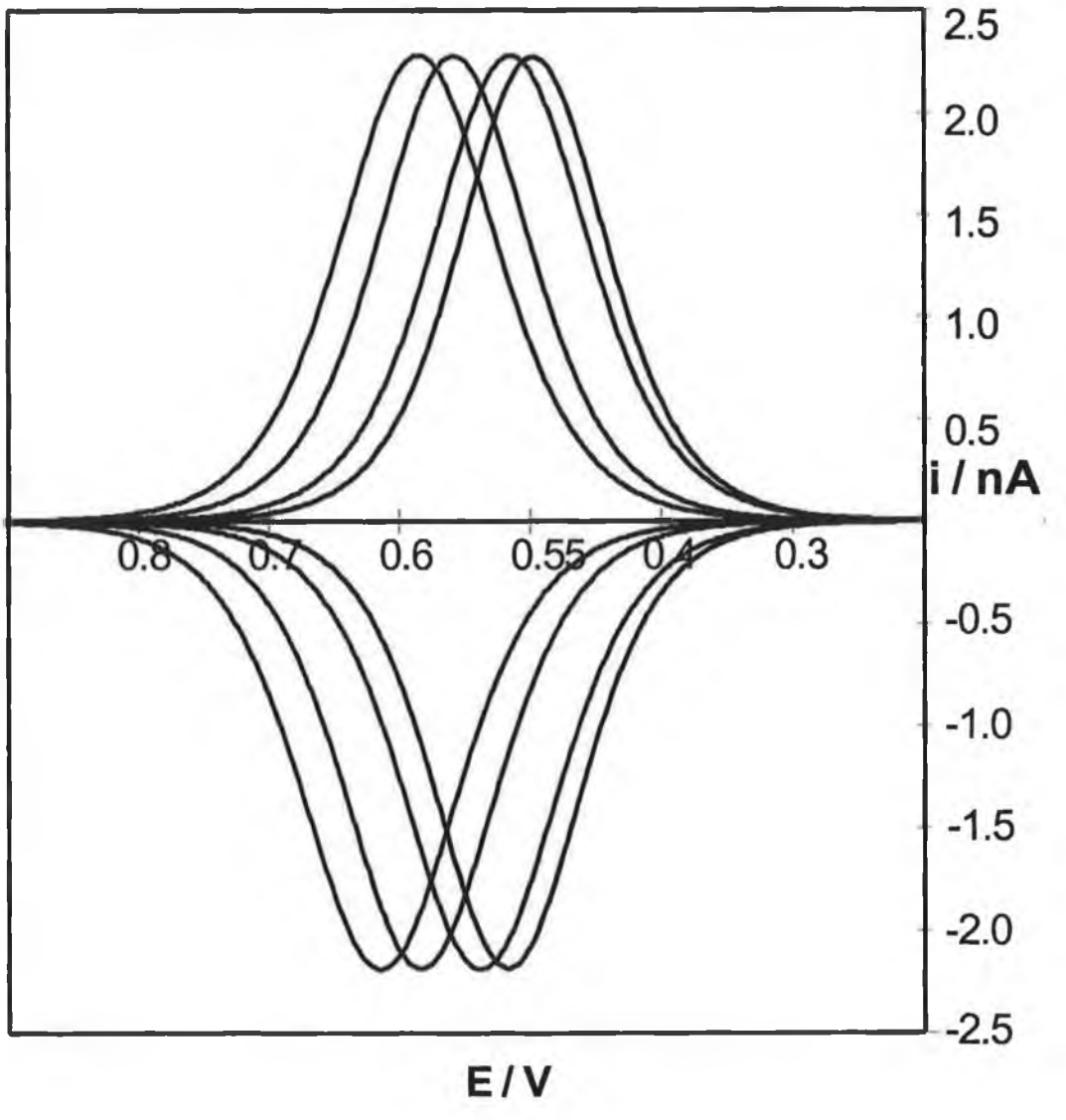

Figure 10 Electrolyte dependence of the electrochemical response. The electrolyte concentrations are, from left too right, 0.05 0.1, 0.5, and 1.0 M. The supporting electrolyte is $LiClO_4$ and the electrode radius is 25 μm. The scan rate is 1 V/s.

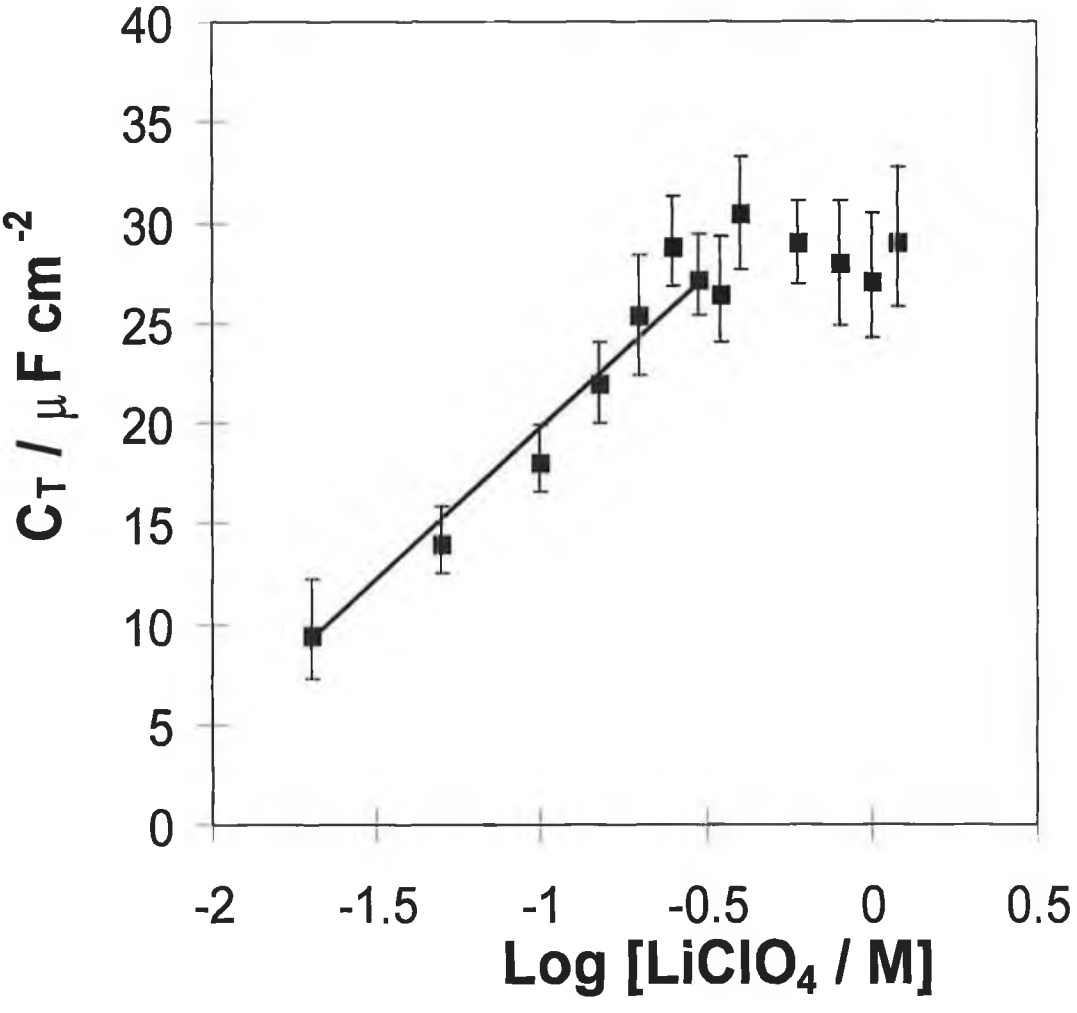

Figure 11 Dependence of the total interfacial capacitance for a spontaneously adsorbed $(p3p)_2$ monolayer on the logarithm of the supporting electrolyte concentration. The capacitance was determined using a small amplitude potential step centred on 0.100 V.

5.3.4 Chronoamperometry

For an ideal electrochemical reaction involving a surface bound species, the Faradaic current following a potential step that changes the redox composition of the monolayer exhibits a single exponential decay in time according to:[11,13,32]

$$i_F(t) = kQ \exp(-kt) \quad (6)$$

where k is the apparent rate constant for the overall reaction and Q is the total charge passed in the redox transformation.

Figure 12 illustrates a typical example of the chronoamperometric response observed for the reduction ($Os^{3+} + e^- \rightarrow Os^{2+}$) of a $(p3p)_2$ monolayer, where the electrolyte is 0.1 M aqueous $LiClO_4$ at a pH of 1.05. In this experiment the overpotential η ($\equiv E - E^{o\prime}$) was -0.050 V. This figure shows that on a microsecond time domain two current decays can be separated. These responses, which arise from double layer charging and Faradaic current flow, are time-resolved due to the much shorter time constant of double layer charging compared to that of the Faradaic reaction. In our investigations, we have determined the electron transfer rate constant only when the time constant of double layer charging is at least five times shorter than the time constant of the Faradaic reaction.

While fast charging of the electrochemical double layer is important, the effects of ohmic losses must also be considered.[43] When Faradaic and charging currents flow through a solution, they generate a potential that acts to weaken the applied potential by an amount iR_u, where i is the total current. This ohmic drop can lead to severe distortions of experimental responses resulting in inaccurate measurements of the heterogeneous electron transfer rate. The significance of ohmic effects for these systems can be assessed using the data presented in Table 1. As illustrated in Figure 12, the Faradaic currents that flow in these high speed chronoamperometric experiments are typically in the low microamp range even for 25 μm electrodes. Therefore, using the cell resistance data given in Table 1 the

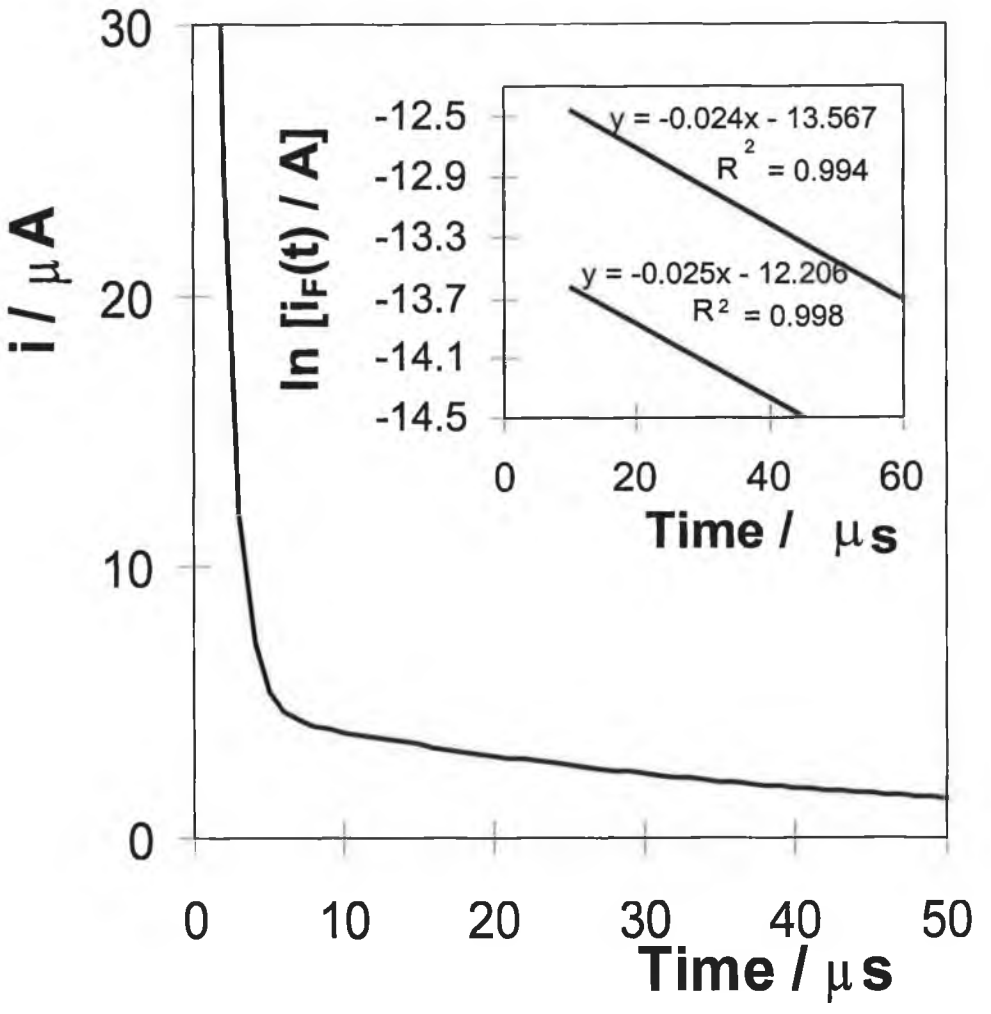

Figure 12 Current response for a 25 μm radius platinum microelectrode modified with a $(p3p)_2$ monolayer following a potential step where the overpotential η was -50 mV. The supporting electrolyte is 0.1 M perchlorate at a pH of 1.05. The inset shows ln $i_F(t)$ vs t plots for the Faradaic reaction for a 25 μm (top) and a 12.5 μm (bottom) radius platinum microelectrode.

calculated iR_u drop is less than 20 mV for supporting electrolyte concentrations above 0.1 M. However, not only does the concentration of the supporting electrolyte play an important role in determining the magnitude of the uncompensated resistance, so too does the pH. For example, for the pH 1.05 system illustrated in Figure 12, the uncompensated resistance is approximately 2500 Ω making the average ohmic loss approximately 5 mV.

The linearity of the ln $i_F(t)$ vs t plot shown in the inset of Figure 12 indicates that electron transfer is characterised by a single rate constant over the time required to collect greater than 95% of the Faradaic charge. At supporting electrolyte concentrations greater than 0.1 M, the monolayers always gave linear first order decays over about two lifetimes. Deviations from linearity would be expected if ohmic drop was present. Uncompensated resistance causes the applied potential, and hence the apparent rate, to evolve with time. Therefore, iR_u drop produces negative deviations in the observed current at short times.[32] That such non-idealities are not observed, at least for high concentrations of supporting electrolyte, is consistent with negligible ohmic losses. We have further probed the existence of ohmic effects by reducing the radius of the microelectrode. This approach is useful since the resistance increases with decreasing electrode radius but the current decreases as the square of the radius leading to reduced ohmic effects for smaller electrodes. The inset in Figure 12 shows that the slope of the semi-log plot obtained for a 12.5 μm platinum electrode modified with a spontaneously adsorbed $(p3p)_2$ monolayer is indistinguishable from that obtained at a 25 μm electrode. This observation is consistent with ohmic losses being negligible under the experimental conditions employed. Moreover, we find that the heterogeneous electron transfer rate constant measured at an overpotential of -50 mV is independent of the supporting electrolyte concentration, maintaining a value of $2.5 \pm 0.2 \times 10^4$ s^{-1} as the $LiClO_4$ concentration was systematically varied from 0.1 to 1.0 M. On the basis of the measured cell resistances, and the insensitivity of the apparent heterogeneous rate constant to changes in electrode size or supporting electrolyte concentration, we conclude that ohmic drop and double layer effects on the interfacial kinetics are negligible for electrolyte concentrations greater than about 0.1 M.

Further evidence suggesting the predominance of a single rate constant is obtained by examining the intercept of the semi-log plot at zero time. As indicated in Equation 5, the intercept for a single exponential decay is ln (kQ). Nernst plots of the redox composition as a function of potential (vide supra) confirm that an absolute overpotential of 100 mV decreases the number of oxidised species within the monolayer to less than 2 % of the total. Therefore, such a potential step effectively causes complete reduction of the film, and the full surface coverage, Γ, can be calculated from the intercept of Figure 12 using the relation,[34,35]

$$\Gamma = \frac{Q}{nFA} \tag{7}$$

where n is the number of electrons transferred, F is Faraday's constant, and A is the real or microscopic electrode area. This chronoamperometric determination of the charge passed can then be compared with the value determined using cyclic voltammetry in order to further test the ideality of the chronoamperometric response. We find that the charges passed in these two independent experiments agree within 10 %. This agreement indicates that all of the surface confined molecules are redox active on a microsecond timescale, i.e., relatively few, if any, sites are kinetically isolated.

5.3.5 Effect of solution pH on heterogeneous kinetics

Plots of ln $i_F(t)$ vs t, obtained at an overpotential of 102 mV, remain linear ($R^2 > 0.99$) as the pH of the contacting electrolyte solution is systematically varied from 5.05 to 1.07, and heterogeneous electron transfer rate constants have been evaluated from their slopes. Figure 13 shows that there is a sigmoidal relationship between the heterogeneous electron transfer rate constant and the pH of the electrolyte, with k decreasing from $3.4\pm0.2\text{x}10^5$ to $6.6\pm0.4\text{x}10^4$ s^{-1} when the solution pH is decreased from 5.05 to 1.07. That k is sensitive to the solution pH, yet plots of ln $i_F(t)$ vs t remain linear over a wide pH range, is significant. One might imagine that if the system were in two different states, protonated and non-protonated, each with different rate constants, that the corresponding semi-log plots would be nonlinear or, in the extreme case, would exhibit dual slope behaviour. That such nonlinear behaviour is not observed suggests that protonation equilibrium occurs more rapidly than redox equilibrium.

It is important to note that the cell resistance decreases as the pH of the electrolytic solution decreases. Therefore, one would expect ohmic effects to be more significant at high, rather than low, pH which would cause the heterogeneous electron transfer rate constant to be underestimated at high pH. That the opposite trend is experimentally observed, i.e., k increases with increasing pH, supports our conclusion that ohmic effects do not adversely affect the chronoamperometric determination of k.

The inflection point of Figure 13 is located at a pH of approximately 2.9, which is consistent with the pK_a of the p3p ligand.[61] These data suggest that protonating the unbound p3p ligand alters the rate of heterogeneous electron transfer across the electrode/monolayer interface. Figure 13 also shows that the rate of heterogeneous electron transfer to spontaneously adsorbed $[Os(bpy)_2$ pyridine $(p3p)]^{2+}$ monolayers, which do not contain groups capable of becoming protonated, is independent of solution pH in this range. This observation suggests that the second

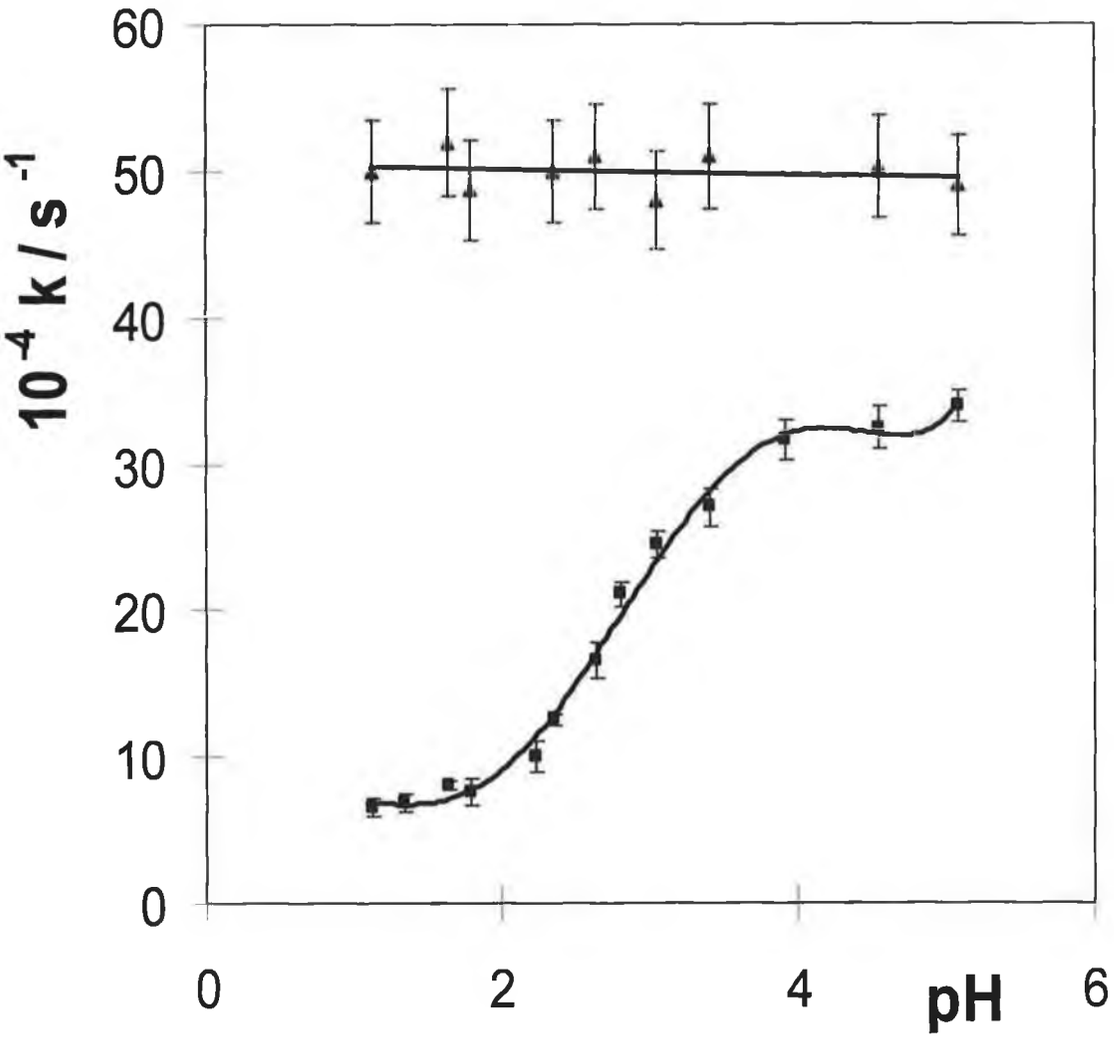

Figure 13 Dependence of the heterogeneous electron transfer rate constant at spontaneously adsorbed $(p3p)_2$ (lower curve) and $[Os(bpy)_2\ (p3p)\ pyridine]^{2+}$ (upper line) monolayers on the pH of the contacting electrolyte. The supporting electrolyte concentration is approximately 0.1 M perchlorate. The overpotential η is 102 mV.

p3p ligand within the coordination shell of the osmium complex plays a central role in making *k* sensitive to the solution pH.

A possible explanation of this pH dependence is that protonating the free pyridine ring of the p3p ligand alters the electron density on the redox centre. However, the degree of electronic coupling between the pyridine rings of the p3p ligand is expected to be weak given that they are separated by three methylene spacer groups. Our experimental observation that the formal potential of the $Os^{2+/3+}$ redox reaction remains constant within 23 mV as the pH of the contacting solution is changed from 5.05 to 1.07, supports this conclusion. Moreover, solution phase absorption spectroscopy of the complex dissolved in DMF indicates that the position of the metal to ligand charge transfer band remains constant when the p3p ligands are protonated. This observation further suggests that protonation does not significantly affect the electron density on the osmium redox centre.

The heterogeneous electron transfer rate is considered to depend on a frequency factor and a Franck-Condon barrier and can be expressed as.[62-64]

$$k = \Gamma_n \kappa_{el} \upsilon_n exp\left(\frac{-\Delta G^{\neq}}{RT}\right) \qquad (8)$$

where Γ_n is the nuclear tunnelling factor, κ_{el} is the electronic transmission coefficient, υ_n is the nuclear frequency factor and $\Delta G^{\neq}$ is the free energy of activation.[61-62] Since the experimental frequency factors are always less than $k_B T$ / h (h is Planck's constant), the nuclear tunnelling factor is unity.[62-64] From Equation 8, it is evident that the sensitivity of the heterogeneous electron transfer rate to the solution pH could be caused by changes in the free energy of activation or the pre-exponential factor. Since the free energy of activation equals $\lambda/4$, where λ is the total reorganisation energy associated with switching the oxidation state of the monolayer, one strategy for estimating $\Delta G^{\neq}$ is to fit the dependence of the logarithm of the rate constant on the overpotential.[6,11,13,63,64]

5.3.6 pH Effects on the Potential dependence of k

Figure 14 illustrates the effect of various overpotentials ($\eta \equiv E - E^{o\prime}$) on the ln $i_F(t)$ vs t plots, where the supporting electrolyte is 0.1 M $HClO_4$. This figure shows that linear responses are observed at each of the overpotentials investigated. These linear responses are consistent with negligible ohmic effects despite the higher Faradaic currents that flow when a larger overpotential is applied. These data highlight another advantage of high speed electrochemistry. As illustrated in Figure 1, the background current in cyclic voltammetry tends to rise as the positive potential limit is approached. This increasing background current arises from the initial electrochemical cleaning of the platinum surface and is caused by incomplete removal of adsorbed oxygen or platinum oxide. However, the processes responsible for these background currents appear to be slow, and take place on a millisecond timescale. By probing the electron transfer dynamics on a microsecond timescale, these background currents can be effectively eliminated so that the chronoamperometric data are not affected even at overpotentials where the background in cyclic voltammetry may be increasing.

Figure 15 illustrates Tafel plots of ln k vs overpotential, η, for monolayers in contact with perchlorate electrolytes at different pHs. For overpotentials less than about 200 mV, ln k depends approximately linearly on η. The standard heterogeneous electron transfer rate constant k^o has been determined by linearly extrapolating ln k to zero overpotential, and Table 2 contains these data. However, at large overpotentials the response is clearly nonlinear, and the slopes decrease in magnitude with increasing overpotential in both the anodic and cathodic directions. In the conventional Butler-Volmer formulation of electrode kinetics,[43] these slopes represent $(1 - \alpha_a) F / RT$ and $-\alpha_c F / RT$ for the oxidation and reduction reactions, respectively, where α_a is the anodic, and α_c the cathodic, transfer coefficient. Therefore, in contrast with the expectations of the Butler-Volmer formulation, Figure 15 suggests that the transfer coefficients are potential dependent. Furthermore, as reported previously for $[Os(bpy)_2 Cl (p3p)]^+$ monolayers,[67] α_a tends toward zero more

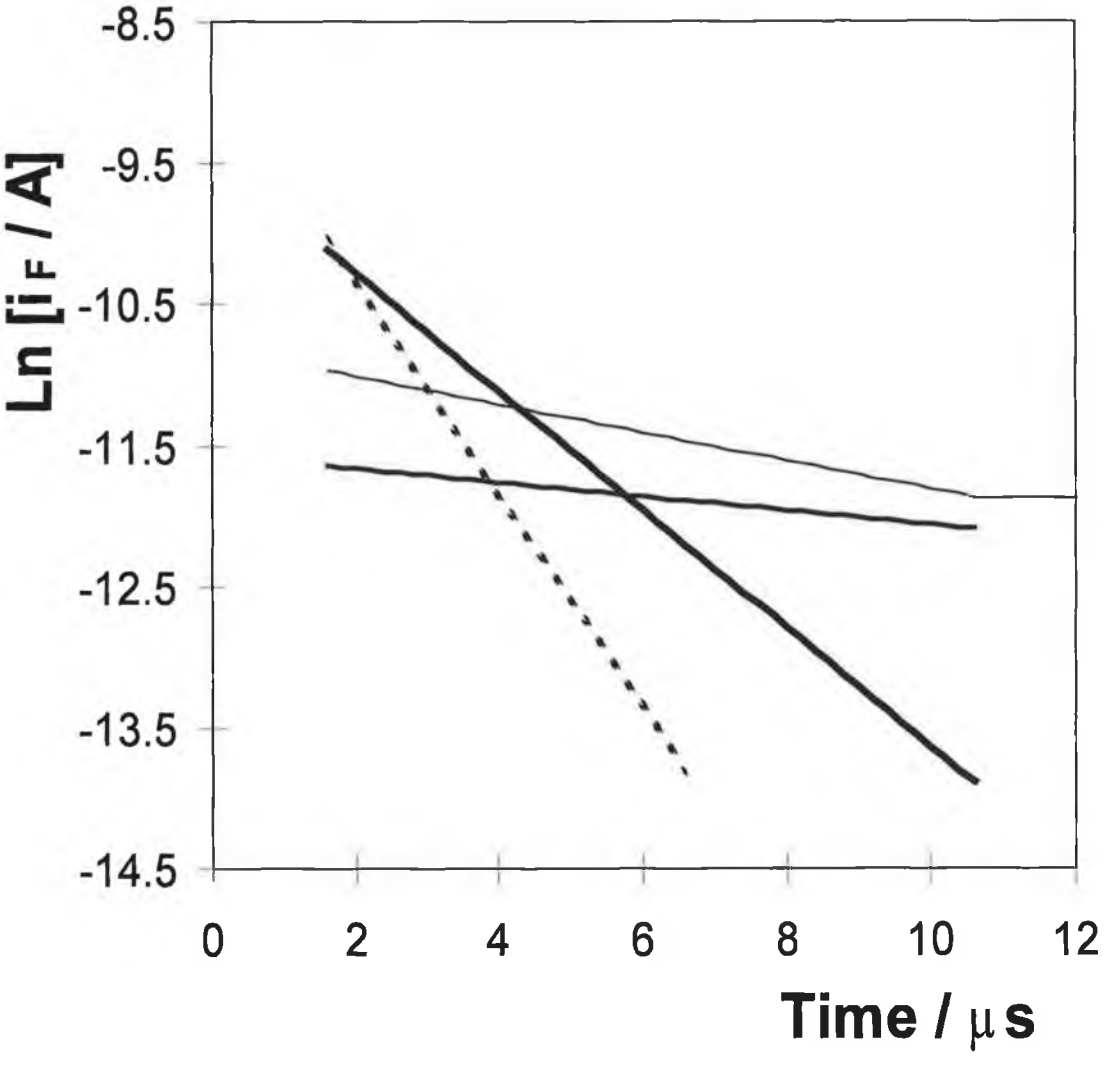

Figure 14 Effect of various overpotentials η, on the ln $i_F(t)$ vs t plots for a spontaneously adsorbed $(p3p)_2$ monolayer. The supporting electrolyte is 0.1 M $HClO_4$. Taken on the right-hand side, the overpotentials are from top to bottom, 0.051, 0.103, 0.200, and 0.349 V, respectively.

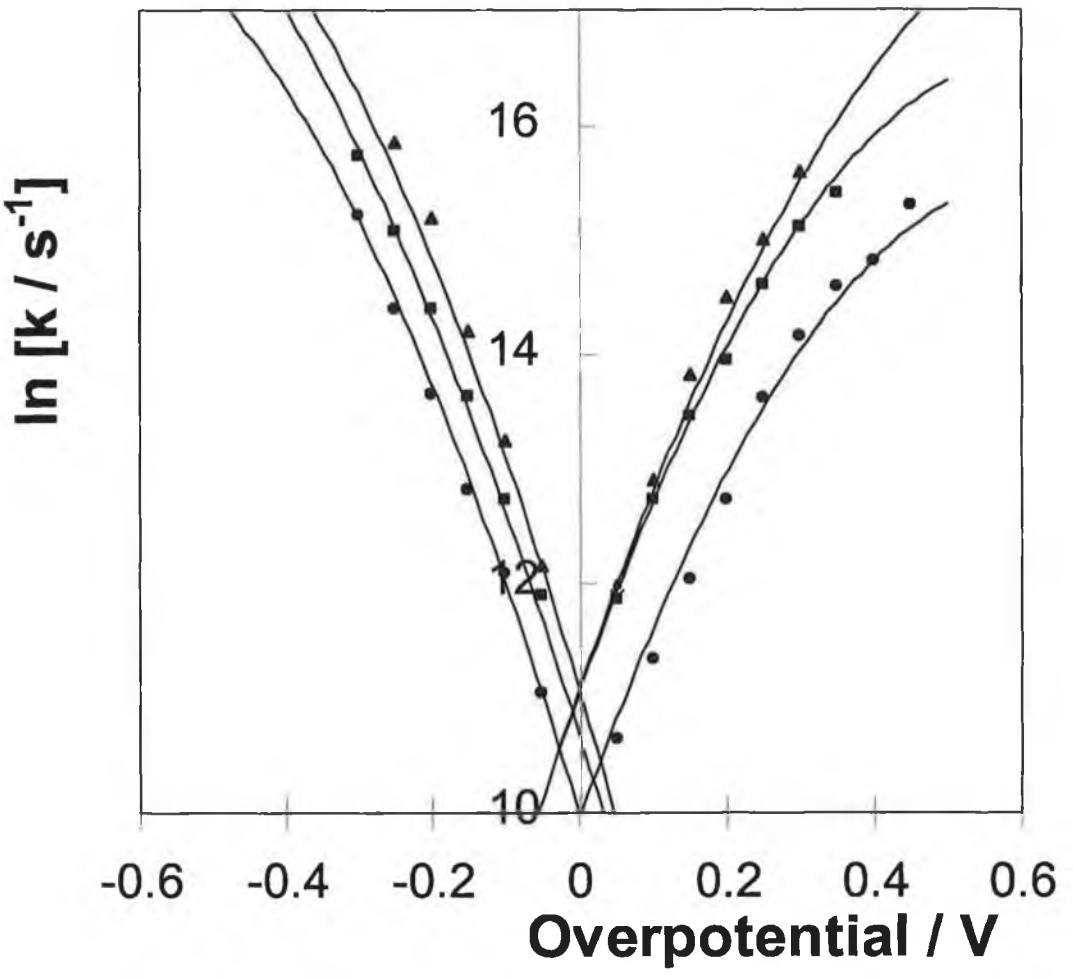

Figure 15 Tafel plots for $(p3p)_2$ monolayers as a function of the supporting electrolyte pH. The data (top to bottom, right hand side) represent electrolyte pH's of 5.05, 3.10 and 1.07, respectively. The solid lines denote theoretical fits obtained from a through-space tunnelling model where λ equals 100, 68, and 56 kJ mol^{-1} from top to bottom, respectively. The errors are approximately equal to the size of the symbols.

Table 2. Effect of Electrolyte pH on Activation Parameters and Pre-exponential Factors[a]

Electrolyte pH	10^{-4} k°, [b] s^{-1}	λ, kJ mol^{-1}	$\Delta H^{\neq}$, kJ mol^{-1}	$\Delta G_c^{\neq}$, [c] kJ mol^{-1}	10^{-6} A_{et}, [d] s^{-1}
5.05	6.1(0.2)	100	37.5(2.1)	25.1(2.2)	1547(345)
3.95	6.0(0.2)	93	34.6(1.8)	22.1(1.7)	451(78)
3.10	4.3(0.1)	68	30.3(1.3)	17.0(0.9)	41(6)
2.08	2.0(0.1)	54	26.1(2.2)	13.8(1.4)	5.3(0.6)
1.07	1.6(0.1)	56	24.6(1.5)	14.3(1.1)	5.2(0.4)

a Numbers in parentheses represent the standard deviations for at least three individual monolayers. Supporting electrolyte is 0.1 M perchlorate.

b All standard rate constants were determined at 298 K.

c Free energy of activation determined from the cathodic ideal electrochemical enthalpies using $\Delta S_{rc}°$.

d Pre-exponential factor extracted from the standard heterogeneous electron transfer rate constant using $\Delta G^{\neq}$.

rapidly than α_c. The Marcus theory of electron transfer predicts these nonlinear Tafel plots, because it includes a term that is quadratic in η in the rate equation.[69-72]

Simplified models incorporating the basic concepts of the Marcus theory have been developed to model heterogeneous electron transfer across electrode/monolayer interfaces.[11,13] Chidsey has developed a model describing through-bond electron tunnelling across metal/monolayer interfaces.[11] However, this model predicts that Tafel plots will be symmetric with respect to overpotential. That we experimentally observe larger cathodic than anodic heterogeneous electron transfer rate constants for a given absolute value of the overpotential suggests that through-bond electron tunnelling is not an appropriate model for our system. Finklea and Hanshew[13] have assembled a model describing through-space electron tunnelling that predicts our experimental observation of asymmetric Tafel plots. In Finklea's model, the heterogeneous electron transfer rate constant is given by the integral over energy of three functions, namely, the Fermi function of the metal, the distribution of energy levels for acceptor or donor states in the monolayer (assumed to be Gaussian), and a

rate parameter for electron tunnelling at a given energy. In order to fit this model to the experimental data shown in Figure 15, estimates are required for the average barrier height to heterogeneous electron transfer, the total reorganisation energy associated with switching the redox state of the monolayer, and the pre-integral factor.

The average barrier height for electron tunnelling at $[Os(bpy)_2\ Cl\ pNp]^+$ monolayers, where pNp is 4,4'-dipyridyl, 1,2-bis(4-pyridyl)ethane or 4,4'-trimethylenedipyridine, has previously been estimated from the distance dependence of $k°$.[67] Given that the same bridging ligand is used here, we employ the same value of the average barrier height, 200 kJ mol^{-1}, in the present analysis. The total reorganisation energy λ, dictates the degree of curvature in the Tafel plots. Therefore, λ was chosen so that there was satisfactory agreement between shapes of the theoretical Tafel plots and the experimental data. Finally, the pre-integral factor was adjusted to give the experimental value of k^o.

Figure 15 shows the experimental dependence of ln k on overpotential for solution pH's of 5.05, 3.10 and 1.07. This figure indicates that the degree of curvature of these Tafel plots depends on pH suggesting that the reorganisation energy depends on the extent of monolayer protonation. Figure 15 shows that satisfactory agreement between Finklea and Hanshew's model and the experimental data is obtained when λ is 100, 68 and 56 kJ mol^{-1} for solution pH's of 5.05, 3.10 and 1.07, respectively. However, we note that the electron transfer dynamics can only be probed over a restricted range of overpotentials because of the rapid nature of the process. This restriction means that only limited confidence can be placed in these fitted values of the reorganisation energy.

The Marcus theory can provide a theoretical estimate of the reorganisation energy.[69-72] In the Marcus model, λ is considered to be the sum of an inner sphere and outer sphere component. The inner sphere component describes the distortion of bond angles and lengths accompanying electron transfer, while the outer sphere component reflects solvent reorganisation effects. Crystallographic data demonstrate

that switching the oxidation state of osmium and ruthenium polypyridyl complexes does not significantly change either the bond lengths or angles. This observation suggests that the inner sphere reorganisation energy for this system is negligible, at least in the solid state. The outer sphere solvent reorganisation energy λ_{OS} is given by:

$$\lambda_{os} = \left(\frac{e^2}{2}\right)\left(\frac{1}{r} - \frac{1}{R_e}\right)\left(\frac{1}{\varepsilon_{op}} - \frac{1}{\varepsilon_{SOLN}}\right) \qquad (9)$$

where e is the absolute electronic charge, r is the radius of the metal complex (6.7 Å), R_e is the reactant-image distance, ε_{op} is the optical dielectric constant of water (5.5), and ε_{SOLN} is the static dielectric constant (78.5) . As discussed previously,[67] we have neglected imaging effects, i.e., $R_e \rightarrow \infty$, in calculating the theoretical solvent reorganisation energy. Equation 9 yields a solvent reorganisation energy of 56.9 kJ mol^{-1}, which agrees with the value of 56 kJ mol^{-1} obtained from fitting the data in Figure 15 when the monolayer is fully protonated. This observation suggests that the activation energy barrier to heterogeneous electron transfer at a protonated monolayer is dictated by solvent reorganisation. In contrast, the experimental reorganisation energy for non-protonated monolayers (100 kJ mol^{-1}) is significantly larger than that predicted by Equation 9 for solvent reorganisation. There are a number of factors that may cause the activation barrier to heterogeneous electron to depend on the monolayer's state of protonation. For example, the interfacial potential distribution may be different with the higher ionic strength of the low pH solutions causing the potential to drop more sharply at the electrode/monolayer interface. These differences in electric field strength may change the solvent or ion content of the film. It is important to note, that the experimental semi-log current vs time responses remain linear over the pH range investigated. The linearity of these responses suggests that diffusional processes, e.g., the motion of charge compensating counterions does not influence the rate of, or the barrier to, heterogeneous electron transfer. Alternatively, redox induced changes in the film structure, e.g., a change in the tilt angle θ (Chart 3), may accompany oxidation of the monolayer. This reorientation of the adsorbate could act as an "inner sphere"

reorganisation energy making the experimental λ larger for non-protonated monolayers.

In the Marcus theory, the free energy of activation $\Delta G^{\neq}$ is equal to $\lambda/4$. Therefore, while the largest heterogeneous electron transfer rate is observed for non-protonated monolayers (Figure 13), this process is associated with the largest free energy of activation (Figure 15). If the pre-exponential factor of Equation 8 did not change as the monolayer became protonated, then a higher free energy of activation would give a lower, not a higher, heterogeneous electron transfer rate. This is an important observation and suggests that changes in the pre-exponential factor with monolayer protonation cause the heterogeneous electron transfer to be pH sensitive.

To eliminate the inherent inaccuracy of fitting Tafel plots over a limited potential range to estimate $\Delta G^{\neq}$, and to obtain a more quantitative insight into the origin of the pH sensitivity of k, we have performed temperature-resolved measurements of the formal potential and heterogeneous electron transfer rate to independently probe the pH dependence of the activation entropy and enthalpy, respectively.

Chart 3

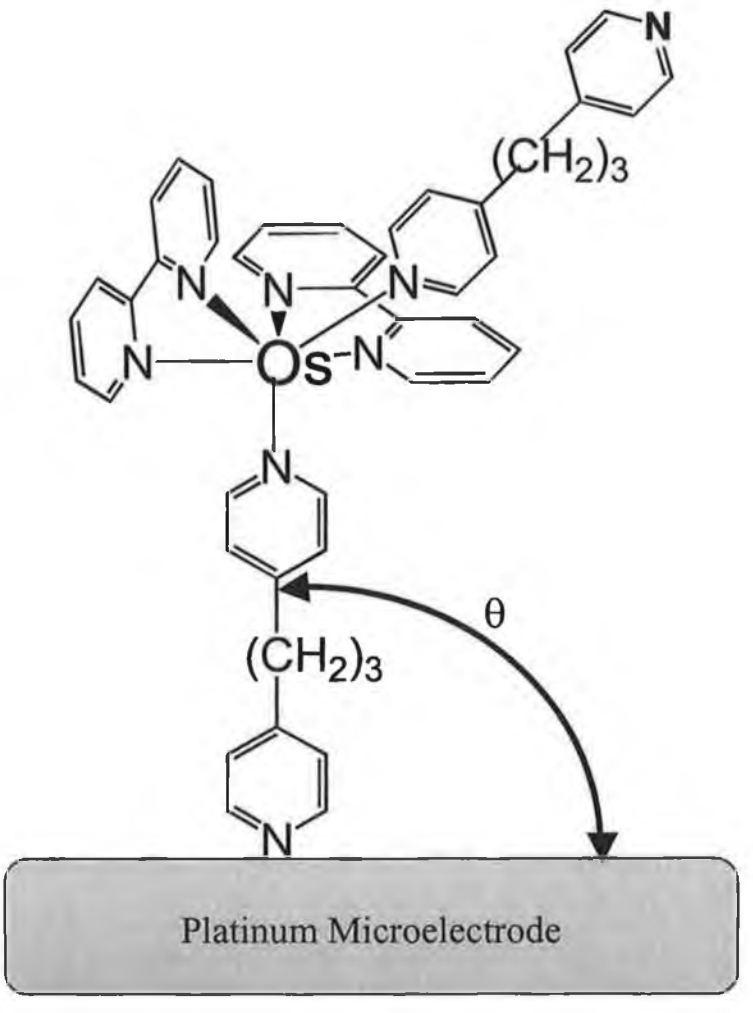

5.3.7 Reaction Entropies

One might anticipate that since protonating the monolayer changes its charge, the reaction entropy $\Delta S_{rc}°$, quantifying the difference in entropy between the reduced and oxidised forms of the redox couple, would depend on the pH of the contacting electrolytic solution.[73] If $\Delta S_{rc}°$ was pH dependent, then it could explain the pH dependence of the free energy of activation suggested by Figure 15.

The reaction entropy has been determined using a nonisothermal cell by measuring the temperature dependence of the formal potential obtained from cyclic voltammetry as the pH of the contacting solution was systematically varied. As discussed by Weaver and coworkers, the temperature dependence of the formal potential can be expressed as:[73, 74]

$$\Delta S^{\circ}_{rc} = F\left(\frac{\partial E^{\circ\prime}}{\partial T}\right) \tag{10}$$

Figure 16 shows typical cyclic voltammograms for a platinum electrode modified with a monolayer of $(p3p)_2$ as a function of supporting electrolyte pH. It is apparent from this data that E°′ does not shift significantly with pH. Figure 17 shows the dependence of the voltammetric response on temperature. For all situations investigated, the formal potential shifts in a positive potential direction with increasing temperature indicating positive reaction entropies and a higher degree of local ordering in the oxidised than in the reduced state. Figure 18 shows that plots of E°′ vs. T are linear over the pH range 5.2 to 1.5, and reaction entropies have been calculated from the slopes according to Equation 10. The slopes of these lines do not depend on the pH of the contacting solution, and Figure 19 shows that $\Delta S_{rc}°$ remains constant at 82±7 $Jmol^{-1}K^{-1}$ over the pH range 5.2 to 1.5. This observation clearly demonstrates that changes in the activation entropy are not responsible for the pH dependence of the free energy of activation suggested by Figure 15. Moreover, there is no difference in reaction entropy for these monolayers adsorbed onto gold or platinum electrodes.

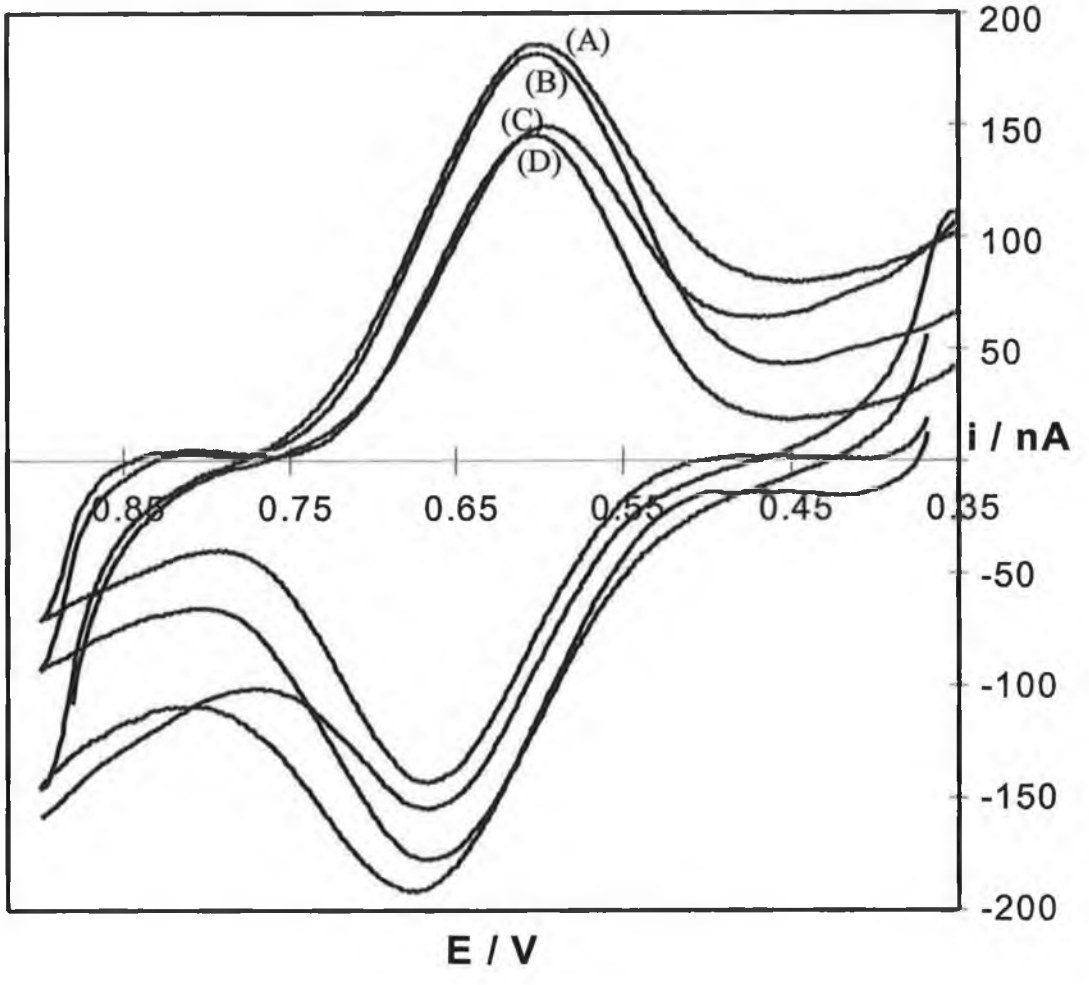

Figure 16 Cyclic voltammograms of adsorbed $(p3p)_2$ as a function of supporting electrolyte pH. The solution pH's are (A) 5.2, (B) 4.9, (C) 3.0, and (D) 2.5. The pH was adjusted by addition of $HClO_4$ to 0.1 M $LiClO_4$ solutions. The scan rate is 1 V/s and the electrode radius is 250 μm.

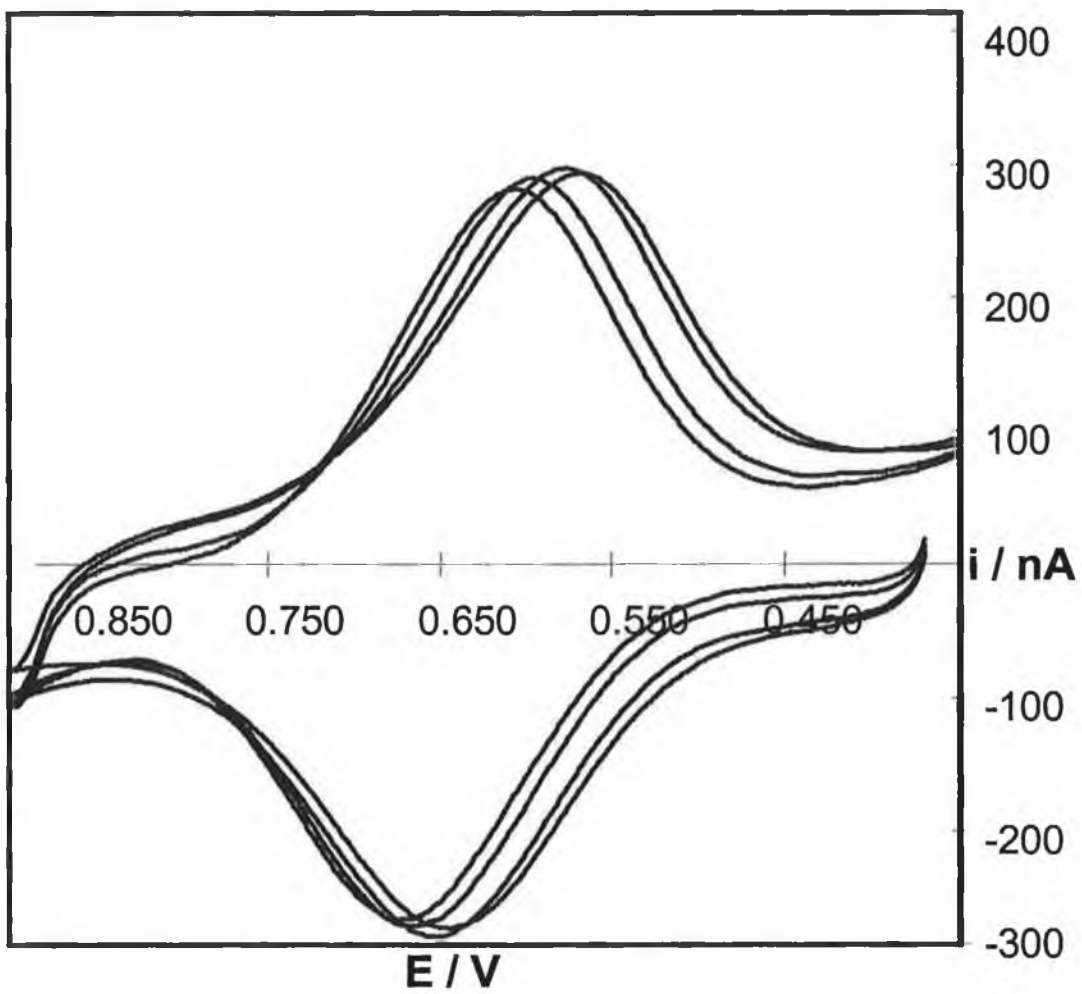

Figure 17 Cyclic voltammograms of adsorbed $(p3p)_2$ as a function of temperature. The voltammograms are, from right to left, -5, 5, 25, and 35 °C. The scan rate is 1 V/s and the pH of the solution is 3.6.

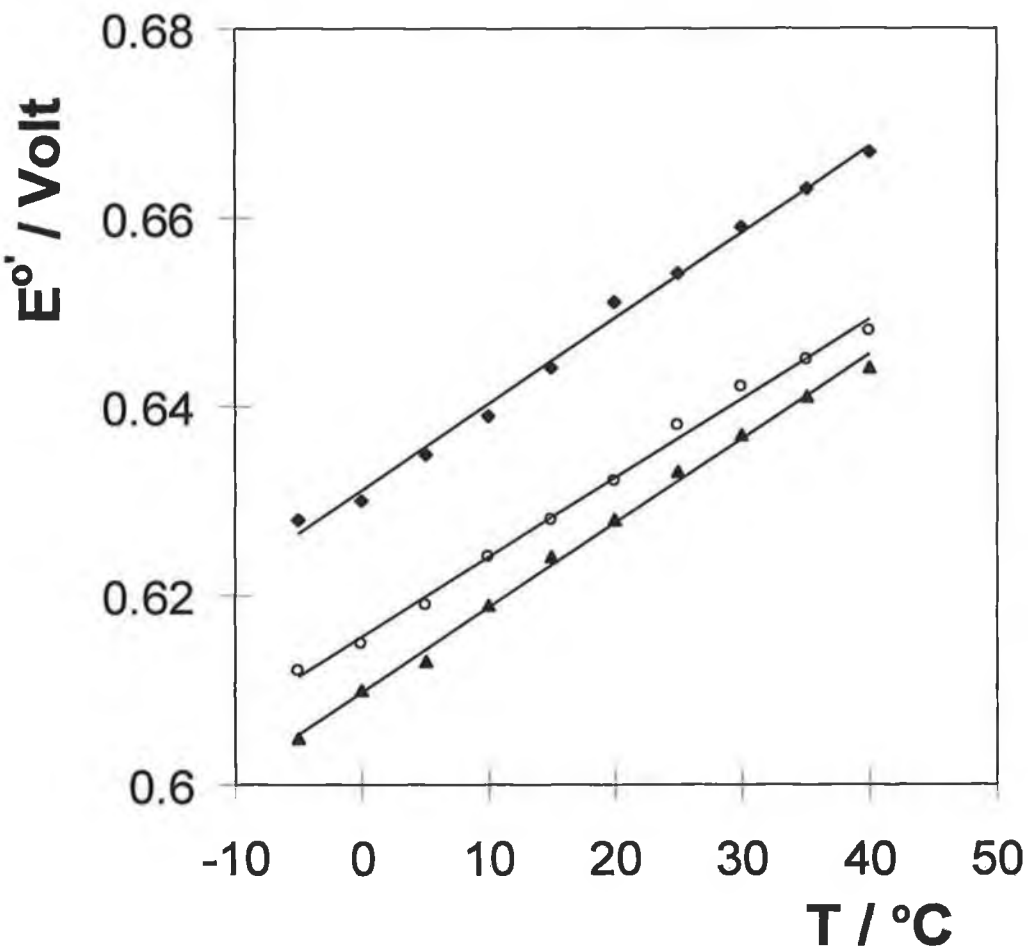

Figure 18 Effect of the pH of the contacting electrolyte solution on the temperature dependence of the formal potential for $(p3p)_2$ monolayers spontaneously adsorbed on platinum microelectrodes. The data represent (top to bottom) electrolyte pH's of 1.5, 5.2, and 3.6, respectively.

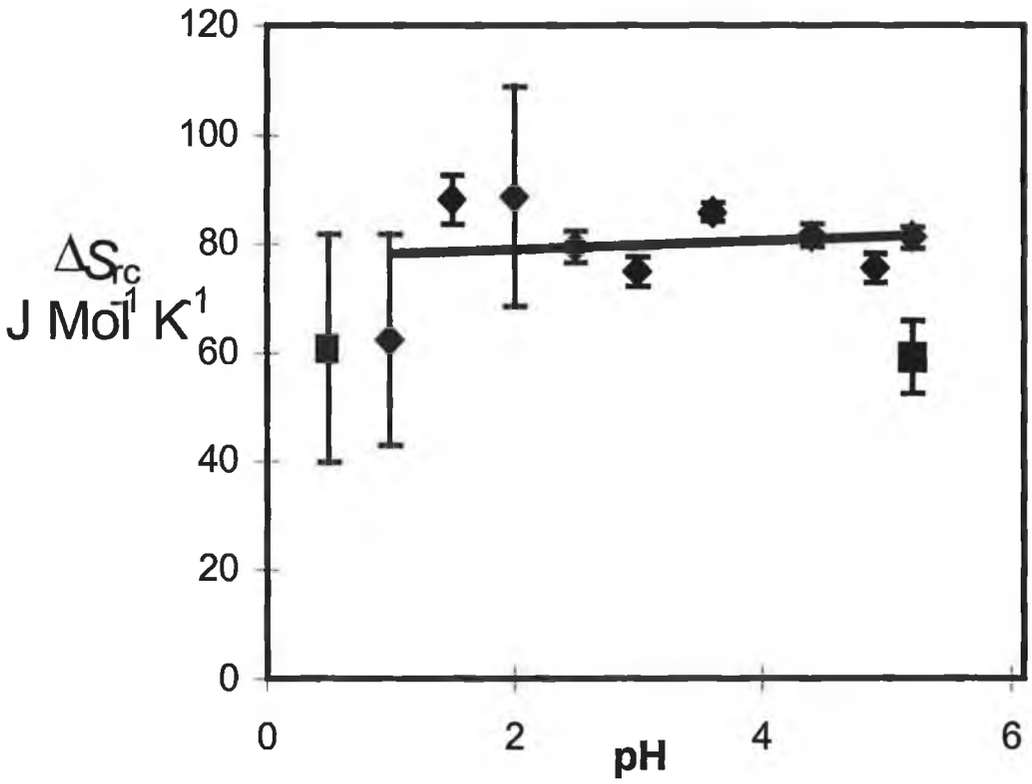

Figure 19 Dependence of the reaction entropy, $\Delta S_{rc}°$, as a function of solution pH for surface confined $(p3p)_2$, ◆, and freely diffusing $[Os(bpy)_3]^{2+}$, ■.

5.3.8 Temperature Dependence of k

Weaver and co-workers[75-76] have established that a temperature independent Galvani potential difference, ϕ_m, across the metal/solution interface can be achieved using a nonisothermal cell. The electrochemical activation enthalpy determined from an Arrhenius plot of ln k vs T^{-1}, where ϕ_m is held constant, has been termed "ideal",[77-77] and we label it here as $\Delta H_I^{\neq}$. For a reduction or cathodic reaction, this electrochemical activation enthalpy can be separated into "chemical", $\Delta H^{\neq}$, and "electrical", $\alpha_c F\phi_m$, contributions according to:

$$\Delta H_{I,c}^{\neq} = -R\left.\frac{\partial \ln k}{\partial\left(\frac{1}{T}\right)}\right|_{\phi_m} = \Delta H^{\neq} - \alpha_c F\phi_m \qquad (11)$$

We have investigated the temperature dependence of the heterogeneous electron transfer rate using temperature-resolved chronoamperometry over the temperature range -5 to 40 °C. An overpotential of -50 mV, as determined at 298 K, was used throughout these experiments, and the resulting current-time transients were similar to those illustrated in Figure 12. The corresponding semi-log plots were linear over approximately two lifetimes, and the heterogeneous electron transfer rate was evaluated from the slopes. In a typical set of experiments, the temperature was systematically varied over a range and then returned to the initial temperature. The same slope, $-k$, and intercept, ln (kQ), were observed within experimental error for the initial and final transients. This consistency indicates that cycling the temperature does not change the heterogeneous kinetics or the quantity of material immobilised on the electrode surface. The heterogeneous electron transfer rate increases with increasing temperature as anticipated for a thermally activated process. Arrhenius plots of ln k vs T^{-1} are linear ($R^2 > 0.995$) over the temperature range -5 to 40 °C. Table 2 contains the activation enthalpies, $\Delta H^{\neq}$, obtained from the slopes of these plots after using the experimental transfer coefficient to correct for the electrical driving force (-50 mV) according to Equation 11. These data confirm that the activation enthalpy changes as the monolayer becomes protonated decreasing from 37.5±2.1 to 24.6±1.5 kJ mol^{-1} as the pH is reduced from 5.05 to 1.07.

In principle, it is possible to use the experimental enthalpies and entropies to calculate free energies of activation. Comparing these values with the value of the reorganisation energy provided by Finklea and Hanshew's model is an important test of consistency between these two independent experiments. We have calculated the cathodic free energy of activation according to Equation 12:[67, 77, 78]

$$\Delta G_c^{\neq} = \Delta H_{I,c}^{\neq} - T\alpha_c \Delta S_{rc}^{o} \tag{12}$$

and Table 2 contains the data. These data show that, at the five pH's investigated, $\Delta G_c^{\neq}$ and $\lambda/4$ agree to within 5 %.

5.3.9 Pre-exponential Factor

That both $\Delta G_c^{\neq}$ and k decrease with decreasing electrolyte pH suggests that the pre-exponential factor of Equation 8 decreases as the monolayer becomes protonated. Table 2 contains values of A_{et} ($\equiv \kappa_{el}\ \upsilon_n$) that have been determined using our experimental free energies of activation and the standard heterogeneous electron transfer rate constant. To isolate the effects of the electronic transmission coefficient, we have calculated the nuclear frequency factor, υ_n, using the dielectric continuum model,[79]

$$\upsilon_n = \frac{1}{\tau_l}\left(\frac{\Delta G_c}{4\pi k_B T}\right)^{1/2} \tag{13}$$

where τ_l^{-1} is the inverse longitudinal relaxation time for water (1.9 ps^{-1}). These values have then been used to estimate κ_{el} from the experimental pre-exponential factor. Figure 20 shows that for all pH's investigated the electronic transmission coefficient is considerably less than unity. This observation indicates that there is a low probability of electron transfer once the nuclear transition state has been attained, suggesting a nonadiabatic reaction involving weak coupling between the metallic states of the electrode and the localised orbitals of the redox centre. The pH

dependency of log κ_{el} is illustrated in Figure 20. Significantly, κ_{el} increases dramatically from $4.4\pm2.0\times10^{-6}$ to $9.1\pm2.4\times10^{-4}$ on going from a protonated to a non-protonated monolayer.

As discussed above, our observation of larger cathodic than anodic heterogeneous electron transfer rate constants for a given absolute value of the overpotential is consistent with through-space rather than through-bond electron tunnelling. This is an important point since, unlike a through-space tunnelling mechanism, the electron transfer distance for a through-bond tunnelling process is not sensitive to the tilt angle (Chart 3) between the electrode and the redox site. There are several possible causes of the observed dependence of the electronic transmission coefficient, and hence the heterogeneous electron transfer rate, on the pH of the contacting solution. For example, it is possible that at high pH immobilisation occurs through both uncomplexed pyridine nitrogens and that lowering the solution pH causes desorption of one of the pyridine rings which then becomes protonated. We note however, that the experimental area of occupation as measured at high pH, is considerably smaller than that predicted for the situation in which both uncomplexed pyridine groups bind to the electrode surface. Moreover, the pK_a's of both uncomplexed pyridines are identical making selective desorption of one of them from the electrode surface unlikely. Alternatively, protonating the monolayer may either cause the tilt angle (Chart 3) between the bridging ligand and the electrode surface to increase, or the methylene spacer groups to adopt a more extended configuration. It is possible that this proton induced restructuring of the monolayer arises because the formal potential of the adsorbed complex is positive of the potential of zero charge. This situation is expected to cause repulsive interactions between the positively charged electrode and the highly charged protonated (4+) complexes causing the redox centres to move away from the electrode thus increasing the through-space tunnelling distance.

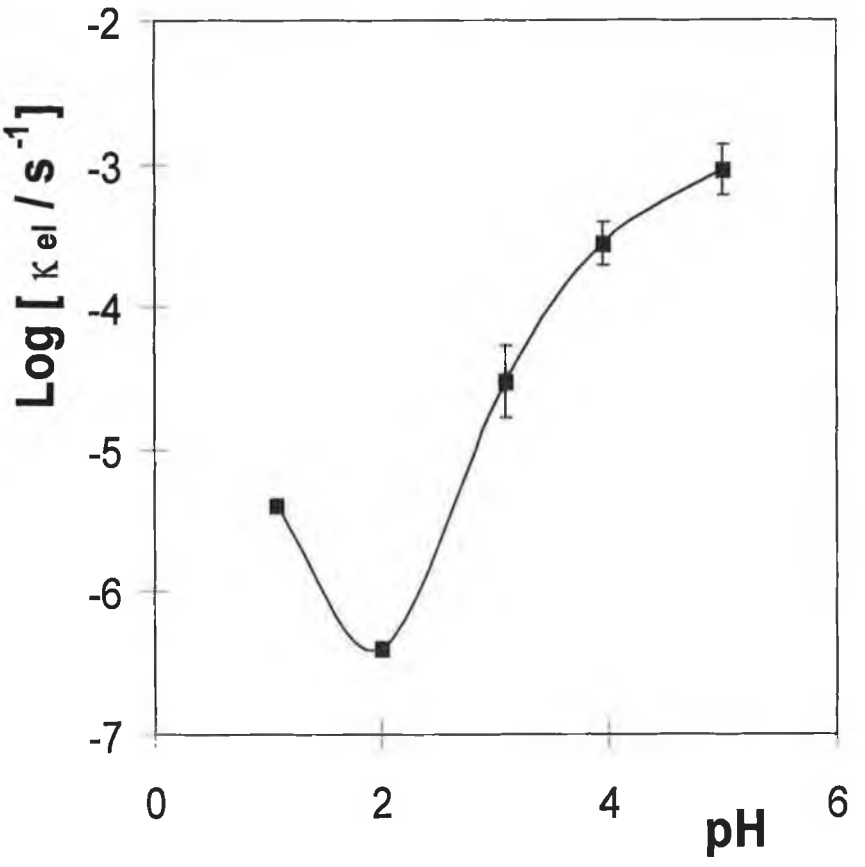

Figure 20 Dependence of the logarithm of the electronic transmission coefficient κ_{el} for heterogeneous electron transfer across platinum/$(p3p)_2$ monolayer interfaces on the pH of the supporting electrolyte.

If this model is appropriate, then the change in the through-space tunnelling distance between the protonated and non-protonated forms of the monolayer can be estimated from the data illustrated in Figure 20 by assuming that the tunnelling parameter β° is identical to that found previously[67] for $[Os(bpy)_2\ Cl\ p3p]^+$ monolayers (1.5 $Å^{-1}$). Using this value of β°, a increase in the through-space electron transfer distance of approximately 3.5 Å would be required to cause κ_{el} to decrease from $9.1\pm2.4x10^{-4}$ to $4.4\pm2.0x10^{-6}$ as the monolayer goes from a non-protonated to a fully protonated state. When any directional component in the electronic coupling between the metallic states of the electrode and the orbitals of the adsorbed complex is ignored, this difference in through-space electron transfer distance could be accounted for by a change in the tilt angle from approximately 40° in the non-protonated state to 90° in the protonated state.

5.4 Conclusions

The adsorbed monolayers considered here exhibit nearly ideal cyclic voltammetry and chronoamperometry as the pH, temperature and experimental timescale are varied over a wide range. Chronoamperometry has been used to probe the rate of heterogeneous electron transfer across the monolayer/microelectrode interface. This process can be characterised by a single rate constant at high electrolyte concentrations suggesting that heterogeneous electron transfer across these metal/monolayer interfaces is mechanistically uncomplicated. This unusual ideality has allowed us probe the nature of the activation barrier to electron transfer, and the degree of electronic coupling between the remote redox centres and the microelectrode, in considerable detail. Measurements of the potential dependence of the heterogeneous electron transfer rate constant, k, suggest that electron transfer occurs via a through-space rather than a through-bond tunnelling mechanism and that it depends on the pH of the contacting solution. By determining the free energy of activation using two independent methods, we have shown that changes in the pre-exponential factor rather than $\Delta G^{\neq}$ cause this pH sensitivity. It appears that the interaction of the highly positively charged protonated complexes with the interfacial electric field causes the through-space electron transfer distance to increase, perhaps by altering the tilt angle between the adsorbate and the electrode surface or by causing the methylene spacer groups to become extended.

Although the change in heterogeneous electron transfer rate constant on going from non-protonated to fully protonated monolayers is less than an order of magnitude, this pH induced "conformational gating" of the electron transfer rate offers the possibility of developing pH triggered electrical switches. We expect that fundamental investigations focusing specifically on the role that the local medium, particularly the bridging structure linking the reactants, plays in dictating the rate and pathway for electron transfer, will make it possible to design molecular systems that maximise electron transfer efficiency and their sensitivity to specific chemical triggers.

5.5 References

1 Abrûna, H. D. "*Electroresponsive Molecular and Polymeric Systems*" Skoteim, T. Ed., Marcel Dekker: New York, 1988.

2 Stoddart, J. F. "*Frontiers in Supramolecular Organic Chemistry and Photochemistry*" Schneider, H. J.; Dürr, H., Eds., Weinheim:VCH, 1990.

3 Murray, R. W. "*Molecular Design of Electrode Surfaces*" Wiley-Interscience: New York, 1992.

4 Ulman, A. "*An Introduction to Ultra-thin Organic Film From Langmuir-Blodgett to Self-Assembly*". Academic Press: San Diego, 1991.

5 Chidsey, C. E. D.; Loiacono, D. N. *Langmuir* 1990, 6, 682.

6 Finklea, H. O.; Snider, D. A.; Fedik, J. *Langmuir* 1990, 6, 371.

7 Strong, L.; Whitesides, G. M. *Langmuir* 1988, 4, 546.

8 Nuzzo, R. G.; Dubois, L. H.; Allara, D. L. *J. Am. Chem. Soc.* 1990, 112, 558.

9 Yamada, S.; Kawazu, M.; Matsuo, T. *J. Phys. Chem.* 1994, 98, 3573.

10 Shi, X.; Caldwell, W. B.; Chen, K.; Mirkin, C. A. *J. Am. Chem. Soc.* 1994, 116, 11598.

11 Chidsey, C. E. D. *Science*, 1991, 251, 919.

12 Dudois, L. H.; Nuzzo, R. G. *Annu. Rev. Phys. Chem.* 1992, 43, 437.

13 Finklea, H. O.; Hanshew, D. D. *J. Am. Chem. Soc.* 1992, 114, 3173.

14 Acevedo, D.; Abrûna, H. D. *J. Phys. Chem.* 1991, 95, 9590.

15 Acevedo, D.; Bretz, R. L.; Tirado, J. D.; Abrûna, H. D. *Langmuir*, 1994, 10, 1300.

16 Becka, A. M.; Miller, C. J. *J. Phys. Chem.* 1993, 97, 6233.

17 Rubinstein, I.; Steinberg, S.; Tor, Y.; Shanzer, A. *Nature*, 1988, 332, 426.

18 Franzen, S.; Goldstein, R. F.; Boxer, S. G. *J. Phys. Chem.* 1993, 97, 3040.

19 Nordyke, L. L.; Buttry, D. A. *Langmuir*, 1991, 7, 380.

20 Li, T. T.-T.; Weaver, M. J. *J. Am. Chem. Soc.* 1984, 106, 6107.

21 Forster, R. *J. Chem. Soc. Rev.* 1994, 289.

22 Faulkner, L. R., Walsh, M. R., Xu, C. *Contemporary Electroanalytical Chemistry*, Plenum Press: New York, 1990.

23 Andrieux, C. P.; Hapiot, P. Savéant, J. M. *Chem. Rev.* 1990, 90, 723.

24 Amatore, C. A., Jutand, A.; Pflüger, F. *J. Electroanal. Chem.* 1987, 218, 361.

25 Penner, R. M.; Heben, M. J.; Longin, T. L.; Lewis, N. S. *Science*, 1990, 250, 1118.

26 Sabatani, E.; Rubinstein, I. *J. Phys. Chem.* 1987, 91, 6663.

27 Smith, C. P.; White, H. S. *Anal. Chem.* 1992, 64, 2398.

28 Creager, S. E.; Weber, K. *Langmuir*, 1993, 9, 844

29 Andreu, R.; Fawcett, W. R. *J. Phys. Chem.* 1994, 98, 12753.

30 Gao, J.; Shopes, R. J.; Wright, C. A. *Biochim. Biophys. Acta* 1990, 1015, 96.

31 Kaminskaya, O.; Konstaninov, A. A.; Shuvalov, V. A. *Biochim. Biophys. Acta* 1990, 1016, 153.

32 Forster, R. J.; Faulkner, L. R. *J. Am. Chem. Soc.* 1994, 116, 5444.

33 Yee, E. L.; Cave, R. J.; Guyer, K. L.; Tyma, P. D.; Weaver, M. J. *J. Am. Chem. Soc.* 1979, 101, 1131.

34 Laviron, E. *J. Electroanal. Chem.* 1974, 52, 395.

35 Brown, A. P.; Anson, F. C. *Anal. Chem.* 1977, 49, 1589.

36 Feldberg, S. W.; Rubinstein, I.; *J. Electroanal. Chem.* 1988, 240, 1.

37 Goodwin, H. A.; Kepert, D. L.; Patrick, J. M.; Skelton, B. W.; White, A. H. *Aust. J. Chem.* 1984, 37, 1817.

38 Ferguson, J. E.; Love, J. L.; Robinson, W. T. *Inorg. Chem.* 1972, 11, 1662.

39 Rillema, D. P.; Jones, D. S.; Levy, H. A. *J. Chem. Soc., Chem. Commun.* 1979, 849.

40 Forster, R. J. *Inorg. Chem.*, submitted for publication.

41 Forster, R. J. *Langmuir*, 1995, 11, 2247.

42 Forster, R. J.; Vos, J. G. *Langmuir*, 1994, 10, 4330.

43 Bard, A. J.; Faulkner, L. R. *Electrochemical Methods : Fundamentals and Applications,* Wiley, New York, 1980.

44 Bretz, R. L.; Abruña, H. D. *J. Electroanal. Chem.* 1996, 408, 199.

45 Hudson, J. E.; Abruña, H. D. *J. Phys. Chem.* 1996, 100, 1036.

46 Tirado, J. D.; Abruña, H. D. *J. Phys. Chem.* 1991, 100, 4556.

47 Campbell, J. L. E.; Anson, F. C. *Langmuir* 1996, 12, 4008.

48 Bryant, M. A.; Crooks, R. M. *Langmuir* 1993, 9, 385.

49 Ksenzhek, O. S.; Petrova, S. A.; Oleinik, S. V.; Kokodyashnyi, M. V.; Moskovskii, V. Z. *Elektrokhimiya* 1977, 13, 182.

50 Sun, L.; Johnson, B.; Wade, T.; Crooks, R. M. *J. Phys. Chem.* 1990, 94, 8869.

51 Porter, M. D.; Bright, T. B.; Allara, D. L.; Chidsey, C. E. D. *J. Am. Chem. Soc.* 1987, 109, 3559.

52 Wightman, R. M.; Wipf, D. O. *Electroanalytical Chemistry*, Vol. 15, Bard, A. J. Ed.; Marcel Dekker; New York, 1989.

53 Widrig, C. A.; Chung, C.; Porter, M. D. *J. Electroanal. Chem.* 1991, 310, 335.

54 Nuzzo, R. G.; Allara, O. L. *J. Am. Chem. Soc.* 1983, 105, 4481.

55 Chidsey, C. E. D.; Bertozzi, C. R.; Putvinski, T. M.; Mujsce, A. M. *J. Am. Chem. Soc.* 1990, 112, 4301.

56 Gerischer, H.; Scherson, D. A. *J. Electroanal. Chem.* 1985, 188, 33.

57 Rowe, G. K.; Creager, S. E. *Langmuir* 1991, 7, 2307.

58 Nagamura, T.; Sakai, K. *Chem. Phys. Lett.* 1987, 141, 553.

59 Nagamura, T.; Sakai, K. *J. Chem. Soc., Faraday Trans.* 1988, 84, 3529.

60 Creager, S. E.; Rowe, G. K. *Anal. Chim. Acta*. 1991, 246, 233.

61 Dean, J. A. "*Handbook of Organic Chemistry*", McGraw-Hill: New York, 1987.

62 Weaver, M. J. *Chem. Rev.* 1992, 92, 463.

63 Bagchi, G. *Ann. Rev. Chem.* 1989, 40, 115.

64 Sutin, N. *Acc. Chem. Res.* 1982, 15, 275.

65 Barr, S. W.; Guyer, K. L.; Li, T. T.-T.; Liu, H. Y.; Weaver, M. J. *J. Electrochem. Soc.* 1984, 131, 1626.

66 Sutin, N. Brunschwig, B. S. *ACS Symp. Ser.* 1982, 198, 105.

67 Forster, R. J.; Faulkner, L. R. *J. Am. Chem. Soc.* 1994, 116, 5453.

68 Richardson, J. N.; Rowe, G. K.; Carter, M. T.; Tender, L. M.; Curtin, L. S.; Peck, S. P.; Murray, R. W. *Electrochim. Acta,* 1995, 40, 1331.

69 Marcus, R. A. *J. Chem. Phys.* 1956, 24, 966.

70 Marcus, R. A. *J. Chem. Phys.* 1965, 43, 679.

71 Tender, L. M., Carter, M. T.; Murray, R. W. *Anal. Chem.* 1994, 66, 3173.

72 Weber, K.; Creager, S. E. *Anal. Chem.* 1994, 66, 3164.

73 Hupp, J. T.; Weaver, M. J. *J. Phys. Chem.* 1984, 88, 1860.

74 Barr, S. W.; Guyer, K. L.; Li, T.T.-T.; Liu, H. Y.; Weaver, M. J. *J. Electrochem. Soc.* 1984, 131, 1626.

75 Li, T. T.-T.; Guyer, K. L.; Barr, S. W.; Weaver, M. J. *J. Electroanal. Chem.* 1984, 164, 27.

76 Yee, E. L.; Weaver, M. J. *Inorg. Chem.* 1980, 19, 1077.

77 Weaver, M. J. *J. Phys. Chem.* 1979, 83, 1748.

78 Weaver, M. J. *J. Phys. Chem.* 1976, 80, 2645.

79 Morgan, J. D.; Wolynes, P. G. *J. Phys. Chem.* 1987, 91, 874.

Chapter 6

Electrochemistry of a Novel Spontaneously Adsorbed Anthraquinone based Transition Metal Complex

6.1 Introduction

Quinones have been the subject of intense research mainly because their coupled electron (e^-) and proton (H^+) transfer reactions play key roles in biological redox processes.[1,2,3,4,5,6,7,8,9,10] For example, during the primary process of photosynthesis, incident light produces a charge separated species and triggers electron transfer reactions resulting in the reduction of a terminal acceptor, which then picks up two protons. This proton transfer step initiates the formation of the proton gradient that provides the driving force for the formation of high energy compounds. Thus, coupled electron and proton transfers play pivotal roles in the overall reaction. A desirable property of any model system designed to enhance our understanding of these processes is that the system's architecture be controlled, i.e., that the reactant's separation and relative orientation be well-defined. While considerable attention has been focused on the dynamics of electron transfer within monolayers,[11,12,13,14,15,16] there have been relatively few reports on the electrochemical properties of monolayers in which electron and proton transfer are coupled.[4,9,10,17] Toward this objective, we have adsorbed an alizarin based transition metal complex on carbon fibre microelectrodes and examined its electrochemical properties. This complex has been synthesised using $[Ru(bpy)_2Cl_2]$ and alizarin, where Ru is ruthenium, bpy is bipyridyl, and alizarin is 1,2-dihydroxy-9,10-anthraquinone. The synthesised complex is called $QCat^{2-}$Ru-1,2 because the ruthenium is bound to the 1 and 2 positions on the anthraquinone.

A wide variety of intermediates and products can be produced by the redox reactions of quinones and it is this unique behaviour that has made them a popular focus of attention. Quinones are now used in many diverse areas of research. These include the medical field where they are used as antitumor[18,19,20] and anticancer agents,[21] for the cleavage of DNA,[22,23] and the oxidation of alcohol.[24] Quinones are also important in the growing area of research that seeks to develop sensors and molecular devices,[25,26,27,28,29] and in catalysis,[30,31] corrosion inhibition,[32] and polymer science.[33] They are widely available, easily handled under ordinary experimental conditions and exhibit well behaved electrochemistry. In particular, Hubbard and

coworkers have done much to increase our knowledge of quinones and anthraquinones, by examining their electrochemical and spectroscopic properties. The surface electrochemistry and molecular orientation of hydroquinones using electrochemical and spectroscopic techniques[34,35] have been studied while the effects of solute concentration,[36] potential,[37] and surface pretreatment[38] on a large number of surface active species has been investigated.

In this work, we have examined the electrochemistry of $QCat^{2-}Ru$,1-2 in order to explore its suitability as a model system for examining surface confined species as molecular switches. We have probed the thermodynamics and kinetics of electron transfer for $QCat^{2-}Ru$,1-2 in solution at platinum and mercury electrodes and as spontaneously adsorbed monolayers on carbon fibre microelectrodes. This is an attractive model system for probing these issues since the electrochemical response of $QCat^{2-}Ru$,1-2 is unusually ideal and carbon fibre microelectrodes provide a large potential region in which to examine the electrochemical response allowing both ligand and metal based processes to be investigated. The intention is that by analysing the electrochemical response of spontaneously adsorbed monolayers of $QCat^{2-}Ru$,1-2 as a function of voltammetric scan rate, temperature, and potential we might begin to understand those factors that influence the mechanism of coupled electron and proton transfer in organised assemblies. Cyclic voltammetry has been used to determine the ideality of the solution phase and surface confined electrochemical response, to probe the reaction entropy and to provide the standard heterogeneous electron transfer rate constants and the reaction enthalpies. Normal Pulse Voltammetry has been employed to determine of the electron transfer coefficients and rate constants for the solution phase species. Finally, potential step chronoamperometry has been used to determine the dependence of heterogeneous electron transfer rate constant on overpotential and temperature.

6.2 Experimental

6.2.1 Materials and procedures

The surface active complex $QCat^{2-}Ru$-1,2 was synthesised and characterised as described in Chapter 2. Unless otherwise stated, Milli-Q purified water (18 mΩ cm^{-1}) was used as the solvent and the electrolyte was 1.0 M $LiClO_4$ for surface confined measurements. For solution phase investigations, the solvent was dimethylformamide (99%) and the electrolyte was tetraethylammonium tetrafluoroborate ($TEABF_4$). Platinum and carbon fibre microelectrodes were fabricated and characterised as outlined in Chapter 3 while the mercury electrode employed was that described in Chapter 4. Spontaneously adsorbed monolayers were typically formed by immersing the carbon fibre microelectrodes in millimolar solutions of the complex in either 50:50 aqueous dimethylformamide or 50:50 acetone:dimethylformamide. Deposition times averaged approximately 3-4 hours. No precautions were taken to exclude oxygen during monolayer formation. Before electrochemical experiments were carried out the electrodes were rinsed with the electrochemical solvent to remove unbound material. Subsequent measurements were performed in blank electrolyte solutions.

6.2.6 Apparatus

Electrochemical cells were of conventional design and were thermostated within ±0.2 °C using a Julabo F10-HC refrigerated circulating bath. All potentials are quoted with respect to a BAS Ag/AgCl reference electrode while a platinum counter electrode was also employed. Cyclic and normal pulse voltammetry and potential step chronoamperometry were performed using a CH Instruments Model 660 potentiostat and a conventional three electrode cell. All solutions were degassed using nitrogen, and a blanket of nitrogen was maintained over the solution during all experiments. For the temperature resolved experiments, a non-isothermal cell was

used in which the reference electrode was isolated from the main compartment by a salt bridge and held at a constant temperature. The non-isothermal salt bridge contained saturated KCl since it has a low resistance, and the salt remains soluble at the lowest temperature employed (-5 °C). The high electrolyte concentration and the design of the bridge minimise any systematic error in the reported temperature effects on $E^{\circ\prime}$ due to changes in the liquid junction potential with temperature.[39]

6.3 Results and discussion

6.3.1 Solution Phase Voltammetry

Scheme 1(A) shows the structure of the $QCat^{2}$-Ru-1,2. Figures 1 and 2 show solution phase voltammograms of a 10 mM solution of the complex at platinum and mercury electrodes, respectively. With the initial potential being the open circuit potential of –0.3 V, and the initial scan direction in the positive direction, the redox couples as assigned in Chapter 2 are as follows. The redox peak at approx. 200 mV is due to oxidation of one of the semi-quinones in the 1 or 2 position to the quinone (as shown by Scheme 1(b)). The peak at approx. 1200 mV is due to oxidation of the second semi-quinone to the quinone (as shown by Scheme 1(c)). On the reverse scan the peaks at 1200 mV and 200 mV represent reduction of the peaks to their semi-quinone states. The peaks at approx. –800 mV and –1200 mV are the reduction of the semi-quinones in the 1 and 2 positions to the hydroquinone forms. The peaks at more negative potentials are due to reduction of the bipyridyl moieties. The corresponding peaks on the oxidation side of these four peaks represent the return of the redox centres to their former states. In order to obtain information about the reversibility and the diffusion coefficients of the redox couples in this complex, solution phase cyclic voltammetry at platinum and mercury electrodes has been carried out. Figures 3 to 5 show scan rate dependent cyclic voltammetry of some of the individual redox couples on the complex. From these experiments the diffusion coefficients of each of the redox couples at both electrodes was obtained. Figures 6 to 8 show representative examples of the scan rate dependencies of the peak currents associated with these voltammetric experiments. Using Equation 1 the slopes of these plots were used to calculate diffusion coefficients.

$$i_p = 2.69\text{x}10^5 n^{3/2} D^{1/2} v^{1/2} CA \qquad (1)$$

Where i_p is the peak current, n is the number of electrons involved in the reaction, D is the diffusion coefficient, v is the voltammetric scan rate, C is the concentration of the redox species in solution and A is the electrode area.

Table 1 shows the diffusion coefficients for the redox couples of the $QCat^{2-}Ru$-1,2 complex at both mercury and platinum. The diffusion coefficients for the complex at mercury are more uniform with a value of $1.65 \pm 0.16 \times 10^{-4}$ cm^2/sec for the entire range of redox couples and $1.53 \pm 0.61 \times 10^{-4}$ cm^2/sec for the couples at platinum. The mercury electrode appears to give more precise results. However, the most significant result from these experiments is that all of the redox couples appear to be reversible. In fact, apart from the redox couple at –0.800 V, the oxidation and reduction reactions for all of the other couples are reversible to the same extent. This is a significant consideration for the determination of transfer coefficients and heterogeneous electron transfer rate constants.

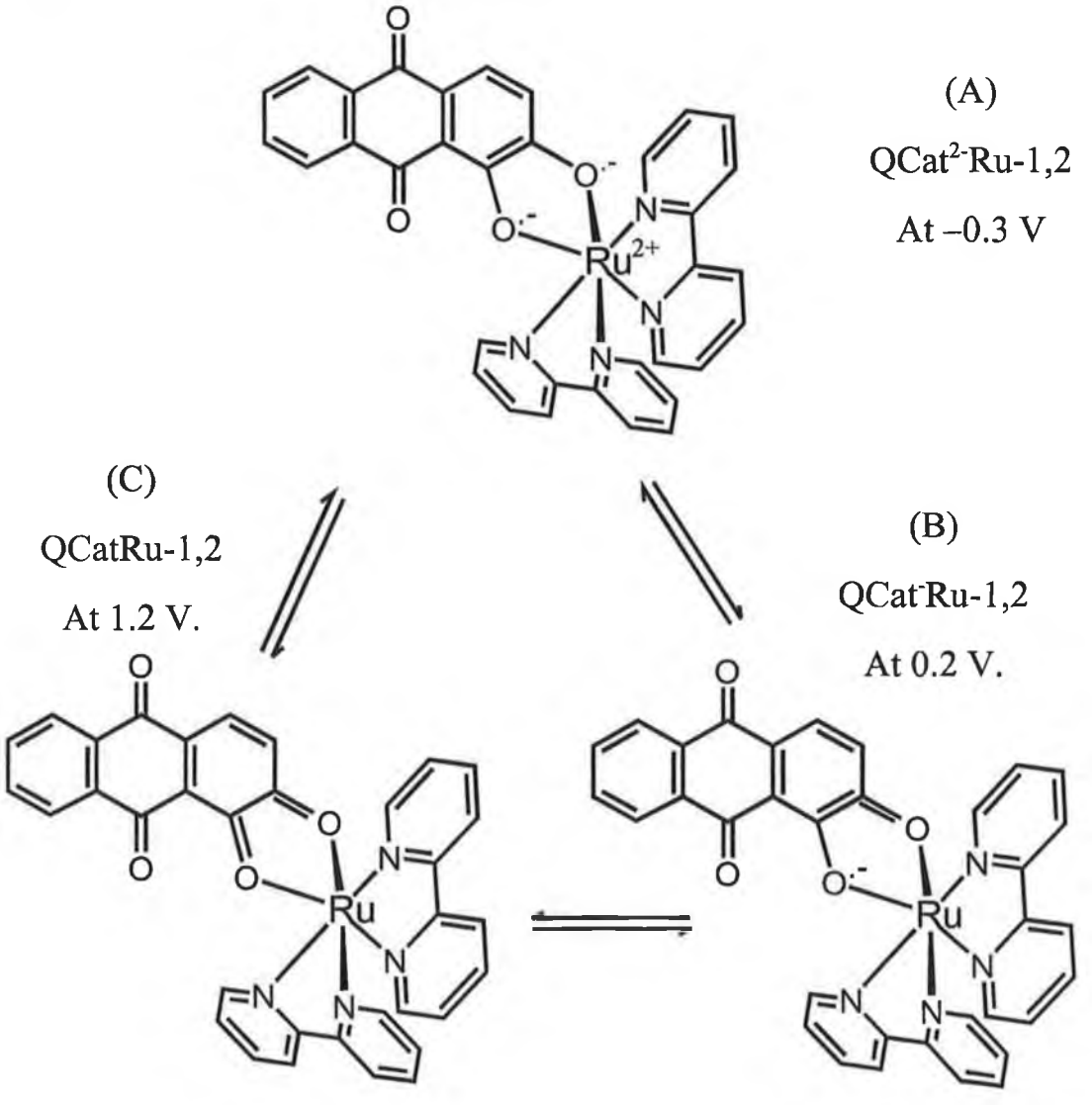

Scheme 1 $QCat^{2-}Ru$-1,2 as synthesised (A), oxidised at200 mV (B), and further oxidised at 1200 mV (C).

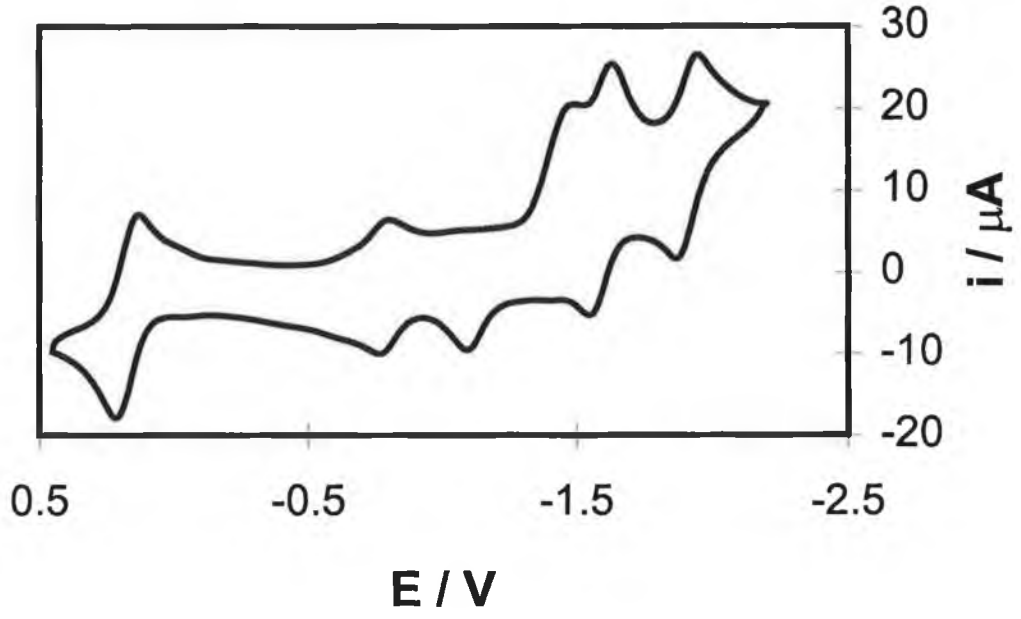

Figure 1 Cyclic voltammogram of 10 mM $QCat^{2-}$Ru-1,2 in DMF at a mercury electrode. The supporting electrolyte is 0.1 M $TEABF_4$ and the scan was initiated at the OCP. Cathodic currents are and anodic currents are down.

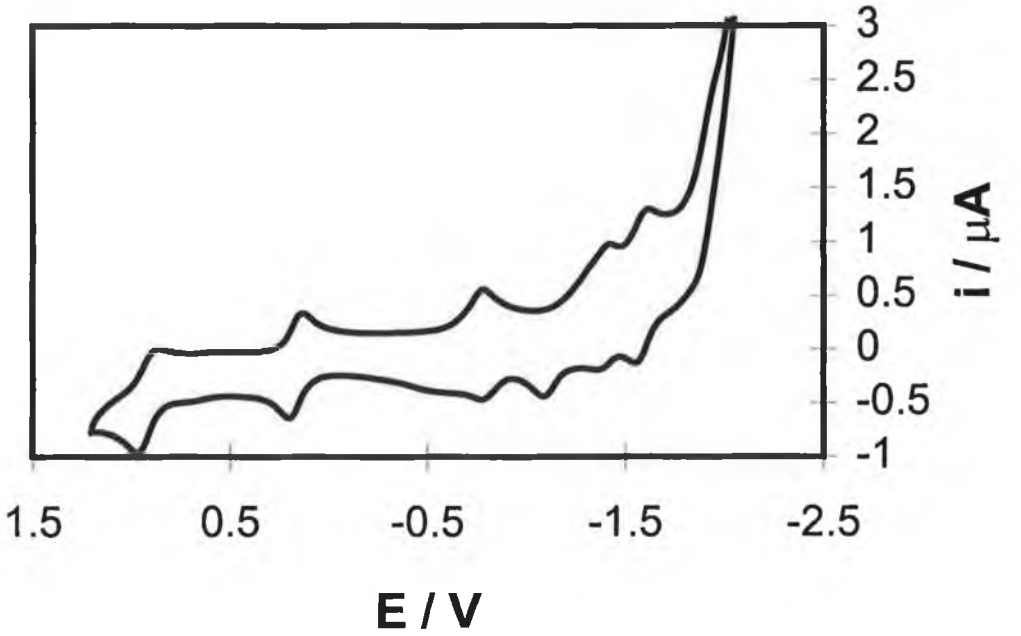

Figure 2 Cyclic voltammogram of 10 mM $QCat^{2-}$Ru-1,2 in DMF at a platinum electrode. The supporting electrolyte is 0.1 M $TEABF_4$ and the scan was initiated at the OCP. Cathodic currents are and anodic currents are down.

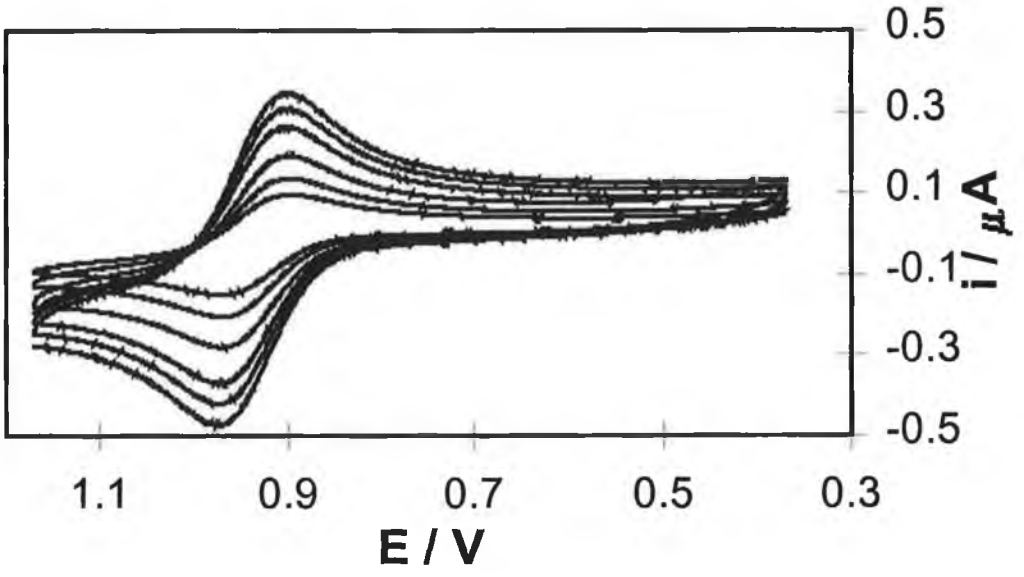

Figure 3 Cyclic voltammetry of the semi-quinone/quinone redox couple in the 1 position as a function of voltammetric scan rate. The scan rates from top to bottom are 1.0, 0.8, 0.6, 0.4, 0.2, and 0.1. The working electrode is 25 μm radius platinum. The concentration of $QCat^{2-}$Ru-1,2 is 10 mM and the electrolyte is 0.1 M $TEABF_4$. The solvent is DMF and the initial potential is 0.37 V.

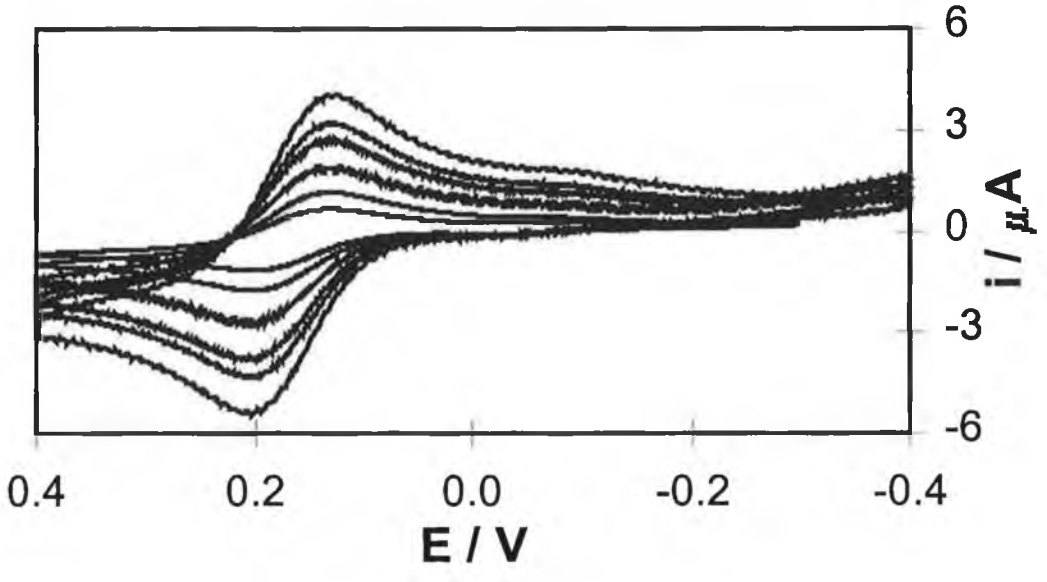

Figure 4 Cyclic voltammetry of the semi-quinone/quinone redox couple in the 9 position as a function of voltammetric scan rate. The scan rates from top to bottom are 0.5, 0.3, 0.2, 0.1, 0.05, and 0.02 V/s. The working electrode is mercury and the initial potential is –0.4 V. Other conditions are as in Figure 1.

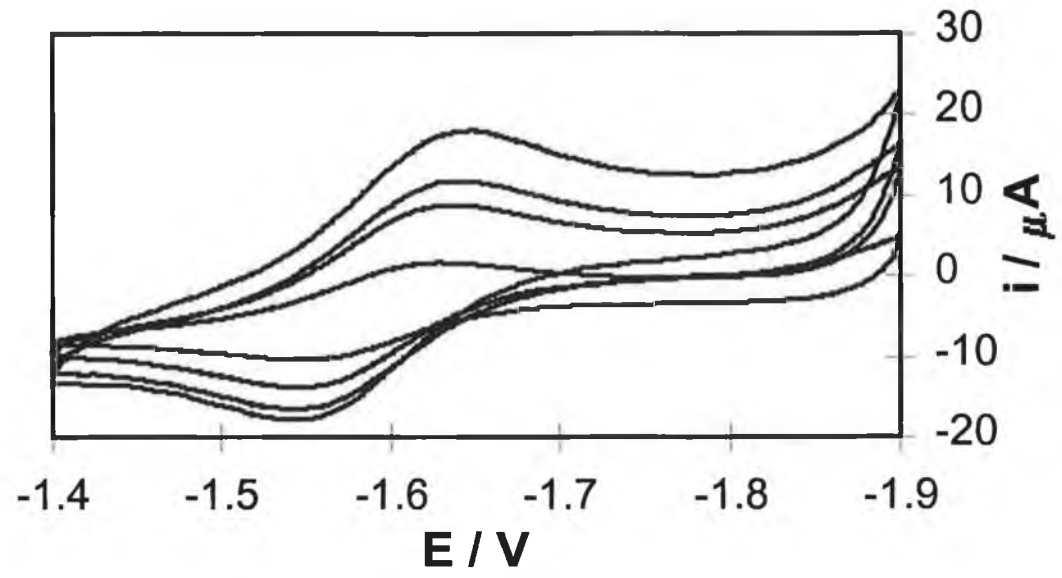

Figure 5 Cyclic voltammetry of the first bipyridyl reduction/oxidation redox reaction as a function of voltammetric scan rate. The scan rates from top to bottom are 1.5, 1.0, 0.6, and 0.2 V/s. The working electrode is mercury and the initial potential is –1.4 V. Other conditions are as in Figure 1.

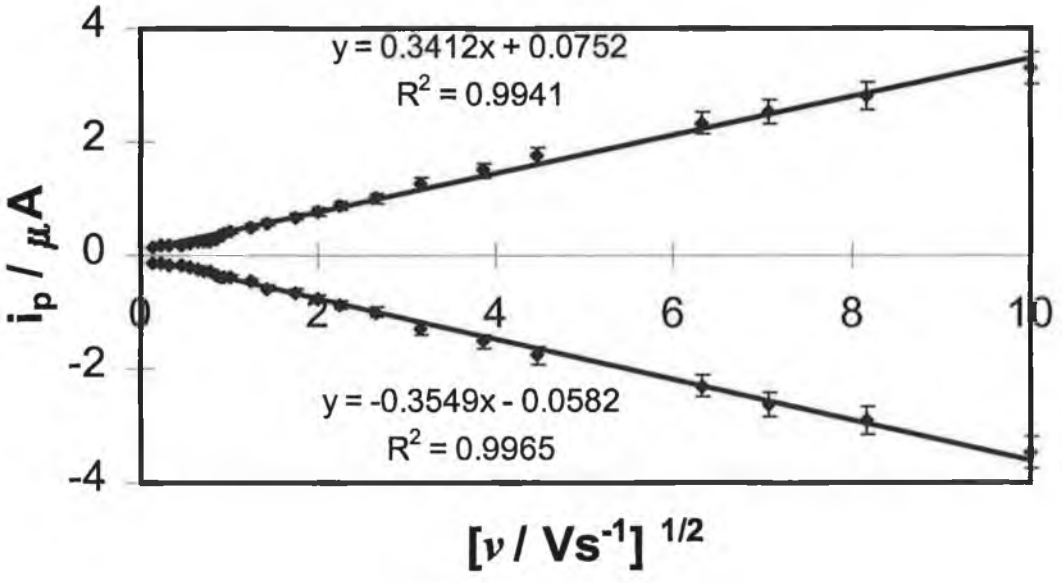

Figure 6 Dependence of peak currents for voltammetric wave centred at –1.6 V on scan rate for a 10 mM solution of $QCat^{2}$-Ru-1,2. Cathodic currents are up, anodic currents are down. The working electrode is 25 μm radius platinum.

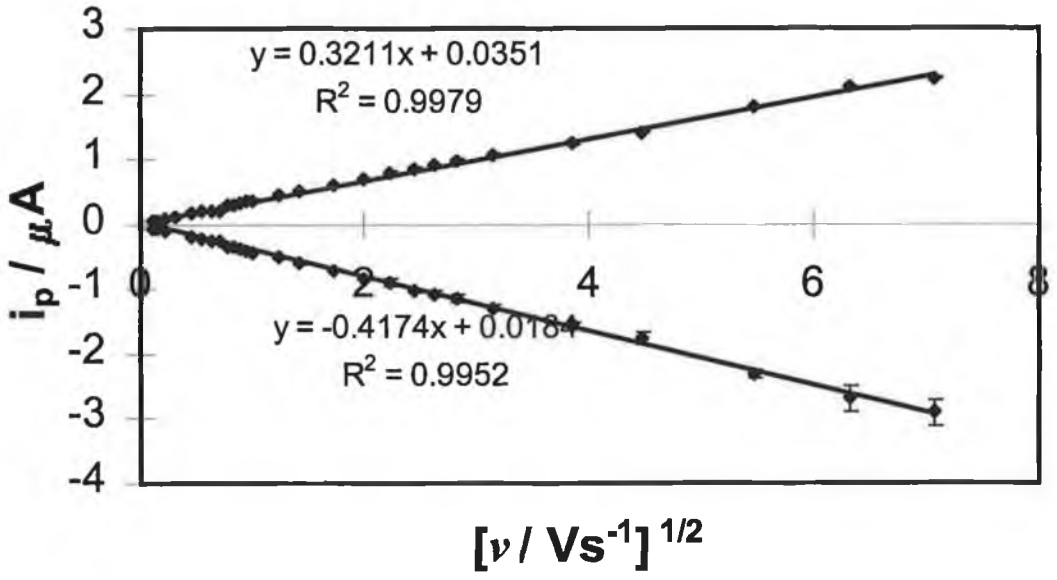

Figure 7 Dependence of peak currents for voltammetric wave centred at 0.165 V on scan rate for a 10 mM solution of $QCat^{2-}$Ru-1,2. Cathodic currents are up, anodic currents are down. The working electrode is 25 μm radius platinum.

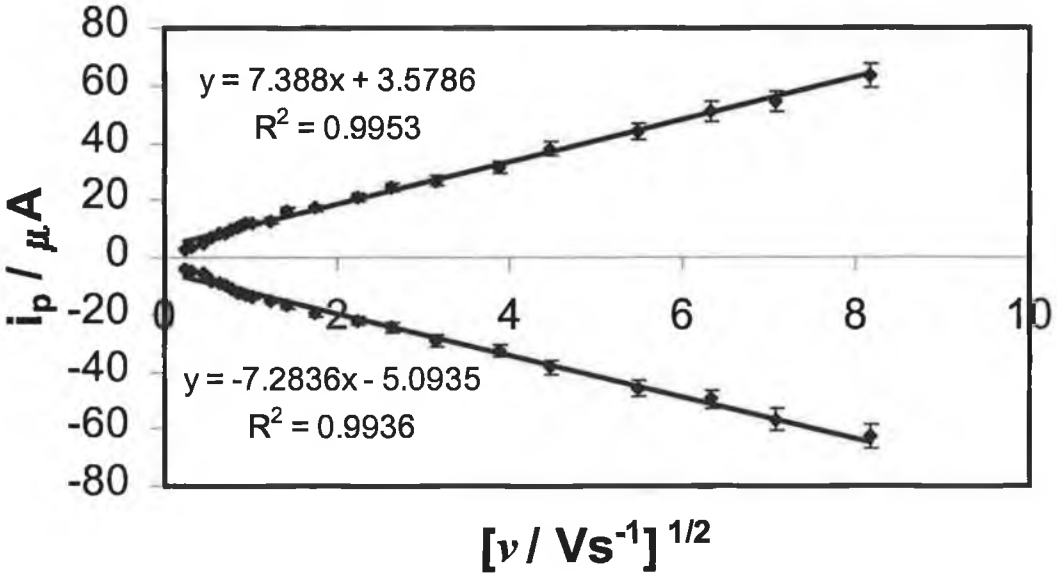

Figure 8 Dependence of peak currents at –1.4 V on scan rate for a 10 mM solution of $QCat^{2-}$Ru-1,2. Cathodic currents are up, anodic currents are down. The working electrode is 0.17 cm^2 mercury.

Table 1. Diffusion coefficients for $QCat^{2}$-Ru-1,2 at platinum and mercury electrodes. Values are in cm^2/sec.

Redox couple	Mercury		Platinum	
(V)	D_C / cm^2 s^{-1}	D_A / cm^2 s^{-1}	D_A / cm^2 s^{-1}	D_C / cm^2 s^{-1}
1.000	N/A	N/A	1.12×10^{-4}	1.16×10^{-4}
0.165	1.65×10^{-4}	1.58×10^{-4}	1.46×10^{-4}	1.88×10^{-4}
-0.800	1.61×10^{-4}	N/A	2.14×10^{-4}	N/A
-1.400	1.68×10^{-4}	1.81×10^{-4}	1.30×10^{-4}	N/A
1.600	1.63×10^{-4}	1.60×10^{-4}	1.61×10^{-4}	1.55×10^{-4}
-1.800	1.62×10^{-4}	1.67×10^{-4}	N/A	N/A

Normal pulse voltammetry (NPV) was performed over a wide range of sampling times in order to probe the electron transfer coefficients and standard heterogeneous electron transfer rate constants of the solution phase redox couples. Figures 9 and 10 show representative NPV recorded using sampling times between 5 and 10 ms.

Consistent with the Cottrell equation the anodic and cathodic currents increase with decreasing sampling time. The rising portion of the waves can be analysed according to Equation 2 to 5 to obtain transfer coefficients and heterogeneous electron transfer rate constants for each of the redox couples.

$$E = E^{*} \pm \frac{RT}{\alpha_{\pm} nF} ln \left\{ X \left[\frac{1.75 + X^{2}\left[1 + exp\left(\pm \xi\right)\right]^{2}}{1 - X\left[1 - exp\left(\pm \xi\right)\right]} \right]^{1/2} \right\} \qquad (2)$$

$$E^{*} = E^{o} \pm \frac{RT}{\alpha_{\pm} nF} ln \left\{ \frac{4}{3^{1/2}} \frac{k^{o} \tau^{1/2}}{D^{1/2}} \right\} \qquad (3)$$

where E is the electrode potential, E^o is the reversible half wave potential, α is the transfer coefficient, k^o is the standard heterogeneous electron transfer rate constant, ξ a dimensionless parameter expressed as

$$\left\{\left(\frac{nF}{RT}\right)\left(E - E^o\right)\right\} \tag{4}$$

τ the sampling time, D is the diffusion coefficient as determined by cyclic voltammetry, and X is the ratio of the current at the potential E to the anodic limiting diffusion controlled current.

A plot of the right hand side of Equation 2 versus E is linear with a slope of

$$\left(\left(\frac{RT}{\alpha nF}\right)^{-1}\right) \tag{5}$$

and an intercept of E*, for the anodic branch. Assuming D is the same for the anodic and cathodic processes, and using the value of the formal potential obtained from cyclic voltammetry, k^o and α can be evaluated. This method of estimating the kinetic parameters of a system has been used successfully by several authors.[40,41,42] Figures 13 and 14 show representative examples of these plots from which the transfer coefficients are obtained. In all cases the heterogeneous electron transfer rate constant for the redox couples is of the order of 10^{-2} cm^2 s^{-1} while the transfer coefficients are always 0.50 ± 0.05. This measure of the transfer coefficients may be significant, as we shall see later in the chapter.

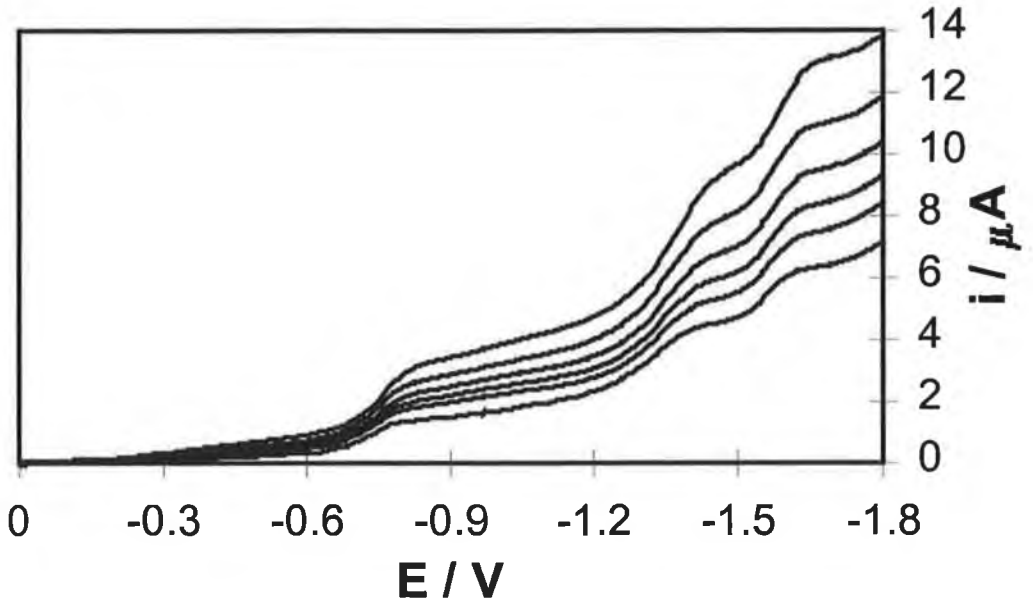

Figure 9 Normal pulse voltammetry of $QCat^{2-}Ru$-1,2 showing the redox couples situated around –0.8, -1.4 and –1.6 V. The sampling times from top to bottom are 5, 6, 7, 8, 9, and 10 ms respectively. The initial potential is 0.0 V.

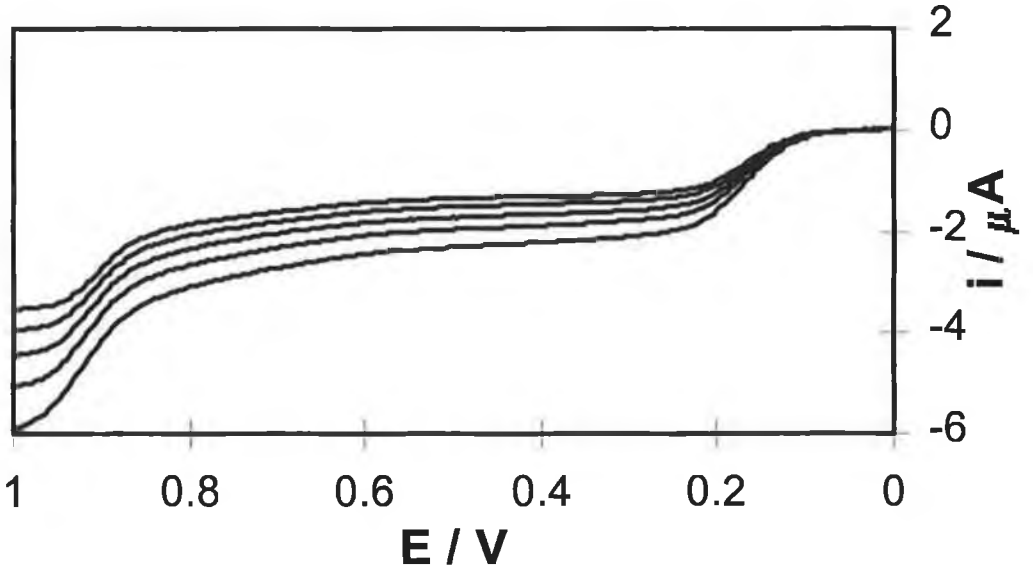

Figure 10 Normal pulse voltammetry of $QCat^{2-}Ru$-1,2 showing the redox couples situated at 0.16 and 0.95 V. The sampling times from top to bottom are 9, 8, 7, 6, and 5 ms respectively. The initial potential is 0.0 V.

6.3.2 Surface Confined Voltammetry

Attempts to adsorb $QCat^{2-}$Ru-1,2 onto several electrode materials including gold, platinum and mercury met with varying degrees of success. While the complex did not appear to adsorb onto mercury, low surface coverages were obtained at both platinum and gold electrodes after soaking electrodes for up to 12 hours. However, the voltammetry of the species when adsorbed onto platinum and gold is non-ideal and difficult to interpret making these electrode/monolayer interfaces unattractive for the study of thermodynamics and kinetics using electrochemical techniques. The material onto which the complex adsorbed most successfully was carbon fibre. Monolayers of $QCat^{2-}$Ru-1,2 were typically formed by immersing a carbon fibre microelectrode in millimolar acetone/DMF or aqueous/DMF solutions of the complex for up to 4 hours.

A cyclic voltammogram of $QCat^{2-}$Ru-1,2 surface confined on a carbon fibre microelectrode is shown in Figure 11. Two redox couples are observed which correspond to oxidation of the parent dianion radical to form the complexes denoted (b) and (c), respectively, in Scheme 1. These species shall be denoted for the purpose of this discussion as $Q^{\cdot\cdot 2-}/Q^{\cdot-}$ and $Q^{\cdot-}/Q$, respectively. Starting at a potential of -0.3 V, scanning positively, the CV in Figure 11 represents firstly, oxidation of the semi-quinone in the 1 position of Scheme 1(a) to the anthraquinone of scheme 1(b) which exists at ~0.5 V. Oxidation of the second semi-quinone leads to the formation of the anthraquinone of scheme 1(c). These assignments of the redox couples are consistent with the characterisation of the complex, which has been described in detail in Chapter 2.

The formal potentials of the redox couples in Figure 11 are 0.190 and 0.730 V respectively. This voltammetric response is consistent with that expected for an electrochemically reversible reaction involving a surface confined redox-active species.[43,44] For example, Figure 12 shows that the peak shapes are independent of scan rate, ν up to at least 10 V/s and Figures 13(a) and 13(b) show that the peak height varies linearly with sweep rate rather than the $\nu^{1/2}$ dependence

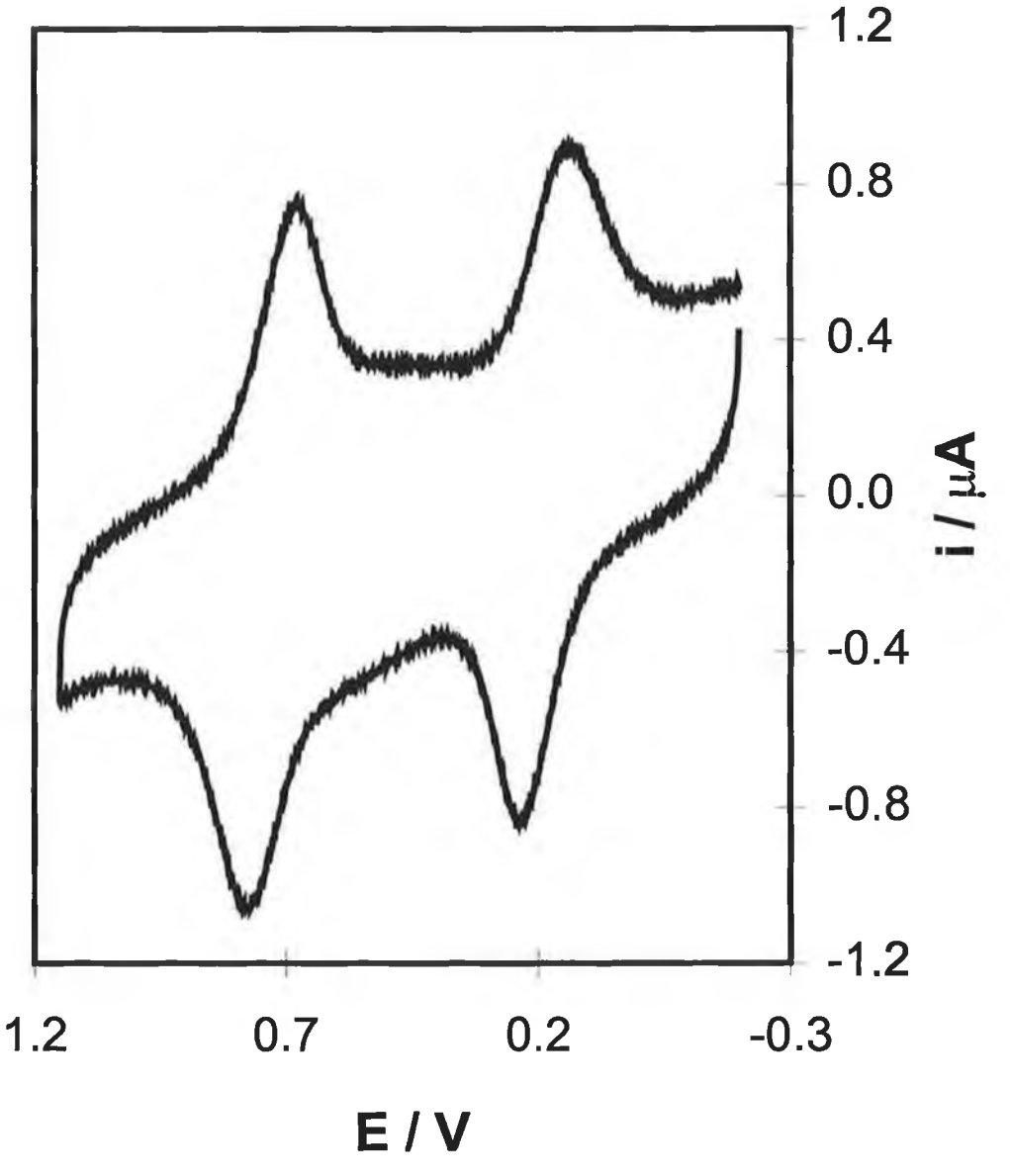

Figure 11 Cyclic voltammogram of $QCat^{2-}Ru$-1,2 immobilised on a carbon fibre microelectrode. Cathodic currents are up and anodic currents are down. The supporting electrolyte is aqueous 1.0 M $LiClO_4$. The scan rate is 2 V/s and the initial potential is –0.2 V.

expected for a freely diffusing species. Therefore, consistent with other reports on monolayer modified electrodes it appears that $QCat^{2-}$Ru-1,2 adsorbs onto the surface of a carbon fibre microelectrode to give an electroactive film.[43,44] For a surface confined species in which there are no interactions between adsorbates, and an equilibrium is rapidly established between the applied potential and the redox composition of the film, a zero peak-to-peak splitting and a full width at half maximum (FWHM) of 90.6/n, where n is the number of electrons transferred, are expected. We typically observe peak-to-peak splitting and FWHM values of 60 to 80 mV and 100 to 120 mV respectively, at scan rates slower than 10 V/s in 1.0 M $LiClO_4$. The non zero nature of the peak-to-peak splitting has been interpreted by Feldberg as unusual quasi-reversibility (UQR).[45]

In this model, hysteresis is observed in cyclic voltammetry because some processes, e.g., heterogeneous electron transfer, ion movement, changes in monolayer structure that accompany redox switching, etc., are slow compared to the time scale of the experiment. These issues are not considered here except to note that neither heterogeneous electron transfer nor double layer assembly limits the voltammetric response at these scan rates. Since the experimental timescale is in the order of 0.1 ms and the timescale of electron transfer is at least two orders of magnitude faster, as indicated by cyclic voltammetry, slow heterogeneous electron transfer is are not considered to be the origin of the non-zero ΔE_{peak}.

The magnitude of the FWHM suggests that both redox reactions observed in Figure 1 each involve the transfer of one electron. Brown and Anson,[44] as well as Laviron,[43] have demonstrated that the full width at half maximum is sensitive to the degree of interaction between adsorbates. As the potential is scanned, the reduced (R) and oxidised (O) forms of the redox couple exist near $E^{o\prime}$. Where there are no lateral interactions between surface confined redox centres, or where the interactions between O and O, R and R, and O and R are large but similar to one another, a FWHM of 90.6 mV is expected for a redox reaction involving the transfer of a single electron. Therefore, while the voltammetric response of these monolayers is electrochemically reversible, our experimental observation of a FWHM of between

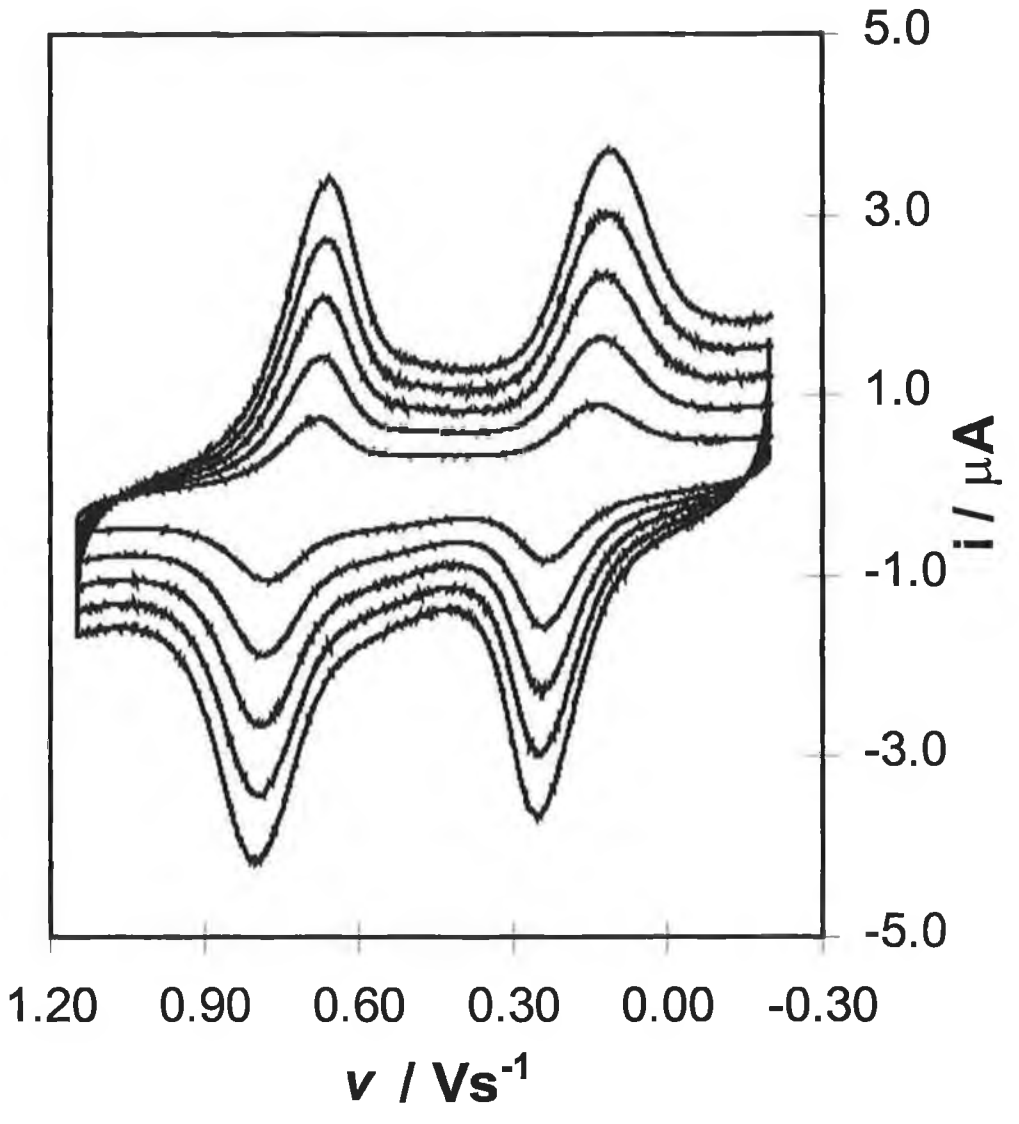

Figure 12 Cyclic voltammograms of $QCat^{2}$-Ru-1,2 immobilised on a carbon fibre microelectrode. Scan rates from top to bottom are 10, 8, 6, 4, and 2 V/s. The supporting electrolyte is aqueous 1.0 M $LiClO_4$ and the initial potential is –0.2 V.

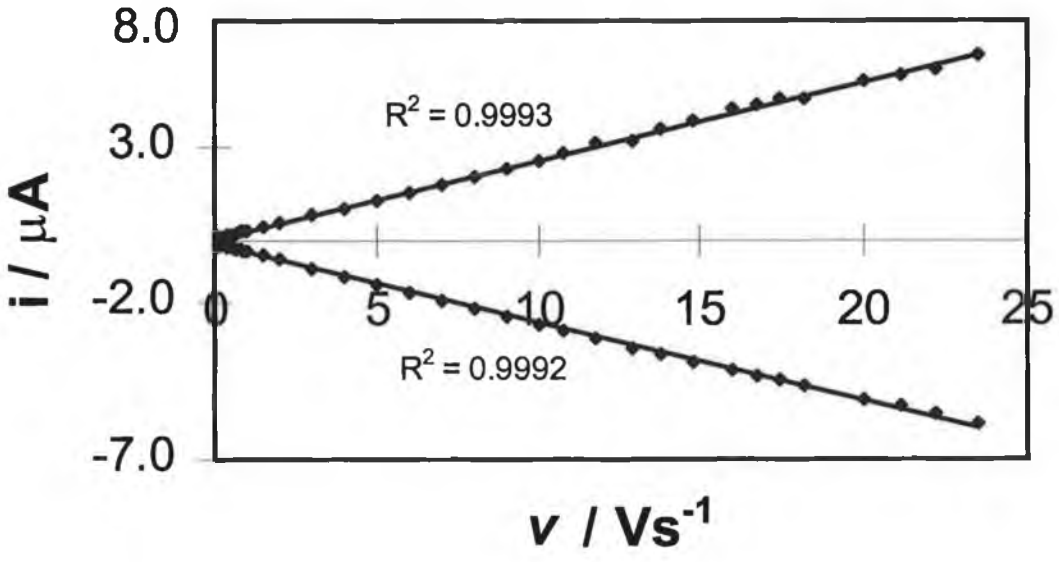

Figure 13(a) Dependence of peak currents for the $Q^{\cdot 2-}/Q^{-}$ redox couple immobilised onto a carbon fibre microelectrode up to 23.5 V/s. Cathodic currents are up, anodic currents are down.

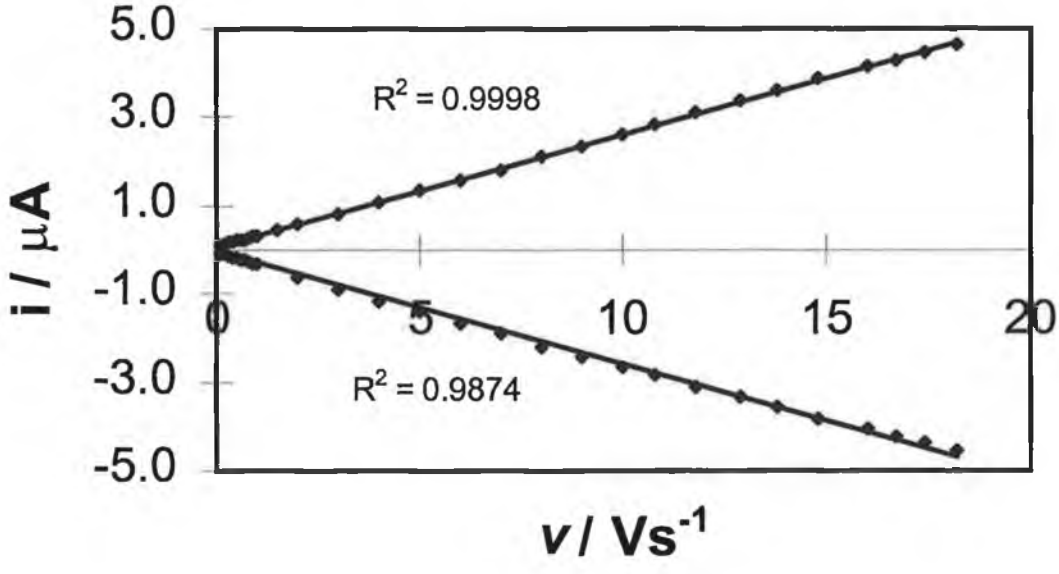

Figure 13(b) Dependence of peak currents for the Q^{-}/Q redox couple immobilised onto a carbon fibre microelectrode up to 18.2 V/s. Currents as in Figure 3(a).

100 and 120 mV suggests that destabilising lateral interactions exist within the assemblies.

The surface coverage, which can be determined from the charge under a voltammetric wave, after correcting for background charging, together with the geometric area of the electrode. Unfortunately, due to problems outlined in Chapter 3, it is difficult to obtain the real surface area of carbon fibre microelectrodes. The methods used above for determining the area of gold and platinum electrodes are not applicable as carbon undergoes neither hydrogen or oxygen adsorption from solution. The redox active probe method is not applicable since the surface is rarely atomically smooth. For these reasons, the microscopic area of our carbon fibre microelectrodes has not been accurately determined.

When the time constants of the voltammetric experiment and electron transfer are comparable, one expects the rate of electron transfer across the metal/film interface to influence the voltammetric response. A shift in both the anodic and cathodic peak potentials, that cannot be attributed to iR drop, and a non unity slope magnitude in a plot of the peak current, i_p, versus the scan rate are evidence that the electrode kinetics influence the overall response. Figures 13(a) and 13(b) show that the experimental i_p increases linearly with increasing ν up to approximately 20 V/s with absolute slopes of near unity (|slope| = 0.96±0.06 and 0.97±0.04) for the $Q^{\bullet 2-}/Q^{\bullet -}$ and $Q^{\bullet -}/Q$, redox couples respectively, thereby indicating that for scan rates up to approximately 20 V/s the experimental timescale is longer than that for electron transfer. For scan rates above 23.5 V/s for the $Q^{\bullet 2-}/Q^{\bullet -}$ reaction and 18.2 for the $Q^{\bullet -}/Q$ reaction, Figures 15(a) and 15(b) indicate that the slopes observed for plots of i_p versus ν decrease significantly as the influence of heterogeneous electron transfer kinetics becomes apparent, and the current tends to become independent of the scan rate for values greater than approximately 100 V/s. The scan rate at which the peak current begins to vary significantly from unity can be used to estimate the rate of heterogeneous electron transfer, k^o, using Equation 6;

$$k^{o} \approx \frac{Fv}{RT} \quad (6)$$

where F is Faradays constant, v is the voltammetric scan rate, R is the gas constant and T is the absolute temperature. Given that the time constant for a cyclic voltammetry experiment in which the scan rate is 20 V/s is approximately 130 ms, these observations suggest that the standard electron transfer rate constants, k^{o}, for the $Q^{\cdot\cdot 2-}/Q^{\cdot -}$ redox centre and the $Q^{\cdot -}/Q$ moiety are at least 900 and 700 s^{-1} respectively.

For potentials far from E°′, the voltammetric response is dominated by the double layer charging current, i_c. The charging current observed in the absence of dissolved $QCat^{2-}$Ru-1,2 is at least twice as large as that observed in Figure 11. Therefore, that the charging current observed in Figure 11 remains much lower than that of the bare carbon fibre microelectrode between approximately 1.2 and -0.30 V suggests that $QCat^{2-}$Ru-1,2 remains adsorbed over the entire potential range investigated and desorbs only at potentials outside of this range. That the peak shapes do not change significantly when cycled repeatedly at temperatures up to 40 °C, over at least 6 hours, indicates that adsorbed films of $QCat^{2-}$Ru-1,2 are both electrochemically reversible and thermally stable.

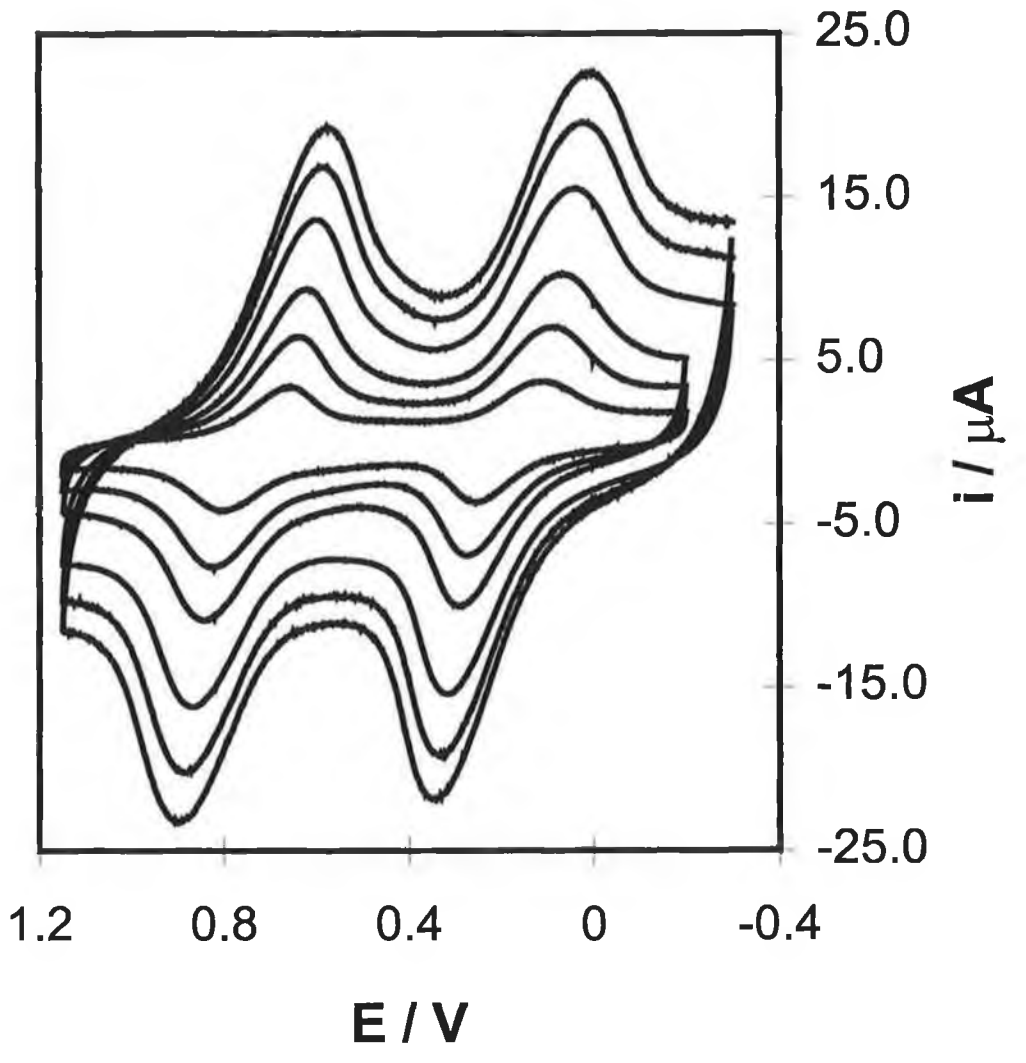

Figure 14 Scan rate dependence of the cyclic voltammetric response for $QCat^{2-}$Ru-1,2 immobilised on a carbon fibre microelectrode. Scan rates from top to bottom are 80, 66.7, 50, 30.8, 20, and 10 V/s. The initial potential is –0.2 V for the voltammograms recorded at 10, 20, and 30.8 V/s and –0.3 V for those recorded at 50, 66.7, and 80 V/s. The supporting electrolyte is aqueous 1.0 M $LiClO_4$.

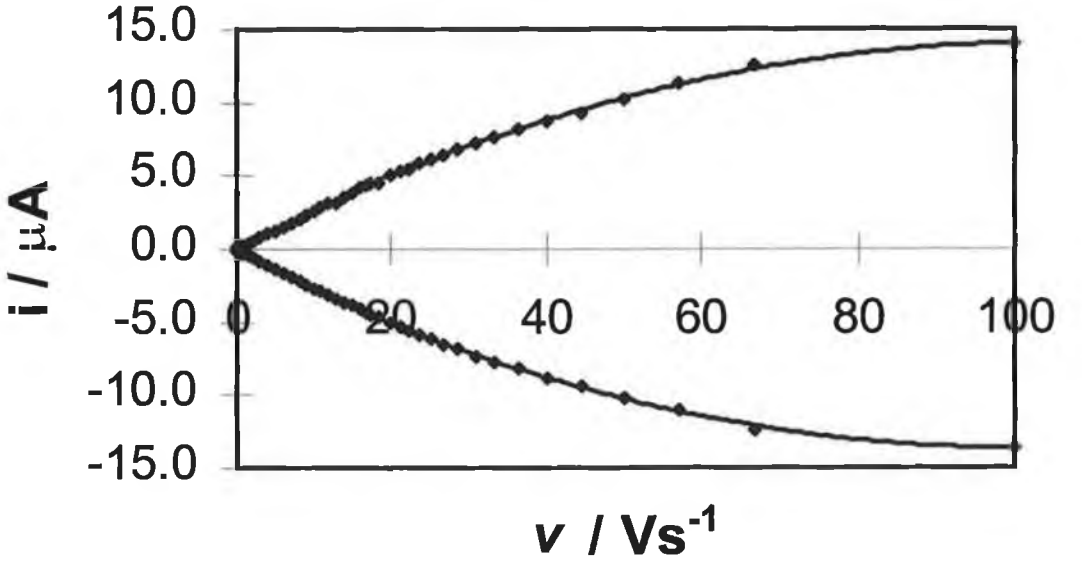

Figure 15(a) Dependence of peak currents for the $Q^{\bullet-2}/Q^{\bullet-}$ redox couple immobilised onto a carbon fibre microelectrode up to 100 V/s. Cathodic currents are up, anodic currents are down.

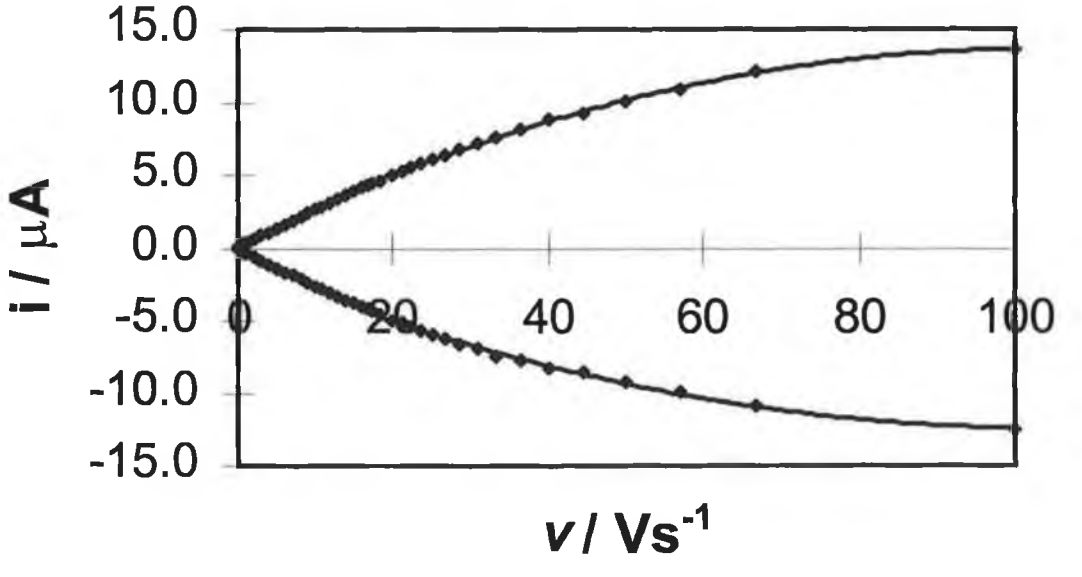

Figure 15(b) Dependence of peak currents for the $Q^{\bullet-}/Q$ redox couple immobilised onto a carbon fibre microelectrode up to 100 V/s. Cathodic currents are up, anodic currents are down.

6.3.3 Chronoamperometry

Chronoamperometry has been used to determine the ideality of the electrochemical response and to probe the heterogeneous electron transfer kinetics of the monolayer modified electrode. In these experiments, the potential was stepped from an initial value E_i where the monolayer is redox active to a region in which Faradaic currents were recorded. Figures 16 and 17 show typical examples of potential step experiments in which the capacitive and Faradaic currents can be observed. The semi-log plots of these data yield dual slope behaviour typically associated with processes involving two single exponential decays.

At short times the capacitive current associated with double layer charging is recorded. This capacitive current can be analysed using a plot of ln i_c versus t to obtain the total cell resistance, R, and the double layer capacitance, C_{dl}, according to Equation 7;

$$i_c(t) = \left(\frac{\Delta E}{R}\right) exp\left(\frac{-t}{RC_{dl}}\right) \tag{7}$$

where ΔE is the pulse amplitude. Using this equation it is possible to obtain RC cell time constants associated with the carbon fibre microelectrodes used here. Determination of RC cell time constants is an important consideration when one considers the electron transfer rates being probed. Cyclic voltammetry indicates that the standard heterogeneous electron transfer rate constant is approximately 1000 s^{-1}. If our only requirement were to examine the kinetics of electron transfer near $E^{o\prime}$, then an electrode with an RC of 200 μs would be adequate. However, since we are interested in probing the kinetics of electron transfer as a function of potential and temperature, in order to obtain information about the electron transfer coefficients, free energies of activation, reorganisation energies, etc., of the system, we require electrodes with RC values that will not interfere with the Faradaic responses observed at high overpotentials and temperatures. Using Equation 7 we have confirmed that the RC cell time constants associated with the carbon fibre

microelectrodes employed throughout the course of this work were always less than 50 μs.

At times longer than those for decay of the capacitive current, the Faradaic current associated with the redox process of interest is observed. For an ideal electrochemical reaction involving a surface bound species, the Faradaic current following a potential step that changes the redox composition of the monolayer exhibits a single exponential decay in time. That a single exponential decay is observed for the Faradaic reactions in Figures 16 and 17 indicates that the electrochemical response of these monolayers is ideal, i.e., that the kinetics of charge transfer are not limited by ion motion, that iR drop is not large enough to significantly change the overpotential and that electron hopping to a population of fast redox centres does not occur. The rate of heterogeneous electron transfer across the electrode/monolayer interface can be determined from plots such as Figures 16 and 17 according to Equation 8

$$i_F(t) = kQexp(-kt) \tag{8}$$

where k is the apparent rate constant for the overall redox reaction and Q is the total charge passed in the redox transformation. Using chronoamperometry electron transfer rates can be probed as a function of overpotential and temperature to obtain information about the energetics of the system. The data in Figures 16 and 17 was recorded from starting potentials of 0.45 and 0.40 V using pulse amplitudes of 0.43 and 0.37 V, respectively, which lead to the chronoamperometric responses being recorded at overpotentials of 0.15 and -0.16 V. The inset of these diagrams provides the semi-log plot required for determination of the rate constant k. That these semi-log plots are linear over at least one and a half lifetimes suggests that the behaviour of these monolayers is indeed ideal. Rate constants determined from Figures 16 and 17 are approximately 1100 s^{-1}. In order to determine k^o using chronoamperometry it is necessary to determine k as a function of potential and then extrapolate out the value of k^o.

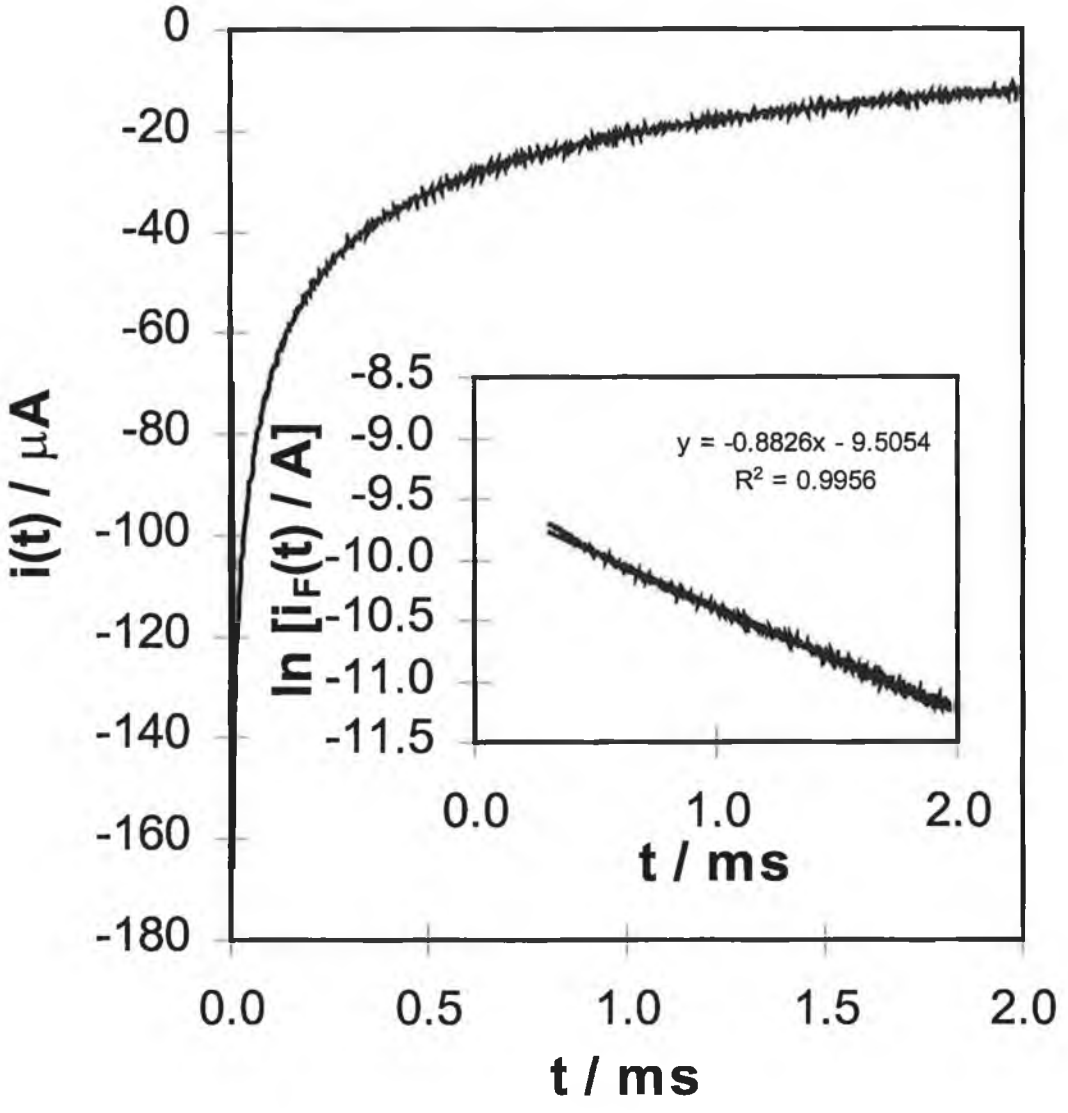

Figure 16 Current-time transient and semi-log plot for a chronoamperometric experiment in which a $QCat^{2-}$Ru-1,2 modified carbon fibre microelectrode was immersed in 1.0 M $LiClO_4$. The initial potential is 0.45 V and a pulse amplitude of 0.43 V in the positive potential direction was applied. The overpotential is 0.15 V.

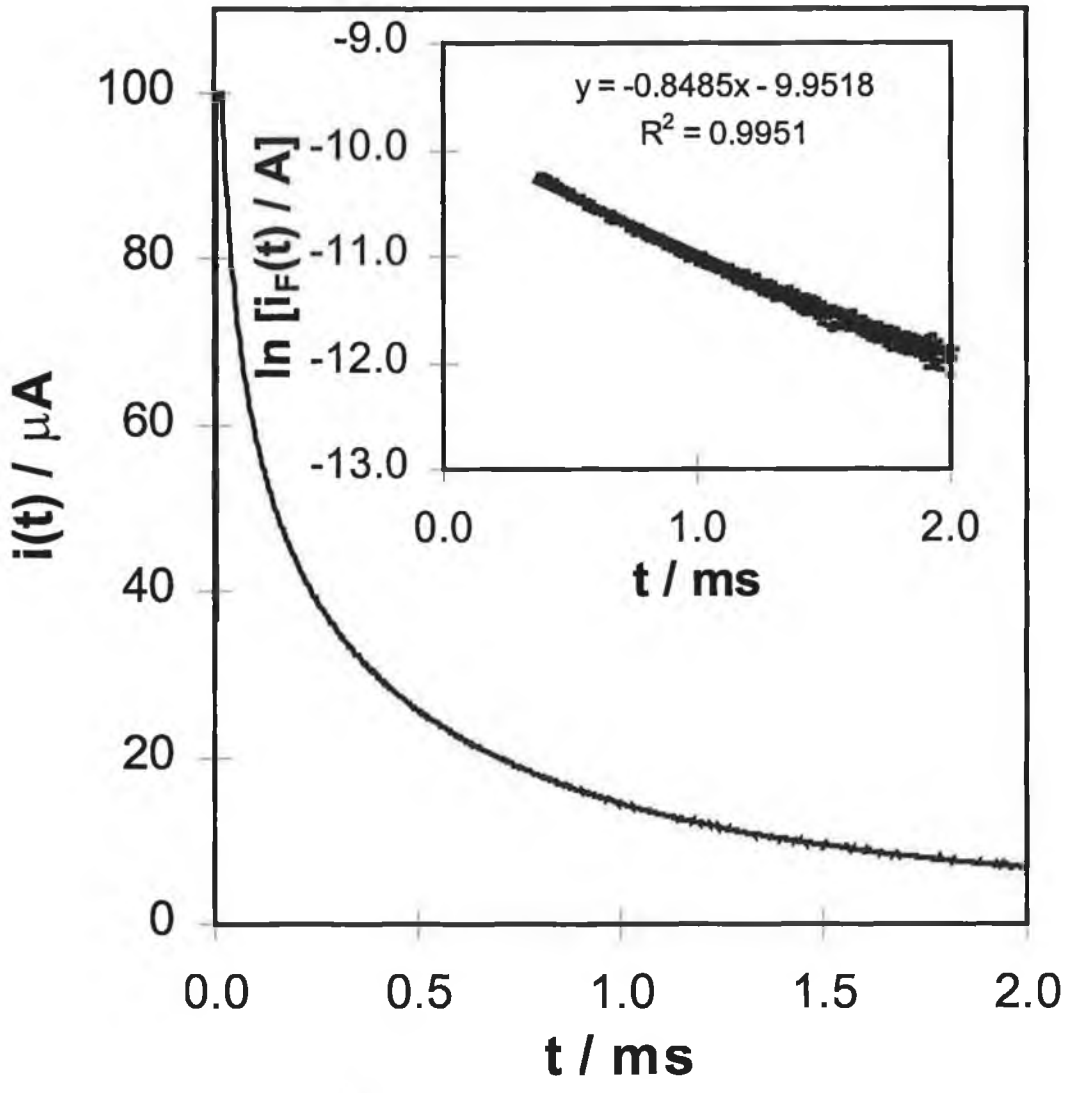

Figure 17 Current-time transient and semi-log plot for a chronoamperometric experiment in which a $QCat^{2-}$Ru-1,2 modified carbon fibre microelectrode was immersed in 1.0 M $LiClO_4$. The initial potential is 0.40 V and a pulse amplitude of 0.37 V in the positive potential direction was applied. The overpotential is -0.16 V.

6.3.4 Potential dependence of k

In an amperometric experiment, an increased potential step relative to the formal potential increases the free energy driving force of the reaction and causes increased electron transfer rates to be observed. In fact, the Butler-Volmer formulation predicts that for electrode reactions that are limited only by the interfacial kinetics, the heterogeneous electron transfer rate k will increase exponentially with increasing overpotential, $\eta \equiv (E - E^{o\prime})$, where $E^{o\prime}$ is the formal potential. Figure 18 shows the chronoamperometric response of a carbon fibre microelectrode modified with $QCat^{2-}$Ru-1,2 as a function of applied potential. Using an initial pulse amplitude of 400 mV, the potential was stepped from a value E_i where there was no redox activity taking place to a region in which Faradaic currents were observed and the resulting current responses were recorded. Between successive measurements, E_i remained the same but the pulse amplitude was increased monotonically by 30 mV. The charging current, i_c, decays exponentially in time according to Equation 7 with Faradaic currents increasing as the overpotential is increased. Figure 19 shows the semi-log plots of the current-time transients of the $Q^{\cdot-}/Q$ redox couple (Figure 18) as a function of applied potential. The slopes of these lines provide the heterogeneous electron transfer rates. This figure shows that k increases significantly with increasing overpotential. The magnitudes of the slopes at low overpotential suggest that the heterogeneous electron transfer rate constant is of the order of 1000 s^{-1} which agrees with the cyclic voltammetric data presented earlier.

Figure 20 illustrates the Tafel plot of ln k versus η associated with this redox reaction. k increases exponentially with applied potential as predicted by Butler-Volmer theory. For overpotentials less than about 300 mV on the anodic branch and 400 mV on the cathodic branches, ln k depends approximately linearly on η. The standard heterogeneous electron transfer rate constant k^o has been determined by linearly extrapolating ln k to zero overpotential. The standard heterogeneous electron transfer rate constant for both redox processes is approximately 900 s^{-1}. At high overpotentials the dependence of ln k on η is clearly nonlinear, and the slopes decrease in magnitude with increasing overpotential. This response contrasts with

the Butler-Volmer formulation of electrode kinetics,[46] which suggests that transfer coefficients are potential independent. Furthermore, the branches of the Tafel plot become unsymmetrical at large overpotentials, with the anodic branch showing more curvature than the cathodic. Finklea and Hanshew have interpreted this asymmetry as indicating through space tunnelling between the underlying electrode and the redox centres.[47]

The slopes, m, of the linear portions of both branches in this plot are 3.4. Using Equation 9 transfer coefficients, α, of 0.09 was calculated for the oxidation and reduction processes.

$$m = \frac{\alpha n F}{RT} \tag{9}$$

These are low and unexpected values for the transfer coefficients. Figure 20 also shows the slopes associated with transfer coefficients of 0.5. One might expect since our solution phase NPV experiments consistently yield electron transfer coefficients of 0.5±0.05, that our Tafel plots would also provide transfer coefficients of 0.5. Due to this contradiction in the two sets of experimental results we have not attempted to fit Finklea's model to our data to estimate the reorganisation energies associated with the processes under investigation.

We have not investigated the nature of the observed response except to point out that Creager[11] has interpreted Tafel plots of decreased slope as being caused by a potential difference between the plane of electron transfer and bulk solution. Factors which affect this potential difference are surface coverage, electrolyte concentration and the charge on the immobilised before and after application of a potential step. Future work will no doubt focus on these issues and calculation of the potential difference across the interface in order to determine whether these factors have a pronounced effect on the rate constant as a function of potential. Although we did not achieve the expected slopes in our Tafel plots, it was possible to use

chronoamperometry at relatively low overpotentials in order to study the rate constant as a function of temperature.

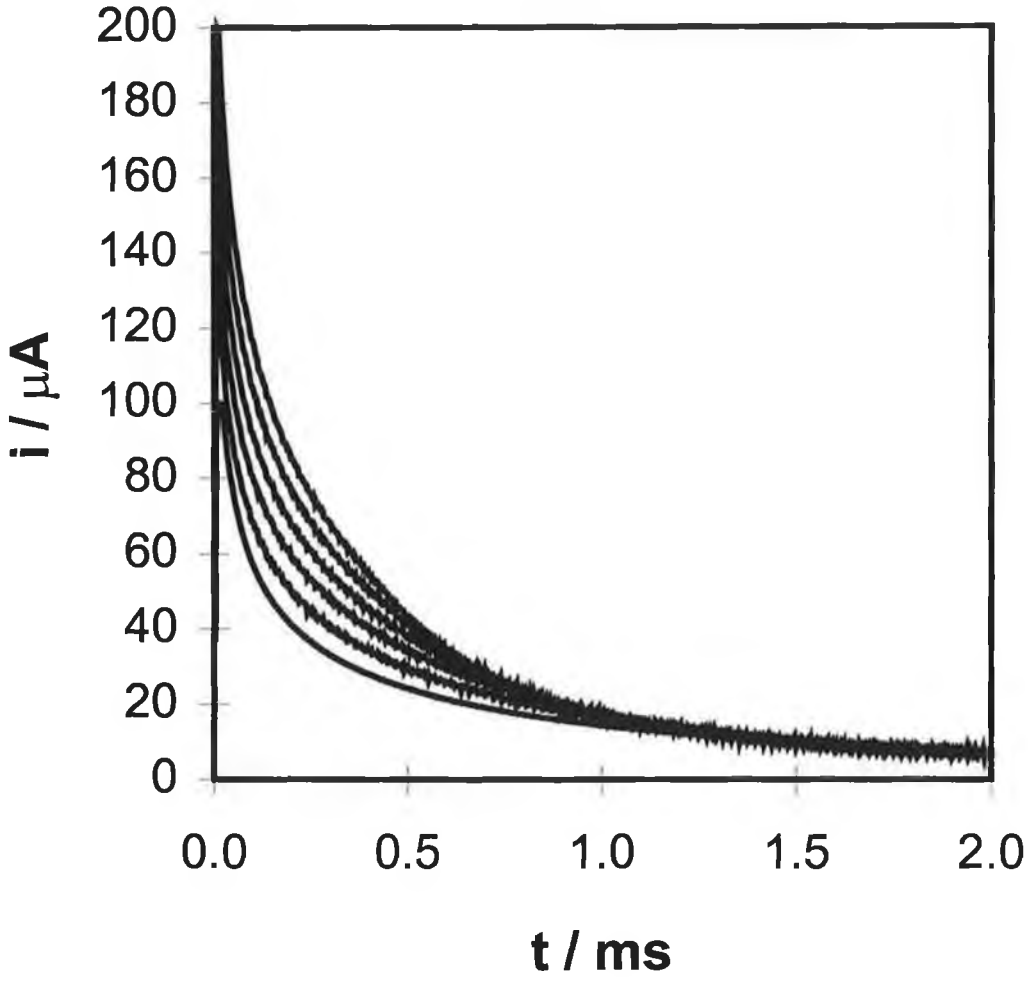

Figure 18 Current-time transients for $QCat^{2-}$Ru-1,2 spontaneously adsorbed onto a carbon fibre microelectrode. The supporting electrolyte is 1.0 M $LiClO_4$ and the initial potential is 1.0 V. The overpotentials from top to bottom are, -0.42, -0.36, -0.30, -0.24, -0.18, and -0.12 V.

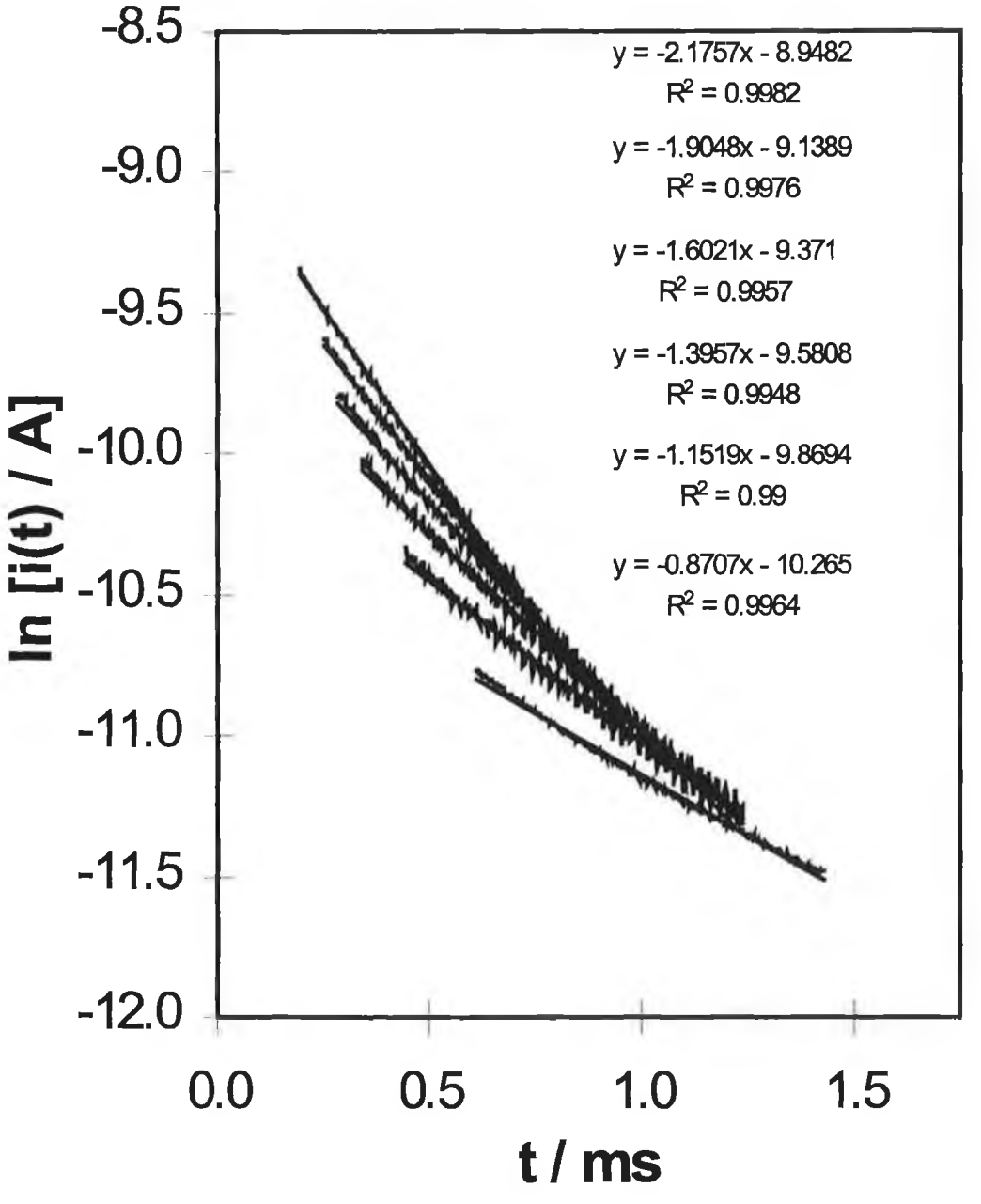

Figure 19 Semi-log plots of current-time transients shown in Figure 18. The overpotentials from top to bottom are -0.42, -0.36, -0.30, -0.18, -0.24, and -0.12 V.

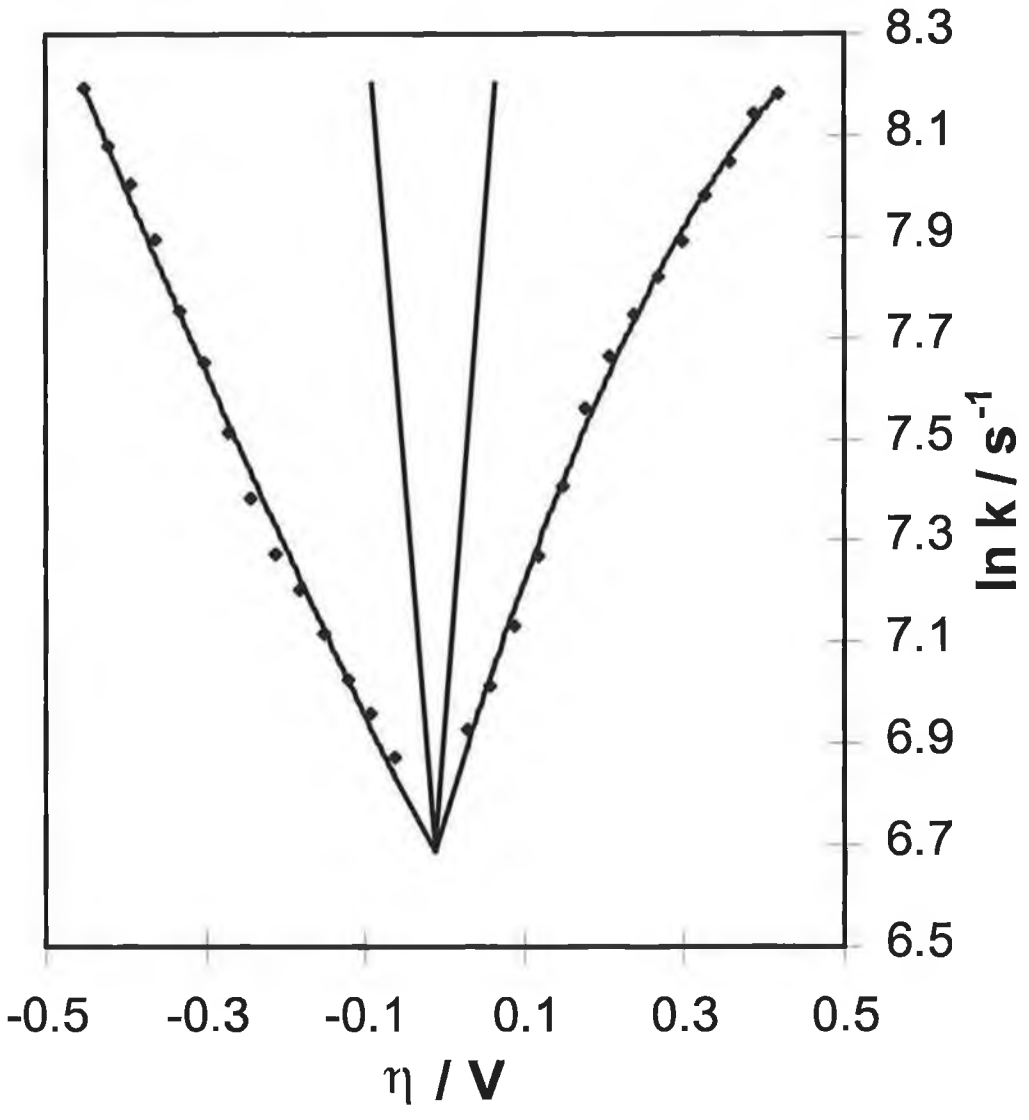

Figure 20 Tafel plot for$QCat^{2-}$Ru-1,2 monolayer. The redox couple is Q^{-}/Q.

6.3.5 Temperature dependence of k

The activation enthalpy, ΔH, can be determined from the temperature dependence of the heterogeneous electron transfer rate constant. The activation enthalpy quantifies the change in enthalpy upon oxidation or reduction of the redox active species. Together with the reaction entropy, it can be used to determine the free energy of activation, ΔG.

The electrochemical activation enthalpy determined from an Arrhenius plot of ln k vs T^{-1}, where ϕ_m, the potential difference across the electrode/solution interface, is held constant, has been termed "ideal",[32] and we label it here as $\Delta H_I^{\neq}$. For a reduction or cathodic reaction, this electrochemical activation enthalpy can be separated into "chemical", $\Delta H^{\neq}$, and "electrical", $\alpha_c F\phi_m$, contributions according to Equation 10.

$$\Delta H_{I,c}^{\neq} = -R\left.\frac{\partial \ln k}{\partial\left(\frac{1}{T}\right)}\right|_{\phi_m} = \Delta H^{\neq} - \alpha_c F\phi_m \qquad (10)$$

The temperature dependence of k has been investigated in order to determine the activation enthalpy for the system under investigation. In a typical experiment, the temperature was systematically varied from its initial value, through the entire range between -5 to 40 °C and returned to its initial value. The same slope, $-k$, and intercept, $\ln(kQ)$ was observed within experimental error for the initial and final transients. This consistency indicates that cycling the temperature does not alter the electron transfer kinetics or the surface coverage. Overpotentials of 150 mV were employed in the case of both redox couples. Figure 21 illustrates semi-log plots as a function of temperature for the $Q^{\cdot-}/Q$ redox couple. It is clear from these transients that the slope of the Faradaic portion of the curve becomes larger with increasing temperature. The corresponding semi-log plots were linear over approximately two lifetimes, and the heterogeneous electron transfer rate was evaluated from the slopes.

Figure 22 displays an Arrhenius plot of ln k vs. T^{-1} for the QCat^{2-}Ru-1,2 monolayer immobilised on an electrode surface. That the electron transfer rate increases with temperature is consistent with a thermally activated process.

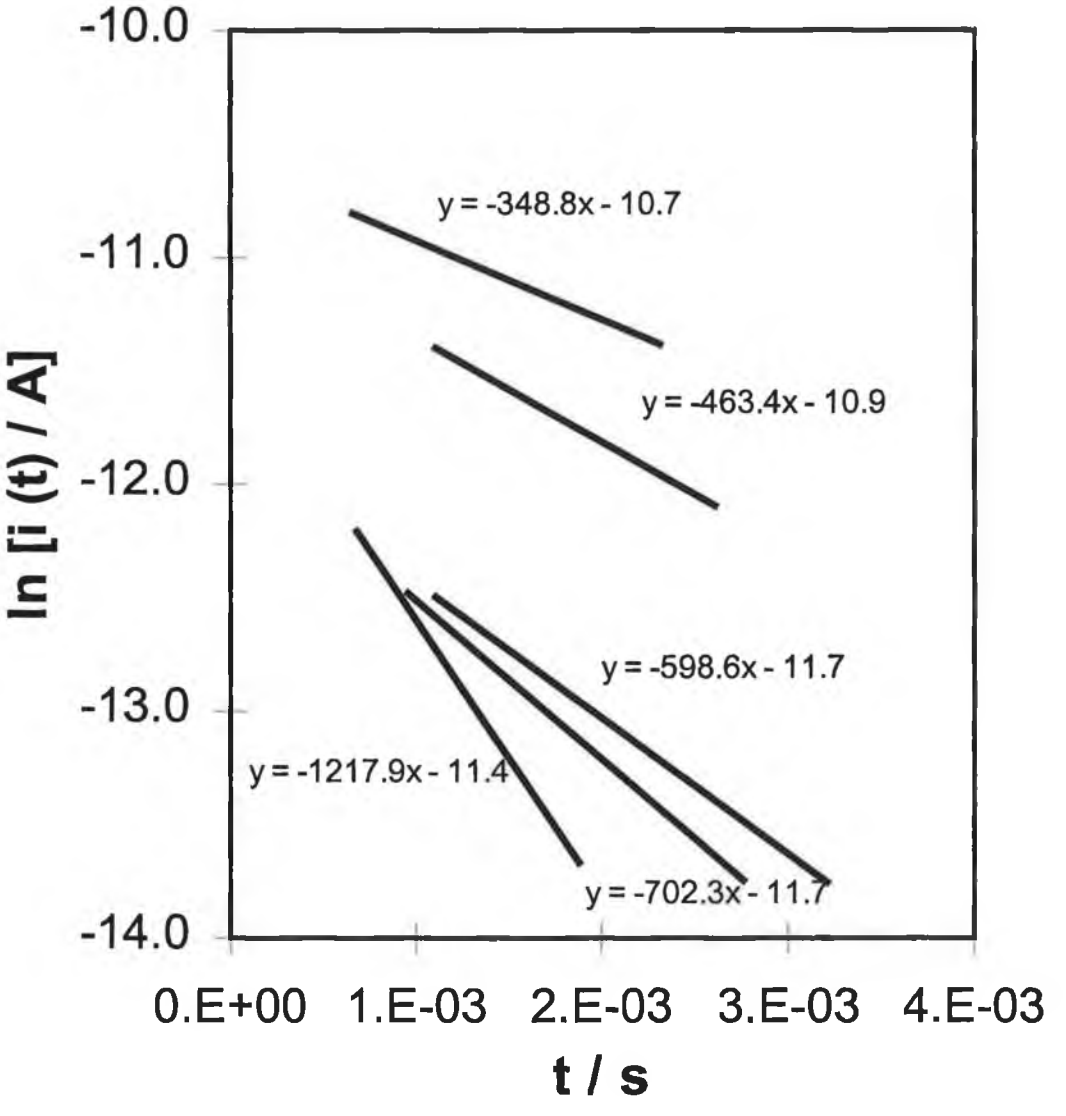

Figure 21 Semi-log plots for a carbon fibre microelectrode modified with spontaneously adsorbed Qcat^{2-}Ru-1,2. The semi-log plots represent, from top to bottom, temperatures of –5, 0, 5, 10, and 20. The overpotential is 0.15 V and the supporting electrolyte is 1.0 M $LiClO_4$. The redox couple is $Q^{\cdot-}$/Q.

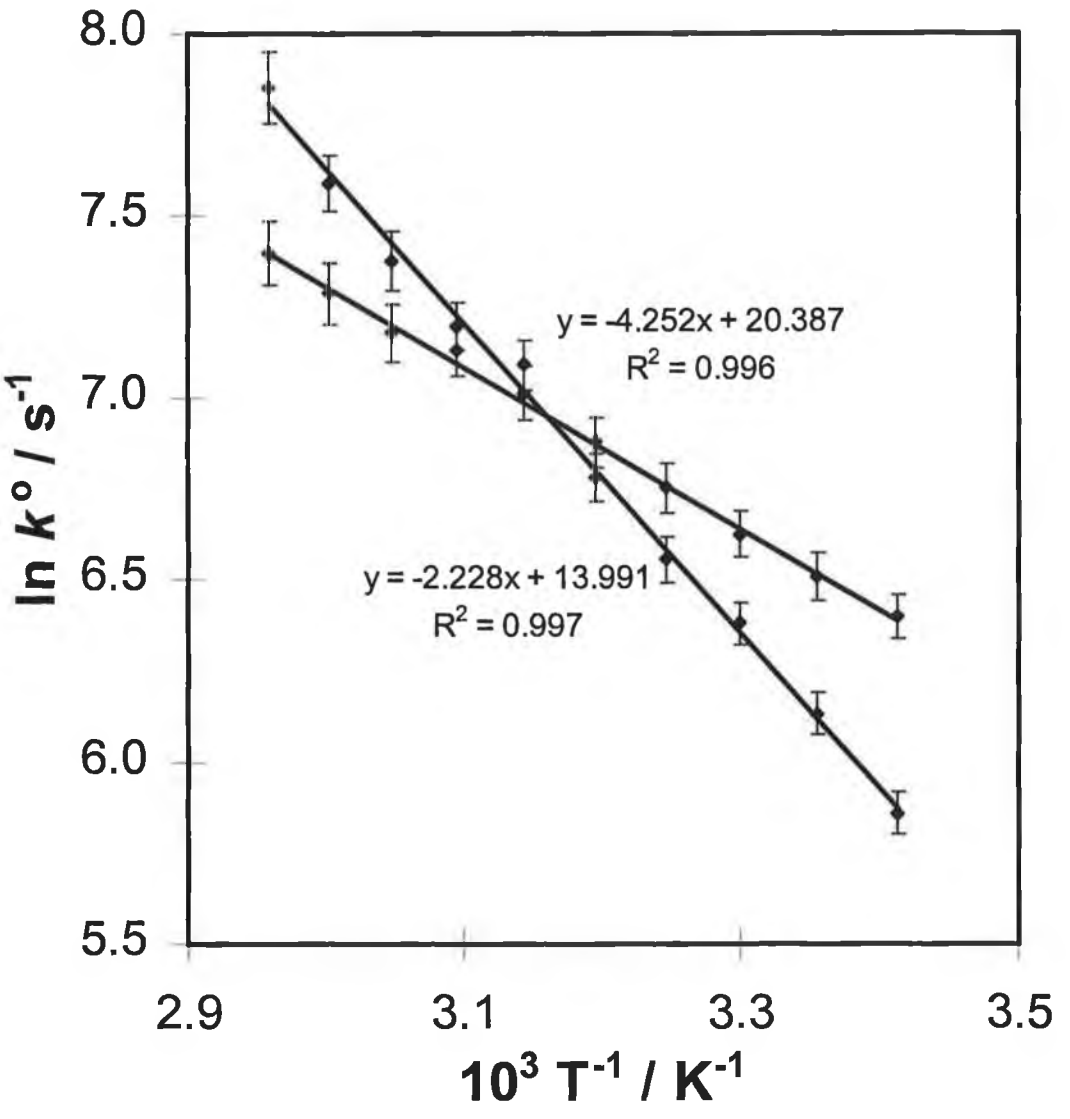

Figure 22 Arrhenius plot showing the dependence of the heterogeneous electron transfer rate constant, *k*, on temperature. Experiments were carried out as illustrated in Figure 21 in which an overpotential of 0.1 V at 298 K was employed. The experiments represent, from top to bottom on the left hand side, the temperature dependence of the $Q^{\cdot-}/Q$ and $Q^{2-\cdot}/Q^{\cdot-}$ redox couples respectively. The lines fitted to the points are the best fit linear lines, the slope of which is used to determine the reaction enthalpy.

6.3.6 Reaction Entropies

The reaction entropy, ΔS_{rc}, quantifies the difference in entropy between the reduced and oxidised forms of the redox couple. Weaver has shown that for solution phase reactants involving 2+/3+ 1+/2+ and 0/1+ redox reactions, ΔS_{rc} decreases with decreasing overall charge, i.e., $\Delta S_{rc}^{2+/3+} > \Delta S_{rc}^{1+/2+} > \Delta S_{rc}^{0/1+}$. Forster has also shown similar trends for spontaneously adsorbed monolayers. Therefore, one might expect that ΔS_{rc} would be larger for the $Q^{\bullet 2-}/Q^{-}$ redox reaction than $Q^{\bullet -}/Q$ since the $Q^{\bullet 2-}/Q^{\bullet -}$ based reaction involves a net increase in charge from 2- to 1-, whereas the $Q^{\bullet -}/Q$ moiety involves an increase from –1 to 0.

The temperature dependence of the formal potential can be expressed as

$$\Delta S_{rc} = F\left(\frac{\partial E^{o\prime}}{\partial T}\right) \tag{11}$$

Figure 23 shows the temperature dependence of the voltammetric response for $QCat^{2-}Ru$-1,2 monolayers adsorbed on a carbon fibre microelectrode. These voltammograms were recorded using a non-isothermal cell and the formal potentials were plotted as a function of temperature. As Figure 24 shows, $E^{o\prime}$ varies linearly with temperature over the range -5 to 40 °C and the slopes of these lines can be used to calculate the ΔS_{rc} according to Equation 9. Surprisingly, the reaction entropy for the $Q^{\bullet -}/Q$ couple(100 J mol^{-1} K) is considerably larger than that for the $Q^{\bullet 2-}/Q^{-}$ moiety (7 J mol^{-1} K).

Together with reaction enthalpies, these reaction entropies can be used to calculate the free energies of activation for the two redox processes. According to Equation 10 the free energy of activation, ΔG, depends on the activation enthalpy, reaction entropy, temperature, and the transfer coefficient.

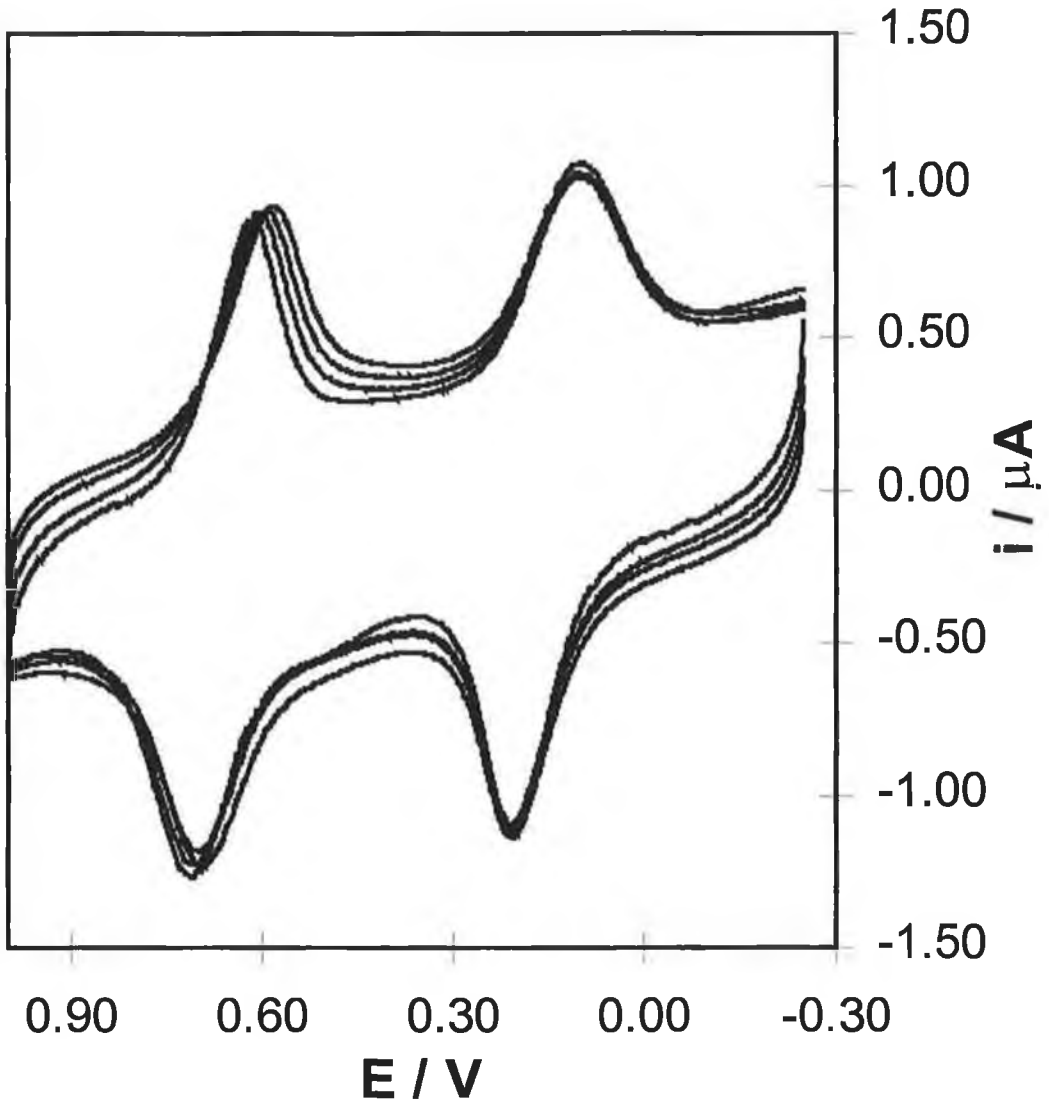

Figure 23 Temperature dependence of the cyclic voltammetric response for $QCat^{2-}$Ru-1,2 spontaneously adsorbed onto a carbon fibre microelectrode. Cathodic currents are up and anodic currents are down. The temperatures from right to left on the cathodic side of the more positive redox couple are 0, 10, 20, and 30 °C. Scans were initiated at –0.3 V and the supporting electrolyte is 0.1 M.

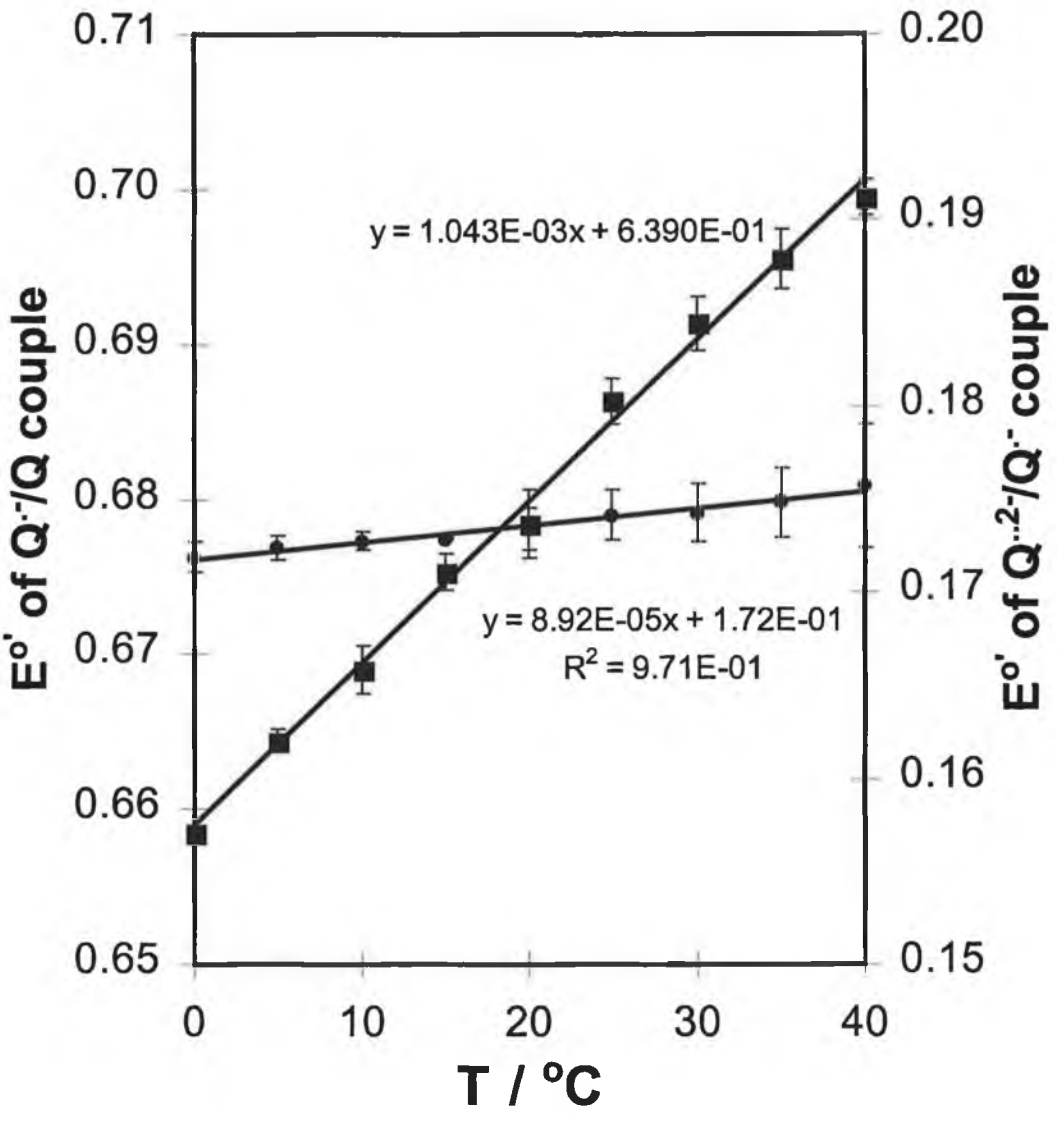

Figure 24 Plot of formal potential, E°′, versus temperature for the redox couples $Q^{2-\cdot}/Q^{\cdot-}$ (●) and $Q^{\cdot-}/Q$ (■) which are observed for $QCat^{2-}Ru$-1,2 immobilised on a carbon fibre microelectrode.

In principle, it is possible to use the experimental enthalpies and entropies to calculate free energies of activation. We have calculated the cathodic free energy of activation according to Equation 12:[27,32]

$$\Delta G_c^{\neq} = \Delta H_{I,c}^{\neq} - T\alpha_c \Delta S_{rc}^{o} \quad (12)$$

Assuming a transfer coefficient of 0.5 from our NPV experiments, the free energy of activation for the metal based and the quinone/hydroquinone redox reactions have been calculated. Table 2 summarises the results which provide the first estimation of activation free energies, activation enthalpies and reaction entropies for such a system.

Table 2 Enthalpies, entropies, free energies of activation, and reorganisation energies for the Q^{2-}/Q^{-} and Q^{-}/Q redox couples.

Redox couple	$\Delta H^{\neq}$, kJ mol^{-1}	ΔS_{rc}^{o}, Jmol^{-1}K^{-1}	$\Delta G^{\neq}$, kJ mol^{-1}	λ kJ mol^{-1}
Q^{2-}/Q^{-}	18.5(0.9)	8.6(0.6)	20.4(0.5)	81.6
Q^{-}/Q	35.3(2.2)	100.3(5.2)	17.3(0.7)	69.2

The free energy of activation can be used to estimate the reorganisation energy, λ, for the system. The reorganisation energy which provides a measure of the energy required to rearrange the solvent around the redox centre when electron transfer takes place can be estimated using Equation 13

$$\lambda = 4\Delta G \quad (13)$$

The values of λ in Table 2 indicate that the reorganisation for the system is large. Tafel plots of low slope, as observed in Figure 20, would indicate low reorganisation energies. However, this does not appear to be the case and based on this evidence the reorganisation energy for quinone based ruthenium complexes appears to be large.

6.4 Conclusions

Quinones are an important group of molecules that play a significant role in many areas of science. The co-ordination chemistry of these potential ligands with transition metals has been relatively slow in development and in most cases characterisation has been confined to elemental analysis. However, in recent years much interest has been paid to complexes that comprise of quinones attached to a ruthenium redox centre. Much of the work that has been carried out on the electrochemistry of ruthenium-quinone systems has been carried with these complexes being dissolved in solution. However, we have concentrated on probing the thermodynamics and kinetics of heterogeneous electron transfer associated with monolayers of these species adsorbed onto carbon fibre microelectrodes.

That the adsorbed monolayers considered here exhibit nearly ideal cyclic voltammetric behaviour is significant. It suggests that electron transfer between the underlying electrode surface and the two surface confined redox centres is mechanistically uncomplicated and agrees with our NPV analysis. However, chronoamperometric data, recorded on a timescale approximately two orders of magnitude shorter than typical cyclic voltammetric experiments, is more complicated. The potential dependence of the heterogeneous electron transfer rate constant provides Tafel slopes an order of magnitude less than that expected on the basis of the NPV results. The reason for this low transfer coefficient is unclear although it may be due to the applied potential not being fully realised at the plane of electron transfer. Further work will no doubt focus on this issue and others such as determining the surface coverage of the adsorbed species and hence its orientation on the electrode surface.

Reported here is one of the first studies on the thermodynamics and kinetics of heterogeneous electron transfer involving a transition metal – quinone monolayer spontaneously adsorbed onto an electrode surface. These monolayers may play an important role in furthering our understanding of biological assemblies and may provide the basis for molecular technology. Further work such as the pH dependence of the electrochemical response is of great interest and will impact on our understanding of these materials.

6.5 References

1 Keita, B.; Nadjo, L. *J. Electroanal. Chem.* 1984, 163, 171.

2 Chen, X.; Zhuang, J.; He, P. *J. Electroanal. Chem.* 1989, 271, 257.

3 Wipf, D. O.; Wehmeyer, K. R.; Wightman, R. M. *J. Org. Chem.* 1986, 51, 4760.

4 He, P.; Crooks, R. M.; Faulkner, L. R. *J. Phys. Chem.* 1990, 94 1135.

5 Chambers, J. Q. In *The Chemistry of Quinonoid Compounds, Vol II*; Patai, S., Rappoport, Z. Eds.; Wiley: New York, 1988; Ch 12..

6 Gamage, R.S.K.A.; McQuillan, A.J.; Peake, B.M. *J. Chem. Soc. Faraday Trans.* 1991, 87, 3653.

7 Turovska, B.; Stradins, J.; Logins, J.; Strazdins, I.; Dregeris, J. *J. Electroanal. Chem.* 1995, 394, 229.

8 Vijayan, M.; Krishnan, V. *Electroanalysis*, 1995, 7 197.

9 Hubbard, A. T.; Stickney, J. L.; Soriaga, M. P.; Chia, V. K. F.; Rosasco, S. D.; Schardt, B. C.; Solomun, T.; Song, D.; White, J. H.; Wieckowski, A. *J. Electroanal. Chem.* 1984, 168, 43.

10 Stern, D. A.; Laguren-Davidson, L.; Frank, D. G.; Gui, J. Y.; Lin, C.-H.; Lu, F.; Salaita, G. N.; Walton, N.; Zapien, D. C.; Hubbard, A. T. *J. Am. Chem. Soc.* 1989, 111, 877.

11 Creager, S. E.; Weber, K. *Langmuir*, 1993, 9, 844.

12 Forster, R. J.; Faulkner, L. R. *J. Am. Chem. Soc.* 1994, 116, 5444.

13 Forster, R. J.; Faulkner, L. R. *J. Am. Chem. Soc.* 1994, 116, 5453.

14 Hamelin, A. *J. Electroanal. Chem.*, 1992, 329, 247.

15 Chidsey, C.E.D.; Bertozzi, C.R.; Putvinski, T.M.; Mujsce, A.M. *J. Am. Chem. Soc.* 1990, 112, 4301.

16 Chidsey, C.E.D. *Science* 1991, 251, 919.

17 Forster, R. J. *J. Electrochem. Soc.* 1997, 144, 1165

18 Moret, E. E.; de Boer, M.; Hilbers, H.W.; Tollenaere, J. P.; Janssen, L. H. M.; Holthuis, J. J .M.; Driebergen, R. J.; Verboom, W.; Reinhoudt, D. N. *J. Med. Chem.*1996, 39, 720.

19 Haung, Z.-H.; Chen, Y.-N.; Menon, K.; Teicher, B. A. *J. Med. Chem.* 1993, 36, 1797.

20 Saito, H.; Hirata, T.; Kasai, M.; Fujimoto, K.; Ashizawa, T.; Morimoto, M.; Sato, A. *J. Med. Chem.* 1991, 34, 1959.

21 Kuo, S.C.; Ibuka, T.; Huang, L-J.; Lien, J.-C.; Yean, S.-R.; Huang, S.-C.; Lednicer, D.; Morris-Natschke, S.; Lee, K.-H. *J. Med. Chem.* 1996, 39, 1447.

22 Skibo, E.B.; Schulz, W.G. *J. Med. Chem.* 1993, 33, 3050.

23 Breslin, D. T.; Schuster, G. B. *J. Am. Chem. Soc.* 1996, 118, 2313.

24 Itoh, S.; Ogino, M.; Fukui, Y.; Murao, H.; Komatsu, M.; Ohshiro, Y.; Inoue, T.; Kai, Y.; Kasai, N. *J. Am. Chem. Soc.* 1993, 115, 9960.

25 Barisci, J. N.; Wallace, G. G. *Electroanalysis* 1992, 4, 439.

26 Davidson, V. L.; Jones, L. H. *Anal. Chim. Acta* 1991, 249, 235.

27 Wagner, R. W.; Brown, P. A.; Johnson, T. E.; Lindsey, J. S. *J. Chem. Soc. Chem. Comm.* 1991, 1463.

28 Saika, T.; Iyoda, T.; Honda, K.; Shimidzu, T. *J. Chem. Soc. Perkin Trans.* 1993, 1181.

29 Joulié, L. F.; Schatz, E.; Ward, M. D.; Weber, F.; Yellowlees, L. J. *J. Chem. Soc. Dalton Trans.* 1994, 799.

30 Lorenzo, E.; Sánchez, L.; Pariente, F.; Tirado, J.; Abruña, H. D. *Anal. Chim. Acta* 1995, 309, 79.

31 Kimachi, T.; Tamura, Y.; Bessho, K.; Yoneda, F. *J. Chem. Soc. Perkin Trans.* 1993, 6, 697.

32 Slavcheva, E.; Sokolova, E.; Raicheva, S. *J. Electroanal. Chem.* 1993, 360, 271.

33 Wang, P.; Martin, B. D.; Parida, S.; Rethwisch, D. G.; Dordick, J. S. *J. Am. Chem. Soc.* 1995, 117, 12885.

34 Soriaga, M. P.; Hubbard, A. T. *J. Am. Chem. Soc.* 1982, 104, 2742.

35 Zapien, D. C.; Gui, J. Y.; Stern, D. A.; Hubbard, A. T. *J. Electroanal. Chem.*, 1992, 330, 469.

36 Soriaga, M. P.; Hubbard, A. T. *J. Am. Chem. Soc.* 1982, 104, 3937.

37 Stern, D. A.; Laguren-Davidson, L.; Frank, D. G.; Gui, J. Y.; Lin, C.-H.; Lu, F.; Salaita, G. N.; Walton, N.; Zapien, D. C.; Hubbard, A. T. *J. Am. Chem. Soc.* 1989, 111, 877.

38 Soriaga, M. P.; Hubbard, A. T. *J. Phys. Chem. Soc.* 1984, 88, 1089.

39 Yee, E. L.; Cave, R. J.; Guyer, K. L.; Tyma, P. D.; Weaver, M. J. *J. Am. Chem. Soc.* 1979, 101, 1131.

40 Forster, R. J. Ph.D. Thesis, *Dublin City University*, 1990.

41 Clarke, A. P. Ph.D. Thesis, *Dublin City University*, 1992.

42 Forster, R. J.; Vos, J. G. *J. Electroanal. Chem.* 1991, 314, 135.

43 Laviron, E. *J. Electroanal. Chem.*, 1974, 52, 395.

44 Brown, P.; Anson, F. C. *Anal. Chem.*, 1977, 49, 158.

45 Feldberg, S. W.; Rubinstein, I.; *J. Electroanal. Chem.* 1988, 240, 1.

46 Bard, A. J.; Faulkner, L. R. Electrochemical Methods : Fundamentals and Applications, Wiley, New York, 1980.

47 Finklea, H. O.; Hanshew, D. D. *J. Am. Chem. Soc.* 1992, 114, 3173.

Chapter 7

Concluding Remarks

7.1 Conclusions

Many important and interesting processes occur at the electrode-solution interface. Some of these processes include corrosion of metals, charging of batteries, electroplating of metals, and the operation of electroanalytical sensors. Scientists have long been interested in electrochemical interfaces because of their importance in generating and storing electrical energy and for synthesis. Therefore, a major research focus in modern electrochemistry involves the deliberate modification of the electrode-solution interface.

Structurally well defined films on solid surfaces allow experimentalists to simplify and model a large variety of interfacial phenomena that are often difficult to study at bare electrodes. Well ordered films offer the possibility of precise control of spacing and orientation on a molecular level, a feature of current interest in electron transfer reactions. If it is assumed that the local microenvironment at the electrode surface can be controlled, then the sensitivity and/or specificity of electrode reactions can be influenced. This control may provide fundamental information on the mechanisms of interfacial electron transfer and of electron and ion transport in thin films, as well as advancing electroanalytical chemistry.

Experimental progress has been accelerated by recent advances in the technology of surface characterisation, including the emergence of various surface sensitive techniques based upon spectroscopy, diffraction of electrons and protons, and electrochemistry. Virtually any combination of substrate and adsorbate can now be studied. These advances in experimental capabilities, instrumentation, and electrode dimensions have allowed electrochemical experiments to be carried out on the nanosecond timescale. Recent work has focussed on surface and adsorbed layer structure, elemental composition, purity, stoichiometry, packing density, molecular characteristics, surface chemical bonding, surface layer chemical stability, electrochemical reactivity and mechanistic aspects of heterogeneous electron transfer. Surface electrochemical research is contributing to progress in the interfacial sciences. Studies of the electrical double layer are guiding the development of interfacial theory and have stimulated interest in the role of the electrical double layer in electrode kinetics. Intriguing facts concerning the

electrochemistry of solvents, ions, solutes, and the chemisorption of organic molecules have been revealed.

Redox active monolayers represent an important group of materials which can be used for a variety of functions. The now popular technique of self-assembly has been widely applied in order to provide redox active films. These films provide a high degree of structural order that can be manipulated to provide films of various thickness, densities and compositions. In this work, we have focussed on using these monolayers to probe fundamental issues such as the thermodynamics and kinetics of electron transfer between the underlying electrode and the electroactive redox centre within the adsorbed monolayer. We have investigated the effects of pH and electrolyte on the electrochemical response of the layers, the strength with which these monolayers are adsorbed to the surface, and the heterogeneous electron transfer dynamics for these monolayers. We have examined these aspects of electron transfer due to their importance in the development of new materials for molecular electronics.

The field of molecular electronics ranges from well-defined and well-understood phenomena such as nonlinear optical responses, to the tantalising, and conceptually more difficult, areas of computing and information storage at the molecular level. Supramolecular assemblies, constructed using single electroactive molecules as building blocks, offer a striking way to create electrically conducting materials whose organised architecture makes them suitable for developing molecular electronic devices. The role of electron transfer in molecular electronics, biological processes, photophysics, and sensor technology has received much attention over the past two decades. Depositing monomolecular films using self-assembly or spontaneous adsorption approaches represents an important approach to controlling the properties of the electrode/solution interface. Immobilised, redox-active monolayers using highly ordered materials offer the possibility of being able to control electron transfer distance, mass transfer effects, and the local microenvironment, thus enabling the processes that influence heterogeneous electron transfer to be examined.

Progress toward the strategic goal of developing molecular electronic materials demands not only the development of new synthetic approaches that yield highly ordered materials but also careful attention to those elementary processes that dictate the rate of heterogeneous electron transfer across electrode/monolayer interfaces. However, it is only recently that it has been possible to *directly* probe those factors that govern the rate of electron transfer processes that are complete within a few billionths of a second. In fact, coupling recent advances in the design and fabrication of microelectrodes and electrochemical instrumentation that operate on a nanosecond timescale, with chemical systems that are organised on a molecular level, promise to revolutionise investigations into electron transfer processes.

Toward the objective of understanding those factors that influence heterogeneous electron transfer, we have formed redox active monolayers by spontaneous adsorption onto clean platinum, gold and mercury electrodes. These adsorbed monolayers are stable for long periods at elevated temperatures allowing those factors that control the rate and pathway for electron transfer across electrode/monolayer interfaces to be probed in considerable detail.

Monolayers of the types used in this research are, in general, relatively simple to synthesise and characterise as shown in Chapter 2, and spontaneously adsorb onto a variety of substrates. We have used cyclic voltammetry and chronoamperometry, performed on microsecond timescales, to probe the structure of the monolayer modified interfaces. High speed chronoamperometry has also been used to investigate the dynamics of heterogeneous electron transfer across the electrode/monolayer interface and to determine the strength with which these monolayers are adsorbed. These electrochemical techniques can be used to investigate the suitability of various theoretical models such as the Butler-Volmer and Marcus theories of electron transfer. Although these theories have been in circulation for several decades it is only in recent times that synthetic, instrumental and experimental techniques have been available to test them in a detailed manner. Although the electrode/monolayer systems examined in Chapters 4 and 5 might appear uncomplicated, it is these types of systems that are required to probe existing theories before more complicated model systems such as that described in Chapter 6 can be examined in a meaningful manner.

In general, all of the monolayer assemblies studied in this work have proved stable as a function of time and temperature. The surface confined electrochemical response of the films has been unusually ideal, with peak-to-peak separations as low as 8 mV observed for surface confined anthraquinone-2,7-disulphonic acid. Monolayers of this anthraquinone exist in several forms as a function of electrolyte pH, and further work on the rates of heterogeneous electron transfer as a function of pH should prove illuminating. Investigations of this type are especially important for improving our understanding of those processes that limit the rate of electron transfer within biological assemblies where subtle changes in the chemical microenvironment surrounding the redox site can dramatically alter the electron transfer rates.

The free energy of adsorption of 2,7-AQDS onto mercury electrodes has also been studied. Probing the potential dependence of the interfacial capacitance as the bulk concentration, and hence surface coverage, of a surface active molecule is systematically varied, can provide a useful insight into potential dependent adsorption of electroactive species. We have used high speed chronoamperometry time resolve capacitive and Faradaic current contributions so that we may obtain a useful insight into the potential dependent adsorption of electroactive species that are reversibly adsorbed onto electrode surfaces. Our study has shown that the free energy of adsorption anthraquinone-2,7-disulphonic acid monolayers appears to be relatively independent of oxidation state but dependent on interactions between the oxidised and reduced states of the species at the formal potential.

Monolayers of $[Os(bpy)_2(p3p)_2]^{2+}$, also exhibit nearly ideal electrochemical responses yet display different adsorption and desorption mechanisms from platinum electrodes. Desorption from both electrodes is characterised by an exponential decrease in coverage, indicating a first order process, desorption from gold being approx. twice as fast as that from platinum. Chronoamperometry reveals that the rate of electron transfer is of the order of 10^4 s^{-1}, which is an order of magnitude faster than electron transfer associated with either of the quinone systems investigated. The unusual ideality of the chronoamperometric response has allowed us probe the nature of the activation barrier to electron transfer, and the degree of electronic coupling between the remote redox centres and the microelectrode, in considerable detail.

Measurements of the potential dependence of the heterogeneous electron transfer rate constant, k, suggest that electron transfer occurs via a through-space rather than a through-bond tunnelling mechanism and that it depends on the pH of the contacting solution. By determining the free energy of activation using two independent methods, we have shown that changes in the pre-exponential factor rather than $\Delta G^{\neq}$ cause this pH sensitivity. It appears that the interaction of the highly positively charged protonated complexes with the interfacial electric field causes the through-space electron transfer distance to increase, perhaps by altering the tilt angle between the adsorbate and the electrode surface or by causing the methylene spacer groups to become extended.

Although the change in heterogeneous electron transfer rate constant on going from nonprotonated to fully protonated monolayers is less than an order of magnitude, this pH induced "conformational gating" of the electron transfer rate offers the possibility of developing pH triggered electrical switches. We expect that fundamental investigations focusing specifically on the role that the local medium, particularly the bridging structure linking the reactants, plays in dictating the rate and pathway for electron transfer, will make it possible to design molecular systems that maximise electron transfer efficiency and their sensitivity to specific chemical triggers.

While considerable attention has been focused on the dynamics of electron transfer within monolayers, there have been relatively few reports on the electrochemical properties of monolayers in which electron and proton transfer are coupled. Toward this objective, we have adsorbed an alizarin based transition metal complex on carbon fibre microelectrodes and examined its electrochemical properties. We have combined an anthraquinone similar to that used in earlier work with a transition metal complex also similar to that employed earlier. The resulting complex provides us possibilities for molecular electronic materials in which the electron transfer is pH, temperature and possibly light modulated. This system proved intriguing and demonstrates just how difficult it is to examine electron transfer issues in complicated assemblies. That the surface confined voltammetric response of these monolayers is well behaved is encouraging. However, the

potential dependent electron transfer rates provide an electron transfer coefficients which disagree with those determined from normal pulse voltammetry for the solution phase species. Reaction entropies and activation enthalpies were determined and one of the first accounts of the reorganisation energy for a surface confined transition metal-quinone complex has been provided.

The use of model systems to elucidate the factors that influence the thermodynamics and kinetics of heterogeneous electron transfer is necessary to test existing theories and to further our knowledge of the electrode/monolayer interface. It is hoped that through this work, some insight into those factors that influence electron transfer within these ordered materials has been imparted.

Appendix 1

NMR of $[Os(bpy)_2Cl_2]$ in DMSO.

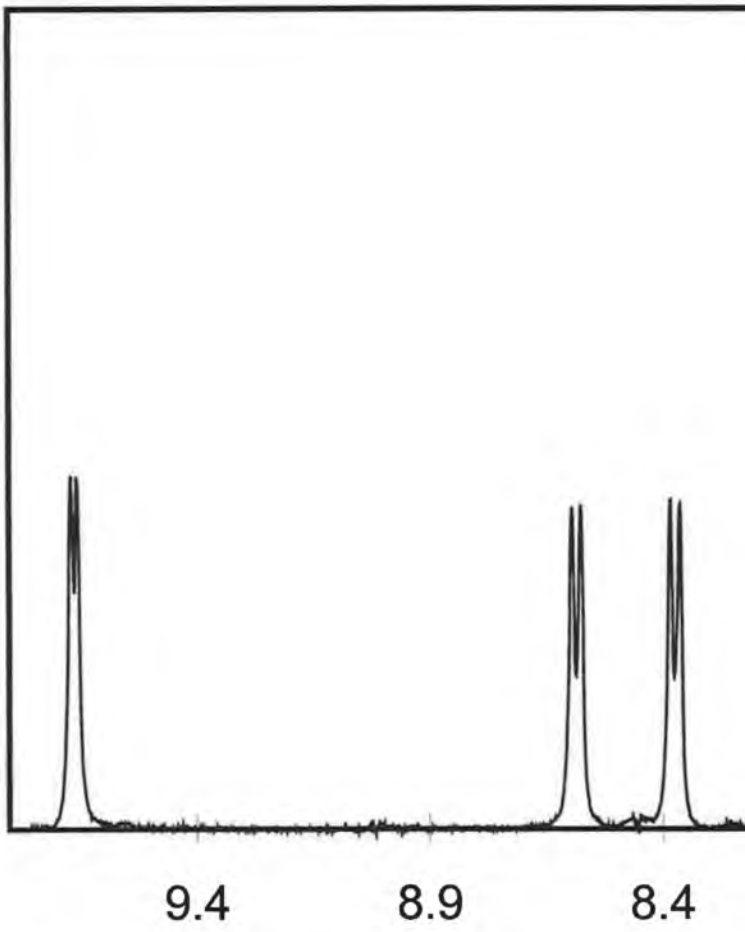

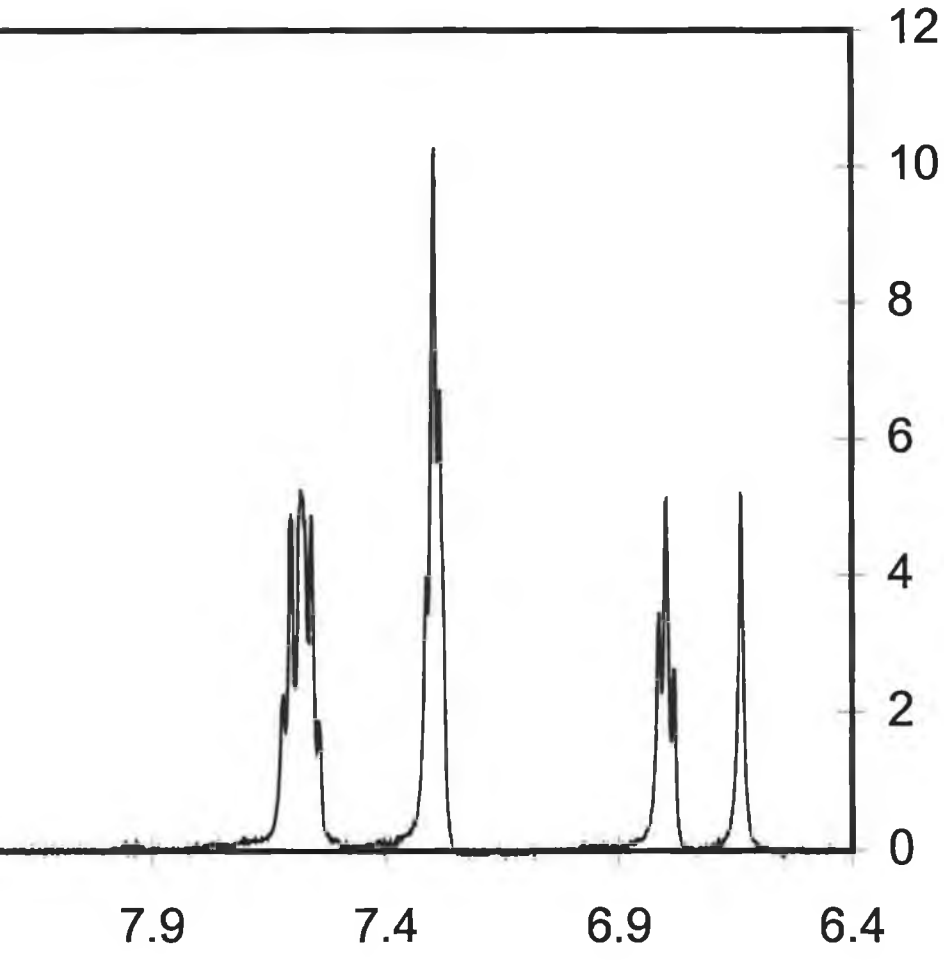
12
10
8
6
4
2
0
7.9
7.4
6.9
6.4
ppm

NMR of $[Os(bpy)_2(p3p)_2]^{2+}$ in DMSO.

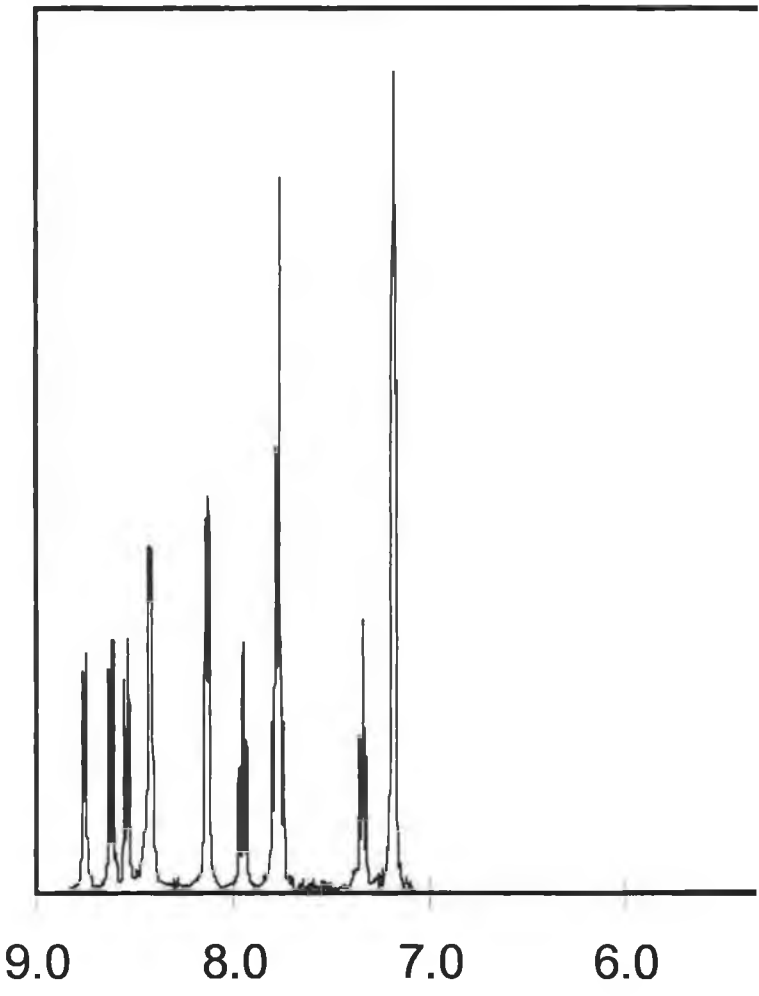

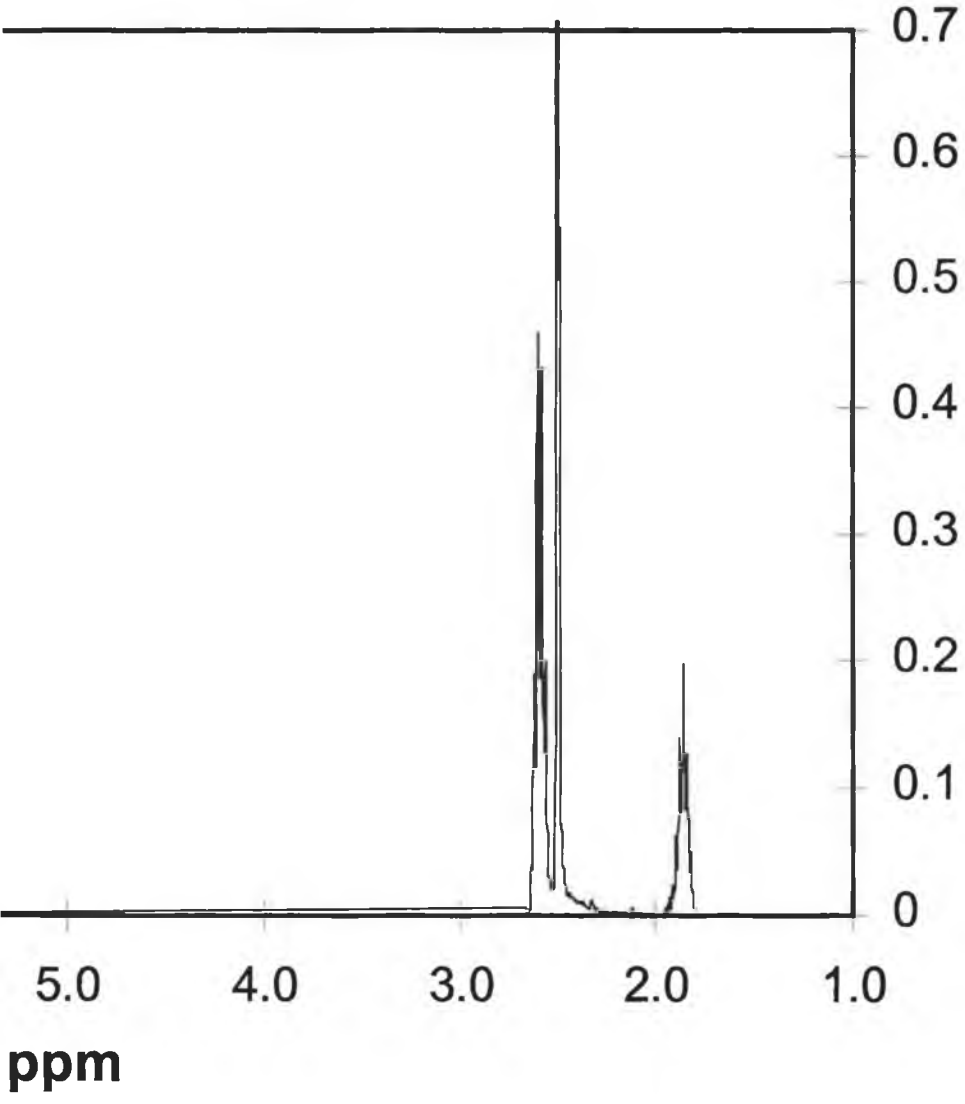
0.7
0.6
0.5
0.4
0.3
0.2
0.1
0
5.0
4.0
3.0
2.0
1.0
ppm

NMR of Alizarin in DMSO.

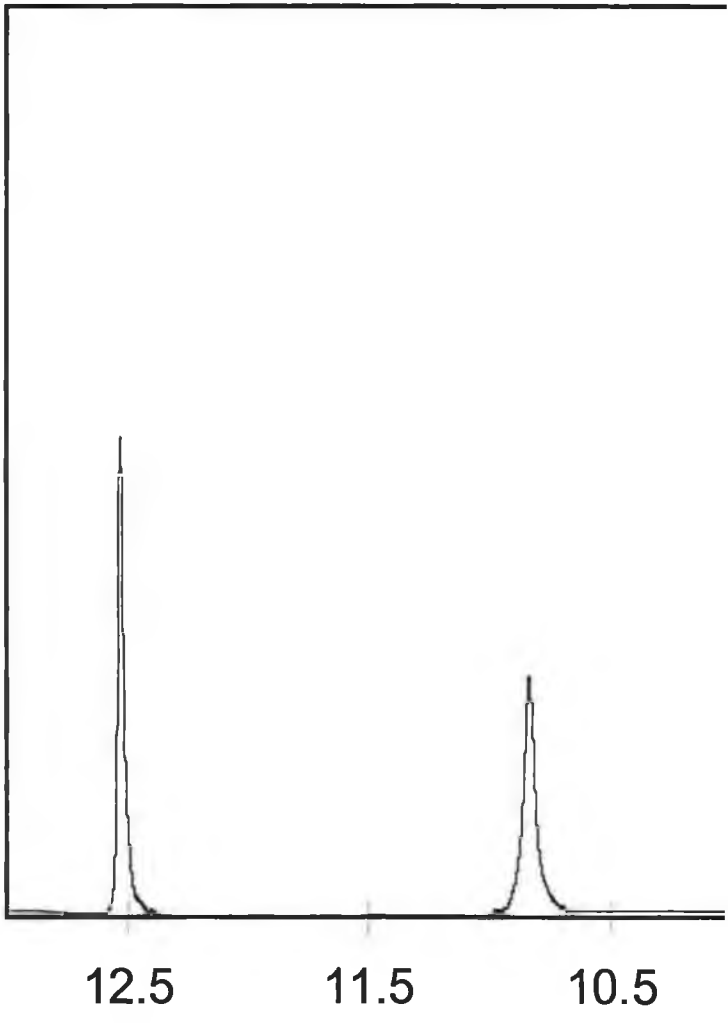

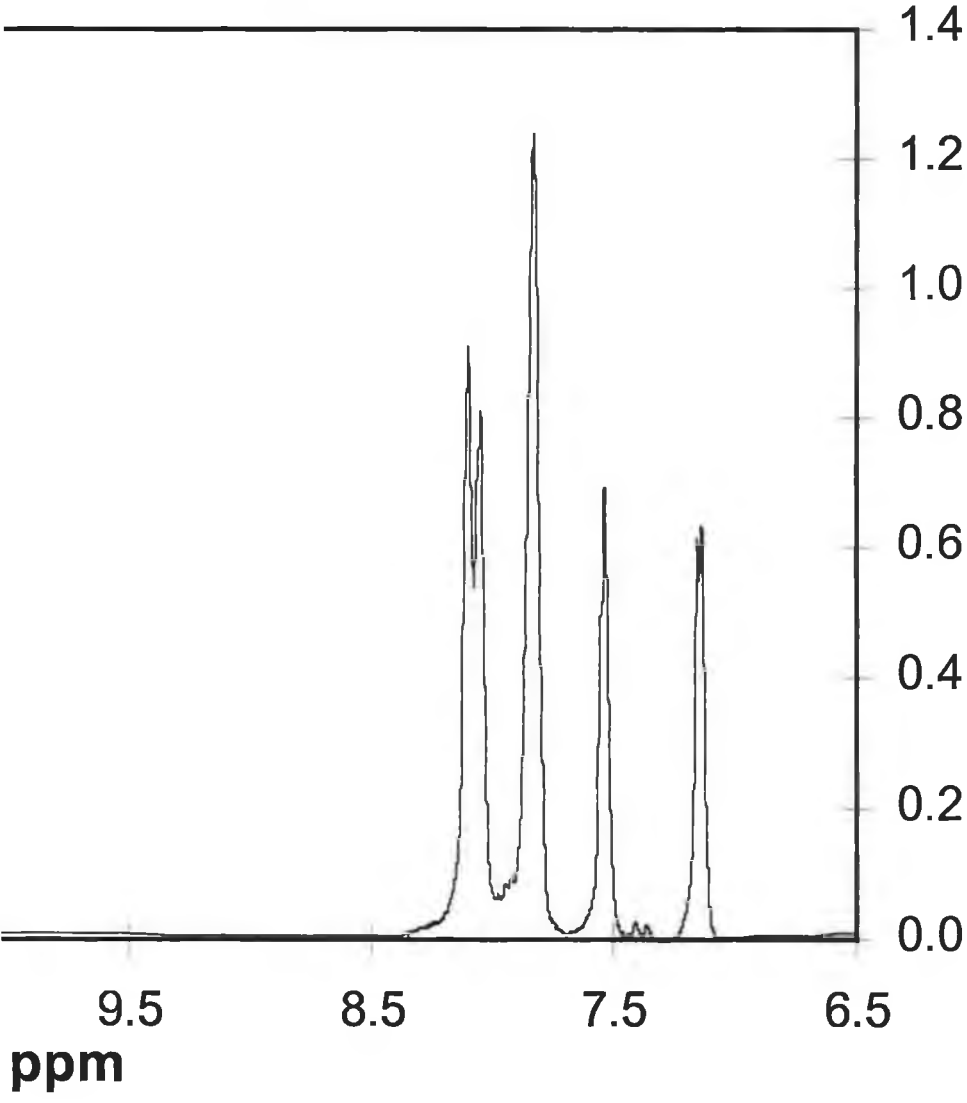
1.4
1.2
1.0
0.8
0.6
0.4
0.2
0.0
9.5
8.5
7.5
6.5
ppm

NMR of $[Ru(bpy)_2Cl_2]$ in DMSO.

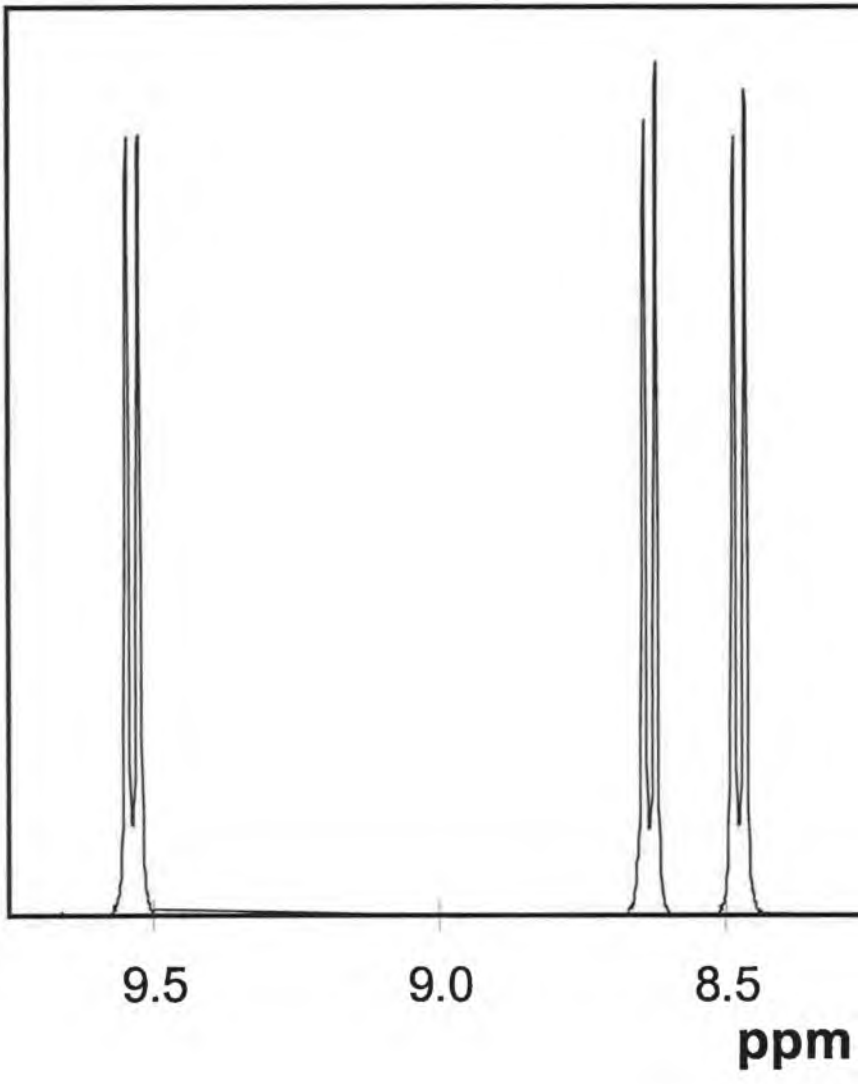

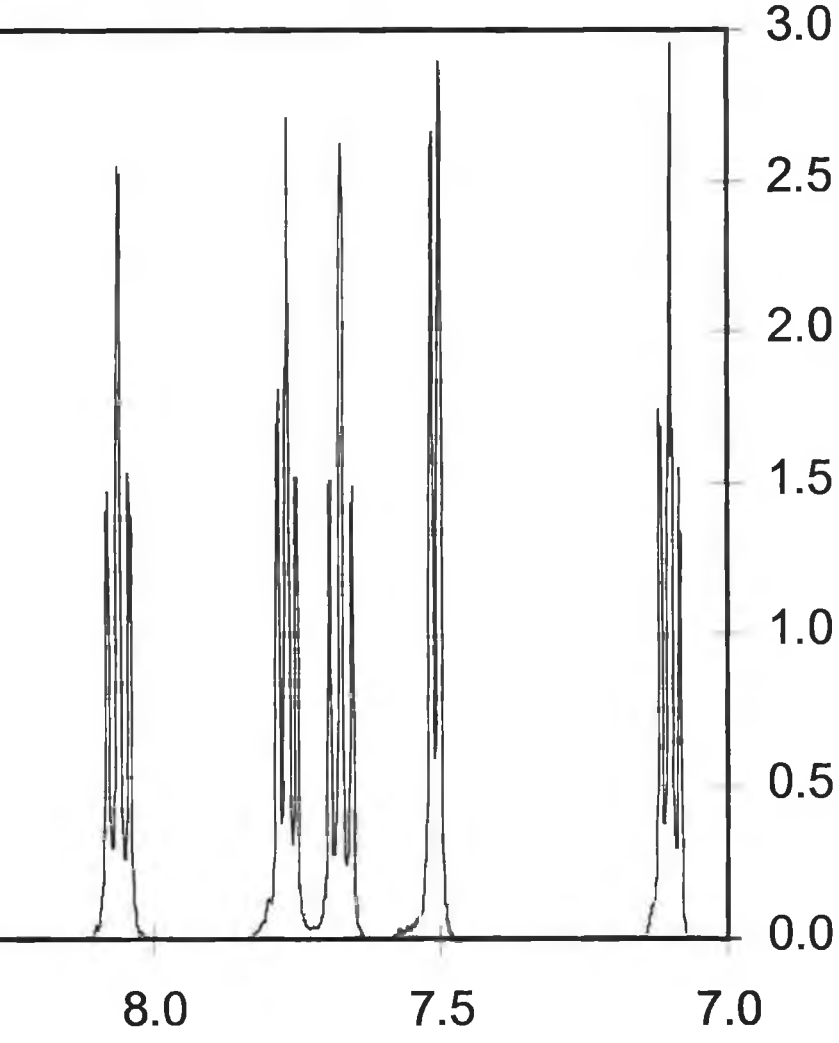
3.0
2.5
2.0
1.5
1.0
0.5
0.0
8.0
7.5
7.0

NMR of $QCat^{2-}$Ru-1,2 in DMSO.

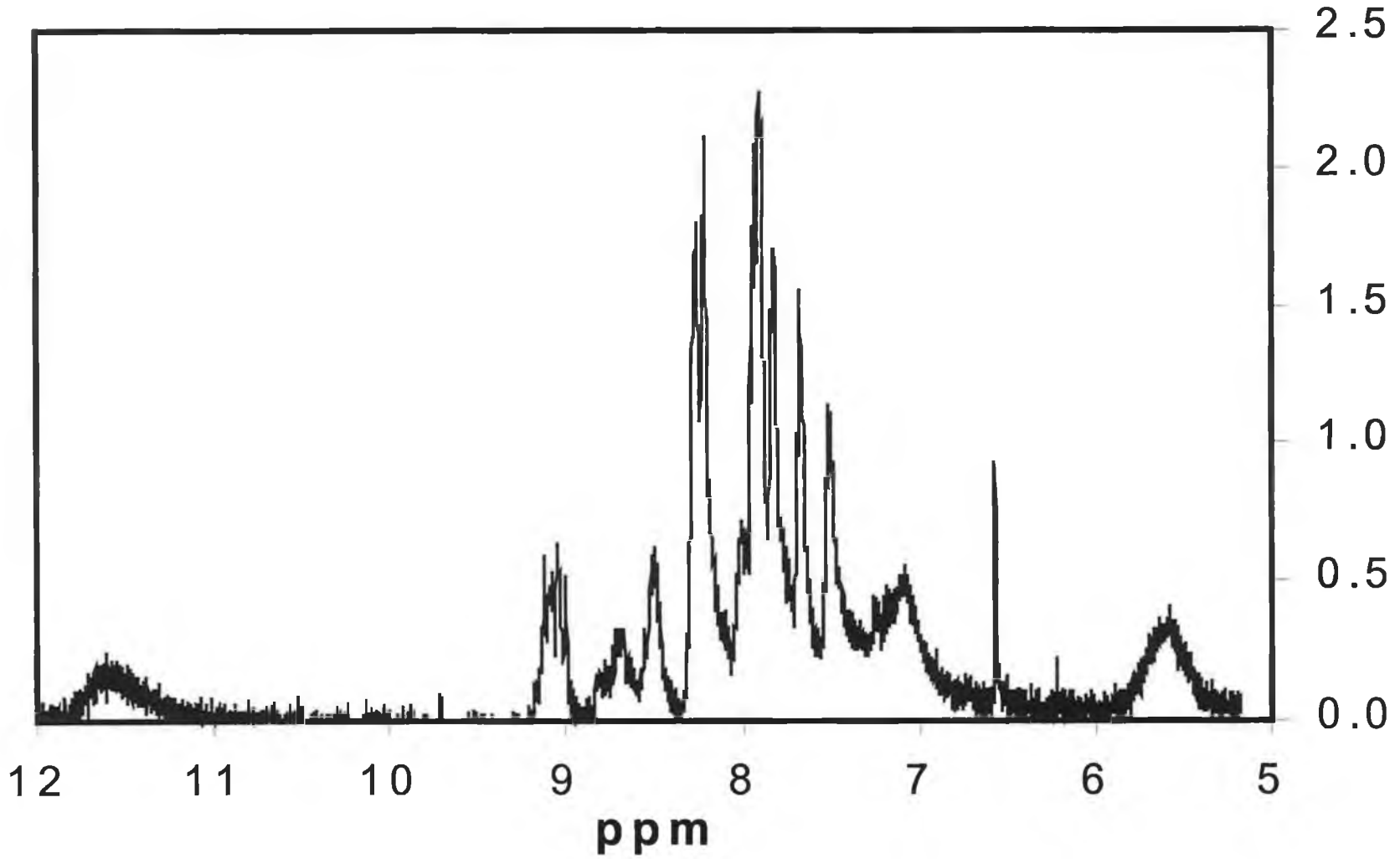

NMR of Anthraquinone-2,7-disulphonic acid in D_2O.

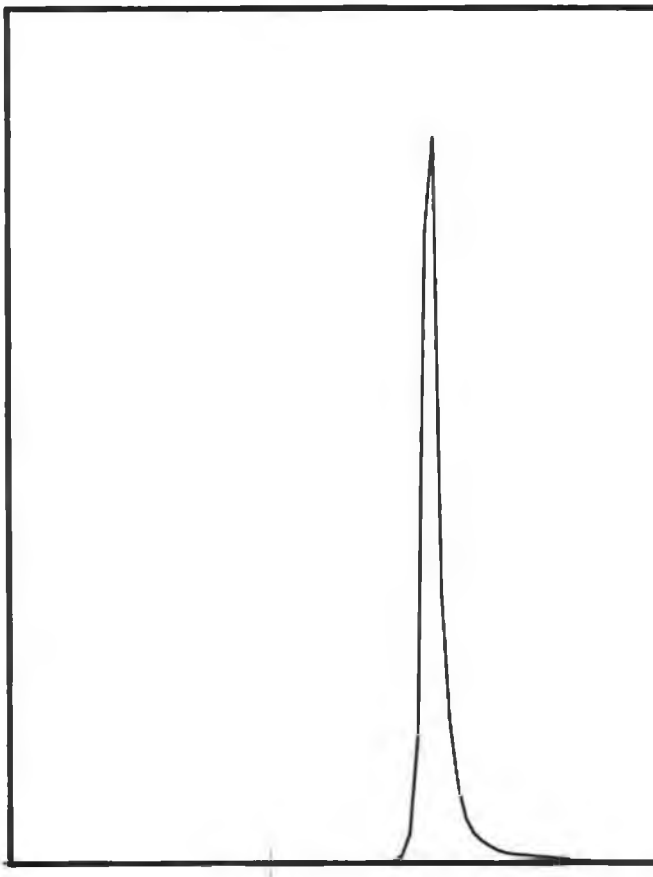

8.15

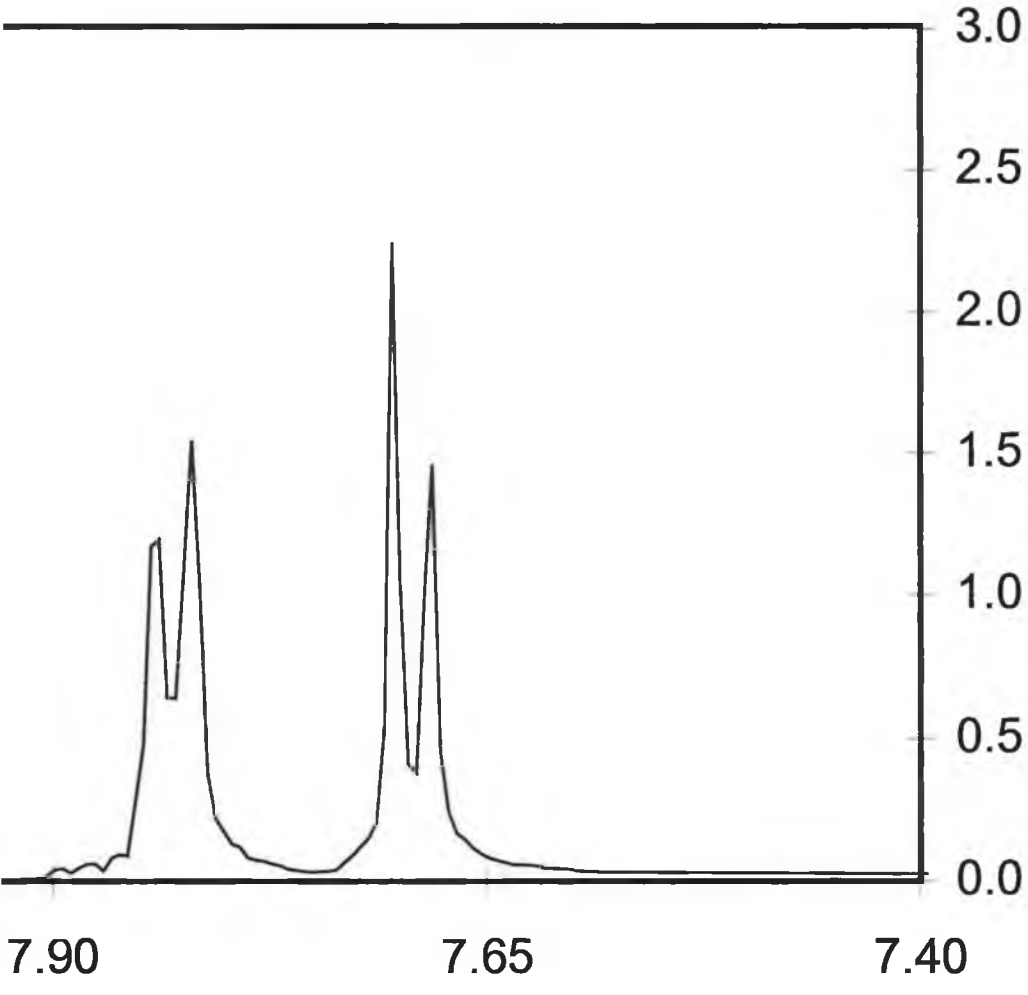
3.0
2.5
2.0
1.5
1.0
0.5
0.0
7.90
7.65
7.40
ppm

Appendix 2

pH Modulated Heterogeneous Electron Transfer across Metal/Monolayer Interfaces

Robert J. Forster* and Joseph P. O'Kelly

School of Chemical Sciences, Dublin City University, Dublin 9, Ireland

Received: July 21, 1995; In Final Form: October 15, 1995[⊗]

Dense monolayers of $[Os(bpy)_2(p3p)_2]^{2+}$, where bpy is 2,2′-bipyridyl and p3p is 4,4′-trimethylenedipyridine, have been formed by spontaneous adsorption onto clean platinum microelectrodes. Cyclic voltammetry of these monolayers is nearly ideal, and the area occupied per molecule suggests that only one of the p3p ligands binds to the electrode surface, the other being available for protonation. Chronoamperometry conducted on a microsecond time scale has been used to measure the heterogeneous electron transfer rate constant k for the $Os^{2+/3+}$ redox reaction. For electrolyte concentrations above 0.1 M, heterogeneous electron transfer is characterized by a single unimolecular rate constant (k/s^{-1}). Tafel plots of the dependence of ln k on the overpotential η show curvature, and larger cathodic than anodic rate constants are observed for a given absolute value of η. This response is consistent with electron transfer occurring via a through-space tunneling mechanism. Plots of k vs pH are sigmoidal, and the standard heterogeneous rate constant k° decreases from $(6.1 \pm 0.2) \times 10^4$ to $(1.6 \pm 0.1) \times 10^4$ s^{-1} as the pH of the contacting solution is decreased from 5.05 to 1.07. When in contact with pH 5.05 electrolyte, the electrochemical enthalpy $\Delta H^\ddagger$ is 37.5 ± 2.1 kJ mol^{-1}, which decreases to 24.6 ± 1.5 kJ mol^{-1} at a pH of 1.07. The reaction entropy ΔS_{rc}° is independent of the pH over this range, maintaining a value of 82 ± 7 J mol^{-1} K^{-1}. In contrast to the behavior expected from the decrease of k with decreasing pH, the free energy of activation $\Delta G^\ddagger$ decreases with decreasing pH. The electronic transmission coefficient κ_{el}, describing the probability of electron transfer once the nuclear transition state has been reached, is considerably less than unity for all pH's investigated. κ_{el} decreases with decreasing solution pH, suggesting an increasingly weaker electronic interaction between the metallic states of the electrode and the orbitals of the redox center as the monolayer becomes protonated. These results suggest that monolayer protonation modulates the heterogeneous electron transfer rate by changing the through-space electron transfer distance. This may be caused either by a change in the tilt angle between the adsorbate and the electrode or by the methylene spacer units within the bridging ligand becoming extended, when the monolayer is protonated.

Introduction

The field of molecular electronics ranges from well-defined and well-understood phenomena such as nonlinear optical responses to the tantalizing, and conceptually more difficult, areas of computing and information storage at the molecular level.[1] Supramolecular assemblies, constructed using single electroactive molecules as building blocks, offer a striking way to create electrically conducting materials whose organized architecture makes them suitable for developing molecular electronic devices.

Progress toward this strategic goal demands not only the development of new synthetic approaches that yield highly ordered materials[2] but also careful attention to those elementary processes that dictate the rate of heterogeneous electron transfer across metal/monolayer interfaces.[3] However, it is only recently that it has been possible to *directly* probe those factors that govern the rate of electron transfer processes that are complete within a few billionths of a second. In fact, coupling recent advances in the design and fabrication of microelectrodes and electrochemical instrumentation that operate on a nanosecond time scale with chemical systems that are organized on a molecular level, promises to revolutionize investigations into electron transfer processes.[4]

Toward the objective of understanding those factors that influence heterogeneous electron transfer, we have formed osmium containing monolayers by spontaneously adsorbing $[Os(bpy)_2(p3p)_2]^{2+}$ complexes (Chart 1), where bpy is 2,2′-bipyridyl and p3p is 4,4′-trimethylenedipyridine, onto clean platinum microelectrodes. For simplicity, we denote these monolayers as $(p3p)_2$. These adsorbed monolayers are stable for long periods at elevated temperatures in aqueous perchlorate solutions allowing those factors that control the rate and pathway for electron transfer across metal/monolayer interfaces to be probed in considerable detail. Moreover, it appears that only one of the pyridine groups binds to the electrode surface, while the other is available for protonation, thus allowing chemical effects on heterogeneous electron transfer to be explored.

CHART 1

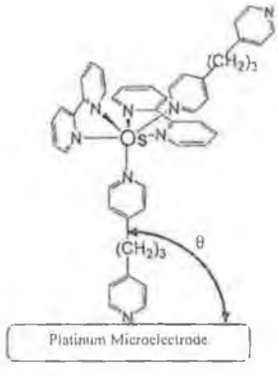

We have used chronoamperometry, performed on a microsecond time scale, to probe the structure of the modified interface, focusing particularly on the extent to which solvent and ions permeate the interior of the monolayer. These investigations are doubly important, since they provide an insight into the relative perfection of the monolayer and allow one to

* To whom correspondence should be addressed.

[⊗] Abstract published in *Advance ACS Abstracts,* January 15, 1996.

0022-3654/96/20100-3695$12.00/0

probe the interfacial potential distribution.[5] High-speed chronoamperometry has also been used to investigate the dynamics of heterogeneous electron transfer across the electrode/monolayer interface. When the supporting electrolyte concentration is greater than about 0.1 M, these chronoamperometric responses are remarkably well-behaved, with heterogeneous electron transfer being characterized by a single rate constant over more than two lifetimes.

Significantly, the solution pH modulates the rate of heterogeneous electron transfer, apparently by protonating the pyridine moiety of the unbound p3p ligand. We have probed the origin of this pH sensitivity by systematically probing the pH dependence of the free energy of activation $\Delta G^{\ddagger}$ and the degree of electronic coupling between the remote redox centers and the electrode. Surprisingly, our investigation suggests that changes in the pre-exponential factor with pH rather than the activation barrier cause the heterogeneous electron transfer rate constant to depend on the extent of monolayer protonation.

Investigations of this type are especially important for improving our understanding of those processes that limit the rate of electron transfer within biological systems where subtle changes in the chemical microenvironment surrounding the redox site can dramatically alter the electron transfer rates.[6]

Experimental Section

Materials. The surface active complex, $[Os(bpy)_2(p3p)_2]^{2+}$, was prepared by first placing 50 mg (0.09 mmol) of $[Os(bpy)_2Cl_2]$ in 40 cm^3 of methanol followed by 10 min reflux to ensure complete dissolution. A solution of 70 mg (0.036 mmol) of 4,4′-trimethylenedipyridine (98%, Aldrich) dissolved in 5 cm^3 of methanol, together with 150 cm^3 of milli-Q water were added, and the resulting solution was refluxed for 15 h. After approximately 10−12 h the color of the solution changed from red-brown to dark green. The progress of the reaction was monitored using HPLC and cyclic voltammetry. After the reaction was complete, the volume was reduced to 5 cm^3 by rotary evaporation. Ammonium hexafluorophosphate (95+%, Aldrich) was then added, and the dark green product was collected by filtration and washed with diethyl ether. The product was recrystallized from aqueous methanol to give dark green-black crystals, yield 66 mg, 82%. The complex was characterized using IR, UV−vis, NMR, and cyclic voltammetry.

Apparatus. Electrochemical cells were of conventional design and were thermostated within ±0.2 °C using a Julabo F10-HC refrigerated circulating bath. All potentials are quoted with respect to a BAS Ag/AgCl gel-filled reference electrode, the potential of which was 35 mV more positive than that of the saturated calomel electrode (SCE). Cyclic voltammetry was performed using an EG&G Model 273 potentiostat/galvanostat and a conventional three-electrode cell. All solutions were degassed using nitrogen, and a blanket of nitrogen was maintained over the solution during all experiments. The degree of monolayer protonation was altered by systematically varying the pH of the contacting electrolyte solution over the range 5.1 to 1.1 by addition of concentrated $HClO_4$ to $LiClO_4$ solutions. These solutions were not pH buffered to avoid difficulties with competitive adsorption effects from buffer ions.

As described previously,[7] a custom built function generator−potentiostat, with a rise time of less than 10 ns, was used to apply potential steps of variable pulse width and amplitude directly to a two-electrode cell. A Pt foil and an Ag/AgCl reference electrode were combined to form a counter electrode. The foil lowered the resistance and provided a high-frequency path.

For the temperature resolved experiments, a nonisothermal cell was used in which the reference electrode was isolated from the main compartment by a salt bridge and held at constant temperature. The nonisothermal salt bridge contained saturated KCl since it has a low resistance, and the salt remains soluble at the lowest temperature employed (−5 °C). The high electrolyte concentration and the design of the bridge minimize any systematic error in the reported temperature effects on $E^{o\prime}$ due to changes in the liquid junction potential with temperature.[8]

Microelectrodes were fabricated from platinum microwires (Goodfellow Metals Ltd.) of radii between 5 and 25 μm by sealing them in soft glass using a procedure described previously.[4b,9] Microdisk electrodes were exposed by removing excess glass using 600 grit emery paper followed by successive polishing with 12.5, 5, 1, 0.3, and 0.05 μm alumina. The polishing material was removed between changes of particle size by sonicating the electrodes in deionized water for at least 5 min. The polished electrodes were electrochemically cleaned by cycling in 0.1 M $HClO_4$ between potential limits chosen to first oxidize and then to reduce the surface of the platinum electrode. Excessive cycling was avoided in order to minimize the extent of surface roughening. Finally, the electrode was cycled between −0.300 and +0.900 V in 0.1 M $NaClO_4$ until hydrogen desorption was complete.

The real surface area of the electrodes was found by calculating the charge under the oxide or hydrogen adsorption−desorption peaks.[10] Typically, the surface roughness factor was between 1.3 and 1.6. Obtaining the real, as opposed to the projected or geometric, surface area of the electrodes is important if the area occupied per molecule is to be accurately measured.

RC cell time constants, measured in blank electrolyte solution, were between 0.03 and 3 μs, depending on the electrode radius and the supporting electrolyte concentration. The interfacial kinetics were measured only at times greater than about 5−10 RC. In chronoamperometry experiments, the initial potential was either 0.000 or +1.000 V, depending on whether oxidation or reduction kinetics were being probed.

Spontaneously adsorbed monolayers were typically formed by immersing the electrodes in a methanol/water solution of the metal complex for 8−12 h. No precautions were taken to exclude oxygen during monolayer formation. Before electrochemical measurements were made, the modified electrodes were rinsed with the electrochemical solvent to remove unbound material. Subsequent measurements were performed in blank electrolyte solutions.

Results and Discussion

General Electrochemical Properties. Figure 1 shows representative cyclic voltammograms for a spontaneously adsorbed $(p3p)_2$ monolayer, where the supporting electrolyte is 0.1 M $LiClO_4$ (pH = 4.8) that does not contain any dissolved $[Os(bpy)_2(p3p)_2]^{2+}$. This voltammetric response is consistent in all respects with that expected for an electrochemically reversible reaction involving a surface-confined species.[11] For example, the peak shapes are independent of scan rate, at least over the range of 1−50 V/s, and the peak height scales linearly with the scan rate v, unlike the $v^{1/2}$ dependence expected for a freely diffusing species. Therefore, it appears that the osmium complex adsorbs onto the surface of the platinum microelectrode to give an electroactive film. Where there are no lateral interactions between surface confined redox centers and a rapid equilibrium is established with the electrode, a zero peak-to-peak splitting (ΔE_p) and a fwhm of 90.6 mV are expected for a reaction involving the transfer of a single electron. As discussed previously for $[Os(bpy)_2Cl(pNp)]^+$ monolayers,[7] where pNp is 4,4′-bipyridyl or 1,2-dipyridylethane, we consis-

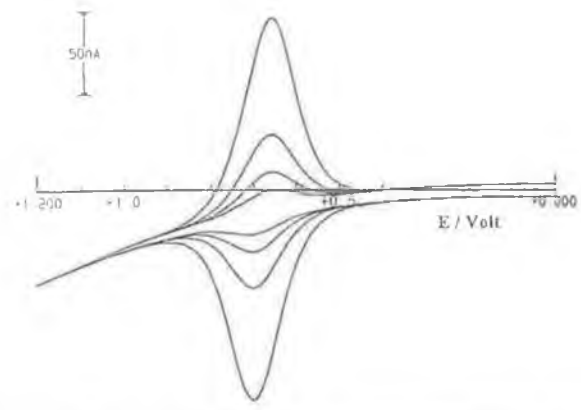

Figure 1. Scan rate dependence of cyclic voltammetry for a spontaneously adsorbed $(p3p)_2$ monolayer. The scan rates are (top to bottom) 50, 20, 10, and 5 V/s. The surface coverage is 9.8×10^{-11} mol cm^{-2}. The supporting electrolyte is 0.1 M $LiClO_4$ at a pH of 4.8. The radius of the platinum microelectrode is 25 μm. The cathodic currents are up, and the anodic currents are down. Each cycle begins at the negative limit.

tently observe a nonzero ΔE_p, even at low scan rates; e.g., ΔE_P is 12 ± 3 mV at a scan rate of 500 mV/s. Feldberg has interpreted nonzero peak-to-peak splitting in terms of unusual quasi-reversibility (UQR).[12] In this model, hysteresis is observed in cyclic voltammetry because some rate processes, e.g., heterogeneous electron transfer, ion movement, changes in monolayer structure that accompany redox switching, etc., are slow compared to the time scale of the experiment. We do not consider this issue in detail here except to note that neither heterogeneous electron transfer or double layer assembly (vide infra) limit the voltammetric response at these scan rates. In general, the voltammetric response is consistent with that expected for a rapid, reversible electron transfer to an immobilized redox active species. The peak height and peak area of the voltammograms do not change by more than 15% when cycled repeatedly over an 10 h period at temperatures up to 40 °C, indicating that the monolayers are both electrochemically and thermally stable. We observe only a 20−30 mV difference between the formal potentials of the solution-phase model compound, $[Os(bpy)_3]^{2+}$, and the monolayer, suggesting that the redox centers within the monolayer are solvated.

The total charge introduced or withdrawn to reduce or oxidize the monolayer can be found from the area under the voltammetric peak after correcting for the background charging current. This charge, together with the real surface area, can then be used to calculate the surface coverage, or the number of moles of $[Os(bpy)_2(p3p)_2]^{2+}$ per cm^2. The surface coverage provides important information about the packing density of the monolayer and may provide a limited insight into the way that the complex adsorbs onto the electrode surface. This is important since the cis configuration of the bpy ligands makes it possible for adsorption to occur through one or both of the p3p ligands.

The surface coverage, Γ, as experimentally determined from the area under the cyclic voltammetric wave, was found to be $(1.05 \pm 0.08) \times 10^{-10}$ mol cm^{-2}, corresponding to an area occupied per molecule of 166 ± 12 Å^2. When the additional contributions to the molecular volume are considered, e.g., a solvent shell or a counterion, this area of occupation is consistent with that expected for a close packed monolayer in which the radius of the metal complex (crystallographic data[13] indicate that the radii of osmium and ruthenium polypyridyl complexes are of the order of 6.7 Å), rather than the length of the bridging ligands, dictates the surface coverage. This area of occupation is smaller than that found for adsorbed $[Os(bpy)_2Cl(p3p)]^+$ complexes[7] (240 Å^2) and is indistinguishable from that found for adsorbed $[Os(bpy)_2(pyridine)(p3p)]^{2+}$ complexes,[14] both of which contain only one p3p bridging ligand. Molecular modeling of the $[Os(bpy)_2(p3p)_2]^{2+}$ complex suggests that if both p3p ligands adsorbed onto the electrode surface, then its area of occupation would be at least 214 Å^2, a value that is approximately 30% larger than that experimentally observed. These observations suggest that only one of the p3p ligands is bound to the electrode surface. This conclusion is supported by our observation (vide infra) that the heterogeneous electron transfer rate constant k depends on the pH of the contacting electrolytic solution. This pH sensitivity of k contrasts with structurally related $[Os(bpy)_2(pyridine)(p3p)]^{2+}$ monolayers where the heterogeneous electron transfer dynamics are independent of the solution pH.

As described previously,[7,15] the ideality of the electrochemical response can be further probed by using chronocoulometry to determine the redox composition as a function of the applied potential.[16] The slopes of plots of ln ([Ox]/[Red]) vs potential are independent of the pH, maintaining a value of 57 ± 3 mV/decade, as the pH of the contacting electrolyte solution is changed from 5.05 to 1.07. This slope is indistinguishable from those predicted for one electron transfer reactions by the Nernst equation,[16] confirming that the thermodynamic aspects of electron transfer at these metal/monolayer interfaces are nearly ideal under the experimental conditions employed.

The formal potential for the $Os^{2+/3+}$ redox reaction shifts from 0.638 to 0.654 V as the pH is systematically varied from 5.05 to 1.07. That $E^{\circ\prime}$ shifts in a positive potential direction indicates that protonation stabilizes the reduced state of the complex. This small shift in $E^{\circ\prime}$ is consistent with the methylene spacer groups preventing effective electronic communication between the two pyridine rings (vide infra). Moreover, the small shift in $E^{\circ\prime}$ suggests that the electrostatic effects of protonating the unbound pyridine ring are minor. This behavior probably arises because the high dielectric constant of water and the high supporting electrolyte concentration efficiently screen the charge on the pyridinium ion that is located 9−10 Å away from the osmium redox center.

Interfacial Capacitance. Probing the double layer capacitance C_{dl} gives an insight into the change in interfacial charge distribution that accompanies monolayer formation, the relative perfection of the monolayer, and perhaps its thickness.[5,7,17] Here, we have used small amplitude potential step chronoamperometry to measure the interfacial capacitance as the electrolyte concentration was systematically varied. The potential step was centered at 0.100 V where the monolayer is redox inactive, and a pulse amplitude ΔE of 25 mV was employed. The pulse amplitude is sufficiently small to allow the measured capacitance to be regarded as an approximate differential capacitance. This potential step does not change the redox composition of the monolayer, and only single exponential decays due to double layer charging were observed. This capacitive current was analyzed using a plot of ln $i_c(t)$ vs t to obtain the resistance R_u and double layer capacitance C_{dl} according to eq 1.[18]

$$i_c(t) = (\Delta E/R_u) \exp(-t/R_u C_{dl}) \quad (1)$$

For an electrochemical double layer, the differential capacitance increases with a decreasing separation between the electrode surface and the plane of closest approach for ionic charge and increases with increasing dielectric constant.[16] There are two limiting cases for the potential profile across an adsorbed monolayer.[5] First, the modified interface could be similar to a bare electrode so that all of the applied potential would be dropped close to the electrode/monolayer interface. In this case, the immobilized redox center would not experience a large

CHART 2

TABLE 1: Electrolyte Concentration Dependence of the Cell Time Constant R_uC_{dl}, Uncompensated Cell Resistance R_u, and Double Layer Capacitance C_{dl} as Measured at +0.100 V[a]

[$LiClO_4$], M	R_uC_{dl}, ns	$10^{-3}R_u$, Ω	C_{dl}, pF
0.02	266(18)	25.1(2.0)	10.6(1.0)
0.05	289(22)	18.3(1.8)	15.8(1.2)
0.10	195(8)	9.6(1.1)	20.4(1.8)
0.15	177(11)	7.1(0.6)	24.9(2.2)
0.21	150(10)	5.2(0.4)	28.7(2.4)
0.26	134(12)	4.1(0.4)	32.6(2.9)
0.29	114(9)	3.7(0.2)	30.8(3.0)
0.35	92(6)	3.1(0.3)	29.9(2.5)
0.40	95(7)	2.8(0.2)	34.5(3.2)
0.61	58(4)	1.8(0.1)	32.8(2.9)
0.80	41(3)	1.3(0.2)	31.7(3.1)
1.0	34(2)	1.1(0.1)	30.5(2.8)
1.2	29(2)	0.9(0.1)	32.8(2.5)

[a] Numbers in parentheses represent the standard deviations for at least three individual monolayers. Supporting electrolyte is lithium perchlorate. The radius of the platinum microelectrode is 5 μm.

electric field (Chart 2A). Second, as discussed recently by Smith and White,[5a] the existence of an impermeable monolayer that has a low dielectric constant may cause the potential to decay linearly across the thickness of the monolayer and then exponentially in the solution phase (Chart 2B). In this case, the surface-confined redox centers would experience a large electric field. An insight into the applicability of either model to our interfaces can be obtained by measuring the interfacial capacitance. This objective is doubly important because we are interested in the electric field effects on heterogeneous electron transfer, and the interaction of the highly charged protonated complexes with the interfacial electric field.

For the model illustrated in Chart 2B,[19] the reciprocal total interfacial capacitance, C_T, is given by the sum of the reciprocal capacitances of the film, C_{film}, and the diffuse layer, C_{dif}

$$C_T^{-1} = C_{film}^{-1} + C_{dif}^{-1} \quad (2)$$

$$C_{film} = \epsilon_0\epsilon_{film}/d \quad (3)$$

$$C_{dif} = \epsilon_0\epsilon_{SOLN}\kappa \cosh[ze(\phi_{PET} - \phi_{SOLN})/2k_BT] \quad (4)$$

where ϵ_0 is the permittivity of free space, ϵ_{film} and ϵ_{SOLN} are the film and solution dielectric constants, respectively, d is the monolayer thickness, z is the charge number of the electrolyte ion, e is the absolute electronic charge, k_B is the Boltzmann constant, T is the absolute temperature, and ϕ_{PET} and ϕ_{SOLN} are the potentials at the plane of electron transfer and in the bulk solution, respectively (Chart 2). The quantity κ is given by $(2n^\circ z^2e^2/\epsilon_{SOLN}\epsilon_0k_BT)^{1/2}$, where n° is the number concentration of the ions in solution.[16]

Only the diffuse layer capacitance depends on the potential or the concentration of supporting electrolyte. Therefore, the relative importance of that component may be probed by systematically varying the supporting electrolyte concentration and measuring the total capacitance. Table 1 contains the cell time constants, uncompensated cell resistances, and double layer capacitances as the concentration of $LiClO_4$ as supporting

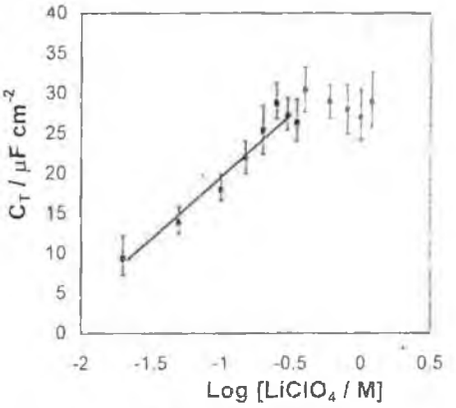

Figure 2. Dependence of the total interfacial capacitance for a spontaneously adsorbed $(p3p)_2$ monolayer on the logarithm of the supporting electrolyte concentration. The capacitance was determined using a small amplitude potential step centered on +0.100 V.

electrolyte is systematically varied from 0.02 to 1.2 M. Figure 2 shows the approximate differential capacitance, determined at 0.100 V, as a function of the logarithm of the supporting electrolyte concentration. The double layer capacitance increases approximately linearly with increasing logarithm of the electrolyte concentration for $LiClO_4$ concentrations less than about 0.2 M. This sensitivity clearly indicates that the diffuse layer capacitance contributes significantly to the total interfacial capacitance over this concentration range. The limiting value of C_T at high electrolyte concentration is at least 28 μF cm^{-2}, which may represent the film capacitance (Chart 2B), or if solvent and electrolyte ions freely diffuse into the interior of the monolayer and the double layer sets up as it would at a bare electrode (Chart 2A), it may correspond to the capacitance of the charges held at the outer Helmholtz plane. If this limiting capacitance is dominated by the film capacitance (Chart 2B), then, assuming a monolayer thickness of approximately 20 Å, the relative dielectric constant within the film is estimated from eq 3 as 63. That the relative dielectric constant within the monolayer is comparable to that of water (ϵ_{SOLN} = 78.5) would suggest that the monolayer is rather permeable to solvent and counterions.

Alternatively, the double layer may set up within the monolayer (Chart 2A), in which case the limiting interfacial capacitance corresponds to the capacitance of the charges held at the outer Helmholtz plane. Given that the distance of closest approach is likely to be of the order of 3 Å, the relative dielectric constant within the double layer would have to decrease from the value of 78.5 for bulk water to approximately 9 before a limiting interfacial capacitance of 28 μF cm^{-2} could be observed. It is important to note that, as discussed above for Chart 2B, this model is consistent with a solvated monolayer interior.

Therefore, based on these capacitance data, we conclude that the interior of the monolayer is at least partially solvated. This conclusion is consistent with the observation that the fwhm in cyclic voltammetry is close to that theoretically predicted for noninteracting redox sites, suggesting that solvent and ions permeate the monolayer and electrostatically insulate adjacent charges.

As described recently by Creager and co-workers,[5b] an insight into the interfacial potential distribution, and hence monolayer permeability, can be obtained by probing the kinetics of heterogeneous electron transfer as the supporting electrolyte concentration is systematically varied. This is possible since a significant potential difference between the plane of the immobilized molecules and the bulk solution means that only

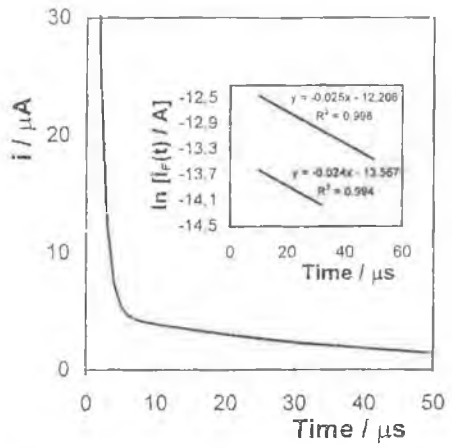

Figure 3. Current response for a 25 μm radius platinum microelectrode modified with a $(p3p)_2$ monolayer following a potential step where the overpotential η was −50 mV. The supporting electrolyte is 0.1 M perchlorate at a pH of 1.05. The inset shows ln $i_F(t)$ vs t plots for the Faradaic reaction for a 25 μm (top) and a 12.5 μm (bottom) radius platinum microelectrode.

a fraction of the total interfacial drop drives the heterogeneous electron transfer process. In fact, the driving force would be governed by an equilibrium electrode potential that is a function of the electrostatic potential at the site for electron transfer. This means that the driving force for electron transfer changes as the redox reaction proceeds, causing the overall dynamics to deviate from first order kinetics.[5b] We note that there are many processes other than interfacial fields that can cause nonexponential current decays, including multiple site geometries, surface activity effects,[11] the presence of defect sites,[20] oxidation state dependent dipole moments,[21] or ion pairing.[22] However, an increased supporting electrolyte decreases the double layer thickness κ, and if ions permeate into the monolayer, the situation is approached where all of the applied potential is dropped close to the electrode/monolayer interface. Therefore, one can probe the ideality of the chronoamperometric response without the complication of interfacial electric fields by employing high concentrations of supporting electrolyte.

Chronoamperometry. For an ideal electrochemical reaction involving a surface bound species, the Faradaic current following a potential step that changes the redox composition of the monolayer exhibits a single exponential decay in time according to[3a,c,7]

$$i_F(t) = kQ \exp(-kt) \tag{5}$$

where k is the apparent rate constant for the overall reaction and Q is the total charge passed in the redox transformation.

Figure 3 illustrates a typical example of the chronoamperometric response observed for the reduction ($Os^{3+} + e^- \rightarrow Os^{2+}$) of a $(p3p)_2$ monolayer, where the electrolyte is 0.1 M aqueous $LiClO_4$ at a pH of 1.05. In this experiment the overpotential η ($\equiv E - E^{o\prime}$) was −0.050 V. This figure shows that on a microsecond time domain two current decays can be separated. These responses, which arise from double layer charging and Faradaic current flow, are time-resolved due to the much shorter time constant of double layer charging compared to that of the Faradaic reaction. In our investigations, we have determined the electron transfer rate constant only when the time constant of double layer charging is at least five times shorter than the time constant of the Faradaic reaction.

While fast charging of the electrochemical double layer is important, the effects of ohmic losses must also be considered.[16] When Faradaic and charging currents flow through a solution, they generate a potential that acts to weaken the applied potential by an amount iR_u, where i is the total current. This ohmic drop can lead to severe distortions of experimental responses resulting in inaccurate measurements of the heterogeneous electron transfer rate. The significance of ohmic effects for these systems can be assessed using the data presented in Table 1. As illustrated in Figure 3, the Faradaic currents that flow in these high-speed chronoamperometric experiments are typically in the low-microamp range, even for 25 μm electrodes. Therefore, using the cell resistance data given in Table 1, the calculated iR_u drop is less than 20 mV for supporting electrolyte concentrations above 0.1 M. However, not only does the concentration of the supporting electrolyte play an important role in determining the magnitude of the uncompensated resistance, so too does the pH. For example, for the pH 1.05 system illustrated in Figure 3, the uncompensated resistance is approximately 2500 Ω, making the average ohmic loss approximately 5 mV.

The linearity of the ln $i_F(t)$ vs t plot shown in the inset of Figure 3 indicates that electron transfer is characterized by a single rate constant over the time required to collect greater than 95% of the Faradaic charge. At supporting electrolyte concentrations greater than 0.1 M, the monolayers always gave linear first order decays over about two lifetimes. Deviations from linearity would be expected if ohmic drop was present. Uncompensated resistance causes the applied potential, and hence the apparent rate, to evolve with time. Therefore, iR_u drop produces negative deviations in the observed current at short times.[7] That such nonidealities are not observed, at least for high concentrations of supporting electrolyte, is consistent with negligible ohmic losses. We have further probed the existence of ohmic effects by reducing the radius of the microelectrode. This approach is useful since the resistance increases with decreasing electrode radius, but the current decreases as the square of the radius leading to reduced ohmic effects for smaller electrodes. The inset in Figure 3 shows that the slope of the semilog plot obtained for a 12.5 μm platinum electrode modified with a spontaneously adsorbed $(p3p)_2$ monolayer is indistinguishable from that obtained at a 25 μm electrode. This observation is consistent with ohmic losses being negligible under the experimental conditions employed. Moreover, we find that the heterogeneous electron transfer rate constant measured at an overpotential of −50 mV is independent of the supporting electrolyte concentration, maintaining a value of $(2.5 \pm 0.2) \times 10^4$ s^{-1} as the $LiClO_4$ concentration was systematically varied from 0.1 to 1.0 M. On the basis of the measured cell resistances, and the insensitivity of the apparent heterogeneous rate constant to changes in electrode size or supporting electrolyte concentration, we conclude that ohmic drop and double layer effects on the interfacial kinetics are negligible for electrolyte concentrations greater than about 0.1 M.

Further evidence suggesting the predominance of a single rate constant is obtained by examining the intercept of the semilog plot at zero time. As indicated by eq 5, the intercept for a single exponential decay is ln(kQ). Nernst plots of the redox composition as a function of potential (vide supra) confirm that an absolute overpotential of 50 mV decreases the number of oxidized species within the monolayer to less than 10% of the total. Therefore, such a potential step effectively causes complete reduction of the film, and the full surface coverage, Γ, can be calculated from the intercept of Figure 3 using the relation[11]

$$\Gamma = Q/nFA \tag{6}$$

where n is the number of electrons transferred, F is the Faraday

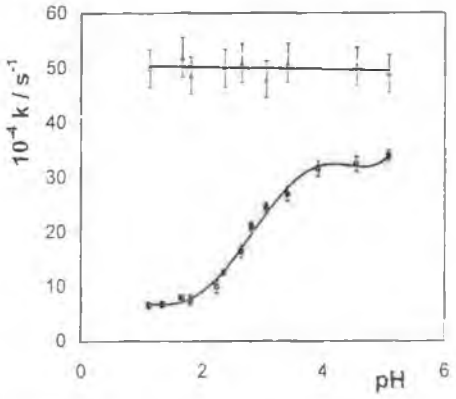

Figure 4. Dependence of the heterogeneous electron transfer rate constant at spontaneously adsorbed $(p3p)_2$ (lower curve) and $[Os(bpy)_2(p3p)(pyridine)]^{2+}$ (upper line) monolayers on the pH of the contacting electrolyte. The supporting electrolyte concentration is approximately 0.1 M perchlorate. The overpotential η is 102 mV.

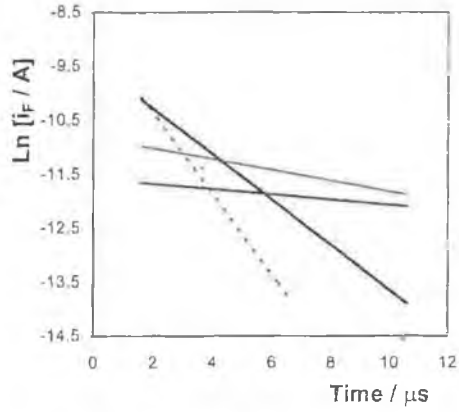

Figure 5. Effect of various overpotentials η, on the ln $i_F(t)$ vs t plots for a spontaneously adsorbed $(p3p)_2$ monolayer. The supporting electrolyte is 0.1 M $HClO_4$. Taken on the right-hand side, the overpotentials are from top to bottom, 0.051, 0.103, 0.200, and 0.349 V, respectively.

constant, and A is the real or microscopic electrode area. This chronoamperometric determination of the charge passed can then be compared with the value determined using cyclic voltammetry in order to further test the ideality of the chronoamperometric response. We find that the charges passed in these two independent experiments agree within 10%. This agreement indicates that all of the surface confined molecules are redox active on a microsecond time scale; i.e., relatively few, if any, sites are kinetically isolated.

Effect of Solution pH on Heterogeneous Kinetics. Plots of ln $i_F(t)$ vs t, obtained at an overpotential of 102 mV, remain linear ($R^2 > 0.99$) as the pH of the contacting electrolyte solution is systematically varied from 5.05 to 1.07, and heterogeneous electron transfer rate constants have been evaluated from their slopes. Figure 4 shows that there is a sigmoidal relationship between the heterogeneous electron transfer rate constant and the pH of the electrolyte, with k decreasing from $(3.4 \pm 0.2) \times 10^5$ to $(6.6 \pm 0.4) \times 10^4$ s^{-1} when the solution pH is decreased from 5.05 to 1.07. That k is sensitive to the solution pH, yet plots of ln $i_F(t)$ vs t remain linear over a wide pH range, is significant. One might imagine that if the system were in two different states, protonated and nonprotonated, each with different rate constants, that the corresponding semilog plots would be nonlinear or, in the extreme case, would exhibit dual slope behavior. That such nonlinear behavior is not observed suggests that protonation equilibrium occurs more rapidly than redox equilibrium.

It is important to note that the cell resistance decreases as the pH of the electrolytic solution decreases. Therefore, one would expect ohmic effects to be more significant at high, rather than low, pH, which would cause the heterogeneous electron transfer rate constant to be underestimated at high pH. That the opposite trend is experimentally observed, i.e., k increases with increasing pH, supports our conclusion that ohmic effects do not adversely affect the chronoamperometric determination of k.

The inflection point of Figure 4 is located at a pH of approximately 2.9, which is consistent with the pK_a of the unbound p3p ligand.[23] These data suggest that protonating the unbound p3p ligand alters the rate of heterogeneous electron transfer across the electrode/monolayer interface. Figure 4 also shows that the rate of heterogeneous electron transfer to spontaneously adsorbed $[Os(bpy)_2(pyridine)(p3p)]^{2+}$ monolayers, which do not contain groups capable of becoming protonated, is independent of solution pH in this range. This observation suggests that the second p3p ligand within the coordination shell of the osmium complex plays a central role in making k sensitive to the solution pH.

A possible explanation of this pH dependence is that protonating the free pyridine ring of the p3p ligand alters the electron density on the redox center. However, the degree of electronic coupling between the pyridine rings of the p3p ligand is expected to be weak given that they are separated by three methylene spacer groups. Our experimental observation that the formal potential of the $Os^{2+/3+}$ redox reaction remains constant to within 23 mV as the pH of the contacting solution is changed from 5.05 to 1.07 supports this conclusion. Moreover, solution phase absorption spectroscopy of the complex dissolved in DMF indicates that the position of the metal to ligand charge transfer band remains constant when the p3p ligands are protonated. This observation further suggests that protonation does not significantly affect the electron density on the osmium redox center.

The heterogeneous electron transfer rate is considered to depend on a frequency factor and a Franck–Condon barrier and can be expressed as[24]

$$k = \Gamma_n \kappa_{el} \upsilon_n \exp(-\Delta G^{\ddagger}/RT) \qquad (7)$$

where Γ_n is the nuclear tunneling factor, κ_{el} is the electronic transmission coefficient, υ_n is the nuclear frequency factor, and $\Delta G^{\ddagger}$ is the free energy of activation.[25,26] Since the experimental frequency factors are always less than $k_B T/h$ (h is the Planck constant), the nuclear tunneling factor is unity.[24] From eq 7, it is evident that the sensitivity of the heterogeneous electron transfer rate to the solution pH could be caused by changes in the free energy of activation or the pre-exponential factor. Since the free energy of activation equals $\lambda/4$, where λ is the total reorganization energy associated with switching the oxidation state of the monolayer, one strategy for estimating $\Delta G^{\ddagger}$ is to fit the dependence of the logarithm of the rate constant on the overpotential.[2c,3a,c,27]

pH Effects on the Potential Dependence of k. Figure 5 illustrates the effect of various overpotentials on the ln $i_F(t)$ vs t plots, where the supporting electrolyte is 0.1 M $HClO_4$. This figure shows that linear responses are observed at each of the overpotentials investigated. These linear responses are consistent with negligible ohmic effects despite the higher Faradaic currents that flow when a larger overpotential is applied. These data highlight another advantage of high-speed electrochemistry. As illustrated in Figure 1, the background current in cyclic voltammetry tends to rise as the positive potential limit is

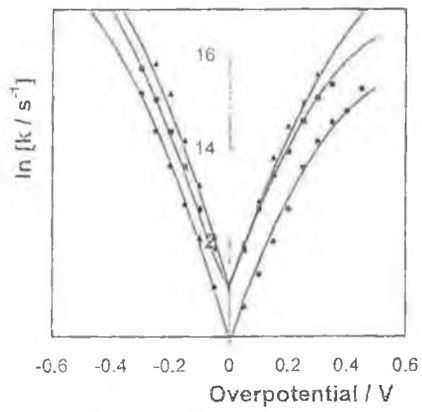

Figure 6. Tafel plots for $(p3p)_2$ monolayers as a function of the supporting electrolyte pH. The data (top to bottom, right hand side) represent electrolyte pH's of 5.05, 3.10, and 1.07, respectively. The solid lines denote theoretical fits obtained from a through-space tunneling model where λ = 100, 68, and 56 kJ mol^{-1} from top to bottom, respectively. The errors are approximately equal to the size of the symbols.

TABLE 2: Effect of Electrolyte pH on Standard Heterogeneous Rate Constants, Activation Parameters, and Pre-exponential Factors[a]

electrolyte pH	$10^{-1}k^{\circ}$,[b] s^{-1}	λ, kJ mol^{-1}	$\Delta H^{\ddagger}$, kJ mol^{-1}	$\Delta G_c^{\ddagger}$,[c] kJ mol^{-1}	$10^{-6}A_{el}$,[d] s^{-1}
5.05	6.1(0.2)	100	37.5(2.1)	25.1(2.2)	1547(345)
3.95	6.0(0.2)	93	34.6(1.8)	22.1(1.7)	451(78)
3.10	4.3(0.1)	68	30.3(1.3)	17.0(0.9)	41(6)
2.08	2.0(0.1)	54	26.1(2.2)	13.8(1.4)	5.3(0.6)
1.07	1.6(0.1)	56	24.6(1.5)	14.3(1.1)	5.2(0.4)

[a] Numbers in parentheses represent the standard deviations for at least three individual monolayers. Supporting electrolyte is 0.1 M perchlorate. [b] All standard rate constants were determined at 298 K. [c] Free energy of activation determined from the cathodic ideal electrochemical enthalpies using ΔS_{rc}°. [d] Pre-exponential factor extracted from the standard heterogeneous electron transfer rate constant using $\Delta G^{\ddagger}$.

approached. This increasing background current arises from the initial electrochemical cleaning of the platinum surface and is caused by incomplete removal of adsorbed oxygen or platinum oxide. However, the processes responsible for these background currents appear to be slow and take place on a millisecond time scale. By probing the electron transfer dynamics on a microsecond time scale, these background currents can be effectively eliminated so that the chronoamperometric data are not affected even at overpotentials where the background in cyclic voltammetry may be rising.

Figure 6 illustrates Tafel plots of ln k vs overpotential, η, for monolayers in contact with perchlorate electrolytes at different pHs. For overpotentials less than about 200 mV, ln k depends approximately linearly on η. The standard heterogeneous electron transfer rate constant k° has been determined by linearly extrapolating ln k to zero overpotential, and Table 2 contains these data. However, at large overpotentials the response is clearly nonlinear, and the slopes decrease in magnitude with increasing overpotential in both the anodic and cathodic directions. In the conventional Butler–Volmer formulation of electrode kinetics,[16] these slopes represent $(1 - \alpha_a)F/RT$ and $-\alpha_c F/RT$ for the oxidation and reduction reactions, respectively, where α_a is the anodic, and α_c the cathodic, transfer coefficient. Therefore, in contrast with the expectations of the Butler–Volmer formulation, Figure 6 suggests that the transfer coefficients are potential dependent. Furthermore, as reported previously for $[Os(bpy)_2Cl(p3p)]^+$ monolayers,[27a] α_a tends toward zero more rapidly than α_c. The Marcus theory of electron transfer predicts these nonlinear Tafel plots, because it includes a term that is quadratic in η in the rate equation.[28]

Simplified models incorporating the basic concepts of the Marcus theory have been developed to model heterogeneous electron transfer across electrode/monolayer interfaces.[3a,c] Chidsey has developed a model describing through-bond electron tunneling across metal/monolayer interfaces.[3a] However, this model predicts that Tafel plots will be symmetric with respect to overpotential. That we experimentally observe larger cathodic than anodic heterogeneous electron transfer rate constants for a given absolute value of the overpotential suggests that through-bond electron tunneling is not an appropriate model for our system. Finklea and Hanshew[3c] have assembled a model describing through-space electron tunneling that predicts our experimental observation of asymmetric Tafel plots. In Finklea's model, the heterogeneous electron transfer rate constant is given by the integral over energy of three functions, namely, the Fermi function of the metal, the distribution of energy levels for acceptor or donor states in the monolayer (assumed to be Gaussian), and a rate parameter for electron tunneling at a given energy. In order to fit this model to the experimental data shown in Figure 6, estimates are required for the average barrier height to heterogeneous electron transfer, the total reorganization energy associated with switching the redox state of the monolayer, and the preintegral factor.

The average barrier height for electron tunneling at $[Os(bpy)_2Cl(pNp)]^+$ monolayers, where pNp is 4,4′-bipyridyl, 1,2-di(4-pyridyl)ethane or 4,4′-trimethylenedipyridine, has previously been estimated from the distance dependence of k°.[27a] Given that the same bridging ligand is used here, we employ the same value of the average barrier height, 200 kJ mol^{-1}, in the present analysis. The total reorganization energy λ, dictates the degree of curvature in the Tafel plots. Therefore, λ was chosen so that there was satisfactory agreement between shapes of the theoretical Tafel plots and the experimental data. Finally, the preintegral factor was adjusted to give the experimental value of k°.

Figure 6 shows the experimental dependence of ln k on overpotential for solution pH's of 5.05, 3.10, and 1.07. This figure indicates that the degree of curvature of these Tafel plots depends on pH, suggesting that the reorganization energy depends on the extent of monolayer protonation. Figure 6 shows that satisfactory agreement between Finklea and Hanshew's model and the experimental data is obtained when λ is 100, 68, and 56 kJ mol^{-1} for solution pH's of 5.05, 3.10, and 1.07, respectively. However, we note that the electron transfer dynamics can only be probed over a restricted range of overpotentials because of the rapid nature of the process. This restriction means that only limited confidence can be placed in these fitted values of the reorganization energy.

The Marcus theory can provide a theoretical estimate of the reorganization energy.[28] In the Marcus model, λ is considered to be the sum of an inner sphere and outer sphere component. The inner sphere component describes the distortion of bond angles and lengths accompanying electron transfer, while the outer sphere component reflects solvent reorganization effects. Crystallographic data demonstrate that switching the oxidation state of osmium and ruthenium polypyridyl complexes does not significantly change either the bond lengths or angles. This observation suggests that the inner sphere reorganization energy for this system is negligible, at least in the solid state. The outer sphere solvent reorganization energy λ_{OS} is given by

$$\lambda_{OS} = (e^2/2)(r^{-1} - R_e^{-1})(\epsilon_{op}^{-1} - \epsilon_{SOLN}^{-1}) \qquad (8)$$

where e is the absolute electronic charge, r is the radius of the

metal complex (6.7 Å), R_c is the reactant-image distance, ϵ_{op} is the optical dielectric constant of water (5.5), and ϵ_{SOLN} is the static dielectric constant (78.5). As discussed previously,[27a] we have neglected imaging effects, i.e., $R_c \rightarrow \infty$, in calculating the theoretical solvent reorganization energy. Equation 8 yields a solvent reorganization energy of 56.9 kJ mol^{-1}, which agrees with the value of 56 kJ mol^{-1} obtained from fitting the data in Figure 6 when the monolayer is fully protonated. This observation suggests that the activation energy barrier to heterogeneous electron transfer at a protonated monolayer is dictated by solvent reorganization. In contrast, the experimental reorganization energy for nonprotonated monolayers (100 kJ mol^{-1}) is significantly larger than that predicted by eq 8 for solvent reorganization. There are a number of factors that may cause the activation barrier to heterogeneous electron to depend on the monolayer's state of protonation. For example, the interfacial potential distribution may be different with the higher ionic strength of the low-pH solutions causing the potential to drop more sharply at the electrode/monolayer interface. These differences in electric field strength may change the solvent or ion content of the film. It is important to note that the experimental semilog current vs time responses remain linear over the pH range investigated. The linearity of these responses suggests that diffusional processes; e.g., the motion of charge compensating counterions does not influence the rate of, or the barrier to, heterogeneous electron transfer. Alternatively, redox induced changes in the film structure, e.g., a change in the tilt angle θ (Chart 1), may accompany oxidation of the monolayer. This reorientation of the adsorbate could act as an "inner sphere" reorganization energy, making the experimental λ larger for nonprotonated monolayers.

In the Marcus theory, the free energy of activation $\Delta G^{\ddagger}$ is equal to $\lambda/4$. Therefore, while the largest heterogeneous electron transfer rate is observed for nonprotonated monolayers (Figure 4), this process is associated with the largest free energy of activation (Figure 6). If the pre-exponential factor of eq 7 did not change as the monolayer became protonated, then a higher free energy of activation would give a lower, not a higher, heterogeneous electron transfer rate. This is an important observation and suggests that changes in the pre-exponential factor with monolayer protonation cause the heterogeneous electron transfer to be pH sensitive.

To avoid the inherent inaccuracy of fitting Tafel plots over a limited potential range to estimate $\Delta G^{\ddagger}$, and to obtain a more quantitative insight into the origin of the pH sensitivity of k, we have performed temperature-resolved measurements of the formal potential and heterogeneous electron transfer rate to independently probe the pH dependence of the activation entropy and enthalpy, respectively.

Reaction Entropies. One might anticipate that since protonating the monolayer changes its charge, the reaction entropy $\Delta S_{rc}°$, quantifying the difference in entropy between the reduced and oxidized forms of the redox couple, would depend on the pH of the contacting electrolytic solution.[29] If $\Delta S_{rc}°$ was pH dependent, then it could explain the pH dependence of the free energy of activation suggested by Figure 6.

The reaction entropy has been determined using a nonisothermal cell by measuring the temperature dependence of the formal potential obtained from cyclic voltammetry as the pH of the contacting solution was systematically varied. As discussed by Weaver and co-workers, the temperature dependence of the formal potential can be expressed as[29,30]

$$\Delta S_{rc}° = F(\partial E°'/\partial T) \qquad (9)$$

For all situations investigated, the formal potential shifts in a positive potential direction with increasing temperature indicating positive reaction entropies and a higher degree of local ordering in the oxidized than in the reduced state. Figure 7 shows that plots of $E°'$ vs T are linear over the pH range 5.2 to 1.5, and reaction entropies have been calculated from the slopes according to eq 9. The slopes of these lines do not depend on the pH of the contacting solution, and $\Delta S_{rc}°$ remains constant at 82 ± 7 J mol^{-1} K^{-1} over the pH range 5.2 to 1.5. This observation clearly demonstrates that changes in the activation entropy are not responsible for the pH dependence of the free energy of activation suggested by Figure 6.

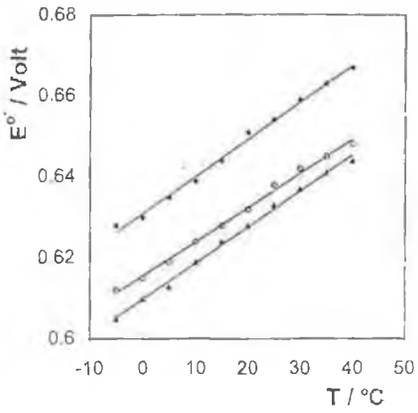

Figure 7. Effect of the pH of the contacting electrolyte solution on the temperature dependence of the formal potential for $(p3p)_2$ monolayers spontaneously adsorbed on platinum microelectrodes. The data represent (top to bottom) electrolyte pH's of 1.5, 5.2, and 3.6, respectively.

Temperature Dependence of k. Weaver and co-workers[31] have established that a temperature independent Galvani potential difference, ϕ_m, across the metal/solution interface can be achieved using a nonisothermal cell. The electrochemical activation enthalpy determined from an Arrhenius plot of ln k vs T^{-1}, where ϕ_m is held constant, has been termed "ideal",[32] and we label it here as $\Delta H_I^{\ddagger}$. For a reduction or cathodic reaction, this electrochemical activation enthalpy can be separated into "chemical", $\Delta H^{\ddagger}$, and "electrical", $\alpha_c F\phi_m$, contributions according to

$$\Delta H_{I,c}^{\ddagger} = -R\left.\frac{\partial \ln k}{\partial(1/T)}\right|_{\phi_m} = \Delta H^{\ddagger} - \alpha_c F\phi_m \qquad (10)$$

We have investigated the temperature dependence of the heterogeneous electron transfer rate using temperature-resolved chronoamperometry over the temperature range −5 to +40 °C. An overpotential of −50 mV, as determined at 298 K, was used throughout these experiments, and the resulting current−time transients were similar to those illustrated in Figure 3. The corresponding semilog plots were linear over approximately two lifetimes, and the heterogeneous electron transfer rate was evaluated from the slopes. In a typical set of experiments, the temperature was systematically varied over a range and then returned to the initial temperature. The same slope, $-k$, and intercept, ln(kQ), were observed within experimental error for the initial and final transients. This consistency indicates that cycling the temperature does not change the heterogeneous kinetics or the quantity of material immobilized on the electrode surface. The heterogeneous electron transfer rate constant increases with increasing temperature as anticipated for a thermally activated process. Arrhenius plots of ln k vs T^{-1} are linear ($R^2 > 0.995$) over the temperature range −5 to +40 °C. Table 2 contains the activation enthalpies, $\Delta H^{\ddagger}$, obtained from the slopes of these plots after using the experimental transfer coefficient to correct for the electrical driving force (−50 mV)

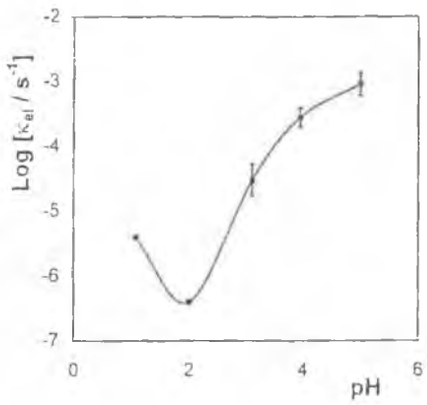

Figure 8. Dependence of the logarithm of the electronic transmission coefficient κ_{el} for heterogeneous electron transfer across platinum/$(p3p)_2$ monolayer interfaces on the pH of the supporting electrolyte.

according to eq 10. These data confirm that the activation enthalpy changes as the monolayer becomes protonated, decreasing from 37.5 ± 2.1 to 24.6 ± 1.5 kJ mol^{-1} as the pH is reduced from 5.05 to 1.07.

In principle, it is possible to use the experimental enthalpies and entropies to calculate free energies of activation. Comparing these values with the value of the reorganization energy provided by Finklea and Hanshew's model is an important test of consistency between these two independent experiments. We have calculated the cathodic free energy of activation according to eq 11,[27a,32] and Table 2 contains the data. These data show that, at the five pH's investigated, $\Delta G_c^{\ddagger}$ and $\lambda/4$ agree to within 5%.

$$\Delta G_c^{\ddagger} = \Delta H_{1,c}^{\ddagger} - T\alpha_c \Delta S_{rc}^{\circ} \qquad (11)$$

Pre-exponential Factor. That both $\Delta G_c^{\ddagger}$ and k decrease with decreasing electrolyte pH suggests that the pre-exponential factor of eq 7 decreases as the monolayer becomes protonated. Table 2 contains values of A_{el} ($\equiv \kappa_{el}\upsilon_n$) that have been determined using our experimental free energies of activation and the standard heterogeneous electron transfer rate constant. To isolate the effects of the electronic transmission coefficient, we have calculated the nuclear frequency factor, υ_n, using the dielectric continuum model,[33]

$$\upsilon_n = \tau_l^{-1}(\Delta G_c^{\ddagger}/4\pi k_B T)^{1/2} \qquad (12)$$

where τ_l^{-1} is the inverse longitudinal relaxation time for water (1.9 ps^{-1}). These values have then been used to estimate κ_{el} from the experimental pre-exponential factor. Figure 8 shows that for all pH's investigated the electronic transmission coefficient is considerably less than unity. This observation indicates that there is a low probability of electron transfer once the nuclear transition state has been attained, suggesting a nonadiabatic reaction involving weak coupling between the metallic states of the electrode and the localized orbitals of the redox center. The pH dependency of log κ_{el} is illustrated in Figure 8. Significantly, κ_{el} increases dramatically from (4.4 ± 2.0) × 10^{-6} to (9.1 ± 2.4) × 10^{-4} on going from a protonated to a nonprotonated monolayer.

As discussed above, our observation of larger cathodic than anodic heterogeneous electron transfer rate constants for a given absolute value of the overpotential is consistent with through-space rather than through-bond electron tunneling. This is an important point since, unlike a through-space tunneling mechanism, the electron transfer distance for a through-bond tunneling process is not sensitive to the tilt angle (Chart 1) between the electrode and the redox site. There are several possible causes of the observed dependence of the electronic transmission coefficient, and hence the heterogeneous electron transfer rate, on the pH of the contacting solution. For example, it is possible that at high pH immobilization occurs through both uncomplexed pyridine nitrogens and that lowering the solution pH causes desorption of one of the pyridine rings which then becomes protonated. We note however, that the experimental area of occupation as measured at high pH is considerably smaller than that predicted for the situation in which both uncomplexed pyridine groups bind to the electrode surface. Moreover, the pK_a's of both uncomplexed pyridines are identical, making selective desorption of one of them from the electrode surface unlikely. Alternatively, protonating the monolayer may either cause the tilt angle (Chart 1) between the bridging ligand and the electrode surface to increase, or the methylene spacer groups to adopt a more extended configuration. It is possible that this proton induced restructuring of the monolayer arises because the formal potential of the adsorbed complex is positive of the potential of zero charge. This situation is expected to cause repulsive interactions between the positively charged electrode and the highly charged protonated (4+) complexes, causing the redox centers to move away from the electrode and thus increasing the through-space tunneling distance.

If this model is appropriate, then the change in the through-space tunneling distance between the protonated and nonprotonated forms of the monolayer can be estimated from the data illustrated in Figure 8 by assuming that the tunneling parameter β° is identical to that found previously[27a] for $[Os(bpy)_2Cl(p3p)]^+$ monolayers (1.5 Å^{-1}). Using this value of β°, an increase in the through-space electron transfer distance of approximately 3.5 Å would be required to cause κ_{el} to decrease from (9.1 ± 2.4) × 10^{-4} to (4.4 ± 2.0) × 10^{-6} as the monolayer goes from a nonprotonated to a fully protonated state. When any directional component in the electronic coupling between the metallic states of the electrode and the orbitals of the adsorbed complex is ignored, this difference in through-space electron transfer distance could be accounted for by a change in the tilt angle from approximately 40° in the nonprotonated state to 90° in the protonated state.

Conclusions

The adsorbed monolayers considered here exhibit nearly ideal cyclic voltammetry and chronoamperometry as the pH, temperature, and experimental time scale are varied over a wide range. Chronoamperometry has been used to probe the rate of heterogeneous electron transfer across the monolayer/microelectrode interface. This process can be characterized by a single rate constant at high electrolyte concentrations, suggesting that heterogeneous electron transfer across these metal/monolayer interfaces is mechanistically uncomplicated. This unusual ideality has allowed us to probe the nature of the activation barrier to electron transfer, and the degree of electronic coupling between the remote redox centers and the microelectrode, in considerable detail. Measurements of the potential dependence of the heterogeneous electron transfer rate constant, k, suggest that electron transfer occurs via a through-space rather than a through-bond tunneling mechanism and that it depends on the pH of the contacting solution. By determining the free energy of activation using two independent methods, we have shown that changes in the pre-exponential factor rather than $\Delta G^{\ddagger}$ cause this pH sensitivity. It appears that the interaction of the highly positively charged protonated complexes with the interfacial electric field causes the through-space electron transfer distance to increase, perhaps by altering the tilt angle between the

adsorbate and the electrode surface or by causing the methylene spacer groups to become extended.

Although the change in heterogeneous electron transfer rate constant on going from nonprotonated to fully protonated monolayers is less than an order of magnitude, this pH induced "conformational gating" of the electron transfer rate offers the possibility of developing pH triggered electrical switches. We expect that fundamental investigations focusing specifically on the role that the local medium, particularly the bridging structure linking the reactants, plays in dictating the rate and pathway for electron transfer, will make it possible to design molecular systems that maximize electron transfer efficiency and their sensitivity to specific chemical triggers.

Acknowledgment. R.J.F. gratefully acknowledges Professor Larry R. Faulkner of the University of Illinois at Urbana-Champaign for the generous loan of the high-speed potentiostat used in this work. Financial support from Forbairt, the Irish Science and Technology Agency, under Basic Research Grant SC/95/209 is gratefully acknowledged.

References and Notes

(1) (a) Abrûna, H. D. In *Electroresponsive Molecular and Polymeric Systems*; Skoteim, T., Ed.; Dekker: New York, 1988. (b) Stoddart, J. F. In *Frontiers in Supramolecular Organic Chemistry and Photochemistry*; Schneider, H. J., Dürr, H., Eds.; VCH: Weinheim, Germany, 1990. (c) Murray, R. W. *Molecular Design of Electrode Surfaces*; Wiley-Interscience: New York, 1992.

(2) (a) Ulman, A. *An Introduction to Ultra-thin Organic Film from Langmuir-Blodgett to Self-Assembly*; Academic Press: San Diego, CA, 1991. (b) Chidsey, C. E. D.; Loiacono, D. N. *Langmuir* **1990**, *6*, 682. (c) Finklea, H. O.; Snider, D. A.; Fedik, J. *Langmuir* **1990**, *6*, 371. (d) Strong, L.; Whitesides, G. M. *Langmuir* **1988**, *4*, 546. (e) Nuzzo, R. G.; Dubois, L. H.; Allara, D. L. *J. Am. Chem. Soc.* **1990**, *112*, 558. (f) Yamada, S.; Kawazu, M.; Matsuo, T. *J. Phys. Chem.* **1994**, *98*, 3573. (g) Shi, X.; Caldwell, W. B.; Chen, K.; Mirkin, C. A. *J. Am. Chem. Soc.* **1994**, *116*, 11598.

(3) (a) Chidsey, C. E. D. *Science* **1991**, *251*, 919. (b) Dudois, L. H.; Nuzzo, R. G. *Annu. Rev. Phys. Chem.* **1992**, *43*, 437. (c) Finklea, H. O.; Hanshew, D. D. *J. Am. Chem. Soc.* **1992**, *114*, 3173. (d) Acevedo, D.; Abrûna, H. D. *J. Phys. Chem.* **1991**, *95*, 9590. (e) Acevedo, D.; Bretz, R. L.; Tirado, J. D.; Abrûna, H. D. *Langmuir* **1994**, *10*, 1300. (f) Becka, A. M.; Miller, C. J. *J. Phys. Chem.* **1993**, *97*, 6233. (g) Rubinstein, I.; Steinberg, S.; Tor, Y.; Shanzer, A. *Nature* **1988**, *332*, 426. (h) Franzen, S.; Goldstein, R. F.; Boxer, S. G. *J. Phys. Chem.* **1993**, *97*, 3040. (i) Nordyke, L. L.; Buttry, D. A. *Langmuir* **1991**, *7*, 380. (j) Li, T. T.-T.; Weaver, M. J. *J. Am. Chem. Soc.* **1984**, *106*, 6107.

(4) (a) Forster, R. *J. Chem. Soc. Rev.* **1994**, 289. (b) Faulkner, L. R.; Walsh, M. R.; Xu, C. *Contemporary Electroanalytical Chemistry*; Plenum Press: New York, 1990. (c) Andrieux, C. P.; Hapiot, P. Savéant, J. M. *Chem. Rev.* **1990**, *90*, 723. (d) Amatore, C. A.; Jutand, A.; Pflüger, F. *J. Electroanal. Chem.* **1987**, *218*, 361. (e) Penner, R. M.; Heben, M. J.; Longin, T. L.; Lewis, N. S. *Science* **1990**, *250*, 1118. (f) Sabatani, E.; Rubinstein, I. *J. Phys. Chem.* **1987**, *91*, 6663.

(5) (a) Smith, C. P.; White, H. S. *Anal. Chem.* **1992**, *64*, 2398. (b) Creager, S. E.; Weber, K. *Langmuir*, **1993**, *9*, 844 (c) Andreu, R.; Fawcett, W. R. *J. Phys. Chem.* **1994**, *98*, 12753.

(6) (a) Gao, J.; Shopes, R. J.; Wright, C. A. *Biochim. Biophys. Acta* **1990**, *1015*, 96. (b) Kaminskaya, O.; Konstaninov, A. A.; Shuvalov, V. A. *Biochim. Biophys. Acta* **1990**, *1016*, 153.

(7) Forster, R. J.; Faulkner, L. R. *J. Am. Chem. Soc.* **1994**, *116*, 5444.

(8) Yee, E. L.; Cave, R. J.; Guyer, K. L.; Tyma, P. D.; Weaver, M. J. *J. Am. Chem. Soc.* **1979**, *101*, 1131.

(9) Xu, C. Ph.D. Thesis, University of Illinois at Urbana-Champaign, 1992.

(10) Trasatti, S.; Petrii, O. A. *J. Electroanal. Chem.* **1992**, *327*, 354.

(11) (a) Laviron, E. *J. Electroanal. Chem.* **1974**, *52*, 395. (b) Brown, A. P.; Anson, F. C. *Anal. Chem.* **1977**, *49*, 1589.

(12) Feldberg, S. W.; Rubinstein, I. *J. Electroanal. Chem.* **1988**, *240*, 1.

(13) (a) Goodwin, H. A.; Kepert, D. L.; Patrick, J. M.; Skelton, B. W.; White, A. H. *Aust. J. Chem.* **1984**, *37*, 1817. (b) Ferguson, J. E.; Love, J. L.; Robinson, W. T. *Inorg. Chem.* **1972**, *11*, 1662. (c) Rillema, D. P.; Jones, D. S.; Levy, H. A. *J. Chem. Soc., Chem. Commun.* **1979**, 849.

(14) Forster, R. J. *Inorg. Chem.*, submitted for publication.

(15) (a) Forster, R. J. *Langmuir* **1995**, *11*, 2247. (b) Forster, R. J.; Vos, J. G. *Langmuir* **1994**, *10*, 4330.

(16) Bard, A. J., Faulkner, L. R. *Electrochemical Methods: Fundamentals and Applications*; Wiley: New York, 1980.

(17) (a) Bryant, M. A.; Crooks, R. M. *Langmuir* **1993**, *9*, 385. (b) Ksenzhek, O. S.; Petrova, S. A.; Oleinik, S. V.; Kokodyashnyi, M. V.; Moskovskii, V. Z. *Elektrokhim.* **1977**, *13*, 182. (c) Sun, L.; Johnson, B.; Wade, T.; Crooks, R. M. *J. Phys. Chem.* **1990**, *94*, 8869. (d) Porter, M. D.; Bright, T. B.; Allara, D. L.; Chidsey, C. E. D. *J. Am. Chem. Soc.* **1987**, *109*, 3559.

(18) Wightman, R. M.; Wipf, D. O. In *Electroanalytical Chemistry*; Bard, A. J., Ed.; Dekker: New York, 1989; Vol. 15.

(19) (a) Widrig, C. A.; Chung, C.; Porter, M. D. *J. Electroanal. Chem.* **1991**, *310*, 335. (b) Nuzzo, R. G.; Allara, O. L. *J. Am. Chem. Soc.* **1983**, *105*, 4481.

(20) Chidsey, C. E. D.; Bertozzi, C. R.; Putvinski, T. M.; Mujsce, A. M. *J. Am. Chem. Soc.* **1990**, *112*, 4301.

(21) Gerischer, H.; Scherson, D. A. *J. Electroanal. Chem.* **1985**, *188*, 33.

(22) (a) Rowe, G. K.; Creager, S. E. *Langmuir* **1991**, *7*, 2307. (b) Nagamura, T.; Sakai, K. *Chem. Phys. Lett.* **1987**, *141*, 553. (c) Nagamura, T.; Sakai, K. *J. Chem. Soc., Faraday Trans.* **1988**, *84*, 3529. (d) Creager, S. E.; Rowe, G. K. *Anal. Chim. Acta* **1991**, *246*, 233.

(23) Denn, J. A. *Handbook of Organic Chemistry*; McGraw-Hill: New York, 1987.

(24) (a) Weaver, M. J. *Chem. Rev.* **1992**, *92*, 463. (b) Bagchi, G. *Annu. Rev. Phys. Chem.* **1989**, *40*, 115. (c) Sutin, N. *Acc. Chem. Res.* **1982**, *15*, 275.

(25) Barr, S. W.; Guyer, K. L.; Li, T. T.-T.; Liu, H. Y.; Weaver, M. J. *J. Electrochem. Soc.* **1984**, *131*, 1626.

(26) Sutin, N. Brunschwig, B. S. *ACS Symp. Ser.* **1982**, *198*, 105.

(27) (a) Forster, R. J.; Faulkner, L. R. *J. Am. Chem. Soc.* **1994**, *116*, 5453. (b) Richardson, J. N.; Rowe, G. K.; Carter, M. T.; Tender, L. M.; Curtin, L. S.; Peck, S. P.; Murray, R. W. *Electrochim. Acta* **1995**, *40*, 1331.

(28) (a) Marcus, R. A. *J. Chem. Phys.* **1956**, *24*, 966. (b) Marcus, R. A. *J. Chem. Phys.* **1965**, *43*, 679. (c) Tender, L. M., Carter, M. T.; Murray, R. W. *Anal. Chem.* **1994**, *66*, 3173. (d) Weber, K.; Creager, S. E. *Anal. Chem.* **1994**, *66*, 3164.

(29) Hupp, J. T.; Weaver, M. J. *J. Phys. Chem.* **1984**, *88*, 1860.

(30) Barr, S. W.; Guyer, K. L.; Li, T. T.-T.; Liu, H. Y.; Weaver, M. J. *J. Electrochem. Soc.* **1984**, *131*, 1626.

(31) (a) Li, T. T.-T.; Guyer, K. L.; Barr, S. W.; Weaver, M. J. *J. Electroanal. Chem.* **1984**, *164*, 27. (b) Yee, E. L.; Weaver, M. J. *Inorg. Chem.* **1980**, *19*, 1077.

(32) (a) Weaver, M. J. *J. Phys. Chem.* **1979**, *83*, 1748. (b) Weaver, M. J. *J. Phys. Chem.* **1976**, *80*, 2645.

(33) Morgan, J. D.; Wolynes, P. G. *J. Phys. Chem.* **1987**, *91*, 874.

JP952057R

Potential dependent adsorption of anthraquinone-2,7-disulfonate on mercury†

The Analyst

Joseph P. O'Kelly and Robert J. Forster*

School of Chemical Sciences, Dublin City University, Dublin 9, Ireland

Received 27th May 1998, Accepted 7th September 1998

Monolayers of anthraquinone-2,7-disulfonic acid, 2,7-AQDS, have been formed by equilibrium adsorption onto mercury electrodes. In low pH electrolytes, cyclic voltammetry is nearly ideal with a peak-to-peak splitting of 8 ± 2 mV, and a full width at half maximum of 57 ± 1 mV, being observed for scan rates less than 3 V s^{-1}. The dependence of the surface coverage of 2,7-AQDS as measured using voltammetry on its bulk concentration is described by the Langmuir isotherm over the concentration range 0.06–9 μM. A saturation surface coverage, Γ_s, of $(8.7 \pm 0.5) \times 10^{-11}$ mol cm^{-2} and an adsorption coefficient, β, of $(5.6 \pm 0.5) \times 10^5$ M^{-1} are observed where the supporting electrolyte is 1.0 M $HClO_4$. Consistent with the formation of an organic film, the double layer capacitance, C_{dl}, as measured at −0.700 V, decreases from approximately 40 μF cm^{-2} in the absence of dissolved 2,7-AQDS to 10 μF cm^{-2} when the bulk concentration exceeds 10 μM. By measuring the potential dependence of C_{dl} as the bulk concentration of 2,7-AQDS is varied systematically, an insight into the potential dependence of the free energy of adsorption, $\Delta G^{\ddagger}_{ads}$, has been obtained. These data reveal that $\Delta G^{\ddagger}_{ads}$ is similar for both fully oxidised and fully reduced monolayers. However, these quinonoid monolayers are least strongly bound ($\Delta G^{\ddagger}_{ads} = -28.5$ kJ mol^{-1}) when the film exists in the quinhydrone form.

Introduction

Depositing monomolecular films using self-assembly or spontaneous adsorption represents an important approach to controlling the properties of the electrode/solution interface.[1–5] While numerous investigations have focused on the physical and chemical properties of these monolayers,[6–8] much less is known about the kinetics and thermodynamics of adsorption in systems of this type. Molecular adsorption onto metal electrodes is known to be profoundly influenced by the specific properties of the substrate and by the state of charge of the surface.[9] In particular, the applied potential plays an important role in determining the stability and configuration of adsorbates.[10,11] For redox active monolayers, the applied potential may influence the adsorption process, not only by changing metal–adsorbate interactions, but also by changing adsorbate–adsorbate interactions through changes in the redox composition of the film.[12]

In recent years, there has been a stronger focus on using Faradaic rather than capacitance measurements to probe these issues. This situation is somewhat surprising given the sensitivity of the interfacial capacitance to the presence of adsorbates. One of the difficulties associated with obtaining accurate capacitance data on redox active films is the difficulty in separating Faradaic and capacitive currents when making measurements close to the formal potential. However, we have demonstrated that by using high speed chronoamperometry, it is possible to efficiently time resolve, and therefore separate, these current contributions under a wide range of experimental conditions.[13,14] In this contribution, we apply this approach to studying the effect of potential on the formation of anthraquinone-2,7-disulfonic acid (2,7-AQDS) monolayers.

. The potential dependence of the differential capacitance of metal electrodes can exhibit well defined maxima at certain voltages in the presence of physically adsorbed neutral molecules.[15] These peaks are interpreted as evidence of adsorption/desorption at the electrode surface. However, the capacitance behaviour of organic monolayers that are chemisorbed to the electrode surface is quite different and adsorption/desorption peaks are absent because a more or less permanent film is formed.[16] We are interested in measuring the interfacial capacitance to diagnose the strength of 2,7-AQDS adsorption over a wide range of potentials encompassing regions where the film is electroactive and regions far from the formal potential of the quinone/hydroquinone redox reaction.

The ability to time-resolve capacitive and Faradaic currents makes it possible to probe the potential dependence of the interfacial capacitance as the bulk concentration, and hence surface coverage, of a surface active molecule is systematically varied. In this way, we have obtained a useful insight into the potential dependent adsorption of electroactive species that are reversibly adsorbed onto electrode surfaces.

Experimental

Materials and procedures

The disodium salt of anthraquinone-2,7-disulfonic acid (2,7-AQDS) was obtained from BASF (Ludwigshafen, Germany). All electrolytes were prepared using Milli-Q purified water. Spontaneously adsorbed monolayers were formed by immersing the electrodes in the supporting electrolyte solution containing the anthraquinone at the desired concentration, typically in the low μM range. Since adsorption is reversible in this system, subsequent experiments were carried out with this concentration of 2,7-AQDS present in solution. The highest concentration of anthraquinone in solution was 10 μM. To ensure that the current observed is dominated by the redox reactions of the monolayer rather than the solution phase anthraquinone, experiments designed to probe the concentration dependence of the surface coverage were performed at relatively short timescales. For example, for the dropping mercury electrode used in this study, for scan rates greater than 10 V s^{-1} the maximum contribution from diffusion to the voltammetric peak current is less than 2% even in 10 μM

† Presented at EIRELEC '98, Howth, Co. Dublin, Ireland, March 26–28, 1998.

2,7-AQDS solutions.[9] All measurements were undertaken when the surface coverage had reached equilibrium with the bulk concentration of 2,7-AQDS, *i.e.*, when repeated voltammetric cycling revealed an unchanging peak current.

Apparatus

All measurements were performed using conventional three-electrode electrochemical cells thermostated to 25 ± 0.2 °C using a Julabo F10-HC (Kutztown, PA, USA) refrigerated circulating bath. The electrolytic solutions were degassed using nitrogen and a blanket of nitrogen was maintained over the solution during all experiments. All potentials are quoted with respect to a BAS (West Lafayette, IN, USA) Ag/AgCl gel-filled reference electrode. Cyclic voltammetry was performed using a PAR EG&G Model 273 (Wokingham, UK) potentiostat/galvanostat interfaced to a PAR EG&G model 270 mercury electrode. Chronoamperometry was carried out using a CH Instruments (Memphis, TN, USA) Model 660 Electrochemical Workstation. The area of the mercury electrode was determined by recording cyclic voltammograms of 1,4-benzoquinone under radial and semi-infinite linear diffusion conditions.[17] Using the values obtained for the limiting and peak currents, an electrode area of 0.017 ± 0 0.002 cm^2 was obtained. This value agrees with that obtained by dispensing, and then subsequently drying and weighing, one hundred mercury drops.

Results and discussion

General electrochemical properties

Fig. 1 shows representative cyclic voltammograms for a mercury electrode immersed in a 5 μM solution of 2,7-AQDS in 1.0 M $HClO_4$. The peak shapes are independent of scan rate up to at least 20 V s^{-1} and the peak height varies linearly with sweep rate, v, rather than the $v^{1/2}$ dependence expected for a freely diffusing species.[9] These voltammograms are consistent with those expected for an electrochemically reversible reaction involving a surface confined redox-active species.[18,19] Therefore, consistent with previous reports on structurally related anthraquinones[20,21] it appears that 2,7-AQDS adsorbs onto the surface of the mercury electrode to give an electroactive film.

For a surface confined species in which there are no interactions between adsorbates, and an equilibrium is rapidly established between the applied potential and the redox

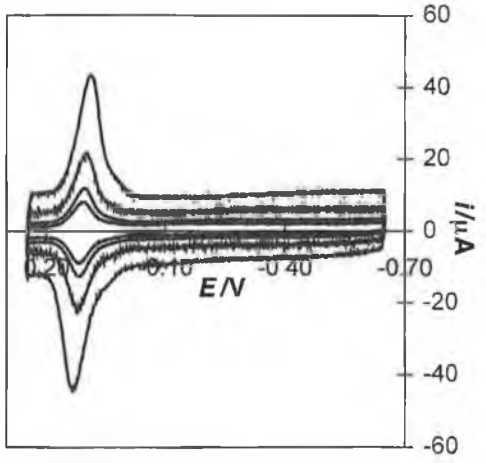

Fig. 1 Cyclic voltammograms for a mercury electrode immersed in a 5 μM solution of 2,7-AQDS in 1.0 M $HClO_4$. Scan rates from top to bottom are 20, 10, 5, and 3 V s^{-1}. Cathodic currents are up and anodic currents are down. The initial potential is −0.650 V and the electrode area is 0.017 cm^2.

composition of the film, a zero peak-to-peak splitting and a full width at half maximum (FWHM) of 90.6/n, where n is the number of electrons transferred, are expected.[9] We typically observe a peak-to-peak splitting and an FWHM of 8 ± 2 and 57 ± 1 mV, respectively, at scan rates slower than 3 V s^{-1} in 1 M $HClO_4$. The magnitude of the FWHM suggests that this redox reaction involves the transfer of two electrons, at least in low pH electrolytes. This result is consistent with our previous work[13,14,21–23] which revealed that in acidic solutions reduction of anthraquinone monolayers proceeds by a two-proton, two-electron transfer mechanism.

When the time constants of the voltammetric experiment and electron transfer are comparable, one expects the rate of electron transfer across the metal/film interface to influence the voltammetric response.[9] A shift in both the anodic and cathodic peak potentials, that cannot be attributed to iR drop, and a non unity slope magnitude in a plot of the peak current, i_p, *versus* the scan rate are evidence that the electrode kinetics influence the overall response. That the experimental i_p increases linearly with increasing v up to 20 V s^{-1} with an absolute slope of near unity (|slope| = 0.98 ± 0.06) indicates that for scan rates up to 20 V s^{-1} the experimental timescale is longer than that for electron transfer. For scan rates above 20 V s^{-1}, the slope observed in a plot of i_p *versus* v decreases significantly, and the current tends to become independent of the scan rate for values greater than approximately 200 V s^{-1}. Given that the time constant for a cyclic voltammetry experiment in which the scan rate is 20 V s^{-1} is approximately 1 ms, these observations suggest that the standard electron transfer rate constant, $k°$, is at least 800 s^{-1}. That electron and proton transfer are coupled in these systems, and that the heterogeneous kinetics are not adequately described by simple Butler–Volmer kinetics, complicates fitting of the data to, for example Laviron's model,[18] to extract accurate heterogeneous rate constants.

For potentials far from $E°'$, the voltammetric response is dominated by the double layer charging current, i_c. The charging current observed in the absence of dissolved 2,7-AQDS is at least twice as large as that observed when its bulk concentration is 10 μM. Therefore, that the charging current observed in Fig. 1 is independent of the applied potential between approximately 0.00 and −0.65 V suggests that the anthraquinone moieties remain adsorbed over the entire potential range investigated and desorb only at potentials negative of −0.65 V.[16] That the peak shapes do not change significantly when cycled repeatedly at temperatures up to 40 °C, over at least 30 min, indicates that adsorbed films of 2,7-AQDS are both electrochemically and thermally stable.

The pH dependence of cyclic voltammograms for surface confined 2,7-AQDS in unbuffered electrolyte is shown in Fig. 2. As discussed above, at a pH of 1.5 the voltammetric response of monolayers of 2,7-AQDS is centred at 0.00 V and is unusually ideal. As the pH of the contacting electrolyte is increased, the voltammetric wave initially shifts in a negative potential direction but becomes independent of the solution pH above pH 4.1. In the very narrow pH range 3.9 to 4.1 two two-electron waves are observed. The sum of the charges under these two peaks, 390 ± 5 nC, is identical to that found under either of the two-electron peaks observed at high or low pH. This observation suggests that over the entire pH range investigated, the redox reactions involve the transfer of two electrons but for 3.9 ≤ pH ≤ 4.1, two chemically distinct species co-exist on the electrode surface.

Adsorption isotherms

The total charge, Q, introduced or withdrawn to reduce or oxidise the immobilised species, can be found from the area under the voltammetric peak after correcting for the background

charging current.[9] This charge, together with the area of the electrode, A, is used to calculate the surface coverage, Γ:

$$\Gamma = \frac{Q}{nFA} \quad (1)$$

where n is the number of electrons transferred, F is Faraday's constant and A is the electrode area.

The surface coverage can be used to determine the area occupied by individual adsorbates which may provide an insight into the orientation of the compound on the electrode, *i.e.*, flat or edge-on.[24] Molecular orientation has important implications in the chemistry of adsorbed compounds, *e.g.*, the oxidation pathway for adsorbed aromatics on Pt is known to depend on their orientation.[25] The saturation surface coverage, Γ_s, as measured using cyclic voltammetry in an electrolytic solution containing a relatively high concentration of 2,7-AQDS (10 μM) was $(7.2 \pm 0.6) \times 10^{-11}$ mol cm^{-2}. This surface coverage gives an area of occupation per molecule of 230 ± 012 Å^2. This area is consistent with that reported by Faulkner and co-workers[20] (200 ± 10 Å^2) for 2,6-AQDS suggesting that the substitution pattern of the anthraquinone does not significantly affect the packing density. It is perhaps important to note that Soriaga and Hubbard[26] observed a limiting coverage of 131 ± 7 Å^2 for 2,6-AQDS adsorbed on platinum indicating that the nature of the electrode material influences the monolayer structure significantly.

In order to define the adsorption isotherm, the surface coverage of 2,7-AQDS at equilibrium was determined using the area under the voltammetric peak, after correcting for the contribution from double layer charging, as the solution concentration of the anthraquinone moiety was systematically varied. Fig. 3 shows the change in surface coverage as the solution concentration of 2,7-AQDS is varied from 5.5×10^{-8} to 9.0×10^{-6} M. These data show that the surface coverage does not increase beyond the plateau value even if the bulk concentration of 2,7-AQDS is increased significantly. This result indicates that this system tends to form monolayers rather than multilayers. Moreover, that Γ is essentially independent of the bulk 2,7-AQDS concentration for 10 μM $\leq C_b \leq$ 1 0 mM suggests that concentration induced molecular reorientation does not occur in this system unlike the situation frequently found for quinones on platinum.[27]

The Langmuir isotherm[9,28] describes equilibrium adsorption for the situation where lateral interactions between the adsorbed molecules are absent or are independent of the surface coverage, the electrode surface is homogeneous, and the limiting surface coverage is dictated simply by the size of the adsorbate. That the voltammetric response illustrated in Fig. 1 is nearly ideal, and that both adsorption and desorption of the anthraquinone occurs rapidly and reversibly, suggests that the Langmuir isotherm may be an appropriate description of adsorption in this case. This isotherm is described by the following expression:

$$\frac{\Gamma_s}{\Gamma_s - \Gamma_i} = \beta_i C_i \quad (2)$$

where β_i and C_i are the adsorption coefficient and the solution phase concentration of species i, respectively. In the following discussions, activity coefficients are incorporated into the adsorption coefficient. The line in Fig. 3 is the best fit Langmuir isotherm. That satisfactory agreement between experiment and theory is obtained suggests that this model may provide an appropriate description of the experimental data.

The Langmuir isotherm predicts that a plot of C_i/Γ_i *vs.* C_i should be linear, and that the saturation surface coverage, Γ_s, and the adsorption coefficient, β_i, can be obtained from the slope and intercept, respectively:

$$\frac{C_i}{\Gamma_i} = \frac{1}{\Gamma_s} C_i + \frac{1}{\Gamma_s \beta_i} \quad (3)$$

The inset of Fig. 3 shows that a plot of this type is satisfactorily linear ($R^2 = 0.98$) and the slope yields an estimate of $(9.0 \pm 0.5) \times 10^{-11}$ mol cm^{-2} for the saturation surface coverage, Γ_s. The adsorption coefficient, β_i, which describes the strength of adsorption, is $(5.2 \pm 0.5) \times 10^5$ M^{-1}. Significantly, the adsorption coefficient for the system investigated here is an order of magnitude smaller than that found for 2,6-AQDS [$(5.2 \pm 0.7) \times 10^6$ M^{-1}].[20] This observation suggests that while the location of the sulfonate groups does not significantly affect the monolayer coverage (*vide supra*) it may be an important factor in determining the strength of adsorption. The adsorption coefficient can be used to calculate the free energy of adsorption, $\Delta G^{\ddagger}_{ads}$:

$$-\Delta G^{\ddagger}_{ads} = RT \ln \beta_i \quad (4)$$

which includes contributions from concentration independent adsorbate–adsorbate and potential dependent adsorbate-electrode interactions. The free energy of adsorption at $E^{o\prime}$ is −32.8 ± 0.3 kJ mol^{-1}.

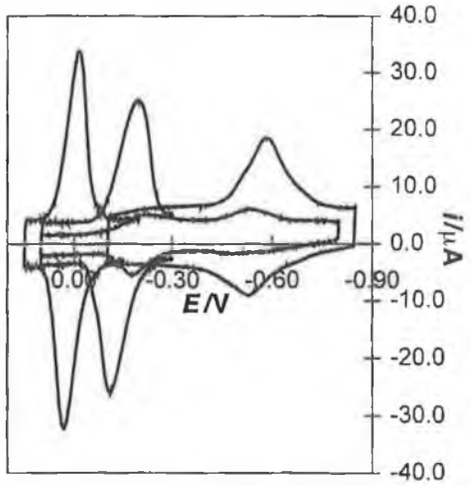

Fig. 2 Cyclic voltammograms for a 0.017 cm^2 mercury electrode immersed in a 5 μM solution of 2,7-AQDS as the pH of the unbuffered contacting electrolyte solution is, from left to right, 1.1, 3.8, 1 (double peak) and 5.1. The scan rate is 10 V s^{-1} and the supporting electrolyte is 0.10 M $LiClO_4$. Cathodic currents are up and anodic currents are down. The initial potential is −0.650 V.

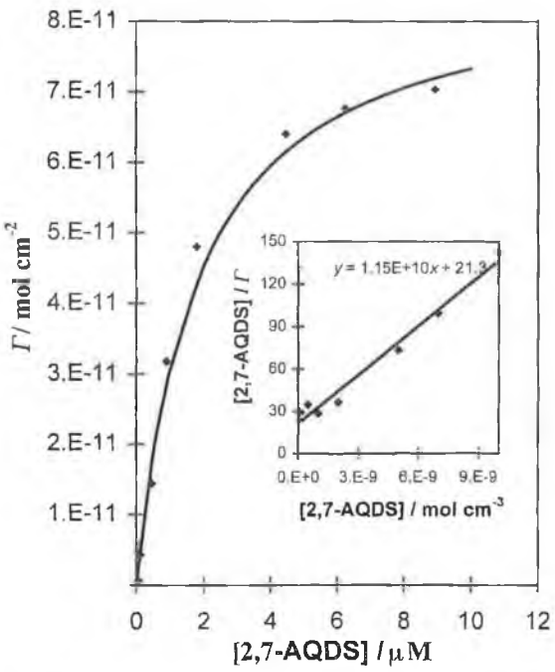

Fig. 3 Relationship between surface coverage and bulk concentration of 2,7-AQDS. The solid line is the best fit to the Langmuir isotherm. The inset illustrates data plotted according to the linearised Langmuir isotherm. The supporting electrolyte is 1.0 M $HClO_4$.

Potential dependence of adsorption strength

Voltammetry can provide a powerful insight into the effect of the applied potential on the surface coverage and strength of adsorption when a molecule adsorbs *irreversibly* onto an electrode surface.[12,29] This understanding can be achieved because the applied potential can be controlled during monolayer deposition and the surface coverage can be measured in a blank electrolyte solution that does not contain any of the adsorbate of interest. This approach is not useful when adsorption is *reversible* since transferring the coated electrode into blank electrolyte would change the equilibrium surface coverage. However, the double layer capacitance, C_{dl}, is sensitive to the nature and extent of surface modification and its potential dependence can be measured in the presence of the dissolved anthraquinone.[14,22] Therefore, we have used potential step chronoamperometry to investigate how the double layer capacitance, C_{dl}, depends on the applied potential as the concentration of 2,7-AQDS in solution is systematically varied. While recognising that chronoamperometry is not an especially sensitive technique for measuring the interfacial capacitance, it has the advantage that double layer charging and Faradaic currents can be time-resolved[13] and the technique is easily implemented.

Chronoamperometry

In these experiments, the potential was stepped from an initial value E_i using a pulse amplitude of 30 mV and the resulting current response was recorded. Between successive measurements, E_i was increased by 30 mV from −0.700 to +0.100 V. The charging current, i_c, decays exponentially in time according to eqn. (5):[30]

$$i_c(t) = (\Delta E/R) \exp(-t/RC_{dl}) \quad (5)$$

where ΔE is the pulse amplitude and R is the total cell resistance.

Eqn. (5) predicts that when the potential is stepped in a region where the redox composition of the monolayer does not change, *i.e.*, far from $E^{\circ\prime}$, a plot of the logarithm of the current observed *vs.* time should be linear. When the potential is stepped in a region close to $E^{\circ\prime}$, the current response at short times is dominated by double layer charging with Faradaic current due to oxidation of the adsorbed 2,7-AQDS moieties occurring at longer times.[13,14] Therefore, a plot of the logarithm of the short timescale current *vs.* time should be linear. Fig. 4 shows how semi-log plots depend on the applied potential for monolayer modified mercury electrodes. The resistance and double layer capacitance were determined from the intercepts and slopes of these lines, respectively, and the data are presented in Table 1.

Fig. 4 reveals that the intercepts of semi-log plots are independent of the applied potential. Moreover, Table 2 shows that the resistance changes by less than 25% as the composition of the electrolyte solution is systematically varied from one that does not contain any dissolved 2,7-AQDS to one where the anthraquinone concentration is 10 μM. That R is relatively independent of both the applied potential and the anthraquinone concentration suggests that the solution resistance dominates the total cell resistance and that the film resistance makes only a minor contribution.

Interfacial capacitance

For an electrode coated with a modifying film, both the diffuse layer capacitance from solution, C_{dif}, and the film capacitance, C_{film}, may contribute to the overall double layer capacitance:[16,31]

$$\frac{1}{C_{dl}} = \frac{1}{C_{film}} + \frac{1}{C_{dif}} \quad (6)$$

Only the diffuse layer capacitance depends on the applied potential and the concentration of supporting electrolyte[9] and the effect of monolayer assembly on the interfacial potential distribution can be diagnosed by measuring C_{dl} as both the applied potential and the bulk concentration of 2,7-AQDS are systematically varied.

The slopes of the best fit lines to the semi-log plots of Fig. 4 depend on the applied potential indicating that the double layer capacitance is potential dependent. Fig. 5 illustrates the potential dependence of the interfacial capacitance as the bulk concentration of 2,7-AQDS is systematically varied. This figure shows that strikingly different voltage dependences are

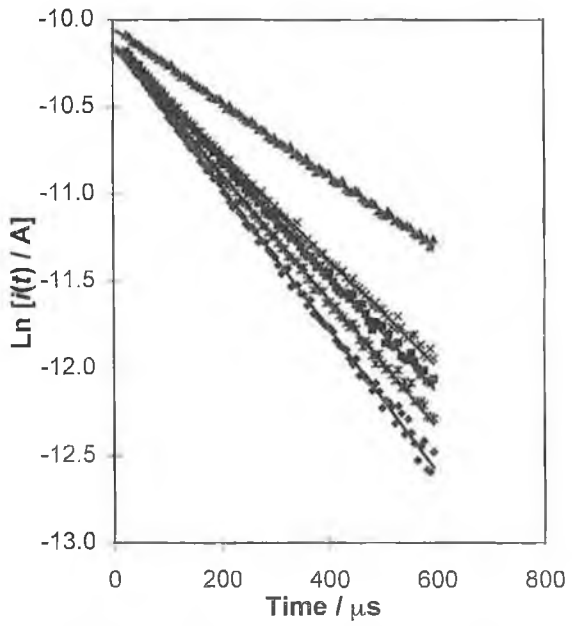

Fig. 4 Effect of the applied potential on plots of the logarithm of the capacitive current *vs.* time for mercury electrodes modified with dense monolayers of 2,7-AQDS.

Table 1 Effect of potential on the total cell resistance and interfacial capacitance observed for a mercury electrode modified with a close packed monolayer of 2,7-AQDS

Potential/V	Resistance[a]/Ω	Capacitance[a]/μF cm^{-2}
−0.220	760(35)	11.6(0.9)
−0.340	750(20)	13.1(1.0)
−0.430	700(25)	15.8(1.1)
−0.520	770(20)	14.7(0.8)
−0.670	770(28)	12.6(0.9)

[a] Resistance and capacitance values quoted are the average of at least three independent chronoamperometric experiments on separate monolayers. The errors are quoted in parentheses.

Table 2 Effect of 2,7-AQDS concentration on the total cell resistance and interfacial capacitance as measured at −0.430 V

[2,7-AQDS]	Resistance[a]/Ω	Capacitance[a]/μF cm^{-2}
0	684(38)	33.1(1.8)
1	756(43)	27.8(1.4)
2	766(51)	25.8(2.1)
7	803(39)	17.2(1.3)
10	890(55)	15.8(0.8)

[a] Resistance and capacitance values quoted are the average of at least three independent chronoamperometric experiments on separate monolayers. The errors are quoted in parentheses.

observed for the monolayer modified electrodes compared to the pristine metal surfaces. In particular, the double layer capacitance is measurably smaller for the coated electrode than for an unmodified interface over the entire potential range investigated, *e.g.*, at the formal potential, the capacitance decreases from 31 μF cm^{-2} for the bare electrode to 17 μF cm^{-2} for a 10 μM solution, and only the clean mercury surfaces show a pronounced minimum. The reduced capacitance in the presence of 2,7-AQDS is consistent with the cyclic voltammetry data presented earlier which indicated that the surface coverage increases from approximately half of a close packed monolayer to approximately full monolayer coverage as the bulk concentration of the anthraquinone is increased from 2 to 10 μM. The data illustrated in this figure are highly reproducible and no detectable hysteresis was observed between successive potential scans, or if the direction of scanning was reversed. These observations suggest that either the structure of the film is static or that it rapidly equilibrates with the applied potential.

A minimum in C_{dl} is expected at the potential of zero charge (p.z.c.) which represents the potential at which there is no excess charge on either the electrode or solution sides of the interface.[9] Fig. 5 reveals that for the clean mercury interface a minimum in the capacitance occurs at −415 ± 15 mV. This value of the p.z.c. is consistent with that expected for a mercury electrode in contact with a dilute, non-surface active electrolyte.[9]

The pK_as of the hydroquinone groups within the reduced form of the adsorbate are 7.7 and 10.5.[32,33] However, the pK_as for the oxidised or quinone form of the monolayer are approximately 6 pH units lower. Therefore, given that the sulfonic acid groups are deprotonated at the pH of this study (5.5), the reduced monolayer is electrostatically neutral while the oxidised form has a charge of 2−. Under these circumstances, one would expect the potential of zero charge for the monolayer to depend on its redox composition. However, it is not possible to identify the p.z.c. for the anthraquinone derivatised electrodes since, even in the presence of 2,7-AQDS concentrations as low as 2 μM, no well-defined minimum in the interfacial capacitance is observed over the potential range investigated. We note that the formal potential in 0.05 M NaF is −415 mV, *i.e.*, the p.z.c. observed for the bare electrode, and $E^{o\prime}$ for the monolayer, are coincident, making it difficult to determine the effect of monolayer formation on the p.z.c.

Fig. 5 shows that a distinct maximum in C_{dl} is observed at approximately −415 mV. That a distinctive peak is observed suggests that this behaviour is not due to imperfections within the anthraquinone monolayer or voltage dependent penetration of water or ionic species into the film. An alternative explanation is that the surface coverage is lower at this potential. To investigate this possibility, we have probed how the interfacial capacitance depends on the bulk concentration, and hence surface coverage, of 2,7-AQDS. The dependence of the interfacial capacitance on the surface coverage can be described using the parallel capacitor model originally proposed by Delahay.[34] In this model, the double layer capacitance for incomplete monolayers is represented by an equivalent circuit composed of two capacitors in parallel representing the contributions from the bare and modified fractions of the electrode surface:

$$C_{dl} = C_{mono} + (C_{bare} - C_{mono})(1 - \theta) \quad (7)$$

where C_{bare} and C_{mono} are the capacitances of the bare and densely coated electrodes respectively, and θ is the fractional surface coverage. Fig. 6 illustrates how the interfacial capacitance, as measured at the formal potential, changes as the bulk concentration is systematically varied from 1 to 10 μM. The capacitance decreases from 31 μF cm^{-2} for the bare electrode to 17 μF cm^{-2} when the concentration in solution is 10 μM. Fig. 3 demonstrated that the Langmuir isotherm provides an adequate description of the dependence of the surface coverage of 2,7-AQDS on its bulk concentration. We have combined Delahay's parallel capacitor model with the Langmuir isotherm to allow the potential dependence of Γ to be probed through measurements of C_{dl}. Eqn. 8 summarises this model:[14]

$$\frac{[2,7\text{-AQDS}]}{(C_{bare} - C_{dl})} = \frac{1}{C_{mono}}[2,7\text{-AQDS}] + \frac{1}{C_{mono}\beta_i} \quad (8)$$

where [2,7-AQDS] represents the solution concentration of 2,7-AQDS. According to eqn. (8), the slope and intercept obtained from a plot of [2,7-AQDS]/(C_{bare} − C_{dl}) *vs.* [2,7-AQDS] can be used to determine the capacitance corresponding to a close packed monolayer and the adsorption coefficient, respectively. The inset of Fig. 6 illustrates a plot of this type using values of C_{dl} measured at $E^{o\prime}$. This plot is linear (R^2 = 0.9936) suggesting that the parallel capacitor model provides an accurate description of adsorption for 2,7-AQDS films. The slope of the inset in Fig. 6 reveals a capacitance for a dense monolayer, C_{mono}, of 22 μF cm^{-2} which compares

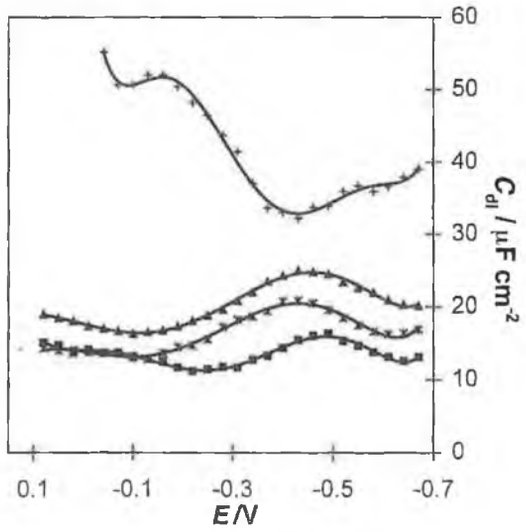

Fig. 5 Double layer capacitance as a function of applied potential as the concentration of 2,7-AQDS in solution is systematically varied. The curves, from top to bottom, represent the capacitance of electrodes immersed in 0.05 M NaF containing 0, 2, 5, and 10 μM 2,7-AQDS. Typical error bars are less than 2 μF cm^{-2}.

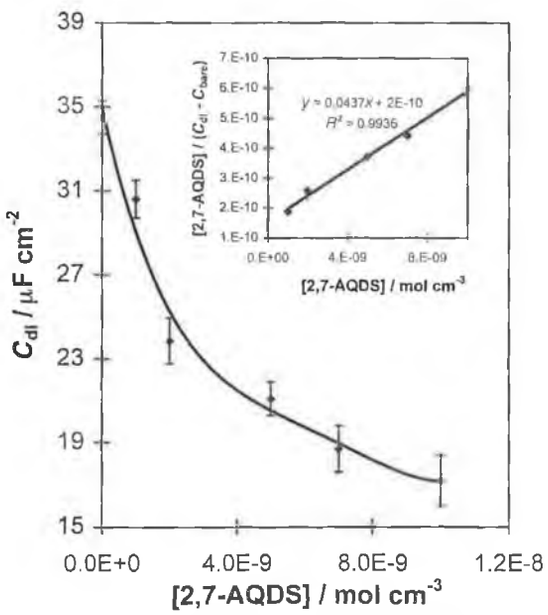

Fig. 6 Dependence of the double layer capacitance as measured at the formal potential on the bulk concentration of 2,7-AQDS. The inset illustrates data linearised according to a parallel capacitor model. The supporting electrolyte is 0.05 M NaF.

favourably with the value of 17 μF cm^{-2} obtained directly from chronoamperometry where the bulk concentration of 2,7-AQDS is 10 μM. The adsorption coefficient of (2.2 ± 0.5) × 10^5 M^{-1} obtained from the intercept of this plot is in reasonable agreement with the value of (5.6 ± 0.5) × 10^5 M^{-1} obtained from the linearised Langmuir isotherm (Fig. 3). That the capacitance and voltammetric results agree, indicates that measurements of C_{dl} can be used to probe the strength of adsorption in this system, at least at $E^{o\prime}$.

Fig. 7 shows data obtained at potentials away from $E^{o\prime}$ and reveals that plots of [2,7-AQDS/($C_{bare} - C_{dl}$) *vs.* [2,7-AQDS] are linear at all potentials investigated. This linearity suggests that the parallel capacitor model provides a meaningful insight into the potential dependence of both C_{mono} and β.

Free energy of adsorption

That adsorption in this system is described by the Langmuir adsorption isotherm suggests that adsorbate–adsorbate interactions are either absent or do not depend strongly on the redox composition or packing density of the monolayer. However, it is possible that adsorbate–electrode interactions depend on the applied potential, thus making the free energy of adsorption, $\Delta G^{\ddagger}_{ads}$, potential dependent. The intercepts of the plots shown in Fig. 7 have been used in conjunction with eqn. (4) and (8) to determine the potential dependence of the free energy of adsorption and the data are illustrated in Fig. 8. At potentials far from $E^{o\prime}$, where only the oxidised or reduced form of the monolayer exist, the free energy of adsorption is large, but is insensitive to the applied potential. For example, $\Delta G^{\ddagger}_{ads}$ differs by only 1.5 kJ mol^{-1} when measured at −0.21 or −0.67 V, where the monolayer is fully oxidised and reduced, respectively. This observation suggests that $\Delta G^{\ddagger}_{ads}$ is relatively insensitive to the applied potential provided that only a single redox form exists on the electrode surface.

The most striking feature of Fig. 8 is that the absolute value of $\Delta G^{\ddagger}_{ads}$ reaches a minimum at approximately −415 mV, *i.e.*, the adsorbates are least strongly bound at this potential. This potential corresponds to both the p.z.c. of the bare mercury surface and the formal potential of the quinone/hydroquinone redox reaction. Unlike potentials that are significantly positive or negative of the formal potential, at $E^{o\prime}$ the monolayer may contain three distinct redox forms of the adsorbate, namely the quinone, hydroquinone and semiquinone forms. Capacitance data do not allow us to discriminate between these different redox states preventing a complete interpretation of the available data. However, a minimum in $\Delta G^{\ddagger}_{ads}$ at the p.z.c. is not expected since the oxidised form of the adsorbate has a 2− charge due to dissociation of the two sulfonic acid groups. Under these circumstances, one would anticipate a larger $\Delta G^{\ddagger}_{ads}$ at potentials positive of the p.z.c. While future papers will report results at other pHs where the p.z.c. and $E^{o\prime}$ are not co-incident, it is likely that the interactions between the electrode and the co-adsorbed quinones, hydroquinones and perhaps semiquinones that exist at $E^{o\prime}$, as well as, acid/base reactions influence the observed response.

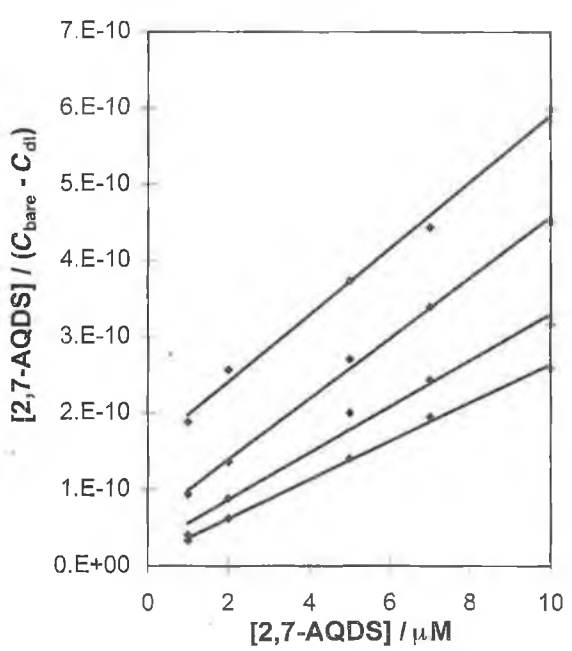

Fig. 7 Potential dependence of capacitance data linearised according to the parallel capacitor model. From top to bottom, the potentials are, −0.460, −0.520, −0.310 and −0.190 V, respectively. The supporting electrolyte is 0.05 M NaF.

Conclusions

The electrochemistry of anthraquinone-2,7-disulfonate monolayers has been investigated and found to be unusually ideal under conditions of low electrolyte pH. In particular, the effects of adsorbate concentration and the applied potential on the adsorption strength have been probed. The dependence of the surface coverage on the bulk concentration of 2,7-AQDS is adequately described by the Langmuir adsorption isotherm. The area occupied per molecule suggests that the adsorbate binds to the surface of the electrode in a flat orientation and that reorientation does not occur, at least not for bulk anthraquinone concentrations up to 10 μM. This resistance to reorientation most likely arises because of entropy considerations. In the flat orientation, each of the three fused rings can interact with the mercury surface, whereas a perpendicular adsorbate would permit only limited anthraquinone–electrode interaction but more extensive lateral interactions through π-stacking.

The double layer capacitance, C_{dl}, has been probed as a function of the applied potential and the solution concentration of 2,7-AQDS. While C_{dl} depends strongly on the concentration of 2,7-AQDS it appears to be only weakly dependent on the applied potential. The concentration dependence of C_{dl} is described by a parallel capacitor model which has been used to probe the potential dependence of the free energy of adsorption. The potential dependence of the free energy of adsorption

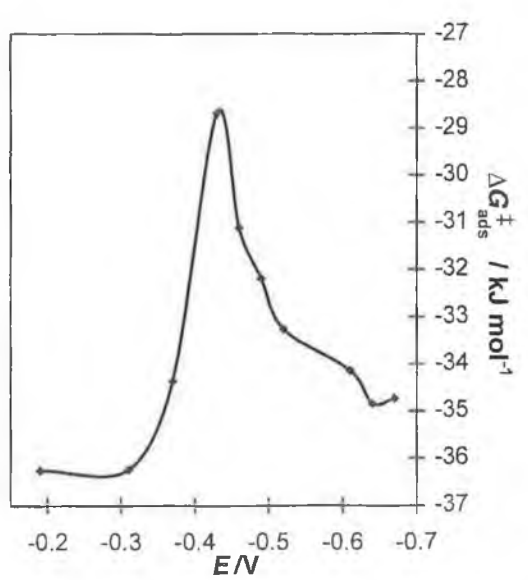

Fig. 8 Dependence of the free energy of adsorption on the applied potential. The supporting electrolyte is 0.05 M NaF.

indicates that the monolayer is least strongly bound at -415 ± 15 mV which coincides with the formal potential of 2,7-AQDS in 0.05 M NaF and the p.z.c. of the unmodified mercury interface. We have found that the ionic strength of the supporting electrolyte solution does not significantly affect the free energy of adsorption. This observation suggests that monolayer formation is best described in terms of the displacement of preadsorbed solvent molecules from the electrode surface rather than the removal of preadsorbed electrolyte ions.

Monolayers of this type represent useful model systems to address outstanding questions regarding how electrons and protons transfer through membranes. Control of how solution phase chemicals interact with these thin films, and what dictates their redox activity, are expected to impact our understanding of the mechanisms of biological reactions.

Acknowledgement

Funding from Forbairt, the Irish Science and Technology Agency, under Strategic Research Grant ST/98/414, is gratefully acknowledged.

References

1 A. Ulman, *An Introduction to Ultrathin Organic Films From Langmuir-Blodgett to Self-Assembly*, Academic Press, UK, 1991.
2 R. W. Murray, in *Molecular design of Electrode Surfaces*, ed. R. W. Murray, Wiley, New York, 1992, ch. 1.
3 M. D. Porter, T. B. Bright, D. L. Allara and C. E. D. Chidsey, *J. Am. Chem. Soc.*, 1987, **109**, 3559.
4 C. E. D. Chidsey and D. N. Loiacono, *Langmuir*, 1990, **6**, 682.
5 R. V. Duevel and R. M. Corn, *Anal. Chem.*, 1992, **64**, 337.
6 R. G. Nuzzo, L. H. Dubois and D. L. Allara, *J. Am. Chem. Soc.*, 1990, **112**, 558.
7 J. M. Tour, L. Jones, D. L. Pearson, J. J. Lamba, T. P. Burgin, G. M. Whitesides, D. L. Allara, A. N. Parikh and S. V. Atre, *J. Am. Chem. Soc.*, 1995, **117**, 9529.
8 R. J. Forster and J. P. O'Kelly, *J. Phys. Chem.*, 1996, **100**, 3695.
9 A. J. Bard and L. R. Faulkner, *Electrochemical methods: Fundamentals and Applications*, Wiley, New York, 1980.
10 B. E. Conway, *Chem. Soc. Rev.*, 1992, 253.
11 R. Parsons, *Chem. Rev.*, 1990, **90**, 813.
12 R. L. Bretz and H. D. Abruña, *J. Electroanal. Chem.*, 1995, **388**, 123.
13 R. J. Forster, *Analyst*, 1996, **121**, 733.
14 R. J. Forster, *Anal. Chem.*, 1996, **68**, 3143.
15 R. De Levie, *Advances in Electrochemistry and Electrochemical Engineering*, Wiley, New York, 1986, vol. 13, p. 1.
16 C. A. Widrig, C. Chung and M. D. Porter, *J. Electroanal. Chem.*, 1991, **310**, 335.
17 R. J. Forster, *Chem. Soc. Rev.*, 1994, 289.
18 E. Laviron, *J. Electroanal. Chem.*, 1974, **52**, 395.
19 P. Brown and F. C. Anson, *Anal. Chem.*, 1977, **49**, 158.
20 P. He, R. M. Crooks and L. R. Faulkner, *J Phys. Chem.*, 1990, **94**, 1135.
21 R. J. Forster, *J. Electrochem. Soc.*, 1997, **144**, 1165.
22 R. J. Forster, *Electrochemical Society Proceedings*, 1996, **96**, 65.
23 R. J. Forster, *Langmuir*, 1995, **11**, 2247.
24 J. Zhang and F. C. Anson, *J. Electroanal. Chem.*, 1992, **331**, 945.
25 M. P. Soriaga, J. L. Stickney and A. T. Hubbard, *J. Electroanal. Chem.*, 1983, **144**, 207.
26 M. P. Soriaga and A. T. Hubbard, *J. Am. Chem. Soc.*, 1982, **104**, 3937.
27 M. P. Soriaga, J. H. White and A. T. Hubbard, *J. Phys. Chem.*, 1983, **87**, 3048.
28 S. Trassatti, *J. Electroanal. Chem.*, 1974, **53**, 335.
29 D. Acevedo, R. L. Bretz, J. D. Tirado and H. D. Abruña, *Langmuir*, 1994, **10**, 1300.
30 R. M. Wightman and D. O. Wipf, *Electroanalytical Chemistry*, ed. A. J. Bard, Marcel Dekker, New York, 1989, vol. 15.
31 C. P. Smith and H. S. White, *Anal. Chem.*, 1992, **64**, 2398.
32 R. S. K. A. Gamage, A. J. McQuillan and B. M. Peake, *J. Chem. Soc., Faraday Trans.*, 1991, **87**, 3653.
33 J. A. Dean, *Handbook of Organic Chemistry*, McGraw Hill, New York, 1987.
34 P. Delahay and I. Trachtenberg, *J. Am. Chem. Soc.*, 1957, **79**, 2355.

Paper 8/03965H